Mesozoic Tectonics of the Aegean

Konstantinos Kydonakis

N° d'ordre : ANNÉE 2014

UNIVERSITÉ DE RENNES 1

THÈSE / UNIVERSITÉ DE RENNES 1
sous le sceau de l'Université Européenne de Bretagne

pour le grade de

DOCTEUR DE L'UNIVERSITÉ DE RENNES 1

Sciences de la Terre

École doctorale Sciences de la Matière (SDLM)

présentée par

Konstantinos A. KYDONAKIS

préparée à l'unité de recherche Géosciences Rennes – UMR6118

Tectonique Mesozoïc de l'Egée

Thèse soutenue à Rennes
le 22 Octobre 2014

devant le jury composé de :

Rapporteur JEAN-PIERRE BURG
Professeur - ETH, Zurich / *Rapporteur*
Rapporteur TORGEIR ANDERSEN
Professeur - University of Oslo / *Rapporteur*
Examinateur CLAUDIO FACCENNA
Professeur - Roma Tre / *Examinateur*
Examinateur DIMITRIOS KOSTOPOULOS
Eldorado Gold / *Examinateur*
Directeur JEAN-PIERRE BRUN
Professeur - Géosciences Rennes / *Directeur de thèse*
Directeur FRÉDÉRIC GUEYDAN
Professeur - Géosciences Montpellier / *Co-directeur de thèse*

Tectonique Mesozoïc de l'Egée

Mesozoic Tectonics of the Aegean

Konstantinos A. Kydonakis

A thesis presented for the degree of
Doctor of Philosophy

Géoscienes Rennes
Université de Rennes1
France

October 2014

To my wife
To my parents who supported my steps

Mesozoic Tectonics of the Aegean

Insights from analogue modelling, petrology, geo- and thermo-chronology

Konstantinos A. Kydonakis

Abstract

The ***Aegean Sea*** started to form since middle Eocene back-arc extension affecting the previously formed ***Hellenic Thrust Wedge***. The latter was made by Mesozoic - Cenozoic accretion of i) three continental fragments, namely ***Rhodopia***, ***Pelagonia*** and ***External Hellenides***, arranged in a SW-verging stack from NNE to SSW in the order listed, and ii) the closure of two intervening oceanic domains now forming, from north to south, the ***Vardar-Axios*** and the ***Pindos Suture Zones***, respectively. The thickened crustal-scale wedge started to collapse, in a process driven by the Hellenic slab rollback, triggering the development of core complexes in the severely stretched Aegean crust. During the early stage of extension, deformation localised to the hinterland of the crustal-scale wedge in the area described as the ***Rhodope Metamorphic Province*** (or simply ***Rhodope***).

The Rhodope is an area of large-scale nappe tectonics and is considered unique for the geology of the Aegean as it recorded both the Mesozoic convergence-related deformation and the subsequent Cenozoic extension of the Aegean during which, part of the earlier fabrics were re-worked. During Cenozoic extension, the southwestermost part of the Rhodope, namely ***Chalkidiki block***, escaped much of the related deformation as it remained in the hanging-wall of the ***Kerdylion Detachment***, a large structure related to the Aegean extension. As a result, we selected the Chalkidiki block to study the Mesozoic tectonics of the Aegean.

This study is based around a multidisciplinary approach that aims to unravel different aspects of the tectonics of North Aegean. For that purpose we have selected to study the Chalkidiki block using a variety of geological methods. 1) We carried out several field mapping campaigns measuring the geometry of structural fabrics. An overview of the regional geometry is given in the compiled regional maps that illustrate the attitude of the measured planar and linear structural fabrics. 2) We evaluated the intensity of the metamorphic conditions using isochemical phase diagram sections calculated by minimisation of the Gibbs free energy. Based on our model results, we inferred the existence of an early eclogite-facies event before the regional amphibolite-facies overprint. 3) We performed high- (U/Pb in zircon and monazite) and medium-temperature ($^{40}Ar/^{39}Ar$ on micas) geochronology coupled with low-temperature thermochronology and inverse thermal history modelling using a Bayesian transdimensional inversion scheme. The modelling results delineated the complete thermal path (T-t) of the study area from Cretaceous heating to Eocene near surface exposure. 4) We modelled the Tertiary geological evolution of the North Aegean with reference to the exhumation of the lower crust during core complex formation. Using scaled laboratory experiments we tested whether the gravity spreading of a crustal-scale thrust wedge that undergoes extension is a suitable process for the development of the Rhodopean core complexes during the early opening of the Aegean. Our analysis suggests that strain localisation and core complex development near the backstop of the area affected by extension is intrinsic to the pre-collapse geometry of the orogenic wedge.

Acknowledgements

I wish to thank Jean-Pierre Brun, the supervisor of this thesis, for his patient guidance, enthusiastic encouragement, useful critiques of this research work and for all the discussions we had on the geology of the Aegean during the last years. He uniquely inspired me.

This study would have been impossible without Claudio Faccenna who is leading TOPO-MOD research project and financially supported the present study.

I would like to express my very great appreciation to Dimitrios Kostopoulos, my mentor in earth sciences, who introduced me, some years ago, to the world of petrology, mineral identification, mineral chemistry, optical microscopy, thermodynamics, igneous and metamorphic petrogenesis, isotopic dating, geochemistry... and a bit of structural geology during several field campaigns in the Hellenic mountains.

Dimitrios Sokoutis supported me during the fieldwork and the physical modelling experiments. We spent lot of time in the field inspecting deformed rocks and, more importantly, eating sardins, tomatoes, cheese and bread under the Hellenic sun. We also spent time in the cold lab of Rennes trying to warm our "kourdoumboulia" during the experimental procedure.

Frédéric Gueydan is thanked for the extensive discussions we had both in the field and the lab.

Maïwenn Cantin is honestly thanked for efficiently undetaking the logistics of the present thesis. Without her it would have been, perhaps, impossible to manage all the paperwork.

Evangelos Moulas is acknowledged for the long-lasting fruitfull discussions on the evolution of the Hellenides. He supported me throughout this dissertation and provided valuable assistance with his -famous- Matlab codes for the calculation of the strain rate of the analogue modelling experiments. His expertise in computer thermodynamic calculations is clearly illustrated on the results of Chapter 3.

Advice given by Marc Poujol has been a great help. He introduced me to the procedure of zircon and monazite dating: from sample collection to the interpretation of the results.

Kerry Gallagher is thanked for introducing me to the Irish Myth: Guiness beer. He patiently explained me (many times) the FT theory and how to use the QTQt.

Marc Jolivet is thanked for introducing me to the FT analysis and for preparing the FT samples used in Chapter 5.

Jean-Pierre Burg and Lucie Tajčmanová are both acknowledged for allowing access to the WDS instrument of ETH, Zurich.

Patrick Monié patiently introduced me to the noble gas measurements and is acknowledged for his support during the Ar/Ar dating which would have been impossible without the aid of Frédéric Lecoeur.

Elias Chatzitheodoridis is thanked for willingly giving me access to the EDS instrument of NTUA, Athens and for spending a lot of time to obtain the mineral chemistry prepented in Chapters 3 and 4.

Andrew Carter and Jocelyn Barbarand are both acknowledged for giving me access to their FT microscopes at Birkbeck University of London and Géosciences Orsay, Université Paris Sud, respectively.

I thank Michel Ballèvre for his warm welcome in Géosciences Rennes and for providing me with a dedicated optical microscope especially for the needs of this dissertation.

Ewald Hejl is thanked for kindly providing me (many times) with raw FT data from the Chalkidiki and Pangeon granitoids that I used for comparison with my FT results.

Benjamin Guillaume is acknowledged for introducing me to the PIVlab software.

Antoine Rozel is thanked for introducing me to LaTeX and saving me a great amount of time during the writing of this dissertation.

Nikolaos Kipouros is greatly acknowledged for preparing many high-quality thin sections for the purposes of this study.

Jessica Langlande (iFremer) and Francis Gouttefangeas (UR1) are both acknowledged for valuable help with the spectrometer of iFremer and UR1, respectively.

I wish to thank David Vilbert, Dominique Bavay, Yann Lepagnot and Xavier Le Coz for their valuable technical support on this project.

Marine Collignon and Marc Odin (TOPOMOD co-workers) and both thanks for helping me with the french translation.

Contents

Résumé

Une brève introduction

Les ***Hellénides***, qui font partie intégrale de la chaine Alpes-Himalaya, affleurent à l'est de la Méditerranée. Elles résultent de la convergence vers le nord et de l'accrétion, à la marge Sud-Européenne, de blocs continentaux appartenant au Gondwana. Dans cette région, les données de tomographie sismique mettent en évidence un seul panneau de lithosphère en subduction, ancré dans le manteau inférieur à 1600 km de profondeur. Les Hellénides résultent de l'empilement vers le Sud-Ouest, du Mesozoique au Cenozoique, de trois microplaques (***Rhodopia***, ***Pelagonia*** et les ***Hellénides Externes***), avec fermeture de deux domaines océaniques, formant maintenant du Nord au Sud, les zones de sutures du ***Vardar-Axios*** et du ***Pinde***.

Une phase d'extension arrière-arc contrôlée par le retrait vers le sud du panneau plongeant Hellénique a commencé à l'Eocène moyen, affectant la croûte précédemment épaissie. Le système ***Egéen*** représente la partie la plus étirée du domaine arrière arc et résulte du retrait de la fosse océanique, d'environ 600 à 700km vers le sud. Les Hellénides internes ont subit une extension de type "core complex" localisée dans ***la province métamorphique du Rhodope*** (ou ***Rhodope***). Puis l'extension a migré vers la partie centrale de l'Egée, dans la région des ***Cyclades***. Depuis le Miocène moyen, l'extension est passée à une extension de type rift large, donnant naissance à de nombreux bassins sédimentaires marins et continentaux.

Le Rhodope est un domaine précieux du système Egéen car la tectonique chevauchante Mesozoïque de grande échelle y est bien conservée malgré les effets ultérieurs de l'extension Egéenne. C'est donc une localité privilégiée pour l'étude de la convergence Jurassique-Crétacé des Hellénides. C'est aussi une région idéale pour étudier l'effondrement gravitaire de la croûte hellénique épaissie au début de l'extension égéenne. Cette superposition des déformations liées à la convergence (épaississement) et de celles liées à l'extension (amincissement) dans un seul système géologique donne au Rhodope une signature particulière dans l'évolution du système Egéen, très favorable pour l'étude des mécanismes de formation et d'effondrement d'une croûte orogénique épaissie.

Contexte Géologique

Le Rhodope, qui constitue la partie interne des Hellénides (nord-est de la Grèce – sud-ouest de la Bulgarie), est considérée comme une région de chevauchements de grande échelle qui enregistrent la déformation compressive d'âge Mésozoïque. Le Rhodope peut être vu comme un empilement, vers le sud-ouest pendant le Mésozoïque, d'unités métamorphiques (facies amphibolite) d'échelle crustale, ensuite fortement affectées par l'extension Cénozoïque de type core complexe ainsi que par du magmatisme syn- et post-orogénique. Le Rhodope est bordé au Nord par la faille décrochant dextre Maritza, à l'Est par le bassin de la Thrace, d'âge Eocène moyen à Quaternaire, à l'Ouest par les bassins Vardar-Axios et Thermaikos, qui sont corrélés avec la zone de suture du Vardar-Axios, et au Sud par la dépression nord

égéenne. On distingue trois domaines majeurs dans le Rhodope, qui sont du Nord-Est au Sud-Ouest: le ***Domaine Nord Rhodope***, le ***Core Complexe du Sud Rhodope*** et le ***Bloc de Chalcidique***.

Le ***Domaine Nord Rhodope*** est la partie la plus septentrionale du Rhodope. Il consiste en un système tectonique imbriqué, constitué principalement de roches métamorphiques de haut-grade, incluant un ancien arc magmatique du Jurassique moyen. Le Domaine Nord Rhodope est composée d'orthogneiss, d'éclogites, d'amphibolites, de paragneiss, d'horizons de marbres parsemés, et plus rarement de roches ultramafiques. Bien que les roches métamorphiques du facies amphibolites soient les plus largement représentées, de nombreuses occurences d'éclogites plus ou moins rétrogrades, témoignent d'une phase antérieure de métamorphisme de haute pression. Le pic de métamorphisme du Jurassique Supérieur, est suivi au Crétacé par un métamorphisme régional de facies amphibolites. La présence d'inclusions de micro-diamants est une preuve indiscutable de conditions d'ultra-haute pression, et suggère une pression locale minimale de 3.0GPa (pour 600^{o}C). Les conditions métamorphiques de la phase de haute pression, enregistrée par les roches mafiques, sont estimées à 1.9GPa et 700^{o}C et pour le métamorphisme régional du facies amphibolites à 1.7GPa et 720^{o}C. Au Nord-Est, les dépôts du Maastrichtien-Paléocène reposent en discordance sur les gneiss du socle, en partie synchrone avec le volcanisme et plutonisme d'âge Crétacé supérieur à Oligocène inférieur.

Le ***Core Complexe du Sud Rhodope*** est un large dôme métamorphique de forme plus ou moins triangulaire, situé immédiatement au Sud-Ouest du Domaine Nord Rhodope. Leur contact correspond à un chevauchement ductile mylonitique, vers le Sud-Ouest et connu sous le nom de "Chevauchement du Nestos". Le core complexe est constitué d'orthogneiss mylonitiques fortement déformés, d'âge Permo-Carbonifère, de micaschistes et d'amphiboles, couverts par une épaisse séquence de marbres. Les gneiss sont affectés par des conditions de métamorphisme du facies amphibolites. Le dôme métamorphique est caractérisé une foliation horizontale à l'échelle régionale. Des plutons, datés de l'Oligo-Miocène, présentant des caractéristiques syn-tectoniques, sont intrusifs dans les gneiss du socle. Des bassins sédimentaires, orientés Nord-Ouest Sud-Est, se développent après le Miocène moyen, bien que des reliques de calcaires nummulitiques de l'Eocène moyen, ont été trouvés localement.

Le ***Bloc de Chalcidique***, qui est la partie la plus méridionale du Rhodope, constitue le toit du ***Détachement du Kerdylion***, la structure qui est responsable de l'exhumation du Core Complex du Sud Rhodope, directement à l'est. Le Bloc de Chalcidique correspond au Massif Serbo-Macedonien, si on exclue sa partie la plus à l'est, l'Unité du Kerdylion qui fait partie intégrante du Core Complexe du Sud Rhodope. Le Bloc de Chalcidique est défini comme un empilement de trois unités: ***l'Unité de Vertiskos***, ***la Ceinture Circum-Rhodope*** et ***la Suite Magmatique de Chortiatis***. Ces unités sont séparées par des contacts tectoniques nets orientés nord-ouest.

L'Unité du Vertiskos, allongée dans une direction nord-ouest, a une histoire tectono-métamorphique complexe. Elle est formée de granitoides du Silurien-Ordovicien, des alternances de paragneiss, de fins horizons de marbre, d'intrusions de leucogranites/pegmatitiques, d'amphibolites déformées, de boudins éclogitiques et de serpentinites. Le métamorphisme régional de moyenne pression et du facies amphibolite est estimé à 0.45-0.75GPa et 510-580^{o}C pour les micaschistes à grenat et staurotide, ainsi que 0.85GPa et 600^{o}C pour les amphibolites à grenat. Le métamorphisme est daté du Jurassique-Crétacé, d'après la bibliographie. La continuité structurale et les fabriques orientées Nord-Ouest/Sud-Est de l'unité du Vertiskos sont interrompues par de petits bassins sédimentaires, post-Miocène moyen. L'unité de Vertiskos est intrudée par des plutons d'âge Eocène et Oligocène-Miocène.

La Ceinture Circum-Rhodope est une séquence méta-sédimentaire du Trias-Jurassique, avec localement des rhyolites et des quartzites à la base. La séquence est considérée comme la couverture sédimentaire Mésozoïque de l'unité du Vertiskos. Le contact entre l'unité de Vertiskos (socle) et la ceinture Circum-Rhodope (couverture sédimentaire) est un chevauchement

orienté nord-ouest, avec par endroits une composante décrochante. La Suite Magmatique de Chortiatis est constituée de roches ignées de type acide à intermédiaire, datées du Jurassique Supérieur. Les données disponibles dans la littérature pour la Ceinture Circum-Rhodope et la Suite Magmatique de Chortiatis suggèrent qu'elles ont subit un métamorphisme de haute pression pendant le Mésozoïque. Cependant, un métamorphisme de haute-pression n'a jamais été documenté pour l'unité de Vertiskos, impliquant la probabilité d'un hiatus métamorphique au niveau du Bloc de la Chalcidique.

Problematic

L'étude présentée dans ce mémoire se fonde sur une approche multidisciplinaire qui vise à éclaircir certains aspects de la tectonique Nord Egéenne. L'extension Egéenne a conduit à une segmentation des structures chevauchantes antérieures en raison de l'exhumation des dômes gneissiques extensifs du Rhodope. Ceux-ci forment: i) un alignement de dômes métamorphiques extensifs, au Nord-Est, appelé ici par simplicité le Core Complexe Nord Rhodope, et ii) le Core Complexe du Sud Rhodope, au Sud Ouest. Le développement du Core Complexe du Sud Rhodope a séparé le Rhodope en deux blocs principaux: la Domaine Nord Rhodope au nord-est, et le Bloc de Chalcidique au Sud-Ouest. La localisation de l'extension dans les Hellenides internes ainsi que la formation de deux zones voisines de dômes gneissiques extensifs, très proche l'un de l'autre, est intrigant et nous a conduit à tenter d'élucider les mécanismes qui ont gouverné les début de l'extension Egéenne.

Le Domaine Nord Rhodope a été plus largement étudié que la partie sud-ouest (Bloc de Chalcidique) et l'évolution P-T-t, bien que toujours débattue dans le détail, est globalement correctement définie. Par contre, le Bloc Chalcidique a fait l'objet de beaucoup moins d'attention et son évolution P-T-t est très mal connue. En Chalcidique, le métamorphisme est beaucoup plus faible, atteignant le facies amphibolite de moyenne pression, et parfois seulement des facies schistes bleus/schistes verts vers l'ouest. Une grande partie du travail présenté ici est dédiée à l'évolution tectono-métamorphique du bloc Chalcidique et à son évolution thermique depuis le début de l'accrétion jusqu'à son exhumation, en surface. Cette étude tentera de répondre à série de questions importantes telles que:

- Pourquoi l'extension s'est-elle localisée à l'arrière du domaine du Rhodope pendant les premiers stages de l'extension Egéenne?
- Pourquoi les core complexes se sont-ils développés dans deux zones distinctes du Rhodope?
- Pourquoi le Détachement Kerdylion qui contrôle l'exhumation du Core Complexe du Sud Rhodope a-t-il un pendage Sud vers l'avant-pays?
- Pourquoi le toit du Détachement Kerdylion s'est comporté comme un bloc cohérent indéformable pendant l'extension ductile du Rhodope?
- Quelles sont les conditions métamorphiques atteintes par les unités géologiques du Bloc de Chalcidique?
- Pourquoi l'enregistrement de conditions moyenne-pression/haute température (Barrovien) dans la plus grande partie du Bloc de Chalcidique ne contredit pas notre hypothèse de travail pour l'implication dans une subduction Mésozoïque?
- Y a-t-il un gradient métamorphique à l'échelle de l'ensemble du Rhodope?
- Quand les évènements métamorphiques enregistrés par le bloc Chalcidique ont-ils eu lieu et comment sont-ils corrélés à ceux du Domaine Nord Rhodope?
- Le Bloc Chalcidique et la région nord-Rhodope sont-ils une unique entité géologique Mésozoïque?
- Le Bloc de Chalcidique a-t-il conservé la mémoire d'évènements tectoniques et métamorphiques qui ont été largement effacés dans le Domaine Nord Rhodope?

Méthodes - Structure de la thèse

Cette étude est consacrée à la géologie de la péninsule Chalcidique (Grèce du Nord) avec un intérêt particulier pour l'Unité du Vertiskos (socle), la Ceinture Circum-Rhodope (couverture) et la Suite Magmatique de Chortiatis (arc). Nous avons : i) cartographié le champ de déformation, ii) évalué l'intensité des conditions métamorphiques et iii) pour dater l'évolution tectonique et métamorphique, utilisé la géochronologie haute température (U/Pb zircon et monazite) et moyenne température ($^{40}Ar/^{39}Ar$ sur micas) couplées à de la thermochronologie à basse température et à de la modélisation inverse de l'histoire thermique. D'un point de vue géodynamique, à l'aide d'expériences de laboratoire à échelle réduite, nous avons modélisé l'extension gravitaire d'un prisme chevauchant pour expliquer la déformation du prisme chevauchant hellénique pendant l'extension égéenne et en particulier la formation de core complexes à l'arrière du prisme.

Dans le ***Chapitre 2***, nous affinons l'âge des roches magmatiques de la région. L'âge du protolithe du socle est défini comme Silurien grâce à des datations Pb/Pb sur zircon. Avec une datation LA-ICP-MS sur zircons, nous montrons que l'âge du protolithe est en fait Ordovicien. Des pegmatites et des amphibolites sont largement intégrées dans les orthogneisses du socle, mais leur âge reste mal connu. Avec des datations sur zircons nous définissons l'âge des pegmatites et des amphibolites intercalées et nous présentons des données choisies sur les zircons détritiques de paragneiss intercalés dans les orthogneiss.

Dans le ***Chapitre 3***, nous étudions l'évolution P-T d'échantillons de méta-pélites sélectionnés parmi micaschistes à grenats et à staurotide, d'âge Mésozoïque et provenant de la partie orientale du socle. Les conditions du pic métamorphique et les chemins rétrogrades sont établis sur la base de micro-textures, des compositions chimiques des minéraux et la construction de diagrammes de phase isochimiques. Nous avons identifié un événement métamorphique Mésozoïque de haute pression (1.9GPa / 520^{o}C), largement effacé mais qui a précédé le ré-équilibrage régional vers des conditions de moyenne pression/haute température (1.2GPa / 620^{o}C).

Dans le ***Chapitre 4***, nous présentons une nouvelle étude de géochronologie de haute température (U/Pb sur monazite) et moyenne température ($^{40}Ar/^{39}Ar$ sur micas) à la fois du socle et de la couverture. Sur la base de datations sur monazite, nous définissons un événement à haute température au Crétacé inférieur (∼130 Ma) pour la partie orientale du socle. Les âges de refroidissement à travers le Bloc de Chalcidique sont compris entre 100 et 125 Ma. Les variations régionales et les tendances géographiques dans le régime (P)-T-t sont mises en évidence et discutées par rapport aux autres domaines de Rhodope.

Dans le ***Chapitre 5***, nous étudions l'évolution thermique post-pic de métamorphisme de la partie orientale du socle en utilisant la thermochronologie à basse température (traces de fission sur apatite). Avec une modélisation inverse bayésienne, nous établissons au Crétacé supérieur, le moment où l'exhumation des gneiss a quasiment atteint la surface. Enfin, nous discutons les variations latérales au sein du Bloc de Chalcidique ainsi que les différences avec les autres domaines de Rhodope.

Dans le ***Chapitre 6***, nous présentons de nouvelles données de géologie structurale acquises au cours de plusieurs campagnes de terrain et l'analyse géométrique et cinématique des structures observées. La structure géologique finale du Bloc de Chalcidique est discutée au travers de coupes d'échelle crustale, de cartes structurales et de cartes cinématiques régionales. Nous proposons une interprétation cinématique de l'évolution géologique du Bloc de Chalcidique en relation avec les données P-T-t présentées précédemment.

Dans le ***Chapitre 7***, nous étudions l'effondrement gravitaire d'un prisme orogénique et la formation de core complexes, à l'aide d'expériences de modélisation analogique. Les modèles fragiles-ductiles (sable-silicone) sont construits avec une géométrie initiale en prisme, représentant la géométrie globale probable du prisme chevauchant hellénique à l'Eocène. Les expériences consistent à les soumettre les modèles à un effondrement gravitaire à vitesse

contrôlée par des moteurs pas-à-pas et à observer la déformation obtenue pour différente structures fragiles-ductiles initiales et vitesses d'extension. On montre que l'extension est toujours localisée à l'arrière du prisme et que le développement des core complexes est favorisé par les résistances fragiles les plus fortes et les vitesses d'étirement les plus lentes. Ces résultats éclairent la dynamique de l'extension du Nord de l'Egée d'un jour nouveau et sont discutés en détail par référence aux données géologiques et géophysiques disponibles.

Le ***Chapitre 8*** résume les principaux résultats acquis dans ce travail.

Extended abstract

A short introduction

The ***Hellenides*** constitute an integral part of the Alpine-Himalayan mountain chain and are exposed at the eastern Mediterranean Sea. They are the product of convergence between the stable South European margin and northward-driven Gondwana-derived continental fragments. Seismic tomography illustrates beneath the Hellenides and down to 1600 Km depth a single northward-dipping slab, anchored into the lower mantle. The Hellenides resulted from Mesozoic - Cenozoic southwestward piling-up of three continental fragments, namely ***Rhodopia***, ***Pelagonia*** and ***External Hellenides***, arranged in a SW-verging stack from NNE to SSW in the order listed, and the closure of two intervening oceanic domains now forming, from north to south, the ***Vardar-Axios*** and the ***Pindos*** Suture Zones, respectively.

The previously built thickened crust started to collapse in middle Eocene in a process driven by trench retreat. The ***Aegean*** represents the more strongly stretched part of the back-arc domain and is the result of accumulated trench retreat of around 600 - 700Km. During the early Aegean opening, slab rollback triggered large-scale extension of core complex type to the hinterland of the Hellenides, in an area described as the ***Rhodope Metamorphic Province*** (or simply ***Rhodope***), synchronous with thrusting close to the retreating subduction trench. With ongoing trench retreat the extension progressively migrated southward in the central part of the Aegean, in the ***Cyclades***. Since middle Miocene, extension shifted toward the wide rife mode causing widespread development of continental and marine sedimentary basins.

The Rhodope is a unique domain of the Aegean. It is an area of large-scale nappe tectonics and the type-locality for the study of the Jurassic - Cretaceous convergence history of the Hellenides. It is also an ideal place to study the gravitational collapse of the thickened Hellenic crust during the early opening of the Aegean. The superposition of convergence- and strong extension-related tectonics in a single geological entity makes the Rhodope a key part for the evolution of the Aegean where one can study the mechanics of both building and collapse of a thickened orogenic crust. For the reasons described, the Rhodope is the centrepiece of this study.

Geological setting

The Rhodope Metamorphic Province (RMP), or simply Rhodope for short, constitutes the hinterland of the Hellenides (northeast Greece - southwest Bulgaria) and is considered an area of large-scale nappe tectonics that keep a record of the Mesozoic convergence-related deformation of the Aegean. The Rhodope can be viewed as a Mesozoic southwestward piling-up, crustal-scale, syn-metamorphic, amphibolite-facies duplex strongly affected by Cenozoic extension of core complex type and syn- to post-tectonic magmatism. It is bordered to the north by the Maritza dextral strike-slip fault, to the east by the Middle Eocene to Quaternary Thrace Basin, to the west by the Vardar-Axios - Thermaikos basins which in turn roughly

correlate with the Vardar Suture Zone and to the south by the North Aegean Trough. We recognise three major domains in the Rhodope that are, from northeast to southwest: (i) the Northern Rhodope Domain, (ii) the Southern Rhodope Core Complex, and (iii) the Chalkidiki block.

The ***Northern Rhodope Domain*** (NRD) is the northeastern extreme part of the Rhodope and represents an imbricate system made mainly of high-grade metamorphics including a former magmatic arc of Upper Jurassic age. The NRD is composed of orthogneisses, eclogites and amphibolites, paragneisses, scarce marble horizons and relatively rare ultramafic rocks. Although upper amphibolite-facies metamorphic rocks are widespread, many occurrences of variably retrogressed eclogites that preserve evidence for a precursor high-pressure stage have been reported in the literature. Peak (pre-)Upper Jurassic metamorphism was followed by Cretaceous upper amphibolite-facies regional overprint. Evidence for ultrahigh-pressure metamorphic conditions is due to the presence of micro-diamond inclusions in metapelites that indicate minimum local pressure of 3.0GPa (for 600^{o}C). Metamorphic conditions for the high-pressure event recorded in mafic rocks are estimated at 1.9GPa / 700^{o}C and for the regional amphibolite-facies overprint at 0.7GPa / 720^{o}C. To the northeast, Maastrichtian - Paleocene deposits rest unconformably on basement gneisses and are related to plutonic rocks and volcanics of uppermost Cretaceous to lowermost Oligocene age.

The ***Southern Rhodope Core Complex*** (SRCC) is a wide metamorphic dome of roughly triangular shape which lies immediately southwest of the NRD. Their contact is located along a mylonite-bearing SW-verging thrust fault known as the Nestos Thrust. The SRCC consists of highly deformed Permian-Carboniferous mylonitic orthogneisses, micaschists, amphibolites and a thick marble sequence. The gneisses experienced upper greenschist/lower amphibolite-facies conditions and the exhumed dome shows a flat-lying foliation over its width. Oligo-Miocene plutonic bodies that show syn-tectonic features intrude the basement rocks. Widespread NW-SE-trending basins were developed after middle Miocene although remnants of mid-Eocene nummulite-bearing transgressive limestones have been locally reported.

The southwestern part of the Rhodope is the ***Chalkidiki block*** which defines the hanging-wall of the ***Kerdylion Detachment***, the structure that is largely responsible for the exhumation of the SRCC immediately to the east. The Chalkidiki block coincides with the so-called Serbo-Macedonian Massif if one excludes the easternmost part of the latter, the Kerdylion Unit. It has been shown that the ***Kerdylion Unit*** shares a common tectono-metamorphic history with the SRCC. The Chalkidiki block is defined as a stack of three units that separate each other by sharp NW-trending contacts that are, from east to west, the ***Vertiskos Unit***, the ***Circum-Rhodope belt*** and the ***Chortiatis Magmatic Suite***.

The Vertiskos Unit is an elongated NW-trending basement belt with a complex tectono-metamorphic history. It is made of Silurian - Ordovician granitoids later transformed into orthogneisses, intercalated paragneisses and thin marble horizons, leucocratic granitic / pegmatitic intrusions, deformed amphibolites, scarce eclogite boudins and serpentinites. Regional medium-pressure amphibolite-facies conditions are estimated at 0.45-0.75GPa / 510-580^{o}C for intercalated garnet-staurolite-mica schists and at 0.85GPa / 600^{o}C for garnet-bearing amphibolites. A wealth of Jurassic - Cretaceous metamorphic ages have been reported in the literature. The structural continuity and the NW-SE-trending fabrics of the Vertiskos Unit are disrupted by small sedimentary basins developed only after middle Miocene. Large Eocene batholiths and limited Oligo-Miocene plutonic rocks, often accompanied by small coeval volcanic extrusions intrude the Vertiskos Unit.

The Circum-Rhodope belt is a Triassic - Jurassic meta-sedimentary sequence locally involving rhyolites and quartzites at the base. The sequence is considered as the Mesozoic stratigraphic covers of the Vertiskos Unit. The rhyolites from the base of the Circum-Rhodope belt yielded Lower Cretaceous metamorphic ages. The contact between the Ver-

tiskos Unit (basement) and the Circum-Rhodope belt (sedimentary cover) is a sharp NW-trending thrust fault locally showing evidence for re-working. Immediately to the west, the Chortiatis Magmatic Suite is made of intensively deformed acidic and intermediate igneous rocks of Upper Jurassic protolith age. Data from the literature suggest a largely erased Mesozoic high-pressure metamorphic event from both the Circum-Rhodope belt and the Chortiatis Magmatic Suite. However, a similar Mesozoic high-pressure event has never been documented for the Vertiskos Unit implying a potential metamorphic gap in the Chalkidiki block.

Problematic

This study is based around a multidisciplinary approach that aims to unravel different aspects of the tectonics of the North Aegean.

The early Aegean extension resulted in the dispersal of the inherited convergence-related structures and in exhumation of two distinct gneiss domes zones in the Rhodope. These are: i) a set of aligned extensional metamorphic domes to the northeast that are collectively called here for convenience as the Northern Rhodope Core Complex (NRCC) and ii) the Southern Rhodope Core Complex to the southwest. The development of the SRCC separated the RMP into two main blocks: the NRD, to the northeast, and Chalkidiki Block, to the southwest. Both i) strain localisation to the hinterland of the Hellenides at the onset of extension and ii) the formation of two distinct gneiss domes zones so close to each other are clearly intriguing and influenced us to launch the present study to investigate the mechanics of the early evolution of the Aegean.

The northeastern extreme part of the Rhodope (the NRD) is more extensively studied compared to its southwestern part (the Chalkidiki block) and the P-T-t evolution, although still debatable in the details, is generally adequately defined. However, the Chalkidiki block has attracted much less attention and thus, our knowledge on the P-T-t evolution is limited. There, the recorded peak metamorphic conditions are significantly lower reaching medium-pressure amphibolite-facies, and even reduce to blueschists/greenschists-facies further to the west. A major part of this study is dedicated to the investigation of the tectono-metamorphic evolution of the Chalkidiki block and its thermal evolution from early accretion to near surface exposure.

During the course of this study, a series of major questions that will be answered include:

- Why the extension localised at the back of the extending domain (i.e., in the Rhodope) during the early stages of the Aegean opening?
- Why core complexes developed sequentially in two distinct zones in the Rhodope?
- Why the Kerdylion Detachment that controls the exhumation of the southern core complex dips toward the foreland?
- Why the hanging-wall of the Kerdylion Detachment (Chalkidiki block) behaved as a coherent non-deforming block during the ductile extension in the Rhodope?
- What are the metamorphic conditions attained by the Chalkidiki block?
- Why the Barrovian medium-pressure/high-temperature imprint recorded in the largest part of the Chalkidiki block does not contradict our working hypothesis for involvement in a Mesozoic subduction?
- Is there any metamorphic gradient across the Rhodope?
- What is the timing of the metamorphic events recorded in the Chalkidiki block and how do they correlate to the northeastern part of the Rhodope?
- Is the Chalkidiki block and the NRD a single Mesozoic geological entity?
- What information can be extracted from the Chalkidiki block that is largely erased from the other Rhodopean domains?

Methods - Thesis structure

This study is dedicated to the geology of the Chalkidiki Peninsula (Northern Greece) with particular interest for the Vertiskos Unit (basement), the Circum-Rhodope belt (cover) and the Chortiatis Magmatic Suite (arc). Toward that direction, we carried out field mapping measuring the geometry of the deformation fabrics. We evaluated the intensity of the metamorphic conditions and we performed high- (U/Pb in zircon and monazite) and medium-temperature ($^{40}Ar/^{39}Ar$ on micas) geochronology coupled with low-temperature thermochronology and inverse thermal history modelling. At the scale of North Aegean, using scaled laboratory experiments we modelled the extension of a thickened orogenic thrust wedge adopting the geological structure of the North Aegean as the initial geometry of the system.

In ***Chapter 2*** we define the age of magmatic rocks of the area. The protolith age of the basement is defined as Silurian based on Pb/Pb zircon dating. Using LA-ICP-MS zircon dating we show that the protolith age is actually Ordovician. Widespread pegmatites and amphibolites are embedded in basement orthogneisses but their age is rather unknown. With zircon dating we define the age of the intercalated pegmatites and amphibolites and we present additional detrital zircon data from selected intercalated paragneisses.

In ***Chapter 3*** we study the P-T evolution of selected pelitic samples from arguably Mesozoic intercalated garnet-staurolite-mica-schists from the eastern part of the basement. Peak metamorphic conditions and retrogression paths are established on the basis of microtextures, mineral chemistry and isochemical phase diagram sections. We identified a largely erased Mesozoic metamorphic high-pressure event at event (1.9GPa / 520^oC) that preceded the regional re-equilibration at medium-pressure/high-temperature conditions (1.2GPa 620^oC).

In ***Chapter 4*** we present new high- (U/Pb on monazites) and medium-temperature geo-chronology ($^{40}Ar/^{39}Ar$ on micas) from both the basement and the cover. Based on monazite dating, we define a high-temperature event at Lower Cretaceous ($\sim$130Ma) for the eastern part of the basement. Cooling ages across the Chalkidiki block are constrained between 100 and 125Ma. Regional variations and geographical trends in the (P-)T-t regime are highlighted and discussed with reference to the rest of the Rhodopean domains.

In ***Chapter 5*** we study the post-peak thermal evolution of the eastern part of the basement using low-temperature thermo-chronology (apatite Fission-Track analysis). Using a Bayesian inverse modelling scheme, we define the timing of the exhumation and near-surface exposure of the gneisses as uppermost Cretaceous. Lateral variations within the limits of the Chalkidiki as well as differences with the other domains of the Rhodope are discussed.

In ***Chapter 6*** we present new field data and the geometry of structural fabrics collected during several field campaigns. The finite geological structure of the Chalkidiki block is discussed based on cross-sections and on compiled regional structural/kinematic maps. A kinematic interpretation is given for the geological evolution of the Chalkidiki block within the scheme set by the previously presented P-T-t data.

In ***Chapter 7*** we study the gravitational collapse and core complex formation of an orogenic wedge subject to extension using analogue modelling experiments. We adopt the Mesozoic structure of the Hellenides, we apply boundary conditions based on geological constraints and we study the early opening of the Aegean with respect to the exhumation of the Rhodopean gneiss domes. We explain important aspects of the mechanics of the early Aegean extension such as strain localisation and geographical spread of the exhumed domes. The influence of the initial geometry of the system and the effect of various tested displacement velocities on the finite deformation pattern of the North Aegean are discussed.

Chapter 8 shortly summarises our new findings so that the reader can readily access our results.

Chapter 1

Introduction

1.1 A short introduction

The **Hellenides** constitute an integral part of the Alpine-Himalayan mountain chain and are exposed at the eastern Mediterranean Sea (Figure 1.1). They are the product of convergence between the stable South European margin and northward-driven Gondwana-derived continental fragments (e.g., Dercourt et al., 1993; Stampfli & Borel, 2002). They resulted from Mesozoic - Cenozoic southwestward piling-up of three continental fragments, namely the **Rhodopia**, the **Pelagonia** and the **External Hellenides** arranged in a SW-verging stack from NNE to SSW in the order listed and the closure of two intervening oceanic domains now forming, from north to south, the Vardar-Axios (VSZ) and the Pindos Suture Zones (PSZ), respectively (Robertson, 2002; van Hinsbergen et al., 2005a; Papanikolaou, 2009, 2013) (Figure 1.2). Seismic tomography illustrates beneath the Hellenides and down to 1600 Km depth a northward-dipping slab, anchored into the lower mantle (Bijwaard et al., 1998). Various aspects of the Alpine geodynamic evolution of the Hellenides has been discussed at length by van Hinsbergen et al. (2005a,b), Jolivet & Brun (2010), Ring et al. (2010), Royden & Papanikolaou (2011) and Papanikolaou (2013). In short, the centrepiece of the above studies is a Mesozoic crustal thickening phase followed by continuous southward retreat of the subducting Hellenic slab since the Eocene that brought about a concomitant southward migration of magmatism in the severely extending lithosphere, a slow-down in the rate of plate convergence coeval with acceleration of the trench retreat as well as a southward shift in the ages of progressively younger subduction-related metamorphism.

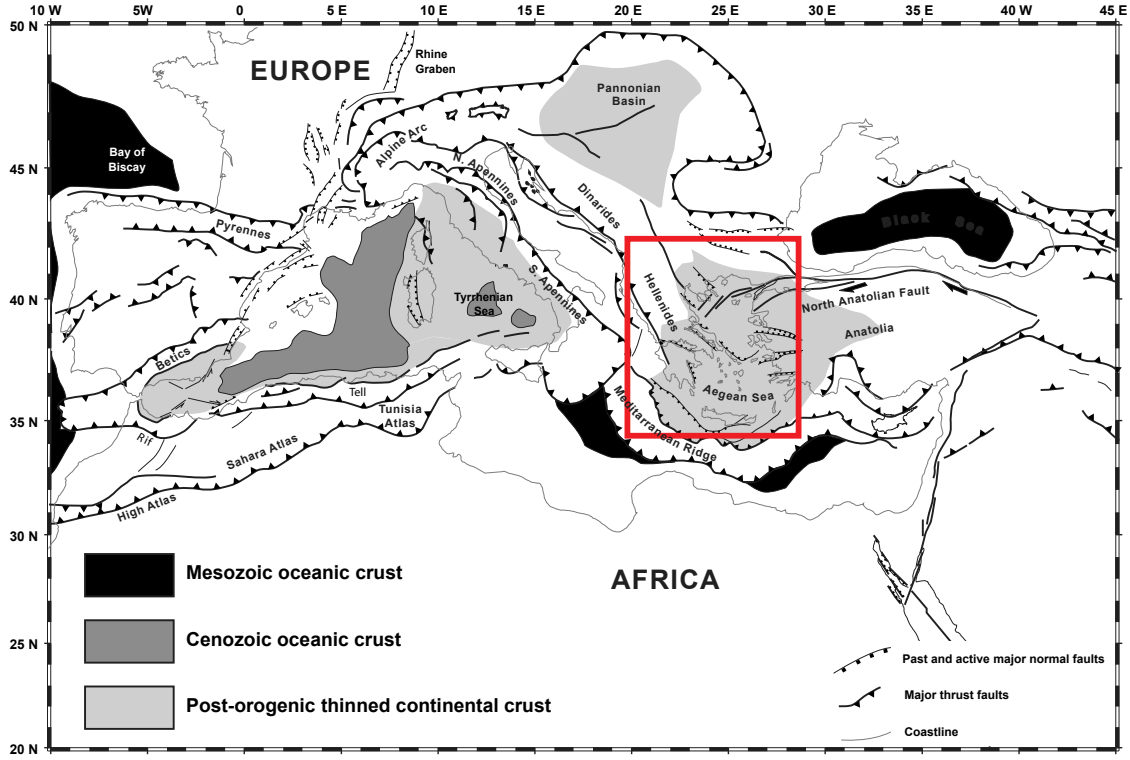

Figure 1.1: Tectonic map of the Mediterranean Sea and location of the Hellenides (red box; see also Fig. 1.2). Major tectonic features and extensional basins are illustrated. Redrawn after Jolivet & Brun (2010).

The **Aegean** represents the more strongly stretched part of the back-arc domain. It started forming during middle Eocene back-arc extension affecting the previously built thickened crust. The thickened crust collapsed, in a process driven by the Hellenic slab rollback, triggering large-scale extension of core complex type synchronous with ongoing thrusting close to the retreating subduction trench. During the early stage of extension, deformation

localised to the hinterland of the thickened crust in an area described as the **Rhodope Metamorphic Province** (or simply **Rhodope**) and progressively migrated southward in the central part of the Aegean, in the **Cyclades**. Since middle Miocene, extension shifted toward the wide rife mode and resulted in widespread development of continental and marine sedimentary basins (see recent reviews of Jolivet & Faccenna, 2000; Burchfiel et al., 2008; Brun & Sokoutis, 2010; Jolivet & Brun, 2010; Ring et al., 2010; Royden & Papanikolaou, 2011; Jolivet et al., 2013).

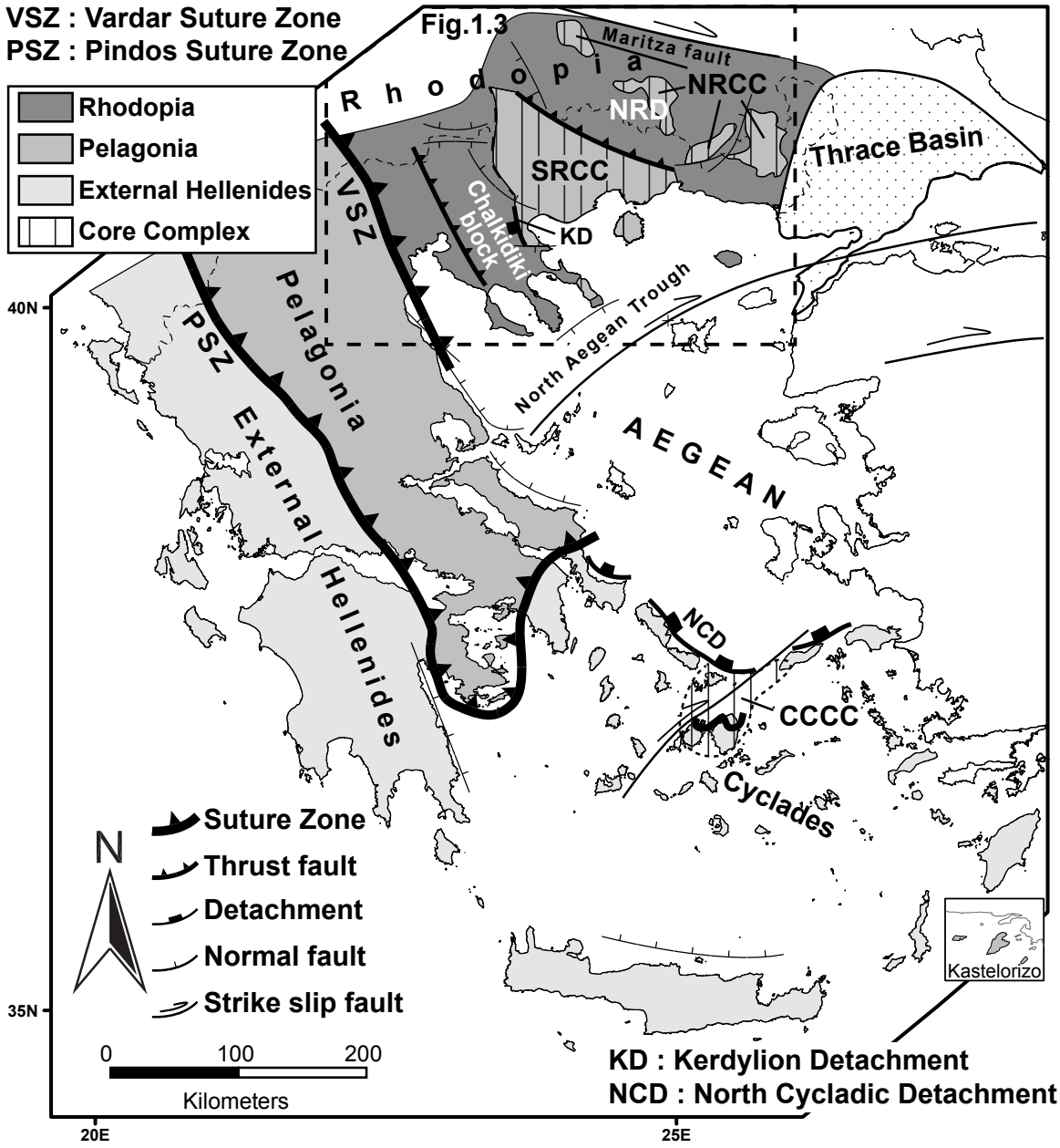

Figure 1.2: Simplified schematic map of the Hellenides where three accreted continental blocks (External Hellenides, Pelagonia and Rhodopia) are separated by two suture zones (Pindos and Vardar Suture Zones). Broadly speaking we study the geological evolution of the North Aegean (see also Fig. 1.3), the hinterland of the Hellenides, and in particular the Chalkidiki block (see also Fig.1.5). NRD: Northern Rhodope Domain, NRCC: Northern Rhodope Core Complex, SRCC: Southern Rhodope Core Complex, CCCC: Central Cyclades Core Complex.

During extension, the western part of the extending domain, from Rhodope to Peloponnese, has undergone up to 50^o-60^o clockwise rotation around an axis located in the vicinity

of the Scutary-Pec in Albania (Kissel and Laj, 1988; van Hinsbergen et al., 2005b). In this kinematic setting the amount of extension increased i) as a function of the distance from the rotation axis and ii) from north to south (Brun & Sokoutis, 2010). The Aegean Sea that represents the more strongly stretched part of the back-arc domain is the result of a southward trench retreat of around 600-700Km (Jolivet & Brun, 2010). In the Aegean, the Moho is rather flat over a distance of around 1000Km in north-south direction, and the crustal thickness has a mean value of 25±2Km except in two structures, namely the North Aegean Through and the Cretan Sea, where the crust is locally thinner than 22Km (Tirel et al., 2004b).

The Rhodope is a unique domain of the Aegean. It is an area of large-scale nappe tectonics and the type-locality for the study of the Jurassic - Cretaceous convergence history of the Hellenides. It is also an ideal place to study the gravitational collapse of the thickened Hellenic crust during the early opening of the Aegean. The superposition of convergence- and strong extension-related tectonics in a single geological entity makes the Rhodope a key part for the evolution of the Aegean where one can study the mechanics of both building and collapse of a thickened orogenic crust. For the reasons described, the Rhodope is the centrepiece of this study. In this introductory chapter, we will briefly describe the geological setting giving the necessary background information; more specific geological data can be found at the corresponding chapters. We will introduce the reader to the problematic, set the working plan and explain the reasons for choosing the westernmost part of the Rhodope (**Chalkidiki block**) as the study area. Toward the end of this chapter we will shortly describe our methodology and the corresponding thesis structure.

1.2 Geological setting

The **Rhodope Metamorphic Province** (RMP), or simply Rhodope for short, constitutes the hinterland of the Hellenides (northeast Greece - southwest Bulgaria) and is considered an area of large-scale nappe tectonics that keep a record of the Mesozoic convergence-related deformation of the Aegean (Burg et al., 1990, 1996; Ricou et al., 1998; Bonev et al., 2006; Krenn et al., 2010; Jahn-Awe et al., 2010, 2012; Nagel et al., 2011; Burg, 2012) (Figure 1.3). The RMP can be viewed as a Mesozoic southwestward piling-up, crustal-scale, syn-metamorphic, amphibolite-facies duplex (Burg et al., 1996; Ricou et al., 1998) strongly affected by Cenozoic extension of core complex type (Sokoutis et al., 1993; Dinter & Royden, 1993; Brun & Sokoutis, 2007) and syn- to post-tectonic magmatism (e.g., Kolocotroni & Dixon, 1991; Jones et al., 1992; Marchev et al., 2004, 2013). It is bordered to the north by the Maritza dextral strike-slip fault, to the east by the Middle Eocene to Quaternary Thrace Basin and to the south by the Vardar-Axios - Thermaikos basins which in turn roughly correlate with the Vardar Suture Zone (VSZ) (Ricou et al., 1998). The continuity of the RMP to the south is hidden beneath the North Aegean Basin deposits (Papanikolaou et al., 2006). With reference to (Figure 1.3), we recognise three major domains, from northeast to southwest: (i) the Northern Rhodope Domain, (ii) the Southern Rhodope Core Complex, and (iii) the Chalkidiki block. A geological map of the area is shown in Figure 1.4.

The **Northern Rhodope Domain** (NRD; Figure 1.3) is characterised by a lithological variability reflecting the diversity of its constituting crustal fragments. It represents an imbricate system made mainly of high-grade metamorphics including a former magmatic arc of Upper Jurassic age (Turpaud & Reischmann, 2010). Several units can be identified in the greek and bulgarian literature, all sharing a common Mesozoic - Cenozoic tectono-metamorphic history (see Burg, 2012, and references therein). The NRD is mainly made of orthogneisses, eclogites and amphibolites, paragneisses and scarce marble horizons (Mposkos & Liati, 1993; Liati & Seidel, 1996; Turpaud & Reischmann, 2010; Janák et al., 2011; Moulas et al., 2013). Volumetrically-low ultramafic rocks also occur usually at high structural levels.

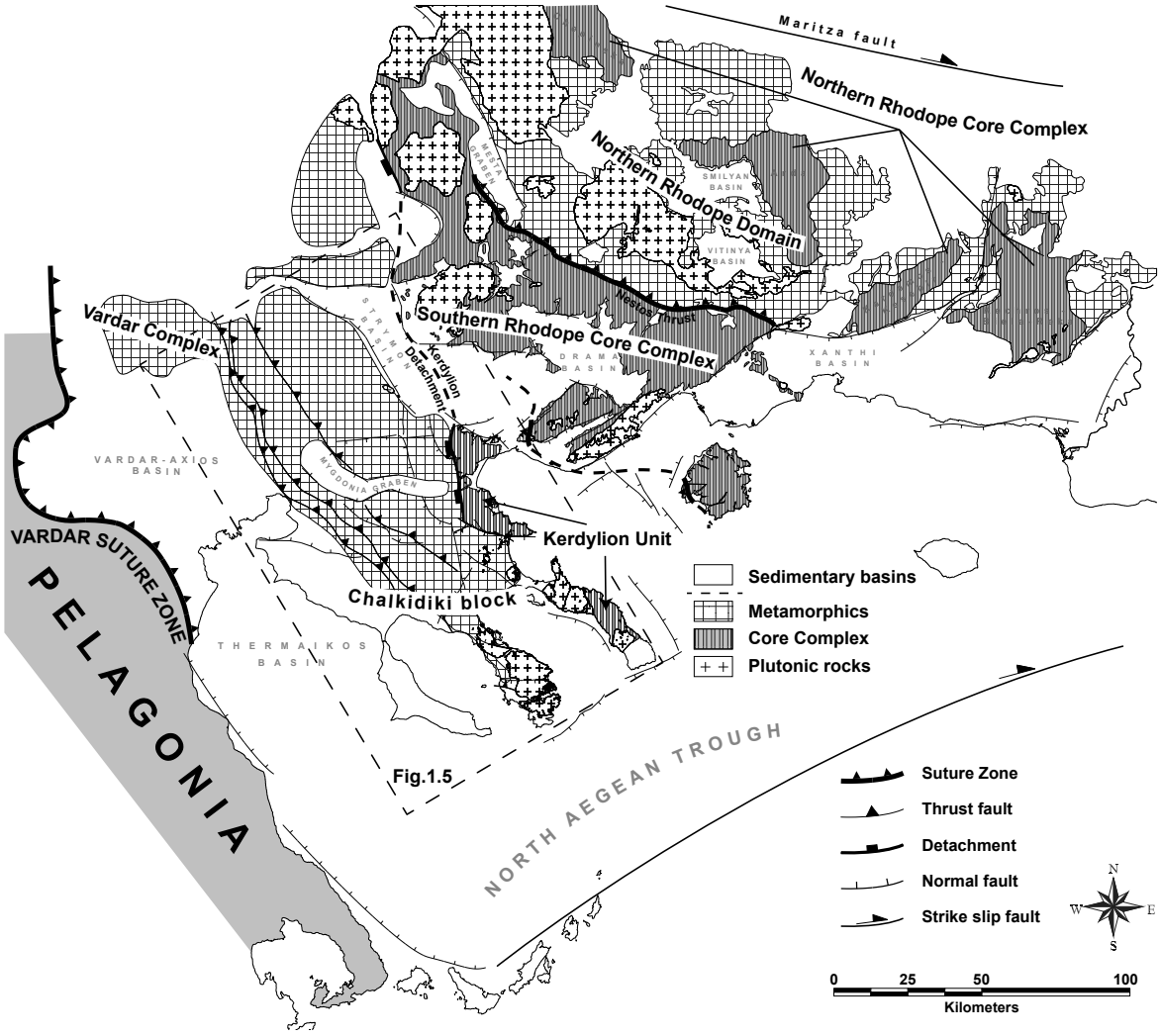

Figure 1.3: Simplified tectonic map of the North Aegean. The different domains of the Rhodope Metamorphic Province (or Rhodope) cover a large part of the North Aegean. The Rhodope is divided into three tectonic domains that are, from northeast to southwest, the Northern Rhodope Domain, the Southern Rhodope Core Complex and the Chalkidiki block. A detailed geological map of the area is shown in Fig. 1.4. See text for details.

Although upper amphibolite-facies metamorphic rocks are widespread, many occurrences of variably retrogressed eclogites that preserve evidence for a precursor HP phase have been reported in the literature. Peak (pre-)Upper Jurassic metamorphism (Reischmann & Kostopoulos, 2002; Hoinkes et al., 2008; Nagel et al., 2011; Liati et al., 2011, and references therein) was followed by Cretaceous upper amphibolite-facies regional overprint (Reischmann & Kostopoulos, 2002; Bauer et al., 2007; Bosse et al., 2010; Krenn et al., 2010; Liati et al., 2011; Moulas et al., 2013). Indisputable evidence for UHP conditions is due to the presence of micro-diamond inclusions in metapelites (Mposkos & Kostopoulos, 2001; Perraki et al., 2006; Schmidt et al., 2010) that sets the RMP as one of the youngest diamondiferous UHP belt and indicate minimum local pressure at 3.0GPa (for 600^{o}C). Metamorphic conditions for the HP event recorded in mafic rocks are estimated at 1.9GPa / 700^{o}C (Liati & Seidel, 1996) and for the regional amphibolite-facies overprint at 0.7GPa / 720^{o}C (Moulas et al., 2013). Metapelite assemblages record higher pressures for the high-temperature overprint at 1.2-1.3GPa / 700-730^{o}C (Krenn et al., 2010).

To the northeast, Maastrichtian - Paleocene deposits rest unconformably on basement gneisses (Boyanov et al., 1982; Goranov & Atanasov, 1992) and are related to plutonic rocks and volcanics of uppermost Cretaceous to lowermost Oligocene age (e.g., Peytcheva

et al., 1998; Soldatos et al., 2001, 2008; Ovtcharova et al., 2003; Marchev et al., 2006, 2010; Jahn-Awe et al., 2010; Filipov & Marchev, 2011) (Figure 1.4). Large-scale extension of core complex type affected the RMP during middle Eocene and resulted in the formation of two distinct core complexes: i) the Northern Rhodope Core Complex (NRCC Bonev et al., 2006, 2013b; Jahn-Awe et al., 2012; Kaiser-Rohrmeier et al., 2013) that developed within the NRD and iii) the larger Southern Rhodope Core Complex (SRCC) that separated the NRD from the Chalkidiki block (Sokoutis et al., 1993; Dinter & Royden, 1993; Brun & Sokoutis, 2007) (see below) (Figure 1.3).

The **Southern Rhodope Core Complex** (SRCC; sensu Brun & Sokoutis, 2007) is a wide metamorphic dome of roughly triangular shape which lies immediately southwest of the NRD (Figure 1.3). Their contact is located along a mylonite-bearing SW-verging thrust fault known as the Nestos Thrust. The development of the SRCC since middle Eocene separated the NRD, to the northeast, from the Chalkidiki block, to the southwest in a kinematic regime described by Brun & Sokoutis (2007). The SRCC consists of highly deformed Permian-Carboniferous mylonitic orthogneisses, intercalated mica-schists and amphibolites capped by a thick marble sequence. The exhumed dome shows a flat-lying foliation over its width (Brun & Sokoutis, 2007). The gneisses experienced upper greenschist/lower amphibolite-facies conditions with the available metamorphic ages being exclusively post-lower Eocene in age (post-51 Ma; Wawrzenitz & Krohe, 1998; Lips et al., 2000). Oligo-Miocene plutonic bodies that show syn-tectonic features intrude the basement rocks (Kolocotroni & Dixon, 1991; Kaufman, 1995; Dinter et al., 1995; Eleftheriadis et al., 2001). Widespread NW-SE-trending basins were developed after middle Miocene (e.g., Strymon and Drama basins; Figure 1.4) (Snel et al., 2006; Burchfiel et al., 2008) although remnants of mid-Eocene nummulite-bearing transgressive limestones have been locally reported (e.g., Xanthi basin).

The southwestern part of the RMP is the so-called Serbo-Macedonian Massif of Kockel et al. (1971). The term "Massif" has been rejected by many, if not all, workers afterward and the term Serbo-Macedonian Domain should be used instead. Much of our knowledge for the different units of that area is due to the mapping of 1:100.000 scale (Kockel & Mollat, 1977) and the accompanying memoir (Kockel et al., 1977) (Figure 1.5). The Serbo-Macedonian Domain is composed, from west to east, of four units namely the Chortiatis Magmatic Suite, the Circum-Rhodope belt, the Vertiskos Unit and the Kerdylion Unit (Kockel & Mollat, 1977; Kockel et al., 1977). The latter unit shares a common tectono-thermal history with the SRCC described before (Brun & Sokoutis, 2007; Himmerkus et al., 2012). The remaining three units define collectively the **Chalkidiki block** and are part of the hanging-wall of the Kerdylion Detachment that is responsible for the exhumation of the SRCC immediately to the east (Figure 1.3). For the purpose of this study we concentrate on the thrust system of the Chalkidiki block. We will proceed with describing the metamorphic units constituting it from east to west (the Vertiskos Unit, the Circum-Rhodope belt and the Chortiatis Magmatic Suite).

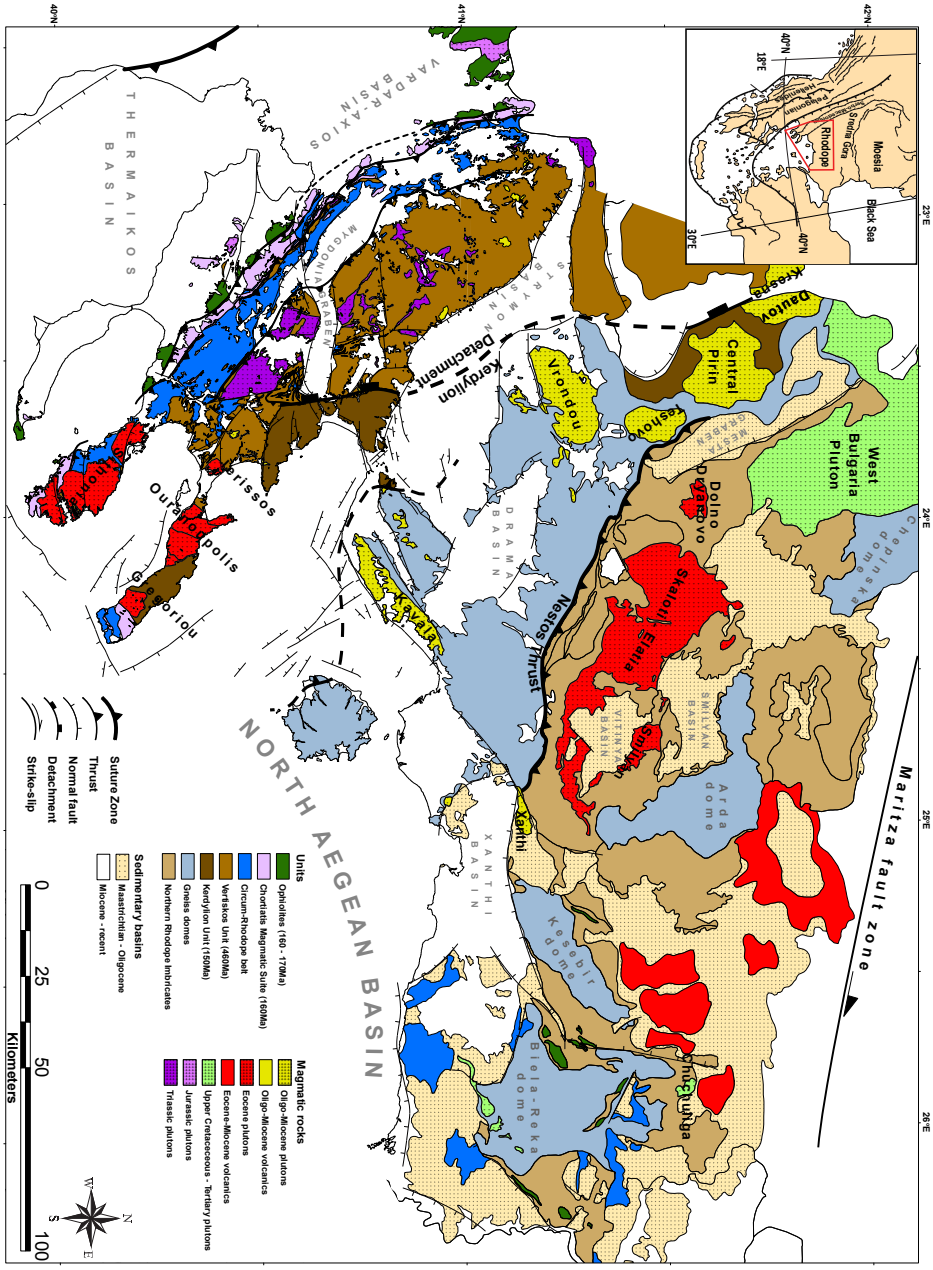

Figure 1.4: Detailed geological map of the Rhodope.

The **Vertiskos Unit** is an elongated NW-trending basement belt with a pretty much constant width of ca. 30 Km and a complex tectono-metamorphic history (Figure 1.5). In Bulgaria, to the north, it is known as the Ograzden Unit (Zagorchev, 1976). It is a distinct basement fragment that detached from Gondwana and incorporated into the Southern European Arcs by the end of the Palaeozoic (Himmerkus et al., 2007; Kydonakis et al., 2014b). In Greece, typical rocktypes are Silurian - Ordovician granitoids later transformed into orthogneisses (Himmerkus et al., 2009a), intercalated paragneisses and thin marble horizons, leucocratic granitic/pegmatitic intrusions, deformed amphibolites, scarce eclogite boudins and serpentinites (Kockel et al., 1971, 1977). The Arnea-Kerkini Magmatic Complex intruded the Silurian - Ordovician orthogneisses during the Lower Triassic and both, as a coherent basement complex, experienced the same post-intrusion tectono-metamorphic history (Himmerkus et al., 2009b). Medium-pressure amphibolite-facies regional conditions are estimated at 0.45-0.75GPa / 510-580^{o}C for intercalated quartz + white mica + biotite + garnet + oligoclase ± staurolite ± kyanite schists (Kilias et al., 1999) and at 0.4GPa /

450-550^{o}C for meta-ultramafics with the assemblage antigorite + Fe-Cr spinel + ilmenite ± chlorite ± talc ± tremolite (Michailidis, 1991). Deformed amphibolites form the basement yield the crucial assemblage amphibole + epidote/zoisite + garnet + quartz + plagioclase ± biotite indicating amphibolite-facies conditions at 0.85GPa / 600^{o}C (Dimitrios Kostopoulos, 2014 pers. comm.). The Volvi meta-mafic body crops out near the eastern part of the Vertiskos Unit and is interpreted as the product of Permian - Lower Triassic intracontinental rifting process (Bonev & Dilek, 2010). A wealth of Jurassic - Cretaceous metamorphic ages (^{40}Ar/^{39}Ar, K/Ar and Rb-Sr) have been reported in the literature (e.g., Harre et al., 1968; Zervas, 1979; Papadopoulos & Kilias, 1985; de Wet et al., 1989; Lips et al., 2000) and they all summarised in Figure 1.6. The structural continuity and the NW-SE-trending planar fabrics of the Vertiskos Unit are disrupted by small sedimentary basins developed only after middle Miocene (Koufos et al., 1995). Large Eocene batholiths (de Wet et al., 1989; Christofides et al., 1990) and limited Oligo-Miocene plutonic rocks (Frei, 1992; Gilg & Frei, 1994), often accompanied by small coeval volcanic extrusions (Tompouloglou, 1981; Harkovska et al., 2010, and our data) intrude the Vertiskos Unit.

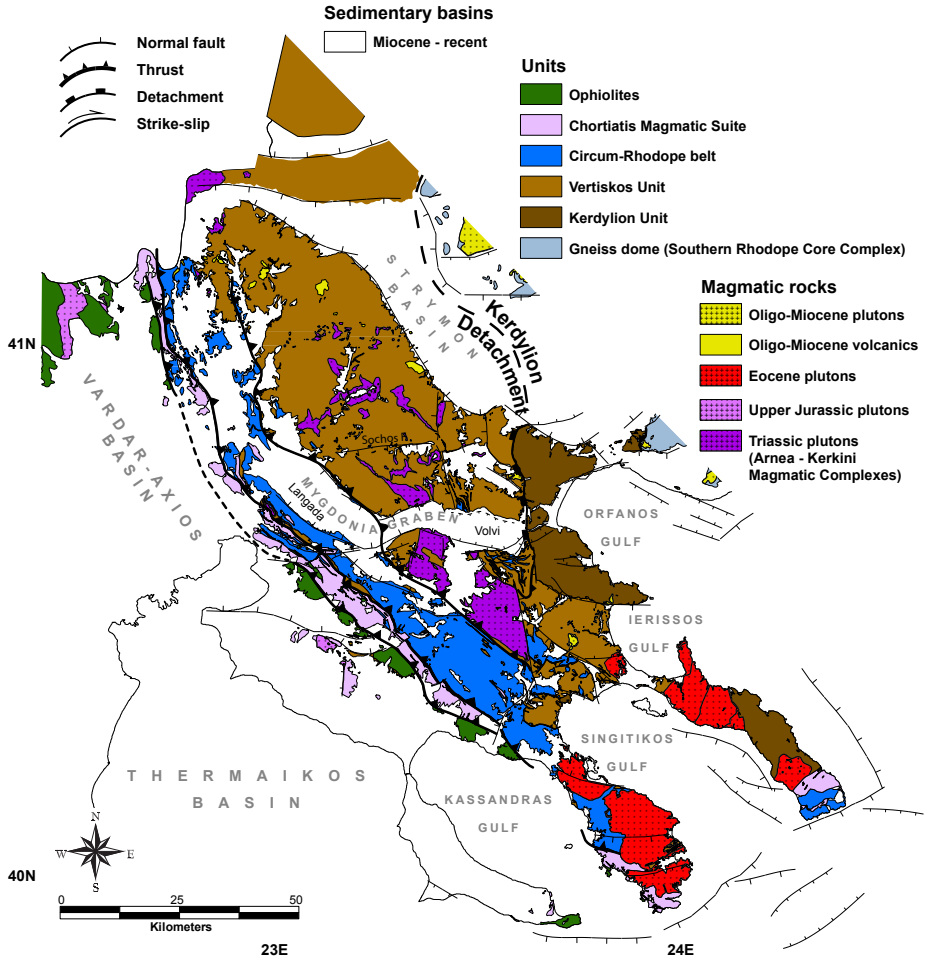

Figure 1.5: Geological map of the Chalkidiki Peninsula (northern Greece) after Kockel & Mollat (1977) and Sakellariou & Dürr (1993). The Chalkidiki forms the southwestern part of the Rhodope and roughly correlates with the so-called "Serbo-Macedonian Massif" of Kockel et al. (1971). Here we study the Mesozoic - Cenozoic geological evolution of the Chalkidiki block which defines the hanging-wall of the Kerdylion Detachment, the structure that is largely responsible for the exhumation of the Southern Rhodope Core Complex immediately to the east. See Figs. 1.2 and 1.4 for location of the study area and text for details.

The **Circum-Rhodope belt** is a Triassic - Jurassic meta-sedimentary sequence locally involving Triassic rhyolites and quartzites at its base (Asvesta & Dimitriadis, 2010; see Mein-

hold & Kostopoulos, 2013, for a review) (Figure 1.5). The term was originally introduced by Kauffmann et al. (1976) to describe low-grade rocks fringing the basement complex of the Vertiskos Unit to the west, thought of as representing its original Mesozoic stratigraphic cover. Indeed, Meinhold et al. (2009) reported detrital zircon ages from the base of the metasedimentary sequences of the Circum-Rhodope belt and assigned the Vertiskos Unit as their source area. Remnants of mappable garnet-kyanite-staurolite-mica schists toward the eastern part of the Vertiskos Unit have been originally mapped as parts of the Circum-Rhodope belt (Kockel et al., 1977). However, they were interpreted later as separate units and local names where assigned to them (i.e., "Nea Madytos Unit" of Sakellariou & Dürr, 1993; "Bunte Serie" of Papadopoulos & Kilias, 1985). Their map continuity with the Circum-Rhodope belt further to the west strongly suggest that those sequences are part of the Mesozoic Circum-Rhodope belt (Dixon & Dimitriadis, 1984) (Figure 1.5). The rhyolites from the base of the Circum-Rhodope belt yield Lower Cretaceous metamorphic ages (K/Ar; Bertrand et al., 1994; Figure 1.6). The contact between the Vertiskos Unit (basement) and the Circum-Rhodope belt (sedimentary cover) is a sharp NW-trending thrust fault locally showing a strike slip component and evidence for re-working (Ricou & Godfriaux, 1994; Tranos et al., 1999).

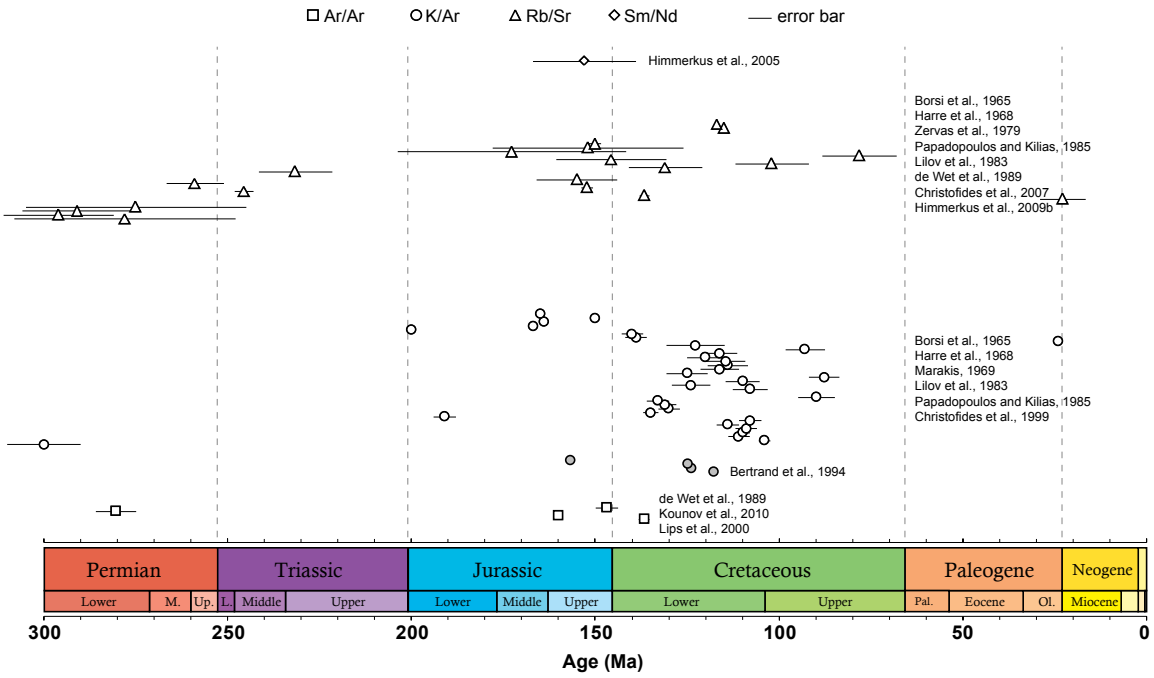

Figure 1.6: Metamorphic ages compilation for the Vertiskos Unit (open symbols) and the Circum-Rhodope belt (filled symbols).

Immediately to the west, the **Chortiatis Magmatic Suite** is made of intensively deformed acidic and intermediate igneous rocks of Upper Jurassic age (Monod, 1964; Zachariadis, 2007) (Figure 1.5). Michard et al. (1994a,b) reported the existence of high-Si phengite (3.52 apfu) from basal rhyolitic meta-tuffs of the Circum-Rhodope belt and relict phengite-glaucophane assemblage from the Chortiatis Magmatic Suite. The latter authors also estimated peak conditions at circa 0.8GPa / 350^{o}C. Asvesta (1992) also reported high-Si phengite from the base of the Circum-Rhodope belt and Monod (1964) mentioned "amphiboles which show sometimes a sodic character" from the Chortiatis Magmatic Suite. However, a pervasive greenschist-facies overprint seems to have almost completely erased the evidence of an earlier HP event of the Circum-Rhodope belt and the Chortiatis Magmatic Suite. The age

of the HP event was speculated by Michard et al. (1994a,b) to be as old as Upper Jurassic. However, Ricou (1965) described Tithonian sediments involved in the thrust system of the Chalkidiki peninsula locally showing neo-formed glaucophane, albite, sericite and epidote - an observation partly ignored by latter workers. The oldest virtually un-metamorphosed sediments involved in the mentioned thrust system are of Albian-Cenomanian age (Meinhold et al., 2009). Thus, the timing for the low-grade HP event can be constrained roughly between uppermost Jurassic and Albian-Cenomanian.

1.3 Problematic

This study is based around a multidisciplinary approach that aims to unravel different aspects of the tectonics of the North Aegean. The latter is the type-locality for both the study of the Jurassic - Cretaceous convergence history of the Hellenides and the gravitational collapse of the thickened Hellenic crust during the early opening of the Aegean.

As mentioned before, the Rhodope (North Greece - South Bulgaria) is one of the youngest UHP belt of the world, forms the hinterland of the Hellenides and can be considered as an area of large-scale nappe tectonics superimposed by strong ductile extension (see Burg, 2012, for a review). Field studies and isotopic work are in line with an early phase of crustal thickening during the Jurassic - Cretaceous that was followed soon after by Tertiary gravitational collapse and core complex formation (Burg et al., 1990, 1996; Ricou et al., 1998; Bonev et al., 2006; Brun & Sokoutis, 2007). The early Aegean extension resulted in the dispersal of the inherited convergence-related structures and in exhumation of two distinct gneiss domes zones in the Rhodope. These are: i) a set of aligned extensional metamorphic domes (Chepinska, Arda, Kesebir - Kardamos and Biela-Reka – Kechros) to the northeast that are collectively called here for convenience as the Northern Rhodope Core Complex (NRCC) and ii) the Southern Rhodope Core Complex (SRCC) to the southwest (Figure 1.3). The development of the SRCC separated Rhodope into two main blocks: the Northern Rhodope Domain (NRD), to the northeast, and the Chalkidiki Block, to the southwest. During the exhumation of the SRCC, the Chalkidiki block, as part of the hanging-wall of the Kerdylion Detachment, a structure that is largely responsible for the exhumation of the SRCC immediately to the east, underwent a circa 30^o clockwise rotation (Kondopoulou & Westphal, 1986). *Both i) strain localisation to the hinterland of the Hellenides at the onset of extension and ii) the formation of two distinct gneiss domes zones so close to each other are clearly intriguing and influenced us to launch the present study to investigate the mechanics of the early evolution of the Aegean.*

The northeastern extreme part of the Rhodope (NRD) is more extensively studied compared to its southwestern part (Chalkidiki block) (Figure 1.3). Within the NRD, peak metamorphic conditions in the eclogite-facies and subsequent amphibolite-facies overprint are recorded by metapelites that locally contain micro-diamond inclusions and by variably retrogressed mafic eclogites (e.g., Reischmann & Kostopoulos, 2002; Liati & Seidel, 1996; Moulas et al., 2013). This part has attracted the attention of many workers during the last decades and the P-T-t evolution, although still debatable in the details, is generally adequately defined (e.g., Lips et al., 2000; Bauer et al., 2007; Jahn-Awe et al., 2010; Krenn et al., 2010; Schmidt et al., 2010; Liati et al., 2011; Kirchenbaur et al., 2012; Mposkos et al., 2012; Bonev et al., 2013b; Moulas et al., 2013). However, the Chalkidiki block has attracted much less attention (Figure 1.5). There, the recorded peak metamorphic conditions are significantly lower reaching medium-pressure amphibolite-facies, and even reduce to blueschists/greenschists-facies further to the west (Michard et al., 1994a,b; Burg et al., 1995; Kilias et al., 1999). Our knowledge on the P-T-t evolution of the Chalkidiki block is rather limited. *A major part of this study is dedicated to the investigation of the tectono-metamorphic evolution of the Chalkidiki block and its thermal evolution from early accretion*

to near surface exposure.

During the course of this study, a series of major **questions** that will be answered include: *why the extension localised at the back of the extending domain (i.e., in the Rhodope) during the early stages of the Aegean extension, why core complexes developed sequentially in two distinct zones in the Rhodope, why the Kerdylion Detachment that controls the exhumation of the southern core complex dips toward the foreland, why the hanging-wall of the Kerdylion Detachment (Chalkidiki block) behaved as a coherent non-deforming block during the ductile extension in the Rhodope, what are the metamorphic conditions attained by Chalkidiki block, why the Barrovian medium-pressure/high-temperature imprint recorded in the largest part of the Chalkidiki block does not contradict our working hypothesis for involvement in a Mesozoic subduction, is there any metamorphic gradient across the Rhodope, what is the timing of the metamorphic events recorded by the different units of the Chalkidiki block and how do they correlated to the northeastern part of the Rhodope, is the Chalkidiki block and the NRD a single Mesozoic geological entity, what information can be extracted from the Chalkidiki block that is largely erased from the other Rhodopean domains?*

In the course of this work we will argue that the Chalkidiki block and the NRD participated into the same Mesozoic convergence both as part of the down-going plate along a northward subduction and that they were separated only after the middle Eocene opening of the SRCC. We will further argue that the Chalkidiki block can provide valuable information on the evolution of the Rhodope as it has preserved much of the convergence-related fabrics and has largely escaped the Tertiary extension and the related thermal overprint.

1.4 Methods - Thesis structure

This study is dedicated to the geology of the Chalkidiki Peninsula (Northern Greece) with particular interest for the Vertiskos Unit (basement), the Circum-Rhodope belt (cover) and the Chortiatis Magmatic Suite (arc). We carried out field mapping measuring the geometry of the deformation fabrics. We evaluated the intensity of the metamorphic conditions and we performed high- (U/Pb in zircon and monazite) and medium-temperature ($^{40}Ar/^{39}Ar$ on micas) geochronology coupled with low-temperature thermochronology and inverse thermal history modelling. On a broader scale, using small-scale laboratory experiments we modelled the core complex formation of orogenic thrust wedges affected by extension adopting the geological structure of the North Aegean as the initial geometry of the system.

In ***Chapter 2*** we refine the age of magmatic rocks of the area. The protolith age of the basement orthogneisses is defined as Silurian based on Pb/Pb zircon dating (Himmerkus et al., 2009a). Widespread pegmatites and amphibolite bodies are embedded within those orthogneisses but their age is rather unknown. Paragneisses appear also intercalated within basement orthogneisses. Using LA-ICP-MS zircon dating we define more accurately the age of the orthogneisses as well as the age of the intercalated pegmatites and amphibolites and we present additional detrital zircon data from selected intercalated paragneisses. In addition, we define the age of the young volcanics exposed along the western part of the study area.

In ***Chapter 3*** we study the P-T evolution of selected pelitic samples from the eastern part of the basement. Peak metamorphic conditions and retrogression paths are established on the basis of micro-textures, mineral chemistry and isochemical phase diagram sections. Regional variations both in the peak pressure and peak temperature are discussed.

In ***Chapter 4*** we present new high- (U/Pb on monazites) and medium-temperature geo-chronology ($^{40}Ar/^{39}Ar$ on micas) from the Chalkidiki block. Regional variations and geographical trends in the P-T-t regime are highlighted and discussed with reference to the rest of the Rhodopean domains.

In ***Chapter 5*** we study the post-peak thermal evolution of the eastern part of the Chalkidiki block using low-temperature thermo-chronology (apatite Fission-Track analysis

and inverse thermal modelling). Using a Bayesian inverse modelling scheme, we define the timing of the exhumation and near-surface exposure of the gneisses. Lateral variations and the differences with the other domains of the Rhodope are discussed.

In ***Chapter 6*** we present new field data and the geometry of structural fabrics collected during several field campaigns. The finite geological structure of the Chalkidiki block is discussed based on balanced cross-sections and on compiled regional structural/kinematic maps. A kinematic interpretation is given for the geological evolution of the Chalkidiki block within the scheme set by the previously presented P-T-t data.

In ***Chapter 7*** we study the gravitational collapse and core complex formation of an orogenic wedge subject to extension using analogue modelling experiments. We adopt the Mesozoic structure of the Hellenides, we apply boundary conditions based on geological constraints and we study the early opening of the Aegean with respect to the exhumation of the Rhodopean gneiss domes. We explain important aspects of the mechanics of the early Aegean extension such as strain localisation and geographical spread of the exhumed domes. The influence of the initial geometry of the system and the effect of various tested displacement velocities on the finite deformation pattern of the North Aegean are discussed.

Chapter 8 shortly summarises our new findings so that the reader can readily access our results.

Chapter 2

Zircon dating: constrain the Palaeozoic - Lower Mesozoic thermal events of the Chalkidiki basement

2.1 Introduction

As mentioned in the previous chapter, the southwestern part of the Rhodope is exposed at the Chalkidiki Peninsula of northern Greece. The Chalkidiki block roughly coincide with the so-called Serbo-Macedonian Massif of Kockel et al. (1971) if one excludes the easternmost unit of the latter that is known as the Kerdylion Unit. The Chalkidiki block defines the hanging-wall of the Kerdylion Detachment whereas the foot-wall is defined by the Kerdylion Unit and the gneiss dome of the Southern Rhodope Core Complex (Figure 1.3).

For the purpose of this chapter we will concentrate to the Chalkidiki block and in particular to its eastern part that is made of the Vertiskos Unit (basement) and the Circum-Rhodope belt (cover) (Kockel et al., 1971, 1977; Kockel & Mollat, 1977) (Figure 2.1). We will describe shortly the geological setting with emphasis on the different rocktypes as well as their reported ages (deposition, crystallisation, metamorphic, etc.). The aim of this chapter is to define the protolith age (and wherever possible the metamorphic age) of various magmatic rocks from the Chalkidiki. We also provide data on the provenance of intercalated paragneisses using detrital zircon dating. This is a special chapter that deals mainly with Palaeozoic magmatic/metamorphic events from the basement complex of the Chalkidiki block whereas the Mesozoic events, as part of the Alpine history of the Chalkidiki block, will be described in detail in the upcoming chapters.

Toward that direction, we will present new U/Pb LA-ICP-MS zircon dating results and discuss our findings with respect to the available literature data. This chapter also includes the results of the MSc dissertation of Charlotte Dubois entitled "*Géochronologie U-Pb sur zircons de filons du massif Serbo-Macédonien (Nord de la Gréce)*" ("*Zircon U-Pb geochronology of dykes from the Serbo-Macedonian Massif (northern Greece)*") presented for her Master 1 studies (Ressources Minérales et Pétrolières, Mai-Juin, 2013) at Géosciences Rennes.

2.2 Geological setting

The **Vertiskos Unit** is an elongated basement complex with a complex tectono-metamorphic history (Figure 2.1). In Bulgaria, to the north, it is known as the Ograzden Unit (Zagorchev, 1976). It is a distinct basement fragment that detached from Gondwana and incorporated

into the Southern European Arcs by the end of the Palaeozoic (Himmerkus et al., 2007; Kydonakis et al., 2014b).

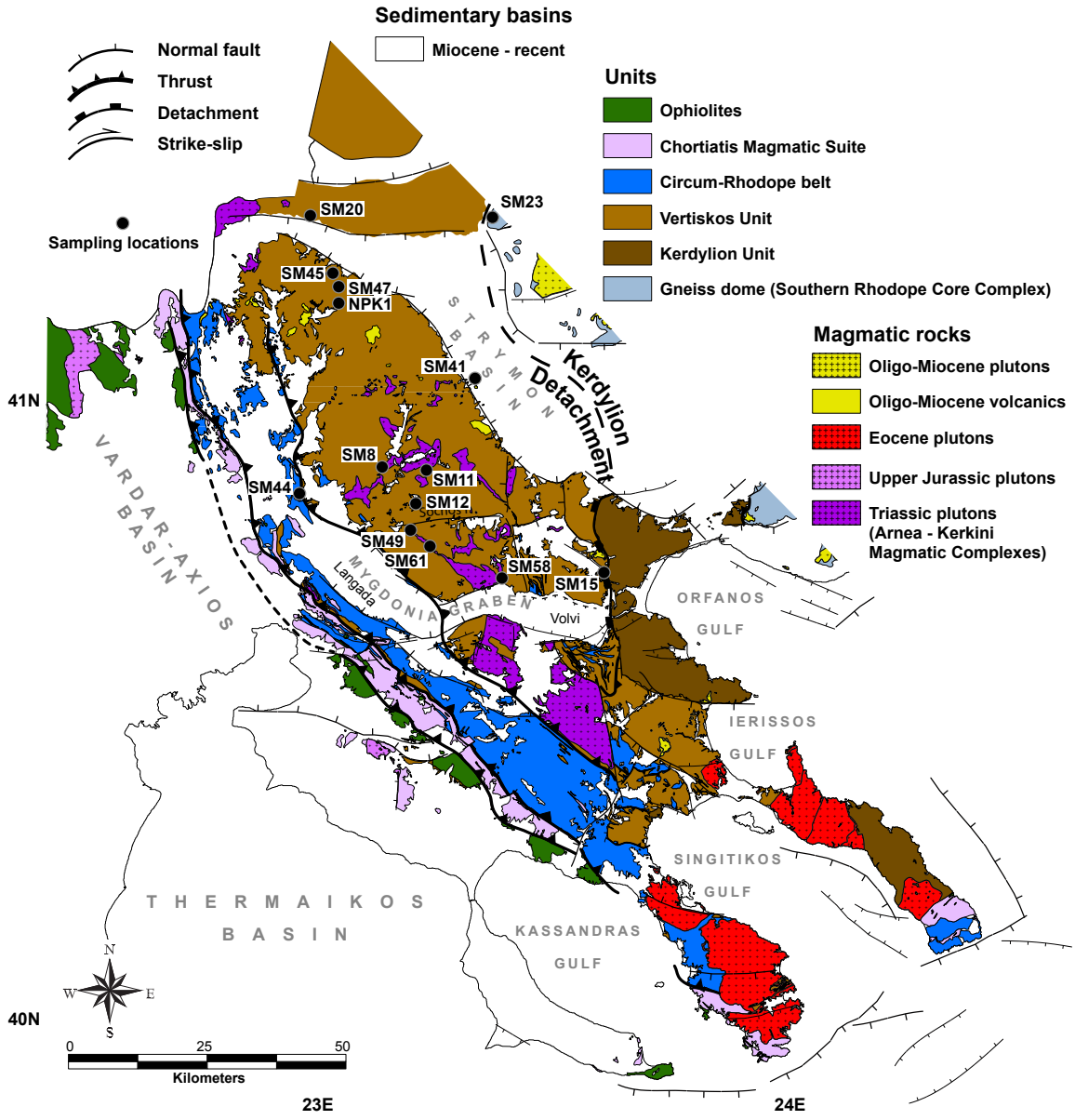

Figure 2.1: Geological map of the Chalkidiki. For locality with reference to the North Aegean see Fig. 1.3. The samples used for U/Pb LA-ICP-MS dating are shown on the map.

In the study area, the most common rocktype are biotite **orthogneisses** whose protolith is dated as Silurian (Himmerkus et al., 2009a). The orthogneisses bear in places intercalated para-gneisses and thin marble horizons, leucocratic granitic/pegmatitic intrusions, deformed amphibolites, scarce eclogite boudins and serpentinites (Kockel et al., 1971, 1977). Widespread and intensely deformed **pegmatites** are common in the study area. Himmerkus et al. (2009a) provided a 431.1 ± 3.6 (sample SH69c, Lachanas village) and a 435.4 ± 2.5 (sample SM1, Oreokastro village) age (Pb/Pb) for the protolith of the pegmatites. Borsi et al. (1965) reported circa 300 Ma Rb/Sr ages for pegmatites located near the western part of the Vertiskos Unit (Nea Santa village). K/Ar metamorphic ages for similar pegmatites are reported also from Harre et al. (1968) and Marakis (1969) and scatter between 104 and 190 Ma.

In many places within the Vertiskos Unit, **amphibolite** bodies crop out. They appear either as intensely deformed, relatively thin, former dykes with their foliation planes being parallel to the foliation of the country rocks (e.g., Kassoli-Fournaraki et al., 1986) or as distinct voluminous bodies, in many cases in association with ultramafics, near the eastern part of the Vertiskos Unit (Therma - Volvi - Gomati complexes) (Dixon & Dimitriadis, 1984; Bonev & Dilek, 2010; Bonev et al., 2012a). The first type of amphibolites are of unknown protolith age. They can be found almost everywhere in the study area and their most typical mineral assemblage is garnet + amphibole + biotite + plagioclase (Kassoli-Fournaraki et al., 1986). Kourou (1991) and Sidiropoulos (1991) reported the existence of rare and variably retrogressed eclogites which, in association with amphibolites, are preserved as lenses within the Silurian gneisses. Dimitriadis & Godelitsas (1991) also reported similar retrogressed eclogites from the southeastern part of the Chalkidiki Peninsula. Arguably equivalent amphibolites from the Mesta Village of Bulgaria are dated at 454.1 ± 8.3 (meta-gabbro) and 446 ± 7 Ma (meta-diorite) (Peytcheva et al., 2009). The second type of amphibolites appears deformed but magmatic textures are still preserved in places of low strain. Himmerkus et al. (2005) reported a circa 228 Ma age from plagiogranites of the Volvi complex (Pb/Pb) and Liati et al. (2011) mentioned a 252 ± 13 Ma (SHRIMP) from a meta-gabbro of the same complex. Metamorphic ages (K/Ar on hornblende) from the Volvi complex peak between 90 and 120 Ma (Harre et al., 1968; Papadopoulos & Kilias, 1985).

Leucocratic two-mica and biotite meta-granites with a pronounced within-plate isotopic signature from the study area are collectively known as the Arnea - Kerkini Magmatic Complexes (Figure 2.1). Their crystallisation age is well-defined at Triassic (Himmerkus et al., 2009b; Poli et al., 2009) based on zircon dating. The evidence for syn-intrusion contact metamorphism into the host Silurian orthogneisses is only very locally preserved as it has been largely erased during post-intrusion deformation. In many places, the Arnea - Kerkini meta-granites are transformed into highly deformed L-mylonites. A similar-looking leucocratic biotite-quartz monzodiorite to granodiorite known as the Flamouri Complex (Kockel et al., 1977) is dated at uppermost Carboniferous (304.1 ± 7.0 Ma) (Dimitrios Kostopoulos unpublished data).

In the southern tip of the Chalkidiki peninsula a first pulse of **Tertiary magmatic intrusions** is recorded. Hornblende-biotite granodiorites (Sithonia, Ierissos, Ouranoupolis and Gregoriou) intrude the basement and are dated at circa 50 Ma (de Wet et al., 1989; Christofides et al., 1990; Frei, 1996). Their continuation to the south is obscured by the North Aegean Trough, while to the north, along the Vertiskos Unit, no magmatism of the same age is recorded. A second pulse of magmatic activity is documented by smaller plutons (Stratoni, Skouries and Olympiada) that are often accompanied by volcanic extrusions (Monolithi and Gerakario). Feeding dykes of the latter intrude the basement complex. To the south they are related to fluid circulation, porphyry copper mineralization, and Pb-Zn-Ag-Au replacement ores. This pulse is as old as Oligo-Miocene (Frei, 1992; Gilg & Frei, 1994; Tompouloglou, 1981). Along the eastern border of the Vertiskos Unit, in proximity to the Strymon basin, a trachyte-rhyolite series known as the Strymoniko volcanics crop out. According to the available literature it is Pliocene-Quaternary in age (Kockel & Walther, 1966; Panagos et al., 1978).

The **Circum-Rhodope belt** is a Triassic - Jurassic meta-sedimentary sequence locally involving Triassic rhyolites and quartzites at its base (Kauffmann et al., 1976; Asvesta & Dimitriadis, 2010; Meinhold & Kostopoulos, 2013). The sequence is considered the Mesozoic sedimentary cover of the Vertiskos Unit (Kockel et al., 1971, 1977; Dixon & Dimitriadis, 1984). Indeed, Meinhold et al. (2009) reported detrital zircon ages from a basal meta-quartzite of the Circum-Rhodope belt and assigned the Vertiskos Unit as one of the possible source areas. However, due to Cretaceous - Cenozoic post-metamorphic deformation, the contact between the basement and its sedimentary cover is a sharp NW-trending thrust

fault often showing a strike slip component and evidence for re-working (Ricou & Godfriaux, 1994; Tranos et al., 1999). The rhyolites from base of the Circum-Rhodope belt yielded Lower Cretaceous metamorphic ages (K/Ar) (Bertrand et al., 1994).

2.3 Sampling strategy

In order to refine the magmatic (or even the metamorphic) ages of selected rocktypes we deployed a sampling grid to the Vertiskos and the Circum-Rhodope belt (Table 2-1). We additionally performed detrital zircon analysis on intercalated paragneisses to refine source areas and to attempt to define the deposition age of the sedimentary protolith, based on the youngest well-constrain age cluster. Sample localities are shown in Figure 2.1. In detail, we selected three orthogneisses from the Vertiskos Unit, one mylonite from the Arnea Magmatic Complex, one orthogneiss from the Southern Rhodope Core Complex bounding Vertiskos Unit immediately to the east and one rhyolite from the arguably Pliocene-Quaternary volcanics exposed at the eastern flank of the basement. We also selected four pegmatites and four intercalated paragneisses from the basement and one additional K-feldspar-bearing schist from the base of the Circum-Rhodope belt. In situ zircon dating was performed on metamorphic zircons of a garnet-amphibolite. Representative cathodoluminescence images are shown in Figure 2.2. The full isotopic dataset for the zircons dated is given in Appendix C1.

Table 2.1: List of samples selected for LA-ICP-MS zircon dating. For sample location see Fig. 2.1.

Sample	Locality	Latitude	Longitude	Elevation	Unit
Amphibolite					
NPK01	Kato Theodoraki	41.14	23.02	610	Vertiskos
Acid Magmatics					
SM12	Ossa	40.84	23.21	675	Vertiskos
SM20	Platanakia	41.31	22.93	551	Vertiskos
SM23	Roupel	41.34	23.35	103	Pangeon
SM41	Strymoniko	41.03	23.33	119	Volcanics
SM58	Vaiochori	40.72	23.38	187	Arnea
Pegmatites					
SM45	Monastiraki	41.21	23.02	308	Vertiskos
SM47	Kato Theodoraki	41.18	23.04	673	Vertiskos
SM49	Pente Vryses	40.81	23.19	384	Vertiskos
SM61	Lofiskos	40.78	23.22	499	Vertiskos
Meta-sediments					
SM8	Dorkada	40.90	23.13	498	Vertiskos
SM11	Vertiskos	40.90	23.22	754	Vertiskos
SM15	Arethousa	40.73	23.61	374	Vertiskos
SM44	Nea Santa	40.85	22.94	129	Circum-Rhodope belt

2.4 Analytical method

A classic zircon separation procedure was followed at the facilities available at Géosciences Rennes, France. The samples were crushed and zircon grains were separated using a Wilfley table, heavy liquids and a Frantz isodynamic separator before being handpicked under a binocular microscope and embedded in epoxy resin. Zircons were imaged by cathodoluminescence (CL) before being dated using in-situ laser ablation inductively coupled plasma-mass spectrometry (LA-ICP-MS) at Géosciences Rennes, France. Ablation spot diameter of 20 μm with repetition rates of 3 Hz were used throughout. The data were corrected for U-Pb and Th-Pb fractionation and for mass bias by standard bracketing with repeated measurements of the GJ-1 zircon (Jackson et al., 2004). Data reduction was carried out using the GLITTER© software package developed by Macquarie Research Ltd. (Jackson et al., 2004). Concordia ages and diagrams were generated using Isoplot/Ex (Ludwig, 2001) updated to

ver. 3.75. Further information on the instrumentation and the analytical technique is detailed in Hurai et al. (2010).

2.5 Uranium/lead LA-ICP-MS zircon dating results

2.5.1 Orthogneisses and volcanics

Samples SM12 and SM20 are both part of the basement (Vertiskos Unit) (Figure 2.1). SM12 is a medium-grained biotite orthogneiss collected near Ossa village (Figure 2.3a). In the field, shear bands indicate a SW-directed shear. The zircons of this sample have inherited cores with typical overgrowths showing oscillatory zoning (Figure 2.2). The inherited cores point toward Gondwanan provenance with age peaks at circa 0.55, 0.65, 0.9 and 2 Ga. The calculated concordia age of 460.7 ± 3.9 Ma from the oscillatory domains is interpreted as the crystallisation age of the protolith (Figure 2.4). SM20 is a spectacular coarse-grained biotite augengneiss from the Kerkini Mountain near Platanakia Village (Figure 2.3b). As for the previous sample, inherited core point to Gondwanan provenance with age peak at circa 0.55, 0.6, 0.7 and 1 Ga (Figure 2.2). The calculated concordia age from the oscillatory domains (462.1 ± 3.8 Ma) is indistinguishable from that of the previous orthogneiss (Figure 2.4).

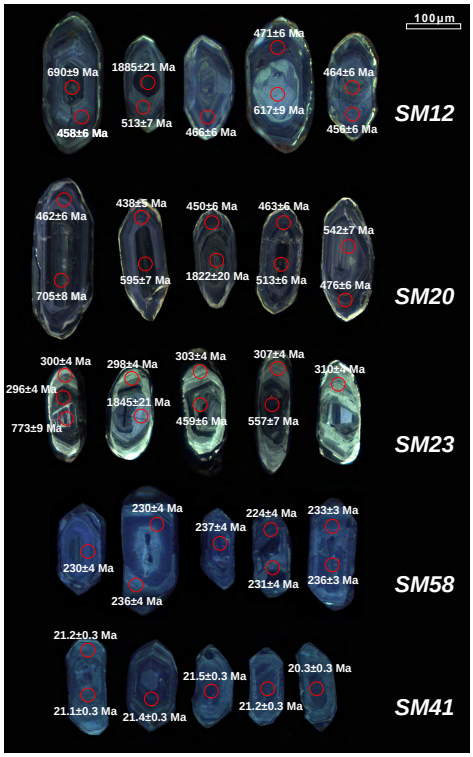

Figure 2.2: Selected zircon cathodoluminescence images for the dated orthogneisses (SM12, SM20, SM23, SM58) and the K-feldspar-bearing clastic sediment. The corresponding $^{238}U/^{206}Pb$ spot age is superimposed.

Sample SM44 has been collected near Nea Santa village (Figure 2.1). It belongs to the base of the Mesozoic Circum-Rhodope belt. It contains angular fragments of potassic feldspar enveloped by groundmass made for quartz and micas. Although that this sample is clearly of sedimentary origin, we describe it here because its zircon population clearly reflect sourcing from the Vertiskos orthogneisses. The youngest coherent age cluster is at 463.3 ± 1.7 Ma (concordia age) and this age is indistinguishable from that of the biotite orthogneisses dated here (e.g., SM12 and SM20) (Figure 2.4).

Sample SM23 has been collected east of the Strymon River near the entrance to the Roupel Fortress (Figure 2.1). It is a medium-grained biotite-rich orthogneiss that belongs to the exposed basement of the Southern Rhodope Core Complex (Figure 2.3). In the field, it is indistinguishable from Vertiskos medium-grained biotite orthogneisses (e.g., sample SM12). Ages obtained from inherited cores peak at 0.55, 0.65, 2 Ga and interestingly at 0.47 Ga (Figure 2.2). The calculated concordia age of 304.8 ± 1.3 Ma is interpreted as the magmatic crystallisation of the rock (Figure 2.4).

Sample SM58 is a coarse-grained two-mica orthogneiss collected near Vaiochori (Figure 2.1). It belongs to the Arnea Magmatic Complex and appears as mega-boudin within enveloping biotite gneisses and amphibolites. Inherited cores are almost absent (Figure 2.2).

The calculated concordia age of 233.1 ± 0.8 Ma is interpreted as the magmatic crystallisation of the rock (Figure 2.4).

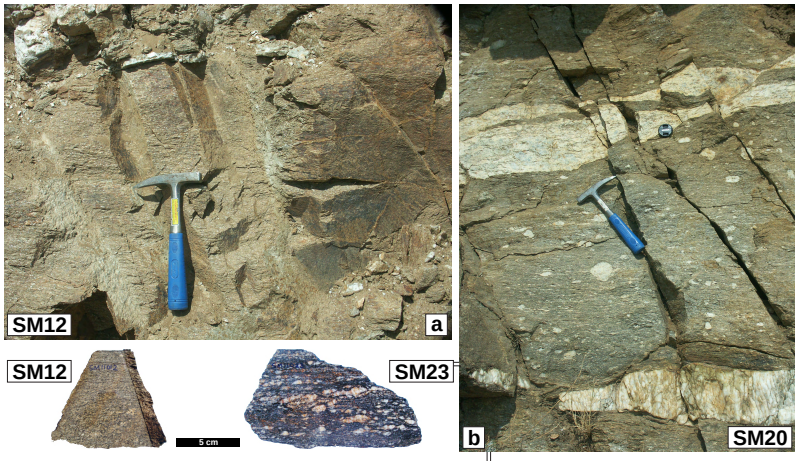

Figure 2.3: Field occurrences and saw-cuts of the dated orthogneisses.

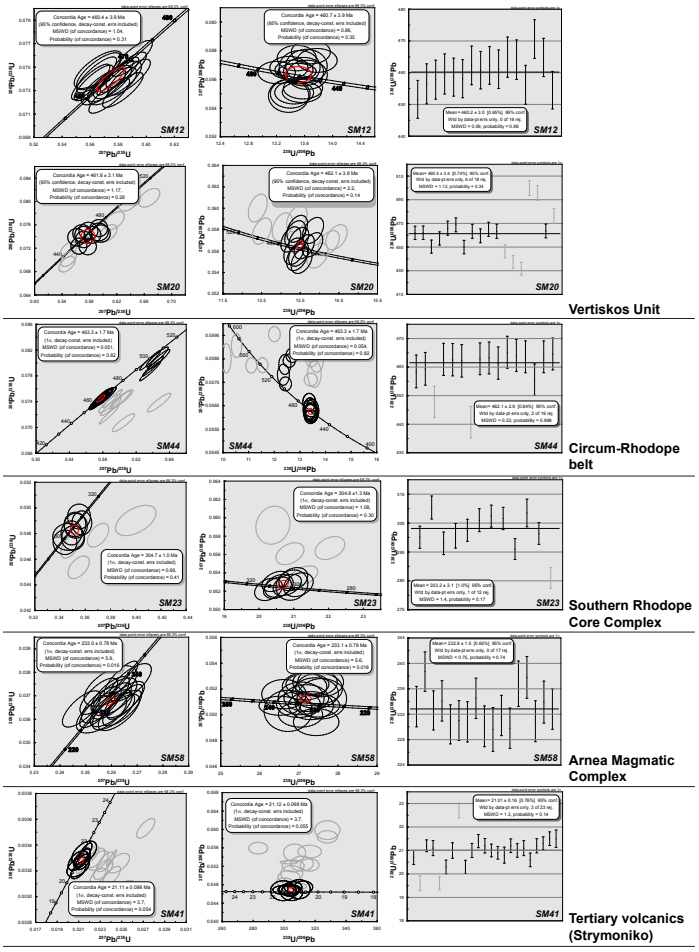

Figure 2.4: Normal and Terra-Wasserburg concordia plots for four meta-granitoid samples from the Vertiskos Unit (SM12, SM58, SM41, SM20), one meta-granitoid from the basement of the Southern Rhodope Core Complex (SM23) and one basal meta-rhyolite from the Circum-Rhodope belt (SM44). Selected $^{238}U/^{206}Pb$ weighted average calculations are also shown.

Sample SM41 is part of the volcanics exposed along the eastern boundary of the Vertiskos

Unit (Figure 2.1). It has been collected from the top of hill near Strymoniko village and belongs to the Strymoniko rhyolite-trachyte series. It has euhedral zircons with oscillatory zoning and completely lack any inherited cores (Figure 2.2). The calculated concordia age of 21.1 ± 0.1 Ma is interpreted as the crystallisation age (Figure 2.4).

2.5.2 Pegmatites

Five pegmatite samples were collected for zircon dating but only four of them contained enough zircon grains for a representative population to be achieved. With the possible exception of one of the samples (SM61), the remaining are strongly deformed as seen in their field occurrences (Figure 2.5).

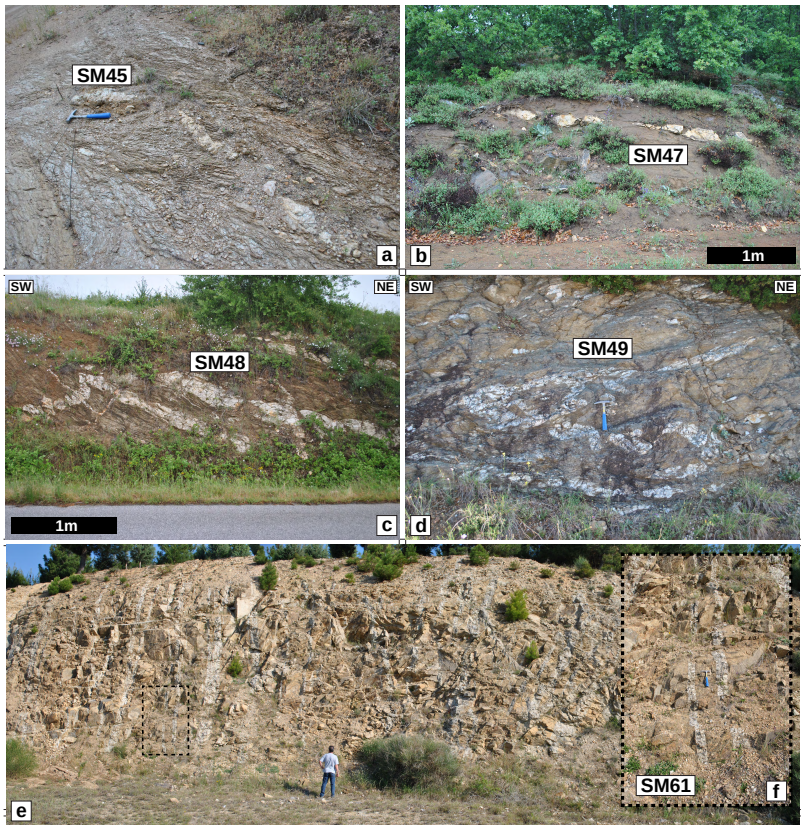

Figure 2.5: Field occurrences of pegmatites. (a),(b),(c),(d) The pegmatites are embedded in basement gneisses and are heavily deformed as a result of Mesozoic deformation. (e) Almost vertical pegmatites intruding an acid granodiorite in the absence of chilled margins (Triassic Arnea Granite according to the geological map of the area). However, the pegmatites yield no post-Carboniferous zircons questioning the assigned age of the country rocks.

Samples SM45 and SM49 gave scattered ages with the youngest age cluster being for both samples at circa 320 Ma (Figure 2.6). However, no reasonable concordia or intercept age could be calculated. For SM45, zircon cathodoluminescence imaging shows inherited cores (commonly dated between 550 and 600 Ma) that are rimmed by thick overgrowths of Carboniferous age (Figure 2.6).

Sample SM47 gave two clear age clusters with the corresponding calculated intercept ages being at 470.0 ± 12.0 and 319.5 ± 3.1 Ma, respectively (Figure 2.6). Zircon cathodoluminescence images reveal that the Carboniferous ages are usually in the outer rims overgrowing inherited Ordovician cores (Figure 2.6).

For sample SM61, most of the ages obtained are Ordovician (474.0 ± 15.0 Ma intercept age) and the youngest age group is defined by two concordant zircon age at 323.2 ± 2.6 Ma

(concordia age) (Figure 2.6).

Overall, two zircon age groups can be envisaged by the four dated pegmatites: an Ordovician and a Carboniferous age cluster. Cathodoluminescence imaging revealed that the most commonly observed pattern is a Carboniferous thick outer rim grown on an Ordovician (or older) core. Based on the calculated Th/U ratios, the Ordovician (and older) age group is characterised by zircons bearing a magmatic signature (high Th/U ratio) whereas the Carboniferous spots show clearly a metamorphic signature (Th/U < 0.1) (Figure 2.6).

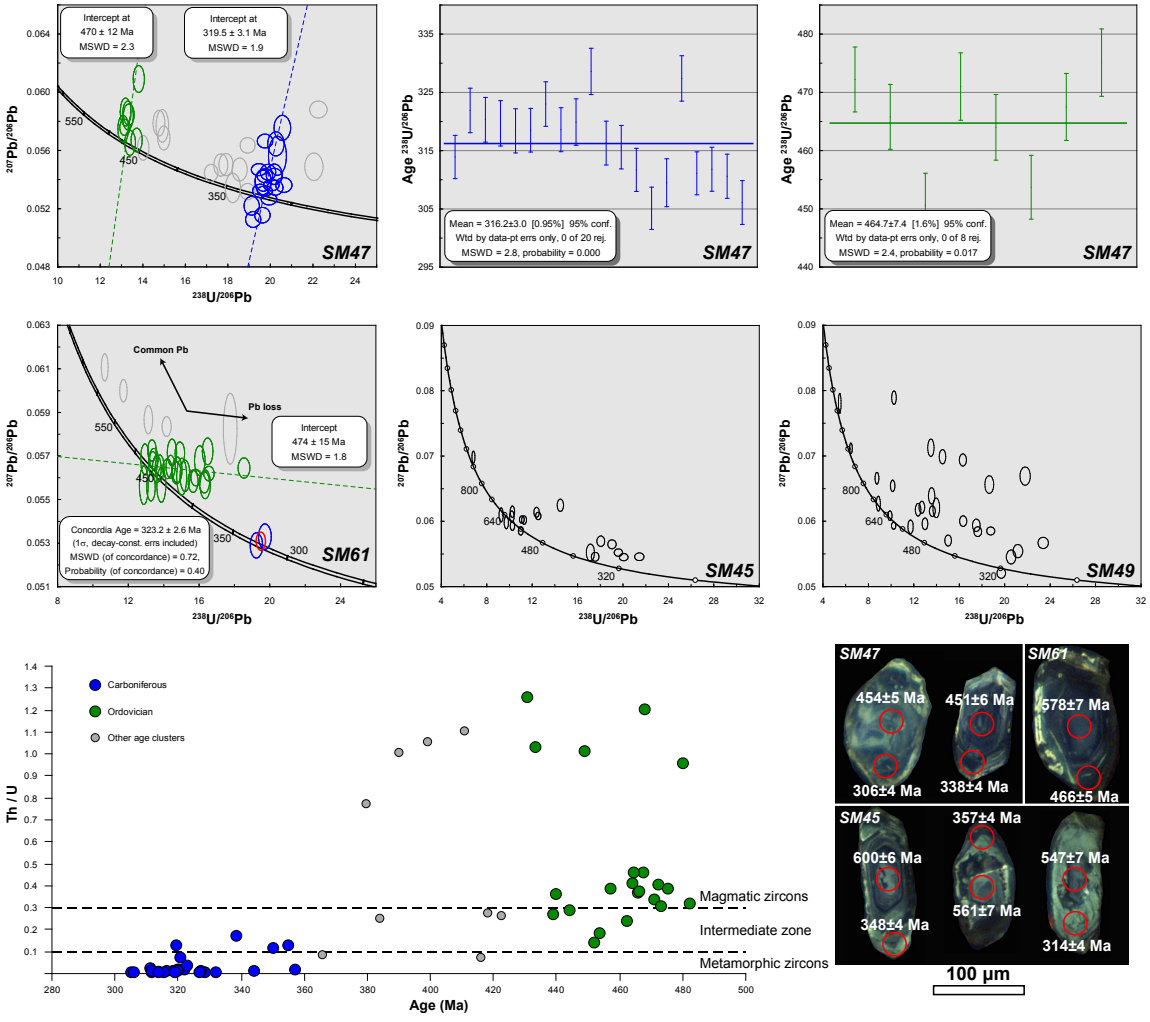

Figure 2.6: Terra-Wasserburg and Th/U plot of four deformed pegmatites (Fig. 2.5) of the Vertiskos Unit (for location see Fig. 2.1). Two of the samples defined tight clusters at ca. 470 and 320 Ma. In the Th/U plot, metamorphic and intermediate-magmatic signatures are illustrated for the Carboniferous and the Ordovician age clusters, respectively. Metamorphic, intermediate and magmatic zircon fields after Teipel et al. (2004).

2.5.3 Intercalated paragneisses

Three paragneisses were selected for provenance analysis using detrital zircon dating (Figure 2.1). Two of them were collected from the central part of the study area near Dorkada (sample SM8) and Vertiskos (sample SM11) villages. They are fine-grained quartz-biotite-white mica gneisses. The youngest concordant zircon is 577 Ma for SM8 and 447 Ma for SM11 and both samples show pronounced age peaks at circa 0.6, 0.75, 0.95 and 1.7-2.6 Ga (Figure 2.7). Sample SM15 is a garnet-staurolite-kyanite-mica schist collected near Arethousa village from the eastern part of the basement. Its zircon population is dominated by circa 240 Ma ages and other age peak are found at 0.3, 0.45 and 0.95 Ga (Figure 2.7).

2.5.4 Amphibolite

One garnet amphibolite (NPK01; courtesy of Dimitrios Kostopoulos and Nikolaos Kartalis) was collected near Kilkis and selected for zircon dating (Figure 2.1). We have chosen to apply in-situ LA-ICP-MS dating of a zircon aggregate from the matrix of the rock (Figure 2.8). In a Terra-Wasserburg plot, the data from seven spots (diameter of 20μm) plot along a common lead trend (Figure 2.8). Five out of the seven spots gave a lower intercept at 341.1 ± 7.9 Ma (MSWD 0.87) (black line, right side of Figure 2.8). Using the same five spots and anchoring a regression line at the 207Pb/206Pb composition at 341 Ma resulted in a lower intercept age of 336.1 ± 6.1 Ma which is considered as the timing of crystallisation of the zircons (dashed line; right side of Figure 2.8). This, coupled with the low Th/U values (¡ 0.12) suggests metamorphic origin of the zircons dated.

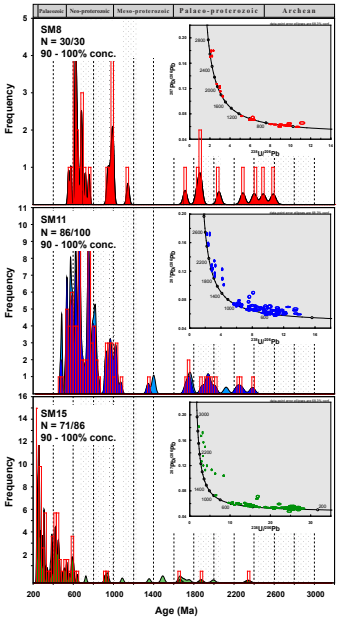

Figure 2.7: Probability-density age distribution patterns and corresponding Terra-Wasserburg plots of detrital zircons for the samples discussed in the text. Concordance-filtered $^{238}U/^{206}Pb$ age was used for the plots. Dark-colored zircon ages within 90-110% concordance; light-colored - zircon ages with more than 10% discordance. Abbreviations: N=number of analyses within the applied concordance limit/number of total analyses. See text for discussion and Fig. 2.1 for sample localities. The binned frequency histograms and the probability-density distributions were created using the AgeDisplay excel workbook (Sircombe, 2004).

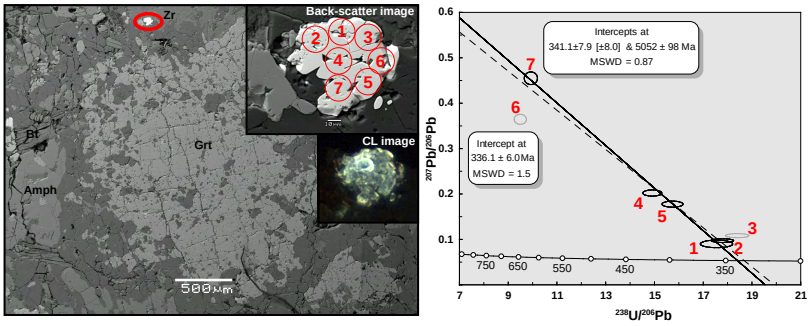

Figure 2.8: (left) Back-scatter and CL image of a zircon aggregate found in a garnet-bearing amphibolite from the basement. (right) Intercept ages for 7 zircon spots (shown to the left). The black line is a regression line through 5 spots that intercepts the concordia at 341 Ma. The dashed line is anchored to the $^{207}Pb/^{206}Pb$ composition at 341 Ma and gives a lower intercept at 336 Ma. Thus, circa 340 Ma is interpreted as the time of crystallisation of the metamorphic zircons.

2.6 Discussion

2.6.1 Refining the protolith age of the Silurian Vertiskos Unit and the Plio-quaternary volcanics

The protolith ages of the basement rocks of Vertiskos Unit are largely known due to the pioneering work of F. Himmerkus and co-workers. In particular, the basement orthogneisses are dated between 398 and 443 Ma (Himmerkus et al., 2009a) and the Arnea Magmatic complex between 222 and 240 Ma (Himmerkus et al., 2009b). However, many, if not all, of the available ages documenting the Vertiskos basement and the Arnea Magmatic Complex as Silurian and Triassic in age, respectively, are based on the Pb-Pb single-zircon evaporation method. It is known that this method is susceptible to mix ages and lacks the capacity for spot dating on specific zircon domains.

Here we sampled basement orthogneisses (SM12, SM20) from the central and the northern part of the study area (Figure 2.1). The obtained concordia ages (460.7 ± 3.9 and 462.1 ± 3.8 Ma) are identical within error (Figure 2.4). This illustrates the dominance of Ordovician zircons, rather than Silurian as considered before, and questions the assigned Silurian age on the basement rocks of the Vertiskos Unit. The age difference between our LA-ICP-MS spot dating results and those obtained from Himmerkus et al. (2009a) is likely due to their used method (Pb-Pb single-grain evaporation) and the problems arising from it. We also note that Meinhold et al. (2009) already reported many Ordovician detrital zircon ages from meta-sedimentary sequences sourced by the Vertiskos basement. *This leave no doubt that the age of the Vertiskos orthogneisses should hereafter considered as Ordovician.* Indeed, Macheva et al. (2006) and Zidarov et al. (2003) reported similar Ordovician ages (circa 452 to 462 Ma) from equivalent basement rocks of the Ograzden Unit from Bulgaria. In addition, Bonev et al. (2013a) recently reported similar Ordovician ages from garnet amphibolites, alkaline basalts and plagiogranites of the eastern Rhodope. *Our findings combined with the above literature data clearly point toward the existence of an Ordovician terrane that includes both acidic and mafic magmatic rocks of Ordovician age and that is largely spread in the Rhodope.*

The calculated concordia age (233.1 ± 0.8 Ma) from the Arnea Magmatic Complex (SM58; Figure 2.4) is identical to the already published ages from Himmerkus et al. (2009b) but it is somewhat younger than those of Poli et al. (2009) (244 - 254 Ma). This illustrates that the magmatic activity of Lower/Middle Triassic that is often correlated to rifting processes (Himmerkus et al., 2009b; Poli et al., 2009; Bonev & Dilek, 2010; Liati et al., 2011; Bonev et al., 2012a) lasted over a time span of approximately 20 m.y.

Turpaud & Reischmann (2010) reported a wealth of zircon ages, using the single-grain evaporation method, from the basement of the Southern Rhodope Core Complex immediately to the east of the study area (Figure 2.1; see also Figure 1.3). Their ages range from 270 to 310 Ma. We calculated here a concordia age for sample SM23 at 304.8 ± 1.3 Ma (Figure 2.4) and although it is within the range of ages reported from Turpaud & Reischmann (2010), it illustrates again that the single-grain evaporation method can potentially shift towards younger, sometimes even un-interpretable, ages (c.f. 270 Ma).

Sample SM41 is an altered rhyolite. It has been collected from a volcanic centre near Strymoniko village along the eastern boundary of the Vertiskos Unit (Figure 2.1). Its age was considered long as Plio-quaternary (Kockel & Walther, 1966; Panagos et al., 1978). However, a tight cluster of ages at 21.1 ± 0.1 Ma was measured here leaving no doubt about the timing of the volcanic eruption near the eastern flank of the basement (Figure 2.4). This sets the Strymoniko volcanic centre as lower Miocene in age and thus, it is necessarily part of the Oligo-Miocene magmatic activity recorded elsewhere in the study area (e.g., Frei, 1992; Gilg & Frei, 1994; Tompouloglou, 1981).

2.6.2 The age of the pegmatites enveloped in basement gneisses

As mentioned in the introduction, the age of the pegmatites found almost everywhere within the basement is rather unknown (Figure 2.5). Based on our dating results, the pegmatites' zircons record Carboniferous growth over Ordovician (or older) cores (Figure 2.6). The nature of the Carboniferous event is unknown and it can be either metamorphic or magmatic in origin. In other words, the pegmatites are: (a) Ordovician in age with a metamorphic overprint during the Carboniferous or (b) they crystallised during the Carboniferous by a magma that was carrying Ordovician (or older) zircons.

Although, the Carboniferous zircon overgrowths of the pegmatites from the basement carry a low Th/U metamorphic signature, the corresponding relatively thick zircon overgrowths that show oscillatory zoning pattern point toward a high-thermal event of magmatic origin (Figure 2.6). In other words, *we envisage crystallisation of the pegmatites during a magmatic event of Upper Carboniferous age (circa 320 Ma).* This makes necessary the existence of a Th-depleted magma that assimilated pre-Carboniferous grains before crystallise at circa 320 Ma. With the exception of the small Flamouri granodiorite which is dated at 304.1 ± 7.0 Ma (SHRIMP; Dimitrios Kostopoulos personal communication), no other plutons of such an age exist in the area and, at a first glance, such a restricted occurrence cannot account for the widespread occurrence of pegmatites across the study area. As such, we cannot confidently discriminate between the magmatic or metamorphic character of the Carboniferous event recorded by the pegmatites.

As shown in Figure 2.5e, the pegmatite SM61 was collected from a set of almost vertical dykes intruding, according to the geological map of the area, the Triassic Arnea Magmatic Complex (see Figure 2.1 for location). The fact that no post-Carboniferous zircon were found in the pegmatite, severely questions the age of the host (Figure 2.6). Based on the similar field-appearance between the Triassic Arnea Magmatic Complex and the Carboniferous Flamouri Complex, the results of SM61 strongly questions the regional mapping as far as those two plutons are concerned. In the absence of more detailed sampling grid and dating, *we suspect that similar Carboniferous plutons are mismapped as parts of the Triassic Arnea Magmatic Complex due to their similar-looking field occurrences.* If true, this could also provide a line of evidence for extensive Carboniferous magmatism in the area and confirm the nature of the Carboniferous event recorded by zircon overgrowths in the pegmatites as magmatic. Based on the above, *we suspect the existence of a largely underestimated and possibly mismapped Carboniferous magmatic rocks from the Vertiskos Unit.* This notion is supported by the finding of Carboniferous grains detrital grains from the sedimentary sequences west of the Vertiskos Unit (Meinhold et al., 2009).

2.6.3 The metamorphic age of the amphibolites from the basement

As mentioned in the introduction, there are many occurrences of amphibolites widespread in the study area (Figure 2.9). Their field occurrences suggest that they possibly represent former mafic dykes within the Silurian hosts. The Volvi Complex to the eastern part of the Vertiskos Unit is probably the best studied example in terms of chemistry, tectonic setting and crystallisation age: it shows a within-plate character and is dated at Lower/Middle Triassic (Himmerkus et al., 2005; Liati et al., 2011) (Figure 2.9e,f). The question that arises is whether the widespread garnet-amphibolites found as syn-folial bodies or boudins (Figure 2.9b,c,d,g) within the Silurian hosts are also Triassic in age or they belong to another generation. In an effort to answer that we applied in-situ dating on a garnet-amphibolite collected near Kilkis. We have shown that its zircons crystallised at middle Carboniferous and bear a metamorphic signature (Figure 2.8). *Thus, contrary to Carboniferous magmatic event recorded by the pegmatites, the Lower Carboniferous (circa 340 Ma) event recorded by the amphibolites is more likely or metamorphic origin.*

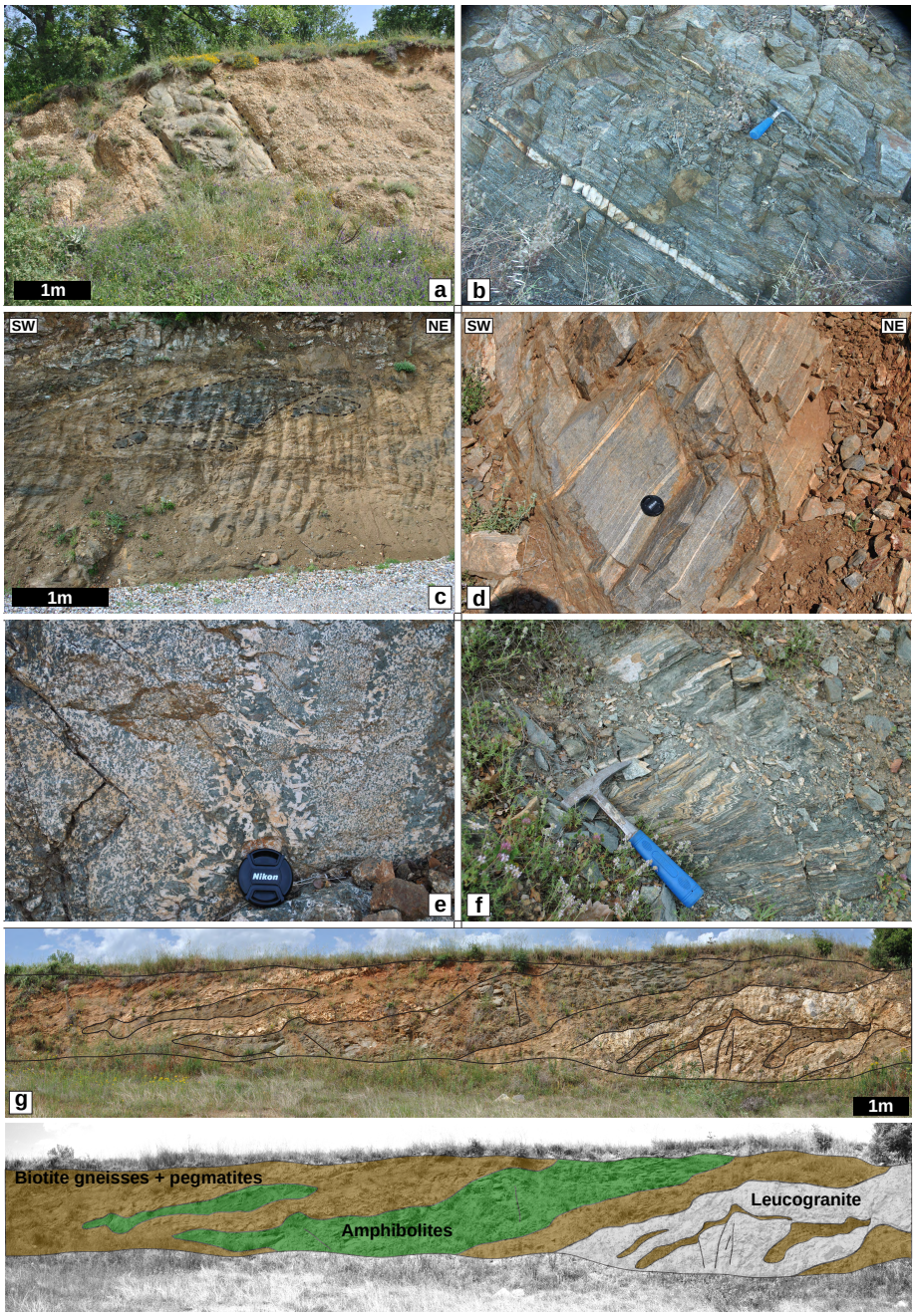

Figure 2.9: Field occurrences of amphibolites from the basement. (a) Almost vertical slightly deformed dioritic dyke parallel to the regional foliation. (b),(d) Banded amphibolites. (c) Amphibolite boudin inside biotite gneisses of the basement. (e) Magmatic gabbroic texture preserved in the Volvi amphibolite. (f) Amphibolite of the Therma amphibolitic body. (g) Alterations of amphibolites, pegmatite-bearing biotite gneisses and leucogranite from the basement.

2.6.4 Palaeozoic/Mesozoic intercalated paragneisses of the basement

Paragneisses appear embedded quite often within the Palaeozoic / Lower Triassic orthogneisses of the Vertiskos Unit (or the Arnea Magmatic Complex). Their deposition age is unknown as no fossils have ever been reported. They were more probably clastic sediments that transformed into gneisses during the Palaeozoic-Mesozoic deformation events.

Here, we applied detrital zircon dating on such intercalated paragneisses from the Vertiskos basement. Based on our findings (Figure 2.7) three age patterns can be deduced: (a) Sample SM8 was collected in proximity to the Triassic Arnea Complex. However, the

youngest concordant zircon is 577 Ma. This excludes the Triassic Arnea Complex as the source area but its age correlates well with the late Neo-Proterozoic orthogneisses found near Pyrgadikia village by Himmerkus et al. (2006) which are interpreted as a remnant arc that was assimilated by the later Ordovician magmatism. Thus, SM8 is interpreted as a former Palaeozoic clastic sediment that sourced mainly by late Neo-Proterozoic zircons. (b) Sample SM11 has also been collected close to the Triassic Arnea Complex but yield no Triassic zircons. On the contrary, the youngest concordant zircon is 447 Ma and point toward sourcing from the Vertiskos Ordovician basement. The shift toward Ordovician sources compared to the SM8 is either due to difference in their deposition age (e.g., SM8 is pre-Ordovician and SM11 post-Ordovician) or simply reflect local variations in the sourcing from different proximal sources. In the latter case there is no need for different deposition age as both samples can be post-Ordovician in age. No matter what, the deposition of the intercalated paragneiss is restricted again to the Palaeozoic. (c) A much different age pattern is that of sample SM15. Although it also appears as intercalated paragneiss within the surrounding Palaeozoic orthogneisses, it bears a dominant age cluster of Triassic zircons. This points towards the Arnea Complex as the main source and limits the possible age of the sedimentary protolith to the Mesozoic.

We have shown that, although extremely similar in appearance, the intercalated paragneisses within the orthogneisses of the Vertiskos Unit can represent both Palaeozoic and Mesozoic clastic sequences. This further demonstrates the complex character of the Vertiskos basement that involves many generations of magmatic rocks and intercalated metasediments. *This implies also that the Mesozoic deformation of the area was rather intense to overprint previous deformation fabrics and to transform the Mesozoic clastic sequences into paragneisses.* The Mesozoic SM15 is the link to the Circum-Rhodope belt further to the west which has been long considered as the Mesozoic sedimentary cover of the Vertiskos Unit (Kockel et al., 1971, 1977; Dixon & Dimitriadis, 1984; Meinhold et al., 2009). *Based on the zircon age spectra of sample SM15 we show that apart from the western flank of the Vertiskos Unit, Mesozoic sequences of currently unknown extend, have been preserved as intercalated paragneisses within the Palaeozoic Vertiskos basement.*

As a last word, we have also shown that a clastic K-feldspar-bearing sediment (SM44) from the base of the Circum-Rhodope belt clearly recycled detritus from the Vertiskos Ordovician basement (Figure 2.4). This is in complete agreement with the notion of the Circum-Rhodope belt being the Mesozoic cover of the Vertiskos Unit.

2.7 Conclusions

A major outcome of this chapter is that the magmatic protolith of the basement orthogneisses (Vertiskos Unit) should now be considered as Ordovician and not Silurian as considered before. This links Chalkidiki with the eastern Rhodope where mafic rocks of similar protolith age have been reported. Widespread pegmatite dykes and amphibolites, whose age is rather unknown, are embedded within the basement. We dated four pegmatites and we envisage a Carboniferous event (at circa 320 Ma) during which they crystallised from a Th-depleted magma. Zircons from a garnet-bearing amphibolite yield also Carboniferous metamorphic ages at circa 340 Ma. This collectively imply that the complex Vertiskos Unit record, apart from the main Ordovician magmatic event, the existence of a Lower Carboniferous metamorphic event that preceded a strong thermal pulse of magmatic origin of Upper Carboniferous age. The latter event crystallised both the pegmatites and largely mismapped and underestimated Carboniferous intrusive rocks.

We have applied zircon dating on a K-feldspar-bearing clastic sediment from the base of the Circum-Rhodope belt that revealed sourcing from the Ordovician orthogneisses of the basement (Vertiskos Unit). We have also conducted detrital zircon dating of intercalated

paragneisses that are embedded in basement orthogneisses. Based on their age spectra, we have concluded that despite the very similar appearance in the field, they belong to clastic sedimentary sequences of different deposition age: Palaeozoic vs Mesozoic. Our findings clearly demonstrates that there are Mesozoic intercalated gneisses within the basement rocks of largely underestimated extend and provide a link with the Mesozoic Circum-Rhodope belt exposed immediately to the west that is known to have been directly sourced from the basement rocks.

Finally, we have also dated an enigmatic trachyte-rhyolite sequence exposed along the eastern part of the basement and which was prior considered as Plio-quaternary. Based on our findings, it is lower Miocene in age and consequently it belongs to the Oligo-Miocene magmatism found elsewhere in the Chalkidiki Peninsula.

Chapter 3

New Mesozoic pelitic eclogites from the western Rhodope (Chalkidiki, northern Greece)

3.1 Introduction

High-Pressure (HP) metamorphic assemblages are commonly overprinted under high temperature (HT) conditions at different stages of the thermal evolution of an orogen (e.g., Laird, 1984; Liati & Seidel, 1996; Parra et al., 2002). At a regional scale, the process responsible for such overprint can be linked to radiogenic heating of a thickened crust, heat produced by viscous dissipation or thermal pulses related to upwelling mantle (e.g., England & Thompson, 1984; Molnar & England, 1990; Burg & Gerya, 2005). A common feature in many orogens is the juxtaposition of rocks that underwent high pressure/low temperature (HP/LT) metamorphism with rocks that are dominated by medium pressure/high temperature (MP/HT) metamorphic assemblages (e.g., Okay, 1989; Whitney et al., 2011). A scenario that explains such juxtaposition can be: either that all rocks experienced an early HP/LT metamorphism but subsequently some of them completely re-equilibrated under HT conditions or that the juxtaposition occurred during a post-metamorphic stage and thus, is of tectonic nature. Deciphering between the mentioned scenarios can be hard in the absence of any preserved HP relicts from the MP/HT rocks.

The Rhodope Metamorphic Province (RMP, northern Greece - southern Bulgaria) is a recently established ultrahigh pressure (UHP) metamorphic province (Mposkos & Kostopoulos, 2001; Perraki et al., 2006; Schmidt et al., 2010; see recent review by Burg, 2012). Peak metamorphic eclogite-facies conditions and subsequent amphibolite-facies metamorphic overprint are recorded by metapelites that locally contain microdiamond inclusions and by variably retrogressed mafic eclogites (e.g., Liati & Seidel, 1996; Mposkos & Kostopoulos, 2001; Moulas et al., 2013). The southwestern part of the RMP is exposed at the Chalkidiki Peninsula of northern Greece and has attracted much less attention compared to the remaining parts of the RMP. There, three major units crop out namely, from west to east: a) a HP Upper Jurassic magmatic arc sequence, b) a HP Triassic - Jurassic meta-sedimentary sequence and c) a Palaeozoic - Lower Mesozoic basement complex that records medium pressure/high temperature (MP/HT) metamorphic conditions. The latter is considered as part of the Rhodopean hanging-wall, an assignment which is supported by the absence of HP relicts and the dominant medium-pressure amphibolite-facies regional metamorphic overprint.

In this contribution we report for the first time, relics of early eclogite-facies conditions of arguably Mesozoic age from the MP/HT rocks of the Chalkidiki. We investigate metapelitic samples by means of micro-textures and mineral chemistry. We then compare selected pelitic samples (chloritoid-bearing garnet-staurolite-mica schists) to modelled mineral assemblages

in the NCKFMASHTiMn (Na_2O-CaO-K_2O-FeO-MgO-Al_2O_3-SiO_2-H_2O-TiO_2-MnO) model system. We use isochemical phase diagram sections (commonly known as pseudosections) calculated by minimization of Gibbs free energy (Connolly, 2005). Model results suggest a high-pressure/medium temperature metamorphic event (1.9GPa / 520^{o}C) that preceded the re-equilibration at MP/HT conditions (1.2GPa / 620^{o}C). Our results are consequential for the geodynamic reconstruction of the Rhodope Metamorphic Province since their interpretation requires the subduction of the MP/HT unit prior to thermal re-equilibration.

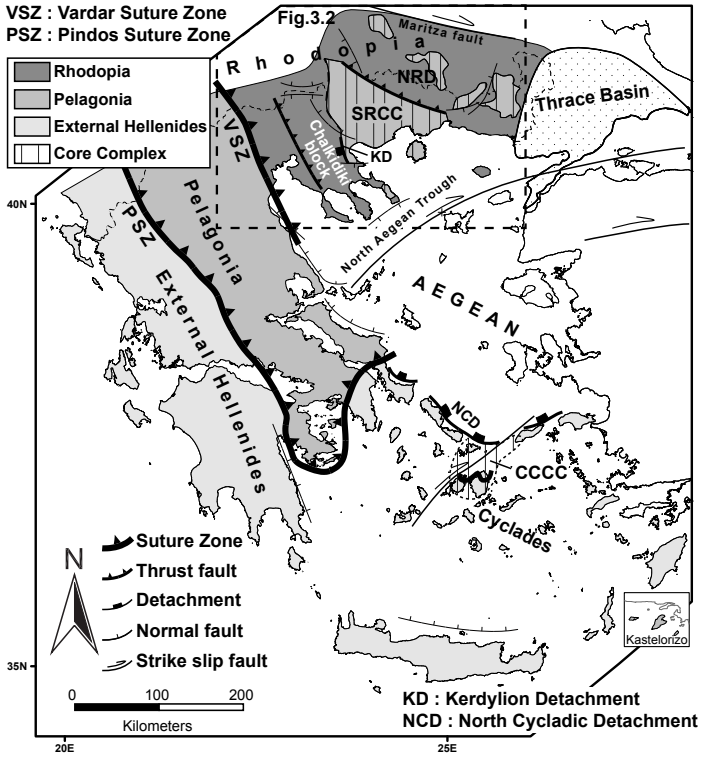

Figure 3.1: Simplified geological map of the Hellenides. The Hellenides are made, from north to south, of three continental blocks (Rhodopia, Pelagonia and External Hellenides) and two intervening sutured oceanic domains (Vardar and Pindos Suture Zones). The study area is located to the hinterland of the Hellenides, in the Rhodope. NRD: Northern Rhodope Domain, SRCC: Southern Rhodope Core Complex, CCCC: Central Cyclades Core Complex.

3.2 Geological setting

3.2.1 The Hellenides

The Hellenides (Figure 3.1) constitute an integral part of the Alpine-Himalayan mountain chain and are the product of convergence between the stable South European margin and northward-driven Gondwana-derived continental fragments (e.g., Dercourt et al., 1993; Stampfli & Borel, 2002). They are formed by Mesozoic southwestward piling-up of three continental blocks (namely the Rhodopia, the Pelagonia and the External Hellenides) and the closure of two intervening oceanic domains, now forming the Vardar-Axios and Pindos Suture Zones, to the north and south, respectively (Robertson, 2002; van Hinsbergen et al., 2005a; Papanikolaou, 2009, 2013) (Figure 3.1). Seismic tomography illustrates beneath the Aegean and down to 1600 Km depth a northward-dipping slab, anchored into the lower mantle (Bijwaard et al., 1998). Various aspects of the Alpine geodynamic evolution of the Hellenides have been discussed at length by van Hinsbergen et al. (2005a), Jolivet & Brun (2010), Ring et al. (2010), Royden & Papanikolaou (2011) and Papanikolaou (2013). In short, the centrepiece of the above studies is a Mesozoic crustal thickening phase followed by

a continuous southward retreat of the subducting Hellenic slab since the Eocene that brought about a concomitant southward migration of magmatism in the severely extending Aegean lithosphere, a slow-down in the rate of plate convergence coeval with acceleration of the trench retreat as well as a southward shift in the ages of progressively younger subduction-related metamorphism. The Rhodope Metamorphic Province is the type-locality to study the Mesozoic convergent history of the Aegean.

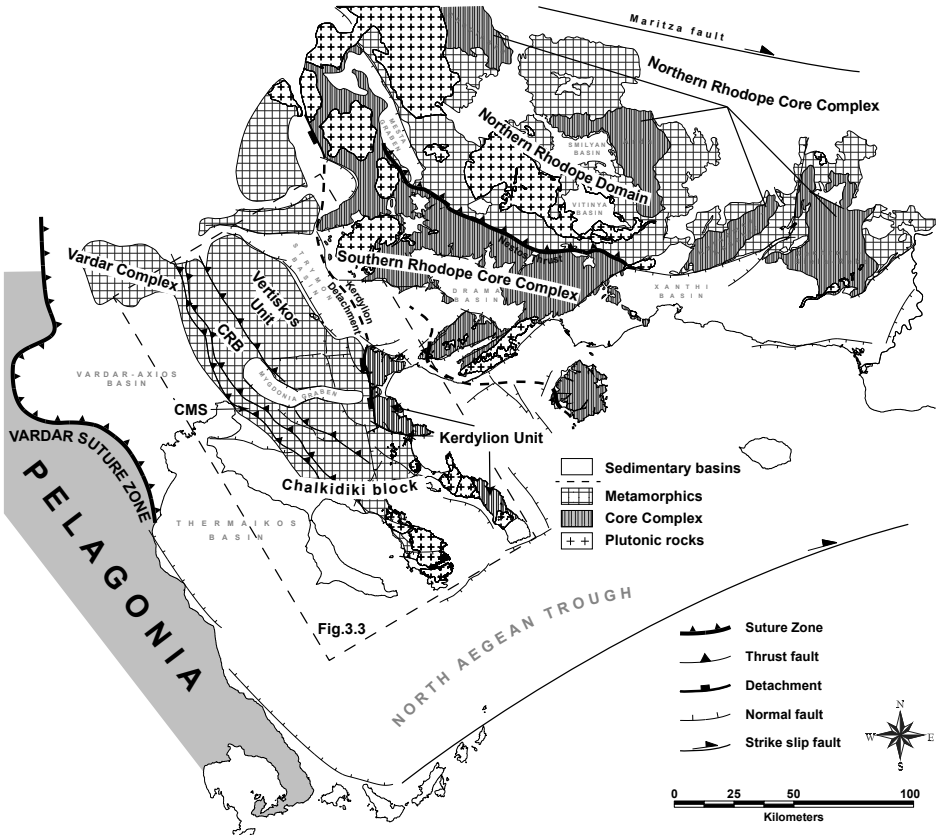

Figure 3.2: Simplified geological map of the North Aegean after Kockel & Mollat (1977), Brun & Sokoutis (2007) and Burg (2012). The Rhodope is composed of three tectonic domains that are, from NE to SW, the Northern Rhodope Domain, the Southern Rhodope Core Complex and the Chalkidiki block. The latter constitute the hanging-wall of the Kerdylion Detachment. CRB: Circum-Rhodope belt, CMS: Chortiatis Magmatic Suite.

3.2.2 The Rhodope Metamorphic Province (RMP)

The *Rhodope Metamorphic Province*, or simply *Rhodope* for convenience, constitutes the hinterland of the Hellenic Orogen (northeast Greece - southwest Bulgaria) (Burg et al., 1990, 1996; Ricou et al., 1998; Krenn et al., 2010; Jahn-Awe et al., 2010; Nagel et al., 2011) (Figure 3.2). It can be viewed as a Mesozoic southwestward piling-up, crustal-scale, syn-metamorphic, amphibolite-facies duplex (Burg et al., 1996; Ricou et al., 1998) strongly affected by Cenozoic extension of core complex type (Dinter & Royden, 1993; Sokoutis et al., 1993; Bonev et al., 2006; Brun & Sokoutis, 2007) and syn- to post-tectonic magmatism (e.g., Kolocotroni & Dixon, 1991; Jones et al., 1992; Marchev et al., 2004, 2013). The Rhodope is bordered to the north by the Maritza dextral strike-slip fault, to the east by the Middle Eocene to Quaternary Thrace Basin, to the south by the Vardar-Axios - Thermaikos basins which in turn roughly correlate with the Vardar Suture Zone (VSZ) (Ricou et al., 1998) and to the south by the North Aegean Trough (Papanikolaou et al., 2006). We adopt a simple threefold division where the Rhodope is divided, from northeast to southwest, into three tectonic domains, from northeast to southwest: (i) the *Northern Rhodope Domain* (NRD),

(ii) the *Southern Rhodope Core Complex* (SRCC), and (iii) the *Chalkidiki block* (Figure 3.2).

To the northeast, within the NRD, typical rocktypes are orthogneisses, eclogites and amphibolites, paragneisses and scarce marble horizons (Mposkos & Liati, 1993; Liati & Seidel, 1996; Turpaud & Reischmann, 2010; Janák et al., 2011; Moulas et al., 2013). Volumetrically-low ultramafic rocks also occur usually at high structural levels. Although upper amphibolite-facies metamorphic rocks are widespread, many occurrences of variably retrogressed eclogites that preserve evidence for a precursor HP phase have been reported in the literature. Evidence for UHP conditions is due to the presence of micro-diamond inclusions in metapelites (Mposkos & Kostopoulos, 2001; Perraki et al., 2006; Schmidt et al., 2010) that indicate minimum local pressure at 3.0GPa (for 600^{o}C). Jurassic and Cretaceous zircon metamorphic ages (circa 150 and 75 Ma) from both garnet-kyanite gneisses and amphibolitised eclogites have been reported (e.g., Bauer et al., 2007; Liati et al., 2011, and references therein). Metamorphic conditions for the HP event recorded in mafic rocks are estimated at 1.9GPa / 700^{o}C (Liati and Seidel, 1996) and for the regional amphibolite-facies overprint at 0.7GPa / 720^{o}C (Moulas et al., 2013). Metapelite assemblages record higher pressures for the high-temperature overprint (1.2-1.3GPa / 700-730^{o}C, Krenn et al., 2008, 2010).

3.2.3 The Chalkidiki block

The southwestern part of the Rhodope is the so-called Serbo-Macedonian Massif of Kockel et al. (1971) (Figure 3.3). The term "Massif" has been rejected by many, if not all, workers afterward and the term Serbo-Macedonian Domain should be used instead. Based on the reference map of Kockel & Mollat (1977) it is composed, from west to east, of four units namely the *Chortiatis Magmatic Suite*, the *Circum-Rhodope belt*, the *Vertiskos Unit* (equivalent to Vertiskos Formation) and the *Kerdylion Unit* (equivalent to Kerdylion Formation) (see also Kockel et al., 1971, 1977; Kauffmann et al., 1976). The latter unit that is located below the Kerdylion Detachment shares a common tectono-thermal history with the SRCC (Brun & Sokoutis, 2007; Himmerkus et al., 2012). The remaining three units define collectively the Chalkidiki block and constitute the hanging-wall of the Kerdylion Detachment that is responsible for the exhumation of the SRCC immediately to the east (Figure 3.3). During exhumation of the latter, the Chalkidiki block underwent a circa 30^o clockwise rotation (Kondopoulou & Westphal, 1986; Brun & Sokoutis, 2007).

The *Vertiskos Unit* is an elongated basement belt with a complex tectono-metamorphic history (Burg et al., 1995; Kilias et al., 1999) (Figure 3.3). In Bulgaria, to the north, it is known as the Ograzden Unit (Zagorchev, 1976). It is a distinct basement fragment that detached from Gondwana and incorporated into the Southern European Arcs by the end of the Palaeozoic (Himmerkus et al., 2007; Meinhold et al., 2010; Kydonakis et al., 2014b). In Greece, typical rocktypes are Silurian - Ordovician granitoids later transformed into orthogneisses (Himmerkus et al., 2009a, see also Chapter 2), intercalated paragneisses and thin marble horizons, leucocratic granitic/pegmatitic intrusions, deformed amphibolites, scarce eclogite boudins and serpentinites (Kockel et al., 1971, 1977). The Arnea-Kerkini Magmatic Complex intruded the Silurian - Ordovician orthogneisses during the Lower Triassic and both, as a coherent basement complex, experienced the same post-intrusion tectono-metamorphic history. Medium-pressure amphibolite-facies regional conditions are estimated at 0.45-0.75GPa / 510-580^{o}C for intercalated quartz + white mica + biotite + garnet + oligoclase ± staurolite ± kyanite schists (Kilias et al., 1999) and at 0.4GPa / 450-550^{o}C for meta-ultramafics with the assemblage antigorite + Fe-Cr spinel + ilmenite ± chlorite ± talc ± tremolite (Michailidis, 1991). Deformed amphibolites from the basement yield the crucial assemblage amphibole + epidote/zoisite + garnet + quartz + plagioclase ± biotite indicating amphibolite-facies conditions at 0.85GPa / 600^{o}C (Dimitrios Kostopoulos, 2014 pers. comm.). Upper Jurassic - Cretaceous metamorphic ages (^{40}Ar/^{39}Ar, K/Ar and Rb/Sr on micas and amphiboles) have been reported for the basement (e.g., Borsi et al., 1965; Harre

et al., 1968; Papadopoulos & Kilias, 1985; de Wet et al., 1989; Christofides et al., 1999, 2007; Lips et al., 2000).

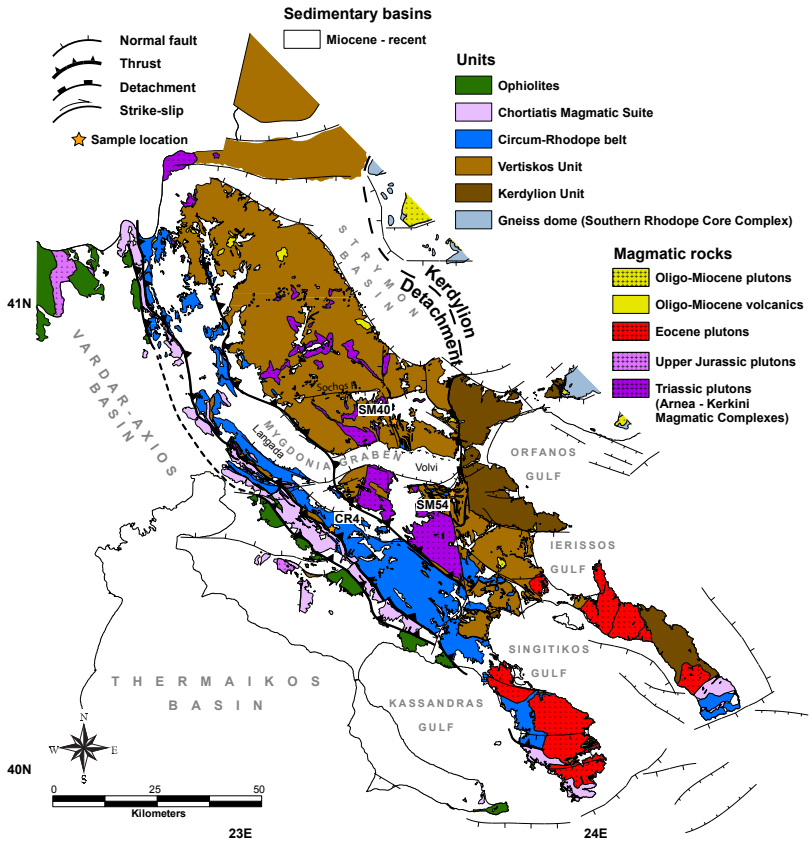

Figure 3.3: Geological map of the Chalkidiki block after Kockel & Mollat (1977) and Sakellariou & Dürr (1993). Sample localities are shown in orange stars.

The *Circum-Rhodope belt* is a Triassic - Jurassic meta-sedimentary sequence locally involving Triassic rhyolites and quartzites at the base (Asvesta & Dimitriadis, 2010, see review in Meinhold & Kostopoulos, 2013) (Figure 3.3). The term Circum-Rhodope belt was originally introduced by Kauffmann et al. (1976) to describe low-grade rocks fringing the basement complex of the Vertiskos Unit to the west, thought of as representing the original Mesozoic stratigraphic cover of the basement. Indeed, Meinhold et al. (2009) reported detrital zircon ages from the base of the meta-sedimentary sequences of the Circum-Rhodope belt and assigned the Vertiskos Unit as their source area. Remnants of garnet-kyanite-staurolite-mica schists toward the eastern part of the Vertiskos Unit have been originally mapped as parts of the Circum-Rhodope belt (Kockel et al., 1977). However, they were interpreted later as separate units and local names where assigned to them (i.e., "Nea Madytos Unit" of Sakellariou & Dürr, 1993, "Bunte Serie" of Papadopoulos & Kilias, 1985). Their map continuity with the Circum-Rhodope belt further to the west strongly suggests that those sequences are part of the Mesozoic sedimentary cover (Dixon & Dimitriadis, 1984) (Figure 3.3). For the purpose of the present study, those garnet-staurolite schists were considered as key elements of the Mesozoic metamorphic evolution of the area and thus, they were selected for thermodynamic calculations (Figure 3.3). The rhyolites from base of the Circum-Rhodope belt yield Lower Cretaceous metamorphic ages (Bertrand et al., 1994). The contact between the Vertiskos Unit and the Circum-Rhodope belt is a sharp NW-trending fault locally showing evidence for multiple re-working (Ricou & Godfriaux, 1994; Tranos et al., 1999).

The *Chortiatis Magmatic Suite*, immediately to the west of the Circum-Rhodope belt, is

made of intensively deformed acidic and intermediate igneous rocks of Upper Jurassic age (Monod, 1964; Zachariadis, 2007) (Figure 3.3). Michard et al. (1994a,b) reported the existence of high-Si phengite (3.52 apfu) from basal rhyolitic meta-tuffs of the Circum-Rhodope belt and relict phengite-glaucophane assemblage from the Chortiatis Magmatic Suite. They also estimated peak conditions at circa 0.8GPa / 350^{o}C. Asvesta (1992) also reported high-Si phengite from the base of the Circum-Rhodope belt and Monod (1964) mentioned "amphiboles which show sometimes a sodic character" from the Chortiatis Magmatic Suite. However, a pervasive greenschist-facies overprint seems to have almost completely erased the evidence of an earlier HP event in most of the Circum-Rhodope belt and the Chortiatis Magmatic Suite.

3.3 Methods / Sampling

3.3.1 Whole-rock chemistry

Selected key samples were first crushed in a steel jaw crusher and then ground in an agate mortar. The powders were digested using standard lithium metaborate ($LiBO_2$) fusion and acid dissolution techniques and subsequently chemically analysed for major elements by ICP-MS (ACME Labs, Vancouver, Canada).

3.3.2 Mineral chemistry

Mineral analyses and garnet elemental maps were obtained at ETH Zurich, Switzerland and at Ifremer (Institut français de recherche pour l'expoitation de la mer), Brest, France using a Jeol JXA 8200 and a Cameca SX 100 electron probe, respectively. Both probes were equipped with 5 wavelength dispersive spectrometers operating at an accelerating voltage of 15 kV with a 2 μm beam diameter and 20 nA beam current. Natural and synthetic materials were used as standards and a CITZAF correction procedure was applied. Back-scattered images were obtained at Université de Rennes1, France and National Technical University of Athens, Greece using a JEOL JSM-7100F Field-Emission Scanning Electron Microscope and a JEOL JSM-6380 Low Vacuum Scanning Electron Microscope, respectively, both operating at an accelerating voltage of 20 kV.

3.3.3 Phase equilibria thermodynamic modelling

Isochemical phase diagram sections were calculated using Gibbs free-energy minimisation (Connolly, 2005). Calculations performed in the NCKFMASHMn(Ti) [Na_2O-CaO-K_2O-FeO-MgO-Al_2O_3-SiO_2-H_2O-MnO-(TiO_2)] model system using the solution models given in Table1 and the thermodynamic database of Holland and Powell (1998, revised 2002). Calcium oxide (CaO) present in apatite was subtracted from the total CaO since apatite is not considered in the thermodynamic calculations.

Table 3.1: Solid solution models used for the calculation of the phase diagram sections.

Mineral / Phase	Solution Model	Source
Biotite	Bio(TCC)	Tajčmanová et al. (2009)
Feldspars	feldspar	Fuhrman & Lindsley (1988)
Garnet	Gt(GCT)	Ganguly et al. (1996)
Ilmenite	IlGkPy	Ideal
White Mica	Mica(CHA1)	Auzanneau et al. (2010); Coggon & Holland (2002)
Chlorite	Chl(HP)	Holland et al. (1998)
Staurolite	St(HP)	parameters from THERMOCALC
Chloritoid	Ctd(HP)	White et al. (2000)
Clino-amphibole	GlTrTsPg	Wei & Powell (2003); White et al. (2003)
Clino-pyroxene	Omph(GHP2)	Diener & Powell (2011)

3.3.4 Sampling grid / Strategy

We have selected three key samples for thermodynamic modelling and P-T estimations (Figure 3.3). CR4 is a phyllite from the Mesozoic cover (Circum-Rhodope belt) that experienced an early HP imprint. As mentioned before, relict HP minerals are extremely rare all along this belt due to later greenschist-facies overprint. Sample CR4 does not contain any HP index mineral and thus, our target is to investigate the conditions of the HT overprint and provide a minimum temperature estimate during that overprint. Samples SM54 and SM40 are typical garnet-staurolite schists from the eastern part of the study area and both belong to a series of small outcrops embedded in basement rocks (Figure 3.3).

3.4 Petrography

Sample CR4 is a fine-grained quartz-mica phyllite. In the field it has a dominant foliation and a prominent NW-trending crenulation lineation. The main mineral phases are, in decreasing amount order, quartz, white mica, chlorite, garnet and opaque minerals. A typical crenulation cleavage is developed by differentiation at the limps of the microlithon domains (Figures 3.4a,b). The microlithons are dominated by quartz and kinked, often chloritised, medium-grained white micas (Figures 3.4a,b). The cleavage domains are made of fine- to medium-grained K-rich white mica or a fine-grained aggregate of K-rich white mica, paragonite and chlorite (Figure 3.4c). Garnet grains (typically 2-3 mm in diameter) appear in the microlithons pseudomorphosed after chlorite (Figure 3.4d). Despite the chlorite alteration, the pseudomorphs still preserve syn-tectonic features. Quartz in the microlithon domains has healing features and is recrystallised with sharp grain boundaries and virtually no undulose extinction.

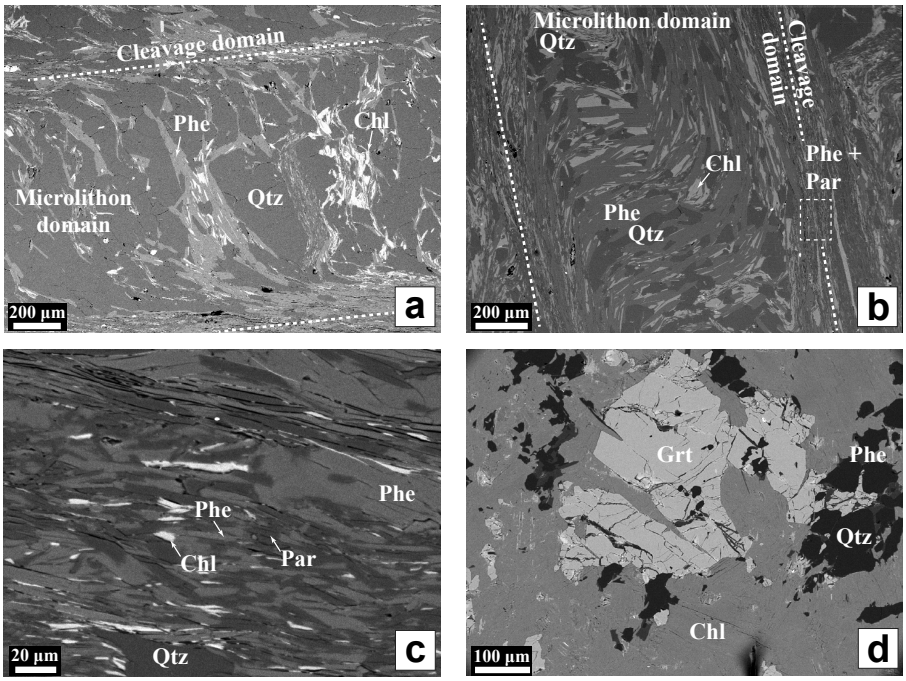

Figure 3.4: Back-scatter images of sample CR4. (a,b) The microlithons are made of coarse-grained phengite, quartz and chlorite whereas the cleavage domains are made of fine-grained intergrowths of phengite, paragonite, chlorite and quartz. (c) Close view of the cleavage domain. (d) Garnet relict from a pseudomorph after chlorite.

Sample SM54 is a representative garnet-staurolite schist. Major phases are white mica,

garnet, staurolite, quartz, biotite, chlorite and sub-ordinate kyanite. Chloritoid also occurs in small amounts but only as inclusion in garnet. Accessory minerals are rutile (almost always rimmed by ilmenite), apatite, zircon and opaques. Garnet appears with exceptionally large grains measuring up to 1 cm in diameter and is the dominant phase enveloped by a medium to fine-grained foliation made of white micas and quartz-rich bands. Shear bands and macroscopically visible spiral garnet indicate a top to SW sense of shear in hand specimen (Figure 3.5a). Under the microscope garnet appears euhedral to subhedral. It contains a relict internal foliation made of aligned quartz, chloritoid, chlorite, margarite, paragonite/muscovite and rutile (often rimmed by ilmenite) which is in continuity with the external foliation implying syn-tectonic garnet growth (Figures 3.6a,b,c). The matrix foliation is made of quartz, phengite and intergrowths of phengite/paragonite (Figure 3.6d). Staurolite shows similar syn-tectonic features and contains quartz, biotite and chlorite as inclusions (Figures 3.6e,f). The internal foliation in garnet and staurolite is virtually linear/flat while the external one is heavily folded. Extremely rare kyanite crystals are observed exclusively in the matrix. Rutile exists in the matrix where it is rimmed by ilmenite. Hematite occurs in trace amounts in the matrix and in association with chlorite in late cracks.

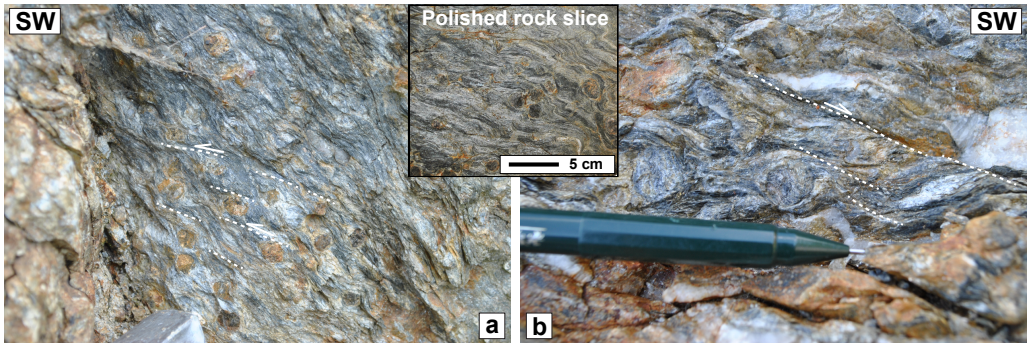

Figure 3.5: Field occurrences of the garnet-staurolite-mica schists.

Sample SM40 is similar to SM54 in terms of texture, mineralogy and deformation pattern. Major phases are quartz, white mica, garnet, staurolite and rutile. Accessory minerals are monazite, zircon, and rarely ilmenite and allanite. The matrix is made of a dominant K-rich white mica, paragonite, rutile and quartz. Garnet appears with euhedral to subhedral grains measuring up to 1.5 cm in diameter (Figure 3.5b). Staurolite is relatively rare compared to SM54 but appears in larger crystals. As in sample SM54, both garnet and staurolite show syn-tectonic features. Rutile also appears as large porphyroblasts in the matrix often surrounded by chlorite. Garnet contains white mica, rutile, ilmenite, chlorite, rare pyrite and an impressive amount of tourmaline as aligned inclusions. Contrary to SM54, no chloritoid was found in this sample.

3.5 Mineral chemistry

A petrogenetic table as well as the bulk composition of the studied samples are given in Table2. Selected mineral analyses from the phyllite and the garnet-staurolite schists are given in Table3. Structural formulas are calculated on the basis of 11 oxygens for micas, 12 oxygens for garnet and chloritoid, 14 oxygens for chlorite and 23 oxygens for staurolite. An overview of the micas and garnet compositions is shown in Figure 3.7 and Figure 3.8, respectively.

CR4: The foliation is made of locally chloritised muscovite/paragonite intergrowths. Paragonite from the matrix has Na/(Na+K) ratio (atoms per formula unit - apfu) around 0.90 and contains small amount of Ca (less than 0.1 apfu). The Si content of the K-rich mica

Table 3.2: Petrogenetic table of the studied samples and corresponding bulk rock compositions.

	Sample	*CR4*	*SM40*	*SM54*
	Latitude	40.526	40.761	40.610
	Longitude	23.222	23.415	23.603
	Rocktype	*garnet phyllite*	*garnet-staurolite-mica schist*	
Major phases	**quartz**	x	x	x
	muscovite	x	x	x
	paragonite	x	x	x
	margarite			*
	chloritoid			*
	biotite		chloritised	x
	garnet	x	x	x
	plagioclase			
	K-feldspar			
	kyanite			x
	staurolite		x	x
	chlorite	x	x	x
Accesory phases	**rutile**		x	x
	titanite			
	ilmenite		x	x
	monazite		x	
	apatite			x
	zircon	x	x	x
	epidote			
	allanite		x	
	fe-oxides	x		x
	xenotime			
	Whole rock chemistry			
	SiO_2	63.67	44.46	56.12
	TiO_2	0.57	1.15	0.82
	Al_2O_3	16.60	27.65	21.77
	Fe_2O_3	4.24	3.00	3.18
	FeO	2.11	5.32	3.61
	MnO	0.06	0.12	0.14
	MgO	1.44	2.26	1.56
	CaO	0.31	0.85	0.80
	Na_2O	1.04	1.55	1.34
	K_2O	2.81	4.68	3.32
	P_2O_5	0.17	0.16	0.19
	LOI	5.30	7.06	5.46
	Total	98.32	98.25	98.32

* Only as inclusion

from the matrix ranges from 3.1 to 3.25 apfu and contains up to 2.4 wt% Na. No systematic chemical variation between the large (microlithon domains) and the smaller (crenulation domains) mica grains was observed. Quartz and iron oxides are also common in the matrix. Garnet is extremely rare as it has been largely pseudomorphosed by chlorite. Garnet composition is between $Alm_{67}Grs_{23}Sps_6Pyr_4$ and $Alm_{60}Grs_{25}Sps_{12}Pyr_6$. The maximum measured Mg# (Mg/(Mg+Fe), apfu) of the chlorite replacing garnet is 0.38.

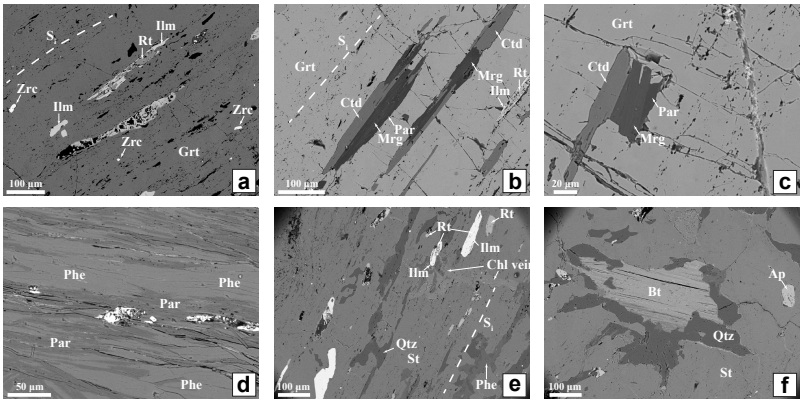

Figure 3.6: Back-scatter images of sample SM54. (a,b,c) The internal foliation (S_i) in the garnet is made of elongated chloritoid, paragonite, margarite and rutile rimmed by ilmenite. (d) Medium- to coarse-grained intergrowths of phengite and paragonite from the matrix. (e,f) The internal foliation(S_i) in the staurolite contains quartz, rutile (often replaced by ilmenite) and biotite.

SM54: White micas show a range of compositions. Potassium-rich white mica is dominant in the matrix and along with paragonite form the main foliation of the rock. The Si

Table 3.3: Representative electron microprobe mineral analyses (in wt %).

sample	*CR4*	*CR4*	*CR4*	*CR4*	*CR4*	*CR4*	*CR4*	*SM54*
rocktype	*phyllite*	*phyllite*	*phyllite*	*phyllite*	*phyllite*	*phyllite*	*phyllite*	*grt-st schist*
mineral	chl	chl	phe	phe	par	grt	grt	chl
texture	pseudomorphs	pseudomorphs	matrix	matrix	matrix	pseudomorphs	pseudomorphs	matrix
SiO_2	24.53	24.47	47.07	48.27	46.66	37.24	37.12	29.52
TiO_2	0.02	0.06	0.37	0.25	0.05	0.09	0.14	2.54
Al_2O_3	21.78	21.35	32.87	32.20	39.91	21.32	21.23	20.35
Fe_2O_3(T)	-	-	-	-	-	-	-	
FeO(T)	30.19	30.88	2.10	2.30	0.78	30.34	28.37	27.01
MnO	0.43	0.51	0.03	-	0.02	2.50	5.27	0.03
MgO	10.57	9.50	1.46	1.64	0.11	1.10	0.92	8.09
CaO	0.01	0.03	-	-	0.25	7.92	7.87	0.30
Na_2O	-	0.03	1.09	0.59	6.54	0.01	0.03	0.11
K_2O	-	0.03	9.72	9.76	1.09	0.01	-	0.80
TOTAL	**87.52**	**86.88**	**94.70**	**95.00**	**95.41**	**100.53**	**100.97**	**88.78**
	[14] O	[14] O	[11] O	[11] O	[11] O	[12] O	[12] O	[14] O
Si	2.66	2.69	3.16	3.22	2.98	2.98	2.97	3.07
Ti	0.00	0.00	0.02	0.01	0.00	0.01	0.01	0.20
Al	2.79	2.77	2.60	2.53	3.01	2.01	2.00	2.50
Fe^{+3}	0.00	0.00	0.00	0.00	0.00	0.00	0.00	0.00
Fe^{+2}	2.74	2.84	0.12	0.13	0.04	2.03	1.90	2.35
Mn	0.04	0.05	0.00	0.00	0.00	0.17	0.36	0.00
Mg	1.71	1.56	0.15	0.16	0.01	0.13	0.11	1.26
Ca	0.00	0.00	0.00	0.00	0.02	0.68	0.67	0.03
Na	0.00	0.01	0.14	0.08	0.81	0.00	0.00	0.02
K	0.00	0.00	0.83	0.83	0.09	0.00	0.00	0.11
TOTAL	9.94	9.92	7.01	6.96	6.96	8.01	8.02	9.54
Mg#	*0.38*	*0.35*	*0.55*	*0.56*	*0.19*	*0.06*	*0.05*	*0.35*

continue...

sample	*SM54*	*SM54*	*SM54*	*SM54*	*SM54*	*SM54*	*SM54*	*SM54*
rocktype	*grt-st schist*	*grt-st schist*	*grt-st schist*	*grt-st schist*	*grt-st schist*	*grt-st schist*	*grt-st schist*	*grt-st schist*
mineral	chl	bt	ctd	ctd	par	par	mar	phe
texture	st inclusion	st inclusion	grt inclusion	grt inclusion	matrix	grt inclusion	grt inclusion	matrix
SiO_2	26.85	38.40	25.32	24.96	45.66	43.35	29.81	46.65
TiO_2	-	1.39	-	-	-	-	-	0.44
Al_2O_3	22.60	21.39	41.13	41.03	40.69	41.74	50.61	35.37
Fe_2O_3(T)	-	-	-	-	-	-	-	-
FeO(T)	20.83	12.54	22.52	23.43	-	1.05	1.10	1.08
MnO	-	-	-	-	-	-	-	-
MgO	17.21	13.30	3.52	2.98	-	-	-	0.97
CaO	-	-	-	-	0.88	1.89	12.22	-
Na_2O	-	-	-	-	6.80	6.57	1.27	1.63
K_2O	-	8.64	-	-	1.17	0.60	0.00	8.85
TOTAL	**87.50**	**98.10**	**92.49**	**92.40**	**95.19**	**95.20**	**95.01**	**95.00**
	[14] O	[14] O	[12] O	[12] O	[11] O	[11] O	[11] O	[11] O
Si	2.75	2.77	2.06	2.04	2.93	2.80	2.00	3.09
Ti	0.00	0.08	0.00	0.00	0.00	0.00	0.00	0.02
Al	2.73	1.82	3.95	3.96	3.08	3.18	3.99	2.76
Fe^{+3}	0.00	0.00	0.00	0.00	0.00	0.00	0.00	0.00
Fe^{+2}	1.78	0.76	1.53	1.61	0.00	0.06	0.06	0.06
Mn	0.00	0.00	0.00	0.00	0.00	0.00	0.00	0.00
Mg	2.63	1.43	0.43	0.36	0.00	0.00	0.00	0.10
Ca	0.00	0.00	0.00	0.00	0.06	0.13	0.88	0.00
Na	0.00	0.00	0.00	0.00	0.85	0.82	0.17	0.21
K	0.00	0.79	0.00	0.00	0.10	0.05	0.00	0.75
TOTAL	9.89	7.64	7.97	7.97	7.00	7.04	7.09	6.99
Mg#	*0.60*	*0.65*	*0.22*	*0.18*	*0.00*	*0.00*	*0.00*	*0.61*

Table 3.3 continue...

sample	*SM54*	*SM54*	*SM54*	*SM54*	*SM54*	*SM54*
rocktype	*grt-st schist*	*grt-st schist*	*grt-st schist*	*grt-st schist*	*grt-st schist*	*grt-st schist*
mineral	st	st	grt	grt	grt	grt
texture	matrix	matrix	rim	rim	core	core
SiO_2	28.99	28.40	37.79	36.88	37.43	36.85
TiO_2	0.48	0.55	0.05	-	0.07	0.14
Al_2O_3	54.66	54.08	21.40	21.70	21.45	21.11
Fe_2O_3(T)	-		-	-	-	-
FeO(T)	13.10	12.87	35.95	35.46	30.05	30.95
MnO	0.02	0.02	0.18	0.11	4.90	4.40
MgO	1.62	2.19	3.53	3.59	1.10	1.12
CaO	0.01	-	2.86	2.79	6.38	6.28
Na_2O	-	-	0.02	-	-	0.02
K_2O	-	-	-	-	-	-
TOTAL	**98.90**	**98.13**	**101.78**	**100.53**	**101.38**	**100.88**
	[23] O	[23] O	[12] O	[12] O	[12] O	[12] O
Si	3.95	3.90	2.98	2.95	2.98	2.96
Ti	0.05	0.06	0.00	0.00	0.00	0.01
Al	8.78	8.76	1.99	2.04	2.01	2.00
Fe^{+3}	0.00	0.00	0.00	0.00	0.00	0.00
Fe^{+2}	1.49	1.48	2.37	2.37	2.00	2.08
Mn	0.00	0.00	0.01	0.01	0.33	0.30
Mg	0.33	0.45	0.42	0.43	0.13	0.13
Ca	0.00	0.00	0.24	0.24	0.54	0.54
Na	0.00	0.00	0.00	0.00	0.00	0.00
K	0.00	0.00	0.00	0.00	0.00	0.00
TOTAL	14.61	14.66	8.02	8.03	8.01	8.03
Mg#	*0.18*	*0.23*	*0.15*	*0.15*	*0.06*	*0.06*

content of the K-rich mica ranges from 3.08 to 3.25 apfu. White micas that are included in the garnet have more paragonite-rich and margarite-rich compositions. Paragonite and margarite inclusions in the garnet show fine-grained intergrowths (Figure 3.6b,c) compared to the more coarse-grained intergrowths of matrix K-rich white mica and paragonite (Figure 3.6d). Paragonite inclusions have Na/Na+K (apfu) ratio up to 0.94 and contain small amount of Ca (less than 0.13 apfu). Margarite contains between 0.17 and 0.39 apfu Na content. Chloritoid is Fe-rich and appears exclusively as inclusion in garnet parallel to an internal, virtually linear/flat, foliation in relation with margarite, paragonite and rutile (sometimes surrounded by ilmenite) (Figure 3.6b,c). Its Mg# range from 0.18 to 0.22 apfu. Annite-rich biotite is dominant in the matrix and phlogopite-rich biotite is found as inclusion in staurolite. In the matrix, the biotite Mg# ranges between 0.32 and 0.47 whereas as inclusion in staurolite, the biotite Mg# reached 0.65 (Figure 3.6f). Similar to biotite, matrix chlorite has lower Mg# (0.35-0.48) compared to the chlorite crystals included in staurolite (0.6). The Al content of biotite varies between 2.5 and 3 apfu. Garnet shows zoning in major elements (Figure 3.9) characteristic for growth during temperature increase (e.g., Harris et al., 2004). Its composition ranges from $Alm_{67}Grs_{18}Sps_{11}Pyr_4$ to $Alm_{79}Grs_7Sps_0Pyr_{14}$ from core to rim. Staurolite Mg# ranges from 0.18 to 0.23.

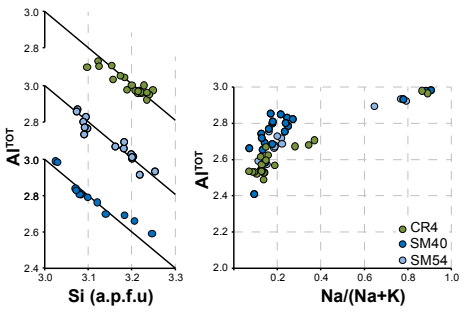

Figure 3.7: White micas chemistry.

SM40: Potassium-rich white mica is dominant in the matrix and its composition has up to 3.25 apfu Si and up to 0.24 apfu Na contents. Paragonite is less abundant with Na/Na+K ratio up to 0.9 and it contains less than 1 wt% Ca (0.04 apfu). Chlorite shows a narrow range of compositions with Mg# between 0.45 and 0.51. Garnet has composition similar to that of SM54 and displays zoning in major elements with $Alm_{65}Grs_{20}Sps_{11}Pyr_4$ cores and $Alm_{80}Grs_9Sps_0Pyr_{11}$ rims. As mentioned before, tourmaline is abundant as inclusion in the garnet but it has never been observed elsewhere. It belongs to the dravite series and it contains about 3 wt% Na and less than 1

wt% Ca. Staurolite Mg# ranges from 0.19 to 0.22.

3.6 Isochemical phase diagram P-T sections

3.6.1 Garnet-bearing phyllite

An isochemical phase diagram section for the sample CR4 has been calculated for the range 0.4-1.6GPa and 350-650^{o}C (Figure 3.10). Due to the absence of rutile, titanite and ilmenite this particular sample composition was modelled in the NCKFMASHMn (i.e., TiO_2 was not considered). For the calculations, total Fe was assumed to be Fe^{+2} and water was taken in excess using the CORK equation of state (EOS) of Holland & Powell (1998). Quadri-variant fields dominate over the calculated P-T area. Penta-variant fields are common at low pressure and low temperature whereas few tri-variant fields are mostly related to the garnet-in and biotite-in reactions. Glaucophane and lawsonite are the Na- and Ca-bearing phases at HP/LT conditions. Potassium- (Wmca1) and Na-white micas (Wmca2) are present in the studied P-T range and they reduce to a single white mica only at T > 600^{o}C for low pressure conditions. Chloritoid is stable above 1.1GPa for T < 550^{o}C. Garnet and biotite are stable at T > 500^{o}C and T > 550^{o}C, respectively. Calculations on the mineral volume and Mg# as well as the garnet end-member molar amounts are given in Supplementary Material #1.

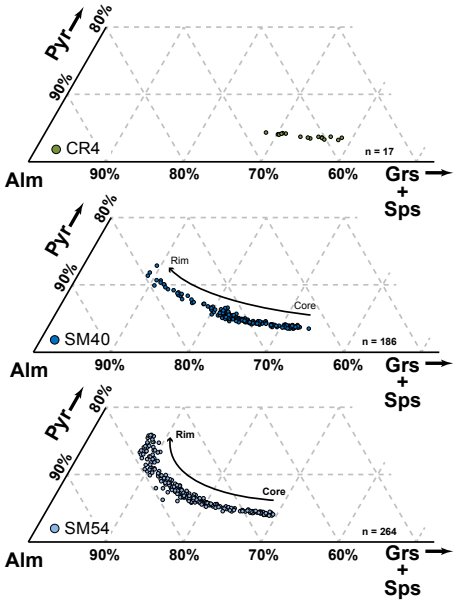

Figure 3.8: Garnet chemistry.

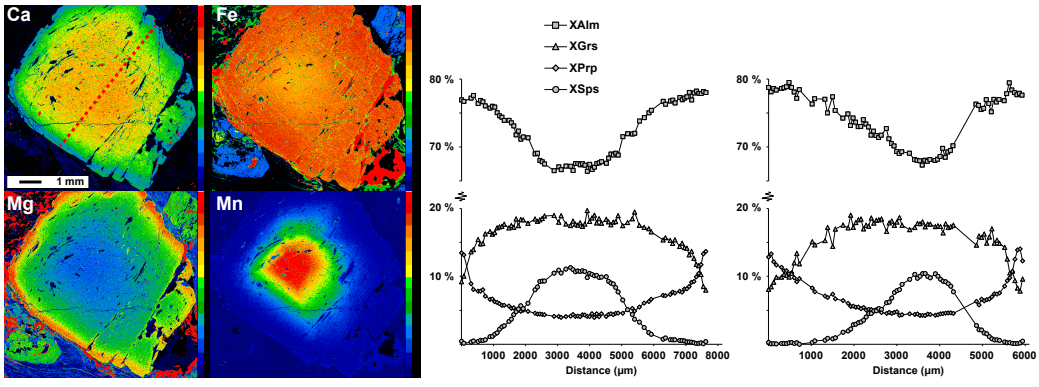

Figure 3.9: Representative garnet element maps (left) and microprobe elemental profiles (right) for sample SM54. The profile to the left corresponds to red dashed line superimposed on the Ca compositional map.

The only evidence for HP metamorphism in the sample can be considered the Si content of the white micas that reaches up to 3.25 apfu. According to the results of the phase diagram section, this is attained at maximum pressure of 1.5GPa (at arbitrarily-chosen temperature of 350^{o}C, see also Supplementary Material #1). At these conditions, chloritoid,

glaucophane and lawsonite participates with 3, 2 and less than 1% in the volume of the rock, respectively, and can be considered as easy to be consumed at a later stage. In the presence of Mn in the system, garnet can be stable at relatively lower temperatures than those predicted for Mn-free systems (Symmes and Ferry, 1992, Mahar et al., 1997, White et al., 2014). Therefore the garnet isograd in the NCKFMASHMn is an excellent marker for the minimum temperature attained during the overprint. As described in the petrography section, garnet is extensively replaced by chlorite (Figure 3.4d) and this can potentially shift garnet's composition (particularly the X_{Fe} and X_{Mg} components) during retrogression. As a result, the measured garnet's compositional isopleths do not cross at a narrow area. The Mn content of garnet suggests that the temperature reached 550^{o}C and this is accordance with the maximum measured chlorite Mg# (Figure 3.10). Based on the intersection of the spessartine content of the garnet and the Mg# of the chlorite from the pseudomorphs, the pressure can be roughly constrained as P $<$ 0.8GPa (Figure 3.10). Biotite is stable at T $>$ 550^{o}C (in small amounts, see Supplementary Material #1) but was not observed in the rock. Thus, although no reliable pressure estimation can be made, the temperature during the retrogression more likely reached 550^{o}C for P $<$ 0.8GPa.

3.6.2 Garnet-staurolite schists

Isochemical phase diagram sections have been calculated in the range 0.4-2.4GPa and 450-750^{o}C for the garnet-staurolite schists (samples SM54 and SM40) in the NCKFMASHMnTi model system. For the calculations, total Fe was assumed to be Fe+2. This is supported by the absence of hematite from the main porphyroblasts (garnet and staurolite). On the contrary, rare hematite is found in the matrix foliation and thus, it is safe to conclude that oxidisation occurred at the post-peak stage of the rock evolution. Water was assumed as a phase in excess using the CORK EOS after Holland and Powell (1998). For reasons of clarity, we will thoroughly describe the results of SM54. Those of the SM40 are given in Supplementary Materials #2, #3 and #4. We note that very similar phase diagram sections were calculated for both samples and the inferred P-T paths are in general agreement.

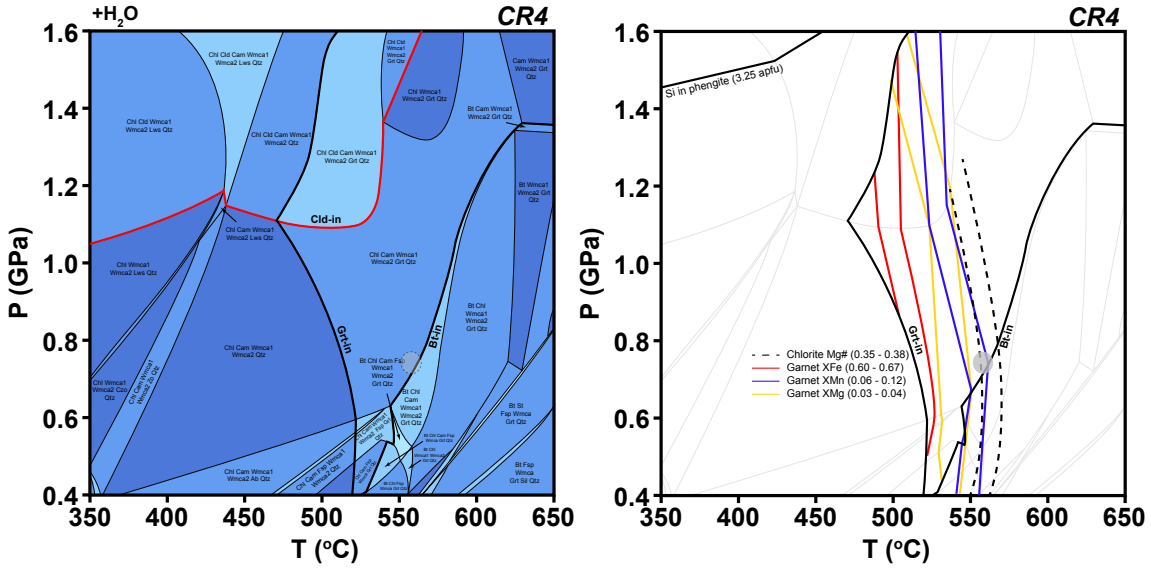

Figure 3.10: Calculated isochemical phase diagram section of sample CR4 (left). Selected compositional isopleths for garnet, phengite and chlorite are superimposed on the section (right). Equilibrium domains are shown in pale grey. See text for details.

The topology of the phase diagram section for sample SM54 is shown in Figure 3.11. Quadri-variant fields dominate over the entire P-T. Tri-variant fields are dominant at medium-

high pressure and low temperature conditions. The P-T phase diagram section predicts the existence of glaucophane and lawsonite as the Na- and Ca-bearing phases at HP/LT conditions. Potassium- (Wmca1) and Na-white micas (Wmca2) are present in the studied P-T range and they reduce to a single white mica only at HT and P < 1.0GPa conditions. Garnet is stable at T > 500^{o}C. Chloritoid is restricted at P > 0.8GPa and it disappears for T > 600^{o}C. Biotite is stable at T > 520^{o}C and both with staurolite are stable at P < 1.3GPa. Calculations on the mineral volume and Mg# as well as the garnet end-member molar amounts are given in Supplementary Material #5.

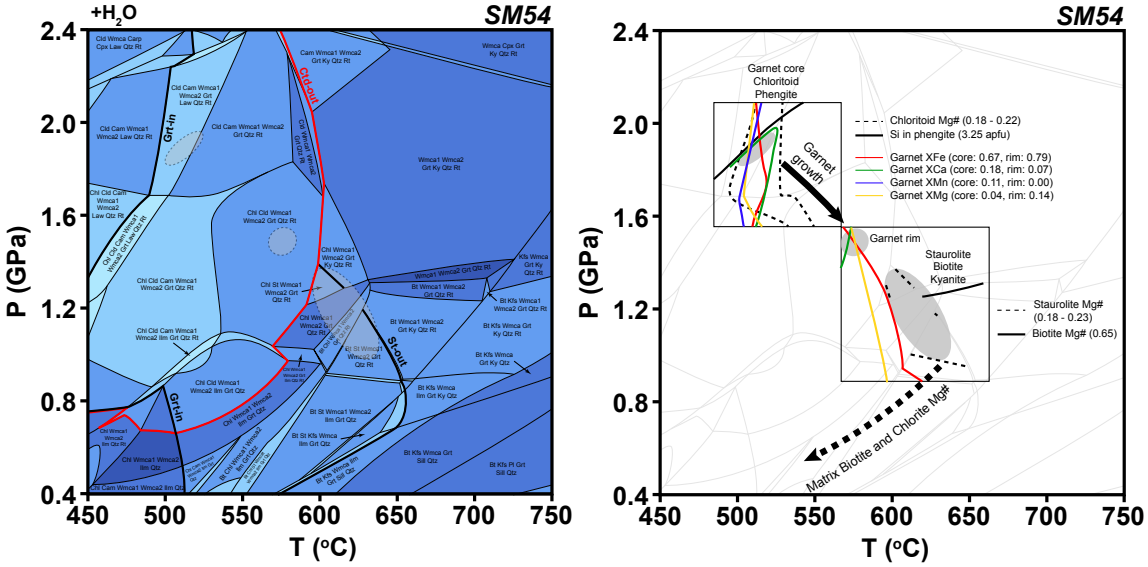

Figure 3.11: Calculated isochemical phase diagram section of sample SM54 (left). Selected compositional isopleths for garnet, chloritoid, phengite, staurolite and biotite are superimposed on the section (right). Equilibrium domains are shown in pale grey. The inferred P-T path is drawn. See text for details.

Based on textural observations, a first HP/LT assemblage is characterised by the co-existence of garnet, chloritoid, white mica and rutile (Figure 3.6b,c). The relative large size of the garnet crystals (cm scale) and the temperature estimate that is below 650^{o}C (see section below) implies that garnet's growth composition is not significantly changed by diffusion (e.g., Caddick et al., 2010). This allow us to use composition isopleths to infer the metamorphic P-T history. Garnet core isopleths and chloritoid Mg# (0.18 - 0.22) cross at 1.8-2.0GPa / 520^{o}C (Figure 3.11). This in agreement with the maximum measured Si content in phengite which also constrains the pressure to a maximum of 2GPa. Based on the calculated P-T section, this first metamorphic assemblage is located within a tri-variant field that also includes lawsonite and/or glaucophane as Ca- and Na-bearing phases (Figure 3.11). Their modal amount is less than 1% for the lawsonite and less than 8% for the glaucophane and thus, it is reasonable to assume that if ever co-existed with chloritoid at the first stage, they were subsequently consumed at a later stage of the evolution of the rock (c.f., Cruciani et al., 2013). Besides, both Ca- and Na-white micas are seen in coexistence with chloritoid inclusion in garnet and may represent phases after former lawsonite and glaucophane (Figure 3.6b,c). The garnet rim composition isopleths cross at 1.5GPa / 570^{o}C, in close proximity to the chloritoid-out reaction. We note that chloritoid is found solely as inclusion in garnet, both in its core and rim. Thus, a heating decompression path within the stability field of chloritoid with increasing garnet volume can be drawn (Figure 3.11). The HT peak overprint is deduced from the co-existence of staurolite (Mg# 0.18 - 0.23 apfu), garnet, biotite (maximum Mg# 0.65 apfu as inclusion in staurolite), chlorite (Mg# 0.6 apfu as inclusion in staurolite) and scarce kyanite. The inferred conditions for that stage are constrained at 1.0 - 1.3GPa and

600 - 640^{o}C (Figure 3.11). Matrix biotite and chlorite record less Mg# compared to that as inclusion in the staurolite, compatible with the P-T section predictions (Figure 3.11) and thus we can infer that they record further cooling/decompression metamorphic conditions.

3.7 Discussion

3.7.1 Summary of the HP events from the Chalkidiki block

Evidence for an early HP from the Chalkidiki block is due to the existence of high-Si phengite and relict glaucophane-bearing assemblages from the base of the Circum-Rhodope belt (cover hereafter) and the Chortiatis Magmatic Suite (arc hereafter), respectively (Asvesta, 1992; Michard et al., 1994a,b) (Figure 3.3). In addition, Tithonian sediments that are involved in the Chalkidiki thrust system locally contain glaucophane (Ricou, 1965). Further to the west, the Paikon Arc, which is considered as equivalent of the Chortiatis Magmatic Suite (Anders et al., 2005; Zachariadis, 2007), contains lawsonite and Na-amphibole (winchite and barroisite) (Baroz et al., 1987). The evidence for an early HP event from the cover and the arc units has been largely erased by later HT overprint.

The age of the HP event recorded by the cover and the arc units is essentially Alpine due to their Triassic - Jurassic protolith ages. Michard et al. (1994a,b) proposed an Upper Jurassic age for the HP event. However, based on existence of Tithonian sediments that are involved in the thrust system of the Chalkidiki and that contain neo-formed glaucophane, albite, sericite and epidote (Ricou, 1965), the HP event should be post-Upper Jurassic in age.

Evidence for a HP episode from the Vertiskos Unit (basement hereafter) is due to rare eclogite occurrences. Sidiropoulos (1991) and Kourou (1991) described eclogite relicts in the cores of amphibolite boudins enclosed in gneisses from the northern and central parts of the study area, respectively. In both occurrences the eclogites are strongly retrogressed and dominated by amphibolite- or even greenschist-facies minerals. Similar retrogressed eclogites were also described by Dimitriadis & Godelitsas (1991) further to the south. Kostopoulos et al. (2000) reported an eclogite lens mantled by trondhjemite enclosed, in turn, in amphibolite near Galarinos Village. The existence of eclogites from the basement is extremely rare and in most cases, if not all, the outcrops have been eroded. Therefore, their direct dating is impossible. In the absence of any radiometric or other criteria, the age of the eclogite-facies event from the basement remains unknown and its attribution to Alpine processes could not be neither inferred nor excluded.

Based on our new findings, we will summarise in the following sections the metamorphic conditions and the timing of the HP from the basement. Then we will link both genetically and temporarily the HP events experienced by the units of the Chalkidiki block defining the nature of the juxtaposition of the HP units (cover/arc) with the Barrovian MP/HT unit (basement). Eventually we will attempt incorporating the southwestern (Chalkidiki block) and the northeastern (Northern Rhodope Domain) parts of the Rhodope into the overall Mesozoic convergence setting.

3.7.2 Revised P-T path of the garnet-staurolite schists: Barrovian paths revisited

The basement complex of the Chalkidiki block has long been considered as showing exclusively a Barrovian medium-pressure amphibolite-facies peak metamorphic conditions and as such it has been considered as part of the Mesozoic Rhodopean hanging-wall. This is supported by i) the predominance of garnet-staurolite schists (typical of amphibolite-facies conditions) that are quite often intercalated within orthogneisses and ii) the lack of any,

reliable, evidence for a Mesozoic HP event. In addition, detrital garnet, kyanite and staurolite have been exhaustively found in recent sedimentary basins sourced from the basement (Georgiadis, 2006) attributing a regional character to the amphibolite-facies overprint.

We have chosen here to study key garnet-staurolite schists (Figure 3.5) exposed as thin slivers toward the eastern part of the basement to investigate the hypothesis of a preceding HP phase of Alpine age before the regional amphibolite-facies overprint (Figure 3.3). The schists belong to the Triassic - Jurassic cover (Kockel & Mollat, 1977; Kockel et al., 1977; Dixon & Dimitriadis, 1984) and therefore they are excellent candidates to record Alpine tectono-metamorphic events. The schists, also studied by Papadopoulos & Kilias (1985) and (Sakellariou & Dürr, 1993), contain a conspicuous mineral assemblage made of garnet, staurolite and chloritoid but no P-T estimations are available.

Experimental data and petrogenetic grids have greatly improved our understanding of the metamorphism of pelitic lithologies (e.g., Albee, 1965, 1972; Thompson, 1976). Since the early petrogenetic grids that incorporated thermodynamic data in the simple system KF-MASH (K_2O-FeO-MgO-Al_2O_3-SiO_2-H_2O) for pelitic schists, it is known that chloritoid can co-exist with garnet at medium to high pressure and low to medium temperature whereas staurolite has a narrow stability field at medium pressure and temperature (e.g., Spear & Cheney, 1989; Powell & Holland, 1990; Xu et al., 1994; Wei & Powell, 2003). Kyanite is predicted to be present with garnet + chloritoid at eclogite-facies conditions for Al-rich/Mg-poor bulk compositions but is restricted to the higher temperature for decreasing Al content (Wei & Powell, 2003). Indeed garnet + chloritoid assemblage (often co-existing with kyanite, phengite and rutile) has been found in eclogite-facies meta-pelites from the Alps (e.g., Spear & Franz, 1986; Vuichard & Ballèvre, 1988; Smye et al., 2010), the Carpathians (e.g., Negulescu et al., 2009), Norway (e.g., Hacker et al., 2003) and Sardinia (Cruciani et al., 2013). More complex thermodynamic systems that involve also Na2O and CaO (NCKFMASH) would lead to stabilisation of Na-bearing phases at high pressure such as Na-pyroxene, Na-amphibole and paragonite shifting at the same time the invariant equilibria to lower pressure and/or lower temperature (Wei & Powell, 2006).

Based on micro-textures, we showed that the eclogite-facies garnet + chloritoid + phengite + rutile assemblage precedes the amphibolite-facies garnet + staurolite ± kyanite assemblage (Figure 3.6). Using phase diagram sections and mineral chemistry (Figures 3.7, 3.8, 3.9) and with reference to the results of SM54, we inferred early HP conditions at 1.8-2.0GPa / 520^{o}C and subsequent re-equilibration at 1.0-1.3GPa / 600-640^{o}C (Figure 3.11). Thus, the garnet-staurolite schists carry evidence for a preceding HP event in the eclogite-facies (close to blueschist/eclogite-facies transition) before the dominant regional amphibolite-facies overprint. Based on their protolith age, the HP event is essentially of Mesozoic age. This has an important consequence and necessitates the re-consideration of the regional evolution of the Chalkidiki (see next paragraph).

3.7.3 Metamorphic evolution of the southwestern Rhodope Metamorphic Province

The Chalkidiki block of northern Greece is the southwestern part of the Rhodope Metamorphic Province and thus, an important element of the latter (Figure 3.2). We mentioned in the introduction that an interesting orogenic characteristic is the juxtaposition of rocks that underwent HP/LT metamorphism with rocks that are dominated by HT metamorphic assemblages (e.g., Maruyama et al., 1996, and references therein). That is the case of the Chalkidiki block where the cover and arc units that carry evidence for a HP event and are in contact with a basement complex that experienced MP/HT metamorphic conditions (Figure 3.3). At a first glance, such juxtaposition seems to impose the existence of a strong discontinuity between the HP units, to the west, and the HT rock units lying to the east. However, as we exemplified here, there is also a preceding HP eclogite-facies from the basement that

was followed by thermal re-equilibration under MP/HT conditions.

On the contrary, at the scale of the whole Chalkidiki block there is a gradient in the metamorphic conditions: from east to the west, they decrease from eclogite-facies (and subsequent amphibolite-facies overprint) to blueschist-facies (and greenschist/lower amphibolite-facies overprint). In details, according to Michard et al. (1994a,b) peak pressure to the west is of the order of 0.8GPa whereas our estimation for the easternmost part is between 1.8 and 2.0GPa (Figure 3.11). The same holds true for the temperature variation. According to Michard et al. (1994a,b) the temperature at the peak pressure event was of the order of 350^oC for the western part and based on our calculations, the HT overprint reached at least 550^oC (Figure 3.10). However, the HT overprint to the east, was of the order of 650^oC (Figure 3.11).

The discovery of an early HP Alpine event from the MP/HT basement fits a model that involves a common early metamorphic history for both the basement and the HP cover/arc units. We envisage here a common genetic metamorphic process responsible for the attained metamorphic conditions that experienced by both the basement and the cover/arc units. Despite the late variable degree of overprint of both the basement and its cover, we argue that their contact should not be considered as an important geological discontinuity (Figure 3.3). It is definitely of tectonic origin but the rock units both in the foot-wall and in the hanging-wall experienced the same, yet of different intensity, metamorphic events.

3.7.4 Mesozoic metamorphic gradient of the Rhodope Metamorphic Province

As briefly described in the introduction, the Rhodope Metamorphic Province forms the hinterland of the Hellenic Orogen. Following a Jurassic - Cretaceous piling-up phase (Burg et al., 1990, 1995, 1996; Ricou et al., 1998), the Tertiary collapse of the Hellenic Orogen resulted in large-scale extension of core complex type, exhumation of migmatitic gneiss domes and dismember of the Rhodopean gneiss imbricates (Dinter & Royden, 1993; Sokoutis et al., 1993; Brun & Sokoutis, 2007; Schenker et al., 2012). Block-type behaviour is shown by the Northern Rhodope Domain (NRD), to the northeast, and the Chalkidiki block, to the southwest, which were separated during the Eocene - Oligocene exhumation of the SRCC (Brun & Sokoutis, 2004, 2007) (Figure 3.2). In other words, restoring the pre-collapse geometry of the Rhodope, thus virtually closing the SRCC, would bring the NRD and the Chalkidiki block in close proximity. It can be further stressed that due to their present-day position the Chalkidiki block occupied a position immediately south of the NRD after restoring the pre-collapse geometry. Based on the fact that the Mesozoic convergence occurred in a northward subduction regime, the attained metamorphic conditions would be expected to increase northward.

In Figure 3.12, we compiled the available P-T estimations for the Chalkidiki block (western and eastern parts) and the NRD. It can be concluded that the metamorphic gradient described before for the western and eastern parts of the Chalkidiki block, can now be expanded to include also the NRD. As shown in Figure 3.12, the metamorphic gradient is valid for both the peak pressure and the attained peak temperature during retrogression. This is additionally strengthened by the discovery of micro-diamonds from the NRD (Mposkos & Kostopoulos, 2001; Perraki et al., 2006; Schmidt et al., 2010) that implies even higher metamorphic conditions toward the northeast. The timing for the peak pressure event is rather unknown for the Chalkidiki block but it is (pre-)Upper Jurassic for the NRD (Reischmann & Kostopoulos, 2002; Liati, 2005; Bauer et al., 2007; Liati et al., 2011). Subsequent retrogression is confined at Cretaceous for both the Chalkidiki block (e.g., Papadopoulos & Kilias, 1985; de Wet et al., 1989; Lips et al., 2000) and the NRD (e.g., Reischmann & Kostopoulos, 2002; Bauer et al., 2007; Bosse et al., 2010; Krenn et al., 2010; Liati et al., 2011; Didier et al., 2014).

From the above, we argue that both the NRD and the Chalkidiki block participated

into the same Mesozoic convergence both as part of the down-going plate along a northward subduction. Both domains record early, possibly (pre-)Upper Jurassic, eclogite-facies metamorphic conditions and subsequent Cretaceous retrogression at amphibolite-facies conditions. The prevailed metamorphic conditions are of different intensity between the domains implying the existence of a metamorphic intensity gradient that shows increasing metamorphic grade toward the northeast.

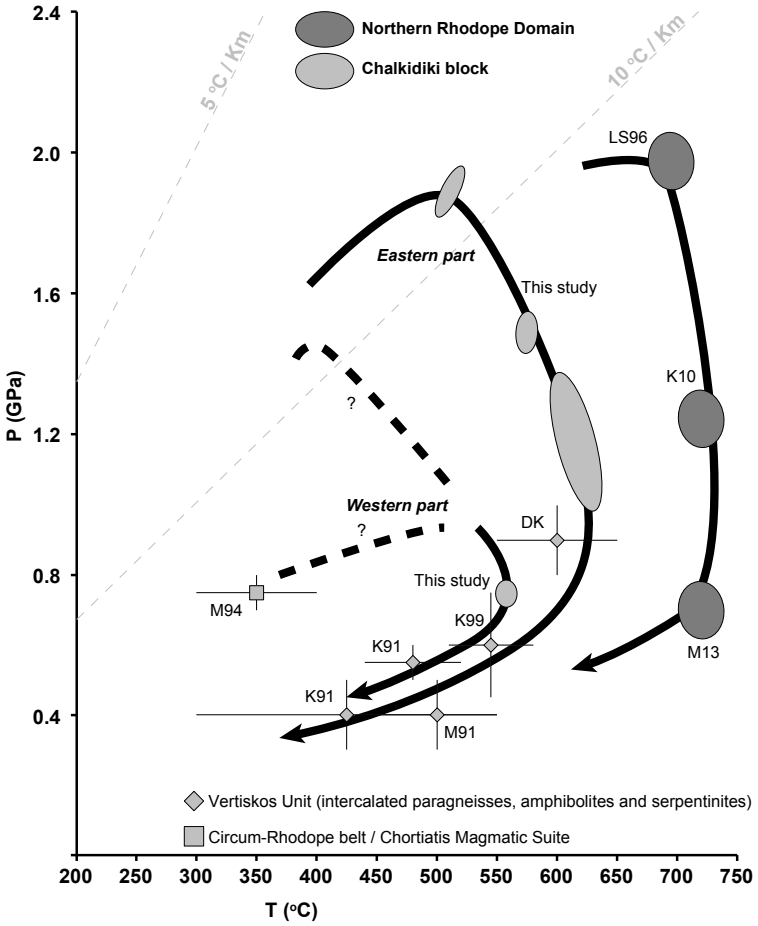

Figure 3.12: Compilation of representative P-T estimations for the Chalkidiki block (light grey) and the Northern Rhodope Domain (dark grey). M94: Michard et al. (1994a), K91: Kourou (1991), K99: Kilias et al. (1999), M91 Michailidis (1991), DK: Dimitrios Kostopoulos, pers. comm. 2014, LS96: Liati & Seidel (1996), K10: Krenn et al. (2010), M13: Moulas et al. (2013). See text for details.

3.8 Conclusions

In this contribution we studied key chloritoid-bearing garnet-staurolite-mica schists (Figure 3.5) from the eastern part of the basement of the Chalkidiki block (northern Greece) (Figures 3.2, 3.3). The basement was prior considered to show exclusively Barrovian medium-pressure amphibolite-facies metamorphic conditions. Based on micro-textures, we documented a relict eclogite-facies mineral assemblage (garnet + chloritoid + phengite + rutile) in an amphibolite-facies matrix composed of garnet + staurolite + phengite ± kyanite (Figure 3.6). Using isochemical phase diagram sections in the system NCKFMASHMnTi and mineral chemistry we inferred early HP conditions at 1.8-2.0GPa / 520^{o}C and subsequent re-equilibration at 1.0-1.3GPa / 600-640^{o}C (Figure 3.11). This finding supports the idea that the regional amphibolite-facies conditions overprinted a largely erased eclogite-facies event of arguably Mesozoic age.

At the scale of the Chalkidiki, the HP metamorphosed rocks share a common metamorphic history with the Mesozoic blueschist-facies rocks exposed to the west in terms of timing and genetic process (Figure 3.3). Based on our results we infer a gradient of the metamorphic conditions in the Chalkidiki that increase from blueschist-facies, to the west, to eclogite-facies toward the east.

In the light of this finding we are able to incorporate the Chalkidiki block into the Mesozoic convergence setting of the Rhodope. Both the Chalkidiki block and the high-grade Rhodopean gneisses, exposed further to the northeast, participated into the same Mesozoic convergence as part of a northward down-going plate prior to their exhumation and incorporation into the upper plate. They both experienced similar metamorphic conditions - yet of varying intensity - that include an early eclogite-facies metamorphic event and subsequently retrogressed at medium-pressure high-temperature conditions during the Cretaceous. The recorded metamorphic conditions increase northward, i.e., from the Chalkidiki block to the Northern Rhodope Domain, compatible with the well-established northward-dipping Jurassic - Cretaceous subduction.

Supplementary Materials

Supplementary Material #1

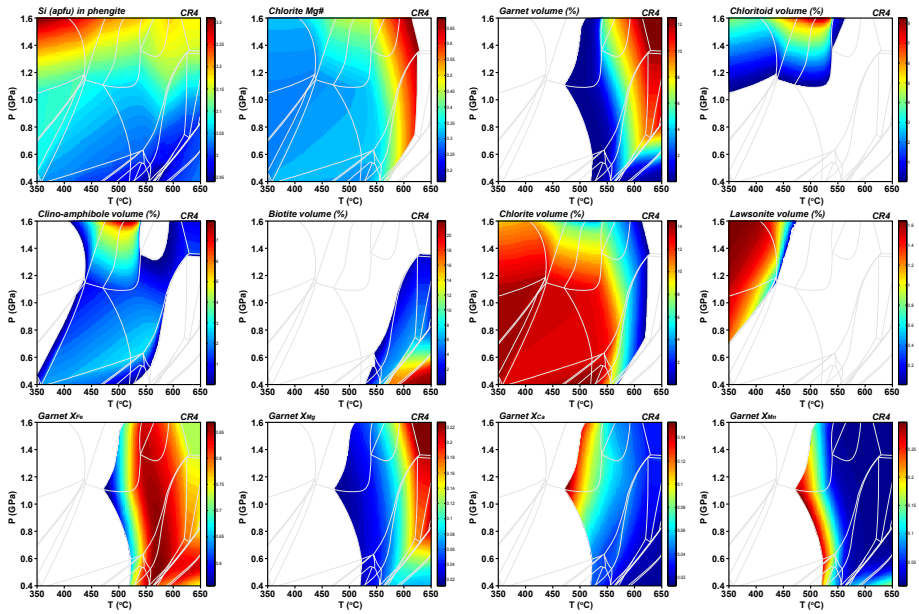

Figure 3.13: Mineral compositional contours for sample CR4.

Supplementary Material #2

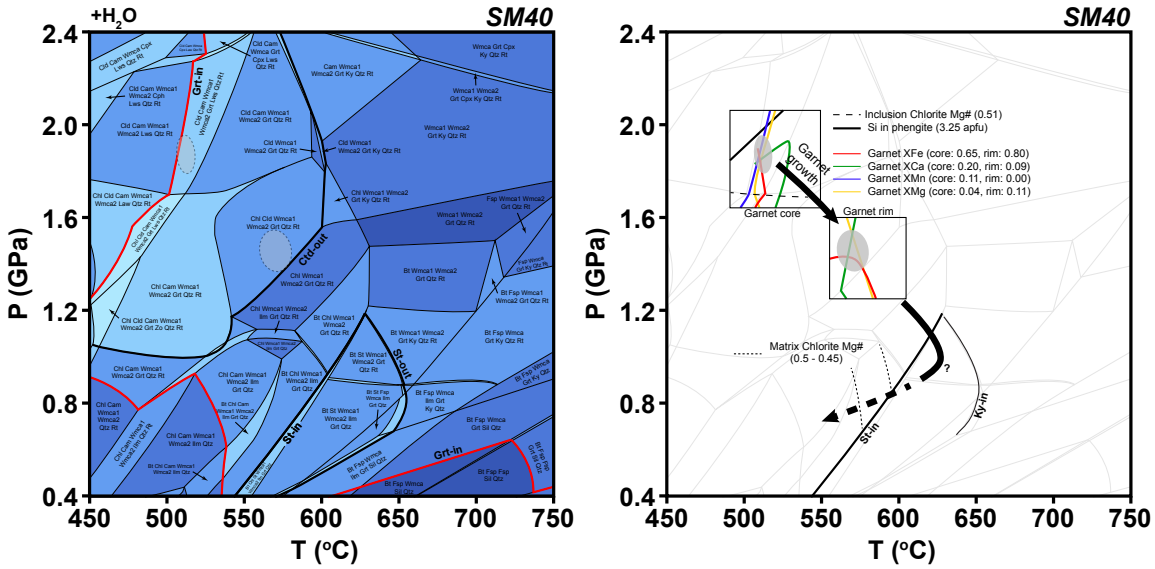

Figure 3.14: Calculated isochemical phase diagram section of sample SM40 (left). Selected compositional isopleths for garnet, phengite and chlorite are superimposed on the section (right). Equilibrium domains are shown in pale grey. See text for details.

Supplementary Material #3

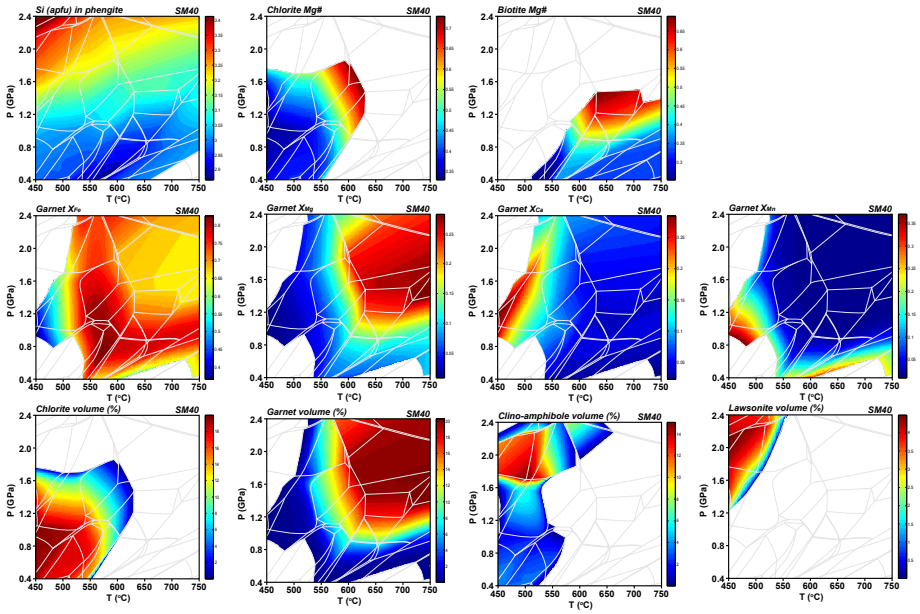

Figure 3.15: Mineral compositional contours for sample SM40.

Supplementary Material #4

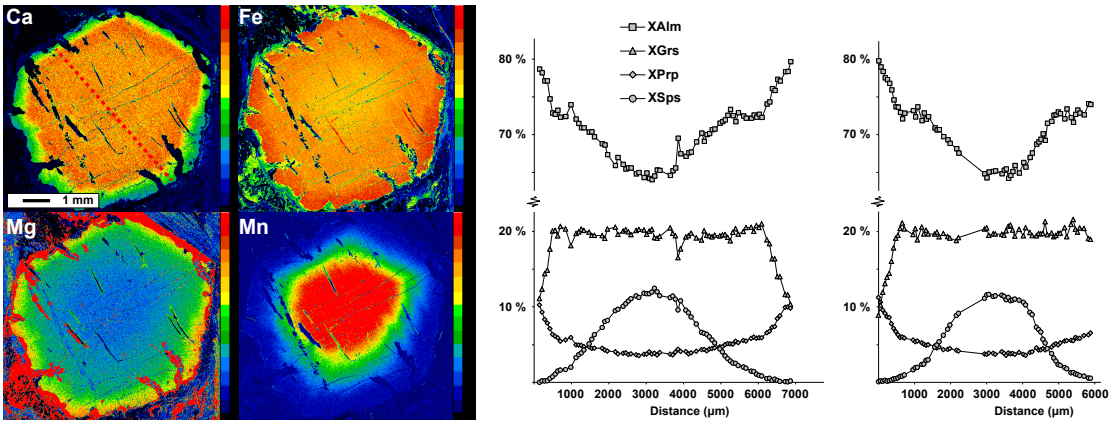

Figure 3.16: Representative garnet element maps (left) and microprobe elemental profiles (right) for sample SM40. The profile to the left corresponds to red dashed line superimposed on the Ca compositional map.

Supplementary Material #5

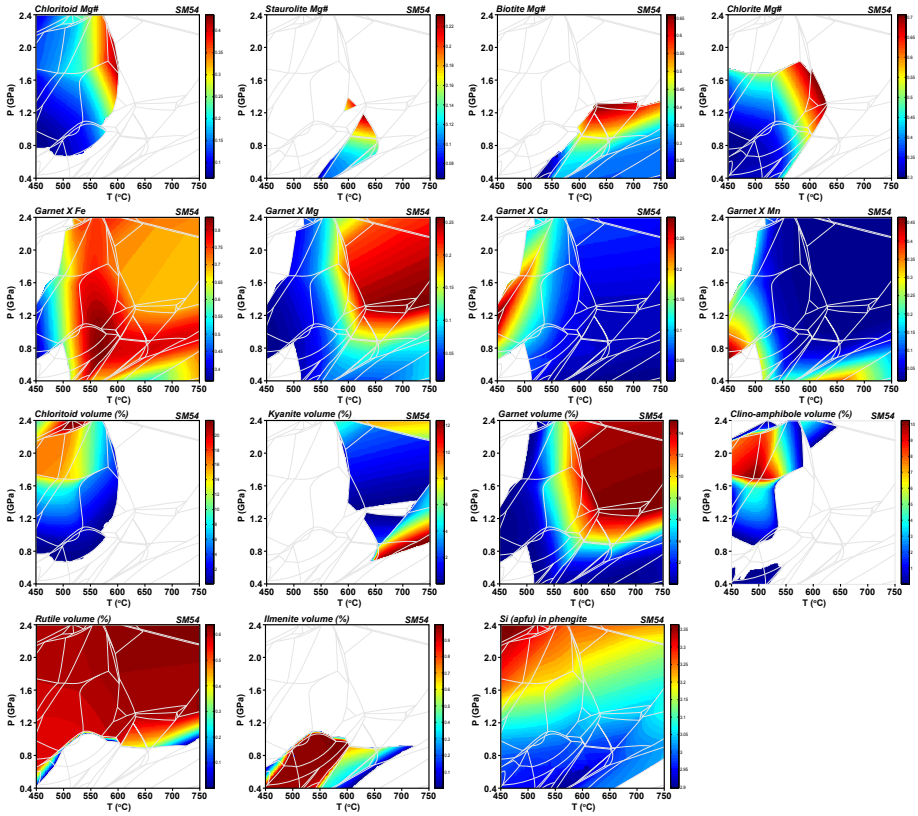

Figure 3.17: Mineral compositional contours for sample SM54.

Chapter 4

Mesozoic thermal evolution of the Chalkidiki block as revealed by $^{40}Ar/^{39}Ar$ and U-Th-Pb dating

4.1 Introduction

The *Hellenic Thrust Wedge* resulted from Mesozoic to early Cenozoic southward-verging convergence of three continental blocks (van Hinsbergen et al., 2005), namely, from top to base, Rhodopia, Pelagonia and External Hellenides, and the closure of two intervening oceanic domains along the two suture zones of Vardar-Axios (VSZ) and Pindos (PSZ) (Robertson, 2002; van Hinsbergen et al., 2005a; Papanikolaou, 2009, 2013) (Figure 4.1). The Mesozoic thrusting history (Burg et al., 1990, 1996; Ricou et al., 1998) was recorded to hinterland of the system that is mostly represented by the Rhodope. The latter can be divided, from northeast to southwest into the Northern Rhodope Domain, the Southern Rhodope Core Complex and the Chalkidiki block (Figure 4.2).

The Aegean represents the most stretched part of the system that was formed during the gravitational collapse of the previously built Hellenic Thrust Wedge. The Aegean extension that started in middle Eocene (Brun & Sokoutis, 2010; Jolivet & Brun, 2010) was driven by slab rollback (Jolivet & Faccenna, 2000). During the earliest phase of the extension the Southern Rhodope Core Complex (Brun & Sokoutis, 2007) exhumed at the wedge rear separating the Chalkidiki block, to the southwest, from the Northern Rhodope Domain, to the northeast. The Chalkidiki block that is the core of the present geochronological study recorded the same Mesozoic large-scale southward thrusting with the Northern Rhodope Domain (see review by Burg, 2012). However, after separation the Chalkidiki block, contrary to the Northern Rhodope Domain, largely escaped the thermal effects of Tertiary tectonics and, therefore, constitute an ideal candidate to attempt defining the Mesozoic post-peak metamorphic evolution of the North Aegean.

The present paper first reviews the tectonic-metamorphic evolution of the Rhodope with particular attention to the similarities between the Northern Rhodope Domain and the Chalkidiki block. Then, after a description of the analytical methods used in this work ($^{40}Ar/^{39}Ar$ step heating method and LA-ICP-MS monazite dating) and the strategy of sampling, the results are presented in details and interpreted. These results are discussed under two complementary perspectives: i) the timing of the peak amphibolite-facies metamorphism as well as the post-peak thermal cooling of the Chalkidiki block ii) the regional correlations and the importance of our findings at the scale of the Rhodope.

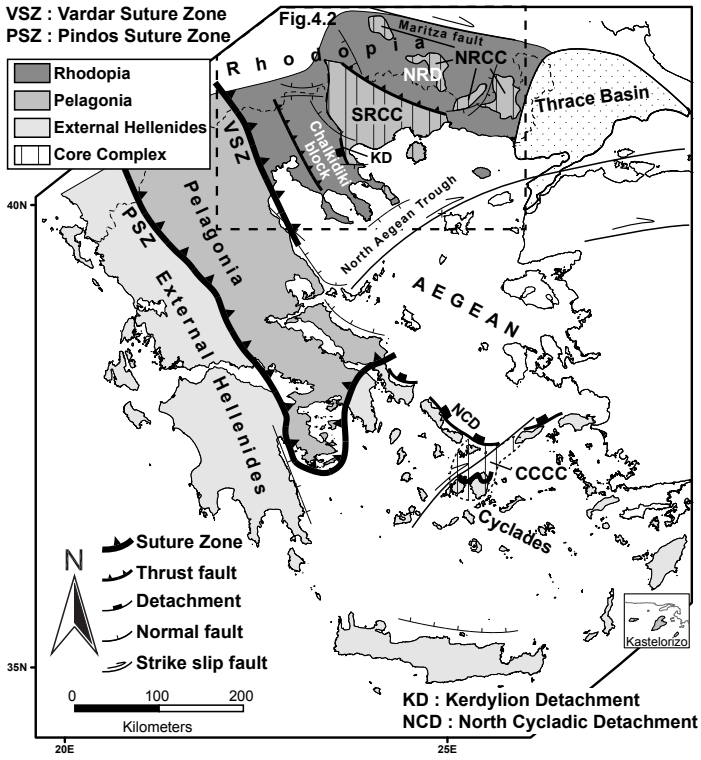

Figure 4.1: Simplified geological map of the Hellenides. The Hellenides are made, from north to south, of three continental blocks (Rhodopia, Pelagonia and External Hellenides) and two intervening sutured oceanic domains (Vardar and Pindos Suture Zones). The study area is located to the hinterland of the Hellenides, in the Rhodope. NRD: Northern Rhodope Domain, NRCC: Northern Rhodope Core Complex, SRCC: Southern Rhodope Core Complex, CCCC: Central Cyclades Core Complex.

4.2 Geological setting

4.2.1 The Rhodope Metamorphic Province

The Rhodope Metamorphic Province, or simply Rhodope for convenience, constitutes the hinterland of the Hellenides (northeast Greece - southwest Bulgaria) and is considered an as area of large-scale nappe tectonics that recorded the Mesozoic convergence-related deformation of the Aegean (e.g., Burg et al., 1990, 1996; Ricou et al., 1998; Krenn et al., 2010; Jahn-Awe et al., 2010; Nagel et al., 2011; Burg, 2012, and references therein) (Figure 4.2). The Rhodope can be described as a Mesozoic southwestward verging crustal-scale pile of syn-metamorphic, thrust units (Burg et al., 1996; Ricou et al., 1998) strongly affected by Cenozoic extension of core complex type (Dinter & Royden, 1993; Sokoutis et al., 1993; Bonev et al., 2006; Brun & Sokoutis, 2007) and syn- to post-extension magmatism (e.g., Kolocotroni and Dixon, 1991, Jones et al., 1992, Marchev et al., 2004, 2013). It is bordered to the north by the Maritza dextral strike-slip fault (Naydenov et al., 2013), to the east by the Middle Eocene to Quaternary Thrace Basin, to the west by the Vardar-Axios - Thermaikos basin that roughly correlate with the Vardar Suture Zone and to the south by the North Aegean Trough. We recognise three major domains in the Rhodope that are, from northeast to southwest: (i) the *Northern Rhodope Domain*, (ii) the *Southern Rhodope Core Complex*, and (iii) the *Chalkidiki block* (Figure 4.2).

The *Northern Rhodope Domain* (NRD) is the northeastern part of the Rhodope and represents an imbricate system mainly made of high-grade metamorphics including a former magmatic arc of Upper Jurassic age (Figure 4.2). The NRD is composed of orthogneisses, eclogites and amphibolites, paragneisses, scarce marble horizons and relatively rare ultra-

mafic rocks (e.g., Mposkos & Liati, 1993; Liati & Seidel, 1996; Turpaud & Reischmann, 2010; Janák et al., 2011). Although upper amphibolite-facies metamorphic rocks are widespread, many occurrences of variably retrogressed eclogites that preserve evidence for a precursor high-pressure stage have been reported in the literature. Evidence for ultrahigh-pressure (UHP) conditions is due to the presence of micro-diamond inclusions in metapelites (Mposkos & Kostopoulos, 2001; Perraki et al., 2006; Schmidt et al., 2010) that indicates minimum local pressure of 3.0GPa (for 600^{o}C). Peak (pre-)Upper Jurassic metamorphism was followed by Cretaceous upper amphibolite-facies regional overprint (Reischmann & Kostopoulos, 2002; Bauer et al., 2007; Hoinkes et al., 2008; Bosse et al., 2010; Krenn et al., 2010; Liati et al., 2011; Nagel et al., 2011; Bonev et al., 2013b). Metamorphic conditions are estimated at 1.9GPa / 700^{o}C for the high-pressure event recorded in mafic rocks and at 0.7GPa / 720^{o}C for the regional amphibolite-facies overprint (Liati & Seidel, 1996; Moulas et al., 2013). To the northeast, Maastrichtian - Paleocene deposits rest unconformably on basement gneisses (Boyanov et al., 1982; Goranov & Atanasov, 1992) and are related to plutonic rocks and volcanics of uppermost Cretaceous to lowermost Oligocene age (e.g., Peytcheva et al., 1998; Soldatos et al., 2001, 2008; Ovtcharova et al., 2003; Marchev et al., 2006, 2010; Jahn-Awe et al., 2010; Filipov & Marchev, 2011).

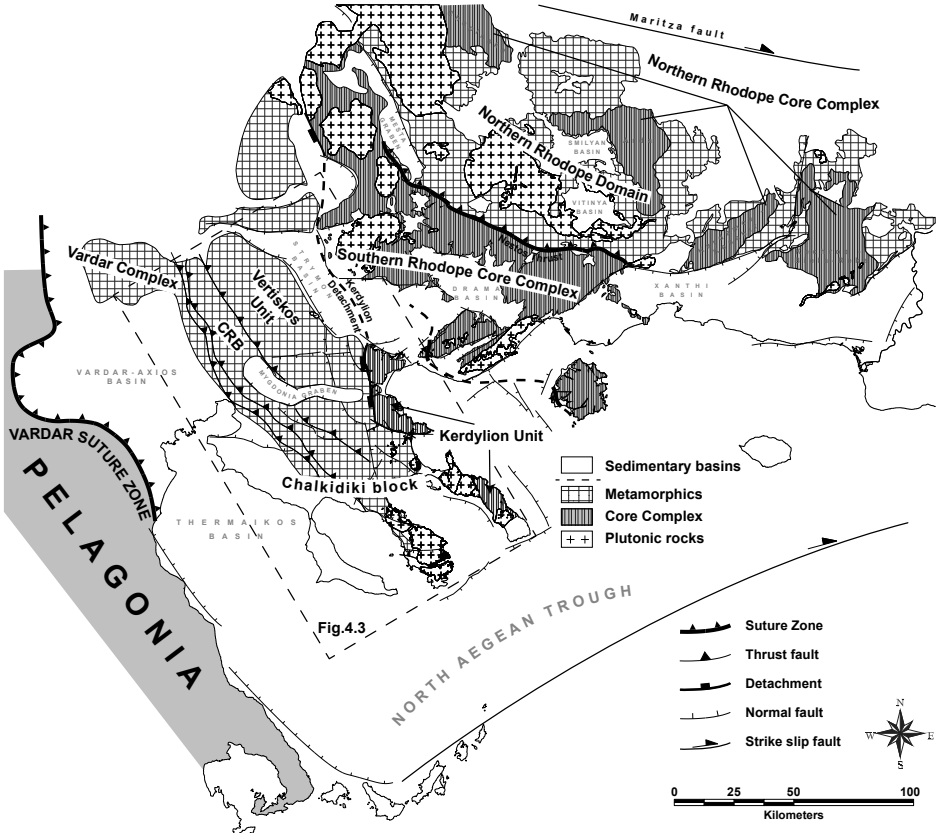

Figure 4.2: Simplified geological map of the North Aegean after Kockel & Mollat (1977), Brun & Sokoutis (2007) and Burg (2012). The Rhodope is composed of three tectonic domains that are, from NE to SW, the Northern Rhodope Domain, the Southern Rhodope Core Complex and the Chalkidiki block. The latter constitute the hanging-wall of the Kerdylion Detachment. CRB: Circum-Rhodope belt.

The *Southern Rhodope Core Complex* (SRCC) (Brun & Sokoutis, 2007) is a wide metamorphic dome of roughly triangular shape that shows a flat-lying foliation over its width and lies immediately southwest of the NRD (Figure 4.2). Their contact is located along a mylonite-bearing syn-metamorphic SW-verging thrust fault known as the Nestos Thrust (e.g., Papanikolaou & Panagopoulos, 1981; Gerdjikov & Milev, 2005). The SRCC consists

of highly deformed Permian-Carboniferous mylonitic orthogneisses, intercalated mica-schists and amphibolites capped by a thick marble sequence (e.g., Kronberg et al., 1970; Turpaud & Reischmann, 2010). The gneisses experienced upper greenschist/lower amphibolite-facies conditions with the available metamorphic ages being exclusively post-Lower Eocene in age (i.e., post-51 Ma) (Wawrzenitz & Krohe, 1998; Lips et al., 2000). Oligo-Miocene plutonic bodies that show syn-tectonic fabrics intrude the basement rocks (Kolocotroni & Dixon, 1991; Kaufman, 1995; Dinter et al., 1995; Eleftheriadis et al., 2001). Widespread NW-SE-trending basins were developed after middle Miocene (e.g., Snel et al., 2006).

Gravitational collapse of the thickened Hellenic crust since the early Aegean extension led to the exhumation of the SRCC that separated the NRD from the Chalkidiki block. Exhumation was controlled by the Kerdylion Detachment whose hanging-wall is defined by the Chalkidiki block. During exhumation, the Chalkidiki block underwent a circa 30^o clockwise rotation (Kondopoulou & Westphal, 1986; Brun & Sokoutis, 2004, 2007).

4.2.2 The southwestern part of the Rhodope: the Chalkidiki block

Three main units separated by sharp NW-trending contacts constitute the Chalkidiki block. From east to west, they are the Vertiskos Unit, the Circum-Rhodope belt and the Chortiatis Magmatic Suite (Kockel et al., 1971, 1977; Kockel & Mollat, 1977) (Figure 4.3). For the present work the two first units are investigated.

The *Vertiskos Unit* is an elongated NW-trending basement belt with a complex tectono-metamorphic history (Figure 4.3). This basement fragment detached from Gondwana and was incorporated into the Southern European Arcs by the end of the Palaeozoic (Himmerkus et al., 2007; Meinhold et al., 2010; Kydonakis et al., 2014b). It is made of Silurian - Ordovician granitoids (Himmerkus et al., 2009a, see also Chapter 2) later transformed into orthogneisses, intercalated paragneisses and thin marble horizons, leucocratic granitic/pegmatitic intrusions, deformed amphibolites, scarce eclogite boudins and serpentinites (Kockel et al., 1971, 1977). The Arnea-Kerkini Magmatic Complex intruded the Vertiskos Unit during the Lower Triassic (Himmerkus et al., 2009b) and both, as a coherent basement complex, experienced the same post-intrusion medium-pressure amphibolite-facies overprint (Burg et al., 1995; Kilias et al., 1999). Peak eclogite-facies metamorphic conditions estimated at 1.9GPa / 520^oC were followed by amphibolite-facies re-equilibration at 1.2GPa / 620^oC (see Chapter 3). Metamorphic K/Ar ages from the basement range between 140 and 90 Ma (e.g., Borsi et al., 1965; Harre et al., 1968; Marakis, 1969; Papadopoulos & Kilias, 1985; Christofides et al., 1999). Rubidium/strontium metamorphic ages are more dispersed but scatter approximately over the same time span (e.g., Zervas, 1979; Papadopoulos & Kilias, 1985; de Wet et al., 1989). Lips et al. (2000) reported a 143 $\pm$ 5 Ma $^{40}Ar/^{39}Ar$ age (white mica, plateau age) from a quartz-calcite mylonite and de Wet et al. (1989) a 136 $\pm$ 1 Ma (biotite, plateau age) from the Arnea Magmatic Complex.

The *Circum-Rhodope belt* is a Triassic - Jurassic meta-sedimentary sequence locally involving Triassic rhyolites and quartzites at the base (Kauffmann et al., 1976; Asvesta & Dimitriadis, 2010; Meinhold & Kostopoulos, 2013) (Figure 4.3). It is largely made of phyllites and carbonates and is considered as the Mesozoic sedimentary cover of the Vertiskos Unit (Kockel et al., 1971; Kauffmann et al., 1976; Dixon & Dimitriadis, 1984). Stratigraphic contacts between basement and cover are rarely, if any, preserved. Due to post-metamorphic deformation, the basement and its cover are mainly separated by a sharp NW-trending contact (Tranos et al., 1999) (Figure 4.3). However, at some places thin intercalated slivers of paragneisses appear in close relationship with the basement and although various local unit names have been attributed to them, most of them belong to the Mesozoic cover. This is particularly true for the garnet-staurolite-kyanite schist that are exposed as thin slivers in the southeastern part of the Vertiskos Unit (Figure 4.3). Basal rhyolites of the Circum-Rhodope belt yield Lower Cretaceous, circa 120 Ma, K/Ar metamorphic ages (Bertrand et al., 1994).

Michard et al. (1994a,b) reported high-Si phengite from basal meta-tuffs and estimated peak metamorphic conditions at 0.8GPa / 350^{o}C.

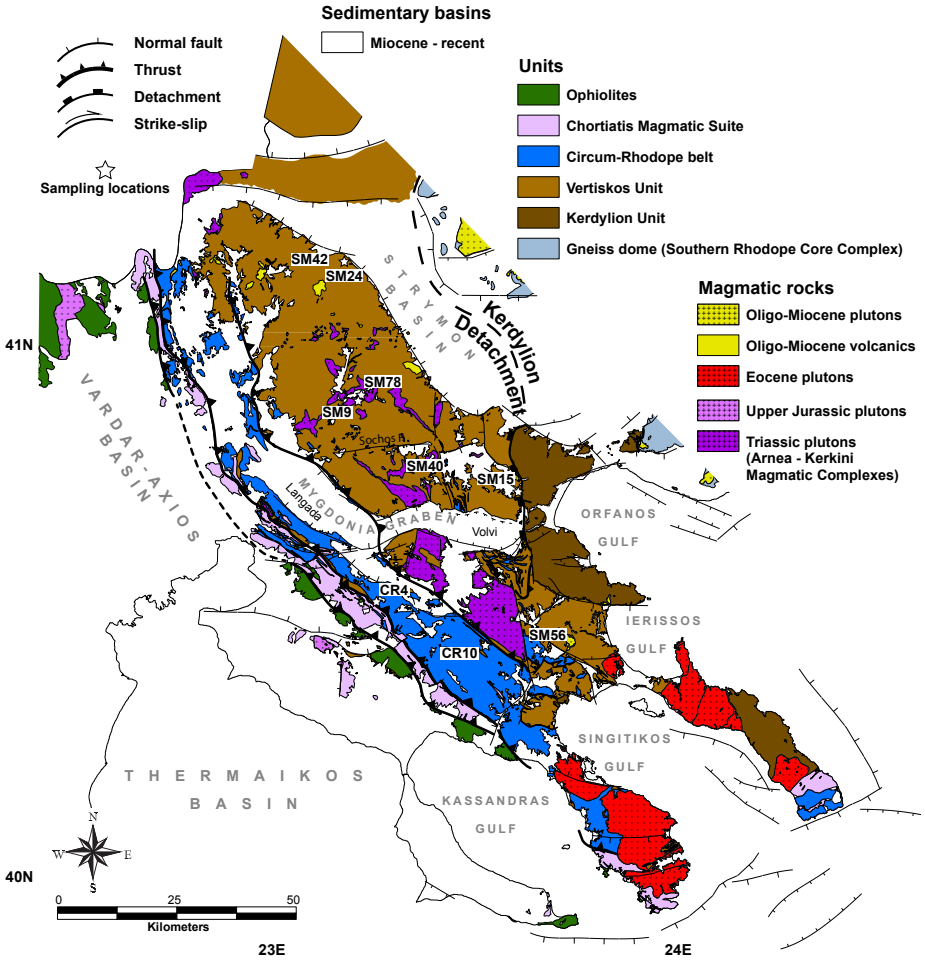

Figure 4.3: Geological map of the Chalkidiki block after Kockel & Mollat (1977) and Sakellariou & Dürr (1993). Sample localities are shown in stars.

4.3 Analytical methods

4.3.1 $^{40}Ar/^{39}Ar$ step heating method

Fresh samples of phyllites, gneisses and mica-schists were selected for step-heating laser probe $^{40}Ar/^{39}Ar$ dating. The samples were crushed, sieved and single grains of micas were handpicked under binocular microscope and cleaned in ultrasonic bath using acetone and distilled water. Biotites and white micas were packaged in aluminium foils and irradiated in the core of the Triga Mark II nuclear reactor of Pavia (Italia) with several aliquots of the Fish Canyon sanidine standard (28.03 ± 0.08Ma) (Jourdan and Renne, 2007) as flux monitor. Argon isotopic interferences on K and Ca were determined by irradiation of KF and CaF2 pure salts from which the following correction factors were obtained: $(^{40}Ar/^{39}Ar)K = 0.00969 \pm 0.00038$, $(^{38}Ar/^{39}Ar)K = 0.01297 \pm 0.00045$, $(^{39}Ar/^{37}Ar)Ca = 0.0007474 \pm 0.000021$ and $(^{36}Ar/^{37}Ar)Ca = 0.000288 \pm 0.000016$. Argon analyses were performed at Géosciences Montpellier (France) with an analytical system that consists of: (a) an IR-CO2 laser of 100 kHz used at 5-15% during 60 sec, (b) a lenses system for beam focusing, (c) a steel chamber, maintained at 10-8 - 10-9 bar, with a drilled copper plate and the four samples on, (d) an inlet line for purification of gases including two Zr-Al getters, (e) a multi-collector

mass spectrometer (Argus VI from Thermo-Fisher). A custom-made software controls the laser intensity, the timing of extraction/purification and the data acquisition. To measure the argon background within the system, one blank analysis was performed every three sample analyses. The ArArCalc software© v2.5.2 was used for data reduction and plotting. The one-sigma errors reported on plateau, isochron and total gas ages include the error on the irradiation factor J. Atmospheric 40Ar was estimated using a value of the initial $^{40}Ar/^{36}Ar$ of 295.5.

4.3.2 LA-ICP-MS monazite dating

Monazites were imaged *in-situ* on well-polished thin sections by back-scattering imaging using a scanning electron microscope (SEM) available at Université de Rennes1, France, prior to isotopic measurements conducted using an in-situ laser ablation - inductively coupled plasma-mass spectrometry (LA-ICP-MS) at the Géosciences Rennes, France. Ablation spot diameters of 7 μm with repetition rate of 3 Hz and laser intensity of 7.5 J/cm2 were used throughout. The data were corrected for U-Pb and Th-Pb fractionation and for mass bias by standard bracketing with repeated measurements of the Moacyr monazite (Itambe, Brasil) with an age of 508 $\pm$ 1 Ma. At regular intervals, the Madagascar monazite was used as unknown to ensure quality control of the isotopic measurements. Data reduction was carried out using the GLITTER® software package developed by Macquarie Research Ltd. (Jackson et al., 2004). Concordia ages and diagrams were generated using Isoplot/Ex (Ludwig, 2001) updated to ver. 2.45.

4.4 Strategy and sample description

Nine samples were selected for $^{40}Ar/^{39}Ar$ step heating and U-Th-Pb dating on micas and monazites, respectively (Table 4.1). The sampling grid is shown in Figure 4.3. Two samples are from the Circum-Rhodope belt lying immediately west of the Vertiskos Unit (CR4 and CR10) and another three are from equivalent Mesozoic sequences (based on regional mapping and our detrital zircon dating results) exposed in close proximity to the basement (SM15, SM40, SM56). Two more samples are from paragneisses of unknown protolith age embedded in the basement (SM24 and SM42) and another from the Triassic Arnea Magmatic Complex (SM9 and SM78). An overview of the micas chemistry is given in Figure 4.4.

Table 4.1: List of samples used for $^{40}Ar/^{39}Ar$ and U-Th-Pb geochronology

Sample	Latitude	Longtitude	Rocktype
Mesozoic sedimentary sequence			
CR4	40.53	23.22	phyllite
CR10	40.45	23.52	phyllite
SM15	40.73	23.61	schist
SM40	40.76	23.41	schist
SM56	40.44	23.65	schist
Sedimentary sequence of unknown protolith age			
SM24	41.13	23.21	schist
SM42	41.13	23.02	schist
Triassic orthogneisses			
SM9	40.91	23.21	orthogneiss
SM78	40.90	23.21	orthogneiss

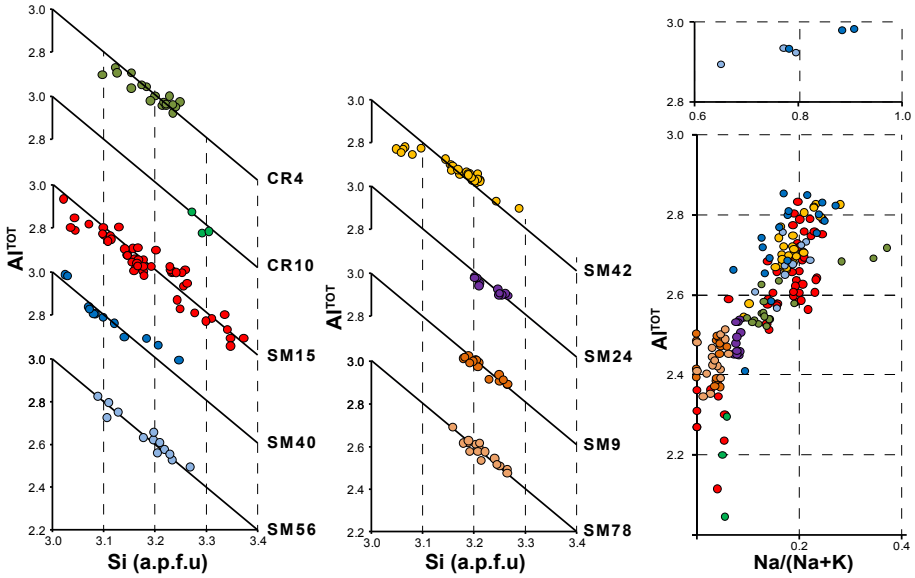

Figure 4.4: White micas chemistry for the samples used for geochronology.

4.4.1 Phyllite/schists of Mesozoic protolith age

Sample CR4 is a fine-grained quartz-mica phyllite. In the field it has a dominant foliation and a prominent NW-SE-trending crenulation lineation. The main mineral phases are, in decreasing amount order, quartz, white mica, chlorite, garnet and opaque minerals. A typical crenulation cleavage is developed by differentiation at the limps of microlithon domains accompanied by pressure solution. The microlithons are dominated by quartz and kinked, often chloritised, medium-grained white micas. The cleavage domains are made of fine- to medium-grained K-rich white mica or a fine-grained aggregate of K-rich white mica, paragonite and chlorite. Paragonite has Na/(Na+K) ratio around 0.90 and contain small amount of Ca (less than 0.1 apfu). The Si content of the K-rich mica range from 3.1 to 3.25 apfu and contains up to 2.4 wt% Na. Garnet grains (typically 2-3 mm in diameter) appear in the microlithons pseudomorphosed after chlorite. Garnet's composition is between $Alm_{67}Grs_{23}Sps_{6}Pyr_{4}$ and $Alm_{60}Grs_{25}Sps_{12}Pyr_{6}$. Despite the chlorite alteration, the pseudomorphs still preserve syn-tectonic features. Quartz in the microlithon domains has healing features and is recrystallised with sharp grain boundaries and virtually no undulose extinction.

Sample CR10 is a fine-grained phyllite with a dominant NW-trending crenulation lineation. Main phases are quartz, phengitic white mica and subordinate chlorite. The bedding can potentially be recognised as the interface between quartz- and white mica-rich layers. An anastomosing network of crenulation cleavage is defined by fine-grained white micas. Chlorite occasionally replaces the white mica. Phengite contains up to 3.31 apfu Si and also small amount of Na (typically less than 0.4 wt%).

Sample SM15 is a medium-grained garnet-kyanite micaschist. It appears in a relatively small isolated outcrop along the eastern part of the Vertiskos Unit and is intercalated with orthogneisses and highly-deformed amphibolites. It has quartz, garnet, kyanite, white mica and rutile as main phases and staurolite, chlorite, biotite (only as inclusion), ilmenite, epidote, phosphates, zircon and opaques as accessory phases. In the field it displays shear bands and rounded garnet/kyanite porphyroclasts surrounded by medium-grained matrix made of K-rich white mica. The K-rich white mica has Si content up to 3.36 apfu, contains up to 1.92 wt% Na (∼0.24 apfu) and is sometimes chloritised especially near the garnet rim. Garnets appear mostly unhedral, range from 500μm to 3mm in diameter and shows a weak zoning in major elements with almost flat spessartine/grossular components, increasing almandine and

decreasing pyrope components towards the rim. Garnet composition typically ranges from $Alm_{64}Grs_5Sps_5Pyr_{26}$ to $Alm_{73}Grs_5Sps_5Pyr_{17}$ from core to rim. Monazites appears mostly in the matrix, often surrounded by a reaction corona, in relationship with apatite or as inclusion in garnet.

Sample SM40 is a garnet-staurolite micaschist from the eastern part of the area. Major phases are white mica, garnet, staurolite, quartz, biotite, chlorite, sub-ordinate kyanite and tourmaline only as inclusion in garnet. Accessory minerals are rutile (almost always rimmed by ilmenite), apatite, zircon and opaques. Garnet appears with exceptionally large grains measuring up to 1 cm in diameter and is the dominant phase enveloped by a medium to fine-grained foliation made of white micas, quartz-rich bands and intergrowths of muscovite/paragonite. Garnet displays zoning in major elements with $Alm_{65}Grs_{20}Sps_{11}Pyr_4$ cores and $Alm_{80}Grs_9Sps_0Pyr_{11}$ rims. Potassium-rich white mica is dominant in the matrix and its composition has up to 3.25 apfu Si and up to 0.24 apfu Na contents. Paragonite is less abundant with Na/Na+K ratio up to 0.9 and it contains less than 1 wt% Ca (¡0.04 apfu). Shear bands and macroscopically visible spiral garnet indicate as SW-directed shearing in hand specimen. Both garnet and staurolite preserve syn-tectonic features.

Sample SM56, although similar to SM40, it is more quartz-rich and its matrix is more fine-grained as a result of deformation. In thin section, garnet porphyroclasts measure up to 0.3 cm in diameter and show consumption textures. Staurolite can barely be recognised in thin sections and is often replaced by shimmer. This sample has suffered grain size reduction compared to SM40 possibly during retrogression.

4.4.2 Paragneisses of unknown protolith age embedded in the basement

Sample SM42 is a medium-grained garnet-bearing micaschist cropping out at the north-central part of the Vertiskos Unit. It has a pronounced foliation and SW-directed shear indicators. It shows a monotonous mineralogy made of small garnet grains (typically less than 2mm) surrounded by matrix made of K-rich white mica, biotite, garnet, quartz, ilmenite and subordinate plagioclase. Chlorite, phosphates, zircon and rutile appear as accessory minerals. Garnet is up to 2 mm in diameter and shows a pronounced prograde zoning in major elements with decreasing spessartine/grossular and increasing almandine/pyrope components. Its composition range from $Alm_{57}Grs_{28}Sps_{12}Pyr_3$ to $Alm_{79}Grs_{10}Sps_1Pyr_{10}$ from core to rim. The foliation is made by biotite and white micas. Biotite, although commonly found along the foliation plane, appears with unhedral grains which look like re-oriented porphyroclasts rather than growing in equilibrium with the white micas of the foliation. According to their textural position and size, two types of white micas are found: i) big mica flakes, commonly at high angle to the foliation, and ii) medium- to fine-grained micas found along the foliation plane. The latter white micas have Si content of up to 3.29 (apfu) and contain less than 1.3 wt% Na.

Sample SM24 is a medium-grained garnet-kyanite micaschist from the eastern part of the Vertiskos Unit. It displays eye-shaped aggregates of garnet, biotite and kyanite surrounded by fine-grained matrix made mostly of white micas and quartz. Accessory minerals are ilmenite, zircon, phosphates and opaques. White micas from the matrix have a phengitic composition (up to 3.26 apfu). Garnet is typically around 2 mm in diameter (few bigger grains with 5 mm diameter were also found). Garnet shows a rather flat major element composition with almandine/pyrope dominating over the spessartine/grossular components and typical composition of $Alm_{75}Grs_{15}Sps_7Pyr_3$. Monazite appears in the matrix or as inclusion in the garnet and displays patchy zoning.

Table 4.2: Overview of the $^{40}Ar/^{39}Ar$ ages.

Sample	Mineral	#Grains	Lat.	Lon.	Total gas age	Plateau age	% ^{39}Ar	Preferred Age	Inverse isochron age	$^{40}Ar/^{36}Ar$ intercept	MSWD
Mesozoic sedimentary sequence											
CR4	w.m.	1	40.53	23.22	124.4 ± 0.9	124.1 ± 0.7	100	124.1 ± 0.7	123.5 ± 1.2	398.3 ± 157.7	0.76
CR4	w.m.	3	40.53	23.22	119.6 ± 0.8	119.2 ± 0.8	79.6	119.2 ± 0.8	118.9 ± 1.0	324.0 ± 23.8	1.68
CR10	w.m.	6	40.45	23.52	116.3 ± 0.5	-	-	117.5 ± 3.2	118.3 ± 3.4	131.8 ± 76.6	¿100
CR10	w.m.	1	40.45	23.52	125.6 ± 0.7	-	-	125.6 ± 0.7	-	-	-
CR10	w.m.	8	40.45	23.52	122.3 ± 0.6	-	-	125.5 ± 3.3	119.0 ± 8.1	3830.7 ± 9743.5	2.43
SM15	w.m.	1	40.73	23.61	102.5 ± 0.5	-	-	104.6 ± 1.2	106.2 ± 1.3	262.1 ± 103.4	5.48
SM15	w.m.	1	40.73	23.61	95.9 ± 0.4	-	-	95.8 ± 1.5	94.2 ± 1.5	374.2 ± 47.4	32.76
SM15	w.m.	1	40.73	23.61	96.6 ± 0.6	-	-	95.4 ± 0.8	94.7 ± 2.9	334.8 ± 166.4	2.03
SM40	w.m.	1	40.76	23.41	97.5 ± 0.4	-	-	97.7 ± 0.8	94.8 ± 1.3	742.2 ± 425.9	15.47
SM40	w.m.	1	40.76	23.41	99.8 ± 0.5	-	-	100.1 ± 0.7	99.3 ± 1.2	819.8 ± 593.1	2.41
SM40	w.m.	1	40.76	23.41	96.9 ± 0.4	-	-	97.2 ± 1.0	94.8 ± 1.9	1365.0 ± 837.7	11.23
SM56	w.m.	5	40.44	23.65	90.9 ± 2.4	92.2 ± 1.9	70	92.2 ± 1.9	93.1 ± 4.0	1842.9 ± 74.2	6.12
Sedimentary sequence of unknown protolith age											
SM42	bt	1	41.13	23.02	128.1 ± 0.6	142.5 ± 0.8	29.9	144.9 ± 2.5	141.4 ± 2.3	313.3 ± 34.7	0.36
SM42	w.m.	1	41.13	23.02	150.0 ± 0.7	-	-	-	141.8 ± 9.0	1022.3 ± 815.3	¿100
SM42	w.m.	1	41.13	23.02	138.6 ± 0.6	-	-	137.5 ± 1.0	137.5 ± 1.1	308.8 ± 63.1	28.69
SM42	w.m.	1	41.13	23.02	126.5 ± 0.5	-	-	127.2 ± 1.9	127.8 ± 2.2	280.8 ± 9.8	4.6
Triassic orthogneisses											
SM9	w.m.	1	40.91	23.21	124.1 ± 0.5	124.3 ± 0.5	86.2	124.3 ± 0.5	124.2 ± 0.5	299.5 ± 39.5	1.86
SM9	w.m.	1	40.91	23.21	124.3 ± 0.5	124.6 ± 0.5	98.1	124.6 ± 0.5	124.6 ± 0.5	302.7 ± 52.4	1.48
SM78	bt	1	40.90	23.21	53.8 ± 0.5	56.7 ± 0.7	34.8	56.7 ± 0.7	-	-	-
SM78	w.m.	1	40.90	23.21	122.1 ± 0.5	123.1 ± 0.5	97.3	123.1 ± 0.5	123.0 ± 0.7	305.2 ± 39.8	1.91

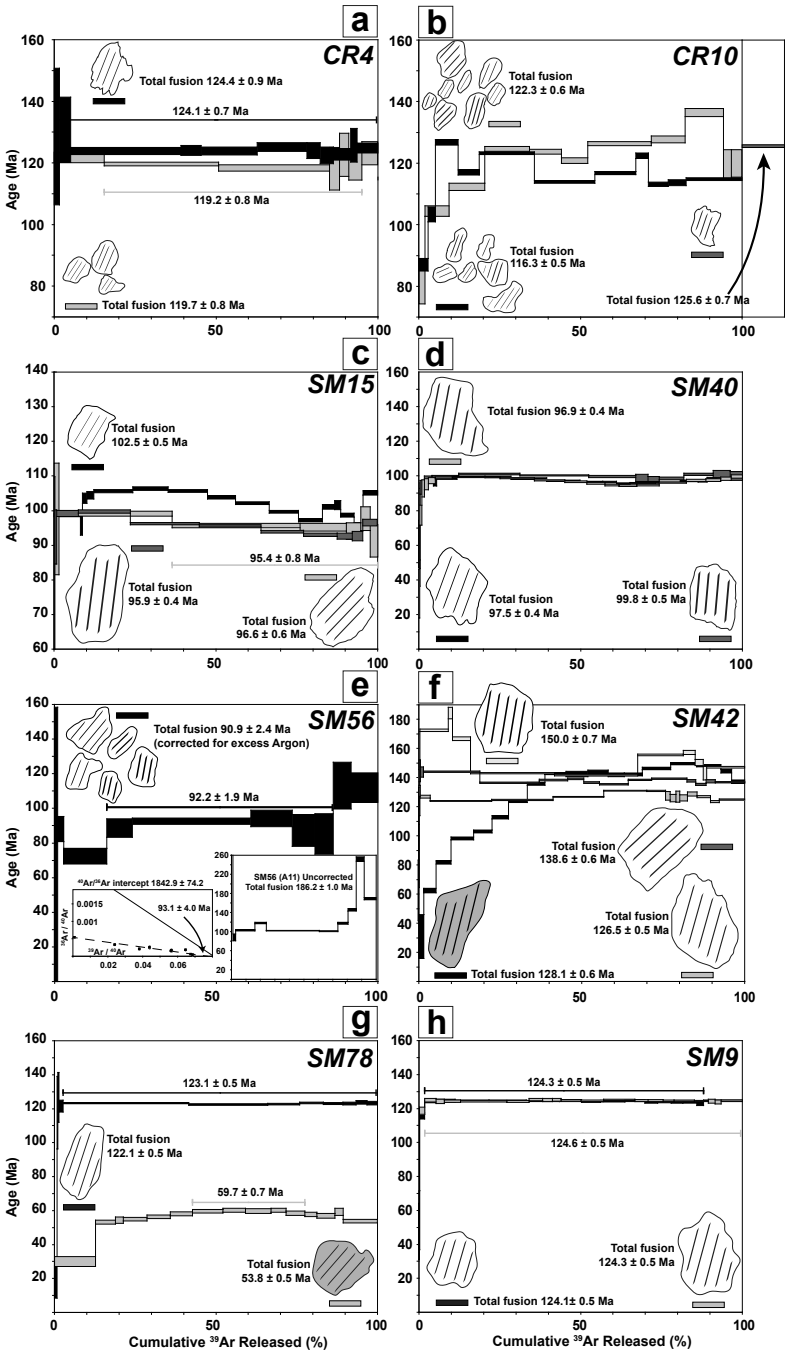

Figure 4.5: Argon/argon age spectra for white micas and biotites from eight samples of the Chalkidiki block, northern Greece. Sample numbers are read at the top right corner of each plot (for location see Fig. 4.3). Total fusion and plateau ages (whenever possible) are calculated. For each sample, a replicate of the grain(s) degassed is shown: white colour for white micas and grey colour for biotites. The scale bar (shown beneath the grain replicates) is 500μm in all samples and its colour corresponds to the colour of the age spectra of each sample. Neglecting all meaningless apparent ages the geologically meaningful ages are constrained between ca. 125 Ma (westernmost samples) and ca. 95 Ma (easternmost samples). See text for details and discussion.

4.4.3 Orthogneisses of the Triassic Arnea Magmatic Complex

Samples SM9 and SM78 are both leucocratic orthogneisses of the Triassic Arnea Magmatic Complex. They contain K-feldspar, quartz, K-rich white mica, plagioclase and subordinate biotite as major mineral phases and zircon, rutile, apatite as accessory minerals. Despite the metamorphic overprint, both samples have preserved magmatic textures (such as myrmekites). Potassium-rich white micas are of metamorphic origin. For both samples,

K-rich white mica from the foliation has up to 3.27 apfu Si content and negligible amount of Na.

4.5 Results

4.5.1 Argon/argon step heating results

Eight samples were used for $^{40}Ar/^{39}Ar$ dating. Degassing data and age spectra plots are shown in Appendix A1 and Figure 4.5, respectively. A synopsis of the $^{40}Ar/^{39}Ar$ ages is given in Table 4.2. For the white mica we adopt a closure temperature of 420 ± 30^{o}C according to Harrison et al. (2009). This has to be considered as a minimum value since the closure temperature increases with the Mg/Fe ratio in phengite (Agard et al., 2002; Augier et al., 2005) as well as with the grain size and the cooling rate. According to Harrison et al. (1985), the closure temperature of the biotite is 320^{o}C ± 30^{o}C.

4.5.1.1 Mesozoic phyllite/schists

For sample CR4, two age spectra were obtained. Two slightly different plateau ages of 124.1 ± 0.7 Ma (100% of ^{39}Ar released) and 119.2 ± 0.8 Ma (80% of ^{39}Ar released) were calculated for a single and three smaller grains, respectively (Figure 4.5a). The obtained ages overlap with the corresponding inverse isochron ages (123.5 ± 1.4 Ma and 118.9 ± 1.0 Ma, respectively). As discussed in the description of the sample, bigger mica grains are commonly found in the microlithons whereas smaller grains are typical for the cleavage domains. The small age difference between the two plateau ages suggests that the obtained age spectra are more likely diffusion-controlled, due to variation in the grain size, and do not reflect different cooling histories between the micas. Thus, the age of ca. 125 Ma is interpreted as the cooling age of the rock.

Two sets of relatively small white micas were analysed from sample CR10. Both age spectra show evidence for partial argon loss and the individual steps for both of them are roughly constrained between ca. 112 and 128 Ma. For the six-grain dataset (black line - Figure 4.5b), the third step produced the oldest age, 126.8 ± 0.9 Ma, which can be considered as the minimum age of an older component and it is very close to plateau age obtained for sample CR4 (i.e. 124.1 ± 0.7 Ma) from the same unit. Six out of the 11 steps yield a weighted age of ca. 115 Ma (67% of ^{39}Ar released) which is similar to the small grains of CR4 (119.2 ± 0.8 Ma). Despite a large MSWD value which is due to the high radiogenic content of the sample, these ages overlap with the inverse isochron age of 118.3 ± 3.4 Ma. For the eight-grain dataset (light grey line - Figure 4.5b) the central part of the spectra (62% of ^{39}Ar released) yielded a weighted mean age of ca. 125 Ma and a meaningless inverse isochron age of 119.0 ± 8.1 Ma. The shape of the two age spectra suggests that several reservoirs contribute to the released argon, yet the convex pattern first described by Wijbrans & McDougall (1986) was not observed. This could indicate that in addition to the two white mica end-members, argon was released from a third component such a interlayered chlorite that partly replaced muscovite. Overall, the age of the sample can be constrained between ca. 112 and 128 Ma. This is supported by the total fusion age of 126.6 ± 0.5 Ma for a single-grain white mica (dark grey line - Figure 4.5b) that is very close to the assumed older end-member. In summary, the most representative age for this sample, ignoring all the complexity involving multi-grain analysis, should be around 125 Ma.

For sample SM15 three single white mica grains were analysed (Figure 4.5c). The smallest one yielded a convex age spectrum (black line) which is reminiscent of the spectra described by Wijbrans and McDougall (1986) for mixture of mica populations. However, the other two gave reasonably flat degassing patterns with 95.4 ± 0.8 Ma (plateau age, 64% of ^{39}Ar released, medium grey line) and 95.9 ± 0.4 Ma (total fusion age, dark grey line). The age

obtained overlap with the calculated inverse isochron ages. These ages are indistinguishable within error with those obtained from samples SM40 (ca. 98 Ma) and SM56 (92.2 ± 1.9 Ma) (see below) from the same Mesozoic schists from the eastern part of the study area.

For sample SM40, three relatively large white mica grains were dated. All of them produced flat to weakly concave age spectra with total fusion ages in the range 97 - 100 Ma, similar to the corresponding inverse isochron ages (Figure 4.5d). Note again the large MSWD values and the error bars due to the clustering of the data points near the abscissa. The reproducibility of the results for the three grains let us suggest an age of 98 ± 2 Ma as the most representative cooling age for this sample.

Five smaller white mica grains separated from sample SM56 display a complex, partially saddle-shaped spectrum that is usually interpreted as due to excess argon contamination (Figure 4.5e inset). In the $^{36}Ar/^{40}Ar$ vs. $^{39}Ar/^{40}Ar$ plot, the data points form a linear array corresponding to an intercept age of 93.1 ± 4.0 Ma, with an initial 40Ar/36Ar value of 1843 ± 74. Correcting the primary age spectrum with this initial argon ratio, a plateau age of 92.2 ± 1.9 Ma can be calculated on 70% of released ^{39}Ar (Figure 4.5e). This age is only ∼4-8 m.y. younger than that of the SM40 probably as a result of a small grain size or different chemical properties.

4.5.1.2 Paragneiss of unknown protolith age embedded in basement orthogneisses

Both biotite and white mica were separated from sample SM42 (Figure 4.5f). The single grain biotite age spectrum shows typical argon pattern with young ages in the first heating increments at about 30 Ma that progressively increase to a relatively tight group of ages between ca. 140 and 150 Ma (mean age of 145.7 ± 2.1 Ma, 57% of ^{39}Ar released). However, no reasonable plateau age can be calculated. The calculated inverse isochron age is 141.4 ± 2.3 Ma. This is identical within error with the 146.9 ± 3.0 Ma plateau age calculated by Lips et al. (2000) from white micas of a mylonite of the Vertiskos Unit further southeast. From the same sample, three single white mica grains of same size were analysed. One of them yield a saddle-shaped spectrum indicative for excess argon (light grey line - Figure 4.5f). However, no linear array was observed in the inverse isochron plot and no correction could be applied to the age spectrum. The other two spectra (dark grey and medium grey lines - Figure 4.5f) yield more concordant age patterns with total fusion ages of 138.6 ± 0.6 Ma and 126.5 ± 0.5 Ma, respectively (inverse isochron ages of 137.5 ± 1.1 and 127.8 ± 2.2 Ma). Complexity on calculating a single age for this particular sample comes from the fact that the three white micas have recorded different apparent ages. This can be the result of variable excess argon incorporation, incomplete resetting or due to complex chemical variations. However, based on the youngest reasonable age (possibly the least affected by excess argon) it seems that the sample cooled below the blocking temperature at maximum at ca. 126 Ma. This sample is more likely part of the intercalated Palaeozoic sequences within the basement and the older age spectra obtained are more probably the result of partial reset of the system during an event around (at maximum) 126 Ma. This conclusion is supported by the fact that the circa 125 Ma event is already well-constrained from samples CR4 and CR10 (described before) and from samples SM78 and SM9 that are described below.

4.5.1.3 Triassic Arnea Magmatic Complex

One white mica and one biotite grain were dated from sample SM78 (Figure 4.5g). The white mica yield a well-defined plateau age of 123.1 ± 0.5 Ma (97% of ^{39}Ar released) (black line) and an identical inverse isochron age of 123.0 ± 0.7 Ma with atmospheric initial argon. This age is very similar to those obtained from the Circum-Rhodope belt few kilometres to the south (CR4 and CR10). From the same sample, the biotite produced a convex age spectrum with maximum ages scattering between 55 and 60 Ma (grey line). A plateau age

was calculated at 59.7 ± 0.7 Ma (36% of ^{39}Ar released) but no reliable inverse isochron age could be calculated. The age difference between the two minerals from the same sample cannot be interpreted in terms of their closure temperature differences over a period of about 60 m.y. Due to its higher sensitivity to thermal overprint, it is likely that the biotite shows evidence for, almost complete, reset during late processes. This scenario is indeed compatible with the intrusion in the area of voluminous plutons by early Eocene (e.g., de Wet et al., 1989; Frei, 1996).

Two white micas were dated from sample SM9 both producing identical plateau ages (124.3 ± 0.5 Ma for 86% ^{39}Ar released and 124.6 ± 0.5 Ma for 98% of ^{39}Ar released) which are also similar to the calculated inverse isochron ages (Figure 4.5h) and to that of the white mica of sample SM78 from the same unit.

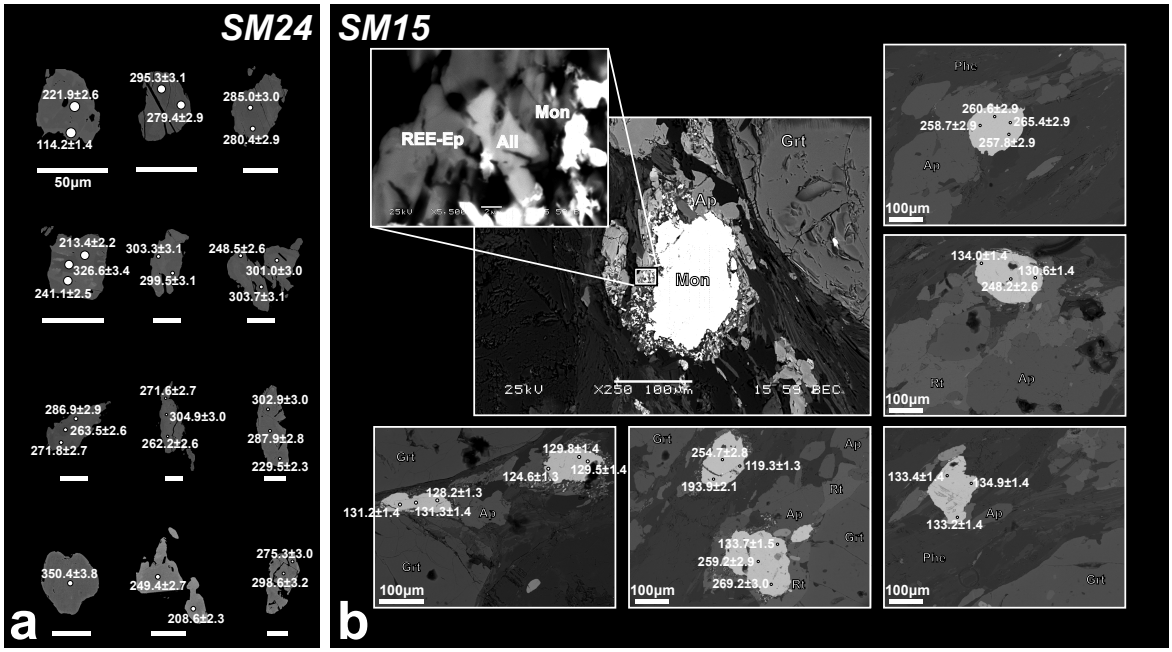

Figure 4.6: Monazite back-scatter images and corresponding ^{232}Th/^{238}U ages for samples SM24 (a) and SM15 (b). For sample SM15 a typical reaction corona surrounding matrix monazites is shown. White dots correspond to the analysed spots with a beam size of 7μm diameter. For sample SM24 the scale bars are 50μm long and for sample SM15 are 100μm long. See text for details.

4.5.2 In situ LA-ICP-MS (U-Th)/Pb monazite dating

Two samples were selected for in situ (U-Th)/Pb monazite dating from the eastern part of the study area (Figure 4.3). The isotopic dataset is given in Appendix C2. Back-scatter imaging of the northernmost sample SM24 revealed patchy zoning for the majority of the grains (Figure 4.6a). Both matrix and inclusion (in garnet and micas) monazites were dated. A concordia age of 302.0 ± 0.8 Ma was calculated from the dominant Carboniferous age cluster and is interpreted as a crystallisation age of the monazite (Figure 4.7a). Scattered ages between ca. 300 and 220 Ma indicate possible partial reset of the isotopic system. The youngest, yet slightly discordant, age from a bright rim (Figures 4.6a, 4.7a) is circa 115 Ma and weakly sets the maximum age for the re-crystallisation in Cretaceous.

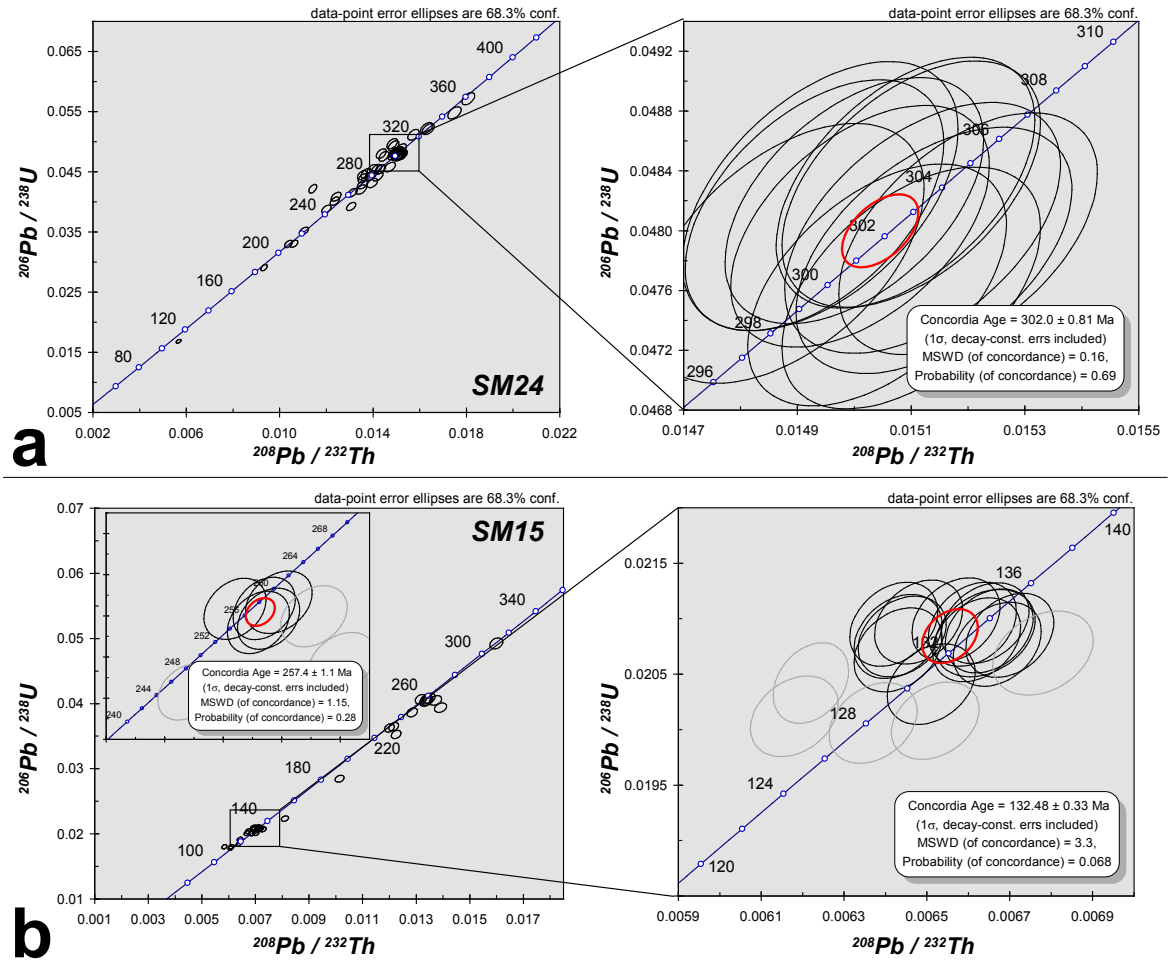

Figure 4.7: Monazite concordia plots and corresponding concordia ages for samples SM24 (a) and SM15 (b).

Back-scatter imaging of the monazite grains from sample SM15 revealed homogenous patterns with no obvious zoning (Figure 4.6b). Monazite is commonly decomposed at its outer parts into a corona made of apatite(ap)-allanite(all)-epidote(ep) according to the reaction (Figure 4.6b):

$$\text{Mon} = \text{Ap} + \text{REE-rich All} + \text{REE-Ep}$$

Similar REE-mobilisation reactions have been described in amphibolite-facies metamorphic rocks (e.g., Broska & Siman, 1998; Finger et al., 1998). Such textures depend on the composition of the metamorphic fluids (Ca bulk content and Ca/Na ratio) in addition to the P-T conditions (Majka & Budzyń, 2006; Budzyń et al., 2011; Krenn et al., 2012, and references therein). For sample SM15, both matrix and inclusion monazites (in garnet, kyanite and white micas) were dated. Among them, only the matrix monazites are surrounded by the coronas mentioned before whereas those protected from fluid interactions, as inclusion in garnet and kyanite, show no reaction textures. Different ages were obtained from cores and rims of the decomposed grains. The dominant age cluster found at their rims is Lower Cretaceous with a calculated concordia age at 132.5 ± 0.3 Ma whereas a late Permian age cluster (concordia age at 257.4 ± 1.1 Ma) is preserved exclusively at their cores (Figure 4.6b,7b). The non-decomposed grain yield late Permian ages. Based on the calculated ages and the micro-textures, we argue that the monazites of this sample crystallised in late Permian and re-crystallised during a Lower Cretaceous Alpine metamorphic event contemporaneous with the formation of the apatite-allanite-epidote coronas (Figure 4.6b,7b).

Based on the above, we conclude that the Carboniferous - Permian monazite ages of both samples reflect crystallisation of primary monazite grains. Based on the findings of the eastern sample SM15, there is evidence for later re-crystallisation in a temperature-assisted process under the effect of metamorphic fluids which is dated at Lower Cretaceous (circa 132 Ma) and is related to REE-mobilisation and breakdown of the monazites to apatite-allanite-epidote (Figure 4.6b). Similar breakdown coronas are absent from the monazites of sample SM24 from the north what implies that this sample escaped any Alpine re-crystallisation preserving the original monazite isotopic composition. Although that it is not safe to conclude a geographical trend for the Alpine re-crystallisation intensity, based on the findings of only two samples, we mention that it is only the eastern sample that recorded such re-crystallisation.

4.5.3 Interpretation of the results

To the eastern part of the Chalkidiki block, monazite re-crystallised in Lower Cretaceous (circa 132 Ma) contemporaneous with REE-mobilisation reaction coronas at the rims of monazites exposed to matrix fluids (Figures 4.6b, 4.7b). Similar reactions have already been described for amphibolite-facies rocks (e.g., Broska & Siman, 1998; Finger et al., 1998) and thus, we interpret the Lower Cretaceous re-crystallisation as the time of the amphibolite-facies overprint. The monazite cores and the non-decomposed monazite grains (usually as inclusions in garnet) preserved their initial isotopic composition and the corresponding calculated ages range between Carboniferous and Permian (Figure 4.7).

Cooling ages were calculated by $^{40}Ar/^{39}Ar$ step heating dating of micas for samples from both the basement and the cover. A reference closure temperature of 420 $\pm$ 30^{o}C (Harrison et al., 2009) that roughly corresponds to greenschist-facies conditions was adopted for the white mica grains. Our results clearly document cooling below the closure temperature at 125 Ma for the western and northern parts and between 95 and 100 Ma for the south-eastern part of the study area. Although that interpreting the age spectra of the Mesozoic phyllites/schists/orthogneisses is rather straightforward (Figure 4.5a-e,g,h), some complexity arises for the paragneisses embedded in basement orthogneisses (Figure 4.5f) due to inheritance and incomplete isotopic reset. However, even in this case consistent data were extracted from the most likely complete reset grain (medium grey line Figure 4.5f).

Based on our results, the oldest cooling age recorded in the area is 125 Ma. However, Lips et al. (2000) reported a spot fusion $^{40}Ar/^{39}Ar$ age at 143 $\pm$ 5 Ma from a basement mylonite close to our CR10 sample (Figure 4.3). Their age is significantly older than those obtained here. Following the above discussion about the inheritance and incomplete isotopic reset in the Palaeozoic basement, we suspect that the Jurassic age of Lips et al. (2000) is due to incomplete reset and does not signify cooling through the white mica closure temperature. In fact, this Jurassic age is quite similar to those obtained here for the incomplete reset white micas (and biotite) of sample SM42 (Figure 4.5f). Our argument on incomplete reset of the micas from the basement is strengthened by the existence of an almost non-reset old age of 275.3 $\pm$ 7.5 Ma few kilometres to the south (Lips et al., 2000).

4.6 Discussion

4.6.1 Cooling of the Chalkidiki block with reference to the metamorphic history

The Chalkidiki block displays an increase in the metamorphic conditions toward its eastern border as recently revealed by the discovery of pelitic eclogites in the Mesozoic sedimentary sequences deposited on top of the Vertiskos basement between Triassic and Jurassic (see Chapter 3). For the eastern part, the peak event (1.9GPa / 520^{o}C) was followed by

amphibolite-facies overprint at 1.2GPa / 620^{o}C. The timing of the amphibolite-facies overprint is determined here by the breakdown and isotopic re-equilibration of Permian monazites (Figure 4.6b) as Lower Cretaceous (∼132 Ma) (Figure 4.7). Subsequent cooling of the eastern part of the Chalkidiki block at mid-crustal level through the white mica closure temperature (420 ± 30^{o}C, Harrison et al., 2009) happened between 95 and 100 Ma (Figure 4.5).

Toward the western part of the Chalkidiki block, the metamorphic conditions decrease to blueschist/greenschist conditions (Michard et al., 1994a,b). The age of the peak-pressure event from the Chalkidiki block is rather unknown. However, based on existence of Tithonian sediments that are involved in the thrust system of the Chalkidiki and that contain neoformed glaucophane, albite, sericite and epidote (Ricou, 1965), the high-pressure event, at least for the western part of the Chalkidiki block, should be post-Upper Jurassic. Our $^{40}Ar/^{39}Ar$ dating on white micas allows a cooling age estimate at 125 Ma for the western part of the Chalkidiki. Overall, the trend for younger cooling ages toward the east correlates well with the increase of the metamorphic conditions toward the same direction.

4.6.2 Monazite dating of the amphibolite-facies re-equilibration in the Rhodope

The oldest available EMPA monazite ages from the Rhodopean imbricates (NRD) are from Reischmann & Kostopoulos (2002), Hoinkes et al. (2008) and Nagel et al. (2011) who found apparent monazite ages at circa 180 Ma age and attributed monazite formation to the UHP event. In a recent work, Didier et al. (2014) reported few monazite cores with similar apparent LA-ICP-MS ages and more importantly, a wealth of Mesozoic monazite ages that scatter between 115 and 165 Ma from the central part of the NRD. They calculated mean age values at 142 ± 11 Ma and at 138 ± 10 Ma for the two studied localities of the NRD and attributed the monazite formation to an upper amphibolite/granulite-facies event. As discussed in the previous section, our work support the existence of a similar amphibolite-facies event in the Chalkidiki block that is dated at 132 Ma (Figure 4.7).

The link between the two extreme parts of the Rhodope (i.e, the Chalkidiki block and the NRD) prior to the exhumation of the Southern Rhodope Core Complex (SRCC), has already been proposed on the basis of structural, kinematic and paleomagnetic data (Brun & Sokoutis, 2004, 2007). In this perspective, Monazite dating (Didier et al., 2014, and this chapter) provides an additional robust argument through the isotopic age of the amphibolite-facies overprint on both sides of the SRCC (Figure 4.2).

4.6.3 Rhodope: from peak eclogite-facies to near surface exposure

In the Rhodope extensive zircon dating carried out over the last decades has identified distinct metamorphic/magmatic events that are often tentatively correlated to large-scale geodynamic processes but without a generally accepted evolution model. In the following lines we will shortly present the metamorphic evidence that coincide with the assumed Mesozoic peak metamorphic conditions in the Rhodope.

The most common zircon metamorphic ages for the early high-pressure metamorphic event of the Rhodope are Upper Jurassic (circa 145 Ma) and were reported from garnet-kyanite gneisses, amphibolitised eclogites and associated paragneisses (e.g., Liati, 2005; Cornelius, 2008; von Quadt et al., 2008; Krenn et al., 2010; Liati et al., 2011). Somewhat older zircon ages from mafic eclogites and related metapelites (Bauer et al., 2007) as well as 160 Ma zircons from migmatitic gneisses that intrude mafic eclogites in the UHP Rhodopean localities (Bonev et al., 2012b) have both used as arguments in favour of a pre-Upper Jurassic age of the (U)HP event. Few circa 75 Ma zircon metamorphic ages from an orthogneisses, a garnet-kyanite gneiss, a garnet-rich mafic rock and an eclogite (Liati et al., 2002, 2011; Bauer et al., 2007) were either attributed to a high-pressure event or related to amphibolite-

facies overprint. These Cretaceous ages are from an upper imbricate unit of the NRD but due to the restricted occurrence of similar metamorphic zircon ages, a regional character of that event is unlikely. Alternatively, these ages could correlate with the Upper Cretaceous magmatism of the Rhodope (von Quadt & Peytcheva, 2005; Marchev et al., 2006; Peytcheva et al., 2007; von Quadt et al., 2010). A 126 Ma metamorphic age (Lu/Hf on garnet) was obtained from the upper imbricate unit (Kirchenbaur et al., 2012). *No matter what is the exact timing of the (U)HP event, it is obvious from the above that peak pressure and/or peak temperature metamorphic conditions span over the Jurassic and part of the Cretaceous.*

On the other hand, Mposkos & Wawrzenitz (1995) provided a 65 Ma age (Rb/Sr) which is indistinguishable from the 62 Ma age (U/Pb on zircon) reported by Liati et al. (2002) both from late pegmatites that crosscut the regional foliation of the gneisses. Contrary to the timing of the (U)HP event in the Rhodope, it is commonly accepted that these ages set an absolute minimum for the end of the metamorphic episodes of the Rhodopean gneisses. This is in agreement with the Maastrichtian - Paleocene deposits that rest on basement gneisses (Boyanov et al., 1982; Goranov & Atanasov, 1992) implying that part of the eastern Rhodope was near surface by uppermost Cretaceous. This is also in agreement with the Eocene apatite fission-track ages (Kydonakis et al., 2014a) that indicate near surface conditions (temperature less than 120^oC) also by uppermost Cretaceous at the western end of the Rhodope (i.e., in the Chalkidiki block). *This rises the next question that concerns the thermal history of the Rhodope between peak metamorphic conditions (Jurassic and part of the Cretaceous) and near surface arrival as deduced from the existence of Maastrichtian - Paleocene unconformable deposits and the upper Cretaceous crosscutting pegmatites.*

4.6.4 Record of post-amphibolite-facies cooling in the Chalkidiki block

The Chalkidiki block started to separate from the NRD in middle Eocene, due to the exhumation of the Southern Rhodope Core Complex (Brun & Sokoutis, 2004, 2007) (Figure 4.2). Consequently, the Chalkidiki block constituted the hanging-wall of the Kerdylion Detachment that controlled the exhumation of the SRCC and i) behaved as a coherent clockwise rotating block during the Paleogene, with moderate internal deformation, ii) underwent moderate brittle north-south extension since middle Miocene and iii) was only locally intruded by magmatic bodies during the Tertiary. This tectonic history of the Chalkidiki block created rather favourable conditions for maintaining isotopic evidence of the cooling path after peak metamorphic conditions.

Cooling after post-peak conditions is better recorded by a robust isotopic system such as the $^{40}Ar/^{39}Ar$. In the eastern Rhodope, the oldest available $^{40}Ar/^{39}Ar$ ages are at circa 150 Ma from allochthonous orthogneisses (Bonev et al., 2010). However, these ages cannot account for regional cooling as they pre-date peak conditions experienced by the Rhodopean gneisses (see section 6.3). Bonev et al. (2013b) obtained an $^{40}Ar/^{39}Ar$ age at circa 65 Ma for an amphibolite from the Byala Reka - Kechros dome of the eastern Rhodope but claimed that such "*anomalously old ages and a disturbed pattern in the low-temperature steps is caused by the presence of excess* ^{40}Ar" and thus, cannot be taken into consideration. Mukasa et al. (2003) reported a circa 45 Ma age (amphibole $^{40}Ar/^{39}Ar$) from a retrogressed eclogite but unfortunately the sample details are not adequately described in their short two-page publication. More importantly, a number of circa 40 Ma and younger $^{40}Ar/^{39}Ar$ ages were obtained from the imbricate units and from the exhumed Rhodopean gneiss domes that clearly document the timing of the regional cooling of the central Rhodope (e.g., Lips et al., 2000; Ovtcharova et al., 2003; Bonev et al., 2006, 2013b; Márton et al., 2010). Consequently, this leaves circa 100 m.y. time lag (from 140 to 45 Ma) between the inferred amphibolite-facies conditions and the timing that the $^{40}Ar/^{39}Ar$ records.

Beyond any doubt the post-45 Ma $^{40}Ar/^{39}Ar$ *ages are related to the early Aegean extension and the resultant exhumation of the Rhodopean domes rather that cooling of the Rhodopean*

gneisses after the peak metamorphic episode. Indeed, severe re-working of the earlier deformation fabrics, exhumation of gneiss domes beneath low-angle detachments (Bonev et al., 2006; Brun & Sokoutis, 2007), extended magmatic activity that includes uppermost Cretaceous - Oligocene magmatic bodies and Eocene-Oligocene volcanic centres and hydrothermal deposits (Pal'shin et al., 1975; Marchev & Singer, 2002; Marchev et al., 2006, 2010; Márton et al., 2010; Filipov & Marchev, 2011; Marchev & Filipov, 2012; Kaiser-Rohrmeier et al., 2013), all contributed to an increased thermal gradient in an active region affected by ductile extension and apparently precluded the existence of any pre-45 Ma medium-temperature isotopic record from the Rhodopean gneisses. The inferred high thermal gradient is further reflected into the relatively young low-temperature thermochronology data from the NRD (see review in Kydonakis et al., 2014a) and is in agreement with the existence of numerous Eocene - Oligocene zircon ages from kyanite eclogites, metapelites, metagabbros, biotite gneisses and pegmatites (e.g., Liati & Gebauer, 1999; Liati, 2005; Cornelius, 2008; Bosse et al., 2009; Liati et al., 2011; Moulas et al., 2013). The latter zircon ages, instead of representing yet another high-pressure event in the Rhodope they should be more likely related, from a geodynamic point of view, to core complex extension coeval with magmatic intrusions of the same age.

Consequently, the post-peak thermal evolution of the central Rhodope can be addressed using the record of the Chalkidiki gneisses. On this basis, we propose that cooling of the Rhodopean gneisses, as given by the white micas blocking temperature, happened around 95 Ma predating for about 50 m.y. the onset of Tertiary ductile extension of the Rhodope.

4.7 Conclusions

Prior to their separation by the exhumation of the Southern Rhodope Core complex in middle Eocene, the Chalkidiki block and the Northern Rhodope Domain underwent the same tectono-thermal history. Contrary to the Northern Rhodope Domain, the Chalkidiki block largely escaped the thermal effects of Tertiary tectonics. Therefore, we selected it as an ideal candidate to attempt defining the Mesozoic post-peak metamorphic evolution of the North Aegean. Based on the available literature data and our new findings, the P-T-t evolution of the Rhodope is compiled in Figure 4.8. Our contribution to the evolution of the Rhodope can be summarised in two main points:

(1) The regional amphibolite-facies re-equilibration was dated at 132 Ma by monazite U-Th-Pb LA-ICP-MS of a garnet-kyanite micaschist from the eastern part of the Chalkidiki block. The conclusion is based on primary Permian - Carboniferous monazite grains that show evidence for complete reset of their isotopic system coeval with REE-mobilisation reaction and formation of a corona made of apatite, allanite and epidote - a reaction that is typically described for amphibolite-facies rocks. The suggested timing for the amphibolite-facies overprint is slightly younger from the corresponding timing proposed recently for the central Rhodope based on monazite dating (circa 140 Ma; Didier et al., 2014 thus, linking the Chalkidiki block with the imbricates of the Northern Rhodope Domain further to the northeast.

(2) Cooling $^{40}Ar/^{39}Ar$ ages are around 125 Ma from the northern and western parts and around 95 Ma for the southeastern part of the Chalkidiki block. This trend for younger cooling ages toward the southeast coincides with the increasing metamorphic conditions toward the same direction. As no medium-temperature geochronology record is preserved prior to 45 Ma in the Northern Rhodope Domain due to strong tectono-thermal reworking by Aegean extension, this cooling around 95 Ma likely corresponds to the time at which the Rhodopean gneisses reached mid-crustal levels.

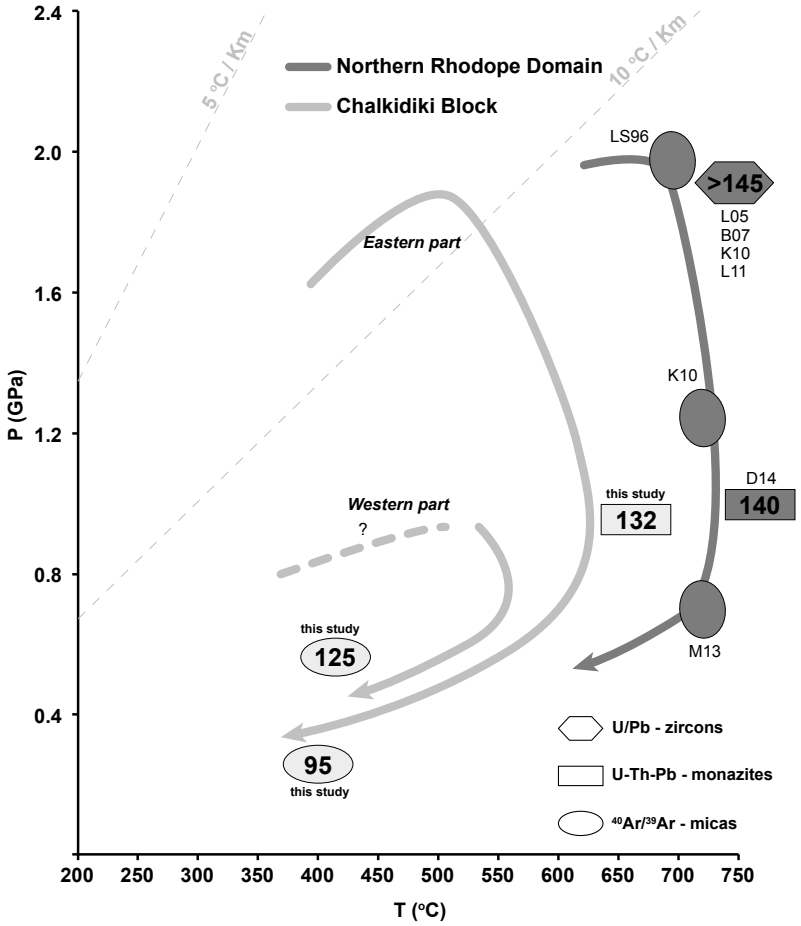

Figure 4.8: Simplified P-T paths for the Chalkidiki Block and the Northern Rhodope Domain (see Chapter 3). The timing of the major metamorphic events, based on literature data and on our results, is also shown. See text for details. LS96: Liati & Seidel (1996), L05: Liati (2005), B07: Bauer et al. (2007), K10: Krenn et al. (2010), L11: Liati et al. (2011), M13: Moulas et al. (2013), D14: Didier et al. (2014).

Chapter 5

Low-temperature thermochronology: apatite Fission-Track analysis and transdimensional inverse thermal modelling

Upper Cretaceous exhumation of the western Rhodope Metamorphic Province (Chalkidiki Peninsula, northern Greece)

Konstantinos Kydonakis[a], Kerry Gallagher[a], Jean-Pierre Brun[a], Marc Jolivet[a], Frédéric Gueydan[b], Dimitrios Kostopoulos[c]

[a]Géosciences Rennes, UMR 6118CNRS, Université Rennes1, Campus de Beaulieu, 35042 Rennes, France
[b]Géosciences Montpellier, UMR 5243CNRS, Université Montpellier2, place E. Bataillon, 34095 Montpellier, France
[c]Faculty of Geology and Geoenvironment, National and Kapodistrian University of Athens, Panepistimioupoli, Zographou, Athens 15784, Greece

AGU PUBLICATIONS

Tectonics

RESEARCH ARTICLE
10.1002/2014TC003572

Key Points:
- The Vertiskos Unit is the western-most part of the Rhodope Metamorphic Province
- Fission track analysis implies Upper Cretaceous exhumation of the Vertiskos Unit
- Our work establishes the Vertiskos Unit as the oldest exhumed basement of Greece

Supporting Information:
- Readme
- Figure S1
- Figure S2

Correspondence to:
K. Kydonakis,
konstantinos.kydonakis@univ-rennes1.fr

Citation:
Kydonakis, K., K. Gallagher, J.-P. Brun, M. Jolivet, F. Gueydan, and D. Kostopoulos (2014), Upper Cretaceous exhumation of the western Rhodope Metamorphic Province (Chalkidiki Peninsula, northern Greece), *Tectonics*, *33*, doi:10.1002/2014TC003572.

Received 4 MAR 2014
Accepted 9 MAY 2014
Accepted article online 22 MAY 2014

Upper Cretaceous exhumation of the western Rhodope Metamorphic Province (Chalkidiki Peninsula, northern Greece)

Konstantinos Kydonakis[1], Kerry Gallagher[1], Jean-Pierre Brun[1], Marc Jolivet[1], Frédéric Gueydan[2], and Dimitrios Kostopoulos[3]

[1]Géosciences Rennes, UMR 6118 CNRS, Rennes, France, [2]Géosciences Montpellier, UMR 5243 CNRS, Montpellier, France, [3]Faculty of Geology and Geoenvironment, National and Kapodistrian University of Athens, Athens, Greece

Abstract The Vertiskos Unit of northern Greece is an elongated basement belt with a complex poly-metamorphic history. It extends from Greece (Chalkidiki peninsula), to the south, up to Serbia, in the north, and arguably represents the westernmost part of the Rhodope Metamorphic Province (northern Greece to southern Bulgaria). The Vertiskos Unit experienced a medium pressure lower amphibolite-facies metamorphic overprint during the Alpine Orogeny. The available medium-temperature geochronology implies that it remained at temperature of approximately 300°C (or slightly higher) during Lower Cretaceous. In order to constrain its post-Lower Cretaceous thermal history, until near-surface exposure, we applied apatite fission track analysis. The central ages obtained range from 68.5 ± 3.8 to 46.6 ± 3.6 Ma (uppermost Cretaceous to Middle Eocene) and mean track lengths between 13 and 13.5 μm. We applied two inverse thermal modeling approaches using either each sample independently (high degree of freedom in the thermal history, better data fit) or all samples together interpreting them as a vertical profile (simpler thermal history, worse data fit). Irrespective of the modeling approach, we conclude that the bulk thermal history of the Vertiskos Unit crosses the high-temperature limit of the apatite partial annealing zone by the uppermost Cretaceous and reaches near-surface conditions as early as lower/middle Eocene. These results contrast with the thermal history of the other domains of the Rhodope Metamorphic Province further east (namely the Southern Rhodope Core Complex and the Northern Rhodope Complex) and establish the Vertiskos basement complex as the oldest exhumed coherent basement fragment of the Rhodope Metamorphic Province and Greece.

1. Introduction

The northeastern part of Greece and southwestern part of Bulgaria is known as the Rhodope Metamorphic Province [see *Burg*, 2012, and references therein] (Figure 1). It constitutes an extended tectonic element between two Alpine Mountain Chains: the Carpathians-Balkanides to the north and the Dinarides-Hellenides to the south. Widespread Jurassic-Cretaceous metamorphic ages [*Reischmann and Kostopoulos*, 2002; *von Quadt et al.*, 2008, 2009; *Krenn et al.*, 2010; *Nagel et al.*, 2011; *Liati et al.*, 2011, and references therein], roughly corresponding to eclogites-facies peak event and subsequent amphibolite-facies overprint, have been described for the whole domain in the literature. The final unroofing, as estimated by low-temperature thermochronology, for the central and northeastern parts is well defined at Eocene-Miocene [e.g., *Hejl et al.*, 1998, 2010; *Wuthrich*, 2009]. Regardless, the cooling history of the westernmost part of the Rhodope Metamorphic Province, known as the Serbo-Macedonian Domain, remains poorly constrained.

Apatite and zircon fission track (AFT, ZFT) analysis is often adopted for determining low-temperature thermal events. A general overview of the basic methodology is given in *Gallagher et al.* [1998] and many different FT applications has been reported in the literature over the past few decades such as investigation of the thermal evolution of basement rocks and sedimentary basins [e.g., *Leech and Stockli*, 2000; *Barbarand et al.*, 2001; *Foster and Raza*, 2002; *Jolivet et al.*, 2007; *Labaume et al.*, 2008; *Balestrieri et al.*, 2011; *Sanchez et al.*, 2011; *Sahu et al.*, 2013; *Yang et al.*, 2013], passive margin denudation history [e.g., *Gunnell et al.*, 2003; *Yi et al.*, 2009; *Cogne et al.*, 2011, 2012; *Dörr et al.*, 2012], detritus supply and provenance studies [e.g., *Carter*, 1999; *Bernet and Garver*, 2005; *Carrapa*, 2009; *Wang et al.*, 2011; *Balestrieri et al.*, 2013]. Apatite FT age data are best coupled with spontaneous track length measurement allowing for the determination of a relatively detailed low-temperature thermal history (T-t). The method can be applied to rocks that have previously been annealed at temperature above the apatite partial annealing zone (PAZ; ~120°C; dependence on the crystal composition) [*Donelick et al.*,

5.1 Introduction

The northeastern part of Greece and southwestern part of Bulgaria is known as the Rhodope Metamorphic Province (see Burg, 2012, and references therein) (Figure 5.1). It constitutes an extended tectonic element between two Alpine Mountain Chains: the Carpathians – Balkanides to the north and the Dinarides – Hellenides to the south. Widespread Jurassic – Cretaceous metamorphic ages (Reischmann & Kostopoulos, 2002; von Quadt et al., 2008, 2009; Krenn et al., 2010; Nagel et al., 2011; Liati et al., 2011, and references therein), and references therein, roughly corresponding to eclogites-facies peak event and subsequent amphibolite-facies overprint, have been described for the whole domain in the literature. The final unroofing, as estimated by low-temperature thermochronology, for the central and northeastern parts is well defined at Eocene – Miocene (e.g. Hejl et al., 1998, 2010; Wuthrich, 2009). Regardless, the cooling history of the westernmost part of the Rhodope Metamorphic Province, known as the Serbo-Macedonian Domain, remains poorly constrained.

Apatite and zircon fission-track (AFT, ZFT) analysis is often adopted for determining low-temperature thermal events. A general overview of the basic methodology is given in Gallagher et al. (1998) and many different FT applications has been reported in the literature over the past few decades such as investigation of the thermal evolution of basement rocks and sedimentary basins (e.g. Leech & Stockli, 2000; Barbarand et al., 2001; Foster & Raza, 2002; Jolivet et al., 2007; Labaume et al., 2008; Balestrieri et al., 2011; Sanchez et al., 2011; Sahu et al., 2013; Yang et al., 2013), passive margin denudation history (e.g. Gunnell et al., 2003; Yi et al., 2009; Cogné et al., 2011, 2012; Dörr et al., 2012), detritus supply and provenance studies (e.g. Carter, 1999; Bernet & Garver, 2005; Carrapa, 2009; Wang et al., 2011; Balestrieri et al., 2013). Apatite FT age data are best coupled with spontaneous track length measurement allowing for the determination of a relatively detailed low-temperature thermal history (T-t). The method can be applied to rocks that have previously been annealed at temperature above the apatite partial annealing zone [PAZ; $\sim 120^{o}$C; dependence on the crystal composition; Donelick et al. (2005)] thus determining their low-temperature cooling path after the peak thermal event. This, combined with other low- ([U-Th]/He) or mid-temperature (^{40}Ar/^{39}Ar) methods, can be used to decipher the regional signal of exhumation and cooling of an area.

In the present work we deal with the timing of regional cooling of the Serbo-Macedonian Domain and in particular its upper part namely the Vertiskos Formation (sensu Kockel et al., 1977; Vertiskos Unit hereafter). For this purpose new apatite FT age data and inverse thermal modelling for basement rocks are presented. We then proceed with comparing the obtained results with those from the central and eastern parts of the Rhodope Metamorphic Province summarising also the available low-temperature data. This allows us to define first order similarities and differences between different areas in terms of their low temperature evolution during Upper Cretaceous – Tertiary.

5.2 Geological setting

The Hellenides constitute an integral part of the Alpine-Himalayan mountain chain and are the product of convergence between the stable South European margin to the north and the North Gondwanan passive margin to the south. Their Alpine geodynamic evolution has been discussed at length by van Hinsbergen et al. (2005a), Jolivet & Brun (2010), Ring et al. (2010), Royden & Papanikolaou (2011) and Papanikolaou (2013). The centrepiece of the above studies is the continuous southward retreat of the subducting Hellenic slab since the Eocene that brought about a concomitant southward migration of magmatism in the severely extending Aegean lithosphere (upper plate), a slow-down in the rate of plate convergence coeval with acceleration of the trench retreat as well as a southward shift in the ages of

progressively younger subduction-related metamorphism.

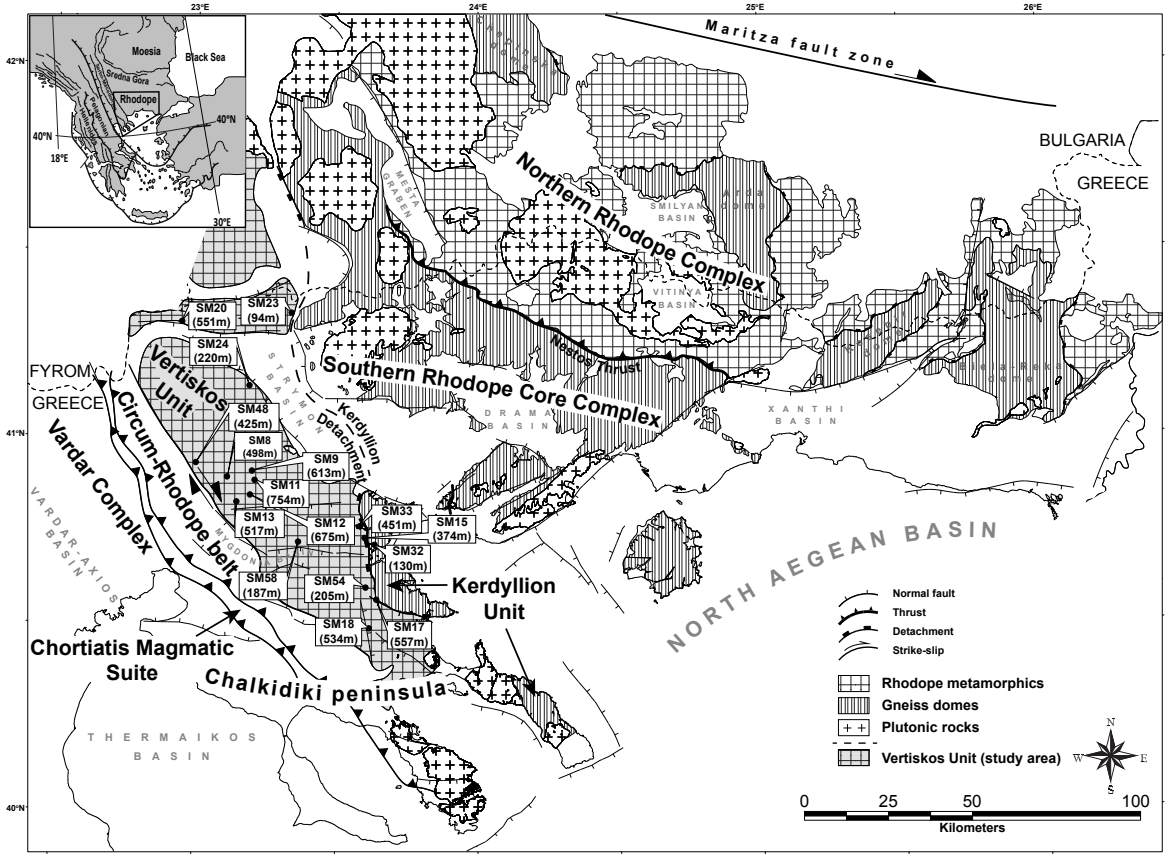

Figure 5.1: Simplified geological map of the Rhodope Metamorphic Province. Three tectonic domains can be distinguished, from northeast to southwest: (i) the Northern Rhodope Complex (NRC), (ii) the Southern Rhodope Core Complex (SRCC) and (iii) Serbo-Macedonian Domain (SMD). The latter is further subdivided into the lower Kerdyllion Unit, to the east, and the upper Vertiskos Unit (our study area) to the west. See text for details. Modified after Kockel & Mollat (1977), Sakellariou & Dürr (1993) and Burg (2012). Normal faults after Sokoutis et al. (1993), Tranos et al. (2003), Papanikolaou et al. (2006) and Brun & Sokoutis (2007). Our sampling locations (sample code and elevation) from the Serbo-Macedonian Domain are also shown.

The Rhodope Metamorphic Province (RMP; Burg et al., 1990; Bonev et al., 2006; Krenn et al., 2010; Jahn-Awe et al., 2010; Nagel et al., 2011) constitutes the hinterland of the Hellenic Subduction System (northeast Greece – southwest Bulgaria) (Figure 5.1). It can be viewed as a southwestward piling-up, crustal-scale, syn-metamorphic, amphibolite-facies duplex (Burg et al., 1996; Ricou et al., 1998) strongly affected by later extension of core complex type (Sokoutis et al., 1993; Dinter & Royden, 1993; Brun & Sokoutis, 2007) and syn- to post-tectonic magmatism (e.g. Kolocotroni & Dixon, 1991; Jones et al., 1992; Marchev et al., 2004, 2013). It is bordered to the north and east by the Maritza dextral strike-slip fault and the Middle Eocene-present Thrace Basin, respectively. Its southwestern limit corresponds to the Vardar – Axios – Thermaikos basins which in turn roughly correlate with the Vardar Suture Zone (VSZ) (Ricou et al., 1998). The continuity of the RMP to the south is hidden beneath the North Aegean Basin deposits [Papanikolaou et al., 2006]. In order to discuss the Upper Cretaceous – Tertiary thermal evolution of the area, we adopt a simple three-fold division where the RMP is divided, from northeast to southwest, into three tectonic domains: (i) the Northern Rhodope Complex (NRC), (ii) the Southern Rhodope Core Complex (SRCC) and (iii) Serbo-Macedonian Domain (SMD; Figure 5.1).

The NRC (Figure 5.1) is characterised by a lithological variability reflecting the diversity of its constituting crustal fragments. Several units can be identified in the greek and bulgar-

ian literature, all sharing a common Mesozoic – Cenozoic tectono-metamorphic history (see Burg, 2012, and references therein). The NRC is mainly made of ortho-gneisses, eclogites and amphibolites, overlain by para-gneisses, schists and scarse marble horizons (Mposkos & Liati, 1993; Liati & Seidel, 1996; Turpaud & Reischmann, 2010; Janák et al., 2011; Moulas et al., 2013). Volumetrically-low ultramafic rocks also occur usually at high structural levels. Micro-diamonds reported from gneisses of the NRC sets the RMP as the youngest diamondiferous UHP belt (Mposkos & Kostopoulos, 2001; Perraki et al., 2006; Schmidt et al., 2010) with pre-Upper Jurassic peak metamorphism (Reischmann & Kostopoulos, 2002; Hoinkes et al., 2008; Nagel et al., 2011; Liati et al., 2011, and references therein) and subsequent Cretaceous upper amphibolite-facies regional overprint (Reischmann & Kostopoulos, 2002; Bauer et al., 2007; Bosse et al., 2010; Krenn et al., 2010; Liati et al., 2011). Basin deposits, unconformably overlying the exhumed metamorphic rocks are dated as early as Maastrichtian - Paleocene (Boyanov et al., 1982; Goranov & Atanasov, 1992) and are related to plutonic rocks and volcanics of uppermost Cretaceous to lowermost Oligocene age (e.g. Peytcheva et al., 1998; Soldatos et al., 2001, 2008; Ovtcharova et al., 2003; Marchev et al., 2006, 2010; Jahn-Awe et al., 2010; Filipov & Marchev, 2011). The deposits mark the initiation of extension affecting the nappe complex (see Burchfiel et al., 2000). Distinct extensional gneiss domes exposed below low-angle detachments formed in late Eocene (Chepinska, Arda, Kesebir and Biela-Reka domes; Figure 5.1) (see Bonev et al., 2006, 2013b; Jahn-Awe et al., 2012; Kaiser-Rohrmeier et al., 2013).

The SRCC (sensu Brun & Sokoutis, 2007) is a wide metamorphic dome of roughly triangular shape which lies immediately southwest of the NRC (Figure 5.1). Their contact is located along a mylonite-bearing SW-verging thrust fault known as the Nestos Thrust. The SRCC consists of highly deformed Permian-Carboniferous mylonitic ortho-gneisses, intercalated mica-schists and amphibolites capped by a thick marble sequence. The exhumed dome shows a flat-lying foliation over its width (Brun & Sokoutis, 2007). The gneisses experienced upper greenschist – lower amphibolite-facies conditions and the available metamorphic ages are exclusively post-Lower Eocene (post-51 Ma; Wawrzenitz & Krohe, 1998; Lips et al., 2000). Oligo-Miocene plutonic bodies that show syn-tectonic features intrude the basement rocks (Kolocotroni & Dixon, 1991; Kaufman, 1995; Dinter et al., 1995; Eleftheriadis et al., 2001). Widespread NW-SE-trending basins have developed after Middle Miocene (e.g. Strymon and Drama basins; Figure 5.1) (Snel et al., 2006; Burchfiel et al., 2008) although remnants of mid-Eocene nummulite-bearing transgressive limestones have been reported locally (e.g. Xanthi basin).

The SRCC is bounded immediately to the west by the Serbo-Macedonian Domain (SMD; equivalent to 'Serbo-Macedonian Massif' sensu Dimitrijević, 1963) (Figure 5.1). The SMD can be traced from the Hellenic territory (Chalkidiki peninsula; see Kockel et al., 1971) until Serbia to the far north. In the Hellenic domain, Kockel et al. (1971) divided the SMD into the lower Kerdyllion Unit and the upper Vertiskos Unit (Figure 5.1). Himmerkus et al. (2012) demonstrated the Rhodopean affinity of the lower Kerdyllion Unit. Brun & Sokoutis (2007) re-interpreted the contact between the Vertiskos and Kerdyllion Units as an extensional detachment fault, namely the Kerdylion Detachment, that accommodated the exhumation of the SRCC since Middle Eocene (Figure 5.1).

The Vertiskos Unit is an isolated and elongated basement belt with a pretty much constant width of ca. 30 Km. In Bulgaria, to the north, it is known as the Ograzden Unit (Zagorchev, 1976). In Greece, typical rocktypes are Silurian granitoids (Himmerkus et al., 2009a), later transformed into ortho-gneisses, intercalated para-gneisses and thin marble horizons, leucocratic granitic/pegmatitic intrusions, deformed amphibolites and scarce eclogite boudins (Kockel et al., 1971, 1977). The Vertiskos Unit was intruded in Lower Triassic by the Arnea-Kerkini magmatic complex (Himmerkus et al., 2009b) with which it experienced the same post-intrusion medium pressure amphibolite-facies overprint (Burg et al., 1995;

Kilias et al., 1999). The Permo-Triassic Volvi meta-mafic body crops out near the eastern part of the Vertiskos Unit and shows rift-related isotopic signatature (Bonev & Dilek, 2010). Similar to the NRC to the northeast where scarce uppermost Jurassic ages ($^{40}Ar/^{39}Ar$ on micas) have been reported in the literature for allochthonous ortho-gneisses (∼155 Ma; Ku-214 and Ku-215 of Bonev et al., 2010), Lips et al. (2000) reported a ca. 147 Ma age for the Vertiskos Unit of Greece. In addition, Kounov et al. (2010) reported a ca. 160 Ma age for the last six high-temperature gas-release steps (white mica) from the equivalent Ograzden Unit of Bulgaria. Lower Cretaceous medium-temperature metamorphic ages are also abundant (ca. 100 – 140 Ma for K/Ar and ca. 80 – 160 Ma for Rb/Sr; Harre et al., 1968; Zervas, 1979; Papadopoulos & Kilias, 1985; de Wet et al., 1989). The structural continuity and the NW-SE-trending fabrics of the Vertiskos Unit are disrupted by small sedimentary basins developed only after Middle Miocene (Koufos et al., 1995). Large Eocene batholiths (de Wet et al., 1989; Christofides et al., 1990) and limited Oligo-Miocene plutonic rocks (Frei, 1992; Gilg & Frei, 1994, and our own data), often accompanied by small coeval volcanic extrusions (Tompouloglou, 1981; Harkovska et al., 2010) intrude the Vertiskos Unit.

In summary, the Mesozoic – Cenozoic history of the three tectonic domains of the RMP is rather contrasted. The NRC is characterised by Jurassic – Cretaceous eclogite- and amphibolite-facies overprint, Maastrichtian basin deposits, Upper Cretaceous to Miocene magmatism and Eocene migmatisation within the exhumed gneiss domes. The SRCC is characterised by post-Lower Eocene metamorphic ages, Middle Miocene basin formation and Oligo-Miocene magmatism. The Vertiskos Unit records uppermost Jurassic - Lower Cretaceous metamorphic ages, Middle Miocene basin formation and Eocene – Miocene magmatism.

5.3 Sampling strategy

As mentioned above, there is clear evidence for Lower Cretaceous re-crystallisation at medium pressure amphibolite-facies conditions in the Vertiskos Unit. Initial exhumation of the unit can be considered as starting in the Upper Cretaceous based on zircon FT ages [71.9 ± 9.4 Ma in northern Greece by Wuthrich (2009) and 87.7 ± 8.6 Ma in southwestern Bulgaria by Kounov et al. (2010)]. In Greece, close-to-surface exposure of the metamorphics is roughly constrained by a 43 ± 6.8 Ma apatite FT age (Wuthrich, 2009). Therefore, a widespread cooling phase during Upper Cretaceous – Eocene seems to be recorded in the Vertiskos - Ograzden Units. However, the regional post-Lower Cretaceous cooling history and any possible lateral variations are yet to be investigated.

Here, we focus on the Vertiskos Unit (Chalkidiki peninsula, northern Greece) with 15 samples: 4 ortho-gneisses, 3 granites, 7 para-gneisses and 1 pegmatite (Figure 5.1; Table 5.1). One additional sample from the underlying Kerdyllion Unit was analysed. The lack of data in the studied area is in stark contrast with the wealth of published ages from the SRCC and the NRC to the east (see discussion below).

5.4 Apatite fission-track analysis

5.4.1 Analytical methods

Apatite separation from the 16 samples was undertaken at Géosciences Rennes, France following the procedure described by Jolivet et al. (2010). The samples were crushed and the apatite grains were separated using a Wilfley table, heavy liquids and a Frantz isodynamic separator before being mounted on glass slides using epoxy resin and polished to expose an internal surface. We used the external detector method to calculate the FT ages (Gleadow, 1981; Hurford & Green, 1982). The polished apatite mounts were etched in 6.5% HNO3

(1.6M) for 45 seconds at 20^{o}C to reveal the spontaneous fission tracks and a low-U external mica sheet was attached before being irradiated with a neutron fluence rate of 1.0 x 1016 neutrons/cm^2 (OSU, Oregon State University, USA). CN5 dosimeters were used to monitor the neutron flux (Hurford & Green, 1983). The induced tracks in the external detector were etched with 60% HF for 40 minutes at 20^{o}C.

The AFT age measurements were made at Géosciences Rennes with a Zeiss M1 microscope at 1250x magnification under dry objectives. For each sample between 18 and 40 c-axis-oriented, inclusion-free apatite crystals were analysed using the Trackscan® and TrackWorks® software packages in manual mode. Age calculations were made with the TrackKey® software (Dunkl, 2002) using a weighted mean ζ value equal to 339.1 ± 6.8 (K.K.) obtained on both Durango and Mt. Dromedary apatite standards. All ages reported are central ages according to Galbraith & Laslett (1993). Errors on ages are quoted at 2σ.

Length measurements of horizontal confined tracks and etch pit dimensions (as a proxy for apatite composition) (Barbarand et al., 2003; Carlson et al., 1999; Ketcham et al., 2007), were made with a Zeiss Axioplan microscope (Birkbeck University of London) equipped with a digitising tablet and computer-driven stage with 1250x magnification using dry objectives. Dpar measurements were calibrated against Durango standards (K.K.).

Table 5.1: Fission track data from the Serbo-Macedonian domain of Northern Greece. Latitude/Longitude are given in WGS1984. ρ_d is the density of induced fissions tracks (per cm^2) that would be obtained in each sample if its U concentration was equal to the U concentration of the CN5 glass dosimeter. Numbers in parantheses are total number of counted tracks. ρ_s and ρ_i are the sample spontaneous and induced track densities per cm^2. U is the calculated uranium concentration in ppm. P(χ^2) is the probability in % of χ^2 for ν degrees of freedom (where ν = number of crystals -1). Age is central age, according to Galbraith & Laslett (1993), given in Ma and calculated using the TRACKKEY software (Dunkl, 2002). Error is given at $\pm 2\sigma$. Mean track length (M.T.L.) is given in μm and measurements were performed on horizontal confined fission tracks in crystal sections parallel to the c crystallographic axis. Dpar is the measured mean diameter (in μm) of the etched trace of the intersection of a fission track with the surface of the analysed apatite crystal, measured parallel to the c axis.

Sample[i]	Rock[ii]	Lat.	Long.	El.[iii]	Gr.[iv]	ρ_d (N_d)	ρ_s (N_s)	ρ_i (N_i)	U (ppm)	P(χ^2)	Age	σ	MTL	sd	Dpar
SM8	O	40.90	23.12	498	40	9.375 (9098)	20.148 (2182)	55.928 (6057)	68	73	57.0	1.9	12.99	1.17	1.17
SM9	G	40.91	23.21	613	40	9.651 (9098)	7.246 (1321)	24.279 (4426)	32	84	48.7	1.9	13.10	1.52	1.48
SM11	P	40.88	23.22	754	40	9.992 (10419)	5.325 (639)	15.558 (1867)	20	63	57.7	3.0	13.18	1.03	1.36
SM12	O	40.84	23.21	675	33	10.087 (10419)	6.876 (647)	23.039 (2168)	27	100	50.8	2.5	13.51	0.90	0.99
SM13	P	40.83	23.16	517	40	10.372 (10419)	5.791 (911)	18.086 (2845)	20	97	56.1	2.5	13.05	1.14	1.04
SM15	P	40.73	23.61	374	26	10.656 (10419)	4.549 (348)	15.32 (1172)	16	92	53.4	3.5	-	-	-
SM17	P	40.57	23.66	557	37	10.846 (10419)	3.263 (218)	11.063 (739)	12	100	54.0	4.3	-	-	-
SM18	P	40.49	23.62	534	28	9.433 (10362)	3.464 (239)	11.855 (818)	14	99	46.6	3.6	-	-	-
SM20	O	41.31	22.93	551	26	9.94 (10362)	2.979 (188)	9.239 (583)	11	92	54.1	4.7	-	-	-
SM23	O	41.34	23.33	94	36	10.431 (10905)	7.599 (785)	27.957 (2888)	30	90	47.9	2.2	13.51	1.06	1.24
SM24	P	41.13	23.21	220	26	10.278 (10362)	4.368 (280)	15.226 (976)	16	48	50.1	3.7	-	-	-
SM32	P	40.71	23.65	130	28	10.16 (10905)	2.449 (226)	9.491 (876)	11	99	44.3	3.4	-	-	-
SM33	G	40.76	23.58	451	33	9.889 (10905)	12.618 (1147)	40.814 (3710)	47	59	51.6	2.1	13.54	1.24	2.12
SM48	PE	40.93	23.01	425	33	10.615 (10362)	8.315 (528)	21.732 (1380)	23	97	68.5	3.8	13.31	0.93	1.13
SM54	P	40.61	23.60	205	18	10.784 (10362)	1.156 (52)	2.4 (108)	3	100	87.4	14.9	-	-	-
SM58	G	40.72	23.38	187	20	11.122 (10362)	1.912 (108)	6.372 (360)	7	95	56.3	6.3	13.26	1.28	-

[i] Italics for sample from the Kerdyllion Unit, regular text for samples from the Vertiskos Complex [ii] [O] Orthogneiss, [G] Granite, [P] Paragneiss, [Pe] Pegmatite [iii] Elevation in meters [iv] Number of grains used

5.4.2 Results

The results of the AFT analysis are presented in Table 5.1 (see supplementary material for the full dataset). For each sample between 18 and 40 single grains were used for the age calculation (supplementary material #1). For the Vertiskos Unit, a tight cluster of apatite FT ages range from 46.6 ± 3.6 to 57.7 ± 3.0 Ma. The westernmost sample (SM48) is a deformed pegmatite which yielded a significantly older age (68.5 ± 3.8 Ma). SM54 gave an exceptionally old age of 87.4 ± 14.9 Ma but due to its poor grain quality (cracked crystals with plenty of inclusions), low uranium content (¡ 3 ppm), wide range of individual grain ages (χ^2 value of 3.72) and the fact that this age doesn't fit the rest of the results, this sample will be excluded from further consideration. The apatite FT age from the Kerdyllion Unit is 44.3 ± 3.4 Ma (SM32), slightly younger than those of the Vertiskos Unit.

Track lengths and the corresponding c-axis angle were obtained for 9 samples of the Vertiskos Unit (supplementary material #2). Hundred individual lengths were measured for the majority of the samples with the exception of 3 samples (41, 81 and 86 length measurements for SM58, SM11 and SM9 respectively). The calculated mean track length (MTL) ranges from 13 to 13.5 μm and the standard deviations from 0.9 to 1.5 μm. Eight samples were used for Dpar measurement. An average of 220 measurements was made for each sample (made on 42 - 67 individual grains). With the exception of SM33 which shows high Dpar value (2.12 μm), the rest of the samples range from 0.99 to 1.48 μm indicating F-rich apatites.

5.5 Inverse thermal history modelling

5.5.1 Methodology

Given the fission track analysis for a given sample, we can infer the thermal history of each sample individually using an inverse modelling scheme. Here, we adopted the Markov Chain Monte Carlo (MCMC) approach described by Gallagher (2012), implemented in the software QTQt. Details of the specific implementation can be found in Gallagher (2012) and other implementations of MCMC can be found in Gallagher et al. (2009), Charvin et al. (2009), Hopcroft et al. (2007) and Sambridge et al. (2006). In brief, the applied inversion scheme is based on Bayesian transdimensional sampling in which the complexity of the thermal history solutions (defined as the number of discrete time-temperature points forming the thermal history) are inferred from the data rather than being specified in advance. The Bayesian approach naturally prefers simpler thermal history models and so reduces problems associated with over interpreting the data (i.e. introducing unwarranted structure in the inferred thermal histories). The output of the method is a population of thermal histories, which reflects the range of acceptable models in terms of a (posterior) probability distribution. Individual models, such as the best data-fitting (maximum likelihood) model or the expected model (effectively the weighted mean thermal history from the posterior distribution) can be also extracted from the posterior distribution to visualise a single thermal history. Additionally, the QTQt implementation allows a group of individual samples of different elevations to be treated as a vertical profile (equivalent to a borehole in the upper crust). In this approach, we make the implicit assumption that all the samples have experienced a similar form of thermal history, with lower elevation samples having always been hotter or at least as hot as the higher elevation samples and there have been no major disruptions of this geometrical/structural relationship since the samples cooled through the apatite fission-track PAZ (Gallagher et al., 1998).

5.5.2 Results

As mentioned earlier, a wealth of available medium-temperature geochronology data exist in the literature for the basement rocks of the Vertiskos Unit. They include Ar/Ar, K/Ar and Rb/Sr data from ortho-gneisses, biotite gneisses, intercalated pegmatites and garnet-mica schists. The Ar/Ar system peaks at ca. 150 Ma (Lips et al., 2000; Kounov et al., 2010). The K/Ar system culminates at Lower Cretaceous (between 100 and 140 Ma; Harre et al., 1968; Marakis, 1969; Papadopoulos & Kilias, 1985). The Rb/Sr isochrons points variably between uppermost Jurassic and Upper Cretaceous times (Zervas, 1979; Lilov et al., 1983; Papadopoulos & Kilias, 1985; de Wet et al., 1989). For this, we can safely conclude that the temperature remained high-enough to cause complete annealing in the FT data at least until the end of Lower Cretaceous. To respect this independent geological evidence we constrained the model histories to pass through 350 ± 50^{o}C at 100 - 140 Ma. As this is well above the apatite partial annealing zone, there is no significant effect on the thermal history models inferred from the inverse modelling.

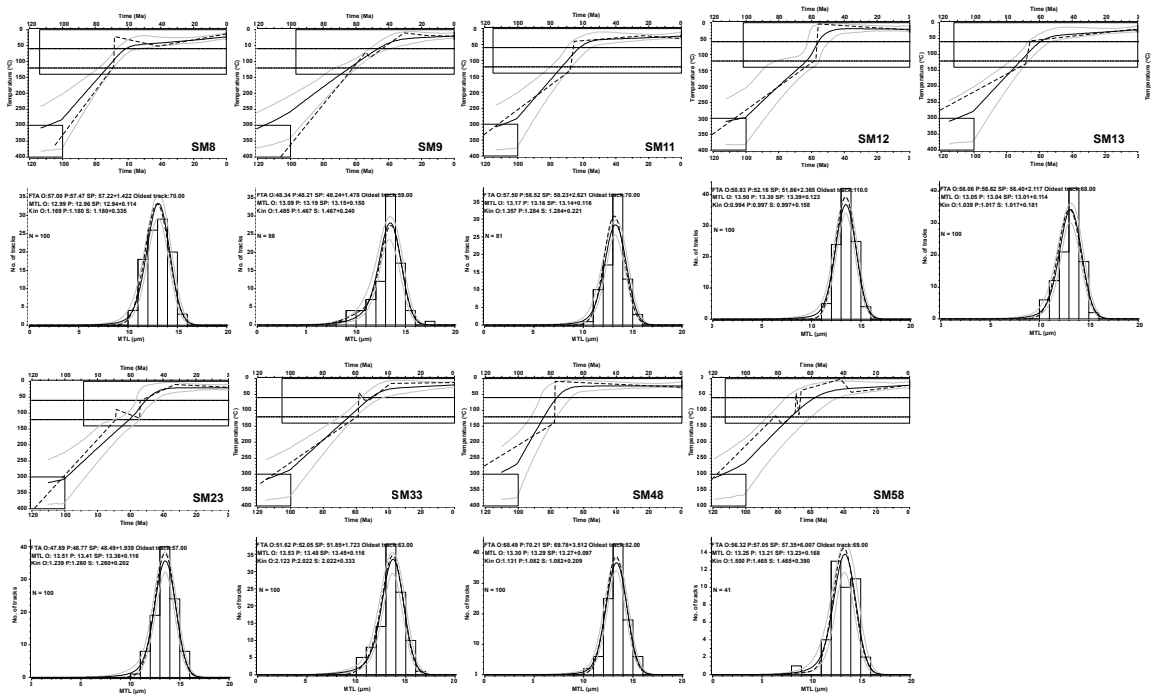

Figure 5.2: Summary of model results and predictions for 9 samples from the Vertiskos Unit (see Fig. 5.1 for sample location). For each sample the upper graph shows the inferred thermal history for the expected model (solid black line with 95% credible interval range represented by grey solid lines) and the maximum likelihood model (dashed line). The lower graph shows the predicted and observed length distributions, for the expected model in black line with 95% credible interval range represented by grey solid lines and for the maximum likelihood model in dashed line. See Gallagher (2012) for details of the modelling procedure adopted here.

5.5.2.1 Individual sample inverse modelling results

We used the 9 samples from the Vertiskos Unit for which length data were obtained (Table 5.1). At this stage we treat each sample individually and allow the Dpar (proxy for apatite composition) to vary within the variance obtained from the measurements). The results for the expected and maximum likelihood models as well as the predictions on the FT age, MTL and the sampled values for Dpar are shown in Figure 5.2. A summary of the observed vs. predicted/sampled values for the FT age, MTL and Dpar is shown in Figure 5.3.

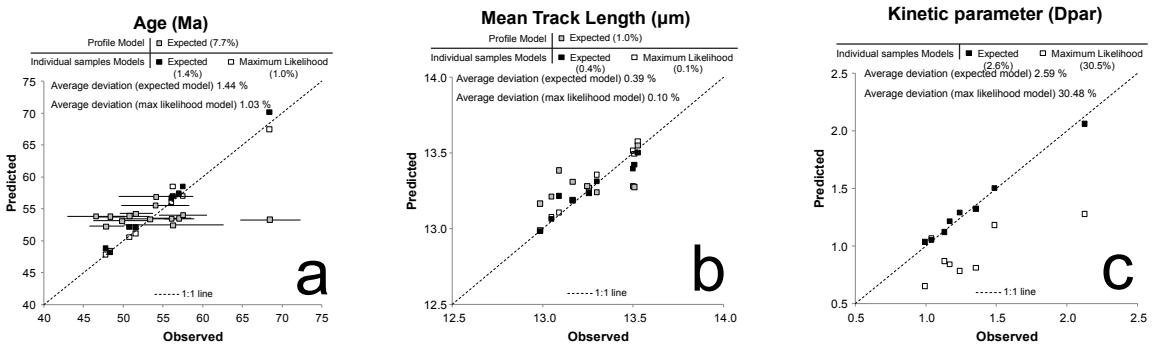

(a) Age (Ma) (b) Mean Track Length (μm) (c) Kinetic parameter (D_{par})

Figure 5.3: Observed vs. predicted values of both the individual sample modelling (expected and maximum likelihood models) and the joint profile modelling approaches adopted here for (a) the age, (b) the Mean Track Length and (c) the sampled kinetic parameter. Error bars on the observed age are also shown for part of the dataset. Numbers in parentheses is the average percentage deviation from the observed values for each dataset.

The thermal history represented by the expected model tends to be simpler or smoother than the maximum likelihood model (Figure 5.2), although predictions using the latter will be closer to the measured data. As a result, the maximum likelihood model fits the AFT age and MTL data (Figures 5.3a and 5.3b) but not the sampled parameter Dpar (Figure 5.3c). The deviation from the observed values tends to be as low as 1% (average for both models) with the exception of the Dpar prediction for the maximum likelihood model (30% on average). The maximum likelihood model arrives at systematically lower mean Dpar than the measured values. However, as a test on the significance of the actual Dpar value on the inferred thermal history we fixed its value to the observed one and re-ran the inversions. The results were not significantly different in terms of the timing of cooling episodes.

Overall, the thermal histories of the 9 modelled samples are similar in that they all show one major period of cooling in the Upper Cretaceous. Figure 5.4 summarises the results of inverse modelling (we show both the maximum likelihood and expected models). For the vast majority of the samples (SM48 excluded) the maximum likelihood models show rapid cooling through the apatite FT partial annealing zone roughly between 50 and 70 Ma without any reheating thereafter (Figure 5.4). SM48 shows the same general trend but its rapid cooling phase is at 80 Ma; this is caused by its old FT age (68.5 $\pm$ 3.8 Ma). A more complicated history (more T-t points), yet the same general shape, is inferred for sample SM58 but this may be due to the fact than only 41 length measurements were obtained.

The expected models show the same general form but tend to be smoother than the maximum likelihood models (Figure 5.4). These average thermal histories show more or less linear cooling from the constrained T-t area to close-to-surface temperature (below 50^{o}C). Eight out of the 9 modelled samples (SM48 excluded) form a cluster and their thermal history crosses the high-temperature limit of the apatite partial annealing zone ($\sim$120^{o}C) between ca. 55 and 75 Ma, $\sim$5 m.y. later than the rapid cooling shown by the maximum likelihood models. This reflects the level of uncertainty on the timing of cooling for all the thermal histories accepted by the MCMC sampling. Sample SM48 crosses the same temperature boundary at 84 Ma. All samples are at temperature lower than 50^{o}C since 45 Ma at the latest.

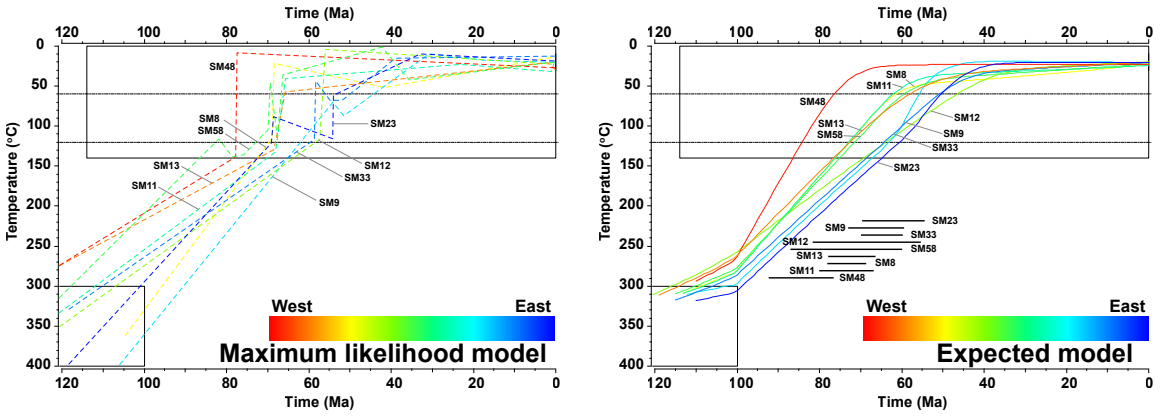

Figure 5.4: Compilation of the calculated maximum likelihood (left) and expected models (right) for 9 samples of the Vertiskos Unit that inferred using the individual samples approach (shown also in fig. 5.2). See fig. 5.1 for sample locations. For the expected model (right), the timing (2 sigma uncertainty included) that each individual thermal path (sample) crosses the high-temperature boundary of the apatite PAZ (∼120^{o}C) is also indicated.

In Figure 5.5, all the samples are plotted along a WSW-ESE transect over a swath profile covering the width of the Vertiskos Unit (sampling area). There is potentially a geographical trend for younger ages towards the east (SM54 excluded). However, if the uncertainty on the age calculation is considered, this trend becomes less obvious and the ages of adjacent samples often overlap within error. Considering the inferred thermal histories for the expected model in more detail, they show the same general form but from the westernmost sample (SM48) to the easternmost ones (SM23 and SM33), the thermal paths enter the PAZ at younger times following the geographic trend mentioned above (Figure 5.4). However, this intriguing geographical pattern needs to be considered in the context of the uncertainties on the thermal histories. Plotting the uncertainties (2 sigma) on the timing that each thermal path crosses the high-temperature boundary of the PAZ (∼120^{o}C), significant overlap exists for all, but SM48, samples (black horizontal lines; Figure 5.4). This suggests that the apparent geographical trend is either not real and/or the AFT data are not sensitive enough to record unambiguously such variation especially taking into consideration the relatively narrow width (∼30 Km) of the studied area (Figure 5.1).

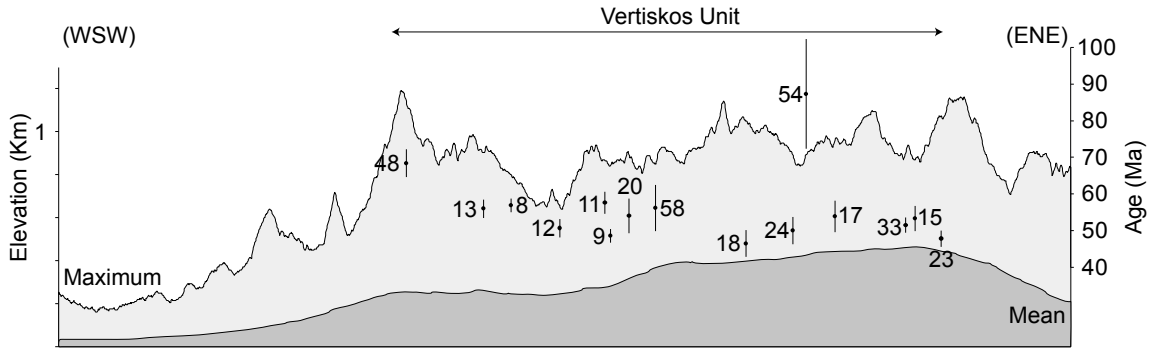

Figure 5.5: WSW-ENE-trending swath elevation profile of the Chalkidiki Peninsula extracted from the ASTER Global DEM v2. The profile stretches from the Vardar-Axios basin to the Strymon basin (see fig. 5.1). The AFT ages for the samples used for the joint profile modelling approach are plotted and the corresponding calculated apatite FT ages are read on the right vertical axis.

Irrespective of the details of the individual thermal histories, the overall picture extracted from modelling each sample independently implies that the basement rocks of the

Vertiskos Unit cooled through the apatite PAZ between the uppermost Cretaceous and the Lower/Middle Eocene.

5.5.2.2 Profile modelling results

Having modelled the thermal history for each sample independently, we now consider them as representing a vertical profile. The aim of this is to determine whether we can explain the data from all samples with a simple and common thermal history to assess whether the geographical variation in the thermal histories described above is real. In this approach, we model all samples simultaneously, using the present day elevation differences as a proxy for different depth in the crust during cooling (Gallagher et al., 2005a,b; Stephenson et al., 2006). As shown by Gallagher et al. (2005a), this joint modelling approach minimises artefacts in the resulting thermal histories (such as the re-heating events in Figure 5.4 for some of the maximum likelihood solutions). The differences in elevation are then used to estimate the temperature difference between the uppermost and lowermost samples, and the thermal histories for samples between them are calculated using linear interpolation of this temperature offset. All the samples are considered to have experienced the same form of thermal history and the reasonable assumption is that the lowest elevation samples were always hotter (deeper in the crust prior to exhumation) than their highest elevation counterparts which remained shallower in the crust. Under these assumptions, we can extract the regional thermal history of the sampled area. In such an approach we exploit the spatial link between different samples in the vertical sense. This includes the implicit assumption that any syn- or post-cooling vertical displacement (e.g. faulting) between sampling locations is negligible. As seen in Figure 5.1, there is no basin of significant size fragmenting the Vertiskos Unit. One exception is the relatively small Middle Miocene Mygdonia basin which is known to be quite shallow (not exceeding 200 meters; Koufos et al., 1995).

Given the assumptions above, this approach allows us to (i) integrate samples with no track length measurements with those that do have them, (ii) to minimise the complexity of the inferred thermal histories of individual samples (previous paragraph) and (iii) to illustrate the thermal evolution of the study area as a whole, grouping the individual samples. Comparing the thermal histories obtained by modelling all samples together to those obtained by modelling them individually, we can heuristically assess the validity of the approach and the assumptions above.

We used 14 of the basement samples from the Vertiskos Unit (Table 5.1; SM54 excluded). All of the samples contain age data and 9 of them have both age and FT length data. The measured central ages range between 46.6 $\pm$ 3.6 Ma and 68.5 $\pm$ 3.8 Ma and the elevation range from 94 m to 754 m. The resultant thermal history is relatively simple (Figure 5.6) and similar in form to those inferred for each sample individually (Figure 5.4). For comparison, the non-constrained profile model is also shown in Figure 5.6. The inferred thermal history shows linear-type of cooling between the constrained T-t area and the near-surface conditions. The cooling path crosses the high-temperature limit of the apatite FT partial annealing zone between 62 and 70 Ma (uncertainties included) and it stays at temperature below 50^{o}C since 55 Ma. The inferred temperature difference between the highest and the lowest elevation samples is 9 $\pm$ 7^{o}C (1 sigma), which implies that the data do not necessarily require very different thermal histories. Although we have grouped together a suite of samples spread over a relatively large area to search for a common form of the thermal history, the data fit is still acceptable in terms of predicted vs. observed age and the same for the MTL and sampling of the kinetic parameter (Figures 5.3 and 5.6). Only 3 out of the 14 samples did not have predicted ages within error, while all of the predicted/sampled values for MTL and Dpar were within error of the observed values.

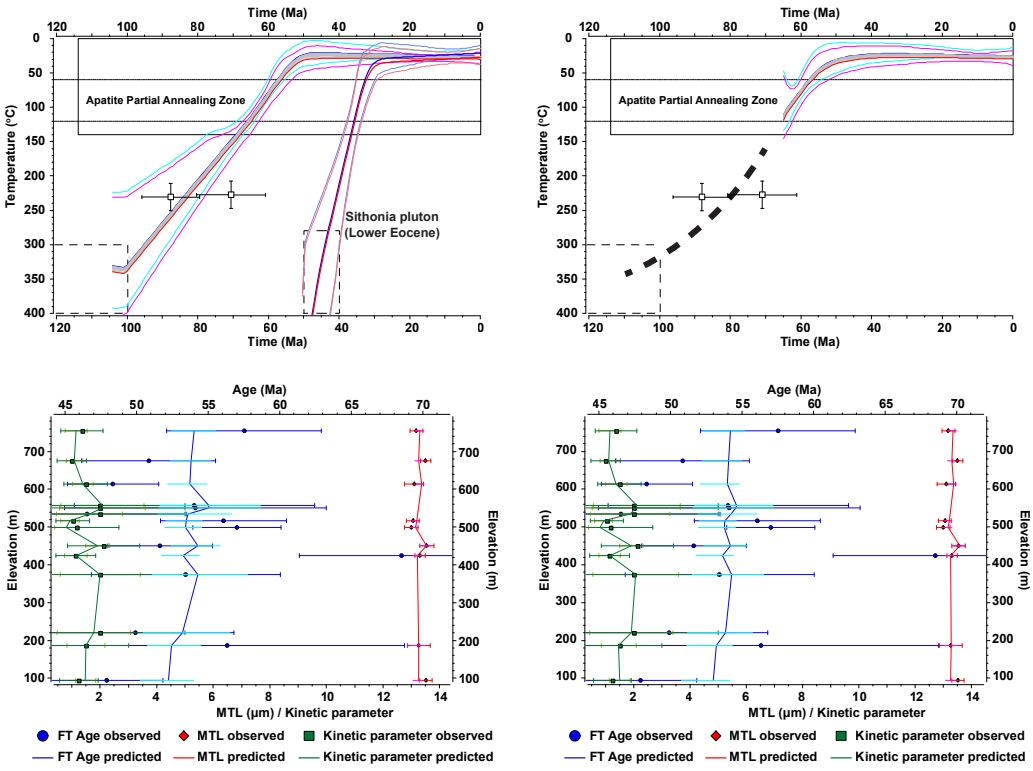

Figure 5.6: (up) The inferred expected model for 14 basement samples of the Vertiskos Unit treated as a vertical profile. The samples used are also shown in fig. 5.5 (SM54 excluded). The modelling approach is described in Gallagher et al. (2005b) and Gallagher (2012). The model on the left originates from a constrained T-t area (dashed box; 350 ± 50 °C at 120 ± 20 Ma) based on the geological evidence and the available geochronology data (see text for details). The two empty squares correspond to the published ZFT age from the Vertiskos/Ograzden Units. For comparison, the result of the non-constrained model is shown on the right. Red thick line is used for the thermal path of the hottest (lowest elevation) sample (red thin lines 95% credible interval range) and blue thick line for the thermal path of the coolest (highest elevation) sample (blue thin lines 95% credible interval range). Using the same modelling approach and the samples GR117, GR126, GR132 and GR134 from Hejl et al. (2010) we calculated, for comparison, the thermal path of the Lower Eocene Sithonia pluton from the southern edge of the Chalkidiki peninsula (see fig. 5.1 for location). (bottom) The corresponding FT age (blue), mean track length (red) and kinetic parameter (green) predictions for the constrained and non-constrained models are shown.

5.6 Discussion

5.6.1 Comparing the two modelling approaches

We have used here AFT analysis and two inverse modelling approaches to investigate the post-Lower Cretaceous cooling path of the Vertiskos Unit (Figure 5.1). In the first approach we modelled each sample independently allowing, thus, for different solutions for each sample (Figure 5.4). In the second approach, we modelled all samples together assuming that they represent a vertical profile and restricting the possible solutions to one common (and simple) thermal history (Figure 5.6). As expected, the first approach resulted in better data fit than the second one (Figure 5.3; see also Gallagher et al., 2005a,b).

From the swath profile shown in Figure 5.5, a possible eastwards younging of the ages can be inferred. This trend becomes ambiguous when considered in the context of the age uncertainties (overlapping ages within error). Using the first approach (individual sample modelling), the same trend is reflected in the resulting thermal histories which also tend to show a later (younger) cooling into the PAZ towards the east (Figure 5.4). Using the second approach (joint profile modelling) under assumptions mentioned earlier (see para-

graphs 5.5.1 and 5.5.2.2), a similar (in form and timings) thermal history is inferred from the data (Figure 5.6). In this case, the FT age for the westernmost sample (SM48), which gives the earliest cooling through the PAZ (around 80 - 85 Ma) is not so well predicted by the joint profile thermal histories (Figure 5.6), suggesting that this sample is not consistent with the profile modelling assumptions. However, the similarity in the form and spread of the individual expected thermal histories (Figure 5.4) and the profile thermal histories (with their uncertainties shown in Figure 5.6) for the other samples suggests either that overall the assumptions are valid or that the data are not sensitive enough to answer which of the two modelling approaches is better for the case of the Vertiskos Unit. To resolve that and to assess whether the geographical variation in the AFT ages (Figure 5.5) is real, a more dense sampling grid coupled with both lower ([U-Th]/He) and higher temperature methods (Ar/Ar on potassic feldspars, ZFT) would be necessary.

Overall however, the results of the two approaches are not significantly different in terms of form of the cooling path and timing. Considering the Vertiskos Unit and independently of the chosen modelling approach, the outcome of our AFT analysis is that it remained at temperature of ca. 120^{o}C until uppermost Cretaceous and it was at near-surface temperature (less than 50^{o}C) by Lower/Middle Eocene (Figures 5.4 and 5.6). With the current state of knowledge and available data and in the absence of any conclusive evidence, both approaches will be discussed independently in the following paragraphs and a possible mechanism for explaining the geographical variation, treated in the first approach, will be presented.

5.6.2 Regional geological and thermal evolution of the Vertiskos Unit

The Vertiskos Unit of the Chalkidiki peninsula, northern Greece is a complex unit with a poly-metamorphic history (Figure 5.1). Its pre-Jurassic history can be described in terms of a coherent metamorphic fragment that detached from the northern Gondwanan margin and was incorporated into the Variscan Arc of southern Europe during the Carboniferous (Kydonakis et al., 2014b). Equivalent units can now be traced to Bulgaria and to Serbia farther north (Zagorchev, 1976; Dimitrijević, 1963; Kounov et al., 2010, 2012). In Greece it mainly comprises Silurian granitoids, later transformed into ortho-gneisses, intercalated garnet-mica schists, amphibolites and thin marble horizons (Himmerkus et al., 2006, 2009a; Kockel et al., 1971, 1977). In Bulgaria, the protolith age of equivalent ortho-gneisses (Ograzden Unit) is defined as Ordovician (Zidarov et al., 2003; Macheva et al., 2006; Bonev et al., 2013a). An extensive rifting event dispersed the arc systems of southern Europe during the Triassic and caused the opening of oceanic basins. In northern Greece, the Vertiskos Unit represents such a rifted part of the European Arc systems, south of which the Vardar Oceanic Domain opened. The rifting event is clearly documented by widespread Triassic granitic intrusions known collectively as the Arnea-Kerkini Complexes (de Wet et al., 1989; Himmerkus et al., 2009b; Poli et al., 2009) and the related Volvi meta-mafic body (Himmerkus et al., 2005; Bonev & Dilek, 2010; Liati et al., 2011).

During the Alpine Orogeny and the closure of the Vardar Ocean, the Vertiskos Unit was incorporated into the southern European active margin reaching lower amphibolite-facies conditions (garnet-staurolite degree). Based on the available medium temperature geochronological data for the basement rocks of the Vertiskos Unit, the temperature remained high enough to reset the K/Ar (and partly the Rb/Sr) system during the Lower Cretaceous (Harre et al., 1968; Zervas, 1979; Papadopoulos & Kilias, 1985; de Wet et al., 1989). In the southern tip of the Chalkdiki peninsula a first pulse of magmatic intrusions is recorded (Figure 5.1). Hornblende-biotite granodiorites (Sithonia, Ierissos, Ouranoupolis, Gregoriou), dated at ca. 50 Ma (de Wet et al., 1989; Christofides et al., 1990; Frei, 1996), intruded the basement complex. Their continuation to the south is obscured by the sea while to the north, along the Vertiskos Unit, no magmatism of the same age is recorded. They belong to an extensive magmatic pulse that is recorded further to the northeast in the NRC (see below).

Within the Vertiskos Unit, a second pulse of magmatic activity is documented by smaller plutons (Stratoni, Skouries, Olympiada) that are often accompanied by volcanic extrusions (Monolithi, Gerakario). Feeding dykes of the latter intrude the basement complex marking the time of its final surface exposure. To the south they are related to fluid circulation, porphyry copper mineralization and Pb-Zn-Ag-Au replacement ores. This pulse is as old as Oligo-Miocene (Frei, 1992; Gilg & Frei, 1994; Tompouloglou, 1981, and our own data). It can be traced at least up to southwest Bulgaria (Kozhuh volcanic body; Pecskay et al., 2011) where it intrudes the equivalent Ograzden Unit.

The post-Lower Cretaceous cooling of the Vertiskos Unit as a coherent block can be inferred from the results of the vertical profile modelling (Figure 5.6). The cooling path crosses the high-temperature limit of the apatite FT partial-annealing zone (∼120^{o}C) at uppermost Cretaceous (between 62 and 70 Ma) and remains at temperature ¡50^{o}C since the Lower Eocene. Using the available geochronology data (Hejl et al., 2010) for a typical Lower Eocene pluton of the first magmatic pulse (Sithonia pluton from the southern tip of the Chalkidiki peninsula; Figure 5.1) and the profile modelling technique described in a previous paragraph we can demonstrate that this pluton cooled to 50^{o}C as early as lowermost Oligocene (∼33 Ma), i.e. 10 - 15 m.y. later than the surrounding basement rocks (Figure 5.6). Thus, it can be concluded that none of the two magmatic pulses penetrating the Vertiskos Unit (Eocene and Oligo-Miocene) were strong enough to cause regional thermal perturbations. Local thermal perturbations are possible, but, to first order, do not appear to be too significant, given the overall similarity of the profile and individual sample modelling results.

In summary, the Vertiskos Unit preserves evidence for Upper Cretaceous exhumation and Lower/Middle Eocene near-surface exposure documented by low-temperature thermochronology data. This robust and systematic low-temperature record over a distance of several tens of kilometres is a unique feature of the Rhodope Metamorphic Province. The regional exhumation of the Vertiskos Unit clearly pre-dates any basin formation and the two described thermal pulses caused by plutonic intrusions.

5.6.3 Lateral variations of the cooling histories in the Vertiskos Unit

In order to evaluate the scale and significance of lateral variations in the cooling history of the Vertiskos Unit we return to the results of the individual sample modelling (Figure 5.4). Lateral variations in the measured apatite FT ages have already been discussed (see paragraph 5.6.1); they young towards the east (Figure 5.5). This trend is clearly reflected into the corresponding individual thermal histories which also become younger towards the east (Figure 5.4). In other words, the relatively young unroofing of the eastern part of the Vertiskos Unit is in contrast to the earlier cooling recorded in its western part. Here we consider possible explanations for this variation.

The Vertiskos Unit is bordered along its western side by a pile of Mesozoic meta-sediments (known as the 'Circum-Rhodope' belt sensu Kauffmann et al., 1976) and a Jurassic magmatic arc (namely the 'Chortiatis Magmatic Suite'; see Kockel et al., 1971) via composite contacts showing thrust and dextral strike-slip components (Ricou & Godfriaux, 1994; Tranos et al., 1999) (Figure 5.1). The youngest involved sediments are virtually un-metamorphosed calcareous clastics of Albian-Cenomanian age (Meinhold et al., 2009). This implies that thrusting was active at shallow crustal conditions during the Upper Cretaceous along the western border of the Vertiskos Unit. During the same time, we have shown evidence for exhumation of the Vertiskos Unit from mid-crustal level to the surface (Figure 5.4). Assuming that differential erosion occurred, exhumation of its western shoulder through a thrusting mechanism would have resulted in younger ages towards the west. Therefore, this mechanism cannot explain the observed FT age and inferred thermal history variations.

Brun & Sokoutis (2007) described the Kerdyllion Detachment as the structure which

controlled the exhumation of the SRCC from Middle Eocene to Middle Oligocene immediately east of the Vertiskos Unit (Figure 5.1). During that time, the Vertiskos Unit was the hanging-wall of the detachment on top of the exhuming mylonitic gneisses. As illustrated in Figure 5.4, the Vertiskos Unit was already at shallow depth and at temperature less than 50^oC before the formation of the SRCC. Therefore, any thermal disturbance related to the exhumation of the mylonitic gneisses and the syn-tectonic plutons post-dates the exhumation of the Vertiskos Unit and can neither affect its thermal evolution nor explain the observed lateral variations in age or cooling through the PAZ. We argue that the observed geographical age geographical pattern can be explained with passive post-exhumation asymmetric uplift and erosion of the eastern Vertiskos shoulder due to extensional doming of the SRCC immediately to the east (Figure 5.1). In such a way its deeper parts are exposed along the eastern side resulting to younger FT ages and later cooling through the PAZ (Figure 5.4). Indeed, the eastern side of the Vertiskos Unit stands at higher elevation compared to its western side, showing, overall, an asymmetric relief (Figure 5.5). The asymmetry decays towards the west, away from the exhuming SRCC, where the oldest ages are recorded. The same result can be also triggered by the Middle Miocene, NW-trending, NE-dipping normal faults bordering the Strymon basin along the eastern part of the Vertiskos Unit (Figure 5.1). Exhumation along their footwall would expose deeper parts of the Vertiskos Unit.

In summary, the younger FT ages (and their associated thermal histories) towards the east within the Vertiskos Unit is arguably the result of post-exhumation passive tilting essentially combined with increased erosion rates towards the east. The relatively young extensional exhumation of the SRCC immediately to the east of the Vertiskos Unit and/or the Middle Miocene normal faulting along its eastern border both account for possible mechanisms.

5.6.4 Comparing the Vertiskos Unit to the Rhodope Metamorphic Province

The Rhodope Metamorphic Province is made of three main tectonic domains that display first-order similarities and differences in terms of cooling to near-surface temperature (Figure 5.7). The available low-temperature thermochronology data (from Bigazzi et al., 1994; Kyriakopoulos et al., 1997; Hejl et al., 1998, 2010; Magganas et al., 2004; Wuthrich, 2009; Kounov et al., 2010; Márton et al., 2010, and the results of this study) are summarised in the histograms of Figure 5.7. For the NRC low-temperature data are from both the migmatitic gneiss domes and their peripheries. With reference to the histograms of Figure 5.7, the zircon FT ages range from 25 to 40 Ma, the apatite FT ages from 10 to 50 Ma and the apatite (U-Th)/He ages from 10 to 40 Ma. For the SRCC the available data are less abundant. The zircon FT ages are from 10 to 45 Ma, the apatite FT ages from 5 to 30 Ma (both Oligo-Miocene plutons and basement rocks) and the three apatite (U-Th)/He ages from 15 to 40 Ma. For the Vertiskos Unit (or the equivalent Ograzden Unit) the two available zircon FT ages are at ca. 80 Ma. The apatite FT ages of the Eocene plutons range from 10 to 40 Ma and from basements rocks from 40 to 70 Ma.

Much of the Mesozoic convergence that affected the Rhodope Metamorphic Province is preserved within the NRC. High-temperature zircon crystallisation ages peak at Jurassic and is often interpreted as the time of the eclogite-facies metamorphism (in places within the diamond stability field). The eclogite-bearing gneisses of the NRC are variably retrogressed to amphibolite-facies conditions (see Moulas et al., 2013, and references therein). The time of this event is constrained at Cretaceous (e.g. Reischmann & Kostopoulos, 2002; Bauer et al., 2007; Bosse et al., 2010; Liati et al., 2011, see also Burg, 2012 0and references therein). A second zircon/monazite growth phase scatters between uppermost Cretaceous and Oligocene and correlates with an elevated thermal gradient caused by voluminous intrusive and extrusive rocks (Figure 5.1). Simultaneously, widespread extensional basins deposited on top of exhumed metamorphic rocks, mark the initiation of extension in the Bulgarian Rhodope.

The area remained active and at an elevated thermal gradient during the exhumation of the gneiss domes prevailing any pre-Lower Eocene (pre-50 Ma) low-temperature record. Indeed the low-temperature record starts at ca. 50 Ma for the domes and their peripheries (Figure 5.7).

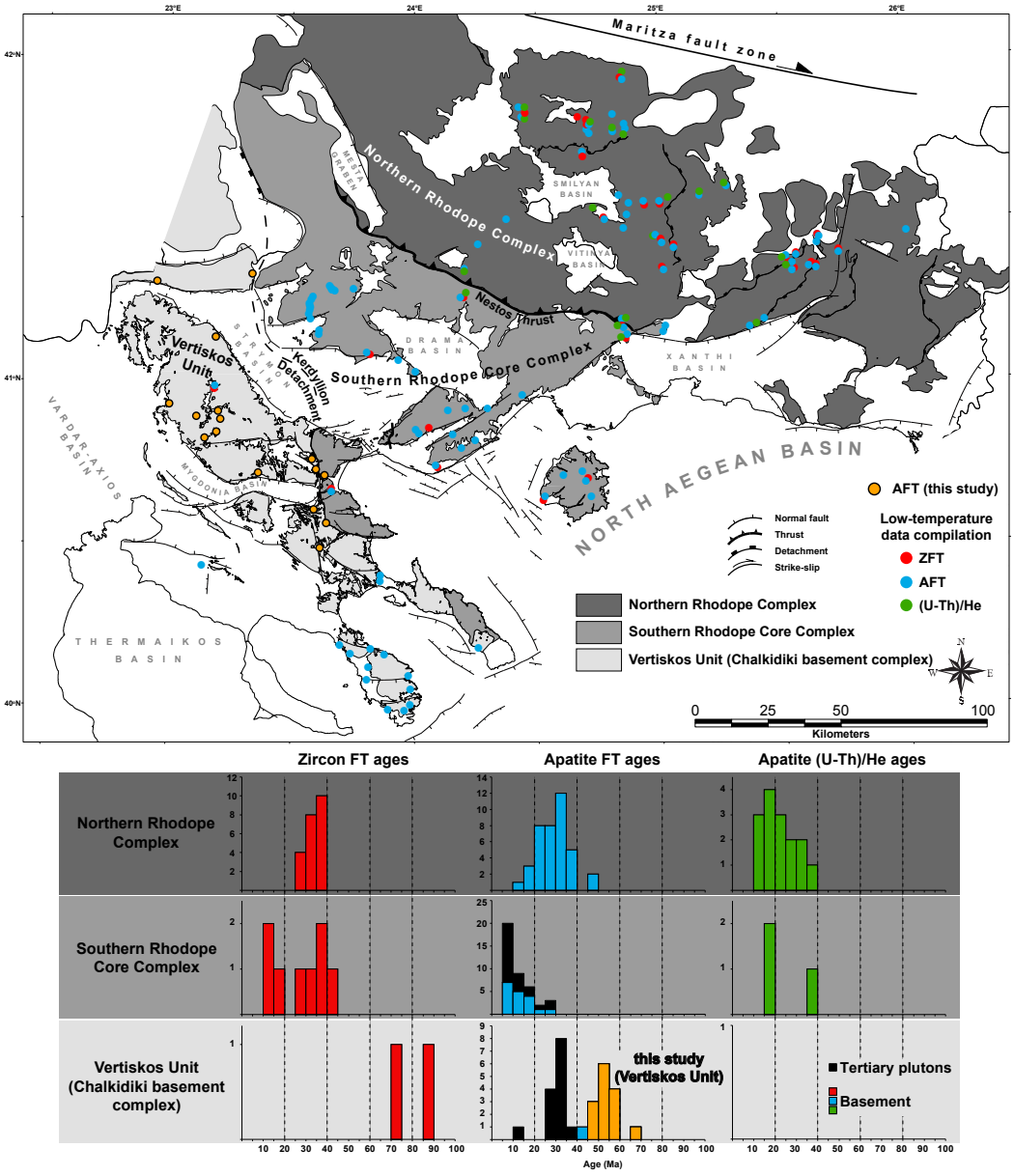

Figure 5.7: The Rhodope Metamorphic Province (fig. 5.1) is divided, from northeast to southwest, into three tectonic domains: The Northern Rhodope Complex (NRC), the Southern Rhodope Core Complex (SRCC) and the Vertiskos Unit. Low-temperature data compilation (ZFT, AFT, (U-Th)/He) is shown on the map (orange-filled circles for our data; red-, blue- and green-filled circles for literature data) and summarised in the histograms. The three tectonic domains are in gray-shaded colours as the corresponding histograms.

Similar to the NRC, the Vertiskos Unit preserves evidence for Upper Jurassic and Cretaceous metamorphism based on the available medium-temperature geochronology data mentioned earlier. Zircon FT ages (uppermost Cretaceous) pre-date the Eocene apatite FT ages for basement rocks (Figure 5.7). Contrary to the elevated thermal gradient in the NRC to the northeastern edge of the RMP, the Vertiskos Unit has been intruded only locally by plutonic bodies. Thus, the thermal history inferred from the FT data can be interpreted as a clear cooling signal of the basement block excluding any thermal overprint due to the plu-

tons/volcanics emplacement. As described above, the Eocene and Oligo-Miocene plutonism and volcanism were not sufficient to increase the thermal gradient to such a degree to erase the evidence for the Upper Cretaceous exhumation. In addition, no significant-sized sedimentary basins have formed in the Vertiskos Unit which remained as a coherent basement zone to the southwest termination of the RMP.

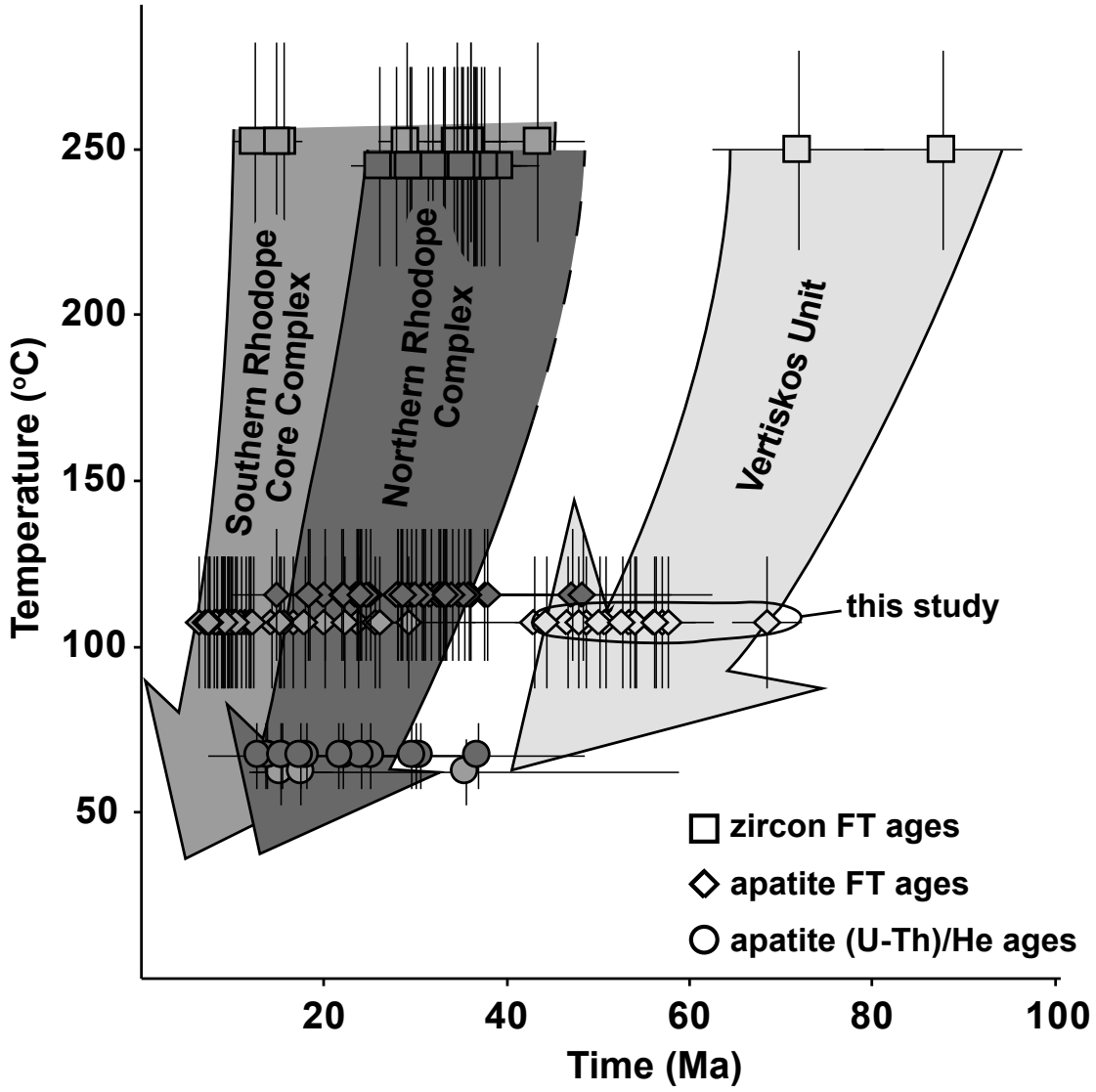

Figure 5.8: Simplified thermal paths (and data compilation) for the three tectonic domains shown in fig. 5.7. The available ZFT, AFT and apatite (U-Th)/He ages are plotted against an 'average' closure temperature (ca. 250, 110 and 60°C respectively). The colour fill of the three thermal paths (and the low-temperature data compilation) corresponds to the colour fill of each of the three tectonic domains shown in fig. 5.7.

This is in contrast to the SRCC where widespread extensional post-Middle Miocene basins developed on top of the exhumed metamorphic complex. As shown in Figure 5.7, the SRCC records the youngest population of ages (well illustrated in the apatite FT data with 20 samples with age less than 10 Ma) among the three domains of the RMP. The Eocene metamorphic ages, the Oligo-Miocene syn-tectonic intrusions and the relatively young low-temperature data point collectively towards a highly active area that remained at a high thermal gradient during the Tertiary before its fragmentation by post-Middle Miocene sedimentary basins. The relatively young ages of the SRCC attest for its denudation after both the NRC, to the northeast, and the Vertiskos Unit immediately to the southwest.

The thermal gradient for the SRCC remained relatively high and only decreased sufficiently enough for low-temperature record to be preserved after Upper Miocene times.

In summary, simple but distinct thermal paths (Figure 5.8) corresponding to the three tectonic domains of the RMP (Figure 5.7) can be defined. To the southwest, the Vertiskos Unit records Upper Cretaceous exhumation (Figures 5.7 and 5.6). No later episodes of pluton intrusion and basin formation erased the evidence for this exhumation. To the northeast, the NRC is characterised by high thermal gradient due to Upper Cretaceous – Oligocene intrusive and extrusive rocks, gneissic domes formation often accompanied with Eocene partial melting and basin development since Maastrichtian. The elevated thermal regime prevented any pre-Eocene exhumation phase to be recorded by low-temperature thermochronological systems. However, a lowermost Paleocene cooling phase is locally inferred from medium-temperature geochronology (Ar/Ar on white micas) on the hanging-walls of the exhuming domes and is in line with Maastrichtian - Eocene syn-tectonic clastics deposited on the metamorphic basement (Bonev et al., 2006, 2013b). Finally, the intermediate SRCC provides the record of the youngest cooling history in the area in agreement with young syn-tectonic plutonism.

5.7 Conclusions

The Vertiskos Unit of the Chalkidiki peninsula (Figure 5.1) is a distinct Silurian fragment of Gondwanan provenance with a complex poly-metamorphic history. Its Alpine thermal history is documented by the available medium-temperature geochronology data that culminates in the Lower Cretaceous and is often correlated to a lower amphibolite-facies overprint. In an effort to constrain its post-Lower Cretaceous cooling history until close-to-surface temperature we applied apatite FT analysis coupled with inverse thermal modelling. Our results can be summarised as:

(i) The central ages obtained for basement rocks of the Vertiskos Unit range from uppermost Cretaceous to Middle Eocene (46.6 $\pm$ 3.6 to 68.5 $\pm$ 3.8 Ma) with mean track lengths between 13 and 13.5 μm (Table 5.1).

(ii) In the Vertiskos Unit there is potentially a geographic trend for younger AFT ages towards the east (Figure 5.5). This trend becomes less well defined when considered in the context of the age uncertainties (overlapping ages within error). This suggests that either the AFT dating is not sensitive enough to record clearly such variation over such a narrow width ($\sim$ 35 Km) or that the observed pattern simply reflects scatter in the data. In the lack of any conclusive evidence, we have chosen to a) model each sample independently examining this geographical trend and b) model the thermal history of all samples together treating them as a vertical profile and interpreting the geographical trend as an artefact. To assess whether the geographical variation in the AFT ages is real, a more dense sampling grid coupled with both lower ([U-Th]/He) and higher temperature methods (Ar/Ar on potassic feldspars, ZFT) would be necessary.

(iii) However, both of the modelling approaches produced similar results in terms of form of the cooling path and timing (crossing the high temperature limit of the PAZ; near-surface exposure). Considering the Vertiskos Unit and independently of the chosen modelling approach, its overall thermal history implies that it cooled through the apatite PAZ in uppermost Cretaceous and was at near-surface temperature (less than 50^{o}C) by Lower/Middle Eocene (Figures 5.4 and 5.6). Thus, the Vertiskos Unit preserves the evidence for uppermost Cretaceous exhumation.

(iv) The Vertiskos Unit is the westernmost extreme of the Rhodope Metamorphic Province (Figure 5.7). The other constituents are the Southern Rhodope Core Complex in the centre and the Northern Rhodope Complex to the northeast. The inferred thermal evolution of the Vertiskos Unit (Figures 5.7 and 5.6) is in contrast to the one of the Southern Rhodope Core Complex and the Northern Rhodope Complex where the apatite fission-track ages range

from ca. 10 to 30 Ma and from ca. 10 to 40 Ma respectively (Figure 5.7). Figure 5.8 summarises, in a simplified way, the distinct thermal paths of the three tectonic domains of the Rhodope Metamorphic Province (Figure 5.7). It shows clearly the difference in terms of timing of close-to-surface exposure between them and establishes Vertiskos Unit as the oldest exhumed basement complex in the Rhodope. We can also safely conclude that the Vertiskos Unit represents the oldest exhumed coherent basement complex of Greece.

ACKNOWLEDGEMENTS

This work was funded by the European Union FP7 Marie Curie ITN "TOPOMOD", contract no. 264517. Andrew Carter and Jocelyn Barbarand are gratefully acknowledged for providing access to the FT microscopes at Birkbeck University of London and Géosciences Orsay, Université Paris Sud, respectively. We thank Ewald Hejl for kindly providing us with the necessary data for the inverse modelling of the Eocene Sithonia granite shown in Figure 5. Editorial handling by Claudio Faccenna is greatly appreciated. Nikolay Bonev and Ewald Hejl are thanked for their valuable suggestions and critical comments that greatly improved our manuscript.

Supplementary Materials

Supplementary Material #1

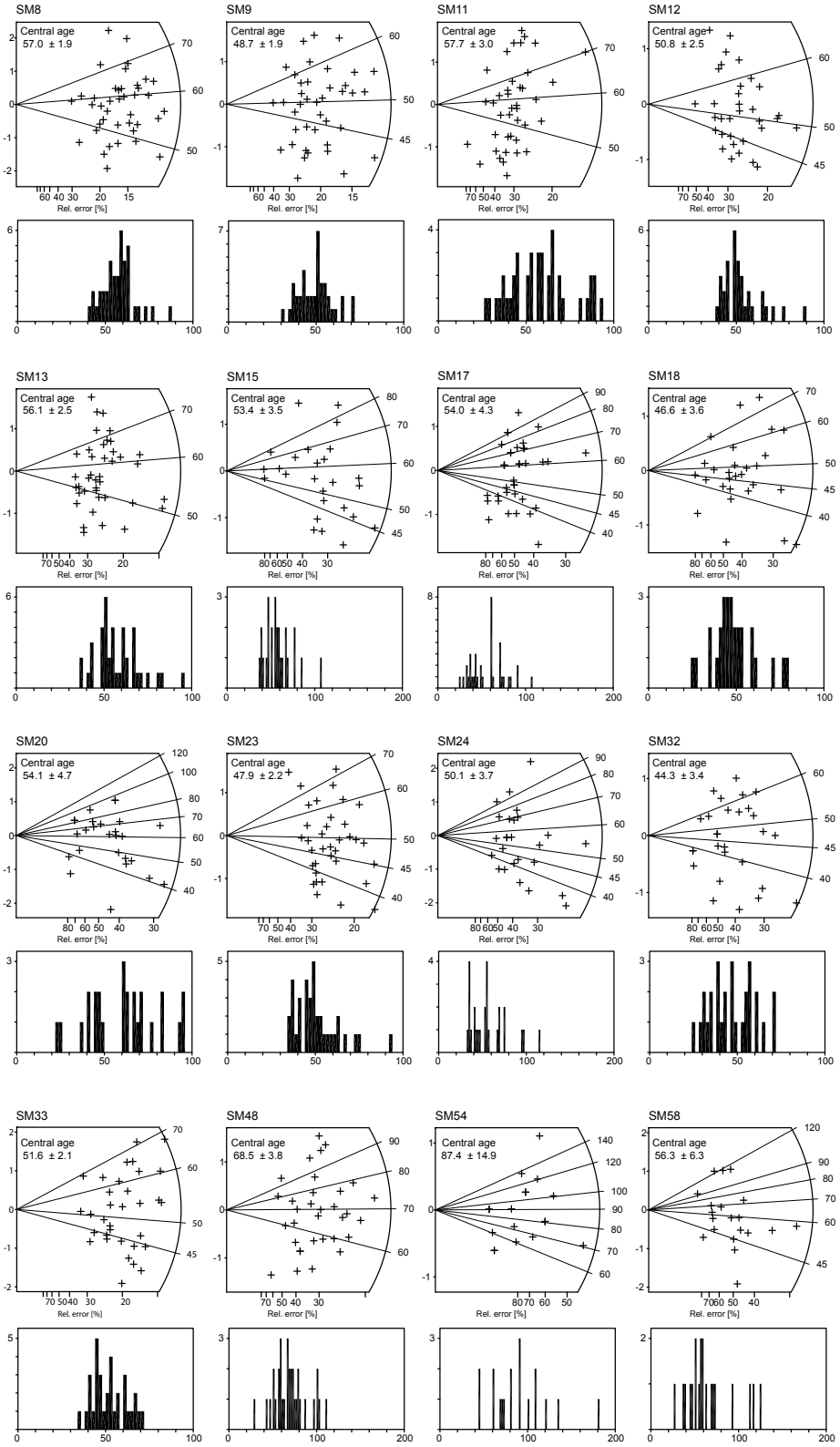

Figure 5.9: Fission-track age radial plots and age histograms of individual grains.

Supplementary Material #2

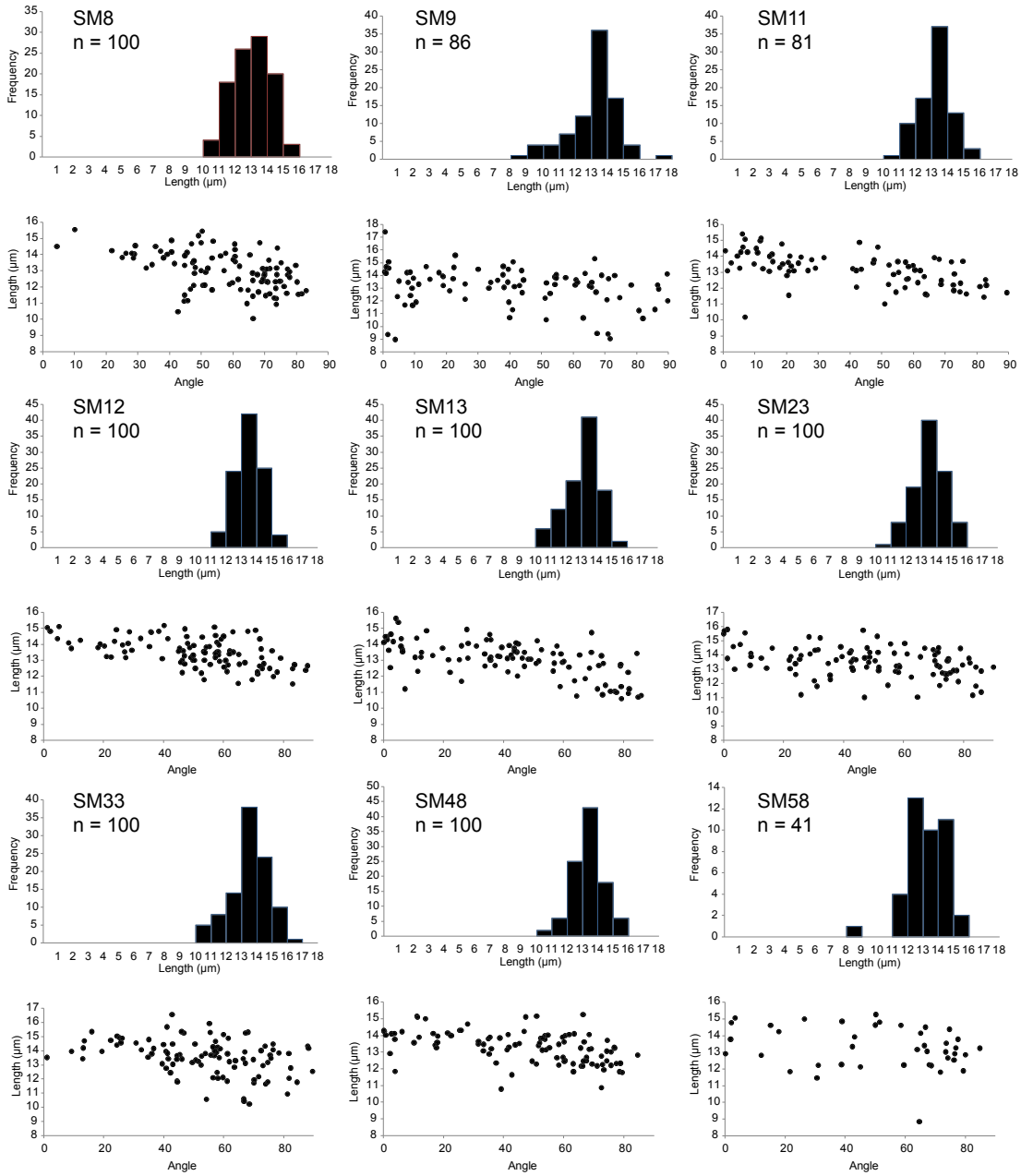

Figure 5.10: FT c-axis-parallel lengths and length vs. c-axis angle plots.

Chapter 6

The Chalkidiki block of North Aegean, from Cretaceous thrusting to Tertiary extension

6.1 Introduction

The Hellenides constitute an integral part of the Alpine-Himalayan mountain chain and are the product of convergence between the stable South European margin and northward-driven Gondwana-derived continental blocks (e.g., Dercourt et al., 1993; Stampfli & Borel, 2002). They resulted from Mesozoic - Cenozoic southwestward piling-up of three continental fragments, namely Rhodopia, Pelagonia and External Hellenides, arranged in a SW-verging stack from NNE to SSW in the order listed, and the closure of two intervening oceanic domains now forming, from north to south, the Vardar-Axios and the Pindos Suture Zones, respectively (Robertson, 2002; van Hinsbergen et al., 2005a; Papanikolaou, 2009, 2013) (Figure 6.1). Seismic tomography illustrates beneath the Hellenides and down to 1600 Km depth a northward-dipping slab, anchored into the lower mantle (Bijwaard et al., 1998). Convergence that took place between Jurassic and Cretaceous is recorded in the innermost part of the Hellenides - i.e., in the North Aegean Domain. Subsequent extension started in middle Eocene, soon after suturing of the Pindos oceanic domain (Brun & Sokoutis, 2010; Jolivet & Brun, 2010) and was driven by the southward retreat of the Hellenic subduction (McKenzie, 1978; Mercier et al., 1979; Mercier, 1981; Dewey & Sengör, 1979; Le Pichon & Angelier, 1979, 1981; Jolivet & Faccenna, 2000). The Aegean represents the most strongly stretched part of the Hellenic domain.

The domain of North Aegean covers a large part of northern Greece and forms the hinterland of the Hellenides (Figure 6.2). It is bordered to the north by the Maritza dextral strike-slip fault (Naydenov et al., 2013) and to the south by the Vardar-Axios Suture Zone. In the mainland of northern Greece and southern Bulgaria, the North Aegean Domain can be divided, from northeast to southwest into the *Northern Rhodope Domain*, the *Southern Rhodope Core Complex* and the *Chalkidiki block*. The Southern Rhodope Core Complex, which resulted from Aegean extension since Middle Eocene, separated the Northern Rhodope Domain from the Chalkidiki block (Brun & Sokoutis, 2004, 2007). Before this separation, the Northern Rhodope Domain and Chalkidiki block recorded during the Mesozoic a crustal-scale southwestward piling-up of metamorphic units (Burg et al., 1990, 1996; Ricou et al., 1998) that resulted in imbricate sheets of paragneisses, orthogneisses, marbles, amphibolites, meta-ophiolites and relicts of a Jurassic magmatic arc (Mposkos & Liati, 1993; Liati & Seidel, 1996; Turpaud & Reischmann, 2010; Janák et al., 2011; Moulas et al., 2013). This thrust system is broadly speaking, the core of the present contribution.

The present paper, after a review of the previous work, describes the Cretaceous syn-

metamorphic deformation pattern of the Chalkidiki block through (i) description of strain markers and superposition of fabrics, (ii) maps of regional foliation, stretching lineation and associated shear sense, (iii) folding pattern and (iv) kinematic interpretation of thrusting toward the SW and extension associated to top-to-NE shear. Finally, the superposed effects of structures related to Tertiary extension are analysed with reference to the clockwise rotation of the Chalkidiki block.

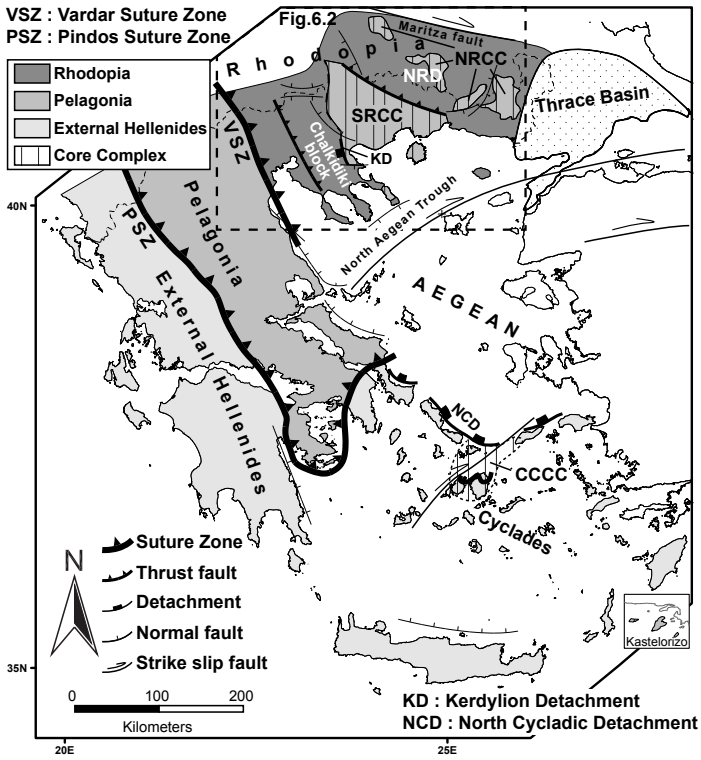

Figure 6.1: Simplified geological map of the Hellenides. The Hellenides are made, from north to south, of three continental blocks (Rhodopia, Pelagonia and External Hellenides) and two intervening sutured oceanic domains (Vardar and Pindos Suture Zones). The study area is located to the hinterland of the Hellenides, in the Rhodope. NRD: Northern Rhodope Domain, NRCC: Northern Rhodope Core Complex, SRCC: Southern Rhodope Core Complex, CCCC: Central Cyclades Core Complex.

6.2 Geological setting

6.2.1 The Northern Rhodope Domain

The *Northern Rhodope Domain* (NRD) is the northeastern part of the Rhodope (Figure 6.2). The gneisses exposed there are locally turned into mylonites and ultra-mylonites and record intense close to plane strain non-coaxial ductile deformation (Burg et al., 1990, 1993). A regional NNE-trending stretching lineation associated to a top-to-SW sense of shear developed during thrusting (Burg et al., 1990; Kilias & Mountrakis, 1990; Barr et al., 1999) in amphibolite-facies conditions (Burg et al., 1996). Evidence for ultrahigh pressure (UHP) metamorphic conditions is due to the presence of micro-diamond inclusions from metapelites (Mposkos & Kostopoulos, 2001; Perraki et al., 2006; Schmidt et al., 2010) that indicate minimum local pressure of 3.0GPa (for 600^{o}C). Jurassic and Cretaceous zircon metamorphic ages (circa 150 and 75 Ma) were obtained from both garnet-kyanite gneisses and amphibolitised eclogites (e.g., Bauer et al., 2007; Liati et al., 2011, and references therein). Peak conditions for the regional high-pressure event are estimated at 1.9GPa / 700^{o}C (Liati & Seidel, 1996) and for the amphibolite-facies overprint at 0.7GPa / 720^{o}C (Moulas et al., 2013). To the northeast, Maastrichtian - Paleocene sediments rest unconformably on basement gneisses

(Boyanov et al., 1982; Goranov & Atanasov, 1992).

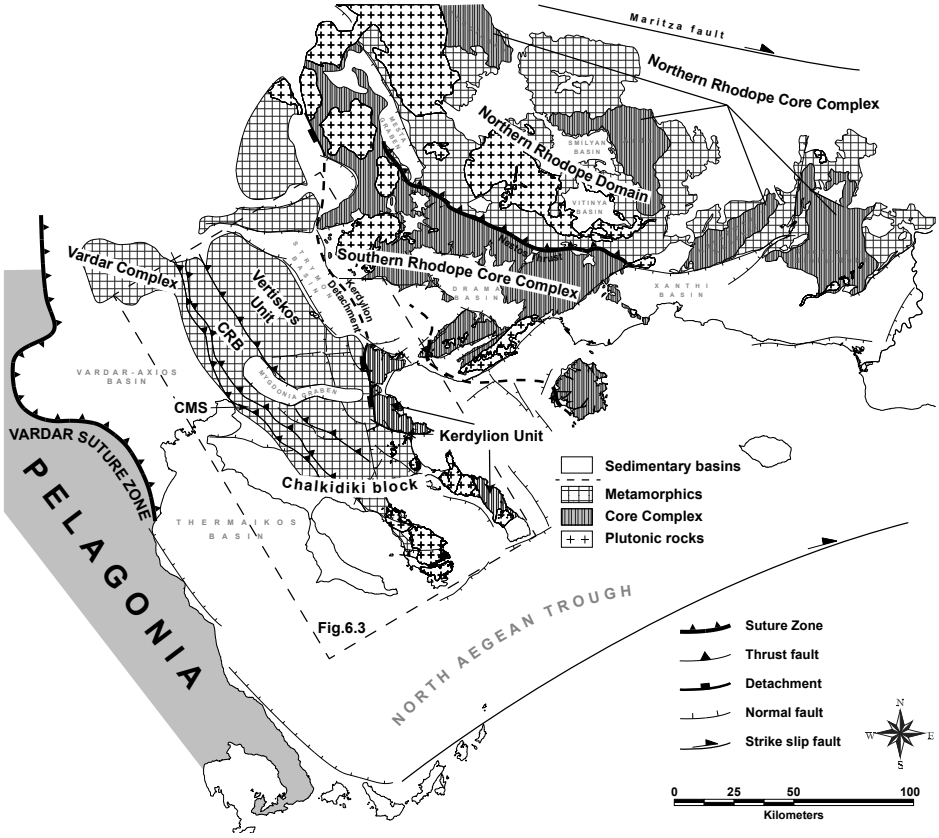

Figure 6.2: Simplified geological map of the North Aegean after Kockel & Mollat (1977), Brun & Sokoutis (2007) and Burg (2012). The Rhodope is composed of three tectonic domains that are, from NE to SW, the Northern Rhodope Domain, the Southern Rhodope Core Complex and the Chalkidiki block. The latter constitute the hanging-wall of the Kerdylion Detachment. CRB: Circum-Rhodope belt, CMS: Chortiatis Magmatic Suite.

Large-scale extension of core complex-type affected the Rhodope since middle Eocene resulting in formation of two distinct zones of core complexes: i) an array of four extensional gneiss domes (Chepinska, Arda, Kardamos - Keshebir and Kechros - Biela-Reka, see review in Burg, 2012) that developed within the NRD and ii) the larger *Southern Rhodope Core Complex* (SRCC) (Dinter & Royden, 1993; Sokoutis et al., 1993; Brun & Sokoutis, 2007) that separated Rhodope into two extreme parts: the NRD and the Chalkidiki block (as defined in Brun & Sokoutis, 2007), to the northeast and southwest, respectively (Figure 6.2). The formation of these two distinct core complex zones in the Rhodope appear to be the result of gravity spreading of a thick and weak thrust wedge of crustal scale (see Chapter 7). Exhumation of the partially-molten gneiss domes was accompanied by syn-extensional plutonic and volcanic activity (e.g., Kolocotroni & Dixon, 1991; Jones et al., 1992; Marchev et al., 2004, 2013). Widespread fault-bounded basins developed only since middle Miocene, segmenting the SRCC (Brun & Sokoutis, 2004, 2007; Snel et al., 2006).

6.2.2 The Chalkidiki block

The *Chalkidiki block* is the southwestern part of the Rhodope and constitutes the hanging-wall of the Kerdylion Detachment that is responsible for the exhumation of the SRCC, immediately to the east (Figures 6.2 and 6.3). The Chalkidiki block coincides with the so-called Serbo-Macedonian Massif (Kockel et al., 1971), if one excludes the easternmost part of the latter, the Kerdylion Unit that has a common tectono-metamorphic history with the

SRCC (Brun & Sokoutis, 2007). Before separation of the Chalkidiki block from the NRD, both parts participated into the same Mesozoic northward subduction as parts of the down-going plate and experienced metamorphic conditions whose intensity increases toward the northeast (see Chapter 3). The Chalkidiki block is composed of three units separated by sharp NW-trending contacts. From east to west, they are the *Vertiskos Unit*, the *Circum-Rhodope belt* and the *Chortiatis Magmatic Suite* (Kockel et al., 1971, 1977; Kockel & Mollat, 1977).

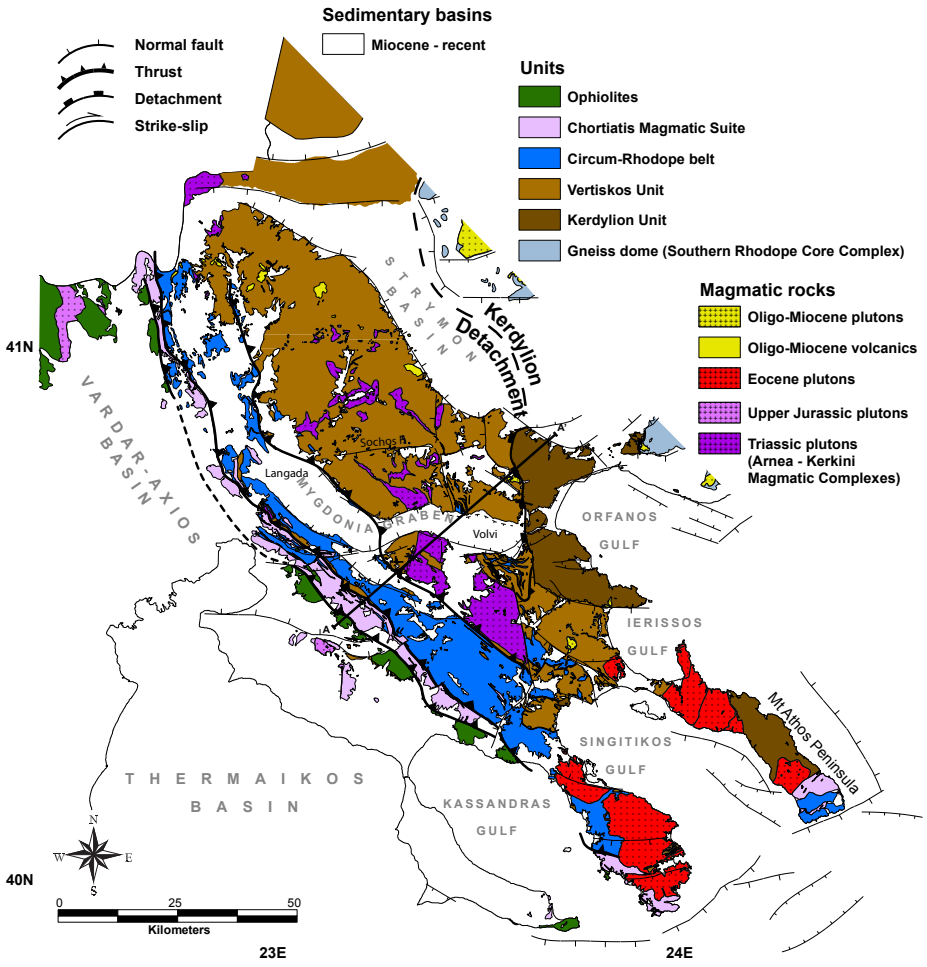

Figure 6.3: Geological map of the Chalkidiki block after Kockel & Mollat (1977) and Sakellariou & Dürr (1993). Cross-section A-A' is shown in Figure 6.15.

The *Vertiskos Unit* is an elongated basement belt with a complex tectono-metamorphic history (Burg et al., 1995; Kilias et al., 1999). The Vertiskos Unit is the oldest exhumed coherent basement complex of the Rhodope (Kydonakis et al., 2014a) (Figure 6.3). It is a distinct basement fragment that detached from Gondwana and was incorporated into the Southern European Arcs by the end of the Palaeozoic (Himmerkus et al., 2007; Kydonakis et al., 2014b). It is made of Silurian - Ordovician granitoids, later transformed into orthogneisses (Himmerkus et al., 2009a, see also Chapter 2), with intercalated paragneisses, thin marble horizons, leucocratic granitic/pegmatitic intrusions, deformed amphibolites, scarce eclogite boudins and serpentinites (Kockel et al., 1971, 1977). Part of the basement is the Arnea-Kerkini Magmatic Complex that intruded the Silurian - Ordovician orthogneisses during the Lower Triassic (Himmerkus et al., 2009b). The Vertiskos Unit was affected by Palaeozoic deformation whose fabrics were re-worked during a Mesozoic amphibolite-facies overprint (e.g., Burg et al., 1995; Kilias et al., 1999) the timing of which is delineated by a wealth of

Upper Jurassic - Cretaceous metamorphic ages ($^{40}Ar/^{39}Ar$, K/Ar and Rb/Sr on micas and amphiboles) (e.g., Borsi et al., 1965; Harre et al., 1968; Papadopoulos & Kilias, 1985; de Wet et al., 1989; Christofides et al., 1999, 2007; Lips et al., 2000). Peak metamorphic conditions, inferred from intercalated metapelites toward the eastern part of the complex, are estimated at 1.9GPa / 520^{o}C followed by re-equilibration at 1.2GPa / 620^{o}C as (see Chapter 3).

Burg et al. (1995) found a systematic regional NE-trending stretching lineation and a consistent top-to-SW shear sense coeval with the regional amphibolite-facies overprint during thrusting. The same authors described also late and mostly brittle SW- and NE-trending shear zones deforming and retrogressing the earlier fabrics. Kilias et al. (1999) described a penetrative NW-striking foliation associated to an ENE-WSW- to WNW-ESE-trending stretching lineation. They deduced a top-to-ENE to -ESE sense of shear contemporaneous with W- to SW-ward flow during a Lower Cretaceous amphibolite-facies ductile event. The same authors also suggested an approximately threefold predominance of the first over the latter shear direction and they attributed them both to a coaxial deformation regime. Fabrics of the previous event were overprinted by low-angle conjugate top to NE- and SW senses of mylonitic shear that developed during formation of a retrograde greenschist mineral assemblage on a NW-striking schistosity coeval with a NE-trending stretching lineation (Kilias et al., 1999).

The *Circum-Rhodope belt* is a Triassic - Jurassic meta-sedimentary sequence locally involving Triassic rhyolites and quartzites at the base (Meinhold et al., 2009; Asvesta & Dimitriadis, 2010; Meinhold & Kostopoulos, 2013) (Figure 6.3). The term Circum-Rhodope belt was originally introduced by Kauffmann et al. (1976) to describe low-grade rocks fringing the basement complex of the Vertiskos Unit thought of as representing its original Mesozoic stratigraphic cover (Dixon & Dimitriadis, 1984). The rhyolites from the base of the Circum-Rhodope belt yield Lower Cretaceous metamorphic ages (Bertrand et al., 1994).

Immediately to the west, the *Chortiatis Magmatic Suite* is made of intensively deformed acidic and intermediate igneous rocks (Monod, 1964; Kockel et al., 1971, 1977) of Upper Jurassic protolith age (Zachariadis, 2007). Michard et al. (1994a,b) reported traces of high-pressure metamorphic overprint for the Circum-Rhodope belt and the Chortiatis Magmatic Suite that includes phengitic white mica for the former and relict glaucophane-bearing mineral assemblage for the latter.

6.3 Ductile deformation in the Chalkidiki block

We investigated the deformation pattern of the three units that constitute the Chalkidiki block (the Vertiskos Unit, the Circum-Rhodope belt and the Chortiatis Magmatic Suite). For convenience, these three units will be called hereafter as “basement”, “cover” and “arc”, respectively. To achieve our structural analysis we studied over thousand sites where we (i) measured the attitude of planar and linear elements of the rock fabrics (foliation, lineations, folds and boudinage), (ii) qualitatively to semi-quantitatively estimated strain intensity and (iii) determined the shear sense associated to the planar-linear fabrics. The following paragraphs describe the bulk deformation pattern at the scale of the Chalkidiki, omitting strain anomalies due to local perturbations.

6.3.1 Strain intensity

The basement is composed of Ordovician arc orthogneisses that essentially carry Hercynian fabrics acquired during late Palaeozoic events (Kydonakis et al., 2014b). Some concern was needed to separate Palaeozoic from Mesozoic fabrics. As we will argue later, the Mesozoic strain intensity is such that all older fabrics would have often been re-oriented during the Mesozoic events. The complexity related to Palaeozoic inherited fabrics only concerns the

basement (Vertiskos Unit) as the cover and the arc units essentially recorded only the Alpine events due to their Triassic - Jurassic and Upper Jurassic protolith ages, respectively.

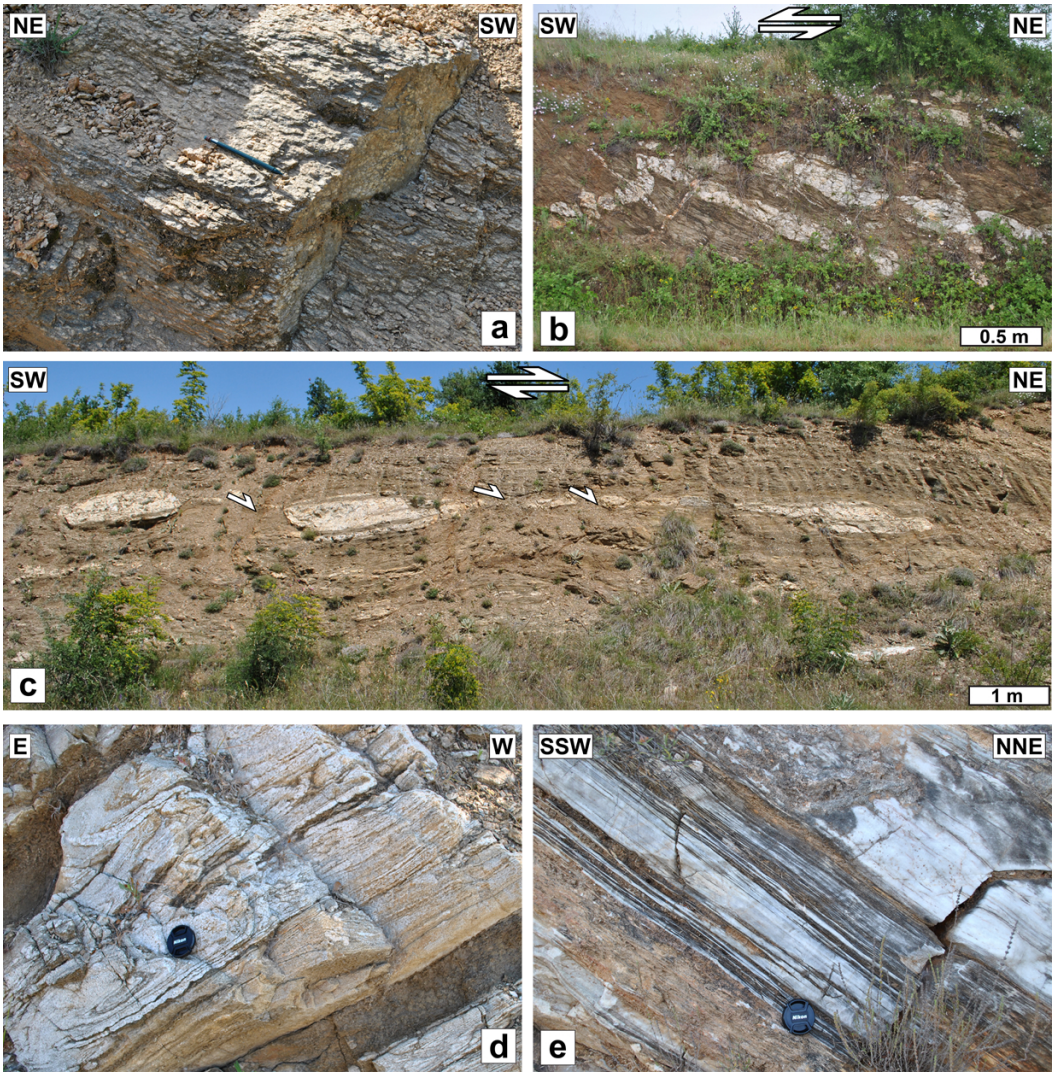

Figure 6.4: Field occurrences of highly deformed rocks. (a) Mylonite of the Triassic Arnea Magmatic Complex. (b,c) Sheared pegmatites embedded in basement orthogneisses. (d) Sheath folds developed in basement gneisses. (e) Strongly sheared marbles of the cover.

Potential strain markers inside basement gneisses are the amphibolites (former mafic intrusions) and the quartz-rich/pegmatite dykes. The mafic intrusions are of unknown age. However, in Bulgaria, the protolith of possibly equivalent meta-gabbros and meta-diorites has been dated as Upper Ordovician (Peytcheva et al., 2009). In situ zircon dating (LA-ICP-MS) of amphibolites from the basement yielded Carboniferous metamorphic ages (341.1 ± 7.9 Ma; see Chapter 2). This implies that their protolith is pre-Carboniferous and that at least part of their deformation is of Carboniferous age. On the contrary, the pegmatites were more probably crystallised between Carboniferous and Triassic (our own U/Pb LA-ICP-MS zircon dating) and together with the Triassic Arnea Granite, to which they are associated, can be considered as better strain markers for the Mesozoic events.

The deformation of the Triassic Arnea Granite is essentially of Alpine age (Figure 6.3). It is pervasively deformed with local mylonitic shear zones (Figure 6.4a). Rare apophyses of the Arnea Granite that locally cut at high angle the shallow-dipping foliation of the surrounding gneisses suggest that part of the basement's deformation is pre-Arnea emplacement (i.e., pre-Lower Triassic) in age. However, the majority of the pegmatites and quartz-rich

veins appear foliated together with the basement gneisses indicating that any earlier fabrics have been largely re-oriented during the Mesozoic / Cenozoic Alpine event(s) (Figure 6.4b). Boudinage of low dipping pegmatite veins is extensively observed at various scales in quartz-rich veins and pegmatites indicate a strong vertical shortening component of the bulk finite strain. However, most boudinaged pegmatites display a clear asymmetry and associated shear bands that are compatible with either top-to-SW or -NE shear sense, suggesting that the vertical shortening is related to low angle shearing (Figure 6.4c). The aspect ratio of boudins depends on the viscosity contrast between the pegmatite and the gneissic matrix whereas the separation (distance between adjacent boudins) depends on strain intensity. In Figure 6.4c, asymmetric boudinaged pegmatites, with aspect ratio about 0.25, are separated by distance equivalent to one to two times their length (i.e., of the order of 2.0-4.0m). This implies stretching amounts in the range 100-200%, giving λ_1 values in the range of 2.0-3.0. In a simple shear regime (see Ramsay, 1967) this would correspond to minimum γ values of circa 1.5-2.7. Such amount of shear strain is enough to re-orient most previously-formed fabrics as for γ=2.0 all lines having initial obliquities up to 90^o with the shear plane are re-oriented to obliquities less than 28^o (see Ramsay, 1967). This is the case where the main foliation is axial planar to meso-scale folds whose axis has rotated close to the stretching lineation. High strain values (γ values higher than 6.0) are also indicated by the presence of sheath folds in the gneisses, amphibolites and marbles (Figure 6.4d). Mylonitic fabrics in the basement gneisses (Burg et al., 1995; Kilias et al., 1999) commonly display strong grain size reduction that indicates γ values higher than 3.0. Such fabrics they also developed in marbles of the Circum-Rhodope belt (Figure 6.4e).

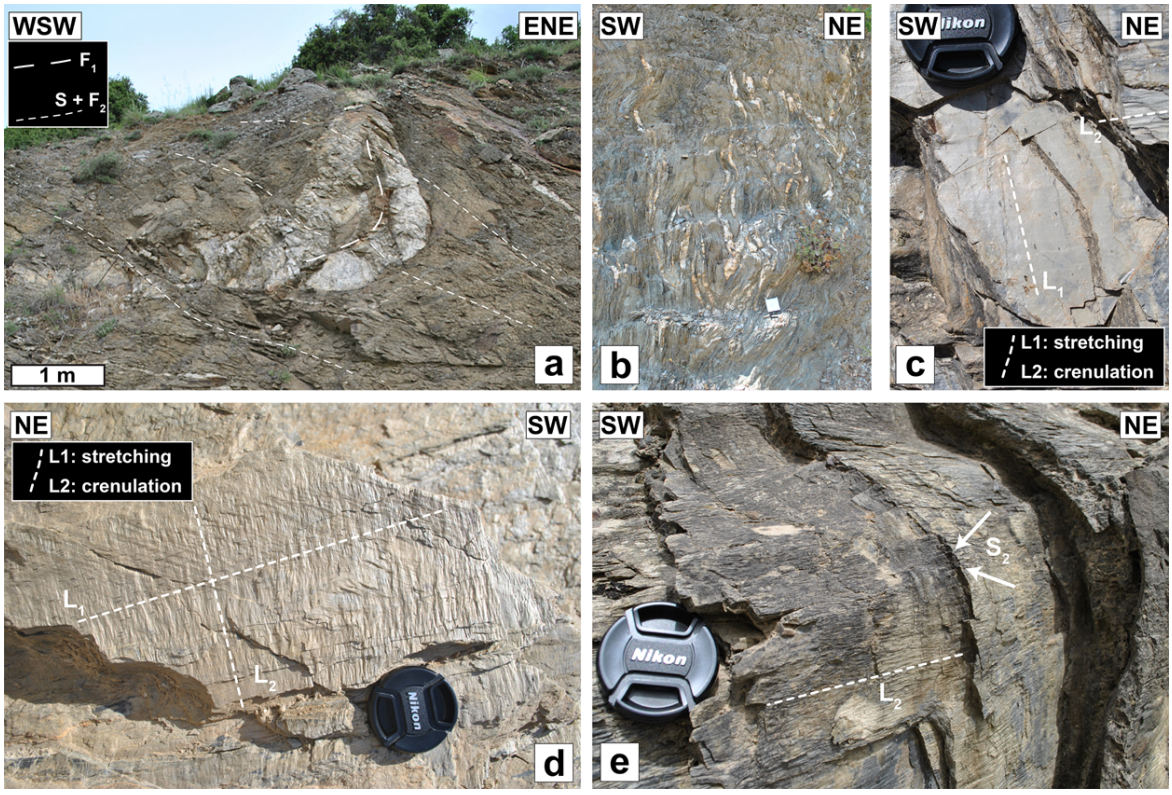

Figure 6.5: "Type 3" fold interference pattern recorded by a pegmatite from the western part of the basement gneisses. (b) Folding after boudinage in quartz-rich layers within micaschists of the cover. (c,d) An early stretching lineation L_1 that developed before the L_2 crenulation lineation. (e) Crenulation cleavage (S_2) developed by dissolution in micaschists from the cover.

The above series of field evidence that characterize the Chalkidiki block indicates that the whole structural pile has undergone high strains commonly giving amount of stretching

higher than 100%.

6.3.2 Superposition of fabrics

Due to high strain intensity features described above it is likely that young deformation (i.e., Mesozoic) have completely re-worked the older structures (i.e. Palaeozoic). There is evidence for superposition of structures both from the basement and the meta-sedimentary cover.

Pegmatites and quartz-rich veins preserve evidence for superposition of two generations of deformation. Close to the basement/cover main contact near Kokkinochori village, the pegmatites preserve evidence for "Type 3" interference pattern (Ramsay, 1967). A first fold generation with horizontal fold axis and vertical axial plane (F_1) affecting a thick pegmatite dyke is re-folded with horizontal fold axis and sub-horizontal axial plane (Figure 6.5a). The latter is parallel to the regional foliation of the enveloping biotite gneisses and thus, they likely developed simultaneously.

In some places within the cover schists, dominantly upright folding affects previously boudinaged quartz veins implying the existence of two deformation phases or a progressive deformation starting with a layer-parallel shear and then followed by folding (Figure 6.5b). This is particularly true close to the contact with the basement where the foliation is close to vertical and is axial planar to the folds. In more detail, within the cover schists, an old S_1 planar fabric bearing a L_1 stretching lineation (Figures 6.5c,d) is pervasively folded throughout the unit producing a closely-spaced crenulation lineation L_2 and a new crenulation cleavage S_2 (Figure 6.5e). The L_2 crenulation lineation trends oblique or perpendicular to the L_1 mineral lineation. With the current state of knowledge the exact timing of the above fabric-forming events from the cover is rather unknown. However, as it will be discussed further these fabrics seem to be rather systematically related to zones of Tertiary faulting and/or strike-slip shearing.

6.3.3 Foliation map

In order to discuss the geological structure and the attitude of the planar/linear fabrics we have compiled several maps illustrating the regional pattern of foliation, stretching lineation, associated shear senses and fold axis/crenulation lineation.

Tight to isoclinal folding affecting all the exposed rocktypes has transposed lithological contacts into the main foliation plane. The latter is pervasive, locally mylonitic and is related to a stretching/crenulation lineation of Mesozoic age (Dixon & Dimitriadis, 1984; Burg et al., 1995; Kilias et al., 1999). The Alpine pervasive planar fabric is chiefly made by quartz and micas in gneisses and schists and by amphiboles, micas and quartz in mafic rocks. A regional foliation map has been compiled using our measurements (n=1054) and those available from the geological map of the area (n=3112 Kockel & Mollat, 1977). Being in general agreement, both datasets were used to draw the regional foliation trajectories map (Figure 6.6).

Despite local perturbations due to late normal faulting and post-metamorphic overprint the strike of regional foliation map is rather constant at the scale of the Chalkidiki block (Figure 6.6). The dominant foliation strike is NW-SE following, in general, the NW-trending lithological contacts along the length of the studied units (Figures 6.7, 6.8 and 6.9). Toward the Kerdylion Detachment, to the east, the foliation dips gently westward. Within the basement, the foliation dips rather gently eastward. On both sides of the SocFhos normal fault that trends approximately E-W in the central part of the area, the basement foliation strikes in different directions: to the south, the foliation strikes NW following the major unit contacts and to the north, it is deflected toward a NE direction. Toward the east, close to the Circum-Rhodope belt, the basement foliation strikes again NW and dips steeply and almost vertical in places. To the east, within the cover, the foliation geometry is rather

homogenous, striking constantly NW-SE and dipping moderately to steeply, sometimes up to vertical, to the NE or SW.

In the central-southern part of the study area, an open NW-trending synform affects the cover (Figure 6.10). Few kilometres to the east, toward the Ierissos and Orfanos Gulfs, another antiform that trends WNW to NNW affects basement rocks (Figure 6.10). Both features resulted from post-metamorphic deformation as they deform the regional foliation. Within the arc unit further to the west, the foliation strikes NW and it is exclusively dipping steeply to the NNE or NE.

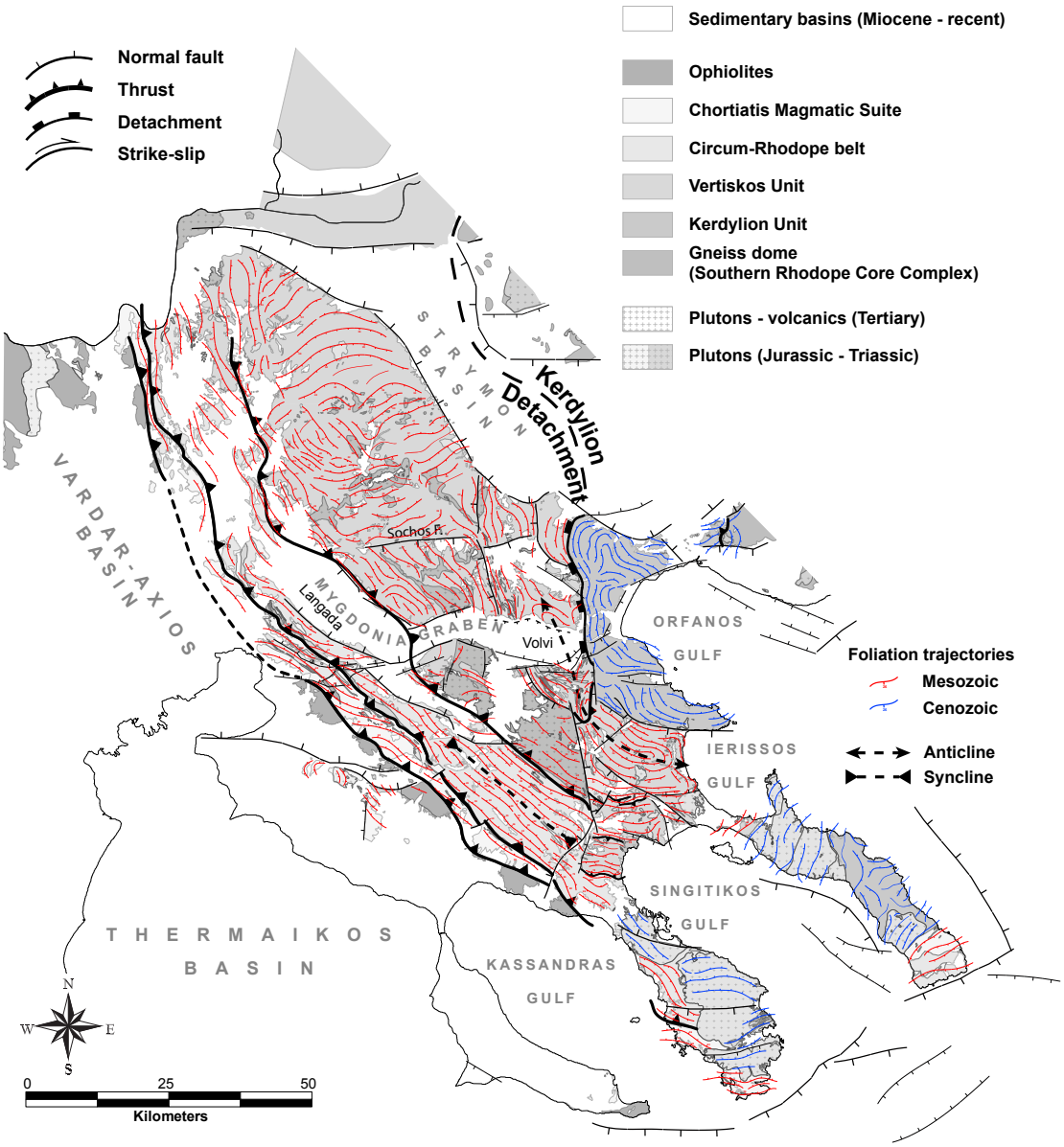

Figure 6.6: Foliation trajectories map compiled using the available literature data (Kockel & Mollat, 1977, n=3112) our measurements (n=1054). Numbers correspond to dip values. For clarity a greyscale version of the geological map of the area (see Figure 6.3) is shown in the background. Red trajectories correspond to Mesozoic deformation whereas blue trajectories are related to Tertiary extension.

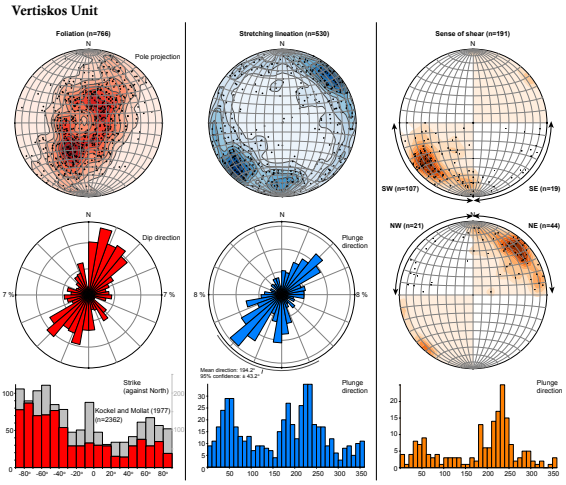

Figure 6.7: Equal area, lower hemisphere stereoplots and corresponding rose diagrams and histograms for various structural fabrics of the basement (Vertiskos Unit). Grey-filled histograms are data from the geological map of the area (Kockel & Mollat, 1977).

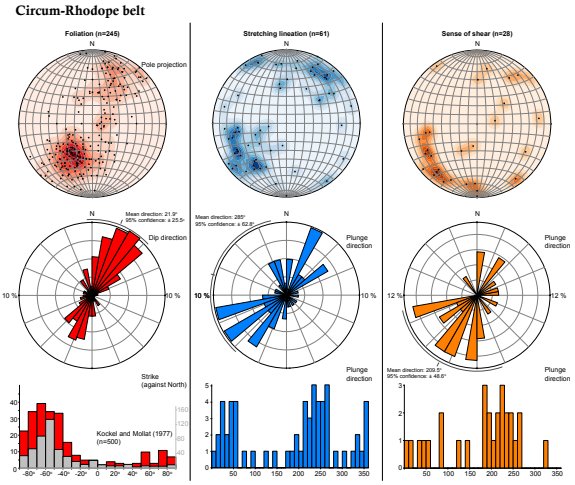

Figure 6.8: Equal area, lower hemisphere stereoplots and corresponding rose diagrams and histograms for various structural fabrics of the cover (Circum-Rhodope belt). Grey-filled histograms are data from the geological map of the area (Kockel & Mollat, 1977).

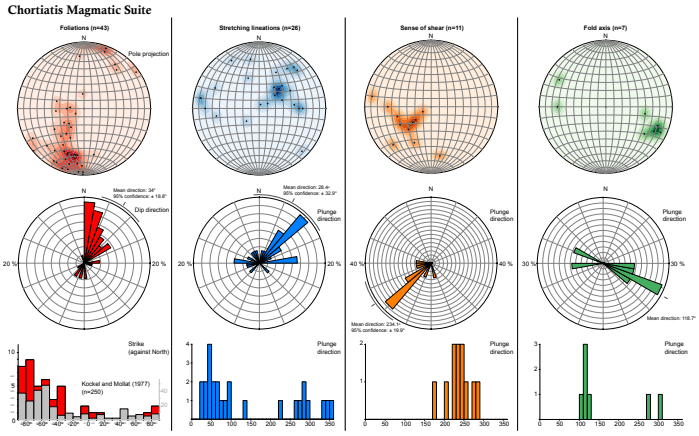

Figure 6.9: Equal area, lower hemisphere stereoplots and corresponding rose diagrams and histograms for various structural fabrics of the arc (Chortiatis Magmatic Suite). Grey-filled histograms are data from the geological map of the area (Kockel & Mollat, 1977).

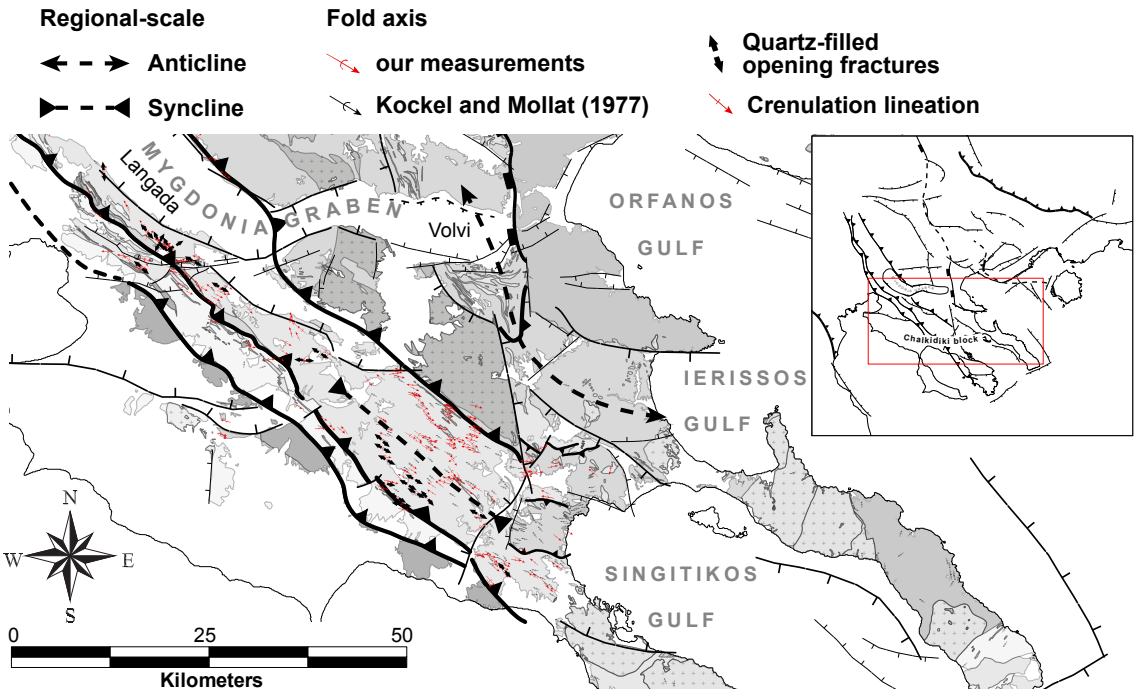

Figure 6.10: Regional fold geometry map.

6.3.4 Map of stretching lineation and sense of shear

A pervasive stretching lineation was measured in all possible lithologies and a regional stretching lineation and shear sense map has been compiled using 617 stretching lineation and 230 senses of shear measurements (Figure 6.11). The stretching lineation is typically defined by micas, elongated quartz aggregates and feldspars. Pressure fringes are commonly developed parallel to the stretching lineation on pre- and syn-tectonic garnets and staurolites in appropriate lithologies. Shear sense criteria (e.g., Berthé et al., 1979; Simpson & Schmid, 1983; van den Driessche & Brun, 1987; Hanmer & Passchier, 1991) were identified at outcrop scale parallel to the stretching lineation (λ_1 axis) and perpendicular to the dominant planar fabric ($\lambda_1\lambda_2$ plane). Wherever needed, saw-cuts and thin sections were studied to define or verify the shear sense based on the asymmetry of structures.

The stretching lineation recorded by the biotite gneisses of the basement maintains a constant SW-trending orientation (around N45^o) in the central part of the area - i.e., north of the Sochos fault. However, to the south of the fault the stretching lineation is deflected toward N-S or E-W possibly as a result of post-ductile deformation associated to normal and strike-slip faulting. On the contrary, the stretching lineation in the cover and the arc units to the west maintains a constant SW orientation without significant lateral along strike variations.

In the basement rocks, two opposing senses of shear, top to SW and top to NE were identified at a regional scale. Representative shear fabrics are shown in Figure 6.12 and although both senses are ductile, the SW one dominates over the NE (Figure 6.11 and Figure 6.7 for basement only). Overlapping relations between the two shear directions were not extensively identified in the field and thus, their time-relation cannot be resolved by overprinting criteria only. The shear sense within the cover and the arc unit is unequivocally toward the SW. This is also true for the western part of the basement close to the cover. In garnet-staurolite-mica-schists, included in the basement, garnet growth during temperature increase (based on major elements zoning not shown here), the shear sense is always top to the SW (Figure 6.12c).

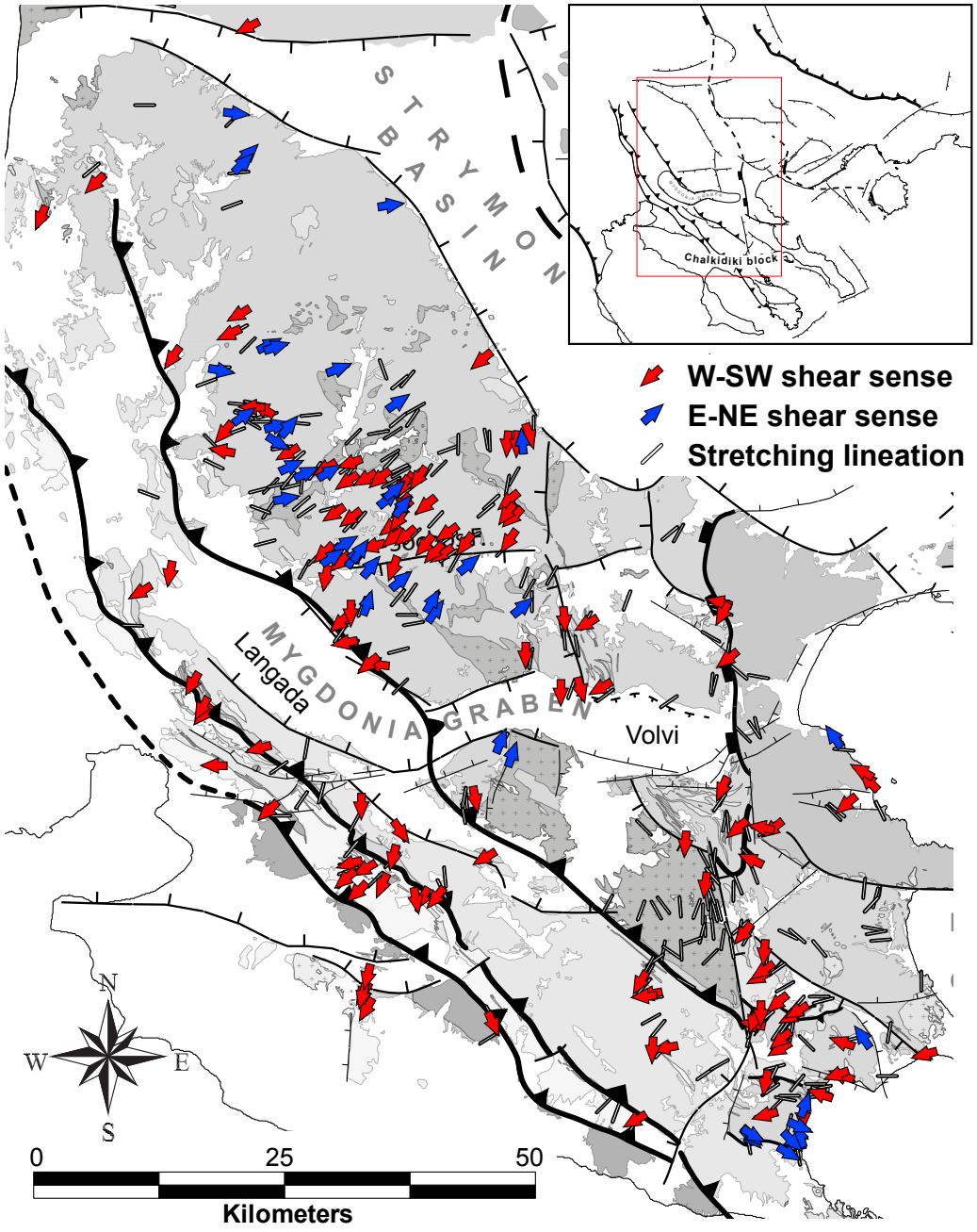

Figure 6.11: Stretching lineation and associated shear sense map.

6.3.5 Timing of ductile fabrics development

In previous studies, the age of the ductile fabrics from the basement was either directly dated (e.g., Papadopoulos & Kilias, 1985) or was deduced from structural relations between plutonic bodies of known age (e.g., Kilias et al., 1999) and country rocks. As already mentioned in section 6.2.2, there is a wealth of available medium-temperature metamorphic ages from the basement rocks and some from the meta-sedimentary cover. Potassium/argon dating of micas and amphiboles from the basement gave consistent cooling ages between 140 and 90 Ma (Borsi et al., 1965; Harre et al., 1968; Marakis, 1969; Papadopoulos & Kilias, 1985; Christofides et al., 1999). The Rb/Sr system gave somewhat more scattered ages between circa 300 and 80 Ma (Borsi et al., 1965; Harre et al., 1968; Zervas, 1979; Papadopoulos & Kilias, 1985; de Wet et al., 1989; Christofides et al., 2007; Himmerkus et al., 2009b). de Wet

et al. (1989) and Lips et al. (2000) reported a 136.8 ± 1.5 Ma $^{40}Ar/^{39}Ar$ age (step heating in biotite) from the Triassic Arnea Granite (part of the basement) and a 149.3 ± 3.0 Ma age (spot fusion in white mica) from a mylonitic zone of the basement, respectively. Bertrand et al. (1994) also reported 120-130 Ma K/Ar age for rhyolites from the base of the Circum-Rhodope belt. More recently, $^{40}Ar/^{39}Ar$ cooling ages were obtained from the basement rocks and the meta-sedimentary cover that range from circa 125 Ma (to the west) to circa 100 Ma (to the east) (see Chapter 4). These younger cooling ages to the east coincide with higher metamorphic conditions in the same direction. The above geochronology input, leaves no doubt that the syn-metamorphic deformation started in Lower Cretaceous when the regional foliation was formed.

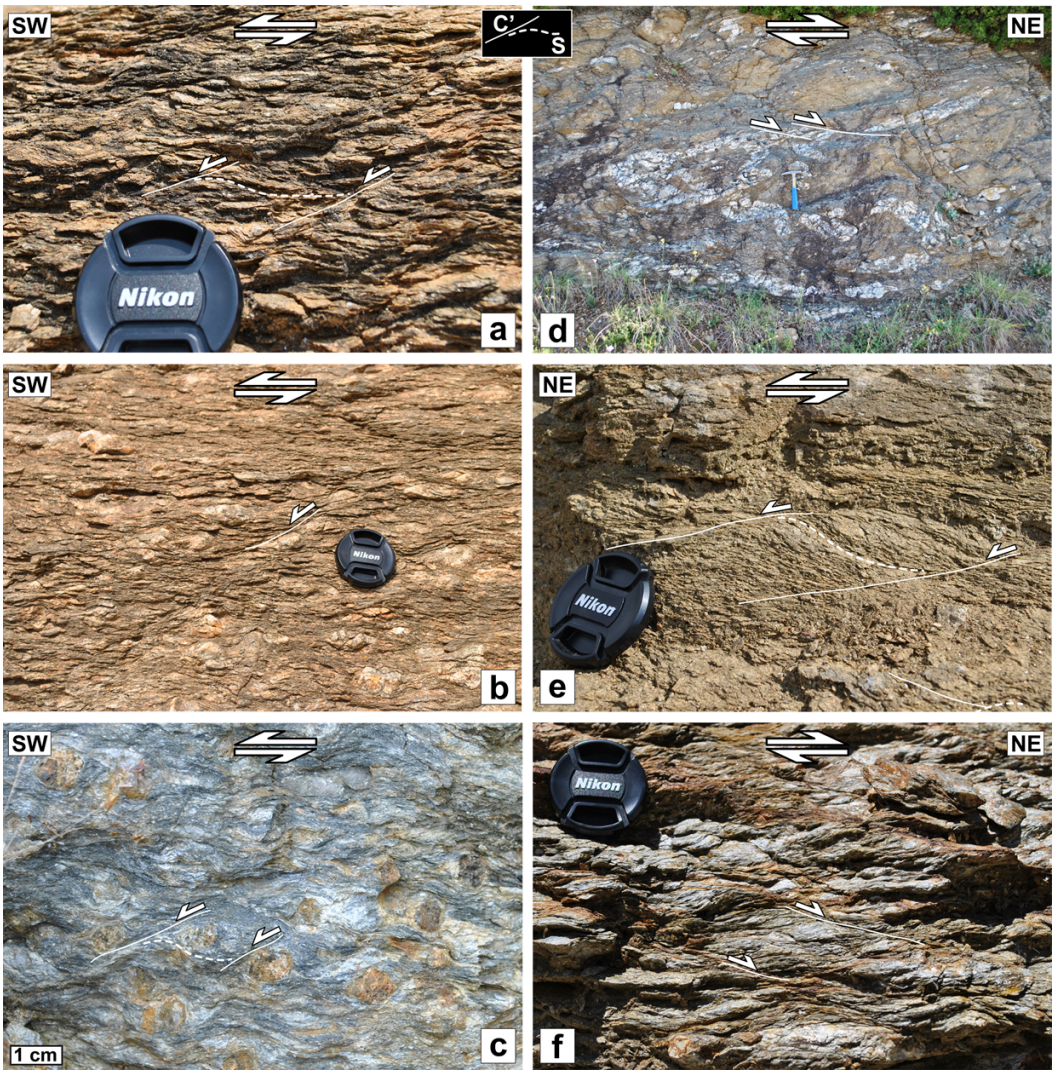

Figure 6.12: Selected shear sense indicators from the basement. (a-c) Top-to-SW shear bands. (d-f) Top-to-NE shear bands.

The Eocene syn-tectonic plutons (e.g., de Wet et al., 1989; Tranos et al., 1993) and the middle Oligocene post-tectonic plutons from the southern part of the Chalkidiki Peninsula were used as time markers for the end of the basement ductile deformation. Based on deformation similarities with the Tertiary plutons, Kilias et al. (1999) suggested that the late greenschist-facies ductile fabrics of the basement were formed between Eocene and lower Oligocene. However, no post-90 Ma mid-temperature metamorphic ages have been reported from the basement and this leaves circa 40 m.y. of time lag between the youngest reported metamorphic age and the assumed end of the ductile deformation. We instead propose that

the bulk ductile deformation must have ceased significantly earlier than the Oligocene or even the Eocene. In line with that, Kydonakis et al. (2014a) reported circa 55 Ma apatite fission-track ages from the basement and this already implies that the rocks were at low temperature already by the uppermost Cretaceous. Therefore, the ductile fabrics of the Chalkidiki block have necessarily been formed between lowermost and uppermost Cretaceous.

6.4 Folding

All units of the Chalkidiki block display folding at various scales. Two strikingly different situations must be distinguished: (i) syn-metamorphic folding mostly observed in basement gneisses and pegmatites and (ii) post-metamorphic folding that affected all units but that was pervasively developed in the cover meta-sediments.

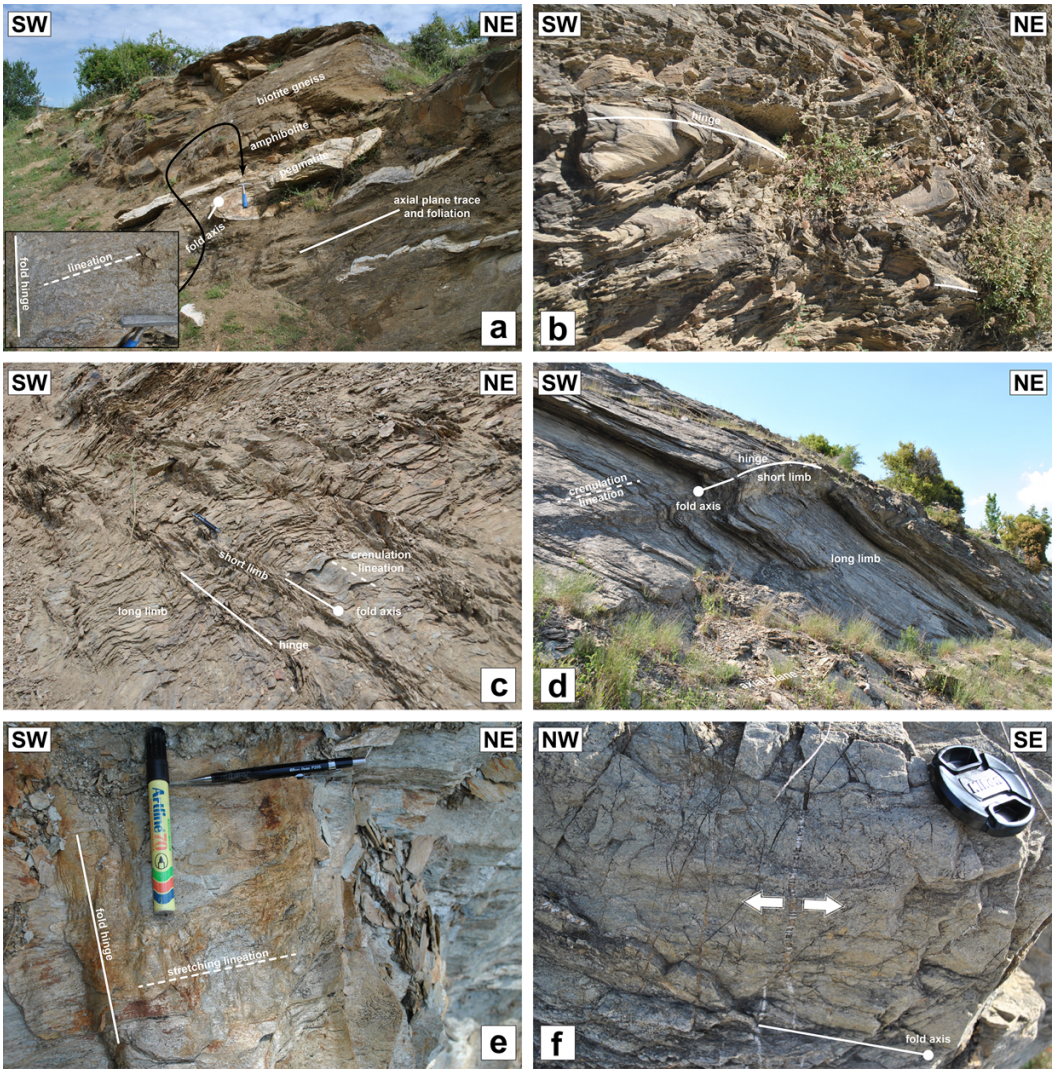

Figure 6.13: Occurrences of folds from the basement (a,b) and from the cover (c-e). (f) Quartz-filled opening fractures developed perpendicular to the fold axis.

6.4.1 In basement rocks

Recumbent folds that are frequently observed in basement rocks are mostly symmetrical with gently dipping or sub-horizontal axial planes, parallel to the regional foliation, and gently plunging fold axes. Such cylindrical and tight to isoclinal folds involving all possible

basement lithologies (biotite gneisses, amphibolites and pegmatites) whatever their initial geometry imply a strong vertical component of shortening (Figure 6.13a). But, meso-scale fold axes were largely re-oriented parallel or at small angle to the stretching lineation in basement mica-schists indicating that they formed and amplified during the same low-angle shear that gave the regional-scale foliation.

6.4.2 In cover meta-sediments

Fold geometry in the Circum-Rhodope Belt strongly differs from that in the basement. The most commonly observed fold type involves asymmetric open to tight folds with moderately to gently plunging fold axes (Figures 6.13c,d). They affect a bedding parallel foliation that bears a mineral stretching lineation. In other terms, these folds developed significantly after metamorphism (Figure 6.13e).

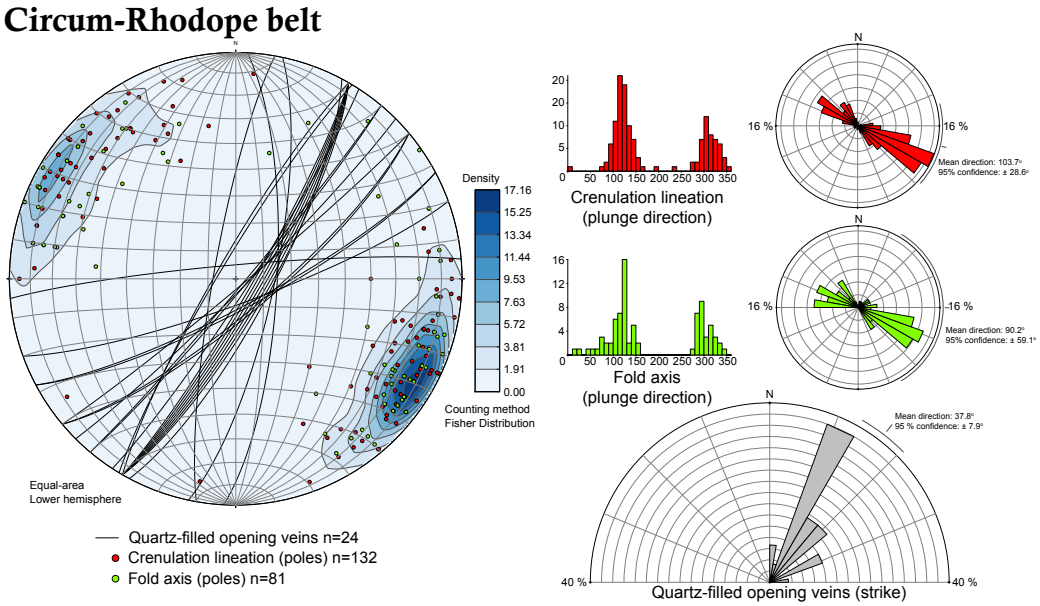

Figure 6.14: Equal area, lower hemisphere stereoplots and corresponding rose diagrams and histograms for fold axis and crenulation lineation of the cover (Circum-Rhodope belt).

The map of fold axes and crenulation lineation along the schists of the Circum-Rhodope belt shows a very constant trend parallel to regional scale lithological contacts (Figures 6.10 and 6.14). With only minor exceptions, tension gashes filled with secondary quartz formed perpendicular to the fold axes and the crenulation lineations (Figure 6.13f) indicating a moderate amount of axis parallel stretching (i.e., along-strike stretching). Locally, curved hinges indicate partial reorientation in the stretching direction (Figure 6.13b).

Although folds are rare within the Chortiatis Magmatic Suite, wherever observed they follow roughly the same NW-SE trend (Figure 6.9).

6.5 Cretaceous thrusting and extension

6.5.1 Kinematics of thrusting

In the Chalkidiki block there is a general agreement concerning the direction of thrusting. Burg et al. (1995) argued for syn-metamorphic SW-directed thrusting based on mylonitic foliation and associated shear criteria developed in basement rocks. Tranos et al. (1999) reported early SW-directed shear fabrics from the contact between basement and cover that was preserved despite later tectonic overprints. Toward the eastern part of the basement,

eclogite-facies meta-sediments, whose garnet grew during temperature increase on a prograde path (our unpublished data), have recorded a SW-directed shear (Figure 6.12c). Step heating ($^{40}Ar/^{39}Ar$) on white micas from the same locality gave lowermost Upper Cretaceous cooling ages (see Chapter 4).

The piling up of the Palaeozoic basement on top of the Mesozoic sedimentary cover and of these two lithologic units on top of the Upper Jurassic arc unit shows that thrusting occurred at the scale of the whole Chalkidiki block. Both thrust contacts are sharp, trend NW and appear heavily re-worked in a post-metamorphic stage (Figure 6.3). In the central part of the Chalkidiki block, the thrust contact between basement and cover is partly obscured by normal faulting related to the middle Miocene Mygdonia graben. Close to the graben, the foliation of both units trend NW, parallel to their contact, and dips steeply either to the NE or to the SW (Figure 6.6). This conspicuous steeply-dipping pattern is due to late brittle strike-slip re-working that makes difficult the observation of basement on top of cover geometry at several places. However, in few places the contact is preserved with a gently NE-dipping foliation with basement on top of cover, associated to SW-directed ductile sense of shear. Further to southwest the contact between the cover and the arc also trends NW-SE. The foliation on both sides of the contact is moderately to steeply dipping toward the NE and brings the older cover on top of the arc with associated to SW-directed ductile sense of shear. As already mentioned, the sense of shear is unequivocally directed to the SW near the thrust contacts (Figure 6.6) leaving no doubt on the kinematics of ductile thrusting at the scale of the whole Chalkidiki block.

A the whole North Aegean scale, Cretaceous syn-metamorphic thrusting toward SW to S is the norm in the Rhodope (Burg et al., 1990, 1996) and is accompanied by a N- to NE-trending stretching lineation (see compilation by Burg, 2012). Along the southward verging Nestos shear zone two units (Papanikolaou & Panagopoulos, 1981) are superposed with the upper unit characterised by eclogite-bearing amphibolite-facies rocks and the lower by greenschist-facies rocks (Burg et al., 1990, 1996) (Figure 6.2). Southward thrusting is also described in an equivalent shear zone to the north of the Nestos shear zone namely Chepelare shear zone (Burg et al., 1990).

To the west, the Vardar Ophiolites are thrust on top of the Pelagonian margin with the kinematics of obduction being again to the southwest (Papanikolaou, 2009; Robertson et al., 2013). Overall, it appears that a continuum exists from Pelagonia, to the west, to the Rhodope, to the Northeast where thrust-related kinematics are always directed toward the southwest.

6.5.2 Cretaceous extension

Two opposing senses of shear, toward the SW and the NE are associated to syn-metamorphic deformation (Figures 6.11 and 6.12) and developed in Cretaceous (Section 3.4). This is at variance with conclusions reached by previous workers in the area.

Kilias et al. (1999) argued that (i) a systematic top-to-ENE to ESE ductile flow of Cretaceous age is recorded in the basement, (ii) this shear sense is dominant over the top-to-WSW to WNW one and (iii) based on similar shear sense to the northern part of the Rhodope, they concluded that the eastward shearing is more likely related to ductile extension. In addition, these authors concluded that both senses of shear characterize both Cretaceous and Eocene-Miocene tectonic events. On the other hand, Burg et al. (1995) argued for a dominant syn-metamorphic SW-directed ductile shear and claimed that the NE shearing in basement rocks is in the brittle regime and likely related to late extension.

Our own work shows that both shear senses are clearly ductile (Figure 6.12). The regional shear sense map (Figure 6.11) and stereoplots (Figures 6.7, 6.8 and 6.9) show that the SW-directed shear is clearly dominant over the NE one. The predominance of thrust-related deformation over the extension-related one implies that extension was somewhat not so

intense and more likely slow. A key observation is that, in the Chalkidiki block, only the basement records the NE shearing which is completely absent from cover and arc units.

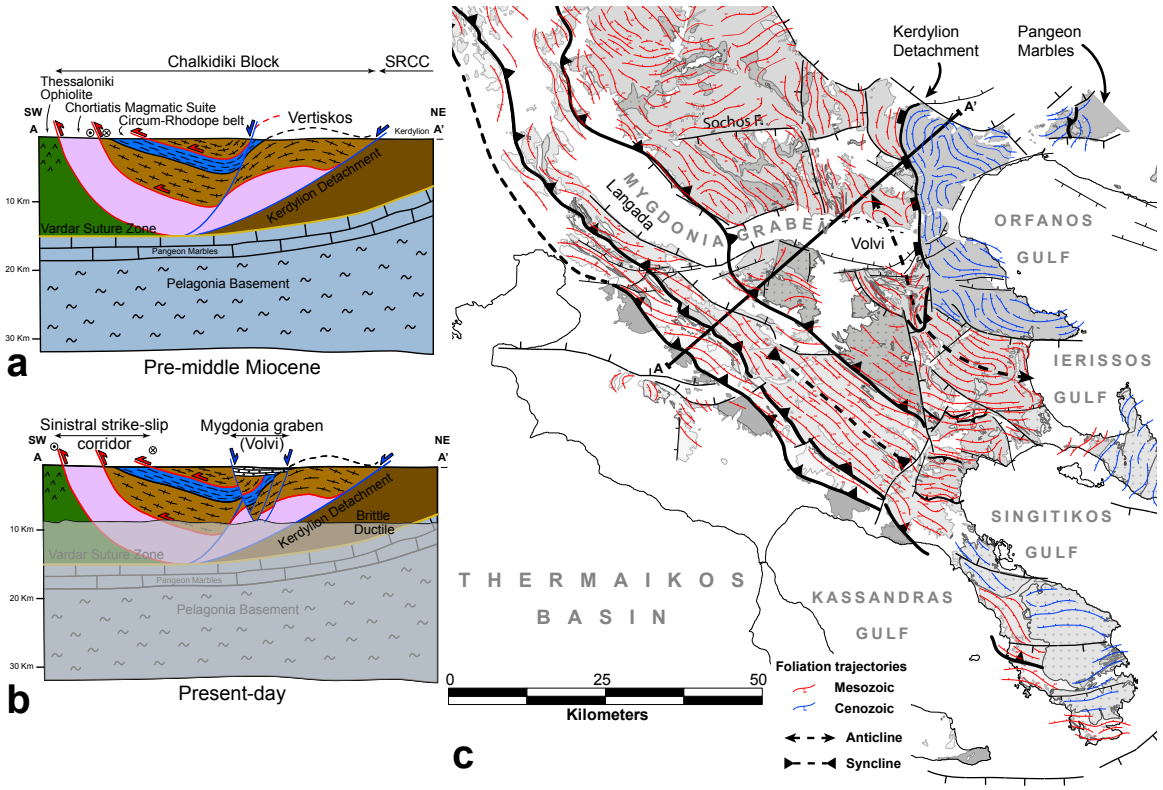

Figure 6.15: Pre-middle Miocene (a) and present-day (b) crustal-scale NE-SW cross-sections as deducted from geophysical data and surface geology. Thrusting is indicated in red and extension-related structures in blue. (c) The regional foliation trajectories map (also shown in Figure 6.6).

6.5.3 Relation between thrusting and extension

Using the only available data, which are mainly surface geology (Figure 6.3) and Moho depth from regional geophysical mapping (e.g., Papazachos, 1998), we attempted portraying the crustal-scale structure of the Chalkidiki block (i) before Neogene extension (i.e., prior to 15Ma) (Figure 6.15a) and (ii) at present-day (Figure 6.15b). The upper one third of the sections is constructed using the geological map of the area (Kockel & Mollat, 1977) (Figure 6.3) and our own structural mapping (Figures 6.6 and 6.11) whereas the lower two thirds of the sections correspond to a downward extrapolation made using the regional scale geological data (Figure 6.2).

Prior to Neogene extension – i.e., before the development of the Mygdonia Graben - the structure of the Chalkidiki block mostly resulted from (i) Cretaceous syn-metamorphic thrusting (main thrust faults in red in Figure 6.15a) and (ii) Paleogene (from 45 to 15Ma) core complex extension (the Kerdylion Detachment that controlled the SRCC exhumation and a secondary normal fault related to the detachment in blue in Figure 6.15a). The Chortiatis Magmatic Suite is thrust on top of the Thessaloniki Ophiolite. Toward the southwest, the Vardar ophiolites are thrust on top of Pelagonia, this thrust being the Vardar Suture Zone (green trace in Figure 6.15a). Toward the northeast, the Kerdylion Unit lays on top of the Pangeon marbles that is the upper metamorphic unit of the SRCC. We interpret this marble layer and its underlying Hercynian gneisses as Pelagonia that reappears as an extensional tectonic window in between the Chalkidiki block and the Northern Rhodope Domain.

This SW-NE section (Figure 6.15a) gives an overall picture of the thrust system and its relation to extension during Cretaceous at the scale of the Chalkidiki block. The basement

(Vertiskos Unit) is duplicated in two main sub-units separated by the sedimentary cover (Circum-Rhodope belt). It is noticeable that the NE directed senses of shear are almost entirely located in the upper basement unit (Figure 6.11). The distributed extension within the upper thrust unit strongly contrast with the absence of NE directed shear in the lower basement unit. This suggests that this extensional shearing resulted from the exhumation of the lower unit (i.e., basement and sedimentary cover that underwent high-pressure metamorphism up to 1.9GPa / 520^{o}C) toward the SW.

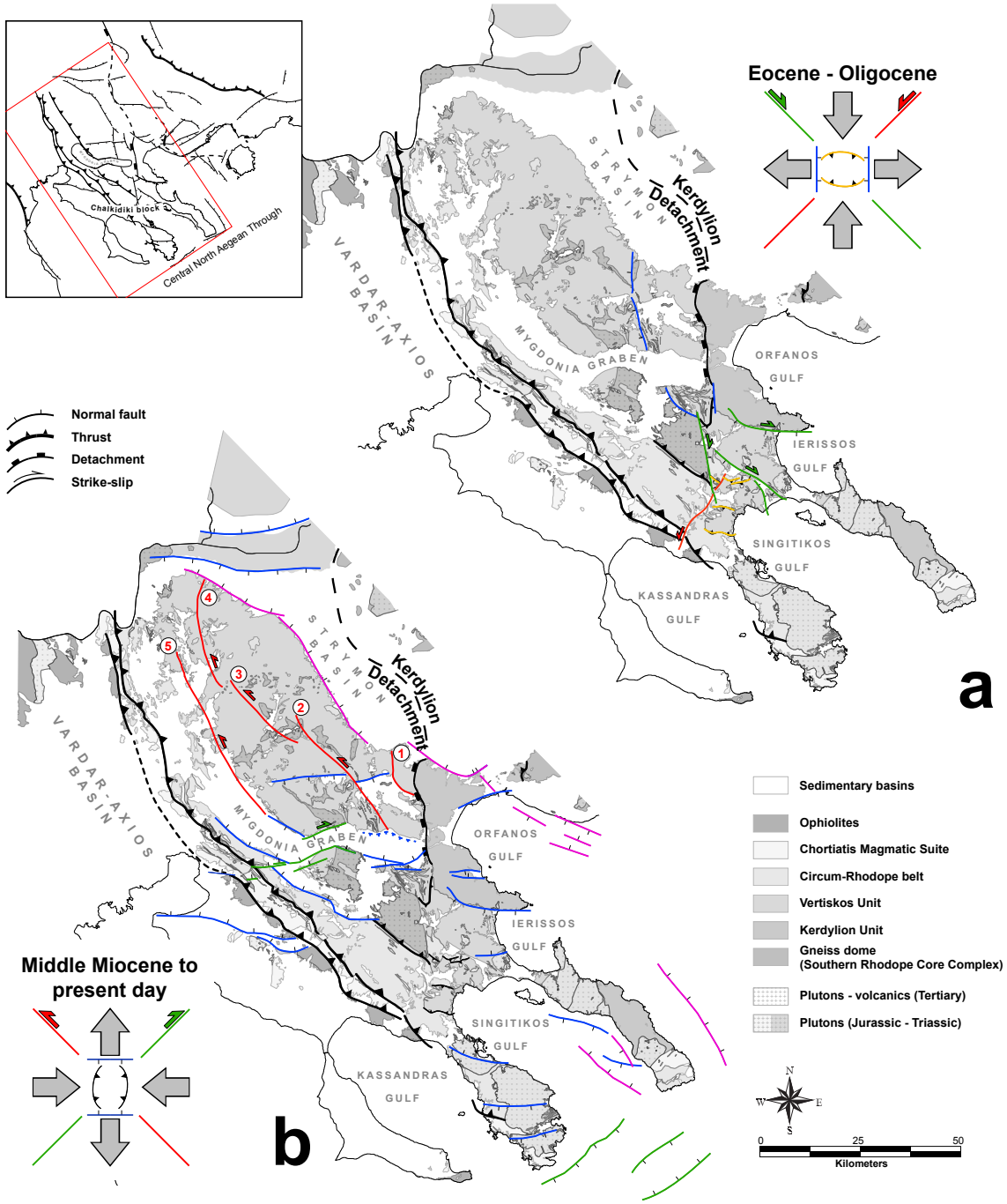

Figure 6.16: The faults of the study area are grouped into two major families that are interpreted here as acting together during (a) Eocene - Oligocene and (b) middle Miocene to present.

Exhumation of high-pressure metamorphic rocks driven by slab rollback, as illustrated by the Cycladic blueschists, offers a simple explanation for the situation observed in the Chalkidiki block. In this process (Brun & Faccenna, 2008; Tirel et al., 2013), the continental

crust that is pulled down during subduction, undergoes high-pressure metamorphism and progressively delaminates from the lithospheric mantle. When full delamination is reached, the downgoing slab starts to rollback, allowing the subducted crust to be exhumed. Due to delamination from its underlying lithospheric mantle, the base of the exhuming crust comes into direct contact with the asthenosphere and then undergoes a strong heating from below. As exemplified in the Cyclades, during subduction and high-pressure metamorphism the sense of shear is directed toward the SW whereas during later core complex extension and high temperature metamorphism the sense of shear is directed to the NE (Philippon et al., 2012). The situation observed in the Chalkidiki block is, to some extent, comparable to the Cyclades. Thrusting and shear directed toward the SW is associated with high-pressure metamorphism. The NE directed shear of rather moderate intensity that affected the hot basement of Vertiskos more likely represents the extension of the upper thrust unit as a consequence of the southwestward exhumation of the lower unit.

Note that a similar sense of shear top to NE, related to Cretaceous extension, is also observed in one of the imbricate units of the northern part of the Rhodope (Burg et al., 1990). This is perhaps the only place in the Northern Rhodope Domain where a systematic NE-shear sense is recorded (see Burg, 2012).

6.6 Tertiary deformation related to Aegean extension

6.6.1 The clockwise rotation of the Chalkidiki block

During the Tertiary, the Chalkidiki block underwent a clockwise rotation of 30^o (Kondopoulou & Westphal, 1986; Kissel & Laj, 1988) that accommodated the exhumation of the Southern Rhodope Core Complex (Brun & Sokoutis, 2004, 2007) (Figure 6.17). The Chalkidiki block is sharply cut to the northeast by northeast dipping normal faults that control the ongoing subsidence of the Strymon Basin and to the southwest by the Thermaikos Basin whose present-day tectonic subsidence is controlled by NE dipping normal faults (Laigle et al., 2000) that trend parallel to the western branch of the North Cyclades Detachment System (Jolivet et al., 2010). Laterally, toward the southeast, the clockwise rotation of the Chalkidiki block should have been accommodated by a sinistral strike-slip shear within the Central North Aegean Through (CNAT) also called Sporades Basin (see review by Koukouvelas & Aydin, 2002. This early sense of strike-slip must not be confused with the dextral strike-slip shear that took place within the CNAT in the last 5Ma when the North Anatolian Fault reached the Aegean (Lyberis, 1984; Armijo et al., 1999) and that is responsible for the oblique pattern of normal faulting that is depicted by seismic data (Roussos & Lyssimachou, 1991) and by detailed seafloor bathymetry (Papanikolaou et al., 2002, 2006).

An early sinistral sense of strike-slip shear has not yet been documented in the CNAT, likely due to the lack of seismic data deep enough to image the early Paleocene - Lower Neogene stages of development. However, in the northeastern end of the CNAT, NE-trending normal faults were inverted by E-W dextral shear related to the westward propagation of the North Anatolian Fault (see fig.3 in Roussos & Lyssimachou, 1991. One of these faults, the so-called "Athos Fault Zone" that is located offshore close to the Mt Athos peninsula (see Figure 6.3) is (according to these authors) "*characterised by dextral strike-slip movement along a pre-existing normal fault*". Normal faults that trend NE-SW extend further to the northeast (Mascle & Martin, 1990), over around 100Km away from the North Anatolian fault. Note that this NE-trending fault belt is in line with the onshore western limit of the Thrace Basin whose first sedimentary deposits in Eocene were made in a transtensional environment (Siyako & Huvaz, 2007).

The southeast end of the Mt Athos Peninsula (Figure 6.3) displays evidence for sinistral strike-slip shear in a NE-SW direction that initiated in Eocene (Georgiadis et al., 2007): "*the*

prevailing structures in the southern Athos peninsula are an asymmetric, SW-plunging, NW-verging mega-scale antiform and a NE-SW striking left-lateral shear zone. These structures are the result of a transpressional deformation that initiated at least since the Eocene under ductile, syn-metamorphic (low-greenschist facies) conditions and progressively changed during the Oligocene-Early Miocene to brittle conditions with E-W striking reverse faults-thrusts and NNW-SSE striking right-lateral and NE-SW striking left-lateral strike-slip faults".

This line of observations indicates that the CNAT is inherited from a fault belt that likely developed in Eocene to accommodate the clockwise rotation of the Chalkidiki block. It was reactivated, in transpression to the northeast and in transtension from its centre to the southwest, when the tip of the propagating North Anatolian Fault reached the Aegean during the Pliocene.

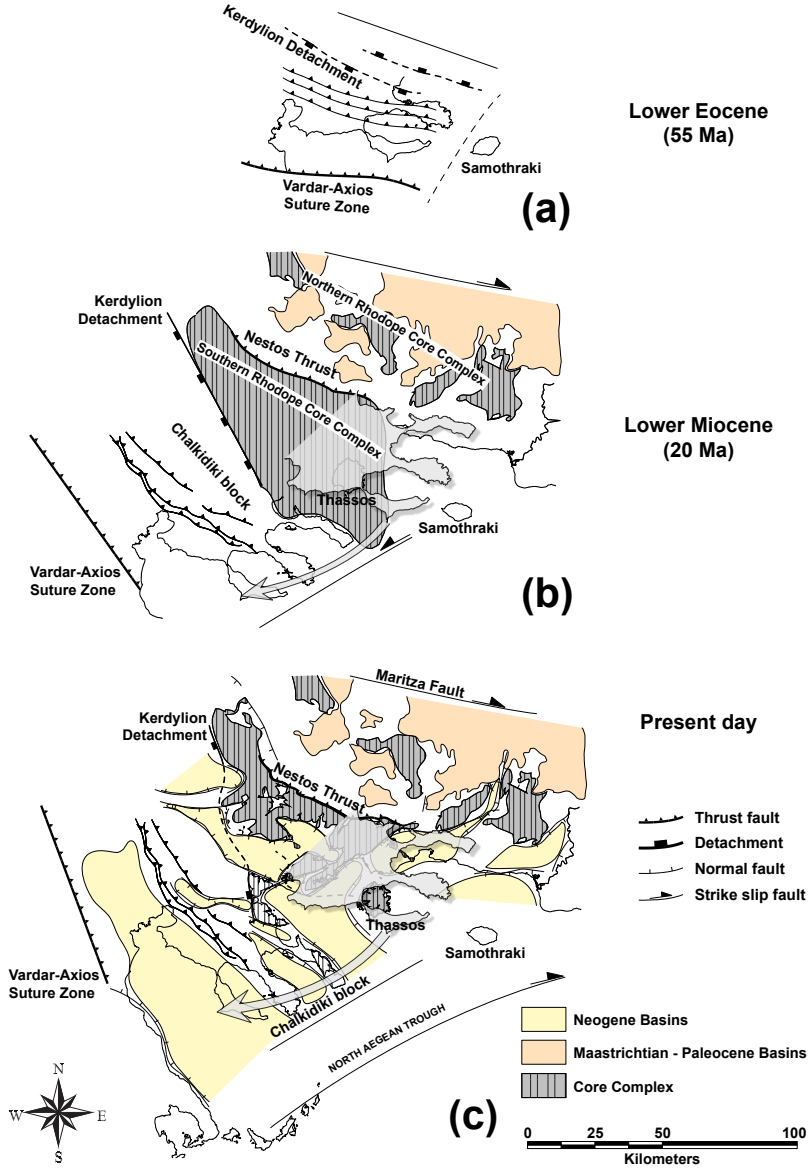

Figure 6.17: Map restoration of the North Aegean Domain. Three key snapshots are shown between lower Eocene and the present-day. Basin fill of Maastrichtian - Paleocene age to the north and post-middle Miocene basins to the south record, overall, a southward swift of the extension. Clockwise rotation of the Chalkidiki block (superimposed in all three subfigures) was accommodated by a sinistral strike-slip fault zone located to the southern limit of the block. This fault zone was overprinted in Pliocene by dextral strike-slip faulting related to the North Anatolian Fault. The latter defines the southern border of the North Aegean Trough.

6.6.2 Paleogene extensional structures

Sedimentary deposits. There are only few remnants of the earliest Tertiary sedimentary deposits in the Chalkidiki block. They mostly consist of middle/upper Eocene transgressive conglomerates, sandstones and nummulite-bearing limestones in the Vardar-Axios - Thermaikos Basin that appear either onshore (Bourcart, 1919; Xydas & Efstratiades, 1983; Maltzaris, 1987) or in drill cores (Christodoulou, 1965; Roussos, 1994; Carras & Georgala, 1998). The sequences were deposited on an eroded Mesozoic substratum in an environment that remained either lacustrine or shallow neritic until lower Oligocene and in places, they were possibly accompanied by pyroclastic sandstones, acid tuffs, rhyolites (e.g., Xydas & Efstratiades, 1983). Similar sequences crop out along the western border of the basement where they are overthrust by biotite gneisses of the basement.

The existence of remnants of middle to late Eocene sediments implies (i) that extension in the Chalkidiki block and surrounding areas started in middle/upper Eocene and (ii) that a significant amount of uplift led to erosion of the previously deposited sequences before being covered by middle/upper Miocene deposits. This is in agreement with the lower Eocene apatite fission-track ages for the basement metamorphic units (Kydonakis et al., 2014a) indicating that they already reached shallow conditions in lower Eocene.

Structures and deformation. As illustrated by the geological map (Figure 6.3) and cross-section (Figure 6.15a) the Kerdylion Detachment, which controlled the exhumation of the Southern Rhodope Core Complex (SRCC) since middle Eocene (Brun & Sokoutis, 2004, 2007), is a major bounding structure of the Chalkidiki block on its eastern side. As already mentioned, the Chalkidiki block is the hanging-wall of the SRCC. All structures related to the SRCC exhumation are located in the southeast part of the Chalkidiki block.

The map of foliation trajectories (Figures 6.6 and 6.15c) shows that an anticline surrounds the Kerdylion detachment whose axis is located at around 10 Km from the detachment trace. This gentle foliation folding is of extensional origin and corresponds to a bending effect in the footwall of a steep normal fault trending parallel to the detachment and that connect with it at depth (Figure 6.15c and in blue in Figure 6.16a). In its southeast termination the anticline is cut by the undeformed Stratoni Pluton dated at circa 30Ma (Gilg & Frei, 1994).

Other structures observable at map-scale are: (i) E-W trending thrust faults in the Singitikos Gulf (in yellow in Figure 6.16a) and (ii) NNW to NW-trending dextral strike-slip faults and NE-trending sinistral strike-slip faults (in green and red, respectively in Figure 6.16a). Note that one of the dextral strike-slip faults is responsible for the eastern sharp and straight boundary of the Triassic Arnea Magmatic Complex (compare Figures 6.3 and 6.16a).

These regional scale structures, when considered all together, indicate a N-S direction of shortening, an E-W direction of stretching and a sinistral sense of shear in the direction of the Central North Aegean Through (NE-SW, see inset in Figure 6.16). Their location in the southeastern part of the Chalkidiki block corresponds to the zone where the Kerdylion Detachment was interacting with the sinistral strike-slip shear during the rotation of the Chakidiki block (see section 5.1 and Figure 6.17). The exact timing of this deformation pattern is difficult to ascertain. However, the available evidence indicates a Paleocene age, from Eocene to lower Miocene (Kilias et al., 1999; Georgiadis et al., 2007) that is directly comparable to the development of the SRCC (Brun & Sokoutis, 2007).

6.6.3 Neogene extensional structures

Sedimentary environment. A period of quiescence between upper Oligocene and middle Miocene was followed by the development of the widespread sedimentary basins and plutonic/volcanic activity, mainly after middle Miocene in the Chalkidiki block and surrounding areas. To the west, the Vardar-Axios - Thermaikos basin (Figure 6.2) trends roughly

NW-SE and is largely made of upper Miocene recent sandstones, marls, limestones and micro-conglomerates with horizons of sandy marls (e.g., Xydas & Efstratiades, 1983). To the northeast, the Strymon basin that also trends NW-SE to E-W started to develop in upper Miocene. It is made of basal fluvio-lacustrine conglomerates and sands followed by shallow marine clastics, carbonates and conglomerates (Gramann & Kockel, 1969; Psilovikos & Syrides, 1983; Syrides, 1998; Snel et al., 2006).

The Mygdonia Graben. At map scale, the most visible structure that results from Neogene extension in the Chakidiki block is the Mygdonia Graben that, together with its sedimentary fill and lakes, cuts through the basement and cover units (Figure 6.16b). It developed during middle Miocene in a fluvio-lacustrine environment (Koufos et al., 1995). Toward the west, the basin trends NW and is bounded to both sides by SW- and NE-dipping faults but it turns E-W toward the east where it is bounded to the south by E-W-trending normal faults - the normal faults to the northern border of the graben are buried by the sedimentary deposits. The exposed sedimentary deposits remains almost flat with no significant deformation implying a period of quiescence after middle Miocene. Its southern border corresponds to the active E-W-trending fault (Mercier et al., 1979; Papazachos et al., 1979; Hatzfeld et al., 1987) known as the Thessaloniki - Rentina Fault Zone (Tranos et al., 2003).

The Mygdonian Graben is a narrow structure whose width is in the range 10-12 Km. Assuming a mean fault dip of 60^o (i.e., upper crust friction of 30^o) such a width indicates that the brittle-ductile transition at the time of graben initiation was at a depth in the range of 8.6-10.4Km (Allemand & Brun, 1991). In the Chalkidiki block crustal-scale section (Figure 6.15b), we draw the Mygdonia Graben using the above geometrical constraints. Such a shallow brittle-ductile transition implies that in middle Miocene the crust was still dominantly ductile and therefore was rather hot with a Moho temperature likely in the order of 800^oC (for more details on the relation between lithosphere rheology and rifting mechanics see Gueydan et al., 2008).

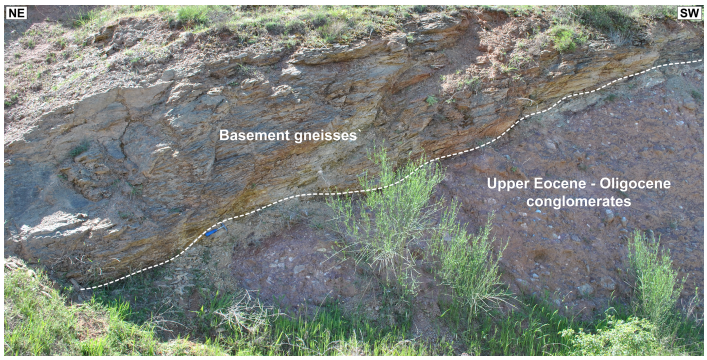

Figure 6.18: Gneisses of the basement thrust on top of upper Eocene - Oligocene deposits along the western part of the basement near Langadas village.

Structures and deformation. The different tectonic features that developed during the same deformation episode are: (i) newly formed normal faults trending around an E-W direction (in blue in Figure 6.16b), (ii) NE-trending dextral strike-slip faults and NW-trending sinistral strike-slip faults (in green and red, respectively, in Figure 6.16b) and (iii) local thrust faults (basement gneisses thrust on Eocene-Oligocene conglomerates from the western part of the basement - Figure 6.18a). These regional scale structures, when considered all together, indicate a N-S direction of stretching, an E-W direction of shortening and a dextral sense of shear in the direction of the Central North Aegean Through (see inset in Figure 6.16).

The northeastern part of the basement is cut by several sinistral strike-slip faults (numbered from 1 to 5 in Figure 6.16b) that in most cases correspond to discontinuities in the foliation trajectory map. The longer one (around 50 Km, Fault 5) runs along the basement-

cover contact along which the metamorphic foliation is often rotated to very steep angles (Figure 6.19). This fault zone is obviously due to a sinistral strike-slip reactivation of the thrust contact between basement gneisses and cover meta-sediments. The other steeply dipping fault zones along which the basement foliation is steepened also correspond to either reactivated pre-existing faults (Figure 6.20) (e.g., fault 3 that likely reactivate a previous thrust fault zone) or localisation along petrological/rheological discontinuities (e.g., faults 1 and 2 along serpentinites or meta-sediments inclusions in gneisses, respectively). Along these fault zones, the sense of strike-slip shear was in general difficult to find at outcrop scale but where it was possible it was sinistral.

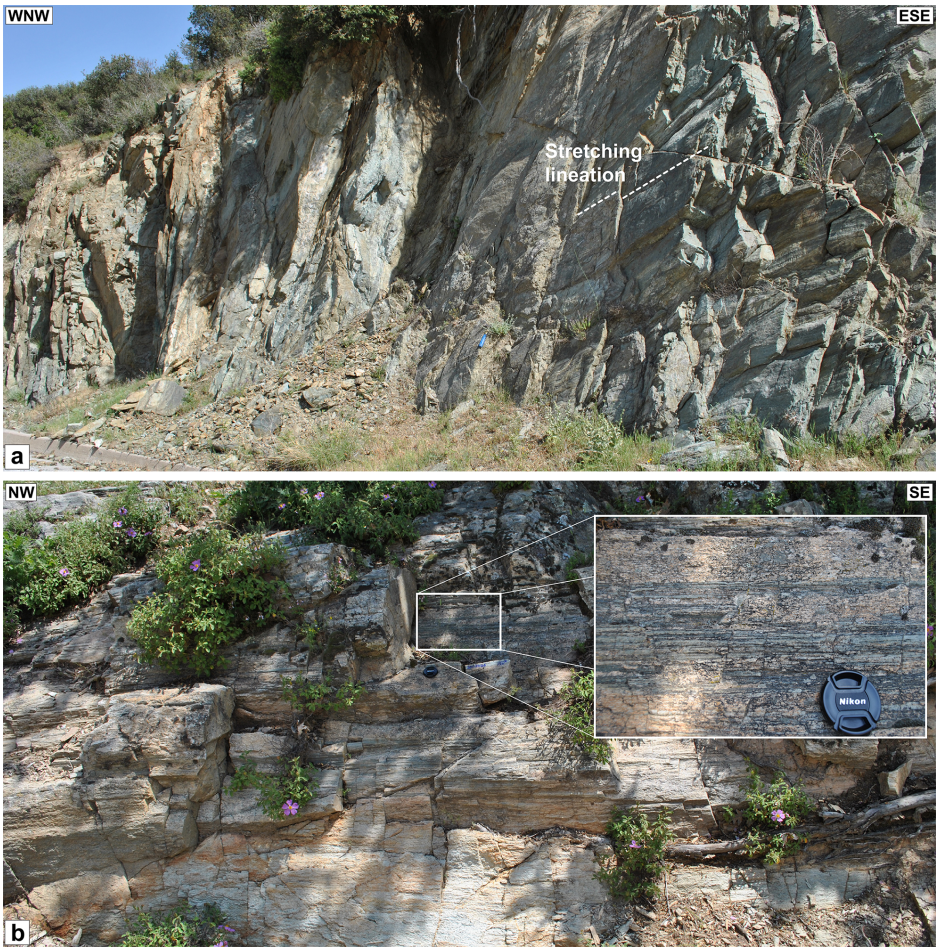

Figure 6.19: Steeply-dipping metamorphic foliation and associated sub-horizontal stretching lineation.

The regional-scale pattern of folding in the Circum-Rhodope belt with fold axes (i) nearly parallel to regional-scale lithological contacts (Figure 6.10) and ii) parallel to the direction of stretching also resulted from an along strike sinitral shear that also involved the neighbouring Chortiatis Magmatic Suite.

One dextral strike-slip fault zone that is located in the middle of the Mygdonia Graben (green in Figure 6.16b) acted as a transfer fault during graben opening. Some normal faults that initiated at an early stage of this deformation episode were rotated clockwise together with the Chalkidiki block (e.g., the Strymon Basin normal faults, in magenta in Figure 6.16b). It is more likely, that the strike-slip fault 5, which is connected to the northern normal fault at the western end of the Mygdonia Graben, has also been rotated clockwise during sinistral shear.

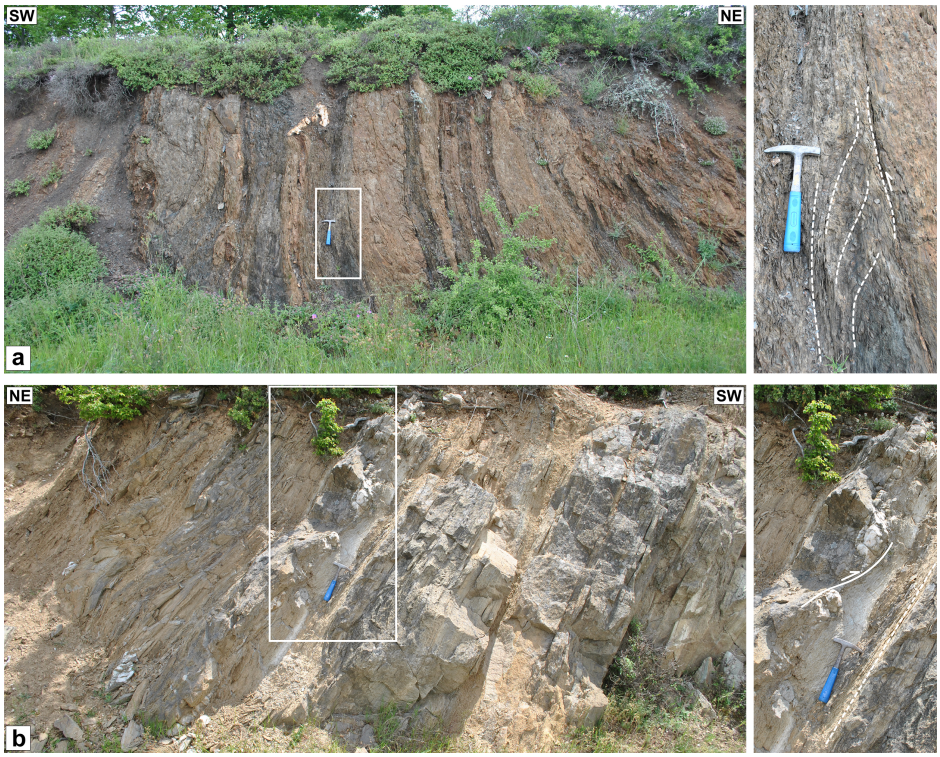

Figure 6.20: Steeply-dipping zones of intense deformation with top-to-SW shear indicators.

6.7 Conclusions

In this study we showed that the Chalkidiki block recorded two distinct series of tectonic events: (i) syn-metamorphic thrusting and extension during the Cretaceous and (ii) moderate brittle deformation during the Tertiary. The most striking features that characterize these two sequences of events can be summarised as follows.

6.7.1 Cretaceous syn-metamorphic thrusting and extension

(1) All syn-metamorphic fabrics result from high *finite strain intensities*, commonly giving amount of stretching higher than 100%. They developed during high-pressure metamorphism followed by a thermal re-equilibration at higher temperature and lower pressure. A review of all available geochronological data demonstrates that all ductile fabrics of the Chalkidiki block have been formed between lowermost and uppermost Cretaceous.

(2) *Foliation* displays three different patterns in the three main units composing the Chalkidiki block: (i) dominantly dipping at low angle in the Palaeozoic basement (Vertiskos Unit), affected by upright folding in the sedimentary cover (Circum Rhodope belt) and systematically steeply dipping to the NE in the arc (Chortiatis Magmatic Suite). In the three units, the dominant foliation strike is NW-SE.

(3) *Stretching lineations* trend dominantly SW-NE in the three main units.

(4) Two opposite *senses of shear*, top to SW and top-to-SE, characterize the basement whereas a single sense of shear top-to-SW is observed in the cover and arc units. Shearing toward the SW is associated to thrusting whereas the NE shearing is more likely extensional and associated to the exhumation of the metamorphic units.

(5) From the *geodynamic* point of view, the above elements that define the deformation pattern at regional scale show that the three units of the Chalkidiki block (i.e., basement - Vertiskos unit, cover - Circum Rhodope Belt, Arc - Chortiatis Magmatic Suite) have undergone a major event of SW thrusting in a high-pressure metamorphic environment that

was followed by a moderate event of shearing toward the NE, likely extensional. Thrusting shear to the SW in a high-pressure metamorphic environment indicates that a continental block (Palaeozoic granitic basement with its Triassic-Jurassic sedimentary cover) has been subducted toward the NE, in the present day geographical reference frame. Top to NE shear in a high temperature metamorphic environment was more likely related to the exhumation of the previously subducted units. The whole subduction-exhumation cycle occurred during the Cretaceous.

6.7.2 Tertiary extension

(1) *During the Paleogene* (upper Eocene-Oligocene), the Chalkidiki block underwent extension along its northeastern (Southern Rhodope Core Complex) and southwestern (Thermaikos Basin) boundaries.

(2) *Structures related to Paleogene extension* are mostly located to the southeast of the Chalkidiki block, close to the Kerdylion Detachment, combine: (i) NS-trending normal faults, (ii) E-W-trending thrust faults and (iii) NW-trending dextral strike-slip faults and NE-trending sinistral strike-slip faults. When considered all together, these structures indicate a N-S direction of shortening, an E-W direction of stretching and a sinistral sense of shear in the direction of the Central North Aegean Through. Their location in the southeastern part of the Chalkidiki block corresponds to the zone where the Kerdylion Detachment was interacting with the sinistral strike-slip shear within the Central North Aegean Through during the clockwise rotation of the Chalkidiki block.

(3) *Since middle Miocene*, contrary to Paleogene extension, the Chalkidiki block undergoes internal deformation.

(4) *Structures related to Neogene extension* combine: (i) newly formed normal faults trending around an E-W direction, (ii) NE-trending dextral strike-slip faults and NW-trending sinistral strike-slip faults and (iii) local thrust faults. These regional scale structures, when considered all together, indicate a N-S direction of stretching, an E-W direction of shortening and a dextral sense of shear in the direction of the Central North Aegean Through.

(5) *The Mygdonia Graben*, the most visible Neogene structure of the Chalkidiki block, started to develop in middle Miocene, in a fluvio-lacustrine environment. Its 10-12 Km width indicates that, at the time of graben initiation, the brittle-ductile transition was in the range of 8.6-10.4 Km depth and therefore that the crust was still dominantly ductile and rather hot.

(6) *Sinistral shear parallel to regional-scale lithological contacts* has affected the northern and western parts of the Chalkidiki block during N-S extension and coeval clockwise rotation of the block. This along-strike shear gave a series of strike-slip fault zones in the basement (Vertiskos) and is responsible for the folding of the bedding-parallel foliation of the cover meta-sediments (Circum Rhodope belt).

Chapter 7

North Aegean core complexes, the gravity spreading of a thrust wedge

7.1 Introduction

Soon after the discovery of metamorphic core complexes and of their significance in terms of crustal-scale extension in the Basin and Range of Western United States (Davis & Coney, 1979; Coney, 1980; Crittenden et al., 1980; Wernicke, 1981, 1985), they have been identified in many other orogenic domains of Alpine age (e.g., Dewey, 1988) or even older (e.g., Proterozoic: Cosca et al., 1995, Caledonian: Norton, 1986; Andersen et al., 1991, Hercynian: van den Driessche & Brun, 1989; Brun & van den Driessche, 1994). The concept of core complex was also adapted to mantle exhumation at mid-oceanic ridges (Karson, 1990; Tucholke & Lin, 1994). Various aspects of their development have been investigated using numerical and physical modelling techniques (e.g., Brun et al., 1994; Tirel et al., 2004a, 2006, 2008; Wijns et al., 2005; Dyksterhuis et al., 2007; Gessner et al., 2007; Rey et al., 2009a,b; Huet et al., 2011a,b; Schenker et al., 2012) and almost three decades after the emergence of the concept considerable progress has been made concerning the mechanisms that control their formation (see comprehensive review by Whitney et al., 2013).

In the Aegean, core complexes developed during back-arc extension in two strikingly different tectonic settings, below and above the Vardar Suture Zone, in the Cyclades and in the Rhodope, respectively (Figure 7.1). The Central Cyclades Core Complex (CCCC), to the south, developed during lower Miocene and display evidence for partial melting within the exhumed domes (Gautier et al., 1993; Gautier & Brun, 1994; Jolivet & Brun, 2010; Jolivet et al., 2010; Philippon et al., 2012) (Figure 7.1). On the other hand, the Rhodopean core complexes to the north developed earlier than the CCCC and correspond i) to an alignment of medium-sized (width of 10-20km in the direction of stretching) gneiss domes in Southern Bulgaria - Northern Greece (see review in Burg, 2012) and ii) to the Southern Rhodope Core Complex (SRCC) (Brun & Sokoutis, 2007) that is a large structure (reaching 120 Km in the direction of stretching in its southeast part) which started to develop during Eocene (Figure 7.1). Evidence for partial melting is also found within the exhumed Rhodopean gneiss domes. Another striking difference between the CCCC and the SRCC is the dip of the detachment responsible for their exhumation that is to the north for the first (North Cycladic Detachment - Jolivet et al., 2010) and to the southwest for the second (Kerdylion Detachment - Brun & Sokoutis, 2007).

While the development of the CCCC is rather well studied and understood, in the frame of the slab rollback-driven extension of the Aegean as summarised above, the origin of the Rhodopean core complexes raises a series of unsolved questions. Why they developed in two zones? Why they are located to the extreme northern part of the domain affected by the Aegean extension and they are separated from the Vardar Suture Zone by a block that

remained undeformed until the Neogene? Why the Kerdylion Detachment that controlled exhumation of lower crust in the SRCC dips to the southwest? Using laboratory experiments presented in this paper, we argue that the gravity spreading of a thrust wedge stimulated by the slab rollback of the Hellenic subduction provides a straightforward answer to all these questions.

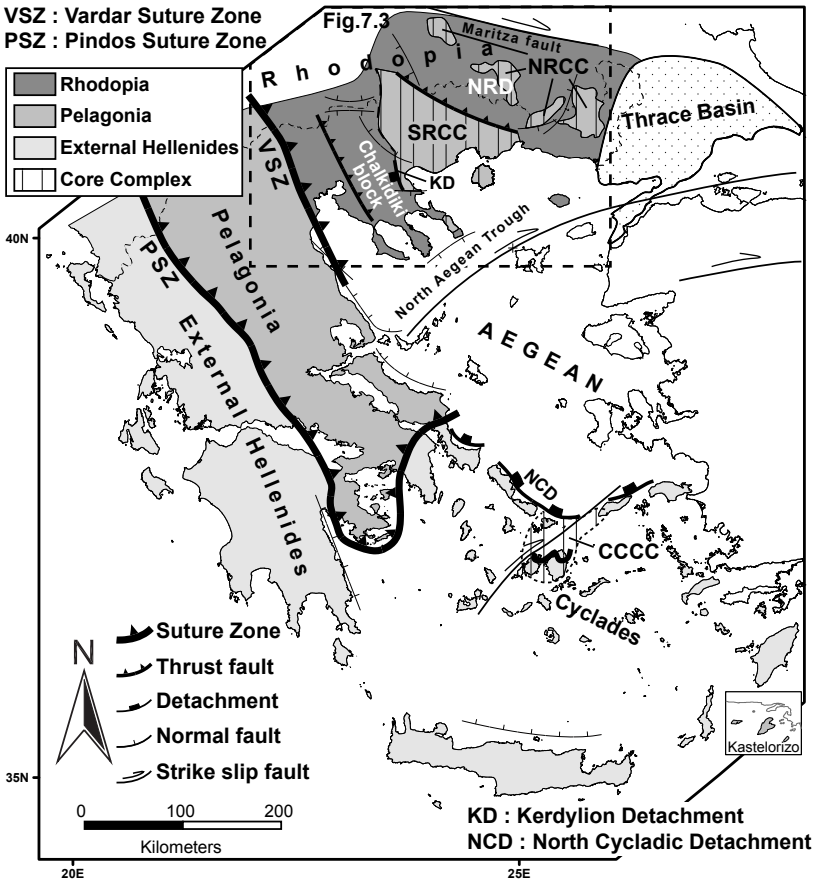

Figure 7.1: Simplified geological map of the Hellenides which are made, from north to south, of three continental blocks (Rhodopia, Pelagonia and External Hellenides) and two intervening sutured oceanic domains (Vardar and Pindos Suture Zones). The Rhodopean and Cycladic Core Complexes are highlighted. NRD: Northern Rhodope Domain, NRCC: Northern Rhodope Core Complex, SRCC: Southern Rhodope Core Complex, CCCC: Central Cyclades Core Complex.

7.2 Tectonic history of the North Aegean in the frame of the Aegean extension

7.2.1 Aegean extension

The Hellenides (Figure 7.1) constitute an integral part of the Alpine-Himalayan mountain chain and are the product of convergence between the stable South European margin and northward-driven Gondwana-derived continental blocks (e.g., Dercourt et al., 1993; Stampfli & Borel, 2002). The Hellenides resulted from the piling-up of three continental blocks (Rhodopia, Pelagonia and External Hellenides) in a south-westerly direction. This also involved the closure of the two intervening oceanic domains represented today by the Vardar-Axios (VSZ) and the Pindos Suture Zones (PSZ) in the north and south, respectively (Robertson, 2002; van Hinsbergen et al., 2005a; Papanikolaou, 2009, 2013) (Figures 7.1, 7.2).

Seismic tomography illustrates beneath the Aegean and down to 1600 Km depth a northward-dipping slab, anchored into the lower mantle (Bijwaard et al., 1998). Aegean

extension that started in middle Eocene was driven by the southward retreat of the Hellenic subduction (McKenzie, 1978; Mercier et al., 1979; Mercier, 1981; Dewey & Sengör, 1979; Le Pichon & Angelier, 1979, 1981; Jolivet & Faccenna, 2000) soon after the suturing of the Pindos oceanic domain (Brun & Sokoutis, 2010; Jolivet & Brun, 2010).

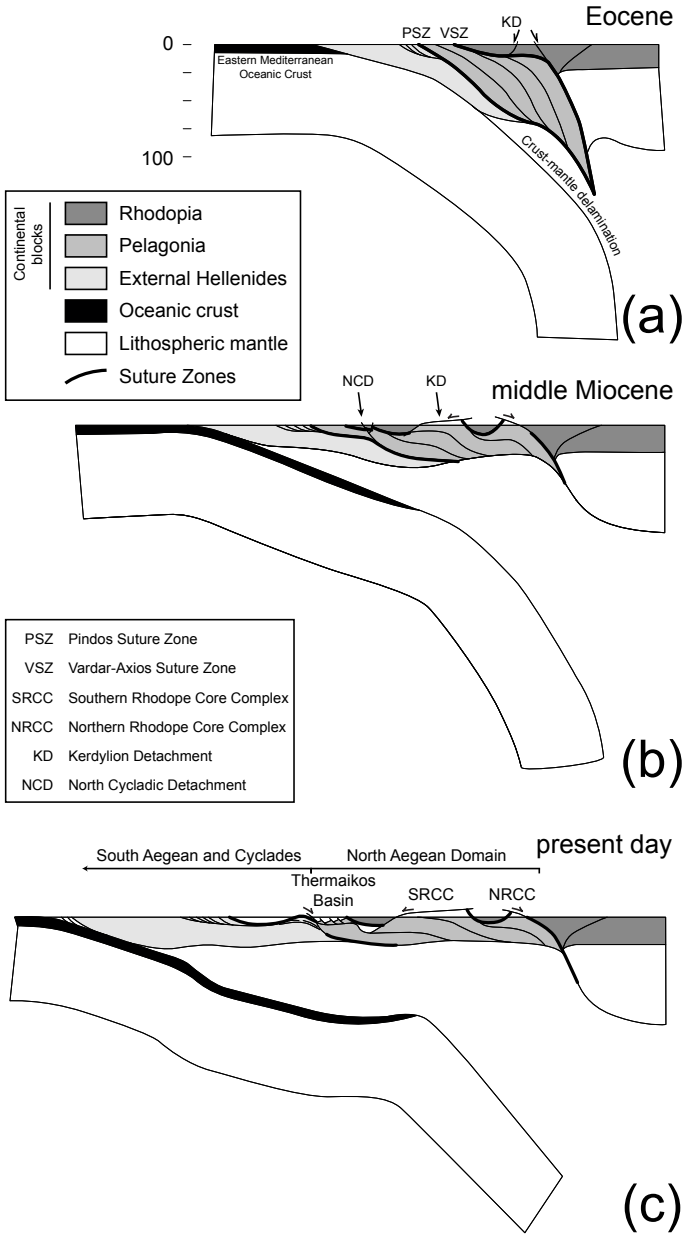

Figure 7.2: Lithospheric cross-section restoration of the Hellenides. The Eocene, middle Miocene and present day structure of the Hellenides is depicted in the corresponding cross-sections. (a) In Eocene the structure of the Hellenides is a crustal-scale wedge, namely the *Hellenic Thrust Wedge* that was formed by the accretion of three continental block and two intervening sutures. The initial geometry of our models is scaled according to this time step. (b) Subduction of the eastern Mediterranean oceanic domain, following crust-mantle delamination, allowed bith southward retreat of the Hellenic trench and upward movement of the accreted blocks simultaneously with the formation of the Rhodopean core complexes to the north. Note that a rather flat moho was established quite early in the collapse history of the Aegean. (c) The Central Cyclades core complex formed later in the sequence. In the present day form, the Hellenides show widespread and relatively shallow basins whereas exhumation of lower crust is restricted to the mentioned core complexes.

In the Aegean, evidence for extension since middle Eocene is due to i) the migration of plutonic activity from the Rhodope to the southern Cyclades, ii) exhumation of high-pressure

metamorphic rocks in the southern Hellenides (Cyclades, Peloponnese and Crete), iii) core complex formation in the Rhodope and the Cyclades. Since middle Miocene, extension resulted in widespread development of continental and marine sedimentary basins (see recent reviews of Jolivet & Faccenna, 2000; Burchfiel et al., 2008; Brun & Sokoutis, 2010; Jolivet & Brun, 2010; Ring et al., 2010; Royden & Papanikolaou, 2011; Jolivet et al., 2013).

During extension, the western part of the extending domain, from Rhodope to Peloponnese, has undergone up to 50^o-60^o clockwise rotation around an axis located in the vicinity of the Scutary-Pec in Albania (Kissel & Laj, 1988; van Hinsbergen et al., 2005b). In this kinematic setting the amount of extension increased i) as a function of the distance from the rotation axis and ii) from north to south (Brun & Sokoutis, 2010). The Aegean Sea that represents the more strongly stretched part of the back-arc domain is the result of a southward trench retreat of around 600-700 Km (Jolivet & Brun, 2010). In the Aegean, the Moho is rather flat over a distance of over 1000 km in north-south direction, and the crustal thickness has a mean value of 25±2 Km except in two structures, namely the North Aegean Through and the Cretan Sea, where the crust is locally thinner than 22 Km (Tirel et al., 2004b).

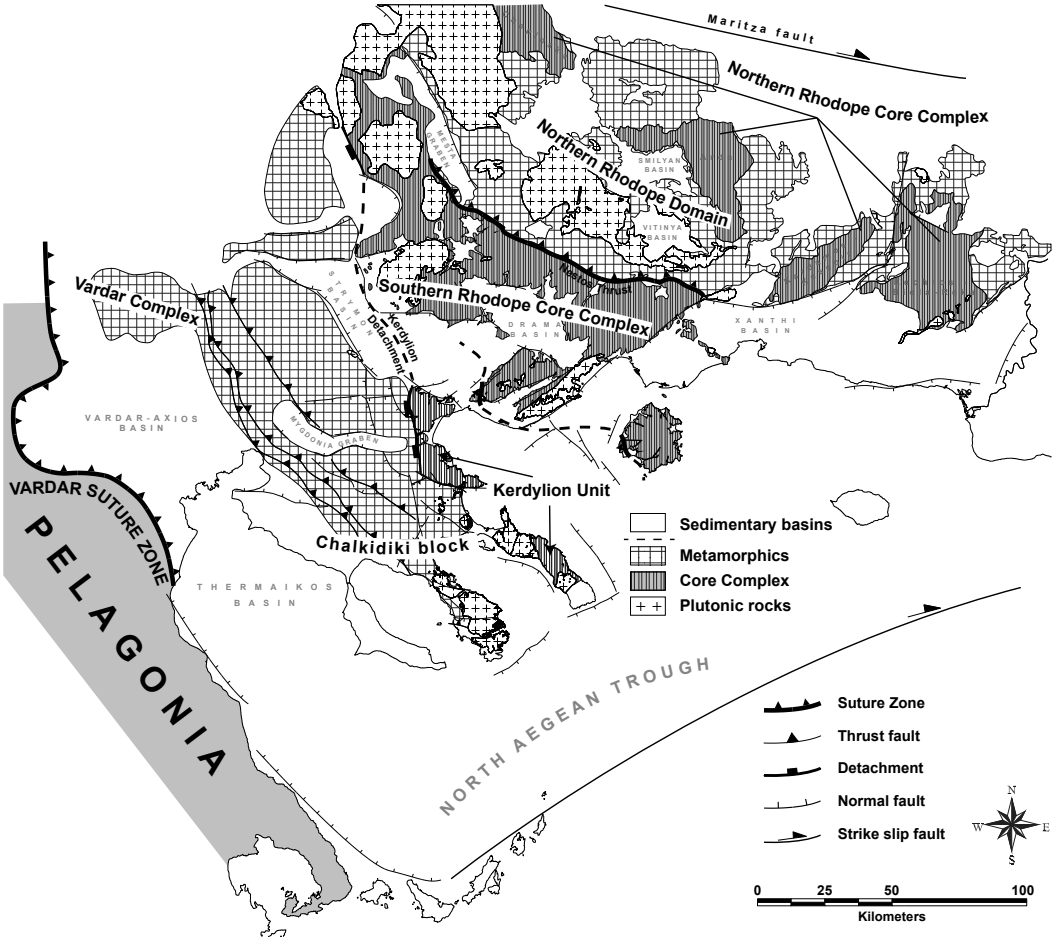

Figure 7.3: Simplified geological map of the North Aegean Domain redrawn mostly after Kockel & Mollat (1977); Brun & Sokoutis (2007) and Burg (2012) with particular interest on the core complexes cropping out in the area. Different tectonic domains can be distinguished, from northeast to southwest: (i) the Northern Rhodope Domain (NRD), (ii) the Southern Rhodope Core Complex (SRCC), (iii) the Chalkidiki block, (iv) the Vardar s.l. units and (v) the Pelagonia. The term Northern Rhodope Core Complex (NRCC) is proposed here to be used collectively for the exhumed gneiss domes (Chepinska, Arda, Kardamos-Kesebir and Kechros-Biela Reka domes) exposed to the northeast within the NRC (see also Fig.7.4) whereas the term Southern Rhodope Core Complex (SRCC) (Brun & Sokoutis, 2007) is adopted for the triangle-shaped gneiss dome exposed at the central part of the map.

7.2.2 Tectonic history of the North Aegean

The domain of North Aegean forms the hinterland of the Hellenic subduction where the early Jurassic - Cretaceous convergence history is recorded (e.g., Burg et al., 1990, 1995, 1996; Ricou et al., 1998). It can be divided, from northeast to southwest, into the Northern Rhodope Domain (NRD), the Southern Rhodope Core Complex (SRCC), the Chalkidiki Block, the Vardar s.l. Units (including the Vardar Complex and the Vardar Suture Zone) and the Pelagonia (Figures 7.1, 7.3). The NRD and the Chalkidiki Block form together the Rhodopia. The domain of North Aegean is bordered to the north by the Maritza dextral strike-slip fault, to the east by the middle Eocene to Quaternary Thrace Basin, to the west by the Vardar-Axios Suture Zone and the Pelagonia, and to the south by the Thermaikos Basin and the North Aegean Through (Figure 7.3).

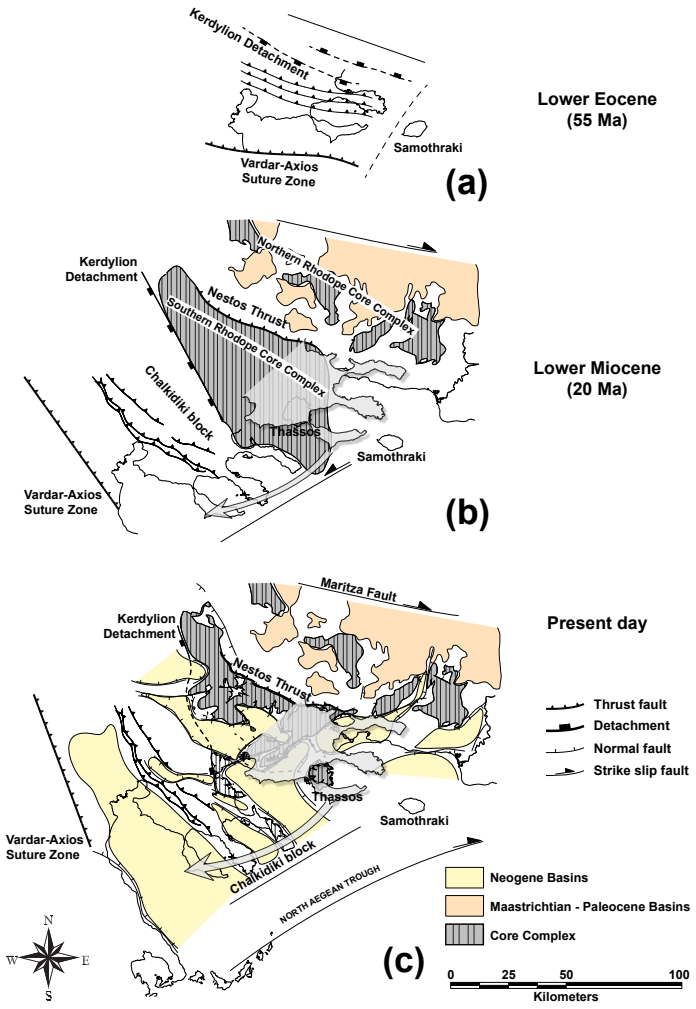

Figure 7.4: Map restoration of the North Aegean Domain. Three key snapshots are shown between lower Eocene and the present-day. Basin fill of Maastrichtian - Paleocene age, to the north, and younger basins developed since middle Miocene, to the southwest, record, overall, a southwestward swift of the extension. For reference, the Chalkidiki block is superimposed in all three subfigures.

From Upper Cretaceous to middle Eocene, the successive closure of the Vardar and Pindos oceanic domains led to the piling-up of Rhodopia, Pelagonia and External Hellenides and the formation of the Hellenic Thrust Wedge (Figure 7.2a). In Eocene the thrust wedge was submitted to extension, likely related to the entrance into the subduction zone of the Eastern Mediterranean Oceanic Lithosphere, leading to the formation of core complexes (Figure 7.2b,

c). In the North Aegean Domain the latter are: i) the aligned extensional metamorphic domes of Chepinska, Arda, Kesebir - Kardamos and Biela-Reka - Kechros to the northeast (Burg, 2012) that will be called hereafter as Northern Rhodope Core Complex (NRCC) for convenience and ii) the Southern Rhodope Core Complex (SRCC) to the southwest (Brun & Sokoutis, 2007). It must be noted here that, whereas the larger SRCC is associated to the well-defined and southwest dipping Kerdylion Detachment, the extensional domes constituting the NRCC are not clearly connected to a detachment (Figure 7.3). As their size is rather small and they are not connected to each other, they likely correspond to core complexes aborted at an early stage of development, prior to detachment localisation (see numerical models of Tirel et al., 2004a, 2008).

The development of the SRCC separated Rhodopia in two main blocks: the NRD, to the northeast, and Chalkidiki Block, to the southwest (Figure 7.3). In other words, the Southern Rhodope Core Complex is a tectonic window inside Rhodopia that exposes Pelagonia at the surface. During the exhumation of the SRCC, the Chalkidiki block, as part of the hanging-wall of the Kerdylion Detachment, underwent a circa 30^o clockwise rotation (Kondopoulou & Westphal, 1986). A southwestward migration of the extension from Paleogene to Neogene can be inferred from the deposition age of sediments and/or volcanic activity centres that becomes younger toward the southwest.

The tectonic history of the northern onshore part of the Aegean is summarized in map view in three selected time frames shown in Figure 7.4: i) In lower Eocene (Figure 7.4a) the Northern Rhodope Domain and the Chalkidiki Block are still attached forming Rhodopia, The two core complexes (NRCC and SRCC) initiated in Eocene, ii) In lower Miocene, whereas the NRCC is already sealed by Paleogene sediments and volcanics , the SRCC is still exhuming (Figure 7.4b), iii) From middle Miocene to present day (Figure 7.4c) extensional Neogene basins developed over the southern part of North Aegean hiding a large part of the SRCC and sealing the Kerdylion detachment.

7.3 Modelling the rotational gravity spreading of a brittle-ductile thrust wedge

7.3.1 Experimental strategy

The conception of the modelling work that we present here is based on the present-day geological setting of the onshore part of the North Aegean and on our understanding of its tectonic history (previous section), including the physical processes involved. Our modelling strategy is based around the gravitational collapse of a brittle-ductile wedge whose frontal boundary is submitted to a rotational extensional displacement and can be decomposed as follows.

Initial wedge geometry. Extension is applied to a thrust wedge whose geometry is deduced from restoration of extensional displacements at the scale of the Aegean (Figure 7.2a) (Brun et al., 2012). On this basis we have chosen a mean initial wedge angle of 20^o.

Topography. To take into account the topography of a crustal thickness of around 70 Km at thrust wedge rear that linearly decreases frontward, we inclined the wedge surface frontward of an angle of 3^o at the onset of extension.

Rheology. Due to high temperature metamorphism, intense magmatic activity and widespread evidence of migmatisation in the Rhodope core complexes (Brun and Sokoutis, 2007, Burg, 2012), we designed the thrust wedge at onset of extension as dominantly ductile.

The thickness of the frictional layer that represents the upper brittle crust should depend on the thermal state of the crust, warmer at the rear than at the front. To take this effect into account the upper frictional layer was built thicker at the front.

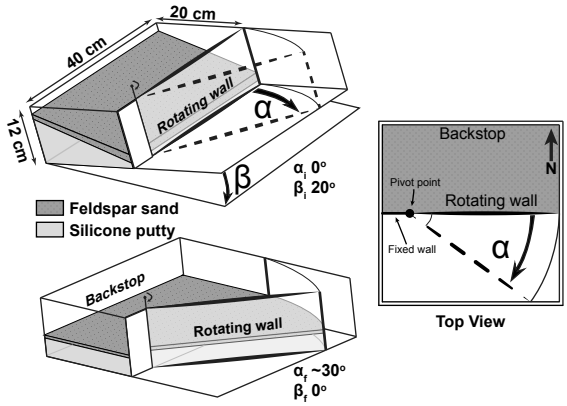

Figure 7.5: The experiments were performed in a Plexiglas box filled with wedge-shaped feldspar sand and silicone putty simulating the behaviour of the brittle and ductile layers of the crust, respectively. The initial geometry of the system is a replicate of the *Hellenic Thrust Wedge* (see Fig.7.2). A rotating wall allowed the model to be spread under its own weight. Both the basal slope of the wedge (crust-mantle boundary in nature) and the displacement of the rotating wall were controlled by stepping motors. Extension applied to the system at a constant displacement velocity. Subscripts "i" and "f" denotes initial and final values.

Displacements applied at model boundaries. As mentioned in the introduction, Aegean extension is driven by the rollback of the Hellenic subduction. During trench retreat, the thrust wedge spreads under its own weight (i.e., gravity spreading). Restoration of displacements at the scale of the Aegean indicates that during the first 30 m.y. of extension, from middle Eocene to middle Miocene, the mean velocity of trench retreat is rather constant and in the order of 0.7 cm/m.y. Consequently, in our models we used a constant velocity for the displacement of the frontal boundary. Its value was calibrated as a function of the free spreading rate of the wedge at the end of the calibration run.

On the other hand, as the extensional history of the Aegean occurred during clockwise rotation (see previous section), the displacement at the wedge front in our models was accommodated by a mobile wall. A bulk angle of rotation of 30^o (angle α in Figure 7.5) was chosen in agreement with the observed value in the SRCC (Kondopoulou & Westphal, 1986; Brun & Sokoutis, 2007).

Variation of wedge angle during extension. To control the initial wedge angle, the model was constructed on top of a rigid plate initially inclined at β_i=20^o (Figure 7.5). To calibrate the decrease of wedge angle during extension, the basal plate was rotated downward at a constant rate to reach the horizontal (β_f=0^o) at the time when the chosen bulk amount of extension is attained.

7.3.2 Scaling

The models were scaled following the principles of geometric, dynamic, kinematic and rheological similarity (Hubbert, 1937; Ramberg, 1981). The experimental method developed at Geosciences Rennes to study the deformation of brittle-ductile tectonic systems uses sand and silicone putty to represent brittle and ductile layers, respectively. The basic principle of the method ground on simulating simplified strength profiles that incorporate both brittle (frictional) and ductile (viscous) rheologies with gravity forces. Scaling relationships between the prototype and the model are obtained by keeping the average strength of the ductile layers correctly scaled with respect to the strength of the brittle layers and the gravity forces. Material properties and scaling parameters age given in Table 7.1.

In analogue experiments under normal gravity, it can be shown from the equation of dynamics that (Brun, 1999):

$$\sigma^* = \rho^* g L^* \quad (1),$$

where σ, ρ, g and L are the stress, density, gravitational acceleration and length. Asterisk denotes model to nature ratio (e.g., σ^*=σ_m/σ_n). With model materials and natural rocks density being of the same order of magnitude the equation reduces to:

Table 7.1: Material properties and scalling parameters of MAK27. The right column is the model/nature ratio. R_m and R_s are the dimensionless Ramberg and Smoluchowski numbers, respectively.

Parameter		Model	Nature	Ratio
Density Brittle Crust	ρ_b (Kgr m^{-3})	1300	2500	0.52
Density Ductile Crust	ρ_d (Kgr $^{-3}$)	1499	2750	0.55
Gravitational Acceleration	g (m/s^2)	9.81	9.81	1
Thickness Brittle Crust	hb (m)	1×10^{-2}	15×10^{3}	6.7×10^{-7}
Thickness Ductile Crust	hd (m)	9.3×10^{-2}	55×10^{3}	1.7×10^{-6}
Cohesive Strength	τ_c (Pa)	15	6×10^{7}	2.5×10^{-7}
Viscosity	η (Pa s)	3×10^{4}	1×10^{20}	3×10^{-16}
Velocity	(m s^{-1})	4.44×10^{-6}	1.1×10^{-9}	4×10^{3}
R_m		955	742	1.3
R_s		8.5	6.1	1.4

$$\sigma^* \approx L^* \quad (2),$$

This means that the stress ratio is roughly equal to the length ratio (i.e., thickness ratio). In our models, where 70 Km in nature (thickness at wedge rear) approximately corresponds to 10 cm in the model, the length ratio, and thus the stress ratio, both equal to circa 1.4 x 10^{-6}.

The rheological-dynamic scaling of the models can be tested using non-dimensional numbers given by ratios between forces acting on the models (Ramberg, 1981; Sokoutis et al., 2005). For the brittle deformation, we consider the ratio between gravitational stress and cohesive strength:

$$R_s = \frac{gravitational\ stress}{cohesive\ strength} = \frac{\rho_b g h_b}{\tau_c} \quad (3),$$

where ρ_b, h_b and τ_c are the density, thickness of the brittle layer and cohesive strength, respectively (Table 7.1). For the viscous deformation we consider the ratio between gravitational and viscous stresses:

$$R_m = \frac{gravitational\ stress}{viscous\ stress} = \frac{\rho_d g h_d}{\eta \dot{\epsilon}} = \frac{\rho_d g h_d^2}{\eta V} \quad (4),$$

where, ρ_d, h_d, η, $\dot{\epsilon}$, V stand for the density of the ductile layer, thickness of the ductile layer, viscosity, strain rate and mean velocity of extension, respectively (Table 7.1). For dynamic similarity to be fulfilled, models should share similar R_s and R_m numbers to nature. In this work, scaling of model to nature is exemplified in Table 7.1 by comparing model MAK27 with mean values of different properties of both upper and lower crust in nature.

7.3.3 Materials and strength profiles

Dry feldspar sand was used in our models to simulate the upper brittle crust whose behaviour is of Mohr-Coulomb-type and follows the formulation $\tau = 50 + 0.6\sigma$, where τ and σ are the shear and normal stresses, respectively (Byerlee, 1978).

For frictional cohesiveness materials the maximum (σ_1) and minimum (σ_3) principal stresses follow the Mohr-Coulomb relation:

$$\sigma_3 = \frac{1-\sin\phi}{1+\sin\phi}\sigma_1 \quad (5),$$

where ϕ is the angle of internal friction. In extension where the vertical stress (σ_v) is $\sigma_v = \sigma_1 = \rho g z$, the differential stress (for $\phi = 30^o$) is given by:

$$\sigma_1 - \sigma_3 = \frac{2}{3}\rho g z \quad (6),$$

The above formulation is used to calculate the strength profiles for the sand layers of the model (Figure 7.6).

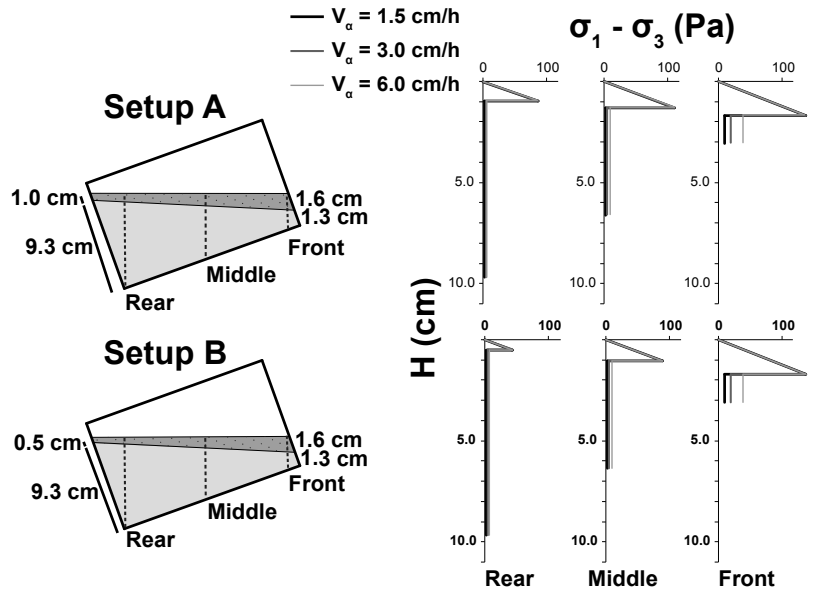

Figure 7.6: Model's side-view and calculated strengths profiles along a central transect for the two different initial geometries (reflecting thickness variation in the frictional layer) used in the experiments. Due to variation of the sand layer thickness and displacement velocity, different strength profiles are calculated for the frontal (near the rotating wall), the middle and the rear part (near the backstop) of the model.

The ductile behaviour of the lower crust is re-produced using a Newtonian silicone putty with viscosity equal to 3×10^4 Pa·s measured at room temperature. The strength of the silicone layers can be calculated using the formula:

$$\sigma_1 - \sigma_3 = 2\eta\gamma \quad (7),$$

where γ is the shear strain rate. The latter can be calculated as the ratio between the displacement velocity of the mobile wall of the model (V) and the thickness of the ductile layer (h): γ = V/h. However, this absolute value is valid only for the initiation of the each experiment and it is anticipated to be reduced during the evolution of model deformation. As a result, for increased displacement velocity and decreased silicone putty thickness the strength of the silicone layer exhibits that of the overlying sand layer, a case unlikely to happen in nature.

Due to the wedge-shaped initial geometry of our models (see next paragraph) three strength profiles (front, middle, rear) have been calculated along the central transect of the model (Figure 7.6).

7.3.4 Experimental setup

According to the modelling strategy defined in section 3.1, we setup the experiments as follows (Figure 7.5). Wedge-shaped sand/silicone models were constructed in a Plexiglas box (40 x 40 x 12 cm) whose walls were lubricated with liquid soap to avoid boundary effects. Models were bounded by a fixed wall at the back and a frontal rotating wall. During model building, the Plexiglas box was inclined ($\beta_i = 20^o$) and the rotating wall was set "closed" ($\alpha_i = 0^o$). The base of the silicone layer corresponds to the Moho in nature. At the onset of each experiment, the model is inclined frontward by 3^o to simulate a foreland-dipping surface slope.

During the experiments, the displacement of the rotating wall allowed the wedge to spread under its own weight at a constant rotation velocity (V_α) of the mobile wall that was controlled by a stepping motor. The maximum aperture α of the rotating wall, attained at the end of each experiment, was circa 30^o. As extension increased with increasing angle α, the basal slope β was decreased at a constant velocity V_β by another stepping motor. To fit the Aegean situation (Figure 7.2), V_α was locked against V_β such as $\alpha_f = 30^o$ when $\beta_f = 0^o$ (Figure 7.5).

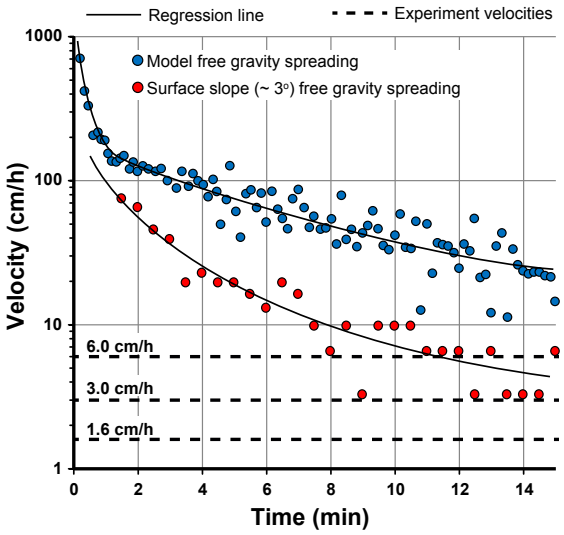

Figure 7.7: Variation of the spreading velocity (logarithmic scale) with time under normal gravity calibration experiments. The free gravity spreading experiments were conducted in the experimental apparatus shown in Fig.7.5 after the removal of the rotating wall so that the system was allowed to flow freely under the effect of gravity. The initial geometry and build of the model is described in the text. Blue and red dots represent the model front propagation velocity measured from surface photographs taken at regular time intervals. For the blue dots, the model was built as described in the text and immediately its basal slope (angle β) turned from 20^o to zero allowing the model to spread under the effect of gravity. The red dots illustrate the velocity-time curve that correspond to the smoothing of the initially imposed $\sim 3^o$ surface slope. During this calibration experiment the basal slope (angle β) remained at 20^o. For comparison, the three velocities used in the experiments are shown in dashed lines.

Whereas the silicone wedge was kept the same in all experiments, two different wedge-shaped feldspar sand layers have been tested (Figure 7.6). The sand thickness was 1.6 cm against the mobile wall whereas it was either 1.0 or 0.5 cm against the backstop in Setup A and B, respectively (Figure 7.6). The effect of the rotating wall velocity (V_α) (locked against the basal slope change - V_β) was examined.

Two free-gravity spreading models have been used to calibrate the velocity values V_α and V_β: one with a 3^o surface slope and one with 20^o initial wedge angle (Figure 7.7). Velocity values of 1.6, 3.0 and 6.0 cm/h used in the experiments and were chosen to be close to the asymptotic abscissa-parallel values of the calculated velocity-time curves of the free gravity spreading models (Figure 7.7).

In order to study displacements and structure development at model surface, top-view photographs were taken at regular time intervals. For one model, we calculated a set of incremental velocity field and the corresponding surface strain rate, from pairs of top-view photographs using PIVlab updated to v.1.35 (Thielicke & Stamhuis, 2014). The various geometric and kinematic parameters used in the series of experiments are summarised in Table 7.2.

7.3.5 Model limitations

The geometry and rheological layering of the models are necessarily simplified compared to nature. However, a simplified setting allows the first-order parameters that control the deformation pattern to be easily highlighted and understood.

Another known limitation of sand-silicone models is due to their incapacity to simulate rheological changes due to temperature variations during deformation. However, representing the lower crust by a uniform layer with depth-invariant properties has been successfully adopted in many analogue modelling experiments and is acceptable in our case study as a

Table 7.2: Geometric and kinematic parameters of the models presented in this paper. V_α is the mobile wall displacement velocity and V_β is the wedge basal slope change velocity. Both velocities are given in cm/h and deg/h.

Model	Sand thickness (cm) (front - backstop)	Silicon thickness (cm) (front - backstop)	V_α (cm/h) or [deg/h]	V_β (cm/h) or [deg/h]	Duration (h)
Setup A					
MAK27	1.6 - 1	1.3 - 9.3	(1.5) [2.5]	(2.8) [1.5]	$\sim$ 13
MAK25	1.6 - 1	1.3 - 9.3	(3) [5]	(5.6) [3]	$\sim$ 6
MAK26	1.6 - 1	1.3 - 9.3	(6) [10]	(11.2) [6]	$\sim$ 3
Setup B					
MAK29	1.6 - 0.5	1.3 - 9.3	(1.5) [2.5]	(2.8) [1.5]	$\sim$ 13
MAK28	1.6 - 0.5	1.3 - 9.3	(3) [5]	(5.6) [3]	$\sim$ 6
MAK30	1.6 - 0.5	1.3 - 9.3	(6) [10]	(11.2) [6]	$\sim$ 3

first order approximation.

7.4 Experimental results

The series of experiments presented here, first aimed at testing whether an initial wedge-shaped crust geometry with a simple two-layer brittle-ductile structure is a sufficient condition to explain the first-order deformation pattern of the North Aegean Domain, with respect to lower crust exhumation and without the addition any complexity such as weak layers or other inherited discontinuities in the system, as commonly done in analogue and numerical models. To match this target, we studied the effects of two parameters on the resulting pattern: i) the displacement velocity imposed by a rotating frontal wall and ii) variations of the brittle crust thickness. Setup A represented a "colder" crust with thicker sand layer and Setup B represented a slightly "hotter" crust with reduced thickness of the sand layer (Figure 7.6). The two tested setups should be considered as small adjustments of an otherwise hot and thick crust and do not at all correspond to a "hot" and "cold" crust at the first place.

Selected top-view snapshots of the experiments at, almost, regular time intervals are shown in Figures 7.8, 7.9. For convenience, the description of structures observed in top-view photographs are oriented with reference to a virtual North that is taken upward and parallel to the lateral walls of the model (see Figure 7.5).

7.4.1 Models with a thick brittle layer (setup A, Figure 7.8)

Three models (MAK25, MAK26 and MAK27) in which the sand layer thickness is 1.0 cm against the backstop were run with displacement velocity of 1.5, 3.0 and 6.0 cm/h at the extremity of the rotating wall (Figure 7.8). *At a stretching velocity of 6.0 cm/h* and 25% of the bulk stretching applied to the model, a domain of faulting is located dominantly in the northeast corner of the model and along the backstop. The main fault that is almost parallel to the rotating wall curves toward the axis of rotation to the west and toward the slipping lateral boundary to the east. This main fault defines a block that rotates with the mobile wall and remains almost undeformed all along the experiment. With increasing deformation, from 25 to 100% of the bulk stretching, the northeast corner of the model is affected by conjugate and narrow spaced faults. In other words, this model is characterized by a distributed extension. At 75% of bulk stretching, a zone of silicone putty is exposed (i.e., exhumed) at the surface along the main fault that defines the undeformed rotating block.

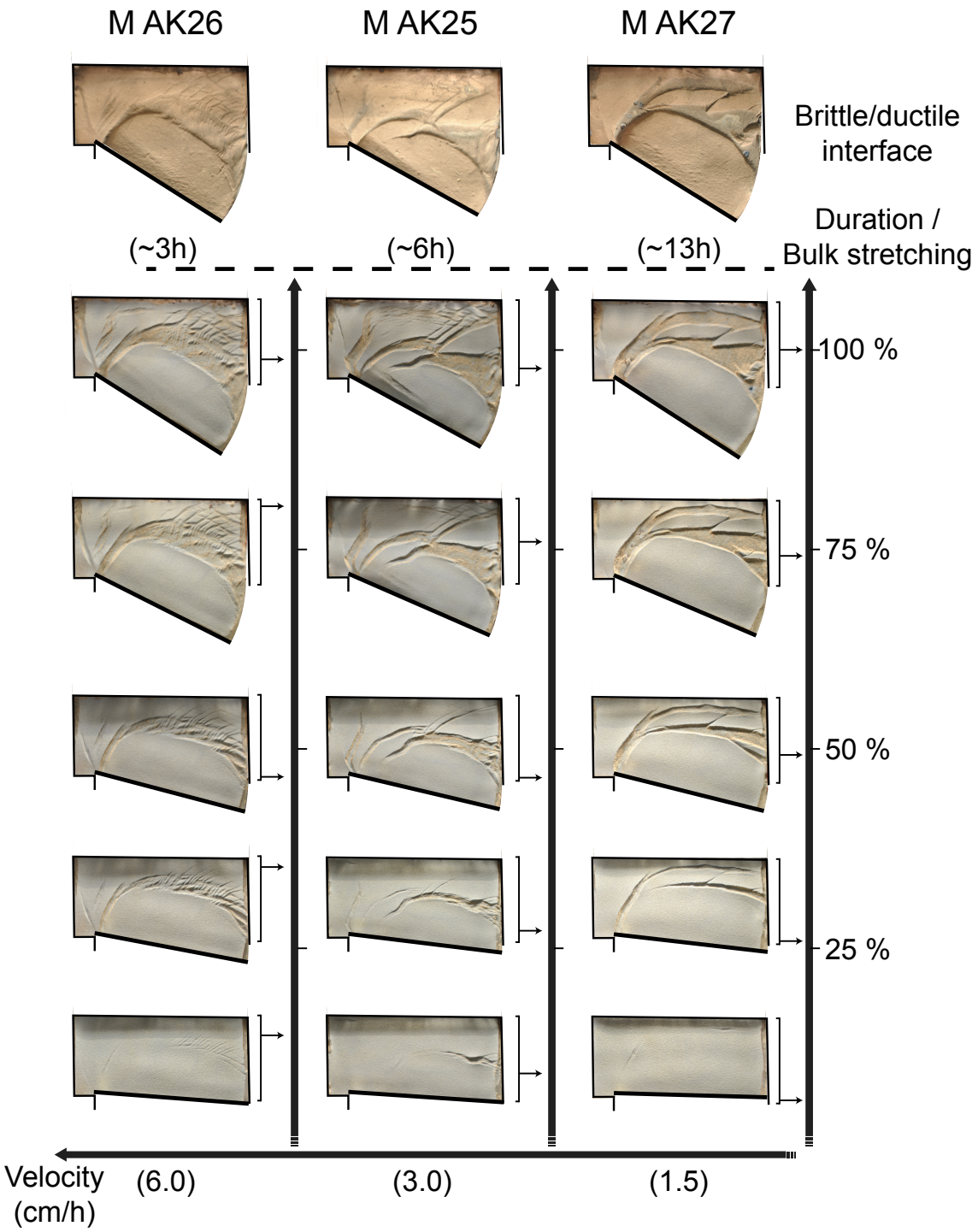

Figure 7.8: Selected top-view snapshots for Setup A experiments (thicker sand layer; see Fig.7.6) using three tested displacement velocities. The brittle/ductile interface at the end of each experiment is also shown. To facilitate the discussion, a virtual north is taken as facing upward. See text for details.

At a stretching velocity of 1.5 cm/h the model's behaviour is strikingly different. At 25% of bulk stretching, the main faults are still propagating. At 50% of bulk stretching they have both reached the rotation axis and have circumscribed a rotating block directly comparable to that of the model described above. Deformation is localised again to the northeast corner of the model. However, it is now localised into two faults parallel to each other at initiation. With ongoing stretching the blocks defined by these faults separate each other progressively allowing the silicone putty to be exhumed in between. During block separation, the borders

of the northern zone of the exhumed silicone putty remained almost parallel to each other. On the contrary, the borders of the southern zone progressively formed a triangular zone of exhumation.

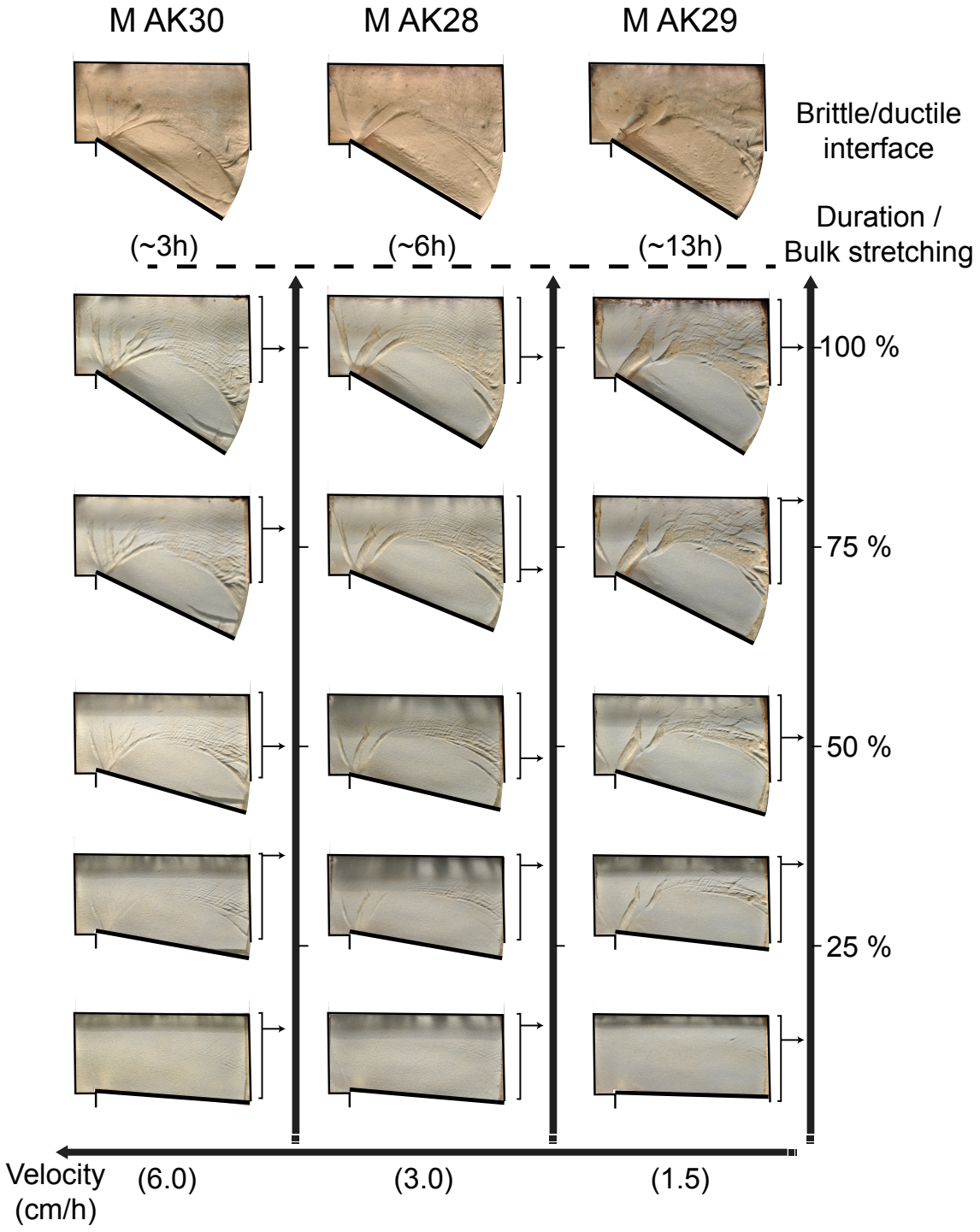

Figure 7.9: Selected top-view snapshots for Setup B experiments (thinner sand layer; see Fig.7.6) using three tested displacement velocities. The brittle/ductile interface at the end of each experiment is also shown. To facilitate the discussion, a virtual north is taken as facing upward. See text for details.

At a stretching velocity of 3.0 cm/h the model behaviour is intermediate, combining a zone of distributed faulting in the northeast corner of the model and along the backstop and a triangular zone of exhumation against the rotating block.

7.4.2 Models with a thin brittle layer (setup B, Figure 7.9)

Three models (MAK28, MAK29 and MAK30) in which the sand layer thickness is 0.5 cm against the backstop were run, like in the previously described models with displacement velocity of 1.5, 3.0 and 6.0 cm/h (Figure 7.9).

These three models display a distributed deformation in the northeast corner of the model and along the backstop. With increasing stretching velocity from 1.5 to 6.0 cm/h fault spacing decreases. It must be noted that the fault pattern of the model run at 1.5 cm/h is close to the one obtained in the previous series at a velocity of 6.0 cm/h (Figure 7.8). In both models, with progressive stretching a zone of silicone putty exhumation occurred along the northern border of the rotating block.

7.5 Interpretation of the experimental data

7.5.1 Core complex vs wide rift mode of extension

Our experiments display either localised or distributed extension that in nature would be correspond to core complex and wide rift modes of extension (see Buck, 1991; Brun, 1999), respectively (Figure 7.10).

The exhumation of the silicone putty starting at the onset of deformation, which is an equivalent of core complexes in nature, was obtained in two models (MAK27 and MAK25, Figure 7.8). One of these two models (MAK27) displays two core complexes whereas the other one (MAK25) corresponds to a mixed mode with one core complex and one wide rift zone to the north of it. The series of models (Figure 7.10) exemplifies that the core complex mode is favoured by thick sand layer (i.e., high frictional strength) and/or low stretching rates (i.e., low ductile strength).

A wide rift mode of extension is obtained in all other models (MAK26, MAK28, MAK29 and MAK30, Figures 7.8, 7.9). In two of these wide rift mode models (MAK26 - Figure 7.8, MAK29 - Figure 7.9) the silicone exhumed against the rotating block after a large amount of strain (50 to 75% of bulk stretching). This exhumation pattern that is a function of strain intensity does not correspond to an initial instability of the brittle-ductile system and therefore is not representative of the core complex mode.

7.5.2 Progressive development of core complexes

Progressive deformation in the model that displays two zones of core complexes (MAK27) is illustrated in Figure 7.8. Shortly after the onset of extension (∼10% of the bulk stretching), deformation localised in a rear graben near the backstop. It was followed soon after (∼15% of bulk stretching) by a frontal graben that formed midway between the rotating wall and the backstop. Both grabens were bordered by a conjugate set of normal faults and both opened at approximately the same rate until almost 25% of bulk stretching. Then, stretching concentrated in the frontal graben that became a zone of silicone exhumation forming, therefore, a core complex. Around 50% of bulk stretching, the frontal core complex had already exhumed silicone over a width twice as large as that of the rear graben. Silicone started to exhume in the rear graben soon after. During the second half of the experiment, the frontal core complex quadrupled its width while the rear core complex only doubled it. Between the two core complexes, a narrow strip of undeformed material remained intact throughout the experiment. A large area, covering half the experiment's surface between the frontal core complex and the rotating wall, remained un-deformed until the end of the experiment.

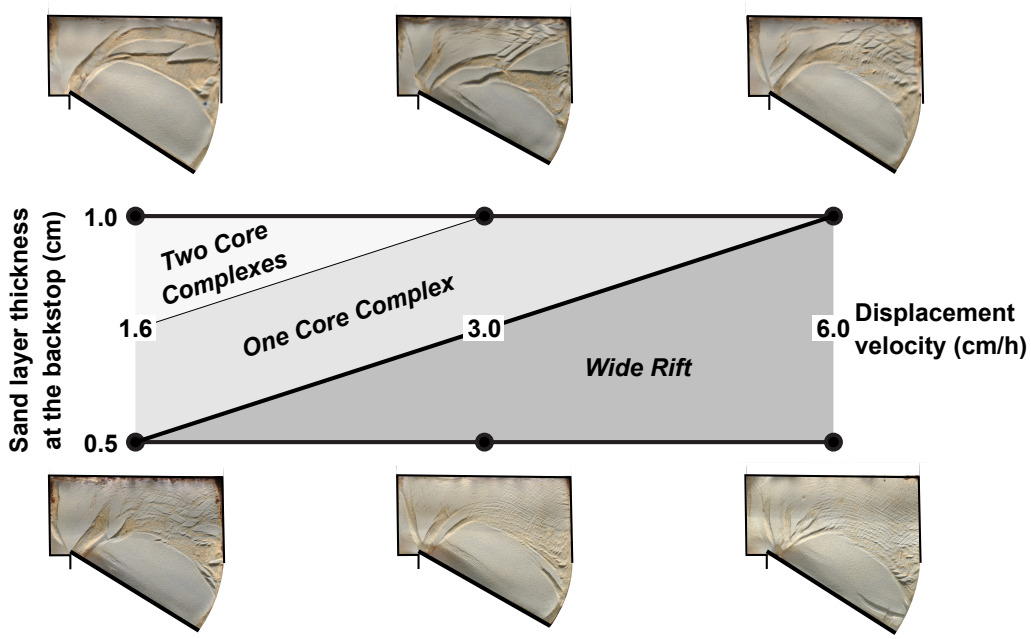

Figure 7.10: Compilation of the finite surface deformation pattern of the six experiments presented in this contribution (Figs.7.8, 7.9) with respect to the resulting mode of extension. Core complex mode of extension is favoured by high frictional strength (i.e., increased brittle crust thickness) and/or low ductile strength (i.e., low viscosity and low strain rate). The case where two different zones of core complex were formed (upper left corner) correspond to the geological setting of the North Aegean Domain discussed in the text (see also Fig.7.11).

The velocity and surface strain rate fields of the same model MAK27 (Figure 7.8) was calculated using couples of successive top-view photographs and is shown in Figure 7.11. Three selected snapshots have been chosen to illustrate the progressive development of the core complexes. At 10% of bulk stretching, deformation occurred mostly in the rear core complex (Figure 7.11a). At approximately 20% of bulk stretching, the activity of this rear localised stretching strongly decreased as the frontal core complex zone initiated. Then up to 60% of bulk stretching the strain localised in the frontal core complex with the maximum strain rate values located against the undeformed rotating block (Figure 7.11b). In nature this high strain rate zone would correspond to the extensional detachment zone that controls core complex exhumation. It is noteworthy that between 30 and 60% of bulk stretching the detachment zone remained located against the undeformed rotating block. After 60% and up to 100% of bulk stretching, strain tend to localise in the largely widening part of the core complex, to the east close to the curved lateral boundary and along strike-slip shear zones that cut through the block that separate the two core complexes (Figure 7.11c).

7.5.3 Location of stretching at the wedge rear

All models have in common: i) the isolation by faulting of a block against the rotating wall that remained undeformed during the whole experiment and ii) the deformation that localised in the northeast corner and along the backstop either appearing with a localised or a distributed pattern (Figures 7.8, 7.9).

With increasing extension, the wedge angle β decreases progressively down to horizontal at the end of experiment. At wedge back the bulk vertical shortening is $\lambda_v = t_f$ / t_b, where t_b is the initial thickness at wedge back and t_f the constant model thickness at the end of experiment. Assuming plane strain in the direction perpendicular to the backstop λ_h $\lambda_v = 1$, where λ_h is the bulk horizontal stretching. Therefore, the bulk horizontal stretching is $\lambda_h = t_b$ / t_f, which for $t_f = 2.9$ cm and $t_b = 9.3$ cm (See Figure 7.6) gives $\lambda_h = 3.2$. This

shows that stretching at wedge rear is higher than 200%. Stretching at the front, against the mobile wall is essentially zero because the frontal part of the model corresponds to the rotating and non-deforming block. As a result, stretching is strongly concentrated in the back part of the wedge. In other terms, the localisation of stretching at model's rear is a direct consequence of the initial wedge shape of the deforming system.

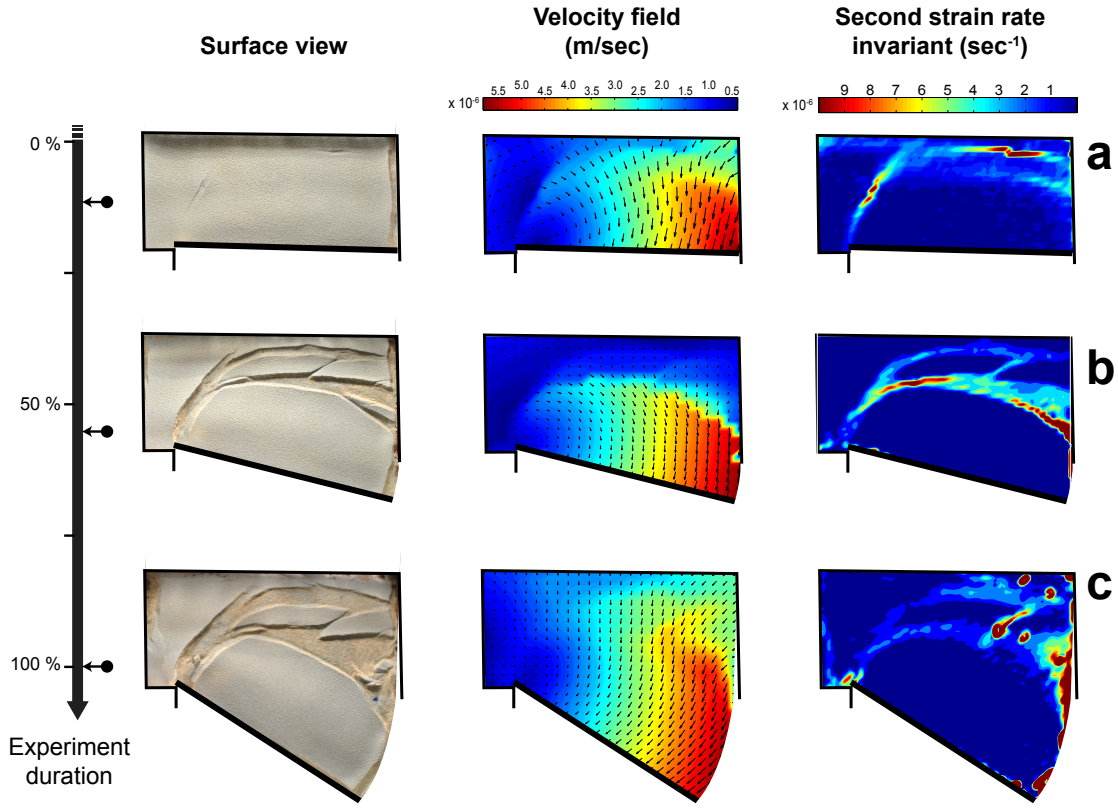

Figure 7.11: Selected top-view snapshots and calculated velocity field and second strain rate invariant of experiment MAK27 approximately at the beginning, midway and at the end of the experiment. The PIV calculations were made using PIVlab v.1.35 software (http://pivlab.blogspot.gr/). The curve-shaped arrow pattern of the velocity field is typical for rotational-driven deformation with the displacement magnitude reducing toward the pivot point. Early in the experiment, the strain is localised in a narrow graben that evolved into the rear core complex near the backstop (see text for an elegant explanation). Soon afterward, the strain localised in another frontal graben, also evolved into a triangle-shaped core complex that accommodated much of the deformation of the system. As shown by the strain rate intensity plot to the right, exhumation of the silicone putty is controlled by a structure (detachment in nature) that is located against and dips toward the non-extending thin frontal part of the wedge.

7.6 Discussion

The set of laboratory experiments presented in this paper have two types of outcomes: first, on a general ground, those concerning core complex development as a result of extension of a thrust wedge and second, those related to application to natural extensional systems and in particular to back-arc extension in the North Aegean Domain.

7.6.1 Core-complex development in a thrust wedge undergoing gravity spreading

7.6.1.1 Stretching located at the wedge rear

Previous models of core complex extension, either analogue (e.g., Brun et al., 1994; Tirel et al., 2006) or numerical (e.g., Tirel et al., 2004a, 2008; Wijns et al., 2005; Rey et al., 2009a,b), considered a brittle-ductile crust with an initial constant thickness. Such an initial geometry requires some type of rheological weakness to be introduced in the model to boost strain localisation during early stages of extension. Such a weakness could either be: i) a pre-existing fault in the upper brittle crust (e.g., Koyi & Skelton, 2001; Gessner et al., 2007; Rey et al., 2009a,b) or ii) a local heterogeneity below the brittle-ductile transition (weaker than the surrounding ductile layer) (e.g., Brun et al., 1994; Tirel et al., 2004a, 2008). However, few models involving strain-dependent fault weakening (e.g., Regenauer-Lieb et al., 2006; Tirel et al., 2009) have been able to stimulate core complex development without the presence of inherited weaknesses.

As demonstrated in our models, contrary to what has been discussed at length for core complex development in a constant thickness brittle-ductile crust, no inherited weak zone (brittle or ductile) or particular mechanism of rheological weakening is required to stimulate the strain localisation and core complex formation in an extending wedge-shaped system. In such common thrust wedges submitted to extension, the only necessary condition for core complex development is the presence of a thick and low-strength (i.e., weak) ductile crust.

During gravity spreading of thrust wedges the horizontal stretching directly depends on the initial layer thickness and thus, stretching intensity increases toward the rear of the extending system where thickness is increased. In other words, *localisation of core complex extension at wedge rear is intrinsically related to the wedge shape of the extending system.*

7.6.1.2 Location and dip of the detachment

As illustrated in our models, the extending domain located at wedge rear is separated from the mobile boundary by a non-extending and only translating block that corresponds to the thin frontal part of the wedge. During core complex exhumation, strain remains localised against this undeforming block (Figure 7.11). This high strain zone corresponds to the detachment of the core complex. In other words, *in an extending brittle-ductile wedge the detachment that controls core complex exhumation is located against and dips toward the non-extending thin frontal part of the wedge.*

7.6.2 Core-complex development in the North Aegean

7.6.2.1 North Aegean Core Complexes

As summarised in section 7.2, the *Hellenic Thrust Wedge* is the result of successive closure of the Vardar and Pindos oceanic domains and the piling-up of Rhodopia, Pelagonia and External Hellenides that assembled by Eocene (Figures 7.1, 7.2a). In Eocene the thrust wedge was submitted to extension, controlled by the onset of the Hellenic slab rollback (Figures 7.2a, 7.2b). This led to the formation of partly migmatised core complexes to the North Aegean that are: i) the aligned extensional metamorphic domes (Chepinska, Arda, Kardamos - Kesebir and Kechros - Biela-Reka) to the northeast (see Burg, 2012) and ii) the larger Southern Rhodope Core Complex (SRCC) to the southwest (Brun & Sokoutis, 2007) (Figure 7.3). The first domes (called here for convenience as the "Northern Rhodope Core Complex" - NRCC) developed within the Northern Rhodope Domain whereas the latter separated Rhodopia into two main blocks: the Northern Rhodope Domain and the Chalkidiki block to the northeast and southwest, respectively (Figures 7.1, 7.3).

The exhumation of the SRCC was controlled by the Kerdylion Detachment whose hanging-wall (the Chalkidiki block) remained almost undeformed for circa 30 m.y. (from middle Eocene to middle Miocene) until formation of the Mygdonia basin (Koufos et al., 1995). During exhumation of the SRCC the Chalkidiki block underwent a circa 30^o clockwise rotation facilitating its exhumation (Kondopoulou & Westphal, 1986). Based on the deposition age of sediments and/or volcanic activity centres that developed on the metamorphics a southwestward migration of the extension from Paleogene to Neogene can be inferred (Figure 7.4).

7.6.2.2 Comparison with models

The wedge geometry of our models was designed on the basis of our reconstruction of the Hellenic Thrust Wedge (Figure 7.2a). To take into account the kinematics of extension in the North Aegean (30^o clockwise rotation of the Chalkidiki Block) the mobile boundary that allowed the model to spread under its own weight was pulled in rotation around a vertical axis (compare Figure 7.4 to Figure 7.5) Model rheology took into account the widespread evidence of partial melting within the NRCC and SRCC indicating that the thrust wedge at the onset of extension was likely dominantly ductile. As information on the initial brittle crust is very poor, we tested different geometries for the upper brittle crust. As the strength of a viscous material depends not only on its viscosity but also on the strain rate, we tested a range of extension velocities. The latter were applied at the mobile boundary (Figure 7.5) and were calibrated against the free spreading of the brittle-ductile wedge model (Figure 7.7). In our experiments, the system stretched approximately 20 cm (140 Km in nature) for a period that corresponds to nature to roughly 30 m.y. This equals to a spreading rate of ∼0.5 cm/yr., compatible with the estimated value from field observations for the same time span ("*significantly less than 1.0 cm/yr.*" according to Brun & Sokoutis, 2010).

This experimental strategy provided a series of models that displayed two main types of extensional patterns: Wide rift versus core complex (Figure 7.10). Whatever the applied extension rate, *in all our experiments the deformation concentrated to the rearmost half of the box leaving an un-deformed block adjacent to the rotating wall.*

The model MAK27 fairly reproduces the main extensional geological features of the North Aegean Domain from middle Eocene to middle Miocene (i.e., from 45 to 15 Ma) (Figure 7.12), prior to the distributed extension that controlled the deposition of Neogene sedimentary basins over the whole Aegean domain (Figure 7.4c). The model displays i) two core complex zones (rear and frontal) located to the north of the extending domain that directly compare with the Northern (NRCC) and Southern (SRCC) Rhodope Core Complexes and ii) an undeformed rotated block that directly compare to the Chalkidiki Block (Figure 7.12). In addition, the mapping of strain rate at model's surface shows that the detachment that controlled the frontal core complex is located against the undeformed rotated block (Figure 7.11b) that directly compare with the Kerdylion Detachment (Figure 7.12). *The fairly good similarities between our model and the North Aegean Domain in terms of timing, location, shape and size of the core complexes is striking, in spite of the gross simplifications of the model.* This validates the restored Eocene geometry of the Hellenic Thrust Wedge (used to design the initial geometry of our models, Figure 7.2). The model demonstrates that *it is the initial wedge geometry of the system and the hot and thick nature of the crust (dominantly ductile) at the onset of extension that controlled the first-order deformation pattern of the North Aegean Domain and especially the development of core complexes.*

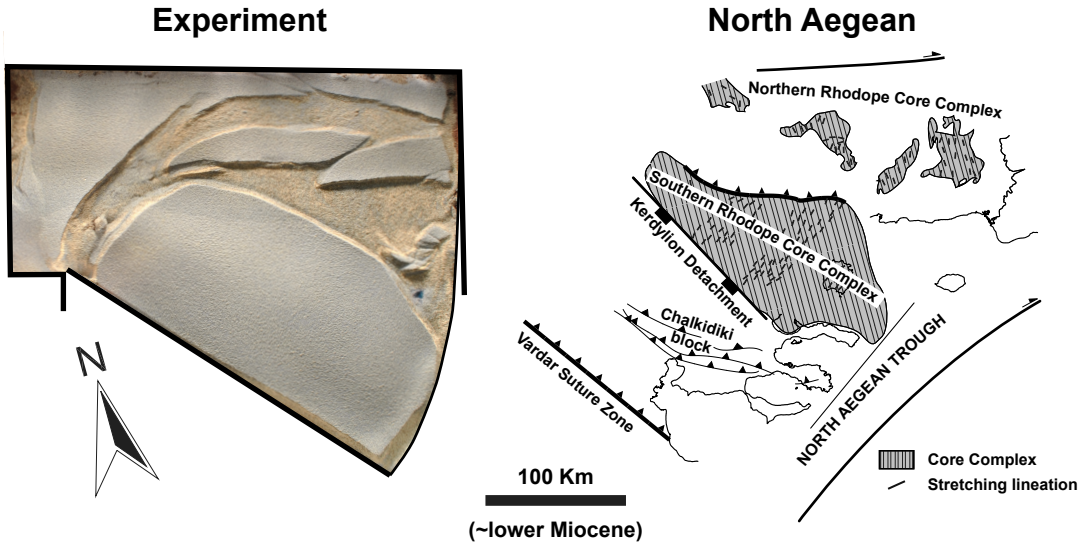

Figure 7.12: On-scale comparison between the surface finite deformation pattern of the experiment MAK27 and the restored geometry of the North Aegean at lower Miocene with respect to the core complex formation. Mark the striking similarities between nature and model in terms of location, size, and shape of lower crust (i.e., silicone putty) exhumation. Mark also the existence of a virtually undeformed block near the rotating wall that corresponds directly to the Chalkidiki block in nature.

Whereas data on the pre-Neogene tectonic story of the North Aegean Through are lacking, the good fit between our model and the North Aegean geology (Figure 7.12) also suggests that this structure that is the most prominent of the North Aegean Sea is inherited from the early Cenozoic tectonic history and that more likely it represents a major transfer zone that accommodated the rotation of the Chalkidiki Block and the exhumation of the Rhodopean Core Complexes. It is noteworthy that the North Aegean Through falls in line with the limit between the Rhodope Core Complexes in which deep hot crust exhumed in Eocene and the Thrace Basin that was a marine sedimentary basin in the same period (Figure 7.1). This strong contrast of extension style on the two sides of the North Aegean Through suggests that the crust was not strongly thickened to the Eastern side allowing sea water to invade the extending domain.

7.7 Conclusions

The set of laboratory experiments presented here aimed at testing gravity spreading of a trust wedge as a suitable process for the development of core complexes with particular application to North Aegean extension, during early evolution of the Hellenic rollback. Beyond their specific application to the North Aegean, our experiments have general outcomes that potentially apply to all tectonic settings when a thrust wedge undergoes extension. They are especially appropriate to the analysis of back-arc extension driven by slab rollback (e.g., Royden, 1993; Brun & Faccenna, 2008; Tirel et al., 2013) as well as to eduction in which a previously subducted continental lithosphere is subsequently exhumed by subduction inversion (e.g., Andersen et al., 1991; Mishin et al., 2008; Duretz et al., 2012).

7.7.1 Extension of a thrust wedge undergoing gravity spreading

On a general ground, our main results can be summarised as follows.

1) Extension, either being distributed (wide rift) or localised (core complex), is located at wedge rear because in gravity spreading the horizontal stretching depends directly on the thickness of the material that is subject to spreading. Thus, the wedge rear being thicker than the frontal part undergoes stronger stretching.

2) The core complex detachment is located against and dips toward the non-extending thin frontal part of the wedge.

3) Core complex location as well as detachment location and dip are interdependent and intrinsically related to the initial wedge shape of the extending system.

4) The experiments presented here show that the development of core complexes is favoured i) by high frictional strength (i.e., increased brittle crust thickness) and/or ii) by low ductile strength (i.e., low viscosity and low strain rate). Therefore, a partially molten crust (very low viscosity) that is slowly stretched is an ideal candidate to undergo core complex mode of extension. We note that this conclusion applies to all core complexes and not only to those developed in a spreading wedge. As already stated in previous studies (e.g., Tirel et al., 2008; Whitney et al., 2013), core complex development is favoured by thick and weak ductile crust.

7.7.2 Extension of the North Aegean Domain

Similarities between structures that developed in our model and those of the North Aegean Domain are striking, in spite of the simplifications inherent to modelling (Figure 7.12). In both cases:

1) *Location*: Two core complexes initiated in the back part of the wedge and are separated from the wedge front by an undeformed block.

2) *Sequence of development*: Extension started close to the wedge backstop (rear core complex / Northern Rhodope Core Complex) and rapidly migrated southward (frontal core complex / Southern Rhodope Core Complex).

3) *Size*: The rear core complex and the Northern Rhodope Core Complex remained smaller (they were likely aborted) whereas the frontal core complex and Southern Rhodope Core Complex constantly enlarged since their initial formation.

4) *Detachment*: Exhumation both in the frontal core complex and the Southern Rhodope Core Complex was controlled by a detachment located against and dipping toward the frontal undeformed block that is direct equivalent to the Chalkidiki Block in nature.

5) *Shape*: The rear core complex and the Northern Rhodope Core Complex remained almost parallel to the backstop whereas the frontal core complex and the Southern Rhodope Core Complex acquired a triangular shape as the detachment's hanging-wall block rotated clockwise during stretching. The model strengthens that it is the initial wedge geometry of the system and the hot and thick nature of the crust at the onset of extension that controlled the extensional pattern of the North Aegean Domain and, in particular, the development of core complexes at the rear of the thrust wedge since the early stages of slab rollback.

Chapter 8

Summary of the results

In ***Chapter 2*** we re-defined the age of the magmatic protolith of the Chalkidiki basement (Vertiskos Unit) as Ordovician; it was considered as Silurian before. This finding provides a linkage to the eastern part of the Rhodope where similar, in age, orthogneisses have been recently reported. The Chalkidiki basement contains embedded widespread pegmatite dykes and amphibolites of unknown age. We proposed here a Carboniferous crystallisation age for the pegmatites based on U/Pb zircon dating. We have also provided a lower Carboniferous metamorphic age for a typical deformed amphibolite. This collectively implies that the Chalkidiki basement record, apart from the main Ordovician magmatic event, the existence of a lower Carboniferous metamorphic event that preceded a strong thermal pulse of magmatic origin of upper Carboniferous age. Based on detrital zircon ages we showed that the base of the Circum-Rhodope belt that has been traditionally considered as the Mesozoic sedimentary cover of the Chalkidiki basement, contains indeed Ordovician zircons pointing toward direct sourcing from the basement. We have also concluded that the intercalated paragneisses within the basement belong to former sedimentary sequences of different deposition age (Palaeozoic vs Mesozoic) despite the fact that they all have very similar appearance in the field. The age of the volcanics along the eastern part of the basement, which was considered as Plio-quaternary before, is now well established as lower Miocene based on our new zircon dating results.

In ***Chapter 3*** we defined the P-T metamorphic conditions of a typical garnet-staurolite micaschist that is part of the Mesozoic sequences of the area exposed to the eastern part of the Chalkidiki block. The sample belongs to a series that was considered before as showing exclusively a Barrovian medium-pressure/high-temperature metamorphic imprint. Based on micro-textures, we documented a relict eclogite-facies mineral assemblage (garnet + chloritoid + phengite + rutile) in an amphibolite-facies matrix composed of garnet + staurolite + phengite ± kyanite. Using isochemical phase diagram sections in the system NCKFMASHMnTi and mineral chemistry we inferred early eclogite-facies conditions at 1.8-2.0GPa / 520oC and subsequent re-equilibration at 1.0-1.3GPa / 600-640oC. This finding supports the idea that the regional amphibolite-facies conditions overprinted a largely erased eclogite-facies event of arguably Mesozoic age. Based on our results we inferred a gradient of the metamorphic conditions in the Chalkidiki that increase from blueschist-facies, to the west, to eclogite-facies toward the east. The gradient can be further extended to include the high-grade Rhodopean gneisses to the northeast. We envisaged here that both the Chalkidiki block and the high-grade Rhodopean gneisses, exposed further to the northeast, participated into the same Mesozoic convergence as part of a northward down-going plate prior to their exhumation and incorporation into the upper plate. Both parts experienced similar metamorphic conditions - yet of varying intensity - that include an early eclogite-facies metamorphic event and subsequently retrogressed at medium-pressure high-temperature conditions.

In ***Chapter 4*** we reported new $^{40}Ar/^{39}Ar$ and U-Th-Pb data on micas and monazites,

respectively. We have shown that primary Permian - Carboniferous monazite grains from garnet-kyanite micaschists show evidence for complete reset of their isotopic system coeval with REE-mobilisation reaction and formation of a corona made of apatite, allanite and epidote - a reaction that is typically described for amphibolite-facies rocks. Based on LA-ICP-MS monazite dating, we defined the timing of re-crystallisation at 132 Ma and thus, we inferred the timing of the amphibolite-facies regional overprint of the eastern part of the Chalkidiki block. The inferred age of the amphibolite-facies overprint is demonstrably slightly younger than that of the corresponding event as recorded in the northeastern part of the Rhodope. Based on $^{40}Ar/^{39}Ar$ cooling white mica ages, we inferred the thermal evolution of the Chalkidiki block after peak-metamorphic conditions. In particular, we proposed that the western Chalkidiki block cooled through the white mica closure temperature at 125 Ma whereas the eastern part cooled around 95 Ma. The younger cooling ages toward the east correlates with the higher metamorphic degree toward the same direction as discussed in Chapter 3.

In ***Chapter 5*** we presented new low-temperature thermochronology data (apatite fission-track analysis) from the Chalkidiki basement. The central ages obtained for basement rocks ranged from uppermost Cretaceous to middle Eocene (46.6 ± 3.6 to 68.5 ± 3.8 Ma) with mean track lengths between 13 and 13.5μ. The obtained ages are in contrast to those of the remaining parts of the Rhodope further to the (north)east where apatite fission track ages range roughly from 10 to 40 Ma. The thermal history of the Chalkidiki basement was defined using a Bayesian transdimensional inverse scheme. We inferred cooling through the apatite partial-annealing zone in uppermost Cretaceous and near-surface exposure by lower/middle Eocene. This implies that the Chalkidiki basement was close to the surface before any of the remaining parts of the Rhodope and thus, our new data set the Chalkidiki basement as the oldest exhumed coherent basement complex of the Rhodope.

In ***Chapter 6*** we presented a series of structural data collected during several field campaigns using regional-scale foliation, stretching lineation and sense of shear maps. We interpreted the geological structure of the Chalkidiki block in terms of a high strain intensity SW-directed thrusting responsible for superposition of a basement slice on top of a basement-cover complex, both being on top of arc and ophiolite units. We also provided a kinematic interpretation for the top-to-NE shearing that is recorded to the basement allochthon as shearing occurring during exhumation of the complex. The inherited Cretaceous fabrics were moderately re-worked and offset along faults formed during the Tertiary Aegean extension. Based on our mapping, we provided a kinematic fault pattern related to the middle Eocene extension. The final assembly of the Chalkidiki block is due to late faulting of post-middle Miocene age for which we also presented a related kinematic model.

In ***Chapter 7*** we performed a series of scaled laboratory experiments to test whether the gravity spreading of an orogenic thrust wedge is a suitable process for the development of the North Aegean core complexes during early back-arc extension driven by the rollback of the Hellenic subduction. Wedge-shaped models were built in a tank with sand to represent the brittle crust and silicone putty to represent the ductile crust. Extension was applied at constant rate at wedge front. The models exemplify that extension can be either distributed (i.e., wide rift mode) or localised (i.e., core complex mode) but always located at the wedge rear. Core complexes developed in models with the thicker brittle layer (higher frictional strength) and lower stretching rates (lower ductile strength). The experimental model displays striking similarities with the extensional pattern of the North Aegean in terms of location, size and shape of core complexes as well as their sequence of development. The model strengthens that it is the initial wedge geometry of the system and the hot and thick (i.e., weak) nature of the crust at the onset of extension that controlled the extensional pattern of the North Aegean Domain and, in particular, the development of core complexes at the hinterland of the Hellenides since the earlier stages of slab rollback.

Overall, in this dissertation we incorporated the Chalkidiki block into the Mesozoic evolution scheme of the Rhodope comparing the inferred P-T metamorphic conditions and timing of the metamorphic events with that of other constituents of the Rhodope.

Bibliography

Agard, P., Monié, P., Jolivet, L., & Goffé, B., 2002. Exhumation of the Schistes lustrés complex: in situ laser probe $^{40}Ar/^{39}Ar$ constraints and implications for the Western Alps, *Journal of Metamorphic Geology*, **20**(6), 599 – 618.

Albee, A. L., 1965. A petrogenetic grid for the Fe-Mg silicates of pelitic schists, *American Journal of Sciences*, **263**(6), 512 – 536.

Albee, A. L., 1972. Metamorphism of Pelitic Schists: Reaction Relations of Chloritoid and Staurolite, *Geological Society of America Bulletin*, **83**(11), 3249 – 3268.

Allemand, P. & Brun, J.-P., 1991. Width of continental rifts and rheological layering of the lithosphere, *Tectonophysics*, **188**(1 - 2), 63 – 69.

Anders, B., Reischmann, T., Poller, U., & Kostopoulos, D., 2005. Age and origin of granitic rocks of the eastern Vardar Zone, Greece: new constraints on the evolution of the Internal Hellenides, *Journal of the Geological Society, London*, **162**, 857 – 870.

Andersen, T. B., Jamtveit, B., Dewey, J. F., & Swensson, E., 1991. Subduction and eduction of continental crust: major mechanisms during continent-continent collision and orogenic extensional collapse, a model based on the south Norwegian Caledonides, *Terra*, **3**(3), 303 – 310.

Armijo, R., Meyer, B., Hubert, A., & Barka, A., 1999. Westward propagation of the North Anatolian fault into the northern Aegean: Timing and kinematics, *Geology*, **27**(3), 267 – 270.

Asvesta, A., 1992. *Magmatism and associated sedimentation during the first stage of the opening of the Vardar oceanic basin in Triassic times (in greek with english abstract)*, Ph.D. thesis, University of Thessaloniki, Greece.

Asvesta, A. & Dimitriadis, S., 2010. Facies architecture of a Triassic rift-related Silicic Volcano-Sedimentary succession in the Tethyan realm, Peonias subzone, Vardar (Axios) Zone, northern Greece; Regional implications, *Journal of Volcanology and Geothermal Research*, **193**(3 - 4), 245 – 269.

Augier, R., Agard, P., Monié, P., Jolivet, L., Robin, C., & Booth-Rea, G., 2005. Exhumation, doming and slab retreat in the Betic Cordillera (SE Spain): in situ $^{40}Ar/^{39}Ar$ ages and P-T-d-t paths for the Nevado-Filabride complex, *Journal of Metamorphic Geology*, **23**(5), 357 – 381.

Auzanneau, E., Schmidt, S., Vielzeuf, D., & Connolly, J. A. D., 2010. Titanium in phengite: a geobarometer for high temperature eclogites, *Contributions to Mineralogy and Petrology*, **159**(1), 1 – 24.

Balestrieri, M., Benvenuti, M., & Tangocci, F., 2013. Detrital fission-track-compositional signature of an orogenic chain-hinterland basin system: The case of the late Neogene Quaternary Valdelsa basin (Northern Apennines, Italy), *Sedimentary Geology*, **289**, 159 – 168.

Balestrieri, M. L., Pandeli, E., Bigazzi, G., Carosi, R., & Montomoli, C., 2011. Age and temperature constraints on metamorphism and exhumation of the syn-orogenic metamorphic complexes of Northern Apennines, Italy, *Tectonophysics*, **509**(3 - 4), 254 – 271.

Barbarand, J., Lucazeau, F., Pagel, M., & Séranne, M., 2001. Burial and exhumation history of the south-eastern Massif Central (France) constrained by apatite fission-track thermochronology, *Tectonophysics*, **335**(3 - 4), 275 – 290.

Barbarand, J., Carter, A., Wood, I., & Hurford, T., 2003. Compositional and structural control of fission-track annealing in apatite, *Chemical Geology*, **198**(1 - 2), 107 – 137.

Baroz, F., Bebien, J., & Ikenne, M., 1987. An example of high-pressure low-temperature metamorphic rocks from an island-arc: the Paikon Series (Innermost Hellenides, Greece), *Journal of Metamorphic Geology*, **5**(4), 509 – 527.

Barr, S. R., Temperley, S., & Tarney, J., 1999. Lateral growth of the continental crust through deep level subduction-accretion: a re-evaluation of central Greek Rhodope, *Lithos*, **46**(1), 69 – 94.

Bauer, C., Rubatto, D., Krenn, K., Proyer, A., & Hoinkes, G., 2007. A zircon study from the Rhodope metamorphic complex, N-Greece: Time record of a multistage evolution, *Lithos*, **99**(3 - 4), 207 – 228.

Bernet, M. & Garver, J. I., 2005. Fission-track analysis of detrital zircon, *Reviews in Mineralogy and Geochemistry*, **58**(1), 205 – 237.

Berthé, D., Choukroune, P., & Gapais, D., 1979. Quartz fabrics and progressive gneissification of granites by simple shear - example of the South Armorican Shear Zone, *Bulletin Mineralogie*, **102**, 265 – 272.

Bertrand, J., Ferriere, J., & Stais, A., 1994. Donées petrographiques et géochronologiques sur des laves des domaines Vardariens de Peonias et d' Almopias (Héllenides Orientales), *Bulletin of the Geological Society of Greece*, **XXX**(1), 213 – 222.

Bigazzi, S. G., Christofides, G., Moro, A. D., & Kyriakopoulos, C., 1994. A contribution to the evolution of the Xanthi pluton (northern Greece): the apatite fission track analysis, *Boll. Soc. Geol. It.*, **113**, 243 – 248.

Bijwaard, H., Spakman, W., & Engdahl, E. R., 1998. Closing the gap between regional and global travel time tomography, *Journal of Geophysical Research: Solid Earth*, **103**(B12), 30055 – 30078.

Bonev, N. & Dilek, Y., 2010. Geochemistry and tectonic significance of proto-ophiolitic metamafic units from the Serbo-Macedonian and western Rhodope massifs (Bulgaria-Greece), *International Geology Review*, **52**(2 - 3), 298 – 335.

Bonev, N., Burg, J.-P., & Ivanov, Z., 2006. Mesozoic-Tertiary structural evolution of an extensional gneiss dome - the Kesebir-Kardamos dome, eastern Rhodope (Bulgaria-Greece), *International Journal of Earth Sciences (Geol Rundsch)*, **95**(2), 318 – 340.

Bonev, N., Spikings, R., Moritz, R., & Marchev, P., 2010. The effect of early Alpine thrusting in late-stage extensional tectonics: Evidence from the Kulidzhik nappe and the Pelevun extensional allochthon in the Rhodope Massif, Bulgaria, *Tectonophysics*, **488**(1 - 4), 256 – 281.

Bonev, N., Dilek, Y., Hanchar, J. M., Bogdanov, K., & Klain, L., 2012a. Nd-Sr-Pb isotopic composition and mantle sources of Triassic rift units in the Serbo-Macedonian and the western Rhodope massifs (Bulgaria-Greece), *Geological Magazine*, **149**(1), 2012.

Bonev, N., Marchev, P., & Moritz, R., 2012b. The Jurassic Rhodope subduction-accretion history: temporal relations between the Circum-Rhodope Belt Evros ophiolite, and the UHP-HP events and the granitoid magmatism in the underlying high-grade metamorphic basement, Thrace region, NE Greece, in *Geophysical Research Abstracts*, vol. 14, pp. EGU2012–7323–1.

Bonev, N., Ovtcharova-Schaltegger, M., Moritz, R., Marchev, P., & Ulianov, A., 2013a. Peri-Gondwanan Ordovician crustal fragments in the high-grade basement of the Eastern Rhodope Massif, Bulgaria: evidence from U-Pb LA-ICP-MS zircon geochronology and geochemistry, *Geodinamica Acta*.

Bonev, N., Spikings, R., Moritz, R., Marchev, P., & D., C., 2013b. $^{40}Ar/^{39}Ar$ age constraints on the timing of Tertiary crustal extension and its temporal relation to ore-forming and magmatic processes in the Eastern Rhodope Massif, Bulgaria, *Lithos*, **180 - 181**, 264 – 278.

Borsi, S., Ferrara, G., & Mercier, J., 1965. Détermination de l'âge des séries métamorphiques du Massif Serbomacédonien au Nord-Est de Thessalonique (grèce) par les methodes Rb/Sr et K/Ar, *Annales de la Societe géologique du Nord*, **84**, 223 – 225.

Bosse, V., Boulvais, P., Gautier, P., Tiepolo, M., Ruffet, G., Devidal, J., Cherneva, Z., Gerdjikov, I., & Paquette, J., 2009. Fluid-induced disturbance of the monazite Th-Pb chronometer: In situ dating and element mapping in pegmatites from the Rhodope (Greece, Bulgaria), *Chemical Geology*, **261**(3 - 4), 286 – 302.

Bosse, V., Cherneva, Z., Gautier, P., & Gerdjikov, I., 2010. Two partial melting events as recorded by the U-Th-Pb chronometer in monazite: LA-ICPMS in situ dating in metapelites from the Bulgarian Central Rhodopes, *Geologica Balcanica*, **39**(1 - 2), 51 – 52.

Bourcart, M. J., 1919. Sur la présence du priabonien dans la région se salonique, *Comptes Rendus de l' Academie des Sciences, Paris*, pp. 855 – 856.

Boyanov, I., Ruseva, M., & Dimitrova, E., 1982. First find of Upper-Cretaceous foraminifers in East-Rhodopes, *Geologica Balcanica*, **12**(4), 20.

Broska, I. & Siman, P., 1998. The breakdown of monazite in the west-Carpathian Veporic orthogneisses and Tatric granites, *Geologica Carpathica*, **49**(3), 161 – 167.

Brun, J.-P., 1999. Narrow rifts versus wide rifts: inferences for the mechanics of rifting from laboratory experiments, *Philosophical Transaction of the Royal Society, London*, **A357**, 695 – 710.

Brun, J.-P. & Faccenna, C., 2008. Exhumation of high-pressure rocks driven by slab rollback, *Earth and Planetary Science Letters*, **272**(1 - 2), 1 – 7.

Brun, J.-P. & Sokoutis, D., 2004. North aegean extension: from the Rhodope core complex to Neogene basins., in *Proceedings of the 5th International Symposium of Eastern Mediterranean Geology, Thessaloniki, Greece, 14-20 April 2004*, vol. 1, pp. 49 – 52.

Brun, J.-P. & Sokoutis, D., 2007. Kinematics of the Southern Rhodope Core Complex (North Greece), *International Journal of Earth Sciences (Geol Rundsch)*, **96**(6), 1079 – 1099.

Brun, J.-P. & Sokoutis, D., 2010. 45 m.y. of Aegean crust and mantle flow driven by trench retreat, *Geology*, **38**(9), 815 – 818.

Brun, J.-P. & van den Driessche, J., 1994. Extensional gneiss domes and detachment fault systems: Structure and kinematics, *Bulletin de la Société Géologique de France, Paris*, **165**(6), 519 – 530.

Brun, J.-P., Sokoutis, D., & van den Driessche, J., 1994. Analogue modeling of detachment fault systems and core complexes, *Geology*, **22**(4), 319 – 322.

Brun, J.-P., Tirel, C., Philippon, M., Burov, E., Faccenna, C., Gueydan, F., & Lebedev, S., 2012. On the role of horizontal displacements in the exhumation of high pressure metamorphic rocks, in *Geophysical Research Abstracts*, vol. 14, pp. EGU2012–9381.

Buck, W. R., 1991. Modes of continental lithospheric extension, *Journal of Geophysical Research*, **96**(B12), 20161 – 20178.

Budzyń, B., Harlov, D. E., Williams, M. L., & Jercinovic, M. J., 2011. Experimental determination of stability relations between monazite, fluorapatite, allanite, and REE-epidote as a function of pressure, temperature, and fluid composition, *American Mineralogist*, **96**(10), 1547 – 1567.

Burchfiel, B. C., Nakov, R., Dumurdzanov, N., Papanikolaou, D., Tzankov, T., Serafimovski, T., King, R. W., Kotzev, V., Todosov, A., & Nurce, B., 2008. Evolution and dynamics of the Cenozoic tectonics of the South Balkan extensional system, *Geosphere*, **4**(6), 919 – 938.

Burchfiel, C. B., Nakov, R., Tzankov, T., & Royden, L. H., 2000. Cenozoic extension in Bulgaria and northern Greece: the northern part of the Aegean extensional regime, *Geological Society, London, Special Publications*, **173**, 325 – 352.

Burg, J.-P., 2012. Rhodope: From Mesozoic convergence to Cenozoic extension. Review of petro-structural data in the geochronological frame, *Journal of the Virtual Explorer*, **42**(1).

Burg, J.-P. & Gerya, T. V., 2005. The role of viscous heating in Barrovian metamorphism of collisional orogens: thermomechanical models and application to the Lepontine Dome in the Central Alps, *Journal of Metamorphic Geology*, **23**(2), 75 – 95.

Burg, J.-P., Ivanov, Z., Ricou, L.-E., Dimov, D., & Klain, L., 1990. Implications of shear-sense criteria for the tectonics evolution of the Central Rhodope massif, southern Bulgaria, *Geology*, **18**, 451 – 454.

Burg, J.-P., Ricou, L. E., Ivanov, Z., Godfriaux, I., Dimov, D., & Klain, L., 1993. Crustal-scale thrust complex in the Rhodope Massif, structure and kinematics, *Bulletin of the Geological Society of Greece*, **XXVIII**(1), 71 – 85.

Burg, J.-P., Godfriaux, I., & Ricou, L.-E., 1995. Extension of the Mesozoic Rhodope thrust units in the Vertiskos-Kerdilion Massifs, *C. R. Acad. Sci. Paris*, **320**(IIa), 889 – 896.

Burg, J.-P., Ricou, L.-E., Ivanov, Z., Godfriaux, I., Dimov, D., & Klain, L., 1996. Synmetamorphic nappe complex in the Rhodope Massif. Structure and kinematics, *Terra Nova*, **8**(1), 6 – 15.

Byerlee, 1978. Friction of rocks, *Pure and Applied Geophysics*, **116**(4 - 5), 615 – 626.

Caddick, M., Konopásek, J., & Thompson, A., 2010. Preservation of Garnet Growth Zoning and the Duration of Prograde Metamorphism, *Journal of Petrology*, **51**(11), 2327 – 2347.

Carlson, W. D., Donelick, R. A., & Ketcham, R. A., 1999. Variability of apatite fission-track annealing kinetics; I. Experimental results, *American Mineralogist*, **84**(9), 1213 – 1223.

Carrapa, B., 2009. Tracing exhumation and orogenic wedge dynamics in the European Alps with detrital thermochronology, *Geology*, **37**(12), 1127 – 1130.

Carras, N. & Georgala, D., 1998. Upper Jurassic to Lower Cretaceous Carbonate Facies of African Affinities in a Peri-European Area: Chalkidiki Peninsula, Greece, *Facies*, **38**, 153 – 164.

Carter, A., 1999. Present status and future avenues of source region discrimination and characterization using fission track analysis, *Sedimentary Geology*, **124**, 31 – 45.

Charvin, K., Gallagher, K., Hampson, G. L., & Labourdette, R., 2009. A Bayesian approach to inverse modelling of stratigraphy, part 1: method, *Basin Research*, **51**, 5 – 25.

Christodoulou, G., 1965. Geological structure of the Thessaloniki - Giannitsa basin (in greek with english abstract), *Bulletin of the Geological Society of Greece*, **VI**(2), 249 – 289.

Christofides, G., D'Amico, C., Moro, A. D., Eleftheriadis, G., & Kyriakopoulos, C., 1990. Rb/Sr geochronology and geochemical characters of the Sithonia plutonic complex (Greece), *European Journal of Mineralogy*, **2**, 79 – 87.

Christofides, G., Koroneos, A., Pe-Piper, G., Katirtzoglou, K., & Chatzikirkou, A., 1999. Pre-Tertiary A-Type magmatism in the Serbomacedonian massif (N. Greece): Kerkini granitic complex, *Bulletin of the Geological Society of Greece*, **XXXIII**, 131 – 148.

Christofides, G., Koroneos, A., Liati, A., & Kral, J., 2007. The A-Type Kerkini granitic complex in North Greece: geochronology and geodynamic implications, *Bulletin of the Geological Society of Greece*, **XXXX**, 700 – 711.

Coggon, R. & Holland, T., 2002. Mixing properties of phengitic micas and revised garnet-phengite thermobarometers, *Journal of Metamorphic Geology*, **20**(7), 683 – 696.

Cogné, N., Gallagher, K., & Cobbold, P. R., 2011. Post-rift reactivation of the onshore margin of southeast Brazil: Evidence from apatite (U-Th)/He and fission-track data, *Earth and Planetary Science Letters*, **309**, 118 – 130.

Cogné, N., Gallagher, K., Cobbold, P. R., Riccomini, C., & Gautheron, C., 2012. Post-breakup tectonics in southeast Brazil from thermochronological data and combined inverse-forward thermal history modeling, *Journal of Geophysical Research*, **117**, B11413.

Coney, P. J., 1980. Cordilleran Metamorphic Core Complexes: An overview, *Geological Society of America Memoirs*, **153**, 7 – 31.

Connolly, J. A., 2005. Computation of phase equilibria by linear programming: A tool for geodynamic modeling and its application to subduction zone decarbonation, *Earth and Planetary Science Letters*, **236**(1 - 2), 524 – 541.

Cornelius, N. K., 2008. *UHP metamorphic rocks of the Eastern Rhodope Massif, NE Greece: new constraints from petrology, geochemistry and zircon ages*, Ph.D. thesis, Johannes Gutenberg-Universität Mainz.

Cosca, M. A., Essene, E. J., Mezger, K., & van der Pluijm, B. A., 1995. Constraints on the duration of tectonic processes: Protracted extension and deep-crustal rotation in the Grenville orogen, *Geology*, **23**(4), 361 – 364.

Crittenden, M., P.J., C., & G.H., D., 1980. Cordilleran metamorphic core complexes, *Geological Society of America Memoirs*, **153**, 1 – 490.

Cruciani, G., Franceschelli, M., Massonne, H.-J., Carosi, R., & Montomoli, C., 2013. Pressure-temperature and deformational evolution of high-pressure metapelites from Variscan NE Sardinia, Italy, *Lithos*, **175 - 176**, 272 – 284.

Davis, G. H. & Coney, P. J., 1979. Geologic development of the cordilleran metamorphic core complexes, *Geology*, **7**(3), 120 – 124.

de Wet, A. P., Miller, J. A., Bickle, M. J., & Chapman, H. J., 1989. Geology and geochronology of the Arnea, Sithonia and Ouranopolis intrusions, Chalkidiki Peninsula, northern Greece, *Tectonophysics*, **161**(1 - 2), 65 – 79.

Dercourt, J., Ricou, L. E., & Vrielynck, B., 1993. *Atlas Tethys palaeoenvironmental maps*, Paris, Gauthier-Villars.

Dewey, J. & Sengör, C., 1979. Aegean and surrounding regions: Complex multiplate and continuum tectonics in a convergent zone, *Geological Society of America Bulletin*, **90**, 84 – 92.

Dewey, J. F., 1988. Extensional collapse of orogens, *Tectonics*, **7**(6), 1123 – 1139.

Didier, A., Bosse, V., Cherneva, Z., Gautier, P., Georgieva, M., Paquette, J. L., & Gerdjikov, I., 2014. Syn-deformation fluid-assisted growth of monazite during renewed high-grade metamorphism in metapelites of the Central Rhodope (Bulgaria, Greece), *Chemical Geology*, **381**, 206 – 222.

Diener, J. F. A. & Powell, R., 2011. Revised activity-composition models for clinopyroxene and amphibole, *Journal of Metamorphic Geology*, **30**(2), 131 – 142.

Dimitriadis, S. & Godelitsas, A., 1991. Evidence for high pressure metamorphism in the Vertiskos group of the Serbomacedonian Massif: the eclogite of Nea Roda, Chalkidiki, *Bulletin of the Geological Society of Greece*, **XXV**(2), 67 – 80.

Dimitrijević, M., 1963. Sur l'âge du métamorphism et des plissements dans la masse Serbo-Macédonièn ne, in *Proc. VI Congr. Carp. Balk. Geol. Assoc.*, pp. 339 – 347.

Dinter, D. A. & Royden, L., 1993. Late Cenozoic extension in northeastern Greece: Strymon Valley detachment system and Rhodope metamorphic core complex, *Geology*, **21**, 45 – 48.

Dinter, D. A., Macfarlane, A., Hames, W., Isachsen, C., Bowring, S., & Royden, L., 1995. U-Pb and $^{40}Ar/^{39}Ar$ geochronology of the Symvolon granodiorite: Implications for the thermal and structural evolution of the Rhodope metamorphic core complex, northeastern Greece, *Tectonics*, **14**(4), 886 – 908.

Dixon, J. E. & Dimitriadis, S., 1984. Metamorphosed ophiolitic rocks from the Serbo-Macedonian Massif, near Lake Volvi, North-east Greece, *Geological Society, London, Special Publications*, **17**, 603 – 618.

Donelick, R. A., O'Sullivan, P. B., & Ketcham, R. A., 2005. Apatite fission-track analysis, *Reviews in Mineralogy and Geochemistry*, **58**(1), 49 – 94.

Dörr, N., Lisker, F., Clift, P. D., Carter, A., Gee, D. G., Tebenkov, A. M., & Spiegel, C., 2012. Late Mesozoic-Cenozoic exhumation history of northern Svalbard and its regional significance: Constraints from apatite fission track analysis, *Tectonophysics*, **514 - 517**, 81 – 92.

Dunkl, I., 2002. Trackkey: a Windows program for calculation and graphical presentation of fission track data, *Computers & Geosciences*, **28**(1), 3 – 12.

Duretz, T., Gerya, T. V., Kaus, B. J. P., & Andersen, T. B., 2012. Thermomechanical modeling of slab eduction, *Journal of Geophysical Research*, **117**(B8).

Dyksterhuis, S., Rey, P., Müller, R., & Moresi, L., 2007. Effects of initial weakness on rift architecture, *Geological Society, London, Special Publications*, **282**, 443 – 455.

Eleftheriadis, G., Frank, W., & Petrakakis, K., 2001. $^{40}Ar/^{39}Ar$ dating and cooling history of the Pangeon granitoids, Rhodope Massif (eastern Macedonia, Greece), *Bulletin of the Geological Society of Greece*, **XXXIV**(3), 911 – 916.

England, P. C. & Thompson, A. B., 1984. Pressure-Temperature-Time Paths of Regional metamorphism i. Heat Transfer during the Evolution of Regions of Thickened Continental Crust, *Journal of Petrology*, **25**(4), 894 – 928.

Filipov, P. & Marchev, P., 2011. U-Pb zircon and $^{40}Ar/^{39}Ar$ ages of Mesta volcanic rocks and Central Pirin pluton, in *Bulgarian National Conference "GEOSCIENCES 2011"*.

Finger, F., Broska, I., Roberts, M. P., & Schermaier, A., 1998. Replacement of primary monazite by apatite-allanite-epidote coronas in an amphibolite facies granite gneiss from the eastern Alps, *American Mineralogist*, **83**(3 - 4), 248 – 258.

Foster, D. A. & Raza, A., 2002. Low-temperature thermochronological record of exhumation of the Bitterroot metamorphic core complex, northern Cordilleran Orogen, *Tectonophysics*, **349**(1 - 4), 23 – 36.

Frei, D., 1996. The extent of inter-mineral isotope equilibrium: a systematic bulk U-Pb and Pb step leaching (PbSL) isotope study of individual minerals from the Tertiary granite of Jerissos (northern Greece), *European Journal of Mineralogy*, **8**, 1175 – 1189.

Frei, R., 1992. *Isotope (Pb,Rb-Sr,S,O,C,U-Pb) geochemical investigations on Tertiary intrusives and related mineralizations in the Serbomacedonian Pb-Zn, Sb+Cu-Mo metallogenetic province in Northern Greece*, Ph.D. thesis, Swiss Federal Institute of Technology (ETH), Zurich.

Fuhrman, M. L. & Lindsley, D. H., 1988. Ternary-feldspar modeling and thermometry, *American Mineralogist*, **71**(3 - 4), 201 – 215.

Galbraith, R. & Laslett, G., 1993. Statistical models for mixed fission track ages, *Nuclear Tracks and Radiation Measurements*, **21**(4), 459 – 470.

Gallagher, K., 2012. Transdimensional inverse thermal history modeling for quantitative thermochronology, *Journal of Geophysical Research*, **117**, B02408.

Gallagher, K., Brown, R., & Johnson, C., 1998. Fission track analysis and its applications to geological problems, *Annual Review of Earth and Planetary Sciences*, **26**, 519 – 572.

Gallagher, K., Stephenson, J., Brown, R., Holmes, C., & Ballester, P., 2005a. Exploiting 3d spatial sampling in inverse modeling of thermochronological data, *Reviews in Mineralogy and Geochemistry*, **58**(1), 375 – 387.

Gallagher, K., Stephenson, J., Brown, R., Holmes, C., & Fitzgerald, P., 2005b. Low temperature thermochronology and modeling strategies for multiple samples 1: Vertical profiles, *Earth and Planetary Science Letters*, **237**(1 - 2), 193 – 208.

Gallagher, K., Charvin, K., Nielsen, S., Sambridge, M., & Stephenson, J., 2009. Markov chain Monte Carlo (MCMC) sampling methods to determine optimal models, model resolution and model choice for Earth Science problems, *Marine and Petroleum Geology*, **26**, 525 – 535.

Ganguly, J., Cheng, W., & Tirone, M., 1996. Thermodynamics of aluminosilicate garnet solid solution: new experimental data, an optimized model, and thermometric applications, *Contributions to Mineralogy and Petrology*, **126**(1 - 2), 137 – 151.

Gautier, P. & Brun, J.-P., 1994. Crustal-scale geometry and kinematics of late-orogenic extension in the central Aegean (Cyclades and Ewia Island), *Tectonophysics*, **238**(1 - 4), 399 – 424.

Gautier, P., Brun, J.-P., & Jolivet, L., 1993. Structure and kinematics of Upper Cenozoic extensional detachment on Naxos and Paros (Cyclades Islands, Greece), *Tectonics*, **12**(5), 1180 – 1194.

Georgiadis, G. A., Tranos, M. D., & Mountrakis, D. M., 2007. Late- and post-alpine tectonic evolution of the southern part of the Athos Peninsula, northern Greece, *Bulletin of the Geological Society of Greece*, **XXXX**(1), 309 – 320.

Georgiadis, I., 2006. *Petrological and geochemical study of Quaternary clastic sediments from the Cherso basin (in greek)*, Master's thesis, University of Thessaloniki, Greece.

Gerdjikov, I. & Milev, P., 2005. Nestos Shear Zone and structure of the metamorphic basement in the area south of Mesta graben, *Comptes rendus de l'Académie bulgare des Sciences*, **58**(2), 197 – 204.

Gessner, K., Wijns, C., & Moresi, L., 2007. Significance of strain localization in the lower crust for structural evolution and thermal history of metamorphic core complexes, *Tectonics*, **26**(2).

Gilg, H. A. & Frei, R., 1994. Chronology of magmatism and mineralization in the Kassandra mining area, Greece: The potentials and limitations of dating hydrothermal illites, *Geochimica et Cosmochimica Acta*, **58**(9), 2107 – 2122.

Gleadow, A. J. W., 1981. Fission track dating methods: What are the real alternatives?, *Nuclear Tracks*, **5**(1 - 2), 3 – 14.

Goranov, A. & Atanasov, G., 1992. Lithostratigraphy and formation conditions of Maastrichtian-Paleocene deposits in Krumovgrad District, *Geologica Balcanica*, **22**(3), 71 – 82.

Gramann, F. & Kockel, F., 1969. Das Neogen im Strimonbecken (Griechisch-Ostmazedonien). Teil 1: Lithologie, Stratigraphie und Paläogeographie, *Geologisches Jahrbuch*, **87**, 445 – 484.

Gueydan, F., Morency, C., & Brun, J.-P., 2008. Continental rifting as a function of lithosphere mantle strength, *Tectonophysics*, **460**(1 - 4), 83 – 93.

Gunnell, Y., Gallagher, K., Carter, A., Widdowson, M., & Hurford, A. J., 2003. Denudation history of the continental margin of western peninsular India since the early mesozoic - reconciling apatite fission-track data with geomorphology, *Earth and Planetary Science Letters*, **215**(1 - 2), 187 – 201.

Hacker, B. R., Andersen, T. B., Root, D. B., Mehl, L., Mattinson, J. . M., & Wooden, J. L., 2003. Exhumation of high-pressure rocks beneath the solund basin, western gneiss region of norway, *Journal of Metamorphic Geology*, **21**(6), 613 – 629.

Hanmer, S. & Passchier, C., 1991. Shear-sense indicators: a review, *Geological Survey of Canada*, **90-17**(M44), 72 pp.

Harkovska, A., Petrov, P. S., Milakovska, Z., & Nakova, V., 2010. "Kozhuh volcano" (SW Bulgaria) - arrangement of the puzzle, 2010 (in bulgarian), *Review of the Bulgarian Geological Society*, **71**(1 - 3), 149 – 166.

Harre, W., Kockel, F., Kreuzer, H., Lenz, H., Müller, P., & Walther, H. W., 1968. Über Rejuvenationen im Serbo-Madzedonischen Massiv (Deutung radiometrischer Altersbestimmungen), in *XXIII International Geological Congress*, vol. 6, pp. 223 – 236.

Harrison, T. M., Duncan, I., & McDougall, I., 1985. Diffusion of ^{40}Ar in biotite: Temperature, pressure and compositional effects, *Geochimica et Cosmochimica Acta*, **49**(11), 2461 – 2468.

Harrison, T. M., Célérier, J., Aikman, A. B., Hermann, J., & Heizler, M. T., 2009. Diffusion of ^{40}Ar in muscovite, *Geochimica et Cosmochimica Acta*, **73**(4), 1039 – 1051.

Hatzfeld, D., Christodoulou, A. A., Scordilis, E. M., Panagiotopoulos, D., & Hatzidimitriou, P. M., 1987. A microearthquake study of the Mygdonian graben (northern Greece), *Earth and Planetary Science Letters*, **81**(4), 379 – 396.

Hejl, E., Weingartner, H., Vavliakis, E., & Psilovikos, A., 1998. Macrorelief features and fission-track thermochronology of the Rila-Rhodope massif (Eastern Macedonia, Greece), *Zeitschrift für Geomorphologie, NF*, **42**(4), 517 – 530.

Hejl, E., Bernroider, M., Parlak, O., & Weingartner, H., 2010. Fission-track thermochronology, vertical kinematics, and tectonic development along the western extension of the North Anatolian Fault zone, *Journal of Geophysical Research*, **115**, B10407.

Himmerkus, F., Zachariadis, P., Reischmann, T., & Kostopoulos, D., 2005. The mafic complexes of the Athos-Volvi-Zone - a suture zone between the Serbo-Macedonian Massif and the Rhodope Massif?, in *Geophysical Research Abstracts*, vol. 7, p. 10240.

Himmerkus, F., Reischmann, T., & Kostopoulos, D., 2006. Late Proterozoic and Silurian basement units within the Serbo-Macedonian Massif, northern Greece: the significance of terrane accretion in the Hellenides, *Geological Society, London, Special Publications*, **260**, 35 – 50.

Himmerkus, F., Anders, B., Reischmann, T., & Kostopoulos, D., 2007. Gondwana-derived terranes in the northern Hellenides, *The Geological Society of America Memoir*, **200**, 379 – 390.

Himmerkus, F., Reischmann, T., & Kostopoulos, D., 2009a. Serbo-Macedonian revisited: A Silurian basement terrane from northern Gondwana in the Internal Hellenides, Greece, *Tectonophysics*, **473**(1 - 2), 20 – 35.

Himmerkus, F., Reischmann, T., & Kostopoulos, D., 2009b. Triassic rift-related metagranites in the Internal Hellenides, Greece, *Geological Magazine*, **146**(2), 252 – 265.

Himmerkus, F., Zachariadis, P., Reischmann, T., & Kostopoulos, D., 2012. The basement of the Mount Athos peninsula, northern Greece: insights from geochemistry and zircon ages, *International Journal of Earth Sciences (Geol Rundsch)*, **101**(6), 1467 – 1485.

Hoinkes, G., Krenn, E., Rubatto, D., Krenn, K., Proyer, A., Bernhard, F., & Bauer, C., 2008. Timing the Rhodope UHP-event using zircon and monazite, in *33rd International Geological Congress. UHP-04 Ultra-high pressure metamorphism: Mineral reactions, geochemistry, thermobarometry and geochronology*.

Holland, T. & Powell, R., 1998. An internally consistent thermodynamic data set for phases of petrological interest, *Journal of Metamorphic Geology*, **16**(3), 309 – 343.

Holland, T., Baker, J., & Powell, R., 1998. Mixing properties and activity-composition relationships of chlorites in the system Mgo-FeO-Al_2O_3-SiO_2-H_2O, *European Journal of Mineralogy*, **10**(3), 395 – 406.

Hopcroft, P. O., Gallagher, K., & Pain, C. C., 2007. Inference of past climate from borehole temperature data using Bayesian Reversible Jump Markov chain Monte Carlo, *Geophysical Journal International*, **171**(3), 1430 – 1439.

Hubbert, K. M., 1937. Theory of scale models as applied to the study of geologic structures, *Geological Society of America Bulletin*, **48**, 1459 – 1519.

Huet, B., le Pourhiet, L., Labrousse, L., Burov, E., & Jolivet, L., 2011a. Post-orogenic extension and metamorphic core complexes in a heterogeneous crust: the role of crustal layering inherited from collision. Application to the Cyclades (Aegean domain), *Geophysical Journal International*, **184**, 611 – 625.

Huet, B., le Pourhiet, L., Labrousse, L., Burov, E., & Jolivet, L., 2011b. Formation of metamorphic core complex in inherited wedges: A thermomechanical modelling study, *Earth and Planetary Science Letters*, **309**(3 - 4), 249 – 257.

Hurai, V., Paquette, J., Huraiova, M., & Konecný, P., 2010. U-Th-Pb geochronology of zircon and monazite from syenite and pincinite xenoliths in Pliocene alkali basalts of the intra-Carpathian back-arc basin, *Journal of Volcanology and Geothermal Research*, **198**(3 - 4), 275 – 287.

Hurford, A. J. & Green, P. F., 1982. A users' guide to fission track dating calibration, *Earth and Planetary Science Letters*, **59**(2), 343 – 354.

Hurford, A. J. & Green, P. F., 1983. The zeta age calibration of fission-track dating, *Chemical Geology*, **41**, 285 – 317.

Jackson, S. E., Pearson, N. J., Griffin, W. L., & Belousova, E. A., 2004. The application of laser ablation-inductively coupled plasma-mass spectrometry to in situ U-Pb zircon geochronology, *Chemical Geology*, **211**(1 - 2), 47 – 69.

Jahn-Awe, S., Froitzheim, N., Nagel, T. J., Frei, D., Georgiev, N., & Pleuger, J., 2010. Structural and geochronological evidence for Paleogene thrusting in the western Rhodopes, SW Bulgaria: Elements for a new tectonic model of the Rhodope Metamorphic Province, *Tectonics*, **29**, TC3008.

Jahn-Awe, S., Pleuger, J., Frei, D., Georgiev, N., Froitzheim, N., & Nagel, T. J., 2012. Time constraints for low-angle shear zones in the Central Rhodopes (Bulgaria) and their significance for the exhumation of high-pressure rocks, *International Journal of Earth Sciences (Geol Rundsch)*, **101**(7), 1971 – 2004.

Janák, M., Froitzheim, N., Georgiev, N., Nagel, T. J., & Sarov, S., 2011. P-T evolution of kyanite eclogite from the Pirin Mountains (SW Bulgaria): implications for the Rhodope UHP Metamorphic Complex, *Journal of Metamorphic Geology*, **29**(3), 317 – 332.

Jolivet, L. & Brun, J.-P., 2010. Cenozoic geodynamic evolution of the Aegean, *International Journal of Earth Sciences (Geol Rundsch)*, **99**(1), 109 – 138.

Jolivet, L. & Faccenna, C., 2000. Mediterranean extension and the Africa-Eurasia collision, *Tectonocs*, **19**(6), 1095 – 1106.

Jolivet, L., Faccenna, C., Huet, B., Labrousse, L., Le Pourhiet, L., Lacombe, O., Lecomte, E., Burov, E., a. Y., Brun, J.-P., Gueydan, F., Philippon, M., Paul, A., Salaün, G., Karabulut, H., Piromallo, C., Monié, P., Okay, A., Oberhänsli, R., Pourteau, A., Augier, R., Gadenne, L., & Driussi, O., 2013. Aegean tectonics: Strain localisation, slab tearing and trench retreat, *Tectonophysics*, **597 - 598**, 1 – 33.

Jolivet, M., Labaume, P., Monié, P., Brunel, M., Arnaud, N., & Campani, M., 2007. Thermochronology constraints for the propagation sequence of the south Pyrenean basement thrust system (France - Spain), *Tectonics*, **26**, TC5007.

Jolivet, M., Dominguez, S., Charreau, J., Chen, Y., Li, Y., & Wang, Q., 2010. Mesozoic and Cenozoic tectonic history of the central Chinese Tian Shan: Reactivated tectonic structures and active deformation, *Tectonics*, **29**, TC6019.

Jones, C. E., Tarney, J., Baker, J. H., & Gerouki, F., 1992. Tertiary granitoids of Rhodope, northern Greece: magmatism related to extensional collapse of the Hellenic Orogen?, *Tectonophysics*, **210**(3 - 4), 295 – 314.

Kaiser-Rohrmeier, M., von Quadt, A., Driesner, T., Heinrich, C. A., Handler, R., Ovtcharova, M., Ivanov, Z., Petrov, P., Sarov, S., & Peytcheva, I., 2013. Post-Orogenic Extension and Hydrothermal Ore Formation: High-Precision Geochronology of the Central Rhodopian Metamorphic Core Complex (Bulgaria-Greece), *Economic Geology*, **108**(4), 691 – 718.

Karson, J., 1990. Seafloor spreading on the Mid-Atlantic Ridge: implications for the structure of ophiolites and oceanic lithosphere produced in slow-spreading environments, in *Ophiolites: Oceanic Crustal Analogues: Proc. Symp. "Troodos 1987": Nicosia, Cyprus (Minist. Agric. Nat. Resour.)*, pp. 547 – 555.

Kassoli-Fournaraki, A., Sklavounos, S., & Michailidis, K., 1986. Garnet composition as a possible indication of retrograde metamorphism, dorkas-ossa area, serbo-macedonian massif, greece, *Geologica Balcanica*, **16**(2), 79 – 84.

Kauffmann, G., Kockel, F., & Mollat, H., 1976. Notes on the stratigraphic and paleogeographic position of the Svoula Formation in the Innermost Zone of the Hellenides (Northern Greece), *Bull. Soc. Géol. France*, **7**(2), 225 – 230.

Kaufman, P. S., 1995. *Extensional Tectonic History of the Rhodope Metamoprhic Core Complex, Greece and Geophysical Modeling of the Halloran Hills, California*, Ph.D. thesis, Massachusetts Institute of Technology.

Ketcham, R. A., Carter, A., Donelick, R. A., Barbarand, J., & Hurford, A. J., 2007. Improved modeling of fission-track annealing in apatite, *American Mineralogist*, **92**, 799 – 810.

Kilias, A. & Mountrakis, D., 1990. Kinematics of the crystalline sequences in the Western Rhodope massif, *Geologica Rhodopica*, **2**, 100 – 116.

Kilias, A., Falalakis, G., & Mountrakis, D., 1999. Cretaceous-Tertiary structures and kinematics of the Serbomacedonian metamorphic rocks and their relation to the exhumation of the Hellenic hinterland (Macedonia, Greece), *International Journal of Earth Sciences (Geol Rundsch)*, **88**(3), 513 – 531.

Kirchenbaur, M., Pleuger, J., Jahn-Awe, S., Nagel, T. J., Froitzheim, N., Fonseca, R. O. C., & Münker, C., 2012. Timing of high-pressure metamorphic events in the Bulgarian Rhodopes from Lu-Hf garnet geochronology, *Contributions to Mineralogy and Petrology*, **163**(5), 897 – 921.

Kissel, C. & Laj, C., 1988. The tertiary geodynamical evolution of the aegean arc: a paleomagnetic reconstruction, *Tectonophysics*, **146**(1 - 4), 183 – 201.

Kockel, F. & Mollat, H., 1977. Geological map of the Chalkidiki peninsula and adjacent areas (Greece), Scale 1: 100000, *Bundesanstalt für Geowissenschaften und Rohstoffe, Hannover*.

Kockel, F. & Walther, H. W., 1966. Der rhyolith von Strimonikon, sein tektonischer rahmen und die junge lagerstattenbildung in seiner umgebung (zentral Mazedonien, Griechenland), *Bulletin of the Geological Society of Greece*, **VII**(1), 1 – 16.

Kockel, F., Mollat, H., & Walther, H. W., 1971. Geologie des Serbe-Mazedonischen Massivs und seines mesozoischen Rahmens (Nordgriechenland), *Geol. Jb.*, **89**(1), 529 – 551.

Kockel, F., Mollat, H., & Walther, H., 1977. *Erlauterungen zur Geologischen Karte der Chalkidiki und angrenzender Gebiete*, Bundesanstalt für Geowissenschaften und Rohstoffe, Hannover, 119 pp.

Kolocotroni, C. & Dixon, J. E., 1991. The origin and emplacement of the Vrondou granite, Serres, NE Greece, *Bulletin of the Geological Society of Greece*, **XXV**(1), 469 – 483.

Kondopoulou, D. & Westphal, M., 1986. Paleomagnetism of the Tertiary intrusives from Chalkidiki (northern Greece), *Journal of Geophysics*, **59**, 62 – 66.

Kostopoulos, D., Ioannidis, N., & Sklavounos, S., 2000. A New Occurrence of Ultrahigh-Pressure Metamorphism, Central Macedonia, Northern Greece: Evidence from Graphitized Diamonds?, *International Geology Review*, **42**(6), 545 – 554.

Koufos, G. D., Syrides, G. E., Kostopoulos, D. S., & Koliadimou, K. K., 1995. Preliminary results about the stratigraphy and the palaeoenvironment of Mygdonia Basin, Macedonia, Greece, *GEOBIOS*, **18**, 243 – 249.

Koukouvelas, I. K. & Aydin, A., 2002. Fault structure and related basins of the North Aegean Sea and its surroundings, *Tectonics*, **21**(5), 10–1 – 10–17.

Kounov, A., Seward, D., Burg, J.-P., Bernoulli, D., Ivanov, Z., & Handler, R., 2010. Geochronological and structural constraints on the Cretaceous thermotectonic evolution of the Kraishte zone, western Bulgaria, *Tectonics*, **29**, TC2002.

Kounov, A., Graf, J., von Quadt, A., Bernoulli, D., Burg, J.-P., Seward, D., Ivanov, Z., & Fanning, C. M., 2012. Evidence for a "Cadomian" ophiolite and magmatic-arc complex in SW Bulgaria, *Precambrian Research*, **212 - 213**, 275 – 295.

Kourou, A. N., 1991. *Lithology, tectonic, geochemistry and metamorphism in the western part of the Vertiskos group. The area NE from the lake Agios Vasilios, northern Greece (in greek)*, Ph.D. thesis, University of Thessaloniki, Greece.

Koyi, H. A. & Skelton, A., 2001. Centrifuge modelling of the evolution of low-angle detachment faults from high-angle normal faults, *Journal of Structural Geology*, **23**(8), 1179 – 1185.

Krenn, E., Harlov, D. E., Finger, F., & Wunder, B., 2012. LREE-redistribution among fluorapatite, monazite, and allanite at high pressures and temperatures, *American Mineralogist*, **97**(11 - 12), 1881 – 1890.

Krenn, K., Bauer, C., Proyer, A., Mposkos, E., & Hoinkes, G., 2008. Fluid entrapment and reequilibration during subduction and exhumation: A case study from the high-grade Nestos shear zone, Central Rhodope, Greece, *Lithos*, **104**(1 - 4), 33 – 53.

Krenn, K., Bauer, C., Proyer, A., Klötzli, U., & Hoinkes, G., 2010. Tectonometamorphic evolution of the Rhodope orogen, *Tectonics*, **29**, TC4001.

Kronberg, P., Meyer, W., & Pilger, A., 1970. Geologie der Rila-Rhodope-Masse zwischen Strimon und Nestos (Nordgriechenland), *Beihefte Geologisches Jahrbuch*, **88**, 133 – 180.

Kydonakis, K., Gallagher, K., Brun, J.-P., Jolivet, M., Gueydan, F., & Kostopoulos, D., 2014a. Upper Cretaceous exhumation of the western Rhodope Metamorphic Province (Chalkidiki Peninsula, northern Greece), *Tectonics*, **33**, 1113 – 1132.

Kydonakis, K., Kostopoulos, D., Poujol, M., Brun, J.-P., Papanikolaou, D., & Paquette, J.-L., 2014b. The dispersal of the Gondwana Super-fan System in the eastern Mediterranean: New insights from detrital zircon geochronology, *Gondwana Research*, **25**(25), 1230 – 1241.

Kyriakopoulos, K. G., Magganas, A. C., Norelli, P., Bigazzi., G., Moro, A. D., & Kokkinakis, A., 1997. Thermochronological evolution of Symvolon and Pangeon pluton and their country rocks, Kavala area, N. Greece: an apatite fission track analysis, *N. Jb. Miner. Mh.*, **H11**(5), 519 – 529.

Labaume, P., Jolivet, M., Souquiére, F., & Chauvet, A., 2008. Tectonic control on diagenesis in a foreland basin: combined petrologic and thermochronologic approaches in the Grés d'Annot basin (Late Eocene - Early Oligocene, French - Italian external Alps), *Terra Nova*, **20**(2), 95 – 101.

Laigle, M., Hirn, A., Sachpazi, M., & Roussos, N., 2000. North Aegean crustal deformation: An active fault imaged to 10 km depth by reflection seismic data, *Geology*, **28**(1), 71 – 74.

Laird, J., 1984. Distribution of Ordovician and Devonian metamorphism in mafic and pelitic schists from northern Vermont, *American Journal of Sciences*, **284**(4 - 5), 376 – 413.

Le Pichon, X. & Angelier, J., 1979. The hellenic arc and trench system: A key to the neotectonic evolution of the eastern mediterranean area, *Tectonophysics*, **60**(1 - 2), 1 – 42.

Le Pichon, X. & Angelier, J., 1981. The aegean sea, *Philos. Trans. R. Soc. London*, **A300**, 357 – 372.

Leech, M. L. & Stockli, D., 2000. The late exhumation history of the ultrahigh-pressure Maksyutov Complex, south Ural Mountains, from new apatite fission track data, *Tectonics*, **19**(1), 153 – 167.

Liati, A., 2005. Identification of repeated Alpine (ultra) high-pressure metamorphic events by U-Pb SHRIMP geochronology and REE geochemistry of zircon: the Rhodope zone of Northern Greece, *Contributions to Mineralogy and Petrology*, **150**(6), 608 – 630.

Liati, A. & Gebauer, D., 1999. Constraining the prograde and retrograde P-T-t path of Eocene HP rocks by SHRIMP dating of different zircon domains: inferred rates of heating, burial, cooling and exhumation for central Rhodope, northern Greece, *Contributions to Mineralogy and Petrology*, **135**(4), 340 – 354.

Liati, A. & Seidel, E., 1996. Metamorphic evolution and geochemistry of kyanite eclogites in central Rhodope, northern Greece, *Contributions to Mineralogy and Petrology*, **123**(3), 293 – 307.

Liati, A., Gebauer, D., & Wysoczanski, R., 2002. U-Pb SHRIMP-dating of zircon domains from UHP garnet-rich mafic rocks and late pegmatoids in the Rhodope zone (N Greece); evidence for Early Cretaceous crystallization and Late Cretaceous metamorphism, *Chemical Geology*, **184**(3 - 4), 281 – 299.

Liati, A., Gebauer, D., & Fanning, C. M., 2011. *Ultrahigh-Pressure Metamorphism: 25 Years After the Discovery of Coesite and Diamond*, chap. Geochronology of the Alpine UHP Rhodope Zone: A Review of Isotopic Ages and Constraints on the Geodynamic Evolution, pp. 295 – 324, Elsevier Inc.

Lilov, P., Zagorčev, I., & Peeva, I., 1983. Rubidium-strontium isochron data on the age of the metamorphism of the Ograždenian Complex, Maleševska Mountain, *Geologica Balcanica*, **13**(2), 31 – 40.

Lips, A. L. W., White, S. H., & Wijbransb, J. R., 2000. Middle-Late Alpine thermotectonic evolution of the southern Rhodope Massif, Greece, *Geodinamica Acta*, **13**, 281 – 292.

Ludwig, K. R., 2001. Isoplot/Ex rev. 2.49, *Berkeley. California, Berkeley Geochronology Center, Special Publication*, **A**(1), 56.

Lyberis, N., 1984. Tectonic evolution of the North Aegean trough, *Geological Society, London, Special Publications*, **17**, 709 – 725.

Macheva, L., Peycheva, I., von Quadt, A., Zidarov, N., & Tarassova, E., 2006. Petrological, geochemical and isotope features of Lozen metagranite, Belasitza Mountain - evidence for widespread distribution of Ordovician metagranitoids in the Serbo-Macedonian Massif, SW Bulgaria, in *Bulgarian National Conference "GEOSCIENCES 2006"*.

Magganas, A., Bigazzi, G., Kyriakopoulos, K., & Balestrieri, M. L., 2004. Low-T thermochronological evolution of the Vrondou composite pluton (northern Greece) using apatite fission track analysis, in *5th International Symposium on Eastern Mediterranean Geology Thessaloniki, Greece, 14-20 April 2004*.

Majka, J. & Budzyń, B., 2006. Monazite breakdown in metapelites from Wedel Jarlsberg Land, Svalbard - Preliminary report, *Mineralogia Polonica*, **37**(1), 61 – 68.

Maltzaris, F., 1987. Geological map of Greece: Evzoni sheet, scale 1:50000, IGME, Athens.

Marakis, G., 1969. Geochronology of granites from Macedonia (Greece) (in greek), *Annales Géologiques des Pays Helléniques*, **21**, 121 – 152.

Marchev, P. & Filipov, P., 2012. First findings of Late Cretaceous magmatic rocks in the Pirin Mts, in *Bulgarian National Conference "GEOSCIENCES 2012"*.

Marchev, P. & Singer, B., 2002. $^{40}Ar/^{39}Ar$ geochronology of magmatism and hydrothermal activity of the Madjarovo base-precious metal ore district, eastern Rhodopes, Bulgaria, *Geological Society, London, Special Publications*, **204**, 137 – 150.

Marchev, P., Raicheva, R., Downes, H., Vaselli, O., Chiaradia, M., & Moritz, R., 2004. Compositional diversity of Eocene-Oligocene basaltic magmatism in the Eastern Rhodopes, SE Bulgaria: implications for genesis and tectonic setting, *Tectonophysics*, **393**(1 - 4), 301 – 328.

Marchev, P., von Quadt, A., Peytcheva, I., & Ovtcharova, M., 2006. The age and origin of the Chuchuliga and Rozino granites, Eastern Rhodopes, in *Bulgarian National Conference "GEOSCIENCES 2006"*.

Marchev, P., Kibarov, P., Spikings, R., Ovtcharova, M., Márton, I., & Moritz, R., 2010. $^{40}Ar/^{39}Ar$ and U-Pb geochronology of the Iran Tepe volcanic complex, Eastern Rhodopes, *Geologica Balcanica*, **39**(3), 3 – 12.

Marchev, P., Georgiev, S., Raicheva, R., Peytcheva, I., von Quadt, A., Ovtcharova, M., & Bonev, N., 2013. Adakitic magmatism in post-collisional setting: An example from the Early-Middle Eocene Magmatic Belt in Southern Bulgaria and Northern Greece, *Lithos*, **180 - 181**, 159 – 180.

Márton, I., Moritz, R., & Spikings, R., 2010. Application of low-temperature thermochronology to hydrothermal ore deposits: Formation, preservation and exhumation of epithermal gold systems from the Eastern Rhodopes, Bulgaria, *Tectonophysics*, **483**(3–4), 240 – 254.

Maruyama, S., Liou, J. G., & Terabayashi, M., 1996. Blueschists and Eclogites of the World and Their Exhumation, *International Geology Review*, **38**(6), 485 – 594.

Mascle, J. & Martin, L., 1990. Shallow structure and recent evolution of the Aegean Sea: A synthesis based on continuous reflection profiles, *Marine Geology*, **94**(4), 271 – 299.

McKenzie, D., 1978. Active tectonics of the Alpine-Himalayan belt: the Aegean Sea and surrounding regions, *Geophysical Journal International*, **55**(1), 217 – 265.

Meinhold, G. & Kostopoulos, D. K., 2013. The Circum-Rhodope Belt, northern Greece: Age, provenance, and tectonic setting, *Tectonophysics*, **595 - 596**, 55 – 68.

Meinhold, G., Kostopoulos, D., Reischmann, T., Frei, D., & BouDagher-Fadel, M. K., 2009. Geochemistry, provenance and stratigraphic age of metasedimentary rocks from the eastern Vardar suture zone, northern Greece, *Palaeogeography, Palaeoclimatology, Palaeoecology*, **277**, 199 – 225.

Meinhold, G., Kostopoulos, D., Frei, D., Himmerkus, F., & Reischmann, T., 2010. U-Pb LA-SF-ICP-MS zircon geochronology of the Serbo-Macedonian Massif, Greece: palaeotectonic constraints for Gondwana-derived terranes in the Eastern Mediterranean, *International Journal of Earth Sciences (Geol Rundsch)*, **99**(4), 813 – 832.

Mercier, J., 1981. Extensional-compressional tectonics associated with the Aegean arc: comparison with the Andean Cordillera of south Peru - north Bolivia, *Philosophical Transactions of the Royal Society of London*, **A300**, 337 – 355.

Mercier, J., Delibassis, N., Gauthier, A., Jarrige, J., Lemeille, F., Philip, H., Sébrier, M., & Sorel, D., 1979. La néotectonique de l'arc égéen, *Rev. Géol. Dyn. Geogr. Phys.*, **21**, 67 – 92.

Michailidis, K. M., 1991. Fe-cr spinel and ilmenite massive mineralization in metamorphic ultramafics from the askos area, northern greece, *Bulletin of the Geological Society of Greece*, **XXV**(2), 203 – 224.

Michard, A., Goffé, B., Liati, A., & Mountrakis, D., 1994a. Blueschist-facies assemblages in the peri-Rhodopian zone, and hints for an Eohellenic HP-LT belt in northern Greece, *Bulletin of the Geological Society of Greece*, **XXX**(1), 185 – 192.

Michard, A., Goffé, B., Liati, A., & Mountrakis, D., 1994b. Decouverte du facies schiste bleu clans les nappes du circum-rhodope: un element d'une ceinture hp-bt eohellenique en grece septentrionale?, *C.R. Acad. Sci. Paris*, **318**(2), 1535 – 1542.

Mishin, Y. A., Gerya, T. V., Burg, J.-P., & Connolly, J. A., 2008. Dynamics of double subduction: Numerical modeling, *Physics of the Earth and Planetary Interiors*, **171**(1 - 4), 280 – 295.

Molnar, P. & England, P., 1990. Temperatures, heat flux and frictional stress near major thrust faults, *Journal of Geophysical Research*, **95**(B4), 4833 – 4856.

Monod, O., 1964. *Etude géologique de massif de Chortiatis (Macédoine greque)*, Ph.D. thesis, Université de Paris.

Moulas, E., Kostopoulos, D., Connolly, J. A. D., & Burg, J.-P., 2013. P-T Estimates and Timing of the Sapphirine-Bearing Metamorphic Overprint in Kyanite Eclogites from Central Rhodope, Northern Greece, *Petrology*, **21**(5), 507 – 521.

Mposkos, E. & Liati, A., 1993. Metamorphic evolution of metapelites in the high-pressure terrane of the Rhodope Zone, Northern Greece, *Canadian Mineralogist*, **31**, 401 – 424.

Mposkos, E. & Wawrzenitz, N., 1995. Metapegmatites and pegmatites bracketing the time of HP-metamorphism in polymetamorphic rocks of the E-Rhodope, N. Greece: petrological and geochronological constraints, *Geological Society of Greece Special Publications*, **4**, 602 – 608.

Mposkos, E., Baziotis, I., & Proyer, A., 2012. Pressure-temperature evolution of eclogites from the Kechros complex in the Eastern Rhodope (NE Greece), *International Journal of Earth Sciences (Geol Rundsch)*, **101**(4), 973 – 993.

Mposkos, E. D. & Kostopoulos, D. K., 2001. Diamond, former coesite and supersilicic garnet in metasedimentary rocks from the Greek Rhodope: a new ultrahigh-pressure metamorphic province established, *Earth and Planetary Science Letters*, **192**(4), 497 – 506.

Mukasa, S. B., Haydoutov, I., Carrigan, C. W., & Kolcheva, K., 2003. Thermobarometry and $^{40}Ar/^{39}Ar$ ages of eclogitic and gneissic rocks in the sredna gora and rhodope terranes of bulgaria, *Journal of the Czech Geological Society*, **48**(1 - 2), 94 – 95.

Nagel, T. J., Schmidt, S., Janák, M., Froitzheim, N., Jahn-Awe, S., & Georgiev, N., 2011. The exposed base of a collapsing wedge: The Nestos Shear Zone (Rhodope Metamorphic Province, Greece), *Tectonics*, **30**, TC4009.

Naydenov, K., Peytcheva, I., von Quadt, A., Sarov, S., Kolcheva, K., & Dimov, D., 2013. The Maritsa strike-slip shear zone between Kostenets and Krichim towns, South Bulgaria - Structural, petrographic and isotope geochronology study, *Tectonophysics*, **595 - 596**, 69 – 89.

Negulescu, E., Săbău, G., & Massonne, H.-J., 2009. Chloritoid-Bearing Mineral Assemblages in High-Pressure Metapelites from the Bughea Complex, Leaota Massif (South Carpathians), *Journal of Petrology*, **50**(1), 103 – 125.

Norton, M., 1986. Late Caledonide Extension in western Norway: A response to extreme crustal thickening, *Tectonics*, **5**(2), 195 – 204.

Okay, A. I., 1989. An Exotic Eclogite/Blueschist Slice in a Barrovian Style Metamorphic Terrain, Alanya Nappes, Southern Turkey, *Journal of Petrology*, **30**(1), 107 – 132.

Ovtcharova, M., von Quadt, A., Heinrich, C. A., Frank, M., Kaiser-Rohrmeier, M., Peycheva, I., & Cherneva, Z., 2003. Triggering of hydrothermal ore mineralization in the Central Rhodopean Core Complex (Bulgaria) - Insight from isotope and geochronological studies on tertiary magmatism and migmatization, in *7th Biennial Meeting, Society for Geology Applied to Mineral Deposits, Mineral exploration and sustainable development*, pp. 367 – 370, Millpress, Rotterdam.

Pal'shin, I., Simov, S. D., Arakelyants, M., & Chernyshev, I., 1975. Absolute age of Alpine activations in Rhodope median massif, Bulgaria, *International Geology Review*, **17**(10), 1161 – 1168.

Panagos, A. G., Pe, G., & Varnavas, S. P., 1978. The volcanic rocks of Strymonikon-Metamorphosis, Central Macedonia, Greece, *Chemie der Erde*, **37**, 50 – 61.

Papadopoulos, C. & Kilias, A., 1985. Altersbeziehungen zwischen Metamorphose und Deformation im zentralen Teil des Serbomazedonischen Massivs (Vertiskos Gebirge, Nord-Griechenland) (in german with english abstract), *Geologische Rundschau*, **74**(1), 77 – 85.

Papanikolaou, D., 2009. Timing of tectonic emplacement of the ophiolites and terrane paleogeography in the Hellenides, *Lithos*, **108**(1 - 4), 262 – 280.

Papanikolaou, D. & Panagopoulos, A., 1981. On the structural style of southern Rhodope, Greece, *Geologica Balcanica*, **11**(3), 13 – 22.

Papanikolaou, D., Alexandri, M., Nomikou, P., & Ballas, D., 2002. Morphotectonic structure of the western part of the North Aegean Basin based on swath bathymetry, *Marine Geology*, **190**(1 - 2), 465 – 492.

Papanikolaou, D., Alexandri, M., & Nomikou, P., 2006. Active faulting in the north Aegean basin, *Geological Society of America Special Papers*, **409**, 189 – 209.

Papanikolaou, D. J., 2013. Tectonostratigraphic models of the Alpine terranes and subduction history of the Hellenides, *Tectonophysics*, **595 - 596**, 1 – 24.

Papazachos, B., Mountrakis, D., Psilovikos, A., & Leventakis, G., 1979. Surface fault traces and fault plane solutions of May-June 1978 major shocks in the Thessaloniki area, *Tectonophysics*, **53**(3 - 4), 171 – 183.

Papazachos, C. B., 1998. Crustal P- and S-velocity structure of the Serbomacedonian Massif (Northern Greece) obtained by non-linear inversion of traveltimes, *Geophysical Journal International*, **134**(1), 25 – 39.

Parra, T., Vidal, O., & Jolivet, L., 2002. Relation between the intensity of deformation and retrogression in blueschist metapelites of Tinos Island (Greece) evidenced by chlorite-mica local equilibria, *Lithos*, **63**(1 - 2), 41 – 66.

Pecskay, Z., Harkovska, A., Petrov, P. S., & Popov, M., 2011. K-Ar dating of Kozhuh volcanic body (SW Bulgaria), *Comptes rendus de l'Académie bulgare des Sciences*, **64**(2), 263 – 268.

Perraki, M., Proyer, A., Mposkos, E., Kaindl, R., & Hoinkes, G., 2006. Raman microspectroscopy on diamond, graphite and other carbon polymorphs from the ultrahigh-pressure metamorphic Kimi Complex of the Rhodope Metamorphic Province, NE Greece, *Earth and Planetary Science Letters*, **241**(3 - 4), 672 – 685.

Peytcheva, I., Kostitsin, Y., Salnikova, E., Kamenov, B., & Klain, L., 1998. Rb-Sr and U-Pb isotope data for the Rila-Rhodope batholith (in bulgarian with english abstract), *Geochemistry, Mineralogy and Petrology*, **35**, 93 – 105.

Peytcheva, I., von Quadt, A., Naydenov, K., Sarov, S., Dimov, D., & Voinova, E., 2007. U-Pb zircon-xenotime-monazite dating and Hf-isotope tracing to distinguish Cretaceous and Paleogene granitoids in the Western Rhodopes and Rila Mountain, in *Bulgarian National Conference "GEOSCIENCES 2007"*.

Peytcheva, I., von Quadt, A., Sarov, S., Voinova, E., & Kolcheva, K., 2009. Ordovician protoliths of metamorphic rocks in Eastern Pirin - Western Rhodopes: Are they part of the Ograzhden Unit?, in *Bulgarian National Conference "GEOSCIENCES 2009"*.

Philippon, M., Brun, J.-P., & Gueydan, F., 2012. Deciphering subduction from exhumation in the segmented Cycladic Blueschist Unit (Central Aegean, Greece), *Tectonophysics*, **524 - 525**, 116 – 134.

Poli, G., Christofides, G., Koroneos, A., Soldatos, T., Perugini, D., & Langone, A., 2009. Early Triassic granitic magmatism - Arnea and Kerkini granitic complexes - In Vertiskos Unit (Serbo-Macedonian Massif, north-eastern Greece) and its significance in the geodynamic evolution of the area, *Acta Volcanologica*, **20 - 21**(1 - 2), 47 – 70.

Powell, R. & Holland, T., 1990. Calculated mineral equilibria in the pelite system, KFMASH (K_2O-FeO-MgO-Al_2O_3-SiO_2-H_2O), *American Mineralogist*, **75**, 367 – 380.

Psilovikos, A. & Syrides, G. E., 1983. Stratigraphy, sedimentation, and palaeogeography of the Strymon Basin, eastern Macedonia/northern Aegean Sea, Greece, *Clausthaler Geologische Abhandlungen*, **44**, 55 – 87.

Ramberg, H., 1981. *Gravity, Deformation, And The Earth's Crust: In Theory, Experiments, And Geological Applications*, 2nd revised edition, Academic Press Inc., London.

Ramsay, J. G., 1967. *Folding and Fracturing of Rocks*, New York: McGraw-Hill.

Regenauer-Lieb, K., Weinberg, R. F., & Rosenbaum, G., 2006. The effect of energy feedbacks on continental strength, *Nature*, **442**, 67 – 70.

Reischmann, T. & Kostopoulos, D., 2002. Timing of UHPM in metasediments from the Rhodope Massif, N Greece, in *Goldschmidt Conference Abstracts*, no. A634.

Rey, P., Teyssier, C., & Whitney, D., 2009a. Extension rates, crustal melting, and core complex dynamics, *Geology*, **37**(5), 391 – 394.

Rey, P., Teyssier, C., & Whitney, D., 2009b. The role of partial melting and extensional strain rates in the development of metamorphic core complexes, *Tectonophysics*, **477**(3 - 4), 135 – 144.

Ricou, L.-E., 1965. *Contribution a l'étude géologique de la bordure sud-ouest du Massif Serbo-macédonien aux environs de Salonique*, Ph.D. thesis, Université de Paris.

Ricou, L.-E. & Godfriaux, I., 1994. The Thessaloniki klippe: a nappe of Vertiskos orogin emplaced upon the Mesozoic flysches of the Vardar basin, *Bulletin of the Geological Society of Greece*, **XXX**(1), 69 – 78.

Ricou, L.-E., Burg, J.-P., Godfriaux, I., & Ivanov, Z., 1998. Rhodope and Vardar: the metamorphic and the olistostromic paired belts related to the Cretaceous subduction under Europe, *Geodinamica Acta*, **11**(6), 285 – 309.

Ring, U., Glodny, J., Will, T., & Thomson, S., 2010. The Hellenic Subduction System: High-Pressure Metamorphism, Exhumation, Normal Faulting, and Large-Scale Extension, *Annual Review of Earth and Planetary Sciences*, **38**, 45 – 76.

Robertson, A. H., 2002. Overview of the genesis and emplacement of Mesozoic ophiolites in the Eastern Mediterranean Tethyan region, *Lithos*, **65**(1 - 2), 1 – 67.

Robertson, A. H., Trivić, B., Derić, N., & Bucurc, I. I., 2013. Tectonic development of the Vardar ocean and its margins: Evidence from the Republic of Macedonia and Greek Macedonia, *Tectonophysics*, **595 - 596**(4), 25 – 54.

Roussos, N., 1994. Stratigraphy and paleogeographic evolution of Palaeocene molassic basins of N. aegean, *Bulletin of the Geological Society of Greece*, **XXX**(2), 275 – 294.

Roussos, N. & Lyssimachou, T., 1991. Structure of the Central North Aegean Trough: an active strike-slip deformation zone, *Basin Research*, **3**(1), 39 – 48.

Royden, L. H., 1993. Evolution of retreating subduction boundaries formed during continental collision, *Tectonics*, **12**(3), 629 – 638.

Royden, L. H. & Papanikolaou, D. J., 2011. Slab segmentation and late Cenozoic disruption of the Hellenic arc, *Geochemistry Geophysics Geosystems*, **12**, Q03010.

Sahu, H. S., Raab, M. J., Kohn, B. P., Gleadow, A. J., & Bal, K. D., 2013. Thermal history of the Krishna - Godavari basin, India: Constraints from apatite fission track thermochronology and organic maturity data, *Journal of Asian Earth Sciences*, **73**, 1 – 20.

Sakellariou, D. & Dürr, S., 1993. Geological structure of the Serbo-Macedonian massif in NE Chalkidiki peninsula (in greek with english abstract), *Bulletin of the Geological Society of Greece*, **XXVIII**(1), 179 – 193.

Sambridge, M., Gallagher, K., Jackson, A., & Rickwood, P., 2006. Trans-dimensional inverse problems, model comparison and the evidence, *Geophysical Journal International*, **167**(2), 528 – 542.

Sanchez, G., Rolland, Y., Jolivet, M., Brichau, S., Corsini, M., & Carter, A., 2011. Exhumation controlled by transcurrent tectonics: the Argentera - Mercantour massif (SW Alps), *Terra Nova*, **23**(2), 116 – 126.

Schenker, F., Gerya, T., & Burg, J.-P., 2012. Bimodal behavior of extended continental lithosphere: Modeling insight and application to thermal history of migmatitic core complexes, *Tectonophysics*, **579**, 88 – 103.

Schmidt, S., Nagel, T. J., & Froitzheim, N., 2010. A new occurrence of microdiamond-bearing metamorphic rocks, SW Rhodopes, Greece, *European Journal of Mineralogy*, **22**, 189 – 198.

Sidiropoulos, N. S., 1991. *Lithology, geochemistry, tectonic and metamorphism of the Disoro mountain area (northwestern part of the Vertiskos unit, North Greece) (in greek)*, Ph.D. thesis, University of Thessaloniki, Greece.

Simpson, C. & Schmid, S. M., 1983. An evaluation of criteria to deduce the sense of movement in sheared rocks, *Geological Society of America Bulletin*, **94**(11), 1281 – 1288.

Sircombe, K., 2004. Agedisplay: an EXCEL workbook to evaluate and display univariate geochronological data using binned frequency histograms and probability density distributions, *Computers & Geosciences*, **30**, 21 – 31.

Siyako, M. & Huvaz, O., 2007. Eocene stratigraphic evolution of the Thrace Basin, Turkey, *Sedimentary Geology*, **198**(1 - 2), 75 – 91.

Smye, A. J., Greenwood, L. V., & Holland, T. J. . B., 2010. Garnet-chloritoid-kyanite assemblages: eclogite facies indicators of subduction constraints in orogenic belts, *Journal of Metamorphic Geology*, **28**(7), 753 – 768.

Snel, E., Mărunţeanu, M., & Meulenkamp, J. E., 2006. Calcareous nannofossil biostratigraphy and magnetostratigraphy of the Upper Miocene and Lower Pliocene of the Northern Aegean (Orphanic Gulf-Strimon Basin areas), Greece, *Palaeogeography, Palaeoclimatology, Palaeoecology*, **238**, 125 – 150.

Sokoutis, D., Brun, J.-P., van den Driessche, J., & Pavlides, S., 1993. A major Oligo-Miocene detachment in southern Rhodope controlling north Aegean extension, *Journal of the Geological Society, London*, **150**, 243 – 246.

Sokoutis, D., Burg, J.-P., Bonini, M., Corti, G., & Cloetingh, S., 2005. Lithospheric-scale structures from the perspective of analogue continental collision, *Tectonophysics*, **406**, 1 – 15.

Soldatos, T., Koroneos, A., Christofides, G., & Moro, A. D., 2001. Geochronology and origin of the Elatia plutonite (Hellenic Rhodope Massif, N. Greece) constrained by new Sr isotopic data, *N. Jb. Miner. Abh.*, **176**(2), 179 – 209.

Soldatos, T., Koroneos, A., Kamenov, B. K., Peytcheva, I., von Quadt, A., Christofides, G., Zheng, X., & Sang, H., 2008. New U-Pb and Ar-Ar mineral ages for the Barutin-Buynovo-Elatia-Skaloti-Paranesti batholith (Bulgaria and Greece): Refinement of its debatable age, *Geochemistry, Mineralogy and Petrology*, **46**, 85 – 102.

Spear, F. & Franz, G., 1986. P-t evolution of metasediments from the Eclogite Zone, south-central Tauern Window, Austria, *Lithos*, **19**(3 - 4), 219 – 234.

Spear, F. S. & Cheney, J. T., 1989. A petrogenetic grid for pelitic schists in the system SiO_2-Al_2O_3-FeO-MgO-K_2O-H_2O, *Contributions to Mineralogy and Petrology*, **101**(2), 149 – 164.

Stampfli, G. & Borel, G., 2002. A plate tectonic model for the Paleozoic and Mesozoic constrained by dynamic plate boundaries and restored synthetic oceanic isochrons, *Earth and Planetary Science Letters*, **196**(1 - 2), 17 – 33.

Stephenson, J., Gallagher, K., & Holmes, C., 2006. Low temperature thermochronology and strategies for multiple samples: 2: Partition modelling for 2d/3d distributions with discontinuities, *Earth and Planetary Science Letters*, **241**(3 - 4), 557 – 570.

Syrides, G. E., 1998. Paratethyan mollusc faunas from the Neogene of Macedonia and Thrace, Northern Greece, *Romanian Journal of Stratigraphy*, **78**, 171 – 180.

Tajčmanová, L., Connolly, J. A. D., & Cesare, B., 2009. A thermodynamic model for titanium and ferric iron solution in biotite, *Journal of Metamorphic Geology*, **27**(2), 153 – 165.

Thielicke, W. & Stamhuis, E. J., 2014. PIVlab - Time-Resolved Digital Particle Image Velocimetry Tool for MATLAB (version: 1.35).

Thompson, A. B., 1976. Mineral reactions in pelitic rocks; I, Prediction of P-T-X(Fe-Mg) phase relations, *American Journal of Sciences*, **276**, 401 – 424.

Tirel, C., Brun, J.-P., & Burov, E., 2004a. Thermomechanical modeling of extensional gneiss domes, *Special Publication, Geological Society of America*, **380**, 67 – 78.

Tirel, C., Gueydan, F., Tiberi, C., & Brun, J.-P., 2004b. Aegean crustal thickness inferred from gravity inversion: Geodynamical implications, *Earth and Planetary Science Letters*, **228**(3 - 4), 267 – 280.

Tirel, C., Brun, J.-P., & Sokoutis, D., 2006. Extension of thickened and hot lithospheres: Inferences from laboratory modeling, *Tectonics*, **25**(1).

Tirel, C., Brun, J.-P., & Burov, E., 2008. Dynamics and structural development of metamorphic core complexes, *Journal of Geophysical Research*, **113**(B4).

Tirel, C., Gautier, P., van Hinsbergen, D. J. J., & Wortel, M. J. R., 2009. Sequential development of interfering metamorphic core complexes: numerical experiments and comparison with the Cyclades, Greece, *Geological Society, London, Special Publications*, **311**, 257 – 292.

Tirel, C., Brun, J.-P., Burov, E., Wortel, M., & Lebedev, S., 2013. A plate tectonics oddity: Caterpillar-walk exhumation of subducted continental crust, *Geology*, **41**(5), 555 – 558.

Tompouloglou, C., 1981. *Les minéralisations Tertiaires, type cuivre porphyrique, du Massif Serbo-Macédonien (Macédoine Grèce) dans leur contexte magmatique (avec un traitement géostatistique pour les donnees du prospect d'Alexia)*, Ph.D. thesis, École Nationale Superieure des Mines de Paris.

Tranos, M., Kilias, A., & Mountrakis, D., 1999. Geometry and kinematics of the Tertiary post-metamorphic Circum Rhodope Belt Thrust System (CRBTS), Northern Greece, *Bulletin of the Geological Society of Greece*, **XXXIII**, 5 – 16.

Tranos, M. D., Kilias, A. A., & Mountrakis, D. M., 1993. Emplacement and deformation of the Sithonia granitoid pluton (Macedonia, Hellas), *Bulletin of the Geological Society of Greece*, **XXVIII**(1), 195 – 210.

Tranos, M. D., Papadimitriou, E. E., & Kilias, A. A., 2003. Thessaloniki-Gerakarou Fault Zone (TGFZ): the western extension of the 1978 Thessaloniki earthquake fault (Northern Greece) and seismic hazard assessment, *Journal of Structural Geology*, **25**(12), 2109 – 2123.

Tucholke, B. E. & Lin, J., 1994. A geological model for the structure of ridge segments in slow spreading ocean crust, *Journal of Geophysical Research*, **99**(B6), 11937 – 11958.

Turpaud, P. & Reischmann, T., 2010. Characterisation of igneous terranes by zircon dating: implications for UHP occurrences and suture identification in the Central Rhodope, northern Greece, *International Journal of Earth Sciences (Geol Rundsch)*, **99**(3), 567 – 591.

van den Driessche, J. & Brun, J.-P., 1987. Rolling structures at large shear strain, *Journal of structural geology*, **9**(5-6), 691 – 704.

van den Driessche, J. & Brun, J.-P., 1989. Un modèle cinématique de l'extension paléozoique supérieur dans le sud du massif central, *Comptes Rendus de l'Académie des Sciences, Paris*, **309**, 1607 – 1613.

van Hinsbergen, D. J. J., Hafkenscheid, E., Spakman, W., Meulenkamp, J. E., & Wortel, R., 2005a. Nappe stacking resulting from subduction of oceanic and continental lithosphere below Greece, *Geology*, **33**(4), 325 – 328.

van Hinsbergen, D. J. J., Langereis, C. G., & Meulenkamp, J. E., 2005b. Revision of the timing, magnitude and distribution of neogene rotations in the western aegean region, *Tectonophysics*, **396**(1 - 2), 1 – 34.

von Quadt, A. & Peytcheva, I., 2005. The southern extension of the Srednogorie type upper Cretaceous magmatism in Rila-Western Rhodopes: constraints from isotope-geochronological and geochemical data, in *Bulgarian National Conference "GEO-SCIENCES 2005"*.

von Quadt, A., Peytcheva, I., Sarov, S., Naydenov, K., & Georgiev, N., 2008. Metamorphic rocks from Dospat area of Western Rhodopes - conventional and in situ U-Pb zircon dating, isotope tracing and correlations, in *Bulgarian National Conference "GEOSCIENCES 2008"*.

von Quadt, A., Sarov, S., Peytcheva, I., & Voinova, E., 2009. Jurassic metagranitoids south of the West-Rhodope batholith - conventional and in situ U-Pb zircon analyses, Sr-Nd-Hf isotope tracing and geodynamic constraints, in *Bulgarian National Conference "GEOSCIENCES 2009"*.

von Quadt, A., Peytcheva, I., Sarov, S., & Liati, A., 2010. Late Cretaceous subduction and magmatism in the Rhodopes: geochronological and isotope-geochemical evidence, in *Bulgarian National Conference "GEOSCIENCES 2010"*.

Vuichard, J.-P. & Ballèvre, M., 1988. Garnet-chloritoid equilibria in eclogitic pelitic rocks from the Sesia zone (Western Alps): their bearing on phase relations in high pressure metapelites, *Journal of Metamorphic Geology*, **6**(2), 135 – 157.

Wang, X., Zattin, M., Li, J., Song, C., Peng, T., Liu, S., & Liu, B., 2011. Eocene to Pliocene exhumation history of the Tianshui-Huicheng region determined by Apatite fission track thermochronology: Implications for evolution of the northeastern Tibetan Plateau margin, *Journal of Asian Earth Sciences*, **42**, 97 – 110.

Wawrzenitz, N. & Krohe, A., 1998. Exhumation and doming of the Thasos metamorphic core complex (S Rhodope, Greece): structural and geochronological constraints, *Tectonophysics*, **285**(3 - 4), 301 – 332.

Wei, C. & Powell, R., 2003. Phase relations in high-pressure metapelites in the system KFMASH (K_2O-FeO-MgO-Al_2O_3-SiO_2-H_2O) with application to natural rocks, *Contributions to Mineralogy and Petrology*, **145**(3), 301 – 315.

Wei, C. & Powell, R., 2006. Calculated Phase Relations in the System NCKFMASH (Na_2O-CaO-K_2O-FeO-MgO-Al_2O_3-SiO_2-H_2O) for High-Pressure Metapelites, *Journal of Petrology*, **42**(2), 385 – 408.

Wernicke, B., 1981. Low-anle normal faults in the Basin and Range Province: nappe tectonics in an extending orogen, *Nature*, **291**, 645 – 648.

Wernicke, B., 1985. Uniform-sense normal simple shear of the continental lithosphere, *Canadian Journal of Earth Sciences*, **22**(1), 108 – 125.

White, R. W., Powell, R., & N., P. G., 2003. A mineral equilibria study of the hydrothermal alteration in mafic greenschist facies rocks at Kalgoorlie, Western Australia, *Journal of Metamorphic Geology*, **21**(5), 455 – 468.

White, S. H., Powell, R., Holland, T., & Worley, B. A., 2000. The effect of TiO_2 and Fe_2O_3 on metapelitic assemblages at greenschist and amphibolite facies conditions: mineral equilibria calculations in the system K_2O-FeO-MgO-Al_2O_3-SiO_2H_2O-TiO_2-Fe_2O_3, *Journal of Metamorphic Geology*, **18**(5), 497 – 511.

Whitney, D., Teyssier, C., Toraman, E., Seaton, N. C. A., & Fayon, A. K., 2011. Metamorphic and tectonic evolution of a structurally continuous blueschist-to-Barrovian terrane, Sivrihisar Massif, Turkey, *Journal of Metamorphic Geology*, **29**(2), 193 – 212.

Whitney, D. L., Teyssier, C., Rey, P., & Buck, W. R., 2013. Continental and oceanic core complexes, *Geological Society of America Bulletin*, **125**(3/4), 273 – 298.

Wijbrans, J. R. & McDougall, I., 1986. $^{40}Ar/^{39}Ar$ dating of white micas from an alpine high-pressure metamorphic belt on Naxos (Greece): the resetting of the argon isotopic system, *Contributions to Mineralogy and Petrology*, **93**(2), 187 – 194.

Wijns, C., Weinberg, R., Gessner, K., & Moresi, L., 2005. Mode of crustal extension determined by rheological layering, *Earth and Planetary Science Letters*, **236**(1 - 2), 120 – 134.

Wuthrich, E., 2009. *Low temperature thermochronology of the North Aegean Rhodope Massif*, Ph.D. thesis, Swiss Federal Institute of Technology, Zurich.

Xu, G., Will, T. M., & P, R., 1994. A calculated petrogenetic grid for the system K_2O-FeO-MgO-Al_2O_3-SiO_2-H_2O, with particular reference to contact-metamorphosed pelites, *Journal of Metamorphic Geology*, **12**(1), 99 – 119.

Xydas, S. & Efstratiades, G., 1983. Geological map of Greece: Koufalia sheet, scale 1:50000, IGME, Athens.

Yang, W., Jolivet, M., Dupont-Nivet, G., & Guo, Z., 2013. Mesozoic - Cenozoic tectonic evolution of southwestern Tian Shan: Evidence from detrital zircon U/Pb and apatite fission track ages of the Ulugqat area, Northwest China, *Gondwana Research*, **In Press, Corrected Proof**.

Yi, Y., Carter, A., Xia, B., Ge, L., Brichau, S., & Xiaoqiong, H., 2009. A fission-track and (U-Th)/He thermochronometric study of the northern margin of the South China Sea: An example of a complex passive margin, *Tectonophysics*, **474**(3 - 4), 584 – 594.

Zachariadis, P., 2007. *Ophiolites of the eastern Vardar Zone, N. Greece*, Ph.D. thesis, Universität Mainz, Germany.

Zagorchev, I., 1976. Tectonic, metamorphic and magmatic markers in the polycyclic ultrametamorphic Ograzdenian complex, *Geologica Balcanica*, **6**(2), 17 – 33.

Zervas, S., 1979. Age determination by the $^{87}Rb/^{87}Sr$ method of some pegmatites in the area of Lagada (Macedonia, Greece) (in greek), *Annales Géologiques des Pays Helléniques*, **XXX**(1), 143 – 152.

Zidarov, N., Peytcheva, I., von Quadt, A., Andreichev, V., Macheva, L., & Titorenkova, R., 2003. Timing and magma souces of metagranites from the Serbo-Macedonian Massif (Ograzhden and Maleshevska Mountains, SW Bulgaria): Constraints from U-Pb and Hf-zircon and Sr whole rock isotope studies, in *Bulgarian Geological Society, Annual Scientific Conference, Sofia, December 11-12*.

Appendix A1

Supplementary $^{40}Ar/^{39}Ar$ step heating data for the samples presented in Chapter 4.

Step	$^{40}Ar^*/^{39}Ar$	2σ	$^{36}Ar/^{40}Ar$ (x1000)	2σ	$^{39}Ar/^{40}Ar$	2σ	$^{37}Ar/^{39}Ar$	2σ	Rel. ^{39}Ar (%)	$^{40}Ar^*$ (%)	Age	2σ
Vertiskos Unit												
SM15	*white mica*	*A2*										
1	11.810	3.887	3.152	0.071	0.006	0.000	11.896	13.636	0.20	6.852	83.12	26.74
2	13.168	1.147	1.820	0.121	0.035	0.001	1.025	7.419	0.62	46.200	92.44	7.85
3	14.151	0.125	0.866	0.019	0.053	0.000	0.307	0.947	6.72	74.369	99.15	0.85
4	14.243	0.063	0.416	0.009	0.062	0.000	0.283	0.412	16.09	87.647	99.78	0.43
5	13.725	0.052	0.185	0.007	0.069	0.000	0.089	0.329	21.31	94.474	96.25	0.35
6	13.633	0.052	0.180	0.007	0.069	0.000	0.004	0.346	19.08	94.622	95.62	0.35
7	13.379	0.062	0.061	0.011	0.073	0.000	0.331	0.515	13.23	98.127	93.88	0.42
8	13.267	0.068	0.089	0.013	0.073	0.000	0.000	0.582	10.33	97.306	93.11	0.46
9	13.204	0.129	0.063	0.029	0.074	0.000	0.450	1.309	4.68	98.082	92.69	0.88
10	13.205	0.194	0.030	0.045	0.075	0.000	0.811	2.038	3.23	99.027	92.70	1.33
11	13.771	0.139	0.020	0.030	0.072	0.000	0.000	1.405	4.51	99.335	96.56	0.95
	J = 0.003983	0.21 (1σ %)								*Total age*	95.79	1.52
SM15	*white mica*	*A3*										
1	13.908	2.357	1.925	0.225	0.031	0.002	2.724	23.727	1.42	43.102	97.50	16.08
2	14.124	0.106	0.498	0.018	0.060	0.000	0.149	0.888	35.00	85.234	98.97	0.72
3	13.630	0.094	0.203	0.018	0.069	0.000	0.145	0.859	39.56	93.941	95.60	0.64
4	13.563	0.156	0.137	0.032	0.071	0.000	0.584	1.520	14.25	95.878	95.14	1.07
5	13.399	0.350	0.083	0.062	0.073	0.001	0.943	2.667	4.57	97.481	94.02	2.39
6	13.924	0.510	0.000	0.090	0.073	0.002	2.960	3.727	2.87	101.297	97.60	3.48
7	12.985	0.695	0.193	0.135	0.073	0.002	4.011	6.226	2.34	94.241	91.19	4.76
	J = 0.003983	0.21 (1σ %)								*Total age*	96.63	0.63
SM15	*white mica*	*A7*										
1	14.082	0.077	0.382	0.011	0.063	0.000	0.000	0.115	8.09	88.670	98.68	0.52
2	13.728	0.446	1.495	0.051	0.041	0.001	0.000	2.402	0.74	55.800	96.27	3.05
3	14.805	0.200	0.492	0.028	0.058	0.001	0.479	1.135	1.35	85.420	103.61	1.36
4	14.932	0.149	0.538	0.021	0.056	0.000	0.000	1.001	2.05	84.070	104.47	1.01
5	15.089	0.065	0.171	0.004	0.063	0.000	0.025	0.169	12.03	94.890	105.54	0.44
6	15.208	0.067	0.068	0.004	0.064	0.000	0.050	0.171	10.92	97.930	106.35	0.45
7	15.107	0.063	0.059	0.004	0.065	0.000	0.132	0.136	12.23	98.200	105.66	0.43
8	14.834	0.073	0.059	0.007	0.066	0.000	0.000	0.184	8.65	98.190	103.80	0.50
9	14.590	0.066	0.033	0.007	0.068	0.000	0.108	0.225	10.45	98.960	102.15	0.45
10	14.228	0.066	0.026	0.007	0.070	0.000	0.000	0.159	8.98	99.170	99.68	0.45
11	13.867	0.081	0.026	0.007	0.072	0.000	0.000	0.310	7.42	99.150	97.22	0.55
12	14.426	0.133	0.026	0.009	0.069	0.001	0.067	0.378	3.81	99.160	101.03	0.91
13	14.507	0.275	0.021	0.021	0.069	0.001	0.984	0.908	1.78	99.320	101.58	1.87
14	14.077	0.094	0.024	0.015	0.071	0.000	0.981	0.427	4.24	99.210	98.65	0.64
15	13.639	0.139	0.017	0.025	0.073	0.001	0.757	0.684	2.78	99.430	95.66	0.95
16	15.035	0.096	0.013	0.013	0.066	0.000	0.073	0.322	4.47	99.540	105.17	0.65
	J = 0.003983	0.21 (1σ %)								*Total age*	102.50	0.45
SM42	*biotite*	*A10*										
1	4.322	2.115	3.284	0.043	0.007	0.000	2.111	2.732	1.50	2.964	30.86	14.98
2	8.815	0.216	1.707	0.033	0.056	0.000	0.000	1.063	3.84	49.533	62.40	1.50
3	11.605	0.174	1.149	0.024	0.057	0.000	0.000	0.906	4.52	66.023	81.71	1.20
4	14.009	0.134	0.961	0.018	0.051	0.000	0.080	0.540	6.97	71.558	98.19	0.91
5	14.714	0.153	0.914	0.019	0.050	0.000	0.044	0.895	5.64	72.943	102.99	1.04
6	16.165	0.171	0.881	0.019	0.046	0.000	0.843	0.734	5.08	73.931	112.83	1.16
7	17.788	0.131	0.821	0.015	0.043	0.000	0.000	0.768	5.79	75.710	123.78	0.88
8	19.587	0.148	0.709	0.014	0.040	0.000	0.006	0.693	5.39	79.016	135.84	0.99
9	20.630	0.122	0.497	0.012	0.041	0.000	0.595	0.757	6.48	85.294	142.80	0.81
10	20.585	0.279	0.375	0.009	0.043	0.001	0.369	0.550	6.65	88.886	142.50	1.86
11	20.686	0.299	0.317	0.011	0.044	0.001	0.130	0.771	6.30	90.600	143.17	1.99
12	20.503	0.177	0.293	0.015	0.045	0.000	0.000	1.064	4.85	91.304	141.95	1.18
13	20.541	0.158	0.352	0.012	0.044	0.000	0.000	0.823	5.61	89.546	142.21	1.05
14	21.167	0.118	0.332	0.010	0.043	0.000	0.000	0.585	8.61	90.164	146.37	0.78
15	21.636	0.108	0.173	0.009	0.044	0.000	0.000	0.612	8.06	94.848	149.48	0.71
16	21.439	0.116	0.093	0.012	0.045	0.000	0.172	0.776	7.38	97.211	148.17	0.77
17	20.882	0.175	0.126	0.018	0.046	0.000	0.000	1.160	3.34	96.230	144.47	1.16
18	19.803	0.155	0.144	0.019	0.048	0.000	0.000	1.104	3.98	95.691	137.28	1.03
	J = 0.003983	0.21 (1σ %)								*Total age*	128.11	0.62
SM42	*white mica*	*A9*										
1	18.652	2.362	1.811	0.168	0.025	0.001	5.058	7.709	0.31	46.465	129.58	15.84
2	25.128	0.116	0.030	0.009	0.039	0.000	0.265	0.232	8.73	99.077	172.49	0.76
3	26.954	0.597	0.056	0.056	0.036	0.001	0.411	1.902	1.25	98.323	184.40	3.88
4	24.251	0.175	0.557	0.015	0.034	0.000	0.357	0.483	5.58	83.510	166.74	1.15
5	20.661	0.070	0.094	0.004	0.047	0.000	0.051	0.098	25.82	97.163	143.00	0.46
6	20.472	0.068	0.021	0.004	0.049	0.000	0.019	0.076	25.49	99.338	141.75	0.45
7	22.549	0.085	0.013	0.006	0.044	0.000	0.112	0.139	13.97	99.562	155.53	0.56
8	22.806	0.208	0.028	0.022	0.043	0.000	0.198	0.569	3.67	99.117	157.22	1.37
9	21.779	0.306	0.020	0.036	0.046	0.000	0.640	0.900	2.44	99.354	150.43	2.03
10	20.664	0.686	0.010	0.086	0.048	0.001	1.142	1.938	1.06	99.650	143.03	4.57
11	21.286	0.090	0.008	0.008	0.047	0.000	0.057	0.191	11.66	99.716	147.16	0.60
	J = 0.003983	0.21 (1σ %)								*Total age*	150.03	0.65
SM42	*white mica*	*A6*										
1	12.255	3.168	2.762	0.152	0.015	0.001	0.000	24.957	0.13	18.391	86.18	21.76
2	20.926	1.109	1.120	0.098	0.032	0.001	0.000	7.283	0.33	66.873	144.77	7.37
3	20.791	0.540	0.906	0.055	0.035	0.000	0.236	4.393	0.91	73.204	143.87	3.59
4	20.830	0.063	0.106	0.004	0.047	0.000	0.032	0.241	17.30	96.831	144.13	0.42
5	19.707	0.060	0.093	0.004	0.049	0.000	0.000	0.230	18.31	97.194	136.65	0.40
6	19.962	0.081	0.140	0.008	0.048	0.000	0.140	0.485	8.63	95.832	138.34	0.54
7	20.096	0.074	0.080	0.008	0.049	0.000	0.064	0.537	4.96	97.605	139.24	0.50
8	19.708	0.074	0.021	0.007	0.050	0.000	0.068	0.472	4.89	99.316	136.65	0.49
9	19.537	0.067	0.043	0.007	0.051	0.000	0.000	0.452	8.76	98.673	135.51	0.45
10	20.005	0.065	0.008	0.006	0.050	0.000	0.622	0.374	7.20	99.721	138.64	0.43
11	20.108	0.062	0.021	0.005	0.049	0.000	0.000	0.336	10.77	99.326	139.32	0.41
12	19.887	0.140	0.035	0.019	0.050	0.000	0.000	1.298	2.75	98.911	137.85	0.93
13	19.521	0.113	0.056	0.014	0.050	0.000	0.000	0.956	3.16	98.307	135.41	0.75
14	19.861	0.171	0.026	0.023	0.050	0.000	0.000	1.596	2.81	99.173	137.67	1.14
15	19.739	0.066	0.012	0.006	0.050	0.000	0.000	0.384	9.10	99.583	136.86	0.44
	J = 0.003983	0.21 (1σ %)								*Total age*	138.62	0.58

Step	$^{40}Ar^*/^{39}Ar$	2σ	$^{36}Ar/^{40}Ar$ (x1000)	2σ	$^{39}Ar/^{40}Ar$	2σ	$^{37}Ar/^{39}Ar$	2σ	Rel. ^{39}Ar (%)	$^{40}Ar^*$ (%)	Age	2σ
Vertiskos Unit	(continue)											
SM42	*white mica*	*A7*										
1	8.850	2.997	3.224	0.049	0.005	0.000	7.359	20.579	0.10	4.740	62.65	20.85
2	18.085	1.106	1.267	0.096	0.035	0.001	10.845	8.858	0.16	62.548	125.78	7.43
3	18.849	0.557	0.819	0.054	0.040	0.001	0.683	4.172	0.37	75.766	130.91	3.73
4	18.270	0.160	0.188	0.021	0.052	0.000	0.056	1.086	3.04	94.389	127.02	1.07
5	17.829	0.052	0.018	0.003	0.056	0.000	0.213	0.130	18.75	99.425	124.06	0.35
6	17.937	0.054	0.010	0.003	0.056	0.000	0.039	0.128	18.84	99.651	124.79	0.36
7	18.255	0.052	0.009	0.003	0.055	0.000	0.036	0.211	15.62	99.679	126.92	0.35
8	18.880	0.055	0.015	0.003	0.053	0.000	0.045	0.214	13.08	99.504	131.11	0.37
9	18.855	0.068	0.022	0.008	0.053	0.000	0.000	0.515	5.78	99.300	130.95	0.45
10	18.359	0.446	0.024	0.079	0.054	0.000	0.000	5.041	1.47	99.229	127.62	2.99
11	18.130	0.380	0.020	0.068	0.055	0.000	0.000	4.287	1.76	99.349	126.08	2.55
12	18.253	0.564	0.014	0.101	0.055	0.000	0.000	6.378	1.15	99.523	126.91	3.78
13	18.139	0.306	0.032	0.054	0.055	0.000	0.000	3.448	2.29	99.014	126.14	2.05
14	18.530	0.220	0.017	0.038	0.054	0.000	0.000	2.438	2.95	99.437	128.77	1.48
15	18.263	0.098	0.015	0.014	0.055	0.000	0.000	0.871	4.12	99.494	126.97	0.66
16	17.769	0.109	0.027	0.017	0.056	0.000	0.000	1.029	2.81	99.150	123.66	0.73
17	17.964	0.070	0.009	0.009	0.056	0.000	0.000	0.552	7.71	99.682	124.97	0.47
	J = 0.003983	0.21 (1σ %)								*Total age*	126.51	0.54
Arnea Granite												
SM78	*biotite*	*B4*										
1	3.891	0.370	2.994	0.031	0.030	0.000	0.014	0.011	12.69	11.515	29.95	2.83
2	6.959	0.148	1.981	0.025	0.060	0.000	0.000	0.026	6.13	41.429	53.21	1.12
3	7.110	0.247	1.976	0.039	0.059	0.001	0.018	0.058	2.53	41.581	54.35	1.86
4	7.188	0.140	1.951	0.023	0.059	0.000	0.000	0.020	7.33	42.327	54.93	1.05
5	7.366	0.145	1.942	0.024	0.058	0.000	0.014	0.022	7.15	42.580	56.27	1.09
6	7.600	0.149	1.914	0.024	0.057	0.000	0.011	0.024	6.88	43.419	58.03	1.12
7	7.809	0.137	1.919	0.020	0.055	0.000	0.010	0.016	9.46	43.278	59.60	1.03
8	7.892	0.158	1.915	0.024	0.055	0.000	0.000	0.021	6.92	43.378	60.23	1.18
9	7.816	0.183	1.939	0.030	0.055	0.000	0.010	0.019	8.03	42.676	59.65	1.37
10	7.885	0.164	1.911	0.024	0.055	0.000	0.003	0.034	4.65	43.509	60.17	1.23
11	7.658	0.173	1.945	0.028	0.056	0.000	0.001	0.025	5.75	42.489	58.47	1.30
12	7.560	0.171	1.955	0.026	0.056	0.000	0.006	0.042	3.72	42.218	57.73	1.29
13	7.455	0.177	1.968	0.026	0.056	0.001	0.003	0.012	5.64	41.828	56.94	1.33
14	7.752	0.281	1.906	0.039	0.056	0.001	0.000	0.039	2.57	43.643	59.18	2.11
15	7.036	0.142	2.026	0.022	0.057	0.000	0.000	0.011	10.56	40.116	53.79	1.07
	J = 0.004291	0.20 (1σ %)								*Total age*	52.82	0.51
SM78	*white mica*	*B5*										
1	2.329	1.236	3.287	0.046	0.012	0.001	0.000	0.112	0.84	2.882	17.99	9.50
2	15.663	2.940	0.970	0.257	0.046	0.007	0.232	0.421	0.26	71.317	117.62	21.37
3	16.904	2.041	0.359	0.212	0.053	0.005	0.000	0.276	0.35	89.349	126.63	14.77
4	16.199	0.469	0.482	0.019	0.053	0.001	0.039	0.088	1.27	85.725	121.52	3.40
5	16.435	0.047	0.157	0.002	0.058	0.000	0.004	0.002	38.87	95.313	123.23	0.34
6	16.326	0.077	0.079	0.001	0.060	0.000	0.003	0.004	24.38	97.604	122.44	0.56
7	16.359	0.063	0.055	0.003	0.060	0.000	0.000	0.006	9.92	98.331	122.68	0.46
8	16.457	0.070	0.045	0.004	0.060	0.000	0.015	0.010	7.38	98.606	123.39	0.51
9	16.408	0.080	0.034	0.004	0.060	0.000	0.018	0.021	5.99	98.950	123.04	0.58
10	16.411	0.116	0.035	0.011	0.060	0.000	0.010	0.024	4.14	98.900	123.05	0.84
11	16.505	0.160	0.020	0.015	0.060	0.001	0.019	0.024	3.38	99.338	123.74	1.16
12	16.443	0.149	0.020	0.014	0.060	0.000	0.008	0.031	3.23	99.360	123.29	1.08
	J = 0.004291	0.20 (1σ %)								*Total age*	121.11	0.53
SM9	*white mica*	*B6*										
1	7.092	2.306	3.233	0.042	0.006	0.000	0.095	0.267	0.22	4.454	54.21	17.36
2	15.399	0.250	1.545	0.019	0.035	0.000	0.000	0.037	1.50	54.317	115.71	1.82
3	16.574	0.105	0.213	0.005	0.057	0.000	0.001	0.015	3.65	93.667	124.24	0.76
4	16.623	0.108	0.051	0.009	0.059	0.000	0.006	0.010	5.85	98.425	124.59	0.78
5	16.626	0.068	0.021	0.005	0.060	0.000	0.001	0.006	10.39	99.326	124.62	0.49
6	16.616	0.064	0.013	0.005	0.060	0.000	0.004	0.006	11.55	99.565	124.54	0.46
7	16.607	0.056	0.009	0.002	0.060	0.000	0.000	0.005	10.32	99.661	124.48	0.41
8	16.624	0.086	0.012	0.003	0.060	0.000	0.000	0.006	6.83	99.598	124.60	0.63
9	16.551	0.079	0.010	0.003	0.060	0.000	0.000	0.009	5.79	99.641	124.07	0.57
10	16.577	0.066	0.010	0.003	0.060	0.000	0.000	0.007	7.57	99.645	124.26	0.48
11	16.623	0.080	0.009	0.003	0.060	0.000	0.000	0.008	6.18	99.679	124.60	0.58
12	16.497	0.078	0.010	0.005	0.060	0.000	0.003	0.024	3.96	99.659	123.68	0.57
13	16.540	0.076	0.011	0.004	0.060	0.000	0.004	0.025	4.18	99.621	123.99	0.55
14	16.498	0.083	0.018	0.005	0.060	0.000	0.000	0.026	3.58	99.397	123.69	0.60
15	16.512	0.074	0.013	0.006	0.060	0.000	0.008	0.013	4.40	99.560	123.79	0.54
16	16.427	0.197	0.007	0.014	0.061	0.001	0.000	0.035	2.01	99.723	123.17	1.43
17	16.621	0.048	0.009	0.003	0.060	0.000	0.008	0.003	12.03	99.669	124.58	0.35
	J = 0.004291	0.20 (1σ %)								*Total age*	124.06	0.50
SM9	*white mica*	*B7*										
1	6.212	2.186	0.003	0.000	0.008	0.001	0.064	0.283	0.23	4.664	47.57	16.52
2	15.804	0.284	0.001	0.000	0.040	0.001	0.007	0.037	1.64	63.191	118.65	2.06
3	16.659	0.139	0.000	0.000	0.057	0.000	0.004	0.019	3.45	94.751	124.85	1.00
4	16.570	0.186	0.000	0.000	0.059	0.001	0.000	0.028	2.60	98.341	124.21	1.35
5	16.577	0.104	0.000	0.000	0.060	0.000	0.000	0.010	5.01	99.305	124.26	0.75
6	16.582	0.053	0.000	0.000	0.060	0.000	0.000	0.003	14.31	99.601	124.29	0.38
7	16.570	0.068	0.000	0.000	0.060	0.000	0.000	0.010	6.83	99.797	124.21	0.49
8	16.720	0.095	0.000	0.000	0.060	0.000	0.000	0.015	4.26	99.859	125.29	0.69
9	16.672	0.134	0.000	0.000	0.060	0.000	0.000	0.026	3.06	99.849	124.95	0.97
10	16.699	0.121	0.000	0.000	0.060	0.000	0.000	0.026	2.64	99.881	125.14	0.87
11	16.656	0.063	0.000	0.000	0.060	0.000	0.000	0.009	6.15	99.723	124.84	0.46
12	16.610	0.058	0.000	0.000	0.060	0.000	0.000	0.009	6.95	99.682	124.50	0.42
13	16.701	0.053	0.000	0.000	0.060	0.000	0.000	0.007	9.71	99.782	125.16	0.39
14	16.630	0.091	0.000	0.000	0.060	0.000	0.000	0.016	4.04	99.754	124.64	0.66
15	16.621	0.080	0.000	0.000	0.060	0.000	0.000	0.014	4.69	99.841	124.58	0.58
16	16.614	0.075	0.000	0.000	0.060	0.000	0.000	0.021	3.35	99.880	124.52	0.54
17	16.630	0.052	0.000	0.000	0.060	0.000	0.000	0.010	6.34	99.806	124.64	0.38
18	16.598	0.059	0.000	0.000	0.060	0.000	0.000	0.016	4.28	99.855	124.41	0.43
19	16.591	0.152	0.000	0.000	0.060	0.000	0.000	0.020	2.07	99.804	124.36	1.10
20	16.523	0.168	0.000	0.000	0.060	0.000	0.000	0.024	1.89	99.818	123.87	1.22
21	16.608	0.060	0.000	0.000	0.060	0.000	0.004	0.010	6.50	99.718	124.48	0.44
	J = 0.004291	0.20 (1σ %)								*Total age*	124.32	0.50

Step	$^{40}Ar^*/^{39}Ar$	2σ	$^{36}Ar/^{40}Ar$ (x1000)	2σ	$^{39}Ar/^{40}Ar$	2σ	$^{37}Ar/^{39}Ar$	2σ	Rel. ^{39}Ar (%)	$^{40}Ar^*$ (%)	Age	2σ
Circum-Rhodope belt (east)	***Nea Madytos Unit***											
SM40	*white mica*	*A8*										
1	6.402	0.732	2.792	0.062	0.027	0.001	3.392	4.578	0.33	17.486	45.53	5.14
2	13.495	0.144	0.483	0.024	0.064	0.000	0.517	1.014	1.50	85.688	94.68	0.99
3	14.004	0.096	0.139	0.015	0.068	0.000	0.000	0.715	2.64	95.827	98.15	0.66
4	13.731	0.442	0.166	0.076	0.069	0.001	0.524	2.167	1.06	95.038	96.29	3.02
5	14.063	0.088	0.080	0.013	0.069	0.000	0.130	0.315	6.31	97.557	98.55	0.60
6	14.196	0.073	0.024	0.009	0.070	0.000	0.119	0.252	8.65	99.234	99.46	0.50
7	14.179	0.085	0.012	0.013	0.070	0.000	0.000	0.188	7.99	99.564	99.34	0.58
8	14.054	0.069	0.018	0.009	0.071	0.000	0.011	0.109	11.05	99.392	98.49	0.47
9	13.859	0.072	0.018	0.010	0.072	0.000	0.040	0.149	10.33	99.386	97.16	0.49
10	13.761	0.069	0.016	0.009	0.072	0.000	0.065	0.212	6.96	99.449	96.49	0.47
11	13.763	0.092	0.009	0.013	0.072	0.000	0.251	0.235	4.33	99.677	96.51	0.63
12	13.618	0.100	0.022	0.017	0.073	0.000	0.012	0.471	4.04	99.275	95.51	0.68
13	13.666	0.074	0.015	0.012	0.073	0.000	0.115	0.183	7.94	99.481	95.84	0.50
14	13.714	0.075	0.018	0.012	0.073	0.000	0.000	0.212	7.65	99.407	96.17	0.51
15	13.853	0.093	0.008	0.017	0.072	0.000	0.076	0.339	5.50	99.698	97.12	0.64
16	13.862	0.102	0.043	0.019	0.071	0.000	0.000	0.597	2.74	98.648	97.18	0.70
17	14.063	0.100	0.010	0.018	0.071	0.000	0.173	0.641	3.11	99.626	98.55	0.68
18	14.152	0.054	0.011	0.006	0.070	0.000	0.210	0.200	7.86	99.593	99.16	0.37
	J = 0.003983	0.21 (1σ %)								*Total age*	94.46	0.42
SM40	*white mica*	*A4*										
1	8.544	1.985	2.762	0.131	0.021	0.002	12.195	18.399	0.45	18.365	60.52	13.82
2	13.310	0.576	0.554	0.102	0.063	0.001	1.366	5.438	1.32	83.587	93.41	3.94
3	14.004	0.275	0.183	0.053	0.068	0.001	0.000	2.635	2.40	94.519	98.15	1.88
4	14.249	0.090	0.053	0.015	0.069	0.000	0.000	0.703	8.22	98.362	99.82	0.61
5	14.421	0.060	0.021	0.009	0.069	0.000	0.000	0.440	18.85	99.326	100.99	0.41
6	14.317	0.067	0.008	0.012	0.070	0.000	0.260	0.555	21.27	99.710	100.28	0.45
7	14.209	0.091	0.007	0.018	0.070	0.000	0.360	0.868	14.57	99.727	99.55	0.62
8	14.100	0.303	0.000	0.070	0.071	0.000	1.472	3.252	3.70	100.068	98.81	2.07
9	14.008	0.223	0.000	0.047	0.072	0.001	1.004	1.978	3.47	100.267	98.18	1.52
10	14.066	0.102	0.000	0.020	0.071	0.000	0.924	0.852	7.65	100.083	98.58	0.70
11	14.394	0.096	0.000	0.019	0.070	0.000	0.617	0.847	9.00	100.208	100.81	0.66
12	14.430	0.311	0.000	0.071	0.069	0.000	0.596	3.520	5.26	100.180	101.06	2.12
13	14.274	0.383	0.020	0.087	0.070	0.000	0.000	4.338	3.83	99.337	100.00	2.61
	J = 0.003983	0.21 (1σ %)								*Total age*	99.77	0.49
SM40	*white mica*	*A5*										
1	4.494	1.997	3.151	0.101	0.015	0.001	4.222	21.213	0.28	6.876	32.08	14.13
2	10.960	0.819	1.335	0.137	0.055	0.001	0.000	6.880	0.70	60.524	77.27	5.65
3	13.213	0.708	0.342	0.138	0.068	0.002	2.151	5.668	0.78	89.841	92.75	4.85
4	13.575	0.456	0.324	0.085	0.067	0.001	1.123	3.562	1.23	90.354	95.22	3.11
5	13.888	0.260	0.204	0.055	0.068	0.000	1.423	2.689	2.13	93.896	97.36	1.77
6	14.105	0.083	0.117	0.015	0.068	0.000	0.121	0.667	5.27	96.478	98.84	0.57
7	14.159	0.046	0.041	0.005	0.070	0.000	0.049	0.241	14.71	98.730	99.21	0.31
8	14.088	0.049	0.013	0.007	0.071	0.000	0.287	0.257	10.64	99.535	98.72	0.33
9	13.890	0.053	0.026	0.007	0.071	0.000	0.000	0.251	9.40	99.178	97.37	0.36
10	13.792	0.066	0.015	0.012	0.072	0.000	0.352	0.470	6.82	99.501	96.70	0.45
11	13.654	0.069	0.005	0.012	0.073	0.000	0.601	0.564	5.58	99.770	95.76	0.47
12	13.486	0.069	0.012	0.010	0.074	0.000	0.563	0.455	4.35	99.572	94.62	0.47
13	13.451	0.081	0.028	0.016	0.074	0.000	0.000	0.746	5.46	99.111	94.37	0.56
14	13.495	0.074	0.027	0.013	0.073	0.000	0.000	0.545	6.94	99.117	94.68	0.50
15	13.711	0.061	0.010	0.009	0.073	0.000	0.202	0.368	8.45	99.641	96.15	0.42
16	13.903	0.088	0.007	0.016	0.072	0.000	0.129	0.683	6.01	99.716	97.46	0.60
17	13.919	0.096	0.019	0.019	0.071	0.000	0.000	0.711	4.59	99.360	97.57	0.66
18	14.035	0.138	0.007	0.030	0.071	0.000	0.169	1.208	3.17	99.738	98.36	0.94
19	14.206	0.141	0.032	0.030	0.070	0.000	0.000	1.274	3.49	98.997	99.53	0.96
	J = 0.003983	0.21 (1σ %)								*Total age*	96.89	0.42
SM56	*white mica*	*A11*										
1	1.470	20.761	0.001	0.000	0.001	0.000	0.000	15.791	1.04	0.128	10.56	148.66
2	12.528	1.045	0.001	0.000	0.056	0.002	0.000	7.271	1.86	70.373	88.05	7.17
3	10.264	0.652	0.000	0.000	0.065	0.000	0.804	0.697	13.32	66.278	72.46	4.51
4	12.612	0.786	0.000	0.000	0.056	0.001	1.212	1.346	7.82	71.058	88.63	5.39
5	13.200	0.272	0.000	0.000	0.067	0.000	0.000	0.357	36.72	89.015	92.66	1.86
6	13.422	0.689	0.000	0.000	0.069	0.000	0.068	0.811	12.79	92.057	94.18	4.71
7	12.413	1.352	0.000	0.000	0.057	0.001	0.000	1.473	6.94	70.101	87.26	9.28
8	12.122	1.692	0.000	0.000	0.044	0.000	0.000	2.054	5.68	53.285	85.27	11.63
9	16.198	1.996	0.000	0.000	0.024	0.000	0.000	2.750	5.57	38.888	113.06	13.50
10	16.041	1.252	0.000	0.000	0.038	0.000	0.000	1.751	8.25	61.145	111.99	8.48
	J = 0.003983	0.21 (1σ %)								*Total age*	90.89	2.38
Circum-Rhodope belt (west)												
CR4	*white mica*	*A4*										
1	18.506	3.309	0.567	0.102	0.045	0.008	0.986	7.236	1.64	83.200	128.61	22.20
2	18.826	1.586	0.280	0.053	0.049	0.004	0.000	3.468	3.50	91.677	130.75	10.63
3	17.800	0.164	0.070	0.007	0.055	0.000	0.003	0.386	33.99	97.870	123.86	1.11
4	17.823	0.237	0.063	0.026	0.055	0.001	0.000	1.428	6.18	98.095	124.02	1.60
5	17.798	0.186	0.025	0.011	0.056	0.001	0.023	0.627	17.38	99.197	123.85	1.25
6	17.984	0.210	0.037	0.012	0.055	0.001	0.000	0.664	15.44	98.866	125.10	1.41
7	17.824	0.380	0.079	0.060	0.055	0.001	0.000	2.812	4.04	97.615	124.02	2.56
8	17.592	0.403	0.034	0.067	0.056	0.001	0.843	3.164	4.03	98.949	122.47	2.71
9	17.642	0.280	0.037	0.045	0.056	0.000	0.000	2.015	5.33	98.848	122.80	1.89
10	18.079	0.806	0.017	0.138	0.055	0.001	1.383	6.642	1.98	99.444	125.74	5.42
11	17.951	0.237	0.036	0.037	0.055	0.000	0.007	1.639	6.49	98.875	124.88	1.60
	J = 0.003983	0.21 (1σ %)								*Total age*	124.38	0.90
CR4	*white mica*	*A5*										
1	17.483	0.245	0.715	0.023	0.045	0.000	0.000	1.107	15.45	78.840	121.73	1.65
2	17.169	0.098	0.129	0.011	0.056	0.000	0.000	0.447	35.40	96.124	119.61	0.66
3	16.975	0.144	0.043	0.013	0.058	0.000	0.072	0.546	34.23	98.684	118.30	0.97
4	16.945	1.024	0.114	0.145	0.057	0.002	0.000	8.401	3.11	96.575	118.10	6.91
5	17.614	1.030	0.000	0.151	0.057	0.002	1.485	8.043	2.93	100.263	122.61	6.93
6	17.103	0.699	0.017	0.098	0.058	0.002	1.221	5.265	3.95	99.455	119.17	4.72
7	17.695	0.560	0.062	0.074	0.055	0.001	0.000	3.953	4.93	98.121	123.16	3.77
	J = 0.003983	0.21 (1σ %)								*Total age*	119.69	0.79

Step	$^{40}Ar^*/^{39}Ar$	2σ	$^{36}Ar/^{40}Ar$ (x1000)	2σ	$^{39}Ar/^{40}Ar$	2σ	$^{37}Ar/^{39}Ar$	2σ	Rel. ^{39}Ar (%)	$^{40}Ar^*$ (%)	Age	2σ
Circum-Rhodope belt (west)	**(continue)**											
CR10	*white mica*	*A1*										
1	11.460	0.947	1.033	0.185	0.061	0.001	0.560	10.553	1.87	69.420	80.71	6.52
2	14.910	0.251	0.312	0.047	0.061	0.000	0.863	2.649	7.47	90.728	104.32	1.70
3	16.076	0.181	0.083	0.033	0.061	0.000	0.947	1.878	10.99	97.498	112.24	1.23
4	17.910	0.115	0.000	0.018	0.056	0.000	2.142	1.087	13.84	100.103	124.61	0.77
5	17.766	0.118	0.015	0.017	0.056	0.000	0.845	1.032	9.90	99.508	123.63	0.79
6	17.339	0.140	0.011	0.019	0.057	0.000	1.473	1.117	8.21	99.630	120.76	0.94
7	18.152	0.099	0.028	0.015	0.055	0.000	0.322	0.949	19.69	99.122	126.23	0.67
8	18.360	0.163	0.005	0.026	0.054	0.000	1.256	1.619	10.44	99.801	127.63	1.09
9	19.661	0.199	0.003	0.022	0.051	0.000	0.718	1.499	11.86	99.872	136.34	1.33
10	17.147	0.725	0.086	0.131	0.057	0.001	0.000	7.925	2.44	97.419	119.46	4.88
11	17.207	0.669	0.006	0.106	0.058	0.001	0.000	3.491	3.29	99.780	119.87	4.51
	J = 0.003983	0.21 (1σ %)								*Total age*	122.27	0.64
CR10	*white mica*	*A6*										
1	12.283	0.310	1.279	0.050	0.051	0.000	0.818	1.914	2.90	62.172	86.38	2.13
2	14.665	0.262	0.167	0.044	0.065	0.001	0.000	2.251	2.27	95.009	102.66	1.78
3	18.183	0.104	0.045	0.010	0.054	0.000	0.010	0.569	7.00	98.608	126.44	0.70
4	16.709	0.091	0.068	0.011	0.059	0.000	0.289	0.548	6.56	97.931	116.51	0.61
5	17.711	0.098	0.023	0.013	0.056	0.000	0.457	0.398	17.04	99.274	123.27	0.66
6	16.323	0.087	0.042	0.012	0.061	0.000	0.000	0.382	18.72	98.699	113.91	0.59
7	16.740	0.122	0.018	0.018	0.059	0.000	0.162	0.560	12.57	99.396	116.72	0.83
8	17.585	0.136	0.009	0.009	0.057	0.000	1.123	0.334	3.96	99.677	122.42	0.91
9	16.217	0.104	0.016	0.012	0.061	0.000	0.820	0.614	6.16	99.478	113.18	0.70
10	16.288	0.137	0.040	0.011	0.061	0.000	0.000	0.521	5.43	98.768	113.66	0.92
11	16.447	0.083	0.048	0.010	0.060	0.000	0.000	0.247	17.38	98.514	114.74	0.56
	J = 0.003983	0.21 (1σ %)								*Total age*	116.29	0.53
CR10	*white mica*	*A6*	*single grain*									
	18.057	0.072	0.040	0.004	0.055	0.000	0.000	0.223	100.00	98.751	125.59	0.48
	J = 0.003983	0.21 (1σ %)										

Appendix B1

Supplementary fission-track dating data for the samples presented in Chapter 5.

Sample	SM11008	
Irradiation Code	R-13-1-C	
Mineral	Apatite	
Ns	2182	
RhoS	20.148	
Ni	6057	
RhoI	55.928	
Area	1083	
Nd	9098	
RhoD	9.375	
Pooled age	57.0	1.9
Mean age	57.6	1.5
Central age	57.0	1.9
Chi-square	33.24	
P(%)	72.93	
Dispersion	0.01	
Kurtosis	1.58	
Skewness	0.75	

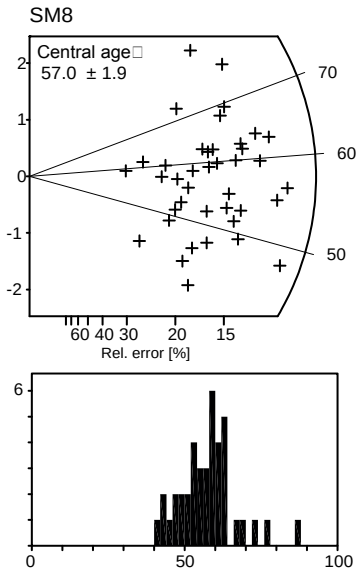

Crystal	Ns	Ni	Area	RhoS	RhoI	Age (Ma)	error (1σ)
1	106	298	40	26.50	74.50	56.3	6.5
2	33	102	18	18.33	56.67	51.2	10.3
3	40	114	20	20.00	57.00	55.5	10.3
4	67	215	30	22.33	71.67	49.3	7.0
5	40	138	25	16.00	55.20	45.9	8.3
6	15	40	18	8.33	22.22	59.3	18.0
7	74	190	28	26.43	67.86	61.6	8.6
8	70	209	24	29.17	87.08	53.0	7.4
9	73	185	25	29.20	74.00	62.4	8.7
10	55	140	20	27.50	70.00	62.1	10.0
11	65	200	40	16.25	50.00	51.5	7.4
12	61	142	24	25.42	59.17	67.9	10.5
13	61	182	30	20.33	60.67	53.1	7.9
14	86	228	30	28.67	76.00	59.7	7.7
15	47	86	32	14.69	26.88	86.3	15.8
16	94	237	35	26.86	67.71	62.7	7.8
17	57	151	30	19.00	50.33	59.7	9.4
18	52	139	36	14.44	38.61	59.2	9.7
19	69	182	24	28.75	75.83	60.0	8.6
20	84	209	40	21.00	52.25	63.6	8.3
21	18	67	20	9.00	33.50	42.6	11.3
22	65	132	25	26.00	52.80	77.8	11.9
23	96	317	36	26.67	88.06	48.0	5.7
24	35	97	24	14.58	40.42	57.1	11.3
25	63	181	30	21.00	60.33	55.1	8.2
26	36	108	21	17.14	51.43	52.8	10.2
27	49	124	24	20.42	51.67	62.5	10.6
28	97	280	40	24.25	70.00	54.8	6.6
29	43	116	18	23.89	64.44	58.7	10.6
30	37	145	25	14.80	58.00	40.4	7.5
31	37	80	18	20.56	44.44	73.1	14.6
32	64	146	40	16.00	36.50	69.3	10.5
33	30	79	28	10.71	28.21	60.1	13.0
34	35	128	30	11.67	42.67	43.3	8.3
35	21	54	24	8.75	22.50	61.5	15.9
36	52	133	24	21.67	55.42	61.8	10.2
37	28	77	21	13.33	36.67	57.5	12.8
38	48	160	24	20.00	66.67	47.5	7.9
39	30	97	18	16.67	53.89	49.0	10.3
40	49	149	24	20.42	62.08	52.1	8.7

Sample	SM11009	
Irradiation Code	R-13-1-C	
Mineral	Apatite	
Ns	1321	
RhoS	7.246	
Ni	4426	
RhoI	24.279	
Area	1823	
Nd	9098	
RhoD	9.651	
Pooled age	48.7	1.9
Mean age	49.4	1.5
Central age	48.7	1.9
Chi-square	30.16	
P(%)	84.4	
Dispersion	0.01	
Kurtosis	-0.18	
Skewness	0.31	

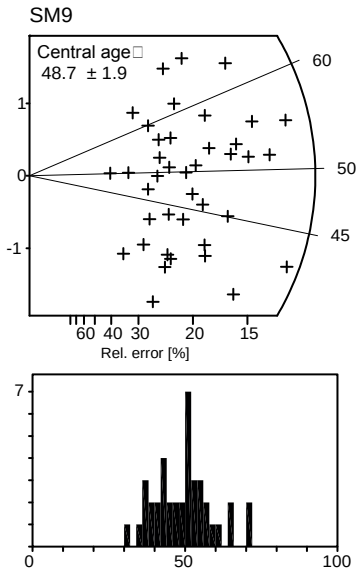

Crystal	Ns	Ni	Area	RhoS	RhoI	Age (Ma)	error (1σ)
1	40	123	70	5.71	17.57	53.0	9.7
2	18	49	100	1.80	4.90	59.8	16.5
3	23	99	40	5.75	24.75	37.9	8.8
4	25	73	40	6.25	18.25	55.8	13.0
5	62	183	40	15.50	45.75	55.2	8.2
6	59	187	40	14.75	46.75	51.4	7.8
7	28	105	35	8.00	30.00	43.5	9.3
8	17	89	30	5.67	29.67	31.2	8.3
9	82	245	100	8.20	24.50	54.5	7.1
10	71	225	50	14.20	45.00	51.4	7.1
11	50	127	30	16.67	42.33	64.1	10.8
12	36	128	40	9.00	32.00	45.9	8.7
13	31	72	32	9.69	22.50	70.1	15.1
14	8	26	24	3.33	10.83	50.2	20.3
15	10	48	50	2.00	9.60	34.0	11.8
16	47	170	60	7.83	28.33	45.1	7.5
17	15	65	50	3.00	13.00	37.7	10.8
18	36	146	100	3.60	14.60	40.2	7.5
19	36	142	40	9.00	35.50	41.4	7.8
20	53	163	30	17.67	54.33	53.0	8.5
21	21	65	30	7.00	21.67	52.7	13.3
22	21	61	32	6.56	19.06	56.1	14.2
23	24	55	25	9.60	22.00	71.0	17.4
24	48	206	40	12.00	51.50	38.0	6.2
25	21	94	100	2.10	9.40	36.5	8.8
26	27	71	25	10.80	28.40	61.9	14.1
27	32	111	40	8.00	27.75	47.0	9.5
28	17	59	40	4.25	14.75	47.0	13.0
29	23	86	25	9.20	34.40	43.6	10.3
30	78	302	100	7.80	30.20	42.1	5.4
31	34	109	50	6.80	21.80	50.8	10.1
32	30	98	30	10.00	32.67	49.9	10.5
33	20	66	30	6.67	22.00	49.4	12.7
34	14	35	40	3.50	8.75	65.1	20.6
35	22	94	40	5.50	23.50	38.2	9.1
36	39	110	36	10.83	30.56	57.8	10.8
37	24	77	24	10.00	32.08	50.8	11.9
38	17	66	40	4.25	16.50	42.0	11.5
39	50	157	25	20.00	62.80	51.9	8.5
40	12	39	50	2.40	7.80	50.2	16.6

Sample	SM11011	
Irradiation Code	R-13-1-E	
Mineral	Apatite	
Ns	639	
RhoS	5.325	
Ni	1874	
RhoI	15.617	
Area	1200	
Nd	10419	
RhoD	9.992	
Pooled age	57.7	2.9
Mean age	57.8	2.8
Central age	57.7	3.0
Chi-square	35.6	
P(%)	62.57	
Dispersion	0.04	
Kurtosis	-0.58	
Skewness	0.33	

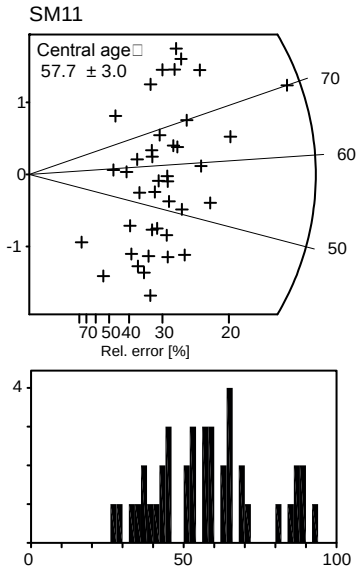

Crystal	Ns	Ni	Area	RhoS	RhoI	Age (Ma)	error (1σ)
1	13	35	15	8.67	23.33	62.6	20.4
2	14	42	40	3.50	10.50	56.2	17.4
3	15	37	25	6.00	14.80	68.3	21.0
4	4	25	20	2.00	12.50	27.0	14.6
5	6	17	25	2.40	6.80	59.5	28.3
6	25	71	40	6.25	17.75	59.4	13.9
7	13	41	25	5.20	16.40	53.5	17.1
8	27	56	30	9.00	18.67	81.2	19.1
9	21	38	30	7.00	12.67	93.0	25.4
10	2	12	20	1.00	6.00	28.2	21.5
11	22	42	35	6.29	12.00	88.1	23.3
12	59	142	15	39.33	94.67	70.0	11.0
13	20	39	30	6.67	13.00	86.3	23.8
14	16	47	24	6.67	19.58	57.4	16.7
15	17	32	18	9.44	17.78	89.4	26.9
16	19	63	25	7.60	25.20	50.9	13.4
17	10	32	30	3.33	10.67	52.7	19.1
18	18	47	56	3.21	8.39	64.6	18.0
19	13	48	30	4.33	16.00	45.7	14.3
20	13	34	30	4.33	11.33	64.5	21.1
21	7	14	15	4.67	9.33	84.2	39.0
22	15	57	64	2.34	8.91	44.4	12.9
23	11	47	24	4.58	19.58	39.5	13.3
24	15	62	36	4.17	17.22	40.9	11.8
25	10	27	32	3.13	8.44	62.4	23.2
26	8	36	24	3.33	15.00	37.5	14.7
27	16	48	27	5.93	17.78	56.2	16.3
28	19	75	64	2.97	11.72	42.8	11.0
29	27	87	27	10.00	32.22	52.4	11.6
30	8	31	20	4.00	15.50	43.6	17.3
31	19	50	30	6.33	16.67	64.1	17.3
32	8	23	15	5.33	15.33	58.7	24.1
33	14	27	30	4.67	9.00	87.3	28.8
34	12	45	48	2.50	9.38	45.0	14.7
35	10	47	24	4.17	19.58	35.9	12.5
36	35	93	15	23.33	62.00	63.4	12.7
37	22	54	36	6.11	15.00	68.7	17.4
38	9	42	30	3.00	14.00	36.2	13.3
39	11	57	36	3.06	15.83	32.6	10.8
40	16	52	40	4.00	13.00	51.9	14.9

Sample	SM11012	
Irradiation Code	R-13-1-E	
Mineral	Apatite	
Ns	647	
RhoS	6.876	
Ni	2168	
RhoI	23.039	
Area	941	
Nd	10419	
RhoD	10.087	
Pooled age	50.8	2.5
Mean age	53.1	1.9
Central age	50.8	2.5
Chi-square	13.23	
P(%)	99.86	
Dispersion	0	
Kurtosis	2.5	
Skewness	1.47	

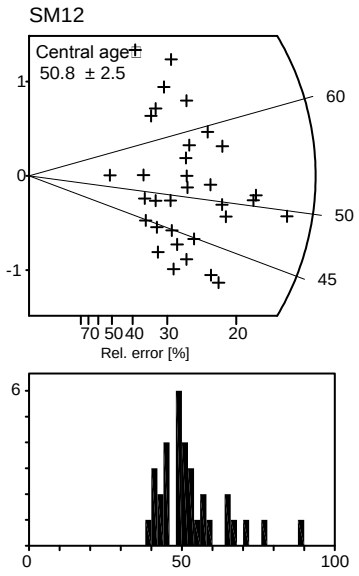

Crystal	Ns	Ni	Area	RhoS	RhoI	Age (Ma)	error (1σ)
1	15	36	25	6.00	14.40	70.9	21.8
2	20	76	32	6.25	23.75	44.9	11.3
3	10	38	30	3.33	12.67	44.9	16.0
4	12	31	25	4.80	12.40	65.9	22.4
5	29	87	56	5.18	15.54	56.8	12.2
6	25	72	40	6.25	18.00	59.1	13.8
7	18	73	40	4.50	18.25	42.0	11.1
8	10	35	30	3.33	11.67	48.7	17.5
9	19	61	30	6.33	20.33	53.1	14.0
10	25	82	20	12.50	41.00	51.9	11.9
11	28	96	30	9.33	32.00	49.7	10.7
12	10	32	21	4.76	15.24	53.2	19.3
13	15	52	24	6.25	21.67	49.1	14.4
14	29	102	50	5.80	20.40	48.4	10.3
15	13	33	18	7.22	18.33	67.0	22.0
16	12	46	24	5.00	19.17	44.5	14.4
17	12	42	32	3.75	13.13	48.7	16.0
18	20	52	30	6.67	17.33	65.4	17.3
19	5	16	20	2.50	8.00	53.2	27.3
20	39	130	40	9.75	32.50	51.1	9.4
21	15	57	32	4.69	17.81	44.9	13.1
22	19	58	18	10.56	32.22	55.8	14.8
23	24	98	25	9.60	39.20	41.7	9.6
24	17	38	25	6.80	15.20	76.1	22.3
25	16	63	24	6.67	26.25	43.3	12.2
26	10	19	24	4.17	7.92	89.4	35.0
27	20	59	25	8.00	23.60	57.7	15.0
28	50	172	24	20.83	71.67	49.5	8.0
29	38	128	30	12.67	42.67	50.6	9.4
30	26	107	28	9.29	38.21	41.4	9.1
31	12	50	21	5.71	23.81	40.9	13.2
32	15	64	20	7.50	32.00	40.0	11.5
33	19	63	28	6.79	22.50	51.4	13.5
34							
35							
36							
37							
38							
39							
40							

Sample	SM11013	
Irradiation Code	R-13-1-E	
Mineral	Apatite	
Ns	911	
RhoS	5.791	
Ni	2845	
RhoI	18.086	
Area	1573	
Nd	10419	
RhoD	10.372	
Pooled age	56.1	2.5
Mean age	57.5	2.0
Central age	56.1	2.5
Chi-square	24.58	
P(%)	96.52	
Dispersion	0	
Kurtosis	1.06	
Skewness	0.85	

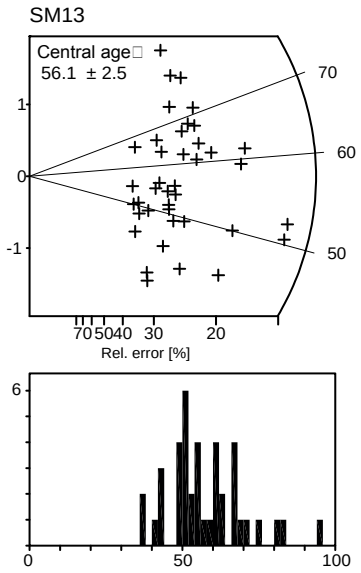

Crystal	Ns	Ni	Area	RhoS	RhoI	Age (Ma)	error (1σ)
1	32	91	40	8.00	22.75	61.5	12.7
2	23	60	35	6.57	17.14	67.1	16.5
3	16	42	25	6.40	16.80	66.6	19.6
4	21	44	35	6.00	12.57	83.4	22.2
5	22	78	36	6.11	21.67	49.4	12.0
6	17	47	20	8.50	23.50	63.3	18.0
7	15	48	36	4.17	13.33	54.7	16.2
8	20	65	36	5.56	18.06	53.9	13.8
9	25	64	40	6.25	16.00	68.3	16.2
10	23	65	40	5.75	16.25	61.9	15.1
11	18	62	40	4.50	15.50	50.9	13.7
12	28	77	50	5.60	15.40	63.6	14.1
13	20	63	40	5.00	15.75	55.6	14.3
14	11	38	24	4.58	15.83	50.7	17.4
15	45	128	40	11.25	32.00	61.5	10.8
16	11	29	21	5.24	13.81	66.4	23.5
17	27	70	30	9.00	23.33	67.5	15.4
18	20	47	28	7.14	16.79	74.4	19.9
19	18	58	30	6.00	19.33	54.3	14.7
20	38	133	60	6.33	22.17	50.1	9.3
21	11	40	36	3.06	11.11	48.2	16.4
22	12	58	36	3.33	16.11	36.3	11.5
23	20	84	30	6.67	28.00	41.7	10.4
24	19	35	32	5.94	10.94	94.8	27.1
25	62	208	100	6.20	20.80	52.2	7.6
26	27	78	50	5.40	15.60	60.6	13.6
27	27	66	40	6.75	16.50	71.5	16.4
28	43	127	70	6.14	18.14	59.3	10.5
29	32	128	60	5.33	21.33	43.8	8.7
30	60	208	100	6.00	20.80	50.5	7.5
31	16	64	32	5.00	20.00	43.8	12.3
32	18	61	40	4.50	15.25	51.7	13.9
33	16	50	30	5.33	16.67	56.0	16.1
34	10	35	28	3.57	12.50	50.1	18.0
35	24	52	40	6.00	13.00	80.7	20.0
36	12	56	36	3.33	15.56	37.6	12.0
37	10	32	18	5.56	17.78	54.7	19.9
38	10	40	24	4.17	16.67	43.8	15.5
39	19	68	40	4.75	17.00	49.0	12.7
40	13	46	25	5.20	18.40	49.5	15.6

Sample	SM11015	
Irradiation Code	R-13-1-E	
Mineral	Apatite	
Ns	348	
RhoS	4.549	
Ni	1172	
RhoI	15.320	
Area	765	
Nd	10419	
RhoD	10.656	
Pooled age	53.4	3.5
Mean age	58.3	3.1
Central age	53.4	3.5
Chi-square	15.78	
P(%)	92.13	
Dispersion	0	
Kurtosis	2.37	
Skewness	1.27	

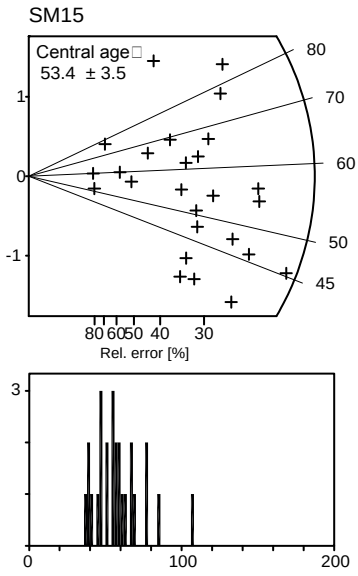

Crystal	Ns	Ni	Area	RhoS	RhoI	Age (Ma)	error (1σ)
1	25	83	42	5.95	19.76	54.2	12.4
2	13	49	24	5.42	20.42	47.8	14.9
3	10	48	25	4.00	19.20	37.5	13.1
4	20	42	18	11.11	23.33	85.5	23.3
5	19	72	27	7.04	26.67	47.5	12.3
6	30	119	60	5.00	19.83	45.4	9.3
7	3	7	25	1.20	2.80	77.0	53.1
8	11	48	36	3.06	13.33	41.3	13.8
9	16	43	36	4.44	11.94	66.9	19.6
10	2	7	35	0.57	2.00	51.4	41.2
11	19	44	42	4.52	10.48	77.5	21.4
12	9	15	18	5.00	8.33	107.5	45.4
13	2	6	20	1.00	3.00	59.9	49.0
14	22	86	42	5.24	20.48	46.1	11.1
15	12	56	25	4.80	22.40	38.6	12.3
16	18	84	27	6.67	31.11	38.6	10.1
17	7	19	18	3.89	10.56	66.2	29.3
18	11	36	21	5.24	17.14	55.0	19.0
19	14	40	35	4.00	11.43	62.9	19.6
20	5	16	21	2.38	7.62	56.2	28.8
21	16	53	30	5.33	17.67	54.3	15.5
22	25	80	40	6.25	20.00	56.2	12.9
23	10	26	30	3.33	8.67	69.1	25.8
24	4	12	15	2.67	8.00	59.9	34.6
25	13	46	28	4.64	16.43	50.9	16.0
26	12	35	25	4.80	14.00	61.6	20.7
27							
28							
29							
30							
31							
32							
33							
34							
35							
36							
37							
38							
39							
40							

Sample	SM11017	
Irradiation Code	R-13-1-E	
Mineral	Apatite	
Ns	218	
RhoS	3.263	
Ni	739	
RhoI	11.063	
Area	668	
Nd	10419	
RhoD	10.846	
Pooled age	54.0	4.3
Mean age	56.9	3.2
Central age	54.0	4.3
Chi-square	17.68	
P(%)	99.56	
Dispersion	0	
Kurtosis	-0.25	
Skewness	0.48	

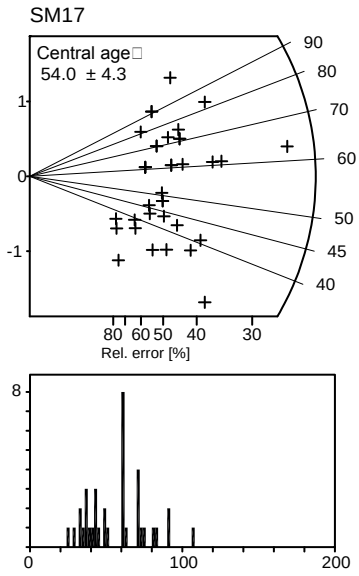

Crystal	Ns	Ni	Area	RhoS	RhoI	Age (Ma)	error (1σ)
1	10	22	20	5.00	11.00	83.1	31.7
2	4	9	12	3.33	7.50	81.2	48.8
3	20	58	28	7.14	20.71	63.1	16.4
4	6	15	16	3.75	9.38	73.1	35.4
5	2	11	14	1.43	7.86	33.3	25.6
6	4	12	15	2.67	8.00	61.0	35.2
7	5	19	10	5.00	19.00	48.2	24.3
8	2	15	12	1.67	12.50	24.5	18.4
9	5	13	24	2.08	5.42	70.3	37.1
10	4	16	20	2.00	8.00	45.8	25.6
11	8	36	40	2.00	9.00	40.7	15.9
12	5	19	24	2.08	7.92	48.2	24.3
13	7	17	14	5.00	12.14	75.3	33.8
14	5	18	25	2.00	7.20	50.9	25.7
15	5	26	24	2.08	10.83	35.3	17.2
16	7	18	25	2.80	7.20	71.1	31.7
17	7	18	18	3.89	10.00	71.1	31.7
18	8	49	16	5.00	30.63	30.0	11.4
19	4	12	12	3.33	10.00	61.0	35.2
20	10	30	20	5.00	15.00	61.0	22.3
21	7	12	18	3.89	6.67	106.4	50.7
22	5	21	21	2.38	10.00	43.6	21.7
23	11	33	24	4.58	13.75	61.0	21.3
24	6	18	16	3.75	11.25	61.0	28.8
25	5	10	10	5.00	10.00	91.3	50.0
26	3	15	16	1.88	9.38	36.7	23.2
27	3	14	12	2.50	11.67	39.3	25.0
28	5	13	10	5.00	13.00	70.3	37.1
29	6	26	30	2.00	8.67	42.3	19.2
30	4	17	16	2.50	10.63	43.1	24.0
31	4	12	15	2.67	8.00	61.0	35.2
32	7	34	16	4.38	21.25	37.7	15.7
33	4	22	15	2.67	14.67	33.3	18.1
34	6	18	14	4.29	12.86	61.0	28.8
35	7	21	18	3.89	11.67	61.0	26.7
36	2	10	12	1.67	8.33	36.7	28.4
37	5	10	16	3.13	6.25	91.3	50.0
38							
39							
40							

Sample	SM11018	
Irradiation Code	R-13-1-H	
Mineral	Apatite	
Ns	239	
RhoS	3.464	
Ni	818	
RhoI	11.855	
Area	690	
Nd	10362	
RhoD	9.433	
Pooled age	46.6	3.6
Mean age	48.6	2.4
Central age	46.6	3.6
Chi-square	12.07	
P(%)	99.4	
Dispersion	0	
Kurtosis	0.84	
Skewness	0.68	

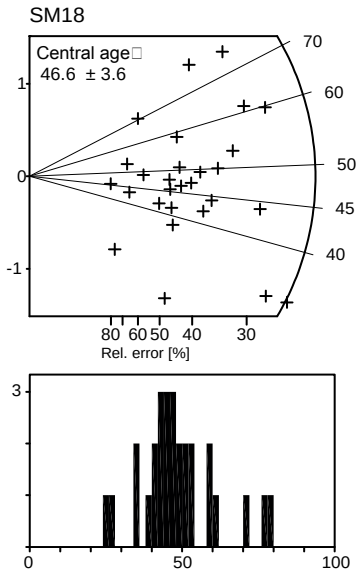

Crystal	Ns	Ni	Area	RhoS	RhoI	Age (Ma)	error (1σ)
1	9	18	30	3.00	6.00	79.5	32.5
2	9	34	40	2.25	8.50	42.2	15.8
3	18	48	40	4.50	12.00	59.7	16.6
4	15	39	30	5.00	13.00	61.2	18.7
5	4	13	16	2.50	8.13	49.0	28.1
6	6	20	18	3.33	11.11	47.8	22.3
7	7	19	20	3.50	9.50	58.7	26.0
8	13	27	21	6.19	12.86	76.6	25.9
9	10	36	32	3.13	11.25	44.3	15.9
10	16	75	32	5.00	23.44	34.0	9.4
11	19	88	50	3.80	17.60	34.4	8.7
12	11	35	25	4.40	14.00	50.1	17.3
13	16	58	25	6.40	23.20	44.0	12.5
14	4	9	15	2.67	6.00	70.7	42.5
15	3	9	15	2.00	6.00	53.1	35.4
16	2	7	15	1.33	4.67	45.5	36.5
17	5	19	21	2.38	9.05	42.0	21.1
18	5	31	24	2.08	12.92	25.7	12.4
19	3	11	24	1.25	4.58	43.5	28.3
20	2	12	15	1.33	8.00	26.6	20.3
21	6	25	20	3.00	12.50	38.3	17.4
22	8	27	28	2.86	9.64	47.2	19.0
23	9	29	24	3.75	12.08	49.4	18.9
24	7	22	15	4.67	14.67	50.7	22.0
25	13	39	32	4.06	12.19	53.1	17.0
26	6	23	24	2.50	9.58	41.6	19.1
27	7	24	15	4.67	16.00	46.5	20.0
28	6	21	24	2.50	8.75	45.5	21.1
29							
30							
31							
32							
33							
34							
35							
36							
37							
38							
39							
40							

Sample	SM11020	
Irradiation Code	R-13-1-H	
Mineral	Apatite	
Ns	188	
RhoS	2.979	
Ni	583	
RhoI	9.239	
Area	631	
Nd	10362	
RhoD	9.94	
Pooled age	54.1	4.7
Mean age	61.0	3.9
Central age	54.1	4.7
Chi-square	15.7	
P(%)	92.36	
Dispersion	0.01	
Kurtosis	-0.66	
Skewness	-0.02	

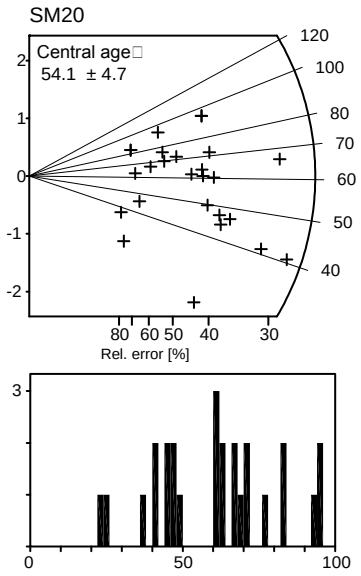

Crystal	Ns	Ni	Area	RhoS	RhoI	Age (Ma)	error (1σ)
1	6	43	28	2.14	15.36	23.5	10.2
2	3	6	15	2.00	4.00	83.7	59.2
3	3	11	18	1.67	6.11	45.8	29.8
4	6	14	18	3.33	7.78	71.8	35.1
5	17	43	35	4.86	12.29	66.3	19.0
6	5	12	25	2.00	4.80	69.8	37.2
7	16	66	40	4.00	16.50	40.7	11.4
8	5	9	16	3.13	5.63	93.0	51.9
9	9	34	16	5.63	21.25	44.5	16.7
10	2	9	16	1.25	5.63	37.3	29.2
11	9	16	40	2.25	4.00	94.1	39.3
12	8	27	16	5.00	16.88	49.7	20.1
13	3	8	16	1.88	5.00	62.9	42.6
14	3	6	12	2.50	5.00	83.7	59.2
15	9	16	30	3.00	5.33	94.1	39.3
16	2	13	14	1.43	9.29	25.9	19.7
17	9	21	25	3.60	8.40	71.8	28.7
18	5	11	21	2.38	5.24	76.2	41.1
19	8	21	20	4.00	10.50	63.9	26.6
20	10	36	21	4.76	17.14	46.6	16.7
21	13	53	81	1.60	6.54	41.2	12.8
22	9	25	18	5.00	13.89	60.4	23.5
23	4	10	20	2.00	5.00	67.1	39.7
24	9	32	20	4.50	16.00	47.2	17.9
25	7	19	25	2.80	7.60	61.8	27.4
26	8	22	25	3.20	8.80	61.0	25.2
27							
28							
29							
30							
31							
32							
33							
34							
35							
36							
37							
38							
39							
40							

Sample	SM11023	
Irradiation Code	R-13-2-G	
Mineral	Apatite	
Ns	785	
RhoS	7.599	
Ni	2888	
RhoI	27.957	
Area	1033	
Nd	10905	
RhoD	10.431	
Pooled age	47.9	2.2
Mean age	50.6	2.1
Central age	47.9	2.2
Chi-square	24.77	
P(%)	90.08	
Dispersion	0	
Kurtosis	2.61	
Skewness	1.38	

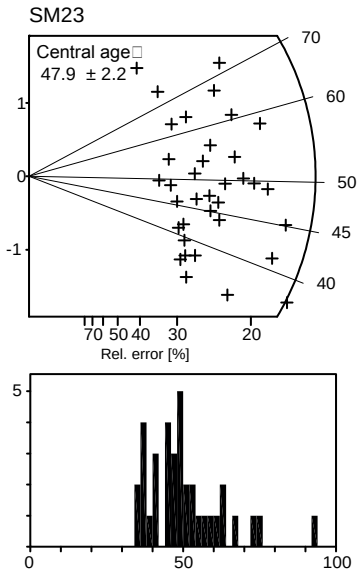

Crystal	Ns	Ni	Area	RhoS	RhoI	Age (Ma)	error (1σ)
1	9	17	18	5.00	9.44	93.0	38.4
2	42	164	36	11.67	45.56	45.1	7.9
3	28	92	30	9.33	30.67	53.6	11.6
4	18	62	32	5.63	19.38	51.1	13.7
5	23	87	21	10.95	41.43	46.6	11.0
6	25	89	30	8.33	29.67	49.5	11.3
7	14	68	20	7.00	34.00	36.3	10.7
8	24	63	20	12.00	31.50	67.0	16.1
9	41	192	40	10.25	48.00	37.7	6.5
10	28	81	36	7.78	22.50	60.8	13.4
11	36	109	30	12.00	36.33	58.1	11.3
12	21	82	36	5.83	22.78	45.1	11.1
13	23	92	24	9.58	38.33	44.1	10.3
14	26	63	21	12.38	30.00	72.6	17.0
15	37	158	40	9.25	39.50	41.3	7.6
16	15	63	20	7.50	31.50	42.0	12.1
17	15	67	32	4.69	20.94	39.5	11.3
18	11	39	27	4.07	14.44	49.7	17.0
19	24	120	40	6.00	30.00	35.3	7.9
20	13	42	15	8.67	28.00	54.5	17.3
21	30	105	30	10.00	35.00	50.3	10.5
22	17	47	30	5.67	15.67	63.7	18.1
23	12	28	20	6.00	14.00	75.4	26.1
24	13	47	21	6.19	22.38	48.7	15.3
25	14	54	20	7.00	27.00	45.7	13.7
26	22	69	30	7.33	23.00	56.1	13.8
27	33	117	50	6.60	23.40	49.7	9.9
28	21	78	28	7.50	27.86	47.4	11.7
29	15	77	36	4.17	21.39	34.4	9.7
30	14	60	30	4.67	20.00	41.1	12.2
31	37	133	40	9.25	33.25	49.0	9.2
32	14	39	20	7.00	19.50	63.2	19.7
33	20	66	24	8.33	27.50	53.4	13.7
34	17	79	24	7.08	32.92	37.9	10.2
35	15	71	30	5.00	23.67	37.3	10.6
36	18	68	32	5.63	21.25	46.6	12.4
37							
38							
39							
40							

Sample	SM11024	
Irradiation Code	R-13-1-H	
Mineral	Apatite	
Ns	280	
RhoS	4.368	
Ni	976	
RhoI	15.226	
Area	641	
Nd	10362	
RhoD	10.278	
Pooled age	49.8	3.6
Mean age	56.6	4.2
Central age	50.1	3.7
Chi-square	26.69	
P(%)	47.96	
Dispersion	0.08	
Kurtosis	1.08	
Skewness	1.17	

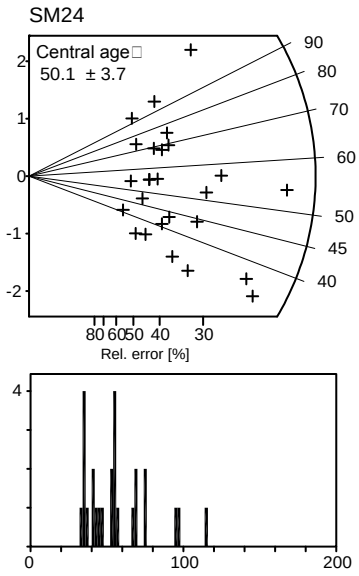

Crystal	Ns	Ni	Area	RhoS	RhoI	Age (Ma)	error (1σ)
1	21	99	50	4.20	19.80	36.9	8.9
2	8	20	21	3.81	9.52	69.3	29.0
3	10	25	28	3.57	8.93	69.3	26.0
4	9	36	28	3.21	12.86	43.4	16.2
5	9	46	30	3.00	15.33	34.0	12.4
6	7	22	21	3.33	10.48	55.2	24.0
7	9	16	21	4.29	7.62	97.3	40.6
8	6	14	15	4.00	9.33	74.3	36.3
9	15	50	20	7.50	25.00	52.1	15.4
10	18	55	28	6.43	19.64	56.8	15.5
11	22	110	50	4.40	22.00	34.8	8.2
12	11	58	30	3.67	19.33	33.0	10.9
13	6	11	14	4.29	7.86	94.4	47.9
14	32	103	50	6.40	20.60	53.9	11.0
15	13	51	25	5.20	20.40	44.3	13.8
16	9	23	20	4.50	11.50	67.8	26.7
17	5	25	21	2.38	11.90	34.8	17.0
18	16	24	18	8.89	13.33	115.1	37.3
19	5	16	15	3.33	10.67	54.2	27.8
20	6	22	18	3.33	12.22	47.4	21.8
21	4	17	16	2.50	10.63	40.9	22.7
22	6	29	20	3.00	14.50	36.0	16.1
23	7	22	20	3.50	11.00	55.2	24.0
24	10	23	20	5.00	11.50	75.3	28.6
25	8	25	18	4.44	13.89	55.5	22.6
26	8	34	24	3.33	14.17	40.9	16.1
27							
28							
29							
30							
31							
32							
33							
34							
35							
36							
37							
38							
39							
40							

Sample	SM12032	
Irradiation Code	R-13-2-G	
Mineral	Apatite	
Ns	226	
RhoS	2.449	
Ni	876	
RhoI	9.491	
Area	923	
Nd	10905	
RhoD	10.16	
Pooled age	44.3	3.4
Mean age	47.1	2.4
Central age	44.3	3.4
Chi-square	11.99	
P(%)	99.43	
Dispersion	0	
Kurtosis	-0.86	
Skewness	0.19	

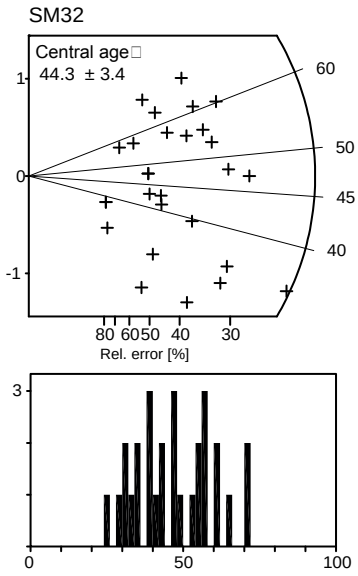

Crystal	Ns	Ni	Area	RhoS	RhoI	Age (Ma)	error (1σ)
1	4	12	28	1.43	4.29	57.2	33.0
2	6	25	30	2.00	8.33	41.2	18.8
3	9	22	24	3.75	9.17	70.1	27.8
4	8	48	30	2.67	16.00	28.6	11.0
5	5	27	32	1.56	8.44	31.8	15.5
6	7	21	40	1.75	5.25	57.2	25.0
7	5	12	30	1.67	4.00	71.4	38.0
8	17	62	100	1.70	6.20	47.1	12.9
9	2	11	20	1.00	5.50	31.2	24.0
10	13	37	50	2.60	7.40	60.2	19.5
11	11	34	50	2.20	6.80	55.5	19.3
12	13	63	60	2.17	10.50	35.4	10.8
13	12	62	50	2.40	12.40	33.3	10.5
14	14	50	36	3.89	13.89	48.1	14.6
15	10	28	30	3.33	9.33	61.2	22.6
16	4	27	24	1.67	11.25	25.5	13.7
17	2	9	20	1.00	4.50	38.2	29.8
18	5	18	20	2.50	9.00	47.7	24.1
19	6	16	28	2.14	5.71	64.3	30.8
20	9	39	30	3.00	13.00	39.6	14.7
21	6	24	24	2.50	10.00	42.9	19.6
22	9	28	28	3.21	10.00	55.1	21.2
23	22	106	40	5.50	26.50	35.7	8.4
24	5	20	24	2.08	8.33	42.9	21.5
25	12	39	24	5.00	16.25	52.8	17.5
26	5	18	16	3.13	11.25	47.7	24.1
27	2	9	21	0.95	4.29	38.2	29.8
28	3	9	14	2.14	6.43	57.2	38.1
29							
30							
31							
32							
33							
34							
35							
36							
37							
38							
39							
40							

Sample	SM12033	
Irradiation Code	R-13-2-G	
Mineral	Apatite	
Ns	1147	
RhoS	12.618	
Ni	3710	
RhoI	40.814	
Area	909	
Nd	10905	
RhoD	9.889	
Pooled age	51.6	2.1
Mean age	52.3	1.7
Central age	51.6	2.1
Chi-square	29.61	
P(%)	58.82	
Dispersion	0.05	
Kurtosis	-0.94	
Skewness	0.34	

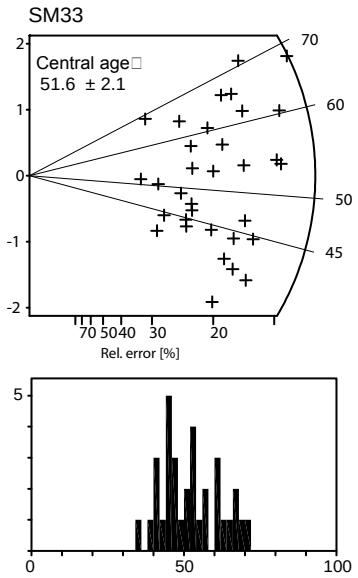

Crystal	Ns	Ni	Area	RhoS	RhoI	Age (Ma)	error (1σ)
1	39	148	35	11.14	42.29	44.0	8.0
2	23	60	18	12.78	33.33	64.0	15.7
3	17	64	25	6.80	25.60	44.4	12.2
4	37	108	30	12.33	36.00	57.2	11.0
5	26	75	20	13.00	37.50	57.9	13.2
6	69	170	50	13.80	34.00	67.7	9.8
7	60	185	40	15.00	46.25	54.2	8.1
8	43	180	30	14.33	60.00	39.9	6.8
9	30	141	24	12.50	58.75	35.6	7.2
10	16	53	20	8.00	26.50	50.4	14.4
11	35	142	30	11.67	47.33	41.2	7.8
12	25	90	20	12.50	45.00	46.4	10.5
13	44	158	40	11.00	39.50	46.5	8.0
14	23	88	30	7.67	29.33	43.7	10.3
15	38	157	28	13.57	56.07	40.5	7.4
16	45	140	30	15.00	46.67	53.7	9.3
17	47	176	30	15.67	58.67	44.6	7.4
18	31	117	30	10.33	39.00	44.3	9.0
19	14	34	15	9.33	22.67	68.7	21.9
20	25	88	24	10.42	36.67	47.5	10.8
21	23	86	20	11.50	43.00	44.7	10.5
22	32	88	25	12.80	35.20	60.7	12.6
23	38	96	24	15.83	40.00	66.0	12.7
24	63	174	40	15.75	43.50	60.4	9.0
25	42	107	24	17.50	44.58	65.5	12.0
26	33	104	30	11.00	34.67	53.0	10.7
27	46	108	25	18.40	43.20	71.0	12.6
28	46	124	25	18.40	49.60	61.9	10.8
29	62	193	40	15.50	48.25	53.6	7.9
30	26	81	30	8.67	27.00	53.6	12.1
31	22	75	15	14.67	50.00	49.0	11.9
32	15	61	18	8.33	33.89	41.1	11.9
33	12	39	24	5.00	16.25	51.4	17.0
34							
35							
36							
37							
38							
39							
40							

Sample	SM12048	
Irradiation Code	R-13-1-H	
Mineral	Apatite	
Ns	528	
RhoS	8.315	
Ni	1380	
RhoI	21.732	
Area	635	
Nd	10362	
RhoD	10.615	
Pooled age	68.5	3.8
Mean age	69.8	3.2
Central age	68.5	3.8
Chi-square	18.58	
P(%)	97.18	
Dispersion	0	
Kurtosis	0.1	
Skewness	0.35	

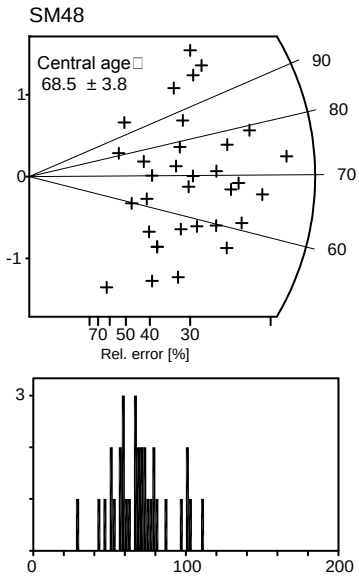

Crystal	Ns	Ni	Area	RhoS	RhoI	Age (Ma)	error (1σ)
1	8	19	12	6.67	15.83	75.3	31.8
2	3	18	12	2.50	15.00	29.9	18.7
3	14	25	12	11.67	20.83	100.0	33.5
4	14	32	20	7.00	16.00	78.3	25.1
5	6	11	10	6.00	11.00	97.4	49.5
6	9	23	18	5.00	12.78	70.0	27.6
7	6	18	12	5.00	15.00	59.7	28.2
8	12	46	15	8.00	30.67	46.8	15.2
9	5	11	12	4.17	9.17	81.3	43.9
10	16	49	30	5.33	16.33	58.5	16.9
11	26	76	30	8.67	25.33	61.3	14.0
12	8	27	12	6.67	22.50	53.1	21.4
13	18	29	15	12.00	19.33	110.8	33.3
14	30	68	30	10.00	22.67	78.9	17.4
15	20	35	24	8.33	14.58	102.0	28.7
16	40	98	36	11.11	27.22	73.0	13.8
17	16	41	12	13.33	34.17	69.9	20.7
18	9	32	24	3.75	13.33	50.4	19.1
19	13	41	16	8.13	25.63	56.8	18.1
20	22	70	30	7.33	23.33	56.3	13.8
21	8	34	16	5.00	21.25	42.2	16.6
22	24	64	18	13.33	35.56	67.1	16.1
23	18	32	20	9.00	16.00	100.5	29.7
24	26	68	24	10.83	28.33	68.5	15.9
25	13	32	18	7.22	17.78	72.7	24.0
26	32	86	32	10.00	26.88	66.6	13.9
27	15	31	16	9.38	19.38	86.5	27.3
28	20	60	24	8.33	25.00	59.7	15.5
29	24	56	20	12.00	28.00	76.7	18.8
30	21	53	16	13.13	33.13	70.9	18.4
31	15	40	20	7.50	20.00	67.1	20.4
32	8	23	15	5.33	15.33	62.3	25.6
33	9	32	14	6.43	22.86	50.4	19.1
34							
35							
36							
37							
38							
39							
40							

Sample	SM12054	
Irradiation Code	R-13-1-H	
Mineral	Apatite	
Ns	52	
RhoS	1.156	
Ni	108	
RhoI	2.400	
Area	450	
Nd	10362	
RhoD	10.784	
Pooled age	87.4	14.9
Mean age	89.7	7.9
Central age	87.4	14.9
Chi-square	3.72	
P(%)	99.97	
Dispersion	0	
Kurtosis	1.93	
Skewness	1.14	

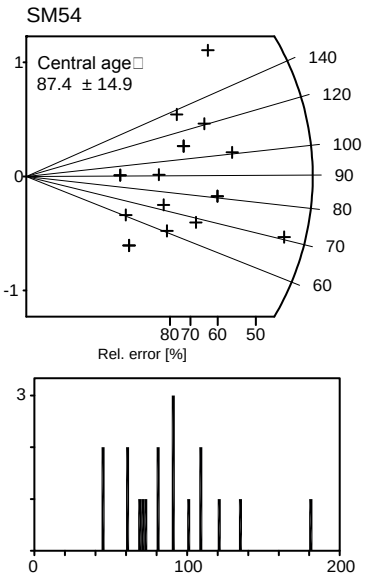

Crystal	Ns	Ni	Area	RhoS	RhoI	Age (Ma)	error (1σ)
1	3	4	16	1.88	2.50	135.7	103.7
2	1	4	20	0.50	2.00	45.5	50.9
3	2	4	20	1.00	2.00	90.8	78.6
4	2	6	16	1.25	3.75	60.7	49.5
5	1	2	16	0.63	1.25	90.8	111.2
6	5	5	20	2.50	2.50	180.3	114.1
7	3	5	16	1.88	3.13	108.8	79.5
8	4	6	35	1.14	1.71	120.8	78.0
9	7	18	30	2.33	6.00	70.7	31.5
10	5	9	25	2.00	3.60	100.8	56.3
11	1	3	18	0.56	1.67	60.7	70.1
12	1	4	20	0.50	2.00	45.5	50.9
13	4	9	40	1.00	2.25	80.8	48.6
14	1	2	40	0.25	0.50	90.8	111.2
15	3	5	35	0.86	1.43	108.8	79.5
16	2	5	28	0.71	1.79	72.7	60.9
17	4	9	20	2.00	4.50	80.8	48.6
18	3	8	35	0.86	2.29	68.2	46.2
19							
20							
21							
22							
23							
24							
25							
26							
27							
28							
29							
30							
31							
32							
33							
34							
35							
36							
37							
38							
39							
40							

Sample	SM12058	
Irradiation Code	R-13-1-H	
Mineral	Apatite	
Ns	108	
RhoS	1.912	
Ni	360	
RhoI	6.372	
Area	565	
Nd	10362	
RhoD	11.122	
Pooled age	56.3	6.3
Mean age	65.2	6.0
Central age	56.3	6.3
Chi-square	10.17	
P(%)	94.86	
Dispersion	0	
Kurtosis	0.42	
Skewness	1.05	

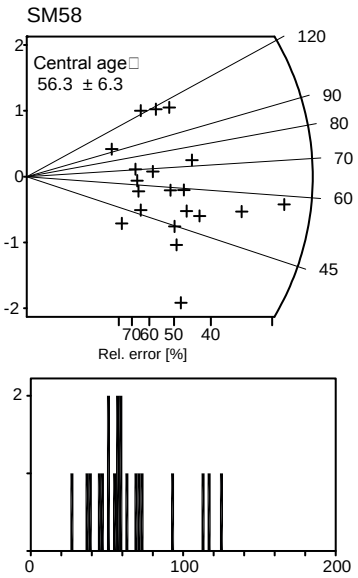

Crystal	Ns	Ni	Area	RhoS	RhoI	Age (Ma)	error (1σ)
1	7	18	14	5.00	12.86	72.9	32.5
2	6	22	16	3.75	13.75	51.2	23.6
3	5	8	12	4.17	6.67	116.8	66.6
4	6	10	15	4.00	6.67	112.2	58.0
5	5	36	40	1.25	9.00	26.1	12.5
6	6	19	32	1.88	5.94	59.3	27.8
7	5	24	32	1.56	7.50	39.2	19.3
8	2	4	30	0.67	1.33	93.6	81.1
9	2	10	24	0.83	4.17	37.6	29.1
10	16	52	30	5.33	17.33	57.8	16.6
11	3	9	28	1.07	3.21	62.6	41.7
12	4	11	28	1.43	3.93	68.2	39.9
13	5	16	28	1.79	5.71	58.7	30.1
14	5	21	40	1.25	5.25	44.7	22.3
15	3	8	24	1.25	3.33	70.3	47.6
16	3	10	35	0.86	2.86	56.3	37.1
17	4	6	32	1.25	1.88	124.5	80.4
18	7	26	40	1.75	6.50	50.6	21.6
19	11	38	50	2.20	7.60	54.4	18.7
20	3	12	15	2.00	8.00	47.0	30.3
21							
22							
23							
24							
25							
26							
27							
28							
29							
30							
31							
32							
33							
34							
35							
36							
37							
38							
39							
40							

Appendix B2

Supplementary fission-track length data for the samples presented in Chapter 5.

SM11008

Sample	#	Length (µm)	C-axis angle	#	Length (µm)	C-axis angle	#	Length (µm)	C-axis angle	#	Length (µm)	C-axis angle
SM11008	1	13.175	73.966	26	12.445	61.858	51	12.355	74.726	76	11.844	62.472
	2	11.798	53.594	27	14.834	53.942	52	13.343	44.744	77	13.664	71.371
	3	12.849	48.022	28	13.019	57.211	53	14.248	21.928	78	13.494	47.246
	4	13.775	38.295	29	13.349	34.451	54	12.575	77.905	79	12.102	50.455
	5	11.436	70.345	30	11.303	73.687	55	13.132	71.638	80	11.407	66.269
	6	11.475	44.756	31	14.743	49.955	56	13.252	62.132	81	15.453	50.269
	7	14.514	35.727	32	13.988	65.541	57	14.321	60.809	82	11.324	73.022
	8	12.921	51.548	33	14.103	45.674	58	13.507	75.165	83	13.932	56.299
	9	15.551	10.091	34	14.513	4.63	59	14.408	73.998	84	10.954	64.442
	10	12.366	75.15	35	10.07	66.564	60	12.336	69.248	85	12.283	80.236
	11	14.002	29.03	36	13.832	25.034	61	13.907	45.007	86	13.577	47.855
	12	15.137	49.09	37	12.283	71.053	62	11.58	71.742	87	11.822	64.784
	13	13.021	49.938	38	13.889	60.834	63	11.874	46.651	88	12.09	51.232
	14	13.183	32.629	39	12.742	73.884	64	12.035	76.313	89	14.092	26.233
	15	12.385	66.297	40	12.71	70.058	65	14.736	68.465	90	13.101	70.696
	16	14.203	37.145	41	13.197	48.065	66	13.79	53.583	91	11.153	45.843
	17	13.418	41.57	42	11.663	68.242	67	14.842	40.82	92	10.487	42.794
	18	12.839	66.375	43	14.135	40.815	68	14.666	46.894	93	10.943	73.75
	19	12.738	67.88	44	12.322	70.689	69	13.143	69.588	94	14.079	57.705
	20	11.615	77.123	45	11.78	83.077	70	13.57	60.747	95	12.498	69.493
	21	12.335	73.611	46	11.889	73.559	71	13.691	60.08	96	13.112	77.211
	22	13.124	52.217	47	14.617	60.605	72	11.14	44.599	97	13.328	80.012
	23	14.526	29.333	48	13.782	28.564	73	12.275	59.956	98	12.953	77.938
	24	12.855	70.04	49	14.091	28.104	74	11.561	80.846	99	12.165	58.913
	25	11.595	81.877	50	12.744	77.468	75	12.1	47.604	100	14.024	39.474

Grain	MDpar	MDprp	NDpar	Grain	MDpar	MDprp	NDpar	Grain	MDpar	MDprp	NDpar
1	1.298	0.492	7	26	1.22	0.525	4	51	1.278	0.537	4
2	1.16	0.392	5	27	1.451	0.563	4	52	1.117	0.454	4
3	1.088	0.524	5	28	1.274	0.35	4	53	1.138	0.448	4
4	1.048	0.386	5	29	1.129	0.459	4	54	1.161	0.479	4
5	1.206	0.351	5	30	1.108	0.467	4	55	1.147	0.343	4
6	1.421	0.619	4	31	1.159	0.544	4	56	0.993	0.347	4
7	1.2	0.379	4	32	1.04	0.464	4	57	1.228	0.39	4
8	1.078	0.378	5	33	1.215	0.402	4	58	0.97	0.499	4
9	1.001	0.421	4	34	1.102	0.363	4	59	1.222	0.572	4
10	1.085	0.435	4	35	1.028	0.395	4	60	1.228	0.635	4
11	1.305	0.488	4	36	1.15	0.481	4	61	1.214	0.515	4
12	1.191	0.51	4	37	1.409	0.494	4				
13	1.266	0.467	4	38	1.331	0.545	5				
14	1.068	0.474	4	39	1.2	0.536	3				
15	1.225	0.475	4	40	1.37	0.371	4				
16	1.112	0.405	4	41	1.039	0.364	4				
17	1.183	0.475	4	42	1.211	0.413	4				
18	1.218	0.428	4	43	1.171	0.463	4				
19	1.126	0.601	4	44	1.244	0.516	4				
20	1.079	0.428	4	45	0.944	0.381	4				
21	1.176	0.509	4	46	1.056	0.525	4				
22	1.058	0.471	4	47	1.13	0.463	4				
23	1.209	0.427	4	48	1.193	0.503	4				
24	1.094	0.515	4	49	1.247	0.45	4				
25	1.123	0.441	4	50	1.148	0.462	4				

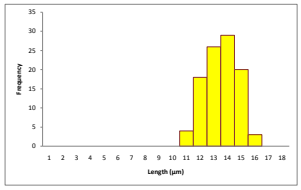

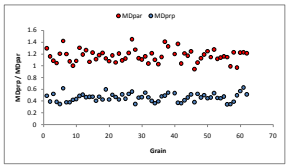

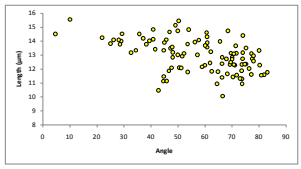

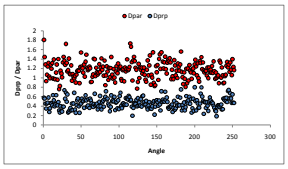

Mean length (µm)	12.991
SD	1.173
Mean Dpar	1.169
SD	0.179
Mean Dprp	0.462
SD	0.116

Minimum length (µm)	10.070
Maximum length (µm)	15.551
Minimum Dpar	0.762
Maximum Dpar	1.806
Minimum Dprp	0.183
Maximum Dprp	0.804

SM11009

Sample	#	Length (µm)	C-axis angle	#	Length (µm)	C-axis angle	#	Length (µm)	C-axis angle	#	Length (µm)	C-axis angle
SM11009	1	17.427	0.66	26	9.053	71.72	51	11.295	85.80	76	10.527	51.47
	2	9.375	1.47	27	13.781	9.55	52	11.862	10.45	77	12.086	70.69
	3	14.339	43.72	28	14.56	1.80	53	13.008	9.31	78	13.328	25.95
	4	13.146	65.15	29	12.648	67.42	54	12.147	25.93	79	13.256	86.66
	5	15.308	66.82	30	14.184	7.53	55	14.008	54.73	80	13.004	33.54
	6	13.444	7.89	31	14.163	63.76	56	12.804	21.07	81	14.482	39.52
	7	10.582	82.21	32	11.693	6.89	57	13.605	44.48	82	14.675	38.14
	8	13.428	51.76	33	14.269	0.49	58	14.02	37.89	83	13.694	14.76
	9	14.69	13.59	34	13.024	38.22	59	14.184	17.62	84	12.338	4.57
	10	12.903	87.04	35	13.67	60.89	60	11.208	80.78	85	12.591	52.94
	11	13.244	78.50	36	13.294	54.44	61	13.455	66.07	86	13.455	61.39
	12	13.822	57.80	37	13.967	68.95	62	15.542	22.96	87		
	13	10.679	40.14	38	13.521	5.02	63	12.02	89.84	88		
	14	14.596	22.33	39	13.431	39.39	64	15.054	1.95	89		
	15	10.626	63.37	40	12.209	51.10	65	12.611	43.93	90		
	16	12.25	74.78	41	13.814	54.39	66	9.463	67.76	91		
	17	13.998	73.31	42	13.735	22.29	67	13.946	18.81	92		
	18	11.621	9.49	43	13.243	60.83	68	13.097	65.82	93		
	19	14.129	89.75	44	13.902	18.97	69	13.773	54.68	94		
	20	12.436	8.80	45	13.462	33.97	70	8.941	3.80	95		
	21	13.208	43.09	46	13.208	19.05	71	9.412	70.99	96		
	22	13.134	41.66	47	11.316	40.88	72	14.225	8.57	97		
	23	13.266	11.21	48	14.137	1.09	73	14.495	30.18	98		
	24	15.056	41.10	49	13.844	54.44	74	14.632	1.04	99		
	25	13.625	36.21	50	13.752	71.20	75	11.868	39.74	100		

Grain	MDpar	MDprp	NDpar	Grain	MDpar	MDprp	NDpar
1	1.793	0.798	4	26	1.6	0.925	4
2	1.301	0.527	4	27	1.31	0.65	4
3	1.572	0.72	4	28	1.406	0.584	4
4	1.707	0.924	4	29	1.67	0.698	4
5	1.343	0.518	4	30	1.79	0.825	4
6	1.429	0.616	4	31	1.633	0.625	4
7	1.613	0.629	4	32	1.148	0.404	4
8	1.868	1.049	4	33	1.229	0.687	4
9	1.413	0.529	4	34	1.319	0.554	4
10	1.222	0.455	4	35	1.455	0.632	4
11	1.607	0.818	4	36	1.242	0.566	4
12	1.732	0.942	4	37	1.044	0.357	4
13	1.704	0.756	4	38	1.256	0.547	4
14	1.552	0.786	4	39	1.086	0.472	4
15	1.479	0.761	4	40	1.617	0.748	4
16	1.724	0.927	4	41	1.512	0.699	4
17	1.517	0.697	4	42	1.41	0.53	4
18	1.559	0.672	4				
19	1.508	0.59	4				
20	1.694	0.709	4				
21	1.544	0.766	4				
22	1.41	0.423	4				
23	1.234	0.57	4				
24	1.459	0.579	4				
25	1.751	0.799	4				

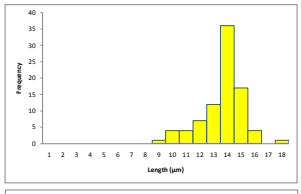

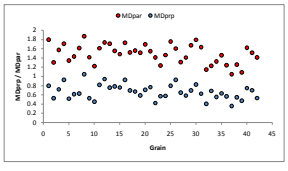

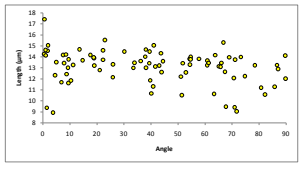

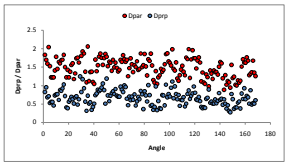

Mean length (µm)	13.097
SD	1.518
Mean Dpar	1.485
SD	0.259
Mean Dprp	0.668
SD	0.198

Minimum length (µm)	8.941
Maximum length (µm)	17.427
Minimum Dpar	0.883
Maximum Dpar	2.063
Minimum Dprp	0.275
Maximum Dprp	1.256

SM11011

Sample	#	Length (µm)	C-axis angle	#	Length (µm)	C-axis angle	#	Length (µm)	C-axis angle	#	Length (µm)	C-axis angle
SM11011	1	13.004	55.385	26	12.232	52.116	51	14.865	43.176	76	13.384	21.587
	2	13.819	68.144	27	13.221	12.698	52	13.648	72.025	77	12.453	68.854
	3	13.603	57.517	28	13.586	47.514	53	13.74	47.568	78	13.355	58.632
	4	10.195	6.851	29	11.586	64.015	54	13.074	26.697	79	15.147	11.912
	5	13.07	20.667	30	13.958	24.609	55	13.296	17.831	80	13.963	14.67
	6	11.694	89.519	31	13.637	15.623	56	14.098	15.57	81	13.096	22.479
	7	12.046	57.433	32	11.724	54.509	57	13.91	66.651			
	8	12.521	82.754	33	11.439	82.319	58	12.888	73.124			
	9	13.081	62.377	34	14.228	7.827	59	14.572	48.824			
	10	15.414	5.986	35	14.011	21.029	60	13.539	23.738			
	11	11.823	72.938	36	11.762	74.715	61	14.971	11.827			
	12	13.23	40.859	37	11.012	50.949	62	13.423	59.959			
	13	13.184	43.599	38	13.108	60.643	63	13.078	42.132			
	14	11.569	64.328	39	13.511	9.728	64	14.782	18.471			
	15	13.61	20.506	40	13.062	14.737	65	12.091	81.202			
	16	12.785	20.29	41	11.522	20.643	66	12.225	68.929			
	17	13.632	55.268	42	13.252	29.156	67	12.6	58.423			
	18	11.643	76.715	43	12.203	72.789	68	14.342	0.695			
	19	14.587	6.228	44	12.316	61.401	69	13.517	18.916			
	20	13.924	31.841	45	15.081	6.885	70	12.857	53.924			
	21	13.1	1.376	46	14.198	10.99	71	13.682	75.794			
	22	12.147	83.197	47	12.566	58.134	72	12.281	74.9			
	23	13.776	27.964	48	12.734	63.392	73	13.45	52.29			
	24	13.598	2.503	49	12.079	42.08	74	14.464	10.468			
	25	13.256	5.252	50	14.023	4.616	75	14.233	5.509			

Grain	MDpar	MDprp	NDpar	Grain	MDpar	MDprp	NDpar	Grain	MDpar	MDprp	NDpar
1	1.222	0.557	4	26	1.159	0.375	4	51	1.364	0.743	4
2	1.156	0.581	4	27	1.328	0.74	4	52	1.664	0.792	4
3	1.275	0.566	4	28	1.251	0.626	4	53	1.557	0.751	4
4	1.192	0.366	4	29	1.323	0.539	4				
5	1.071	0.451	4	30	1.277	0.429	4				
6	1.071	0.377	4	31	1.403	0.587	4				
7	1.452	0.688	4	32	1.183	0.534	4				
8	1.105	0.574	4	33	1.286	0.623	4				
9	1.36	0.571	4	34	1.343	0.425	4				
10	1.267	0.513	4	35	1.151	0.478	4				
11	1.32	0.648	4	36	1.316	0.335	4				
12	1.286	0.645	4	37	1.718	0.811	4				
13	1.168	0.503	4	38	1.632	0.717	4				
14	1.108	0.502	4	39	1.642	0.828	4				
15	1.209	0.552	4	40	1.287	0.706	4				
16	1.226	0.559	4	41	1.773	0.758	4				
17	1.348	0.753	4	42	1.526	0.722	4				
18	1.266	0.496	4	43	1.553	0.747	4				
19	1.288	0.654	4	44	1.498	0.733	4				
20	1.304	0.505	4	45	1.558	0.685	4				
21	1.415	0.586	4	46	1.523	0.997	4				
22	1.232	0.483	4	47	1.844	0.782	4				
23	1.287	0.685	4	48	1.593	0.69	4				
24	1.065	0.325	4	49	1.714	0.699	4				
25	1.046	0.542	4	50	1.734	0.973	4				

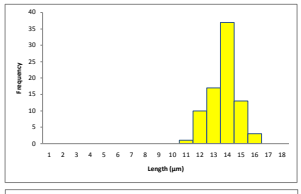

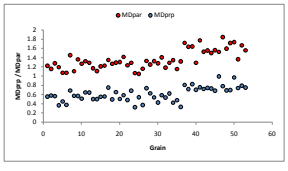

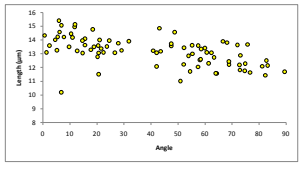

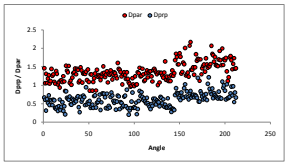

Mean length (µm)	13.178
SD	1.034
Mean Dpar	1.357
SD	0.247
Mean Dprp	0.613
SD	0.186

Minimum length (µm)	10.195
Maximum length (µm)	15.414
Minimum Dpar	0.845
Maximum Dpar	2.173
Minimum Dprp	0.205
Maximum Dprp	1.222

SM11012

Sample	#	Length (µm)	C-axis angle	#	Length (µm)	C-axis angle	#	Length (µm)	C-axis angle	#	Length (µm)	C-axis angle
	1	13.025	49.732	26	12.739	55.717	51	12.629	88.033	76	12.585	60.356
	2	13.521	53.591	27	14.559	57.535	52	14.482	60.167	77	13.249	20.984
	3	13.005	53.804	28	13.488	63.371	53	13.816	48.652	78	13.969	58.439
	4	14.322	72.291	29	13.604	76.355	54	12.706	61.551	79	14.096	8.307
	5	15.129	5.09	30	12.964	60.882	55	12.7	83.831	80	14.077	48.054
	6	13.169	27.347	31	13.688	72.539	56	11.519	82.972	81	12.241	77.831
	7	13.496	58.336	32	13.882	55.288	57	12.272	61.166	82	12.287	71.303
	8	14.349	32.327	33	12.469	75.428	58	13.457	53.926	83	13.911	20.313
	9	14.462	53.047	34	14.328	59.16	59	13.385	65.043	84	13.219	22.684
	10	14.931	24.444	35	12.888	45.632	60	12.763	73.386	85	14.833	38.392
	11	14.076	28.327	36	14.372	41.409	61	14.765	35.85	86	13.843	54.276
	12	14.369	4.653	37	14.791	35.766	62	13.542	27.004	87	11.562	64.908
	13	12.172	52.571	38	15.066	1.213	63	12.47	72.843	88	13.883	35.464
	14	14.492	47.932	39	12.47	50.755	64	12.382	87.587	89	11.788	69.502
	15	15.086	57.146	40	13.262	46.953	65	14.895	70.836	90	12.781	47.175
	16	12.737	65.297	41	13.728	9.28	66	13.018	50.252	91	13.179	72.683
	17	12.956	58.667	42	14.832	2.404	67	14.835	68.043	92	13.99	18.799
	18	14.141	57.811	43	13.297	50.039	68	14.944	47.082	93	15.204	40.203
	19	13.334	58.413	44	13.124	39.733	69	13.93	50.238	94	13.814	18.104
	20	13.561	62.101	45	12.495	82.992	70	14.204	23.632	95	13.163	57.213
	21	13.532	58.031	46	14.265	12.255	71	12.64	71.992	96	13.972	26.243
	22	13.604	46.674	47	13.451	57.232	72	11.792	53.502	97	13.419	62.152
	23	13.014	46.229	48	13.636	29.578	73	12.162	71.539	98	13.728	45.303
	24	14.788	28.656	49	12.204	46.181	74	11.988	76.589	99	12.838	67.266
	25	13.185	49.119	50	14.788	63.062	75	13.148	79.179	100	13.583	45

Grain	MDpar	MDprp	NDpar	Grain	MDpar	MDprp	NDpar	Grain	MDpar	MDprp	NDpar
1	0.877	0.389	4	26	1.099	0.32	4	51	0.98	0.468	4
2	0.894	0.321	4	27	1.143	0.56	4	52	0.959	0.364	4
3	0.932	0.371	4	28	1.144	0.641	4	53	0.96	0.485	4
4	0.969	0.41	4	29	1.121	0.616	4	54	0.913	0.464	4
5	1.029	0.457	4	30	0.896	0.358	4	55	1.011	0.42	4
6	1.104	0.442	4	31	0.948	0.382	4	56	1.065	0.514	4
7	0.921	0.445	4	32	0.827	0.348	4	57	1.066	0.507	4
8	1.024	0.316	4	33	0.916	0.441	4	58	1.02	0.505	4
9	0.796	0.393	4	34	0.946	0.526	4	59	1.023	0.432	4
10	0.811	0.346	4	35	0.916	0.386	4	60	1.085	0.522	4
11	0.962	0.372	4	36	0.921	0.397	4	61	0.871	0.445	4
12	1.445	0.375	4	37	0.968	0.431	4	62	1.063	0.597	4
13	0.846	0.292	4	38	1.07	0.368	4	63	1.177	0.441	4
14	0.98	0.412	4	39	1.033	0.43	4	64	0.904	0.446	4
15	0.83	0.289	4	40	1.045	0.432	4	65	1.108	0.521	4
16	0.969	0.466	4	41	1.164	0.476	4	66	0.909	0.404	4
17	0.709	0.324	4	42	0.92	0.469	3	67	1.166	0.45	4
18	1.081	0.372	4	43	1.113	0.393	4				
19	0.879	0.449	4	44	1.226	0.494	4				
20	0.998	0.382	4	45	0.983	0.364	4				
21	1.002	0.35	4	46	1.138	0.453	4				
22	1.241	0.522	4	47	0.989	0.408	4				
23	0.974	0.46	4	48	0.935	0.455	4				
24	0.903	0.416	4	49	0.796	0.358	4				
25	0.954	0.481	4	50	0.922	0.373	4				

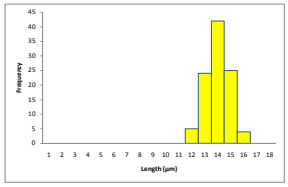

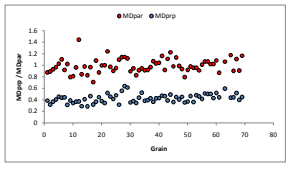

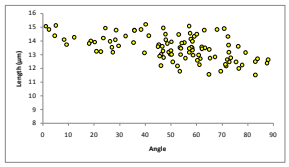

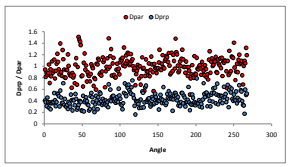

Mean length (µm)	13.505
SD	0.903
Mean Dpar	0.994
SD	0.172
Mean Dprp	0.428
SD	0.114

Minimum length (µm)	11.519
Maximum length (µm)	15.204
Minimum Dpar	0.509
Maximum Dpar	1.514
Minimum Dprp	0.163
Maximum Dprp	0.791

SM11013

Sample	#	Length (µm)	C-axis angle	#	Length (µm)	C-axis angle	#	Length (µm)	C-axis angle	#	Length (µm)	C-axis angle
	1	14.499	1.034	26	12.814	73.297	51	12.322	11.33	76	12.552	2.37
	2	11.353	79.357	27	10.923	81.59	52	12.248	22.316	77	10.817	73.189
	3	14.312	1.33	28	13.237	38.826	53	12.682	71.909	78	13.861	5.932
	4	12.652	78.965	29	12.942	60.114	54	11.187	82.027	79	12.29	41.449
	5	13.44	56.527	30	14.309	35.678	55	14.502	0.782	80	13.406	33.855
	6	11.364	58.864	31	13.345	42.425	56	13.489	44.401	81	11.059	75.843
	7	10.776	64.351	32	13.405	59.314	57	13.517	69.433	82	13.555	43.807
	8	14.917	27.7	33	13.089	35.545	58	14.047	45.061	83	13.64	1.853
	9	11.849	67.168	34	12.574	61.976	59	11.008	77.806	84	11.727	63.594
	10	13.514	12.662	35	14.368	5.898	60	12.256	81.697	85	13.682	52.595
	11	14.242	51.18	36	11.179	71.341	61	14.151	3.232	86	13.153	28.131
	12	14.621	2.566	37	12.673	37.117	62	13.076	49.117	87	13.111	35.641
	13	12.752	79.212	38	13.938	42.055	63	12.017	44.668	88	10.692	85.076
	14	11.187	7.128	39	12.511	68.645	64	13.902	57.817	89	12.927	51.707
	15	13.046	25.249	40	14.409	11.032	65	14.87	14.481	90	14.074	28.361
	16	13.159	10.465	41	14.711	69.38	66	12.603	46.92	91	13.053	21.759
	17	14.622	35.397	42	13.778	43.504	67	13.275	38.007	92	13.512	46.918
	18	12.889	59.82	43	10.808	85.883	68	13.531	6.497	93	10.612	79.255
	19	12.308	56.55	44	13.101	41.193	69	11.702	26	94	13.768	19.823
	20	12.796	56.869	45	13.144	46.196	70	13.452	84.502	95	14.139	0.242
	21	13.074	48.444	46	13.145	43.046	71	14.312	34.313	96	12.807	50.828
	22	13.657	6.147	47	13.788	39.556	72	15.396	5.022	97	13.306	16.37
	23	13.343	65.507	48	13.914	30.934	73	11.409	73.96	98	12.641	33.828
	24	13.265	72.799	49	15.601	4.126	74	14.093	44.327	99	13.893	25.934
	25	13.023	35.833	50	11.073	77.274	75	13.211	35.747	100	13.203	12.41

Grain	MDpar	MDprp	NDpar	Grain	MDpar	MDprp	NDpar
1	1.205	0.444	4	26	1.234	0.502	4
2	1.289	0.414	4	27	0.946	0.499	4
3	0.947	0.362	4	28	1.153	0.51	4
4	1.158	0.542	4	29	1.064	0.521	4
5	1.104	0.352	4	30	1.046	0.406	4
6	1.1	0.386	4	31	1.12	0.49	7
7	1.054	0.381	4	32	0.948	0.366	4
8	0.974	0.442	4	33	1.034	0.453	4
9	0.709	0.247	4	34	1.185	0.489	4
10	0.92	0.295	4	35	0.814	0.478	4
11	0.774	0.354	4	36	0.945	0.493	4
12	0.918	0.339	4	37	1.251	0.442	4
13	1.098	0.349	4	38	1.159	0.377	4
14	1.033	0.406	4	39	1.029	0.575	4
15	0.835	0.426	4	40	1.089	0.472	4
16	0.816	0.322	4	41	0.832	0.485	4
17	1.015	0.428	4	42	1.021	0.393	4
18	1.246	0.363	4	43	0.971	0.47	4
19	1.17	0.362	4				
20	1.185	0.425	4				
21	1.008	0.538	4				
22	1.002	0.38	4				
23	0.979	0.379	4				
24	1.064	0.388	4				
25	1.209	0.41	4				

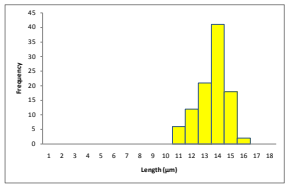

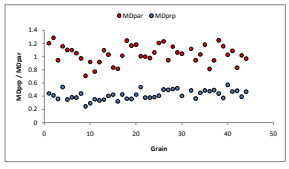

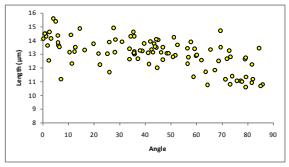

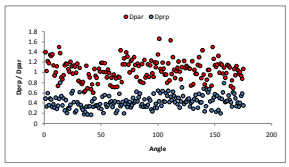

Mean length (µm)	13.052
SD	1.136
Mean Dpar	1.039
SD	0.198
Mean Dprp	0.423
SD	0.126

Minimum length (µm)	10.612
Maximum length (µm)	15.601
Minimum Dpar	0.600
Maximum Dpar	1.660
Minimum Dprp	0.171
Maximum Dprp	0.798

SM11023

Sample	#	Length (µm)	C-axis angle	#	Length (µm)	C-axis angle	#	Length (µm)	C-axis angle	#	Length (µm)	C-axis angle
	1	14.825	60.52	26	14.606	3.223	51	14.473	47.817	76	12.638	23.979
	2	13.16	84.119	27	14.396	69.836	52	13.212	58.477	77	13.596	74.495
	3	15.297	51.24	28	13.983	25.754	53	13.783	12.698	78	12.74	72.871
	4	11.854	71.949	29	12.662	73.76	54	11.84	54.771	79	14.469	23.943
	5	12.881	77.694	30	12.62	74.557	55	11.764	31.09	80	14.475	71.636
	6	14.1	56.87	31	11.139	83.076	56	13.907	9.335	81	12.881	76.623
	7	14.201	48.701	32	14.075	28.81	57	13.859	48.768	82	13.706	43.45
	8	14.484	66.985	33	13.895	22.419	58	11.17	25.773	83	13.168	89.989
	9	13.619	37.448	34	12.744	75.63	59	13.156	47.587	84	13.773	47.214
	10	15.254	28.473	35	13.843	65.659	60	11.354	85.884	85	12.84	85.892
	11	14.485	16.133	36	15.719	0.439	61	13.256	71.124	86	13.103	51.682
	12	12.55	35.664	37	14.554	39.165	62	13.612	70.448	87	12.311	74.093
	13	12.874	51.793	38	13.136	71.986	63	14.208	71.543	88	15.185	32.192
	14	15.576	7.085	39	11.818	84.055	64	13.534	42.455	89	13.723	25.522
	15	13.503	48.398	40	13.737	81.734	65	13.248	8.99	90	14.093	61.2
	16	13.609	50.459	41	12.254	35.503	66	12.64	69.849	91	14.786	55.669
	17	15.477	0.011	42	14.3	42.44	67	13.045	22.298	92	13.017	3.791
	18	15.783	1.231	43	12.204	30.165	68	14.434	78.899	93	13.618	21.822
	19	12.862	57.518	44	14.197	51.662	69	13.42	34.87	94	13.667	44.026
	20	13.895	39.455	45	13.298	79.595	70	14.757	5.52	95	14.344	30.655
	21	14.116	9.072	46	11.04	64.775	71	13.45	82.176	96	10.99	46.914
	22	13.695	75.11	47	15.763	46.653	72	14.379	31.448	97	13.111	42.938
	23	13.076	14.504	48	14.173	42.234	73	12.918	43.308	98	13.364	24.054
	24	13.735	1.191	49	13.592	74.874	74	13.224	57.627	99	13.144	58.774
	25	12.445	62.565	50	12.796	58.395	75	14.004	70.423	100	12.099	78.176

Grain	MDpar	MDprp	NDpar	Grain	MDpar	MDprp	NDpar	Grain	MDpar	MDprp	NDpar
1	1.231	0.454	4	26	1.182	0.475	4	51	1.199	0.704	4
2	1.323	0.526	4	27	0.987	0.483	4	52	1.748	0.484	4
3	1.08	0.482	4	28	1.333	0.453	4	53	1.327	0.529	4
4	1.184	0.392	4	29	1.013	0.54	4	54	0.927	0.475	4
5	1.541	0.672	4	30	1.167	0.526	4	55	1.431	0.624	4
6	1.351	0.475	4	31	1.474	0.642	4	56	1.24	0.65	4
7	1.012	0.338	4	32	1.187	0.437	4	57	1.243	0.49	4
8	1.467	0.47	4	33	1.406	0.605	4	58	1.037	0.48	4
9	1.487	0.487	4	34	1.208	0.441	4	59	1.206	0.477	4
10	1.113	0.457	4	35	1.174	0.478	4	60	1.149	0.396	4
11	1.104	0.309	4	36	0.949	0.393	4	61	1.274	0.587	4
12	1.245	0.573	4	37	1.064	0.449	4	62	1.223	0.446	4
13	1.189	0.497	4	38	1.17	0.549	4	63	1.378	0.573	4
14	1.438	0.493	4	39	1.168	0.511	4	64	1.34	0.495	4
15	1.482	0.634	4	40	1.11	0.364	4	65	1.033	0.331	4
16	1.222	0.661	4	41	0.935	0.388	4	66	1.341	0.536	4
17	1.363	0.558	4	42	1.237	0.551	4				
18	1.217	0.521	4	43	1.292	0.454	4				
19	1.218	0.442	4	44	1.21	0.531	4				
20	1.267	0.435	4	45	1.183	0.551	4				
21	1.227	0.599	4	46	1.231	0.446	4				
22	1.226	0.602	4	47	1.208	0.417	4				
23	1.235	0.573	4	48	1.47	0.616	4				
24	1.31	0.489	4	49	1.456	0.493	4				
25	0.997	0.476	4	50	1.334	0.572	4				

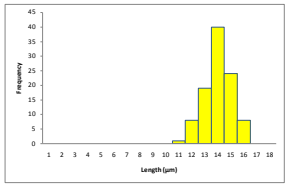

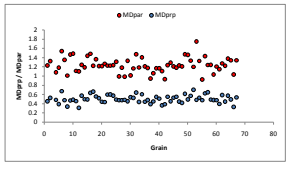

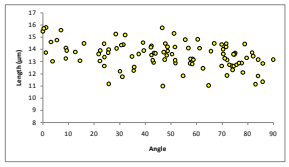

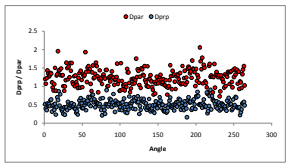

Mean length (µm)	13.514
SD	1.055
Mean Dpar	1.239
SD	0.226
Mean Dprp	0.504
SD	0.135

Minimum length (µm)	10.990
Maximum length (µm)	15.783
Minimum Dpar	0.727
Maximum Dpar	2.061
Minimum Dprp	0.161
Maximum Dprp	0.911

SM112033

Sample	#	Length (µm)	C-axis angle	#	Length (µm)	C-axis angle	#	Length (µm)	C-axis angle	#	Length (µm)	C-axis angle
SM112033	1	15.022	24.615	26	11.724	70.038	51	12.053	58.199	76	13.33	69.886
	2	10.559	54.226	27	13.436	12.995	52	14.131	58.905	77	13.289	64.081
	3	13.188	61.915	28	15.301	46.126	53	11.742	84.432	78	13.534	34.95
	4	13.959	40.666	29	13.694	75.654	54	12.044	81.845	79	13.478	1.013
	5	14.049	32.521	30	13.038	39.476	55	12.738	82.315	80	14.879	26.17
	6	12.084	56.621	31	14.528	25.855	56	12.162	71.691	81	13.788	81.894
	7	12.468	57.774	32	12.527	89.602	57	14.325	88.059	82	15.249	67.464
	8	15.246	46.832	33	12.077	59.78	58	13.459	75.742	83	13.979	56.864
	9	14.114	36.633	34	13.657	56.994	59	14.88	61.468	84	12.995	43.01
	10	12.94	73.013	35	14.238	57.97	60	13.417	41.697	85	13.172	74.638
	11	14.049	76.409	36	13.499	58.506	61	10.402	66.961	86	14.725	22.468
	12	13.833	78.448	37	13.609	52.577	62	10.236	68.741	87	14.221	56.631
	13	13.95	9.185	38	11.796	44.701	63	13.715	45.336	88	13.18	49.674
	14	13.319	63.839	39	14.468	76.502	64	14.697	13.489	89	14.464	50.549
	15	13.742	36.143	40	13.804	53.821	65	14.926	25.179	90	14.391	24.298
	16	11.818	44.392	41	12.41	42.389	66	13.741	61.408	91	13.373	46.038
	17	15.306	15.933	42	13.88	57.685	67	13.776	41.283	92	13.303	50.711
	18	14.741	34.958	43	15.142	59.887	68	13.9	67.059	93	13.079	67.256
	19	10.599	66.657	44	13.239	51.564	69	13.647	44.422	94	15.914	55.377
	20	14.323	73.755	45	14.658	57.257	70	12.754	40.985	95	16.539	42.903
	21	15.633	41.078	46	13.42	66.504	71	15.283	55.513	96	14.436	40.095
	22	12.991	52.457	47	13.683	55.923	72	14.161	88.464	97	11.802	74.634
	23	10.93	81.301	48	11.81	61.135	73	13.972	72.622	98	12.84	63.765
	24	13.95	19.31	49	11.952	70.292	74	15.271	68.034	99	14.464	43.102
	25	11.642	73.911	50	14.157	13.126	75	14.552	30.798	100	13.384	44.544

Grain	MDpar	MDprp	NDpar	Grain	MDpar	MDprp	NDpar	Grain	MDpar	MDprp	NDpar
1	1.615	0.84	4	26	1.79	0.822	4	51	1.831	0.873	4
2	1.901	0.801	4	27	1.925	0.76	4	52	1.981	0.782	4
3	2.067	1.048	5	28	1.968	0.888	4	53	2.992	1.329	4
4	2.185	1.064	4	29	2.501	0.921	4	54	2.596	1.242	4
5	3.551	1.834	4	30	2.332	1.081	4	55	1.815	0.633	4
6	2.688	1.002	4	31	1.665	0.784	4	56	1.877	0.862	4
7	2.334	1.113	4	32	2.745	1.155	4	57	1.952	0.88	4
8	2.701	0.876	4	33	2.531	1.006	4	58	2.19	0.941	4
9	2.024	0.929	4	34	2.096	1.209	4	59	2.461	1.124	4
10	2.043	0.933	4	35	2.232	1.026	4	60	2.853	1.252	4
11	2.022	0.895	4	36	1.821	0.781	4				
12	2.038	0.954	4	37	2.012	0.861	4				
13	2.015	0.899	4	38	2.021	0.956	4				
14	1.807	0.697	4	39	1.935	0.791	4				
15	2.266	1.092	4	40	1.751	0.796	4				
16	1.824	0.949	4	41	2.083	0.988	4				
17	1.732	0.834	4	42	1.342	0.674	4				
18	2.208	0.973	4	43	1.635	0.884	4				
19	1.673	1.004	4	44	2.076	0.853	4				
20	2.01	0.846	4	45	1.928	0.978	4				
21	1.834	0.885	4	46	2.175	0.92	4				
22	2.31	0.957	4	47	2.164	1.07	4				
23	2.189	1.061	4	48	2.443	1.171	4				
24	1.954	0.986	4	49	2.082	0.934	4				
25	2.311	0.947	4	50	2.282	1.016	4				

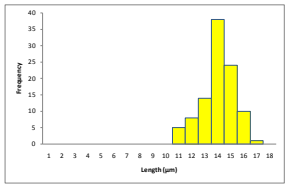

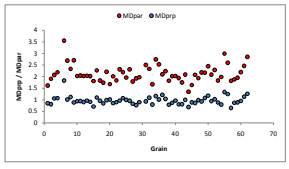

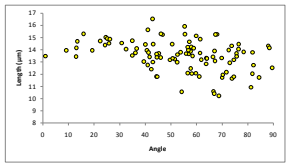

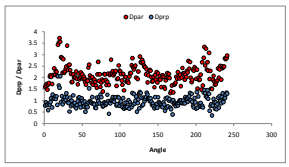

Mean length (µm)	13.540
SD	1.241
Mean Dpar	2.123
SD	0.426
Mean Dprp	0.961
SD	0.239

Minimum length (µm)	10.236
Maximum length (µm)	16.539
Minimum Dpar	0.990
Maximum Dpar	3.708
Minimum Dprp	0.357
Maximum Dprp	2.060

SM12048

Sample	#	Length (µm)	C-axis angle	#	Length (µm)	C-axis angle	#	Length (µm)	C-axis angle	#	Length (µm)	C-axis angle
SM12048	1	12.884	35.301	26	12.454	60.346	51	13.989	53.637	76	13.274	17.757
	2	15.26	66.522	27	15.163	51.091	52	13.591	17.896	77	12.478	67.610
	3	12.835	84.524	28	13.137	54.012	53	13.620	60.106	78	13.277	55.334
	4	13.308	41.855	29	13.494	31.536	54	13.967	18.056	79	15.106	11.225
	5	12.471	60.52	30	11.939	73.451	55	13.650	31.770	80	13.908	11.754
	6	12.489	74.273	31	15.083	47.291	56	13.428	17.380	81	14.245	46.800
	7	14.117	16.687	32	14.079	63.389	57	12.366	37.619	82	12.264	72.854
	8	11.802	78.469	33	14.070	41.451	58	14.018	0.894	83	13.839	52.743
	9	12.711	59.764	34	14.258	0.377	59	13.833	52.260	84	11.799	63.360
	10	12.923	2.33	35	12.168	65.700	60	13.615	66.918	85	12.307	78.962
	11	14.162	21.482	36	13.985	22.249	61	15.174	11.037	86	13.533	45.127
	12	13.535	10.286	37	12.292	69.537	62	13.445	58.323	87	12.273	63.127
	13	13.075	33.361	38	13.987	60.459	63	13.138	41.135	88	12.430	49.398
	14	14.311	25.243	39	12.761	72.539	64	15.010	13.942	89	14.001	22.715
	15	14.7	27.969	40	12.655	67.478	65	12.314	77.422	90	13.182	68.378
	16	13.413	44.004	41	14.053	61.920	66	12.162	66.219	91	11.613	42.680
	17	12.184	75.722	42	11.860	3.834	67	12.664	57.827	92	10.768	39.150
	18	13.448	33.326	43	14.071	2.817	68	14.305	0.086	93	10.868	72.503
	19	13.816	34.85	44	13.202	36.024	69	13.589	18.123	94	14.028	54.847
	20	13.01	75.715	45	13.909	59.542	70	13.102	52.841	95	12.432	66.730
	21	13.223	65.569	46	13.767	53.662	71	13.723	74.477	96	13.220	77.014
	22	13.405	51.566	47	14.056	68.425	72	12.154	71.118	97	13.252	76.749
	23	14.316	25.832	48	13.774	3.906	73	13.548	51.925	98	13.039	74.204
	24	13.209	69.103	49	13.818	38.843	74	14.201	6.081	99	12.225	58.240
	25	11.794	79.365	50	12.296	50.878	75	14.124	3.699	100	13.901	35.429

Grain	MDpar	MDprp	NDpar	Grain	MDpar	MDprp	NDpar	Grain	MDpar	MDprp	NDpar
1	0.891	0.392	4	26	0.909	0.348	4	51	0.976	0.477	4
2	1.283	0.698	4	27	1.078	0.485	4	52	1.182	0.38	4
3	0.936	0.334	4	28	1.453	0.374	4	53	1.118	0.475	4
4	0.729	0.28	4	29	1.266	0.437	4	54	1.133	0.496	4
5	1.106	0.44	4	30	1.146	0.371	4	55	1.303	0.424	4
6	1.243	0.354	4	31	1.01	0.354	4	56	1.035	0.389	4
7	1.196	0.386	4	32	1.076	0.515	4				
8	0.873	0.398	4	33	1.099	0.573	4				
9	0.93	0.458	4	34	1.184	0.322	4				
10	1.13	0.341	4	35	1.39	0.353	4				
11	1.106	0.364	4	36	1.139	0.431	4				
12	1.02	0.302	4	37	1.067	0.406	4				
13	1.248	0.435	4	38	1.303	0.342	4				
14	0.915	0.347	4	39	1.069	0.432	4				
15	0.963	0.479	4	40	1.155	0.457	4				
16	1.457	0.429	4	41	1.324	0.371	4				
17	1.006	0.375	4	42	1.06	0.391	4				
18	1.156	0.307	4	43	0.956	0.308	4				
19	1.248	0.517	4	44	1.355	0.385	4				
20	1.423	0.417	4	45	1.024	0.397	4				
21	1.367	0.44	4	46	1.108	0.536	4				
22	1.019	0.457	4	47	1.205	0.375	4				
23	1.2	0.479	4	48	1.269	0.349	4				
24	1.063	0.387	4	49	1.29	0.4	4				
25	1.092	0.423	4	50	1.077	0.511	4				

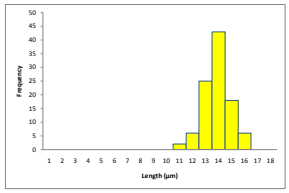

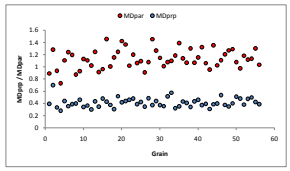

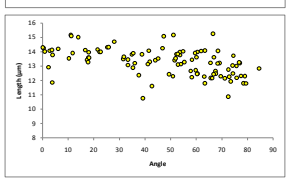

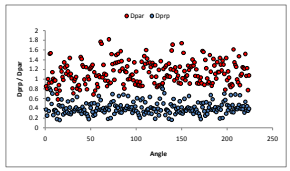

Mean length (µm)	13.307
SD	0.930
Mean Dpar	1.131
SD	0.235
Mean Dprp	0.412
SD	0.130

Minimum length (µm)	10.768
Maximum length (µm)	15.260
Minimum Dpar	0.580
Maximum Dpar	1.822
Minimum Dprp	0.163
Maximum Dprp	0.837

SM12058

Sample	#	Length (µm)	C-axis angle	#	Length (µm)	C-axis angle
SM12058	1	14.346	74.645	26	12.990	73.400
	2	12.66	74.171	27	11.796	71.659
	3	12.228	38.93	28	12.530	76.360
	4	13.745	2.003	29	12.822	11.996
	5	14.606	58.491	30	12.165	68.664
	6	14.777	2.109	31	14.225	17.901
	7	12.227	31.085	32	14.622	15.307
	8	15.061	3.377	33	13.309	42.389
	9	13.542	73.617	34	13.750	77.471
	10	13.024	67.212	35	11.853	79.313
	11	15.23	50.167	36	13.367	66.309
	12	12.199	59.718	37	13.249	76.813
	13	12.258	67.982	38	13.927	43.116
	14	14.146	65.139	39	12.912	0.134
	15	13.215	84.779	40	12.124	45.105
	16	11.452	30.765	41	13.158	64.154
	17	14.993	26.446			
	18	14.819	39.099			
	19	14.468	66.653			
	20	12.915	76.439			
	21	14.596	50.067			
	22	11.837	21.649			
	23	14.804	51.391			
	24	12.856	79.974			
	25	8.846	64.814			

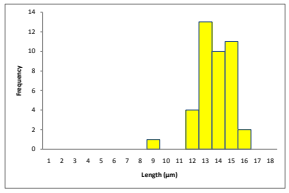

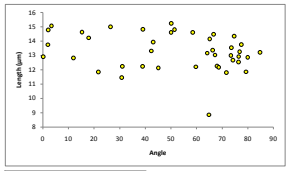

Mean length (µm)	13.260
SD	1.278
Mean Dpar	-
SD	-
Mean Dprp	-
SD	-

Minimum length (µm)	8.846
Maximum length (µm)	15.230
Minimum Dpar	-
Maximum Dpar	-
Minimum Dprp	-
Maximum Dprp	-

Appendix C1

Supplementary zircon isotopic dataset for the samples presented in Chapter 2.

			Isotopic ratios							Ages						
Pb (ppm)	*U (ppm)*	*Th/U*	*$^{207}Pb/^{206}Pb$*	*± 1σ*	*$^{207}Pb/^{235}U$*	*± 1σ*	*$^{206}Pb/^{238}U$*	*± 1σ*	*rho*[1]	*$^{207}Pb/^{206}Pb$*	*± 1σ*	*$^{206}Pb/^{238}U$*	*± 1σ*	*$^{207}Pb/^{235}U$*	*± 1σ*	*Conc.*[2]
SM12	***Ortho-gneiss***															
30	411	0.32	0.0573	0.0009	0.574	0.010	0.0726	0.0010	0.82	503.9	33.4	451.6	6.0	460.3	6.2	98.1
13	188	0.20	0.0570	0.0011	0.576	0.011	0.0734	0.0011	0.73	488.9	41.7	456.5	6.3	461.9	7.3	98.8
15	201	0.27	0.0566	0.0010	0.574	0.010	0.0736	0.0010	0.77	473.5	37.7	457.8	6.1	460.5	6.7	99.4
10	138	0.34	0.0569	0.0011	0.579	0.011	0.0739	0.0011	0.73	485.6	41.6	459.6	6.3	464.0	7.3	99.1
22	307	0.16	0.0551	0.0008	0.560	0.009	0.0737	0.0010	0.84	417.2	32.1	458.6	6.0	451.7	5.9	101.5
23	299	0.43	0.0554	0.0008	0.562	0.009	0.0737	0.0010	0.83	428.2	32.4	458.1	6.0	453.1	6.0	101.1
64	928	0.09	0.0551	0.0008	0.565	0.009	0.0743	0.0010	0.82	415.9	33.7	462.3	6.1	454.5	6.1	101.7
47	652	0.20	0.0566	0.0007	0.578	0.009	0.0741	0.0010	0.89	473.8	28.7	460.8	5.9	463.1	5.5	99.5
44	608	0.16	0.0567	0.0008	0.581	0.009	0.0744	0.0010	0.86	478.0	31.1	462.3	5.9	465.0	5.8	99.4
20	279	0.21	0.0575	0.0009	0.588	0.010	0.0741	0.0010	0.80	510.1	35.1	461.1	6.1	469.4	6.4	98.2
11	145	0.29	0.0549	0.0011	0.566	0.011	0.0748	0.0011	0.71	406.5	42.3	464.9	6.3	455.2	7.3	102.1
21	282	0.30	0.0550	0.0010	0.566	0.010	0.0747	0.0010	0.76	412.3	38.6	464.1	6.2	455.5	6.7	101.9
15	186	0.58	0.0563	0.0010	0.569	0.010	0.0733	0.0010	0.76	464.6	38.6	456.2	6.1	457.6	6.7	99.7
48	630	0.28	0.0565	0.0008	0.590	0.010	0.0757	0.0010	0.83	471.0	32.8	470.6	6.1	470.8	6.1	100.0
41	540	0.30	0.0568	0.0009	0.586	0.010	0.0748	0.0010	0.82	484.0	33.2	464.8	6.0	468.1	6.1	99.3
40	534	0.30	0.0579	0.0009	0.583	0.010	0.0731	0.0010	0.82	526.1	33.3	454.5	5.9	466.5	6.1	97.4
21	330	0.22	0.0657	0.0013	0.592	0.012	0.0654	0.0010	0.73	795.8	40.8	408.4	5.8	472.2	7.6	86.5
36	538	0.18	0.0581	0.0008	0.546	0.009	0.0682	0.0009	0.85	532.1	31.8	425.5	5.6	442.6	5.7	96.1
46	701	0.09	0.0569	0.0008	0.544	0.008	0.0693	0.0009	0.89	488.8	29.1	431.7	5.5	440.8	5.3	97.9
48	679	0.18	0.0551	0.0008	0.551	0.009	0.0726	0.0010	0.87	416.2	30.5	451.5	5.8	445.7	5.6	101.3
90	939	1.34	0.0572	0.0007	0.596	0.009	0.0755	0.0010	0.90	499.0	28.6	469.3	6.0	474.4	5.6	98.9
43	571	0.30	0.0563	0.0008	0.589	0.009	0.0759	0.0010	0.89	461.4	29.4	471.7	6.0	470.0	5.6	100.4
10	143	0.28	0.0602	0.0011	0.599	0.012	0.0722	0.0010	0.74	610.7	40.1	449.6	6.2	476.9	7.4	94.3
7	89	0.56	0.0610	0.0014	0.603	0.013	0.0717	0.0011	0.67	639.6	47.1	446.5	6.4	479.3	8.5	93.2
22	298	0.21	0.0588	0.0009	0.607	0.010	0.0750	0.0010	0.81	558.1	34.7	466.0	6.1	481.8	6.5	96.7
19	247	0.24	0.0577	0.0010	0.605	0.011	0.0761	0.0011	0.75	516.6	39.5	472.5	6.4	480.1	7.2	98.4
27	326	0.11	0.0693	0.0012	0.817	0.014	0.0855	0.0012	0.80	908.3	34.4	529.1	7.2	606.6	8.1	87.2
46	353	0.78	0.0625	0.0008	0.973	0.014	0.1130	0.0015	0.90	691.2	27.5	690.0	8.7	690.2	7.4	100.0
45	305	2.20	0.0594	0.0008	0.778	0.012	0.0950	0.0013	0.88	582.9	29.2	585.1	7.5	584.6	6.8	100.1
16	153	0.37	0.0623	0.0010	0.878	0.015	0.1023	0.0014	0.78	684.2	35.0	627.7	8.3	640.1	8.3	98.1
152	361	0.39	0.1688	0.0020	8.755	0.122	0.3762	0.0050	0.95	2545.6	19.8	2058.7	23.2	2312.8	12.7	89.0
148	417	0.25	0.1245	0.0015	5.828	0.082	0.3396	0.0045	0.94	2021.2	21.2	1884.9	21.4	1950.6	12.1	96.6
14	170	0.25	0.0579	0.0010	0.661	0.012	0.0829	0.0012	0.77	525.4	37.5	513.2	6.8	515.4	7.3	99.6
45	382	1.38	0.0600	0.0008	0.728	0.011	0.0880	0.0012	0.86	603.1	29.7	543.7	7.0	555.2	6.6	97.9
63	613	0.80	0.0589	0.0008	0.719	0.011	0.0885	0.0012	0.89	564.9	28.6	546.4	6.9	550.0	6.3	99.3
33	215	0.54	0.0721	0.0011	1.397	0.024	0.1406	0.0019	0.81	987.8	32.0	848.2	10.9	887.8	10.0	95.5
25	245	0.19	0.0613	0.0009	0.864	0.014	0.1022	0.0014	0.83	648.7	32.1	627.5	8.1	632.1	7.7	99.3
16	189	0.27	0.0561	0.0010	0.651	0.012	0.0841	0.0012	0.75	457.1	38.4	520.5	6.9	508.9	7.4	102.3
9	72	1.10	0.0592	0.0014	0.819	0.020	0.1004	0.0015	0.63	573.1	52.0	617.0	8.9	607.6	11.0	101.5
40	365	0.53	0.0597	0.0009	0.832	0.014	0.1011	0.0014	0.82	591.8	32.7	621.0	8.0	614.7	7.6	101.0
138	491	0.10	0.1222	0.0017	4.675	0.072	0.2774	0.0037	0.87	1989.0	24.5	1578.4	18.6	1762.7	12.8	89.5
22	136	0.57	0.0734	0.0012	1.440	0.025	0.1423	0.0020	0.79	1024.7	32.8	857.8	11.1	905.7	10.4	94.7
66	578	0.32	0.0613	0.0009	0.936	0.015	0.1107	0.0015	0.82	650.5	32.6	676.9	8.7	670.8	8.1	100.9
SM20	***Ortho-gneiss***															
22	306	0.06	0.0571	0.0007	0.585	0.008	0.0743	0.0009	0.92	494.3	26.9	462.0	5.6	467.4	5.2	98.8
17	241	0.11	0.0558	0.0007	0.571	0.008	0.0743	0.0009	0.88	442.3	27.8	462.1	5.7	458.7	5.3	100.7
37	544	0.03	0.0566	0.0007	0.565	0.008	0.0724	0.0009	0.92	475.4	26.2	450.4	5.5	454.5	5.0	99.1
27	375	0.09	0.0564	0.0007	0.572	0.008	0.0735	0.0009	0.92	468.1	26.5	457.3	5.6	459.1	5.1	99.6
16	216	0.06	0.0560	0.0008	0.579	0.009	0.0750	0.0010	0.83	452.0	31.3	466.0	5.9	463.6	5.9	100.5
32	448	0.02	0.0571	0.0007	0.594	0.008	0.0754	0.0010	0.90	494.9	27.5	468.8	5.8	473.3	5.4	99.0
30	438	0.02	0.0579	0.0007	0.577	0.008	0.0723	0.0009	0.89	527.1	27.9	450.0	5.7	462.8	5.4	97.2
22	309	0.06	0.0581	0.0008	0.597	0.009	0.0745	0.0010	0.87	532.6	29.5	463.3	5.9	475.1	5.8	97.5
28	388	0.09	0.0551	0.0007	0.561	0.009	0.0739	0.0010	0.87	416.6	29.4	459.5	5.9	452.4	5.6	101.6
20	271	0.05	0.0576	0.0008	0.594	0.009	0.0748	0.0010	0.86	512.8	30.4	465.0	6.0	473.2	5.9	98.3
18	248	0.08	0.0554	0.0008	0.569	0.009	0.0745	0.0010	0.84	428.9	30.7	463.3	6.0	457.6	5.9	101.2
17	238	0.19	0.0556	0.0007	0.550	0.008	0.0717	0.0009	0.87	436.1	28.8	446.4	5.5	444.7	5.3	100.4
31	464	0.02	0.0568	0.0007	0.550	0.008	0.0702	0.0009	0.92	482.5	26.6	437.5	5.4	444.8	5.0	98.4
37	555	0.02	0.0573	0.0007	0.547	0.008	0.0693	0.0009	0.90	503.0	27.1	431.8	5.3	443.2	5.1	97.4
14	171	0.13	0.0600	0.0008	0.667	0.010	0.0806	0.0011	0.86	604.9	29.3	499.9	6.3	519.1	6.2	96.3
19	232	0.18	0.0579	0.0008	0.638	0.009	0.0799	0.0010	0.88	525.0	28.8	495.7	6.2	500.9	5.9	99.0
25	352	0.03	0.0590	0.0008	0.607	0.009	0.0746	0.0010	0.90	568.7	27.6	463.6	5.8	481.6	5.6	96.3
13	175	0.03	0.0583	0.0008	0.616	0.010	0.0767	0.0010	0.84	539.3	31.4	476.4	6.1	487.4	6.1	97.7
37	299	0.36	0.0661	0.0008	1.053	0.014	0.1157	0.0015	0.93	808.5	24.4	705.5	8.4	730.5	7.0	96.6
41	421	0.19	0.0604	0.0007	0.805	0.011	0.0967	0.0012	0.93	616.7	25.2	595.2	7.2	599.5	6.1	99.3
13	158	0.12	0.0647	0.0009	0.757	0.011	0.0849	0.0011	0.87	765.8	27.9	525.2	6.5	572.5	6.5	91.7
19	141	0.46	0.0651	0.0008	1.101	0.016	0.1227	0.0016	0.90	776.8	26.4	746.2	9.1	753.8	7.6	99.0
161	549	0.13	0.1242	0.0014	4.814	0.065	0.2812	0.0036	0.95	2017.3	20.0	1597.2	18.1	1787.3	11.3	89.4
14	132	0.19	0.0904	0.0012	1.213	0.018	0.0973	0.0013	0.88	1434.4	25.4	598.4	7.6	806.4	8.4	74.2
154	438	0.25	0.1190	0.0014	5.357	0.073	0.3266	0.0042	0.94	1941.0	20.4	1821.9	20.4	1878.0	11.7	97.0
31	369	0.19	0.0583	0.0007	0.666	0.010	0.0828	0.0011	0.89	541.5	28.3	513.0	6.5	518.3	6.0	99.0
29	165	0.26	0.0698	0.0009	1.610	0.024	0.1673	0.0022	0.89	921.5	26.3	997.4	12.2	973.9	9.3	102.4
24	285	0.03	0.0572	0.0008	0.692	0.010	0.0877	0.0012	0.88	499.9	28.8	541.9	6.9	534.0	6.2	101.5
10	106	0.34	0.0612	0.0010	0.722	0.013	0.0856	0.0012	0.78	645.2	34.9	529.4	7.0	551.8	7.5	95.9
63	594	0.86	0.0614	0.0008	0.760	0.011	0.0899	0.0012	0.88	651.7	27.8	554.8	7.1	574.2	6.6	96.6
SM44	***Clastic***															
48	706	0.05	0.0563	0.0006	0.578	0.008	0.0744	0.0009	0.97	464.3	24.5	462.7	5.6	463.0	4.9	99.9
48	700	0.06	0.0561	0.0006	0.576	0.007	0.0745	0.0009	0.98	455.8	23.6	462.9	5.6	461.7	4.7	100.3
18	244	0.38	0.0563	0.0007	0.576	0.008	0.0742	0.0009	0.91	463.1	27.6	461.4	5.6	461.7	5.2	99.9
28	404	0.08	0.0567	0.0007	0.584	0.008	0.0748	0.0009	0.94	477.6	25.7	465.2	5.6	467.3	5.0	99.6
24	342	0.10	0.0564	0.0007	0.580	0.008	0.0747	0.0009	0.92	466.7	26.9	464.1	5.6	464.6	5.1	99.9
34	495	0.06	0.0562	0.0007	0.577	0.008	0.0746	0.0009	0.93	458.2	26.0	463.6	5.6	462.7	5.0	100.2
32	469	0.04	0.0562	0.0007	0.578	0.008	0.0746	0.0009	0.93	460.5	26.0	463.6	5.6	463.2	4.9	100.1
33	475	0.10	0.0563	0.0007	0.581	0.008	0.0747	0.0009	0.93	464.9	26.4	464.6	5.6	464.8	5.0	100.0
28	378	0.08	0.0587	0.0007	0.637	0.008	0.0787	0.0010	0.96	554.8	24.3	488.6	5.9	500.3	5.2	97.7
35	461	0.06	0.0574	0.0006	0.637	0.008	0.0804	0.0010	0.96	508.2	24.1	498.6	6.0	500.3	5.1	99.7
36	490	0.04	0.0584	0.0006	0.640	0.008	0.0795	0.0010	0.97	546.2	23.9	492.9	5.9	502.4	5.1	98.1
18	233	0.23	0.0583	0.0007	0.647	0.009	0.0806	0.0010	0.93	539.3	26.5	499.5	6.0	506.7	5.4	98.6
27	362	0.05	0.0578	0.0007	0.645	0.009	0.0809	0.0010	0.92	523.2	26.5	501.7	6.0	505.5	5.4	99.2

			Isotopic ratios							Ages						
Pb (ppm)	*U (ppm)*	*Th/U*	*$^{207}Pb/^{206}Pb$*	*± 1σ*	*$^{207}Pb/^{235}U$*	*± 1σ*	*$^{206}Pb/^{238}U$*	*± 1σ*	*rho*	*$^{207}Pb/^{206}Pb$*	*± 1σ*	*$^{206}Pb/^{238}U$*	*± 1σ*	*$^{207}Pb/^{235}U$*	*± 1σ*	*Conc.*
SM44	***Clastic***	***(continued)***														
23	336	0.14	0.0579	0.0007	0.588	0.008	0.0737	0.0010	0.89	524.3	28.2	458.5	5.7	469.6	5.4	97.6
24	351	0.07	0.0636	0.0008	0.648	0.009	0.0739	0.0010	0.90	728.3	26.6	459.4	5.7	507.0	5.7	90.6
47	713	0.06	0.0592	0.0007	0.587	0.008	0.0719	0.0009	0.97	575.6	23.8	447.8	5.5	469.2	4.9	95.4
38	525	0.29	0.0589	0.0007	0.604	0.008	0.0744	0.0009	0.92	561.5	26.0	462.6	5.7	479.5	5.2	96.5
40	561	0.20	0.0587	0.0007	0.601	0.008	0.0743	0.0010	0.92	554.3	26.6	462.2	5.7	477.9	5.3	96.7
21	313	0.10	0.0620	0.0008	0.605	0.009	0.0708	0.0009	0.88	674.5	28.1	440.7	5.5	480.3	5.6	91.8
44	645	0.02	0.0576	0.0006	0.592	0.008	0.0745	0.0009	0.97	515.3	23.7	463.2	5.6	472.0	4.9	98.1
29	413	0.15	0.0584	0.0007	0.590	0.008	0.0732	0.0009	0.92	545.0	26.4	455.6	5.5	470.7	5.1	96.8
13	172	0.13	0.0690	0.0008	0.752	0.010	0.0790	0.0010	0.93	899.9	24.5	490.3	6.0	569.4	6.0	86.1
29	331	0.24	0.0582	0.0007	0.723	0.009	0.0901	0.0011	0.96	537.9	24.8	556.0	6.7	552.5	5.6	100.6
30	407	0.08	0.0744	0.0008	0.775	0.010	0.0756	0.0010	0.96	1050.9	22.6	469.9	5.7	582.6	5.8	80.7
26	323	0.17	0.0596	0.0007	0.684	0.009	0.0833	0.0011	0.96	587.8	24.2	515.8	6.2	529.2	5.4	97.5
16	172	0.17	0.0591	0.0007	0.773	0.011	0.0950	0.0012	0.91	570.0	27.0	584.9	7.1	581.7	6.1	100.6
17	161	0.52	0.0585	0.0008	0.797	0.012	0.0988	0.0013	0.88	550.0	29.0	607.3	7.4	595.2	6.6	102.0
48	554	0.26	0.0582	0.0007	0.696	0.009	0.0867	0.0011	0.96	538.2	25.0	535.7	6.4	536.2	5.4	99.9
120	437	0.26	0.0968	0.0010	3.701	0.047	0.2773	0.0035	1.00	1563.7	19.3	1577.6	17.7	1571.6	10.1	100.4
177	711	0.16	0.1123	0.0012	3.901	0.050	0.2519	0.0032	0.99	1837.6	18.9	1448.1	16.4	1613.8	10.3	89.7
15	36	0.81	0.1135	0.0013	5.435	0.072	0.3473	0.0045	0.97	1856.2	20.5	1921.8	21.4	1890.3	11.4	101.7
41	95	1.15	0.1153	0.0012	5.408	0.069	0.3401	0.0043	0.99	1885.2	19.1	1887.2	20.7	1886.1	11.0	100.1
54	206	0.22	0.1216	0.0013	4.228	0.054	0.2522	0.0032	0.99	1979.9	18.7	1449.9	16.4	1679.5	10.5	86.3
127	277	0.81	0.1335	0.0014	7.147	0.091	0.3883	0.0049	0.99	2145.0	18.2	2114.7	22.8	2130.0	11.3	99.3
24	163	0.38	0.0717	0.0009	1.404	0.020	0.1421	0.0018	0.92	977.2	24.9	856.2	10.3	890.6	8.3	96.1
15	84	0.56	0.0729	0.0010	1.639	0.025	0.1632	0.0022	0.86	1010.5	28.5	974.3	11.9	985.4	9.7	98.9
7	57	0.71	0.0644	0.0009	0.979	0.015	0.1103	0.0014	0.86	756.0	29.4	674.3	8.4	693.3	7.7	97.3
144	236	0.57	0.1882	0.0020	13.684	0.171	0.5275	0.0066	1.00	2726.6	17.0	2730.7	27.8	2728.1	11.8	100.1
27	289	0.14	0.0692	0.0008	0.892	0.012	0.0936	0.0012	0.96	903.7	23.1	576.6	6.9	647.5	6.3	89.1
21	349	0.23	0.0610	0.0008	0.538	0.007	0.0640	0.0008	0.92	639.1	26.2	399.8	4.9	437.1	4.9	91.5
30	308	0.39	0.0605	0.0007	0.789	0.011	0.0947	0.0012	0.94	620.1	25.0	583.2	7.0	590.7	6.0	98.7
52	176	0.48	0.1037	0.0012	3.811	0.049	0.2668	0.0033	0.96	1690.5	20.8	1524.3	17.0	1595.2	10.4	95.6
20	190	0.49	0.0606	0.0007	0.847	0.011	0.1014	0.0013	0.94	624.2	25.2	622.8	7.4	623.0	6.2	100.0
40	664	0.06	0.0606	0.0007	0.528	0.007	0.0633	0.0008	0.96	623.5	24.5	395.6	4.8	430.7	4.6	91.9
52	407	0.08	0.0907	0.0010	1.625	0.021	0.1299	0.0016	0.97	1440.8	21.1	787.4	9.2	979.9	8.0	80.4
SM23	***Ortho-gneiss***															
9	212	0.00	0.0533	0.0009	0.350	0.006	0.0477	0.0006	0.75	342.5	36.7	300.1	3.8	304.9	4.5	98.4
11	239	0.00	0.0522	0.0008	0.355	0.006	0.0493	0.0006	0.77	294.6	36.0	310.4	4.0	308.5	4.5	100.6
17	405	0.00	0.0527	0.0009	0.344	0.006	0.0473	0.0006	0.74	316.7	39.2	298.0	3.9	300.1	4.7	99.3
6	142	0.00	0.0527	0.0013	0.347	0.008	0.0477	0.0007	0.61	314.8	53.4	300.6	4.3	302.2	6.2	99.5
12	268	0.00	0.0527	0.0008	0.349	0.005	0.0481	0.0006	0.82	315.9	32.7	302.5	3.8	304.0	4.1	99.5
12	268	0.01	0.0526	0.0009	0.352	0.006	0.0486	0.0006	0.77	311.4	36.9	306.0	4.0	306.5	4.6	99.8
18	401	0.00	0.0531	0.0007	0.357	0.005	0.0488	0.0006	0.87	331.8	29.4	307.4	3.8	310.2	3.9	99.1
10	222	0.00	0.0524	0.0008	0.352	0.006	0.0487	0.0006	0.80	302.5	33.9	306.6	3.9	306.1	4.3	100.2
32	748	0.00	0.0537	0.0007	0.348	0.005	0.0470	0.0006	0.92	358.2	26.9	296.0	3.6	303.1	3.6	97.7
14	286	0.06	0.0592	0.0016	0.400	0.011	0.0490	0.0008	0.60	574.3	58.4	308.5	4.8	341.7	7.7	90.3
14	313	0.02	0.0561	0.0008	0.370	0.006	0.0479	0.0006	0.85	455.9	30.1	301.4	3.8	319.8	4.1	94.2
10	249	0.00	0.0567	0.0008	0.355	0.006	0.0454	0.0006	0.81	479.8	32.5	286.0	3.6	308.3	4.2	92.8
23	220	0.32	0.0629	0.0008	0.895	0.013	0.1032	0.0013	0.89	704.7	26.5	633.1	7.6	649.0	6.8	97.6
21	202	0.30	0.0603	0.0008	0.856	0.012	0.1030	0.0013	0.89	614.5	26.9	632.0	7.6	628.1	6.6	100.6
18	122	0.64	0.0715	0.0009	1.255	0.018	0.1273	0.0016	0.88	971.7	26.7	772.5	9.3	825.6	8.2	93.6
32	223	0.26	0.1242	0.0015	2.071	0.028	0.1209	0.0015	0.93	2017.4	21.0	735.9	8.8	1139.1	9.2	64.6
25	187	1.80	0.0589	0.0009	0.758	0.012	0.0933	0.0012	0.83	564.6	30.5	575.3	7.1	573.1	6.8	100.4
43	402	0.25	0.0637	0.0008	0.955	0.013	0.1088	0.0014	0.93	730.3	24.8	665.8	7.9	680.6	6.7	97.8
9	203	0.00	0.0493	0.0008	0.338	0.006	0.0498	0.0007	0.75	163.0	38.4	313.0	4.0	295.9	4.5	105.8
19	159	0.79	0.0616	0.0008	0.873	0.013	0.1028	0.0013	0.87	659.8	28.2	630.6	7.6	636.9	6.9	99.0
13	139	0.27	0.0635	0.0009	0.771	0.012	0.0880	0.0012	0.83	726.5	31.0	543.8	6.8	580.4	7.0	93.7
35	62	2.67	0.1309	0.0016	5.976	0.083	0.3313	0.0042	0.92	2109.6	21.6	1844.5	20.5	1972.4	12.1	93.5
236	434	0.29	0.1780	0.0020	12.245	0.161	0.4991	0.0062	0.95	2634.0	18.8	2609.8	26.8	2623.3	12.4	99.5
14	205	0.03	0.0568	0.0009	0.590	0.010	0.0754	0.0010	0.80	482.4	33.7	468.6	5.9	471.0	6.1	99.5
63	668	0.51	0.0605	0.0007	0.744	0.010	0.0893	0.0011	0.91	620.2	26.1	551.2	6.7	564.7	6.0	97.6
22	301	0.16	0.0569	0.0008	0.579	0.009	0.0738	0.0010	0.83	487.9	31.7	458.7	5.7	463.7	5.8	98.9
6	48	0.96	0.0666	0.0013	0.897	0.018	0.0976	0.0014	0.70	826.3	41.3	600.6	8.1	650.1	9.7	92.4
26	77	1.37	0.1173	0.0016	3.651	0.054	0.2258	0.0029	0.89	1915.0	24.0	1312.5	15.5	1560.6	11.7	84.1
29	319	0.48	0.0586	0.0008	0.705	0.011	0.0873	0.0011	0.86	551.0	29.6	539.8	6.7	541.9	6.3	99.6
13	285	0.00	0.0533	0.0008	0.361	0.006	0.0491	0.0006	0.83	341.6	32.6	308.8	3.9	312.6	4.2	98.8
SM58	***Alkali granite***															
21	634	0.44	0.0522	0.0008	0.265	0.005	0.0368	0.0005	0.72	294.4	42.1	233.2	3.2	238.8	4.1	97.7
26	762	0.11	0.0507	0.0007	0.264	0.004	0.0377	0.0005	0.81	227.8	34.9	238.7	3.1	237.6	3.5	100.5
17	490	0.38	0.0524	0.0008	0.265	0.005	0.0367	0.0005	0.77	301.3	36.9	232.6	3.1	238.9	3.7	97.4
26	745	0.37	0.0500	0.0008	0.255	0.005	0.0370	0.0005	0.73	196.0	42.1	234.1	3.2	230.7	3.9	101.5
29	870	0.39	0.0507	0.0008	0.255	0.005	0.0364	0.0005	0.75	228.7	39.1	230.4	3.1	230.2	3.7	100.1
17	490	0.48	0.0525	0.0009	0.264	0.005	0.0365	0.0005	0.73	307.8	41.2	231.0	3.1	238.0	4.0	97.1
19	559	0.43	0.0494	0.0009	0.248	0.005	0.0364	0.0005	0.71	168.4	44.6	230.8	3.2	225.2	4.0	102.5
31	891	0.40	0.0508	0.0008	0.259	0.005	0.0371	0.0005	0.73	232.1	42.1	234.5	3.2	234.3	4.0	100.1
14	403	0.67	0.0520	0.0010	0.261	0.005	0.0363	0.0005	0.69	287.1	46.6	230.1	3.2	235.3	4.4	97.8
24	717	0.45	0.0513	0.0010	0.256	0.006	0.0363	0.0006	0.60	252.0	58.0	229.6	3.5	231.5	5.2	99.2
14	404	0.44	0.0507	0.0009	0.256	0.005	0.0366	0.0005	0.70	227.9	44.4	231.8	3.2	231.5	4.1	100.1
17	496	0.36	0.0525	0.0008	0.263	0.005	0.0363	0.0005	0.70	309.1	44.4	229.8	3.2	237.0	4.2	97.0
10	288	0.62	0.0503	0.0010	0.260	0.007	0.0374	0.0006	0.59	209.4	60.1	236.8	3.6	234.3	5.4	101.1
29	807	0.16	0.0516	0.0010	0.267	0.005	0.0376	0.0005	0.70	267.7	45.3	237.8	3.3	240.5	4.3	98.9
13	368	0.65	0.0517	0.0010	0.260	0.005	0.0365	0.0005	0.69	271.6	46.6	230.9	3.2	234.6	4.4	98.4
17	478	0.50	0.0513	0.0009	0.261	0.006	0.0370	0.0005	0.66	253.5	49.2	233.9	3.3	235.7	4.6	99.2
37	1030	0.32	0.0513	0.0009	0.260	0.005	0.0368	0.0005	0.72	254.6	42.8	232.8	3.2	234.8	4.0	99.1
5	146	0.63	0.0527	0.0020	0.257	0.010	0.0353	0.0007	0.50	315.9	86.1	223.8	4.1	232.0	7.7	96.5
4	116	0.46	0.0553	0.0016	0.278	0.009	0.0365	0.0006	0.54	424.5	70.3	231.0	3.8	249.2	6.9	92.7
17	503	0.39	0.0535	0.0009	0.274	0.005	0.0372	0.0005	0.76	348.2	37.6	235.6	3.1	246.2	3.9	95.7
11	317	0.47	0.0537	0.0010	0.273	0.006	0.0369	0.0005	0.67	358.7	48.9	233.8	3.3	245.5	4.8	95.2
10	298	0.46	0.0548	0.0010	0.276	0.006	0.0366	0.0005	0.66	404.7	49.6	231.4	3.4	247.7	5.0	93.4
8	242	0.34	0.0543	0.0014	0.270	0.007	0.0360	0.0006	0.60	383.6	58.4	228.2	3.5	242.5	5.6	94.1
20	553	0.88	0.0549	0.0009	0.279	0.005	0.0369	0.0005	0.75	407.0	38.9	233.7	3.1	250.1	4.1	93.4
23	664	0.63	0.0543	0.0008	0.272	0.005	0.0364	0.0005	0.72	381.6	42.7	230.4	3.2	244.4	4.3	94.3
28	807	0.46	0.0534	0.0009	0.260	0.005	0.0353	0.0005	0.71	344.9	44.3	223.4	3.1	234.3	4.2	95.3
3	80	0.45	0.0547	0.0019	0.281	0.009	0.0373	0.0006	0.50	398.0	74.1	235.8	3.8	251.2	7.4	93.9

			Isotopic ratios							Ages						
Pb (ppm)	*U (ppm)*	*Th/U*	*$^{207}Pb/^{206}Pb$*	*± 1σ*	*$^{207}Pb/^{235}U$*	*± 1σ*	*$^{206}Pb/^{238}U$*	*± 1σ*	*rho*	*$^{207}Pb/^{206}Pb$*	*± 1σ*	*$^{206}Pb/^{238}U$*	*± 1σ*	*$^{207}Pb/^{235}U$*	*± 1σ*	*Conc.*
SM41	***Rhyolite***															
1	452	0.51	0.0525	0.0014	0.023	0.001	0.0032	0.0001	0.61	308.3	58.9	20.7	0.3	23.4	0.6	88.5
3	960	0.62	0.0599	0.0017	0.025	0.001	0.0031	0.0001	0.59	600.6	61.7	19.6	0.3	25.2	0.7	77.8
9	2883	0.46	0.0530	0.0006	0.024	0.000	0.0033	0.0000	0.94	327.0	26.5	21.2	0.3	24.1	0.3	88.0
2	664	0.53	0.0505	0.0014	0.023	0.001	0.0033	0.0001	0.56	217.6	64.1	21.1	0.3	22.9	0.6	92.1
3	1072	0.70	0.0584	0.0012	0.025	0.000	0.0031	0.0000	0.66	545.1	43.4	19.6	0.3	24.6	0.5	79.7
2	834	1.17	0.0553	0.0013	0.024	0.001	0.0032	0.0001	0.69	422.9	50.6	20.3	0.3	24.1	0.5	84.2
1	330	0.50	0.0549	0.0016	0.025	0.001	0.0033	0.0001	0.56	407.4	62.4	21.0	0.3	24.8	0.7	84.7
2	571	0.47	0.0559	0.0012	0.027	0.001	0.0035	0.0001	0.69	448.2	45.6	22.7	0.3	27.3	0.6	83.2
4	1335	0.33	0.0524	0.0011	0.023	0.000	0.0032	0.0000	0.60	301.7	47.4	20.3	0.3	22.9	0.5	88.6
1	456	0.47	0.0521	0.0012	0.023	0.001	0.0033	0.0001	0.68	291.3	51.5	21.0	0.3	23.6	0.5	89.0
3	1006	0.57	0.0486	0.0008	0.022	0.000	0.0033	0.0000	0.70	130.0	38.8	21.4	0.3	22.4	0.4	95.5
2	753	0.62	0.0496	0.0012	0.023	0.001	0.0033	0.0001	0.62	178.0	57.2	21.2	0.3	22.7	0.6	93.4
7	2267	0.41	0.0479	0.0007	0.022	0.000	0.0033	0.0000	0.75	95.1	37.2	21.0	0.3	21.7	0.4	96.8
10	3335	0.21	0.0477	0.0007	0.021	0.000	0.0032	0.0000	0.77	82.5	36.5	20.9	0.3	21.4	0.3	97.7
2	545	0.66	0.0471	0.0016	0.021	0.001	0.0032	0.0001	0.47	51.7	81.0	20.8	0.3	21.1	0.7	98.6
3	842	0.90	0.0467	0.0010	0.021	0.000	0.0033	0.0000	0.57	33.2	49.4	21.2	0.3	21.3	0.4	99.5
3	859	0.69	0.0475	0.0010	0.021	0.000	0.0033	0.0000	0.58	73.7	50.7	21.0	0.3	21.5	0.5	97.7
1	395	0.55	0.0463	0.0014	0.021	0.001	0.0033	0.0001	0.53	11.2	69.0	21.1	0.3	21.0	0.6	100.5
3	1150	0.70	0.0476	0.0011	0.021	0.000	0.0032	0.0000	0.57	76.7	52.6	20.6	0.3	21.1	0.5	97.6
2	570	0.57	0.0470	0.0011	0.021	0.000	0.0033	0.0001	0.66	48.3	54.5	21.2	0.3	21.5	0.5	98.6
7	2164	0.25	0.0470	0.0008	0.021	0.000	0.0033	0.0000	0.70	47.9	38.3	21.3	0.3	21.5	0.4	99.1
6	1887	0.25	0.0469	0.0009	0.022	0.000	0.0033	0.0001	0.75	44.0	45.1	21.5	0.3	21.7	0.4	99.1
1	415	0.56	0.0468	0.0017	0.022	0.001	0.0033	0.0001	0.51	37.1	86.4	21.5	0.4	21.6	0.8	99.5
SM8	***Para-gneiss***															
360	635	0.52	0.1703	0.0018	11.609	0.147	0.4946	0.0061	0.97	2560.2	17.9	2590.7	26.4	2573.4	11.9	100.7
69	140	0.55	0.1798	0.0020	10.564	0.135	0.4262	0.0053	0.97	2651.1	18.1	2288.5	24.0	2485.6	11.9	92.1
36	209	0.42	0.0701	0.0008	1.615	0.022	0.1672	0.0021	0.94	930.1	23.7	996.8	11.6	976.1	8.4	102.1
105	288	0.47	0.1208	0.0013	5.588	0.072	0.3357	0.0042	0.96	1967.5	19.5	1865.9	20.1	1914.3	11.1	97.5
114	277	0.47	0.1272	0.0014	6.567	0.084	0.3744	0.0047	0.97	2060.2	19.2	2049.9	21.8	2054.9	11.3	99.8
38	195	0.24	0.0764	0.0009	2.044	0.027	0.1942	0.0024	0.94	1104.8	22.9	1144.1	13.1	1130.4	9.1	101.2
8	48	0.42	0.0718	0.0010	1.617	0.025	0.1634	0.0021	0.84	979.3	28.8	975.8	11.7	976.8	9.7	99.9
35	345	0.01	0.0597	0.0007	0.922	0.012	0.1120	0.0014	0.92	591.8	25.5	684.5	8.1	663.2	6.6	103.2
19	127	1.00	0.0638	0.0009	1.095	0.016	0.1245	0.0016	0.87	734.5	27.9	756.6	9.1	750.9	7.8	100.8
19	175	0.51	0.0618	0.0008	0.884	0.013	0.1037	0.0013	0.88	667.5	27.2	636.1	7.7	642.9	6.8	98.9
193	589	0.10	0.1239	0.0014	5.732	0.075	0.3357	0.0042	0.95	2012.6	19.8	1865.8	20.2	1936.2	11.3	96.4
82	243	0.34	0.1156	0.0013	5.241	0.069	0.3288	0.0041	0.95	1889.3	20.4	1832.8	20.0	1859.3	11.3	98.6
8	63	1.08	0.0631	0.0010	0.964	0.017	0.1108	0.0015	0.77	712.4	34.1	677.1	8.5	685.2	8.5	98.8
53	415	1.19	0.0606	0.0007	0.862	0.012	0.1032	0.0013	0.91	625.5	26.2	633.0	7.6	631.3	6.5	100.3
77	160	0.33	0.1713	0.0020	10.658	0.143	0.4513	0.0057	0.94	2570.4	19.4	2401.2	25.3	2493.7	12.5	96.3
82	615	1.53	0.0608	0.0007	0.849	0.012	0.1012	0.0013	0.91	632.4	25.7	621.6	7.5	623.9	6.4	99.6
8	45	0.70	0.0714	0.0011	1.637	0.027	0.1662	0.0022	0.81	969.4	30.6	991.3	12.1	984.4	10.2	100.7
13	74	0.46	0.0716	0.0010	1.643	0.025	0.1666	0.0022	0.86	973.2	28.0	993.2	11.9	986.9	9.6	100.6
48	483	0.03	0.0620	0.0008	0.954	0.013	0.1116	0.0014	0.91	673.5	25.7	682.2	8.2	680.1	6.9	100.3
46	462	0.36	0.0617	0.0008	0.863	0.012	0.1016	0.0013	0.90	662.3	26.2	623.5	7.5	631.9	6.6	98.7
213	387	0.73	0.1792	0.0022	11.655	0.161	0.4717	0.0060	0.92	2645.8	19.8	2491.0	26.1	2577.1	12.9	96.7
7	71	0.41	0.0651	0.0011	0.909	0.016	0.1014	0.0014	0.77	776.4	34.5	622.4	7.9	656.6	8.4	94.8
12	122	0.21	0.0619	0.0009	0.865	0.014	0.1013	0.0013	0.81	671.5	31.4	622.2	7.8	632.9	7.5	98.3
3	16	0.56	0.0738	0.0021	1.629	0.045	0.1602	0.0026	0.59	1035.8	56.1	957.6	14.5	981.6	17.4	97.6
9	50	0.68	0.0707	0.0012	1.536	0.026	0.1576	0.0021	0.78	948.5	33.1	943.4	11.8	944.8	10.6	99.9
28	75	1.27	0.1079	0.0015	4.527	0.067	0.3045	0.0040	0.87	1763.4	24.3	1713.5	19.5	1735.9	12.3	98.7
5	49	1.08	0.0656	0.0017	0.812	0.020	0.0897	0.0014	0.62	794.7	51.9	553.9	8.1	603.5	11.3	91.8
45	395	0.36	0.0632	0.0009	1.029	0.015	0.1181	0.0015	0.87	713.6	28.2	719.7	8.8	718.2	7.7	100.2
15	146	0.36	0.0619	0.0009	0.906	0.014	0.1061	0.0014	0.83	671.0	30.6	650.0	8.1	654.7	7.6	99.3
11	128	0.15	0.0595	0.0010	0.767	0.013	0.0936	0.0013	0.78	584.0	34.8	576.5	7.4	578.0	7.6	99.7
SM11	***Para-gneiss***															
19	40	0.71	0.1589	0.0022	9.256	0.144	0.4225	0.0060	0.92	2444.2	23.6	2271.6	27.2	2363.7	14.2	96.1
14	171	0.02	0.0687	0.0012	0.846	0.016	0.0894	0.0013	0.78	889.1	35.9	551.8	7.6	622.6	8.6	88.6
37	99	0.98	0.1127	0.0016	4.839	0.075	0.3115	0.0043	0.90	1843.2	25.0	1748.0	21.3	1791.8	13.0	97.6
20	156	0.46	0.0659	0.0011	1.152	0.020	0.1268	0.0018	0.81	802.7	33.5	769.4	10.2	778.0	9.4	98.9
35	449	0.30	0.0697	0.0010	0.765	0.012	0.0796	0.0011	0.85	920.2	30.2	493.6	6.6	576.9	7.1	85.6
134	1269	0.50	0.0583	0.0008	0.820	0.012	0.1021	0.0014	0.90	539.1	29.4	626.7	8.1	608.1	6.9	103.1
125	1268	0.43	0.0596	0.0008	0.795	0.012	0.0968	0.0013	0.92	589.5	27.5	595.4	7.6	594.2	6.6	100.2
61	357	1.82	0.0653	0.0011	1.076	0.019	0.1194	0.0017	0.81	785.0	34.1	727.2	9.7	741.5	9.2	98.1
32	237	0.95	0.0656	0.0011	1.021	0.018	0.1129	0.0016	0.81	793.4	34.2	689.8	9.2	714.6	9.0	96.5
106	818	2.14	0.0590	0.0008	0.750	0.011	0.0922	0.0012	0.89	566.8	28.1	568.4	7.3	568.1	6.5	100.1
128	997	2.56	0.0574	0.0009	0.724	0.012	0.0916	0.0013	0.82	504.9	34.1	564.7	7.5	553.0	7.2	102.1
74	725	0.26	0.0608	0.0008	0.880	0.013	0.1050	0.0014	0.90	631.8	28.2	643.6	8.2	641.0	7.1	100.4
34	349	0.21	0.0615	0.0009	0.851	0.014	0.1004	0.0014	0.85	655.7	30.8	616.9	8.0	625.3	7.4	98.7
96	852	0.14	0.0641	0.0009	1.041	0.016	0.1178	0.0016	0.90	745.0	28.0	718.1	9.1	724.7	7.8	99.1
63	831	0.47	0.0593	0.0009	0.587	0.010	0.0718	0.0010	0.83	579.1	32.8	446.7	5.9	468.9	6.2	95.3
21	230	0.63	0.0606	0.0010	0.685	0.012	0.0820	0.0011	0.79	625.1	35.3	507.9	6.8	529.8	7.2	95.9
26	327	0.38	0.0649	0.0010	0.665	0.011	0.0744	0.0010	0.81	770.6	32.9	462.4	6.2	517.8	6.8	89.3
26	193	0.44	0.0658	0.0010	1.150	0.019	0.1269	0.0017	0.82	798.4	32.5	769.9	10.0	777.2	9.1	99.1
23	200	0.39	0.0689	0.0011	1.052	0.018	0.1108	0.0015	0.82	895.4	32.4	677.2	8.9	729.9	8.8	92.8
132	388	0.32	0.1344	0.0018	5.858	0.086	0.3161	0.0042	0.90	2156.6	22.9	1770.6	20.7	1955.0	12.8	90.6
116	800	0.09	0.0695	0.0009	1.452	0.022	0.1515	0.0020	0.90	913.9	27.1	909.3	11.3	910.6	8.9	99.9
23	258	0.62	0.0606	0.0012	0.687	0.013	0.0823	0.0012	0.73	624.5	40.8	509.7	7.0	531.1	8.1	96.0
21	186	1.17	0.0598	0.0012	0.731	0.015	0.0887	0.0013	0.73	595.2	42.4	547.6	7.6	557.0	8.5	98.3
52	374	0.51	0.0664	0.0010	1.169	0.019	0.1278	0.0017	0.84	817.5	30.9	775.4	9.9	786.3	8.8	98.6
51	337	0.55	0.0663	0.0010	1.254	0.020	0.1373	0.0019	0.84	814.5	30.6	829.3	10.5	825.2	9.0	100.5
353	464	3.58	0.1719	0.0023	10.592	0.156	0.4471	0.0059	0.90	2575.8	22.0	2382.2	26.4	2488.0	13.7	95.7
39	441	0.04	0.0664	0.0011	0.813	0.014	0.0888	0.0012	0.80	818.8	34.4	548.6	7.3	604.1	7.9	90.8
33	155	1.17	0.0716	0.0011	1.611	0.027	0.1632	0.0022	0.82	974.8	31.5	974.3	12.3	974.4	10.4	100.0
27	149	0.57	0.0734	0.0012	1.598	0.028	0.1579	0.0022	0.80	1024.9	32.8	945.1	12.2	969.3	10.8	97.5
66	295	1.84	0.0716	0.0011	1.488	0.025	0.1507	0.0021	0.82	975.5	31.7	904.7	11.5	925.4	10.1	97.8
36	153	1.46	0.0727	0.0012	1.684	0.029	0.1680	0.0023	0.80	1006.5	32.9	1001.0	12.8	1002.6	10.9	99.8
73	554	0.12	0.0697	0.0010	1.273	0.020	0.1324	0.0018	0.84	920.6	30.3	801.7	10.1	833.8	9.0	96.2
56	419	0.15	0.0707	0.0011	1.287	0.021	0.1321	0.0018	0.83	949.0	31.1	799.8	10.2	840.2	9.3	95.2
16	128	0.17	0.0657	0.0013	1.091	0.021	0.1206	0.0017	0.73	795.1	40.3	733.9	10.0	749.1	10.4	98.0
14	113	0.19	0.0670	0.0014	1.105	0.023	0.1197	0.0018	0.71	837.3	42.6	729.0	10.1	756.0	11.1	96.4

			Isotopic ratios							Ages						
Pb (ppm)	*U (ppm)*	*Th/U*	*$^{207}Pb/^{206}Pb$*	*± 1σ*	*$^{207}Pb/^{235}U$*	*± 1σ*	*$^{206}Pb/^{238}U$*	*± 1σ*	*rho*	*$^{207}Pb/^{206}Pb$*	*± 1σ*	*$^{206}Pb/^{238}U$*	*± 1σ*	*$^{207}Pb/^{235}U$*	*± 1σ*	*Conc.*
SM11	***Para-gneiss***	***(continued)***														
18	149	0.18	0.0659	0.0012	1.094	0.020	0.1204	0.0017	0.77	803.0	36.5	733.0	9.7	750.4	9.6	97.7
23	187	0.16	0.0652	0.0013	1.093	0.021	0.1216	0.0017	0.74	781.1	39.9	739.8	10.0	750.0	10.3	98.6
44	437	0.02	0.0633	0.0010	0.902	0.015	0.1035	0.0014	0.80	716.6	34.3	634.9	8.2	652.9	8.2	97.2
75	306	0.16	0.1009	0.0016	3.186	0.052	0.2292	0.0031	0.83	1639.8	28.6	1330.4	16.2	1453.9	12.6	91.5
135	350	0.42	0.1236	0.0019	5.745	0.092	0.3374	0.0045	0.84	2008.2	26.6	1874.0	21.7	1938.2	13.8	96.7
96	283	0.24	0.1170	0.0018	5.022	0.082	0.3113	0.0042	0.83	1911.5	27.9	1747.0	20.7	1823.0	13.9	95.8
53	451	0.02	0.0714	0.0012	1.177	0.020	0.1196	0.0016	0.79	968.9	33.8	728.1	9.4	789.8	9.5	92.2
195	687	0.34	0.1226	0.0019	4.065	0.066	0.2407	0.0032	0.82	1993.8	27.6	1390.1	16.8	1647.4	13.3	84.4
98	196	0.48	0.1573	0.0025	8.948	0.148	0.4127	0.0056	0.82	2427.0	26.7	2227.1	25.6	2332.7	15.1	95.5
79	146	1.05	0.1721	0.0028	9.221	0.155	0.3887	0.0054	0.82	2578.5	27.0	2116.6	24.8	2360.2	15.4	89.7
52	117	0.81	0.1212	0.0020	5.913	0.099	0.3540	0.0048	0.81	1973.7	28.6	1953.7	22.9	1963.1	14.5	99.5
15	99	0.34	0.0897	0.0018	1.525	0.031	0.1233	0.0018	0.73	1419.4	38.3	749.8	10.4	940.5	12.3	79.7
13	55	1.09	0.0740	0.0015	1.811	0.037	0.1776	0.0026	0.71	1041.2	40.9	1053.6	14.1	1049.3	13.3	100.4
63	450	0.36	0.0720	0.0013	1.241	0.022	0.1252	0.0017	0.77	984.7	35.5	760.2	9.9	819.4	10.1	92.8
20	135	0.36	0.0709	0.0012	1.266	0.023	0.1296	0.0018	0.76	954.3	35.3	785.4	10.1	830.7	10.1	94.5
8	63	0.87	0.0685	0.0014	0.975	0.020	0.1032	0.0015	0.70	883.7	41.6	633.2	8.6	690.8	10.2	91.7
32	151	1.05	0.0790	0.0012	1.726	0.027	0.1584	0.0021	0.84	1172.8	28.6	948.0	11.6	1018.2	10.0	93.1
50	598	0.06	0.0628	0.0009	0.720	0.011	0.0831	0.0011	0.86	701.7	29.0	514.8	6.4	550.5	6.4	93.5
11	81	0.41	0.0696	0.0013	1.112	0.021	0.1160	0.0016	0.73	915.5	38.2	707.2	9.3	759.1	10.2	93.2
10	49	0.71	0.0749	0.0017	1.679	0.037	0.1626	0.0024	0.68	1066.5	43.9	971.0	13.4	1000.6	13.9	97.0
6	30	0.75	0.0733	0.0017	1.704	0.039	0.1687	0.0025	0.66	1021.4	46.0	1005.2	13.9	1010.1	14.5	99.5
18	199	0.01	0.0644	0.0010	0.782	0.013	0.0881	0.0012	0.80	754.6	32.9	544.1	6.9	586.4	7.4	92.8
21	224	0.03	0.0652	0.0010	0.829	0.013	0.0922	0.0012	0.82	780.9	31.4	568.5	7.2	612.8	7.4	92.8
22	101	1.00	0.0709	0.0011	1.638	0.028	0.1677	0.0023	0.80	953.1	32.6	999.2	12.4	984.8	10.6	101.5
29	272	0.01	0.0623	0.0009	0.897	0.014	0.1045	0.0014	0.82	683.5	31.3	640.6	8.0	650.0	7.6	98.6
29	296	0.01	0.0628	0.0009	0.850	0.013	0.0982	0.0013	0.84	701.7	30.7	603.8	7.5	624.7	7.3	96.7
26	294	0.09	0.0655	0.0011	0.767	0.013	0.0850	0.0012	0.78	789.8	34.9	525.7	6.8	578.0	7.7	91.0
21	156	0.59	0.0679	0.0013	1.017	0.019	0.1086	0.0015	0.73	866.1	38.3	664.5	8.8	712.2	9.7	93.3
41	294	0.49	0.0659	0.0009	1.084	0.016	0.1194	0.0016	0.85	803.4	29.2	726.9	8.9	745.8	8.0	97.5
24	205	0.29	0.0614	0.0009	0.909	0.014	0.1074	0.0014	0.82	651.8	31.7	657.7	8.2	656.3	7.7	100.2
24	213	0.29	0.0634	0.0010	0.906	0.015	0.1037	0.0014	0.81	721.1	32.2	636.0	8.0	655.0	7.8	97.1
13	131	0.44	0.0620	0.0011	0.752	0.014	0.0880	0.0012	0.73	675.1	38.8	543.5	7.2	569.5	8.2	95.4
11	78	0.46	0.0652	0.0012	1.077	0.021	0.1199	0.0017	0.72	780.3	39.3	730.0	9.6	742.4	10.1	98.3
38	439	0.11	0.0625	0.0010	0.710	0.012	0.0825	0.0011	0.81	691.3	32.8	510.7	6.5	545.0	6.9	93.7
25	226	0.54	0.0652	0.0011	0.853	0.015	0.0949	0.0013	0.78	780.5	34.8	584.6	7.5	626.3	8.1	93.3
17	146	0.29	0.0621	0.0011	0.889	0.016	0.1039	0.0014	0.76	677.1	36.8	637.2	8.2	646.0	8.6	98.6
3	37	0.12	0.0603	0.0020	0.742	0.023	0.0893	0.0015	0.53	613.6	68.4	551.3	8.8	563.5	13.5	97.8
5	51	0.16	0.0704	0.0020	0.946	0.026	0.0975	0.0016	0.60	939.5	57.1	599.6	9.4	675.9	13.4	88.7
141	312	0.75	0.1214	0.0016	5.824	0.083	0.3480	0.0044	0.90	1977.3	22.7	1924.8	21.3	1950.0	12.3	98.7
9	62	0.18	0.0840	0.0019	1.519	0.034	0.1312	0.0020	0.69	1291.3	44.0	794.9	11.5	938.0	13.6	84.7
12	95	0.40	0.0652	0.0013	0.947	0.018	0.1055	0.0015	0.72	779.3	40.0	646.3	8.6	676.6	9.6	95.5
9	83	0.33	0.0620	0.0017	0.791	0.022	0.0925	0.0015	0.59	675.6	59.0	570.1	8.7	591.6	12.2	96.4
32	271	0.53	0.0610	0.0009	0.828	0.013	0.0985	0.0013	0.81	638.5	32.7	605.8	7.6	612.7	7.5	98.9
5	34	1.05	0.0696	0.0021	0.947	0.027	0.0986	0.0017	0.59	917.5	61.0	606.4	9.8	676.4	14.3	89.7
33	368	0.59	0.0604	0.0010	0.614	0.010	0.0737	0.0010	0.78	619.0	34.7	458.5	5.9	486.1	6.6	94.3
42	243	1.85	0.0617	0.0010	0.895	0.015	0.1052	0.0014	0.79	665.0	33.9	644.9	8.1	649.3	8.0	99.3
19	129	1.49	0.0600	0.0012	0.805	0.016	0.0972	0.0014	0.71	604.9	41.2	598.2	7.9	599.5	8.8	99.8
299	663	0.49	0.1273	0.0017	6.398	0.093	0.3647	0.0047	0.88	2060.7	23.2	2004.3	22.1	2032.1	12.8	98.6
18	86	0.89	0.0747	0.0017	1.617	0.036	0.1570	0.0024	0.68	1060.9	45.5	940.1	13.3	976.9	14.1	96.2
25	133	0.73	0.0732	0.0014	1.519	0.029	0.1505	0.0021	0.74	1019.5	36.8	903.9	11.8	938.1	11.5	96.4
22	99	0.93	0.0733	0.0012	1.717	0.030	0.1699	0.0023	0.78	1022.3	33.2	1011.5	12.6	1014.8	11.1	99.7
162	361	0.66	0.1285	0.0018	6.199	0.092	0.3499	0.0045	0.87	2078.0	23.9	1934.0	21.6	2004.4	13.0	96.5
20	258	0.03	0.0670	0.0014	0.683	0.014	0.0740	0.0011	0.70	837.4	42.5	460.2	6.4	528.8	8.5	87.0
16	112	0.03	0.0769	0.0016	1.409	0.028	0.1329	0.0019	0.72	1119.0	39.9	804.3	10.9	892.8	12.0	90.1
14	90	0.47	0.0657	0.0013	1.177	0.023	0.1300	0.0018	0.72	796.6	40.3	788.0	10.4	790.1	10.8	99.7
89	885	0.01	0.0604	0.0009	0.811	0.013	0.0974	0.0013	0.83	618.9	31.3	599.1	7.5	603.2	7.1	99.3
24	74	0.83	0.1093	0.0020	3.604	0.067	0.2392	0.0034	0.77	1787.6	33.4	1382.7	17.8	1550.5	14.7	89.2
59	684	0.01	0.0594	0.0009	0.682	0.011	0.0833	0.0011	0.80	582.7	33.9	515.5	6.6	528.0	6.8	97.6
31	332	0.02	0.0604	0.0010	0.751	0.013	0.0902	0.0012	0.78	618.3	35.4	556.4	7.1	568.7	7.5	97.8
78	336	1.23	0.0737	0.0012	1.619	0.027	0.1594	0.0021	0.80	1033.2	31.5	953.2	11.8	977.6	10.4	97.5
2	15	0.68	0.0685	0.0032	0.976	0.043	0.1033	0.0021	0.45	884.4	93.1	633.7	12.0	691.4	22.3	91.7
5	32	0.32	0.0667	0.0023	1.220	0.039	0.1327	0.0024	0.56	828.0	69.0	803.1	13.6	809.6	17.9	99.2
50	329	0.66	0.0663	0.0012	1.097	0.020	0.1200	0.0016	0.76	816.4	36.0	730.4	9.4	751.8	9.5	97.2
53	492	0.18	0.0610	0.0010	0.824	0.014	0.0980	0.0013	0.80	638.1	33.3	602.9	7.6	610.2	7.6	98.8
194	518	0.38	0.1278	0.0020	5.351	0.087	0.3038	0.0040	0.82	2067.9	27.0	1709.9	20.0	1877.1	13.9	91.1
SM15	***Para-gneiss***															
4	213	0.01	0.0505	0.0019	0.134	0.005	0.0192	0.0003	0.48	216.9	82.7	122.7	2.1	127.4	4.2	96.3
3	101	1.04	0.0529	0.0016	0.148	0.004	0.0203	0.0003	0.51	324.2	65.2	129.2	1.9	139.8	3.8	92.4
4	202	0.05	0.0974	0.0018	0.273	0.005	0.0203	0.0003	0.75	1574.5	34.0	129.6	1.7	244.7	3.9	53.0
4	223	0.02	0.0516	0.0009	0.145	0.003	0.0204	0.0003	0.73	266.4	40.3	130.0	1.7	137.3	2.3	94.7
4	217	0.05	0.0537	0.0009	0.157	0.003	0.0212	0.0003	0.73	357.7	37.5	135.3	1.7	148.1	2.4	91.4
5	221	0.11	0.0512	0.0009	0.159	0.003	0.0225	0.0003	0.72	251.0	39.4	143.2	1.8	149.5	2.5	95.8
5	256	0.02	0.0523	0.0013	0.164	0.004	0.0228	0.0003	0.57	300.1	56.6	145.3	2.0	154.6	3.5	94.0
2	58	0.64	0.0520	0.0009	0.178	0.003	0.0249	0.0003	0.72	283.3	39.1	158.6	2.0	166.7	2.7	95.1
5	212	0.02	0.0582	0.0013	0.202	0.004	0.0253	0.0004	0.62	534.9	49.2	160.8	2.2	187.2	3.8	85.9
27	1030	0.04	0.0511	0.0006	0.199	0.003	0.0282	0.0003	0.91	246.5	27.0	179.3	2.1	184.1	2.2	97.4
9	341	0.02	0.0515	0.0008	0.224	0.004	0.0315	0.0004	0.81	263.2	33.5	200.2	2.6	205.2	3.0	97.6
6	140	1.30	0.0520	0.0010	0.239	0.004	0.0334	0.0004	0.70	283.5	41.1	211.4	2.8	217.4	3.7	97.2
2	60	0.19	0.0512	0.0017	0.241	0.008	0.0342	0.0005	0.48	248.0	73.4	216.7	3.2	219.3	6.3	98.8
5	143	0.20	0.0523	0.0009	0.258	0.005	0.0358	0.0005	0.72	298.5	40.3	226.7	3.0	233.1	3.9	97.3
4	107	0.73	0.0357	0.0012	0.177	0.006	0.0359	0.0005	0.42	0.1	0.0	227.4	3.1	165.3	5.1	137.6
3	85	0.56	0.0517	0.0011	0.264	0.006	0.0370	0.0005	0.63	272.2	48.3	234.5	3.0	237.9	4.5	98.6
3	89	0.59	0.0498	0.0010	0.254	0.005	0.0371	0.0005	0.66	183.3	43.8	234.8	3.0	230.2	4.0	102.0
3	71	0.82	0.0543	0.0011	0.278	0.006	0.0371	0.0005	0.63	383.3	45.9	234.9	3.1	248.9	4.6	94.4
11	319	0.01	0.0537	0.0009	0.278	0.005	0.0376	0.0005	0.72	358.9	38.6	237.7	2.9	249.2	3.8	95.4
31	890	0.04	0.0522	0.0008	0.273	0.004	0.0379	0.0005	0.77	293.6	35.5	240.1	2.9	245.1	3.5	98.0
10	300	0.01	0.0531	0.0010	0.278	0.005	0.0380	0.0005	0.71	334.4	41.2	240.4	3.0	249.3	4.0	96.4
3	61	0.74	0.0286	0.0017	0.150	0.009	0.0381	0.0006	0.25	0.1	0.0	241.2	3.6	142.2	8.0	169.6
2	58	0.64	0.0520	0.0016	0.277	0.008	0.0387	0.0006	0.50	283.0	68.3	245.0	3.6	248.6	6.7	98.6
6	144	0.23	0.0524	0.0013	0.281	0.007	0.0389	0.0006	0.60	301.7	54.9	245.9	3.6	251.3	5.4	97.9
8	202	0.27	0.0551	0.0019	0.296	0.009	0.0389	0.0007	0.52	417.6	72.6	246.3	4.0	263.3	7.4	93.5
2	44	0.56	0.0535	0.0014	0.288	0.008	0.0390	0.0006	0.54	349.7	59.4	246.6	3.5	256.6	6.0	96.1

			Isotopic ratios							Ages						
Pb (ppm)	*U (ppm)*	*Th/U*	*$^{207}Pb/^{206}Pb$*	*± 1σ*	*$^{207}Pb/^{235}U$*	*± 1σ*	*$^{206}Pb/^{238}U$*	*± 1σ*	*rho*	*$^{207}Pb/^{206}Pb$*	*± 1σ*	*$^{206}Pb/^{238}U$*	*± 1σ*	*$^{207}Pb/^{235}U$*	*± 1σ*	*Conc.*
SM15	***Para-gneiss***	***(continued)***														
3	68	0.81	0.0515	0.0011	0.278	0.006	0.0392	0.0005	0.62	264.3	48.8	247.6	3.3	249.2	4.8	99.4
3	78	0.45	0.0509	0.0012	0.275	0.007	0.0392	0.0006	0.59	237.7	55.3	247.9	3.5	246.9	5.3	100.4
23	632	0.07	0.0554	0.0012	0.299	0.006	0.0392	0.0005	0.64	427.1	47.6	248.0	3.4	265.9	5.0	93.3
7	159	0.42	0.0524	0.0009	0.285	0.005	0.0395	0.0005	0.74	301.2	38.7	249.9	3.3	254.8	4.1	98.1
14	365	0.12	0.0561	0.0011	0.308	0.006	0.0398	0.0005	0.68	455.7	43.4	251.8	3.3	272.7	4.7	92.3
5	107	0.69	0.0508	0.0010	0.280	0.006	0.0399	0.0005	0.67	230.3	44.7	252.5	3.4	250.3	4.5	100.9
4	80	0.86	0.0554	0.0010	0.305	0.006	0.0400	0.0005	0.69	426.5	40.8	252.7	3.3	270.4	4.6	93.5
10	284	0.01	0.0530	0.0007	0.294	0.004	0.0403	0.0005	0.83	328.4	31.2	254.4	3.2	261.8	3.5	97.2
6	148	0.15	0.0477	0.0012	0.266	0.007	0.0405	0.0006	0.57	85.1	58.0	255.7	3.6	239.7	5.3	106.7
52	1415	0.00	0.0531	0.0007	0.297	0.004	0.0406	0.0005	0.88	332.7	28.6	256.7	3.0	264.4	3.2	97.1
14	379	0.03	0.0542	0.0009	0.311	0.005	0.0416	0.0005	0.76	378.7	36.2	262.9	3.2	274.9	4.0	95.6
8	197	0.11	0.0520	0.0010	0.302	0.006	0.0421	0.0006	0.72	284.8	41.3	265.9	3.5	267.8	4.4	99.3
21	527	0.01	0.0513	0.0006	0.298	0.004	0.0421	0.0005	0.90	254.9	27.8	266.1	3.2	265.0	3.2	100.4
26	633	0.02	0.0540	0.0007	0.323	0.005	0.0434	0.0006	0.87	371.5	30.0	274.0	3.5	284.5	3.7	96.3
31	750	0.01	0.0527	0.0007	0.326	0.005	0.0449	0.0005	0.87	313.7	29.2	283.3	3.3	286.6	3.5	98.8
8	179	0.12	0.0593	0.0012	0.369	0.007	0.0451	0.0006	0.67	577.3	42.4	284.6	3.7	318.8	5.3	89.3
58	1366	0.01	0.0528	0.0006	0.332	0.004	0.0456	0.0005	0.95	320.5	24.7	287.4	3.4	291.0	3.2	98.8
31	718	0.01	0.0541	0.0007	0.351	0.005	0.0470	0.0006	0.86	373.7	29.3	296.3	3.5	305.2	3.7	97.1
3	85	0.56	0.0517	0.0007	0.341	0.005	0.0478	0.0006	0.84	272.2	31.0	300.9	3.6	297.6	3.7	101.1
39	874	0.03	0.0540	0.0007	0.358	0.005	0.0480	0.0006	0.86	372.7	29.4	302.1	3.5	310.4	3.7	97.3
6	137	0.00	0.0529	0.0009	0.351	0.006	0.0481	0.0006	0.71	325.6	39.5	302.5	3.7	305.2	4.6	99.1
31	713	0.03	0.0527	0.0007	0.351	0.005	0.0483	0.0006	0.85	316.0	30.7	304.3	3.6	305.7	3.8	99.5
24	541	0.03	0.0540	0.0007	0.365	0.005	0.0490	0.0006	0.86	370.7	29.4	308.3	3.6	315.6	3.8	97.7
30	643	0.01	0.0535	0.0007	0.379	0.005	0.0515	0.0006	0.86	347.7	29.4	323.6	3.7	326.5	3.9	99.1
5	88	0.51	0.0544	0.0010	0.400	0.007	0.0533	0.0007	0.72	388.8	38.3	334.8	4.2	341.7	5.2	98.0
30	527	0.42	0.0542	0.0007	0.434	0.006	0.0581	0.0008	0.87	378.2	29.3	363.9	4.6	365.8	4.5	99.5
6	95	0.45	0.0712	0.0016	0.581	0.013	0.0592	0.0009	0.67	963.7	44.9	370.9	5.2	465.4	8.1	79.7
31	468	0.44	0.0677	0.0009	0.560	0.008	0.0601	0.0007	0.87	858.5	26.7	376.0	4.4	451.7	5.0	83.2
43	759	0.03	0.0548	0.0006	0.460	0.006	0.0608	0.0007	0.94	405.7	25.0	380.5	4.4	384.0	4.1	99.1
50	747	0.54	0.0563	0.0006	0.474	0.006	0.0611	0.0007	0.95	462.9	24.6	382.3	4.5	394.0	4.1	97.0
37	637	0.05	0.0553	0.0006	0.467	0.006	0.0612	0.0007	0.95	424.6	24.4	383.1	4.5	389.0	4.1	98.5
23	372	0.11	0.0581	0.0007	0.511	0.007	0.0638	0.0008	0.92	534.3	26.7	398.8	4.8	419.3	4.7	95.1
60	989	0.01	0.0552	0.0006	0.493	0.006	0.0648	0.0008	0.95	419.0	24.8	404.9	4.9	406.9	4.4	99.5
46	622	0.69	0.0579	0.0008	0.528	0.008	0.0662	0.0008	0.85	524.6	29.9	413.0	4.8	430.4	5.0	96.0
64	1071	0.04	0.0568	0.0007	0.519	0.007	0.0663	0.0008	0.92	484.1	25.9	413.5	5.0	424.5	4.7	97.4
29	507	0.06	0.0553	0.0007	0.508	0.007	0.0667	0.0008	0.88	422.0	28.3	416.1	4.8	417.0	4.7	99.8
72	1088	0.37	0.0592	0.0007	0.545	0.008	0.0668	0.0009	0.90	574.4	27.1	417.1	5.2	442.0	5.2	94.4
41	651	0.02	0.0576	0.0007	0.535	0.007	0.0674	0.0008	0.89	512.8	26.4	420.4	4.8	435.0	4.6	96.6
79	1245	0.02	0.0554	0.0006	0.527	0.007	0.0689	0.0008	0.93	429.3	25.3	429.7	4.8	429.6	4.4	100.0
30	445	0.10	0.0568	0.0007	0.540	0.007	0.0690	0.0008	0.94	482.9	25.2	430.2	5.1	438.7	4.6	98.1
18	269	0.15	0.0595	0.0008	0.580	0.009	0.0707	0.0009	0.85	585.7	29.7	440.2	5.5	464.3	5.7	94.8
64	955	0.01	0.0593	0.0007	0.581	0.008	0.0712	0.0009	0.94	576.2	24.9	443.2	5.4	465.2	5.0	95.3
40	527	0.30	0.0587	0.0008	0.577	0.009	0.0713	0.0009	0.84	554.2	30.9	444.2	5.6	462.4	5.8	96.1
19	276	0.12	0.0559	0.0007	0.555	0.008	0.0721	0.0009	0.89	448.2	27.5	448.6	5.5	448.5	5.1	100.0
43	572	0.27	0.0565	0.0007	0.569	0.008	0.0731	0.0009	0.94	469.9	25.5	454.7	5.5	457.2	4.9	99.5
14	172	0.65	0.0612	0.0009	0.619	0.009	0.0734	0.0010	0.85	645.9	29.8	456.5	5.7	489.2	5.9	93.3
47	521	0.57	0.0593	0.0007	0.647	0.009	0.0792	0.0010	0.90	576.5	26.7	491.4	6.0	506.6	5.6	97.0
68	909	0.01	0.0587	0.0007	0.658	0.008	0.0814	0.0010	0.94	555.2	24.7	504.4	5.7	513.6	5.0	98.2
30	331	0.75	0.0608	0.0009	0.697	0.011	0.0832	0.0011	0.85	633.4	29.7	515.0	6.5	537.2	6.4	95.9
48	563	0.39	0.0608	0.0007	0.718	0.010	0.0857	0.0011	0.91	630.9	25.6	530.0	6.4	549.3	5.8	96.5
54	657	0.37	0.0596	0.0008	0.705	0.009	0.0858	0.0010	0.88	587.8	27.6	530.6	6.0	541.5	5.6	98.0
45	419	0.92	0.0580	0.0007	0.721	0.010	0.0903	0.0011	0.92	527.8	26.6	557.1	6.7	551.3	5.8	101.1
21	179	1.03	0.0619	0.0009	0.802	0.012	0.0939	0.0011	0.85	671.8	29.2	578.5	6.7	597.8	6.5	96.8
33	310	0.61	0.0599	0.0008	0.784	0.011	0.0951	0.0012	0.88	598.0	28.5	585.5	7.2	587.9	6.5	99.6
176	1778	0.31	0.0602	0.0007	0.790	0.011	0.0951	0.0012	0.91	611.5	25.9	585.8	7.1	591.0	6.2	99.1
19	193	0.26	0.0614	0.0007	0.823	0.011	0.0971	0.0012	0.91	654.3	25.8	597.5	7.0	609.5	6.2	98.0
42	350	0.98	0.0610	0.0008	0.821	0.012	0.0976	0.0013	0.88	639.8	27.8	600.1	7.3	608.4	6.7	98.6
24	208	0.69	0.0614	0.0007	0.877	0.012	0.1037	0.0013	0.92	651.9	25.3	636.0	7.4	639.4	6.3	99.5
24	187	0.30	0.1040	0.0014	1.701	0.025	0.1187	0.0015	0.90	1695.9	24.1	722.9	8.9	1008.8	9.3	71.7
48	283	0.88	0.0735	0.0009	1.546	0.020	0.1526	0.0018	0.91	1026.6	24.6	915.7	10.1	948.7	8.0	96.5
66	364	0.82	0.0726	0.0009	1.562	0.020	0.1560	0.0018	0.92	1003.4	23.8	934.6	10.3	955.3	8.0	97.8
141	892	0.14	0.1072	0.0013	2.341	0.031	0.1584	0.0019	0.90	1751.8	22.5	948.0	10.6	1224.7	9.5	77.4
121	577	0.39	0.1133	0.0015	2.877	0.041	0.1843	0.0024	0.89	1852.2	23.1	1090.2	12.9	1375.8	10.8	79.2
22	85	0.63	0.1196	0.0016	3.875	0.054	0.2350	0.0029	0.88	1950.5	24.0	1360.5	15.1	1608.4	11.2	84.6
48	176	0.49	0.1130	0.0014	4.056	0.058	0.2604	0.0034	0.91	1848.1	22.3	1492.0	17.2	1645.5	11.6	90.7
51	168	0.48	0.1496	0.0017	5.411	0.071	0.2624	0.0033	0.96	2341.4	19.5	1502.3	16.9	1886.7	11.3	79.6
161	527	0.11	0.1567	0.0017	6.374	0.082	0.2951	0.0036	0.96	2420.4	18.4	1666.8	18.1	2028.7	11.3	82.2
80	249	0.45	0.1201	0.0014	4.911	0.064	0.2966	0.0037	0.95	1957.8	19.9	1674.4	18.4	1804.1	11.1	92.8
108	309	0.56	0.1349	0.0014	5.662	0.069	0.3044	0.0036	0.98	2163.0	18.5	1713.0	18.0	1925.5	10.6	89.0
71	176	0.75	0.1720	0.0022	7.461	0.108	0.3146	0.0041	0.89	2577.4	21.5	1763.4	19.9	2168.3	13.0	81.3
231	580	0.61	0.1266	0.0014	5.922	0.078	0.3394	0.0043	0.95	2051.4	20.0	1883.5	20.5	1964.5	11.5	95.9
363	889	0.43	0.1668	0.0018	8.400	0.108	0.3654	0.0045	0.96	2525.4	18.2	2007.7	21.4	2275.2	11.7	88.2
127	217	1.19	0.1814	0.0020	11.038	0.143	0.4414	0.0055	0.96	2665.7	18.2	2356.8	24.6	2526.3	12.1	93.3
SM47	***Pegmatite***															
97	2150	0.01	0.0536	0.0006	0.369	0.005	0.0499	0.0006	0.93	355.0	26.0	313.9	3.7	318.8	3.5	98.5
38	775	0.01	0.0564	0.0007	0.410	0.006	0.0528	0.0007	0.89	466.1	28.2	331.9	4.0	349.2	4.1	95.0
90	2160	0.01	0.0588	0.0008	0.364	0.005	0.0449	0.0006	0.88	560.3	27.8	283.3	3.4	315.4	3.8	89.8
45	957	0.02	0.0532	0.0007	0.376	0.005	0.0512	0.0006	0.91	338.8	27.8	321.9	3.8	323.9	3.8	99.4
35	761	0.02	0.0516	0.0007	0.362	0.005	0.0510	0.0006	0.87	266.2	29.4	320.3	3.8	313.8	3.8	102.1
20	428	0.02	0.0539	0.0008	0.378	0.006	0.0509	0.0006	0.82	367.7	32.4	319.7	3.9	325.6	4.3	98.2
101	2172	0.02	0.0567	0.0007	0.396	0.005	0.0506	0.0006	0.91	477.6	27.2	318.4	3.8	338.4	3.9	94.1
196	4258	0.01	0.0532	0.0006	0.372	0.005	0.0507	0.0006	0.94	338.4	25.7	318.5	3.8	320.9	3.5	99.3
151	3183	0.02	0.0646	0.0008	0.447	0.006	0.0501	0.0006	0.93	762.5	24.9	315.2	3.7	374.8	4.1	84.1
95	2006	0.04	0.0547	0.0007	0.387	0.005	0.0514	0.0006	0.92	400.1	25.4	323.0	3.8	332.5	3.7	97.1
54	1174	0.02	0.0543	0.0007	0.379	0.005	0.0507	0.0006	0.91	382.2	27.7	318.6	3.8	326.3	3.8	97.6
19	421	0.01	0.0538	0.0009	0.378	0.006	0.0509	0.0007	0.77	364.0	36.1	319.9	4.0	325.3	4.6	98.3
33	693	0.00	0.0522	0.0007	0.376	0.006	0.0523	0.0007	0.84	294.2	31.8	328.6	4.0	324.4	4.1	101.3
67	1453	0.01	0.0545	0.0007	0.378	0.005	0.0503	0.0006	0.88	392.0	28.3	316.3	3.8	325.5	3.9	97.2
50	800	0.19	0.0577	0.0007	0.513	0.007	0.0644	0.0008	0.89	519.5	28.0	402.4	4.8	420.2	4.7	95.8
53	674	0.41	0.0576	0.0007	0.603	0.008	0.0760	0.0009	0.89	513.9	27.4	472.2	5.6	479.4	5.3	98.5
151	3326	0.01	0.0527	0.0006	0.364	0.005	0.0502	0.0006	0.93	313.9	26.8	315.6	3.7	315.4	3.6	100.1
135	3521	0.01	0.0553	0.0007	0.318	0.004	0.0418	0.0005	0.89	423.7	27.7	263.7	3.2	280.6	3.4	94.0
14	193	0.02	0.1299	0.0021	1.130	0.018	0.0631	0.0009	0.85	2096.2	27.8	394.7	5.1	767.9	8.6	51.4

			Isotopic ratios							Ages						
Pb (ppm)	U (ppm)	Th/U	$^{207}Pb/^{206}Pb$	± 1σ	$^{207}Pb/^{235}U$	± 1σ	$^{206}Pb/^{238}U$	± 1σ	rho	$^{207}Pb/^{206}Pb$	± 1σ	$^{206}Pb/^{238}U$	± 1σ	$^{207}Pb/^{235}U$	± 1σ	Conc.
SM47	***Pegmatite***	***(continued)***														
80	1899	0.01	0.0556	0.0007	0.353	0.005	0.0461	0.0006	0.89	435.9	27.3	290.3	3.5	307.0	3.6	94.6
55	1209	0.01	0.0542	0.0007	0.370	0.005	0.0495	0.0006	0.87	380.2	28.7	311.7	3.7	319.9	3.8	97.4
77	1750	0.01	0.0536	0.0007	0.358	0.005	0.0485	0.0006	0.89	355.2	28.2	305.1	3.6	311.0	3.7	98.1
9	189	0.01	0.0556	0.0012	0.377	0.008	0.0492	0.0007	0.65	437.8	46.0	309.5	4.1	325.1	5.8	95.2
53	1103	0.01	0.0532	0.0007	0.387	0.005	0.0528	0.0006	0.87	336.5	29.0	331.9	4.0	332.5	4.0	99.8
65	1365	0.01	0.0513	0.0007	0.368	0.005	0.0521	0.0006	0.87	252.8	30.0	327.4	3.9	318.4	3.9	102.8
134	2120	0.29	0.1103	0.0014	0.847	0.012	0.0557	0.0007	0.89	1803.7	23.0	349.6	4.2	623.1	6.4	56.1
51	931	0.08	0.0545	0.0007	0.436	0.006	0.0581	0.0007	0.86	390.5	29.2	363.9	4.3	367.5	4.4	99.0
120	2636	0.02	0.0535	0.0007	0.364	0.005	0.0495	0.0006	0.89	347.7	28.2	311.1	3.7	315.5	3.7	98.6
50	1098	0.01	0.0544	0.0008	0.371	0.006	0.0496	0.0006	0.82	386.0	31.7	311.8	3.8	320.7	4.1	97.2
30	396	0.37	0.0585	0.0008	0.604	0.009	0.0749	0.0009	0.83	547.4	30.6	465.8	5.6	479.8	5.7	97.1
122	2666	0.03	0.0842	0.0012	0.520	0.008	0.0448	0.0006	0.85	1296.4	26.9	282.8	3.4	425.4	5.1	66.5
19	412	0.01	0.0565	0.0009	0.384	0.006	0.0494	0.0006	0.79	469.5	33.7	310.6	3.8	330.1	4.5	94.1
85	2117	0.02	0.0635	0.0009	0.371	0.006	0.0424	0.0005	0.82	724.5	30.9	268.0	3.3	320.8	4.2	83.5
27	365	0.29	0.0609	0.0010	0.608	0.010	0.0724	0.0009	0.78	636.3	33.5	450.6	5.5	482.4	6.2	93.4
52	995	0.17	0.0547	0.0008	0.406	0.006	0.0539	0.0007	0.80	400.1	33.2	338.4	4.1	346.3	4.7	97.7
26	335	0.34	0.0587	0.0010	0.613	0.010	0.0758	0.0010	0.76	554.0	35.0	471.0	5.8	485.4	6.4	97.0
31	461	0.26	0.0569	0.0009	0.523	0.008	0.0667	0.0008	0.80	485.6	33.8	416.2	5.1	427.1	5.5	97.4
24	315	0.41	0.0565	0.0009	0.581	0.009	0.0746	0.0009	0.78	472.1	34.4	464.0	5.6	465.4	6.0	99.7
159	3862	0.02	0.0834	0.0012	0.470	0.007	0.0408	0.0005	0.85	1279.1	27.1	258.0	3.1	390.9	4.8	66.0
12	242	0.01	0.0534	0.0010	0.404	0.007	0.0548	0.0007	0.72	347.1	39.8	344.2	4.3	344.5	5.3	99.9
32	778	0.01	0.0549	0.0009	0.343	0.006	0.0454	0.0006	0.75	408.0	36.9	286.0	3.6	299.6	4.4	95.5
49	1079	0.02	0.0576	0.0009	0.386	0.006	0.0486	0.0006	0.79	512.8	33.9	306.1	3.8	331.4	4.5	92.4
42	594	0.18	0.0567	0.0009	0.570	0.009	0.0729	0.0009	0.80	480.1	33.5	453.7	5.5	458.2	5.8	99.0
66	1237	0.12	0.0550	0.0008	0.424	0.007	0.0558	0.0007	0.81	413.9	32.3	350.2	4.2	358.6	4.6	97.7
56	1023	0.13	0.0550	0.0008	0.429	0.007	0.0566	0.0007	0.80	412.5	32.5	354.9	4.3	362.6	4.7	97.9
39	559	0.40	0.0579	0.0009	0.541	0.009	0.0678	0.0009	0.78	525.1	34.2	422.6	5.1	438.9	5.7	96.3
34	427	0.46	0.0584	0.0010	0.606	0.010	0.0752	0.0010	0.75	545.1	36.1	467.5	5.8	480.8	6.5	97.2
27	338	0.39	0.0575	0.0009	0.606	0.010	0.0765	0.0010	0.76	510.6	35.2	475.1	5.8	481.2	6.3	98.7
50	702	0.29	0.0562	0.0009	0.553	0.009	0.0714	0.0009	0.78	459.0	34.5	444.3	5.4	446.7	5.8	99.5
36	529	0.30	0.0577	0.0011	0.533	0.010	0.0670	0.0009	0.71	518.1	40.2	418.3	5.3	433.9	6.5	96.4
SM45	***Pegmatite***															
22	190	0.72	0.0598	0.0010	0.848	0.014	0.1029	0.0013	0.78	597.2	34.3	631.1	7.7	623.6	7.7	101.2
28	258	0.71	0.0593	0.0008	0.797	0.012	0.0974	0.0012	0.85	579.1	29.6	599.2	7.1	595.0	6.6	100.7
16	144	0.46	0.0610	0.0011	0.907	0.016	0.1079	0.0014	0.75	639.0	36.8	660.4	8.2	655.5	8.5	100.7
24	481	0.00	0.0570	0.0009	0.435	0.007	0.0554	0.0007	0.80	489.6	33.2	347.7	4.3	366.9	4.8	94.8
101	1018	1.12	0.0614	0.0009	0.683	0.010	0.0807	0.0010	0.84	653.6	30.5	500.4	6.1	528.8	6.2	94.6
37	435	0.09	0.0603	0.0008	0.749	0.010	0.0901	0.0011	0.89	613.9	27.2	556.4	6.6	567.7	6.0	98.0
16	162	0.30	0.0607	0.0009	0.820	0.013	0.0979	0.0013	0.80	629.9	32.5	602.2	7.3	608.0	7.3	99.0
33	731	0.00	0.0545	0.0007	0.375	0.005	0.0499	0.0006	0.88	393.0	29.0	313.6	3.8	323.2	3.9	97.0
33	364	0.48	0.0602	0.0008	0.735	0.010	0.0886	0.0011	0.87	611.5	28.4	547.1	6.5	559.6	6.1	97.8
160	3182	0.07	0.0879	0.0011	0.611	0.008	0.0505	0.0006	0.91	1379.8	23.4	317.4	3.8	484.5	5.2	65.5
134	1930	0.13	0.0653	0.0008	0.657	0.009	0.0731	0.0009	0.92	782.3	25.3	454.6	5.4	512.9	5.4	88.6
63	1653	0.02	0.0634	0.0008	0.364	0.005	0.0416	0.0005	0.89	722.1	27.4	262.8	3.2	315.0	3.8	83.4
54	1170	0.07	0.0552	0.0007	0.389	0.005	0.0510	0.0006	0.88	421.4	28.7	320.8	3.9	333.3	4.0	96.2
35	508	0.25	0.0625	0.0010	0.595	0.010	0.0691	0.0009	0.79	690.5	33.2	430.5	5.4	473.9	6.2	90.8
21	426	0.02	0.0546	0.0008	0.429	0.006	0.0570	0.0007	0.84	395.4	31.2	357.2	4.4	362.3	4.6	98.6
53	630	0.20	0.0585	0.0008	0.734	0.010	0.0909	0.0011	0.87	550.0	28.6	561.1	6.7	558.8	6.1	100.4
15	291	0.01	0.0552	0.0012	0.445	0.009	0.0584	0.0008	0.67	421.3	45.5	365.8	4.9	373.4	6.5	98.0
55	104	0.70	0.1699	0.0021	10.736	0.147	0.4585	0.0057	0.92	2556.4	20.8	2432.8	25.3	2500.5	12.7	97.3
114	1630	0.01	0.0608	0.0008	0.669	0.009	0.0798	0.0010	0.89	633.6	27.1	494.6	5.9	520.0	5.7	95.1
21	128	0.87	0.0699	0.0010	1.410	0.022	0.1465	0.0019	0.83	923.8	30.1	881.0	10.6	893.2	9.2	98.6
82	2047	0.00	0.0546	0.0007	0.351	0.005	0.0467	0.0006	0.87	395.8	29.3	293.9	3.6	305.5	3.8	96.2
86	1438	0.29	0.0681	0.0009	0.563	0.008	0.0600	0.0008	0.86	870.6	28.5	375.8	4.6	453.7	5.4	82.8
34	709	0.09	0.0565	0.0008	0.409	0.006	0.0526	0.0007	0.84	471.4	31.4	330.2	4.1	348.4	4.5	94.8
22	218	0.66	0.0615	0.0009	0.826	0.013	0.0975	0.0013	0.81	656.5	32.1	599.5	7.4	611.5	7.3	98.0
SM61	***Pegmatite***															
182	3160	0.15	0.0562	0.0006	0.468	0.006	0.0604	0.0007	0.95	459.3	24.9	378.0	4.3	389.7	4.0	97.0
135	2667	0.18	0.0565	0.0007	0.420	0.005	0.0539	0.0006	0.91	469.5	26.7	338.7	3.9	355.9	3.9	95.2
197	2990	0.46	0.0560	0.0006	0.488	0.006	0.0632	0.0007	0.93	452.7	24.9	395.1	4.5	403.6	4.2	97.9
109	1279	1.26	0.0572	0.0008	0.545	0.008	0.0691	0.0008	0.86	497.5	29.1	430.8	5.0	441.5	5.0	97.6
217	4612	0.34	0.0605	0.0007	0.407	0.005	0.0488	0.0006	0.94	623.1	24.2	307.2	3.5	347.0	3.7	88.5
21	241	1.01	0.0557	0.0008	0.554	0.009	0.0721	0.0009	0.79	439.3	32.5	448.9	5.3	447.3	5.6	100.4
38	401	1.20	0.0556	0.0008	0.577	0.008	0.0753	0.0009	0.85	434.8	29.3	468.0	5.4	462.4	5.3	101.2
42	521	0.98	0.0561	0.0009	0.515	0.008	0.0666	0.0008	0.78	454.1	34.2	415.6	5.0	421.5	5.5	98.6
45	586	0.71	0.0564	0.0007	0.526	0.007	0.0677	0.0008	0.86	465.8	29.0	422.4	4.9	429.2	4.9	98.4
47	362	0.25	0.0683	0.0008	1.228	0.016	0.1304	0.0016	0.91	878.7	25.0	790.1	8.8	813.6	7.3	97.1
78	735	1.10	0.0600	0.0007	0.706	0.009	0.0853	0.0010	0.90	603.7	26.2	527.6	6.0	542.1	5.5	97.3
84	1205	0.27	0.0564	0.0007	0.548	0.007	0.0704	0.0008	0.91	468.3	26.3	438.8	5.0	443.6	4.6	98.9
36	325	0.80	0.0611	0.0008	0.790	0.011	0.0938	0.0011	0.87	642.0	27.8	577.8	6.6	590.9	6.2	97.8
63	822	0.38	0.0573	0.0007	0.592	0.008	0.0750	0.0009	0.90	501.3	26.8	466.1	5.3	472.1	5.0	98.7
67	783	1.03	0.0565	0.0007	0.541	0.007	0.0695	0.0008	0.89	472.0	27.8	433.1	5.0	439.3	4.8	98.6
52	284	0.78	0.0728	0.0009	1.602	0.021	0.1597	0.0019	0.89	1008.0	25.3	954.9	10.6	971.0	8.4	98.3
85	1151	0.24	0.0569	0.0007	0.583	0.008	0.0744	0.0009	0.91	486.6	26.7	462.4	5.3	466.5	4.9	99.1
128	2132	0.28	0.0558	0.0007	0.472	0.006	0.0614	0.0007	0.90	444.0	26.6	384.0	4.4	392.6	4.3	97.8
28	339	1.05	0.0561	0.0008	0.509	0.008	0.0658	0.0008	0.82	455.8	31.1	410.6	4.9	417.5	5.1	98.3
81	1066	0.68	0.0562	0.0007	0.527	0.007	0.0680	0.0008	0.89	461.1	27.4	424.0	4.9	429.9	4.7	98.6
36	349	0.16	0.0635	0.0009	0.922	0.013	0.1053	0.0013	0.83	726.1	29.4	645.3	7.5	663.5	7.1	97.3
380	5227	0.36	0.0584	0.0007	0.568	0.007	0.0706	0.0008	0.92	543.6	25.9	439.7	5.0	456.7	4.8	96.3
107	1439	1.01	0.0557	0.0008	0.470	0.007	0.0612	0.0007	0.84	440.8	29.9	382.8	4.5	391.1	4.7	97.9
83	1180	1.02	0.0572	0.0008	0.479	0.007	0.0607	0.0007	0.86	499.6	29.0	379.7	4.4	397.0	4.6	95.6
31	469	0.92	0.0583	0.0014	0.452	0.011	0.0563	0.0008	0.62	539.1	52.7	353.1	5.0	378.8	7.4	93.2
95	1061	0.38	0.0631	0.0008	0.723	0.010	0.0831	0.0010	0.89	712.6	26.7	514.7	5.9	552.6	5.8	93.1
236	3367	0.50	0.0571	0.0007	0.528	0.007	0.0670	0.0008	0.90	496.4	27.5	418.3	4.8	430.5	4.7	97.2
286	4577	0.34	0.0559	0.0007	0.492	0.007	0.0639	0.0008	0.89	446.3	27.0	399.0	4.6	406.0	4.5	98.3
162	2113	0.46	0.0567	0.0007	0.583	0.008	0.0747	0.0009	0.88	477.5	28.5	464.3	5.4	466.5	5.1	99.5
10	61	0.52	0.0797	0.0025	1.516	0.043	0.1380	0.0024	0.60	1188.6	59.5	833.4	13.5	936.7	17.6	89.0
102	1462	0.14	0.0565	0.0008	0.565	0.008	0.0726	0.0009	0.87	470.0	29.3	451.9	5.3	454.9	5.1	99.3
103	1635	0.31	0.0568	0.0008	0.488	0.007	0.0624	0.0008	0.84	483.4	30.7	389.9	4.6	403.7	4.8	96.6
83	886	0.96	0.0569	0.0008	0.606	0.009	0.0773	0.0010	0.83	485.8	31.2	480.0	5.7	481.0	5.6	99.8

			Isotopic ratios							Ages						
Pb (ppm)	*U (ppm)*	*Th/U*	*$^{207}Pb/^{206}Pb$*	*± 1σ*	*$^{207}Pb/^{235}U$*	*± 1σ*	*$^{206}Pb/^{238}U$*	*± 1σ*	*rho*	*$^{207}Pb/^{206}Pb$*	*± 1σ*	*$^{206}Pb/^{238}U$*	*± 1σ*	*$^{207}Pb/^{235}U$*	*± 1σ*	*Conc.*
SM61	***Pegmatite***	***(continued)***														
114	1467	0.31	0.0587	0.0008	0.616	0.009	0.0762	0.0009	0.86	555.2	28.9	473.2	5.5	487.4	5.5	97.1
36	455	0.32	0.0557	0.0009	0.596	0.010	0.0777	0.0010	0.77	438.8	35.0	482.1	5.8	474.6	6.2	101.6
135	2829	0.01	0.0529	0.0007	0.379	0.005	0.0520	0.0006	0.86	325.0	30.0	326.6	3.9	326.3	3.9	100.1
149	1960	0.39	0.0564	0.0008	0.571	0.008	0.0735	0.0009	0.85	468.2	29.7	457.1	5.4	459.0	5.2	99.6
430	9205	0.01	0.0533	0.0007	0.373	0.005	0.0507	0.0006	0.86	342.3	29.6	318.8	3.8	321.6	3.9	99.1
SM49	***Pegmatite***															
27	516	0.07	0.0656	-	0.485	0.009	0.0537	0.0007	0.71	794.9	40.3	336.9	4.5	401.8	6.4	83.8
234	6160	0.02	0.0603	-	0.340	0.005	0.0409	0.0005	0.88	612.5	28.1	258.6	3.2	297.2	3.7	87.0
16	202	0.38	0.0713	-	0.728	0.013	0.0741	0.0010	0.74	965.0	36.9	460.6	6.1	555.1	7.9	83.0
14	206	0.15	0.0714	-	0.682	0.012	0.0693	0.0009	0.75	967.6	36.0	431.8	5.6	527.7	7.4	81.8
42	365	0.29	0.0666	-	1.049	0.016	0.1142	0.0015	0.83	825.5	30.6	697.3	8.5	728.3	8.1	95.7
33	445	0.04	0.0622	-	0.674	0.011	0.0787	0.0010	0.80	679.5	32.9	488.3	6.1	523.3	6.6	93.3
16	135	0.38	0.0627	-	0.974	0.017	0.1126	0.0015	0.75	699.0	36.8	688.0	8.7	690.5	9.0	99.6
28	649	0.01	0.0554	-	0.361	0.007	0.0473	0.0006	0.74	429.8	38.4	297.8	3.9	313.2	4.9	95.1
56	900	0.08	0.0571	-	0.524	0.008	0.0666	0.0009	0.80	493.5	33.9	415.5	5.2	427.6	5.7	97.2
41	429	0.26	0.0594	0.0008	0.800	0.011	0.0978	0.0012	0.90	579.8	27.4	601.5	7.1	596.9	6.2	100.8
15	221	0.01	0.0616	0.0009	0.623	0.010	0.0734	0.0009	0.83	659.5	31.1	456.5	5.6	491.6	6.0	92.9
6	30	0.65	0.0781	0.0015	1.965	0.037	0.1826	0.0025	0.73	1148.8	37.2	1081.2	13.7	1103.7	12.7	98.0
45	905	0.01	0.0585	0.0008	0.430	0.006	0.0533	0.0007	0.87	549.9	28.7	334.7	4.1	363.1	4.3	92.2
18	294	0.09	0.0694	0.0010	0.586	0.009	0.0613	0.0008	0.82	910.8	30.4	383.4	4.8	468.5	5.8	81.8
26	577	0.00	0.0546	0.0010	0.366	0.007	0.0486	0.0007	0.71	393.8	41.1	306.1	4.0	316.4	5.1	96.7
28	399	0.14	0.0699	0.0012	0.663	0.011	0.0688	0.0009	0.78	925.2	33.3	429.2	5.5	516.6	6.8	83.1
12	150	0.22	0.0618	0.0010	0.688	0.011	0.0808	0.0011	0.78	666.7	34.3	500.8	6.3	531.6	6.9	94.2
24	490	0.13	0.0521	0.0008	0.364	0.006	0.0508	0.0007	0.79	288.9	35.3	319.2	4.0	315.5	4.4	101.2
48	157	0.01	0.1314	0.0016	5.613	0.076	0.3098	0.0038	0.92	2117.3	21.6	1739.8	18.9	1918.2	11.6	90.7
33	565	0.04	0.0600	0.0009	0.506	0.008	0.0612	0.0008	0.82	605.0	31.9	382.8	4.7	416.0	5.3	92.0
33	322	0.24	0.0609	0.0009	0.848	0.013	0.1010	0.0013	0.85	634.7	29.9	620.5	7.4	623.5	6.9	99.5
42	458	0.03	0.0655	0.0010	0.890	0.014	0.0986	0.0013	0.82	788.8	30.7	606.4	7.4	646.3	7.4	93.8
40	380	0.26	0.0789	0.0012	1.061	0.016	0.0975	0.0013	0.83	1170.6	29.2	599.8	7.3	734.4	8.1	81.7
21	393	0.03	0.0594	0.0010	0.468	0.008	0.0571	0.0007	0.78	581.7	34.8	358.2	4.5	389.7	5.4	91.9
23	320	0.10	0.0639	0.0012	0.650	0.012	0.0737	0.0010	0.73	738.8	39.2	458.5	6.0	508.2	7.5	90.2
20	449	0.14	0.0669	0.0013	0.423	0.008	0.0459	0.0006	0.71	836.0	40.5	289.1	3.9	358.4	5.9	80.7
33	629	0.01	0.0584	0.0009	0.457	0.007	0.0567	0.0007	0.83	545.8	31.5	355.7	4.4	382.1	4.9	93.1
99	556	0.78	0.0712	0.0010	1.518	0.022	0.1547	0.0019	0.86	962.6	27.7	927.1	10.8	937.5	8.9	98.9
12	140	0.72	0.0621	0.0013	0.612	0.013	0.0716	0.0010	0.66	676.5	45.2	445.5	6.0	485.0	8.1	91.9
41	493	0.33	0.0596	0.0009	0.633	0.010	0.0770	0.0010	0.79	590.1	33.7	478.3	5.9	498.0	6.4	96.0
57	1434	0.00	0.0567	0.0009	0.334	0.005	0.0428	0.0006	0.79	479.6	35.0	269.9	3.4	292.8	4.2	92.2
20	222	0.44	0.0592	0.0010	0.696	0.012	0.0854	0.0011	0.75	573.7	37.1	528.1	6.6	536.6	7.3	98.4
NPK01	***Amphibolite***															
0	5	0.09	0.0901	0.0055	0.708	0.040	0.0570	0.0014	0.44	1427.3	111.4	357.3	8.6	543.4	24.1	65.8
1	23	0.09	0.0973	0.0027	0.754	0.020	0.0562	0.0010	0.65	1573.6	51.1	352.6	5.8	570.8	11.4	61.8
1	19	0.11	0.1083	0.0030	0.812	0.021	0.0544	0.0009	0.67	1770.8	49.2	341.3	5.7	603.4	11.6	56.6
2	23	0.12	0.2022	0.0045	1.869	0.038	0.0671	0.0012	0.85	2843.8	36.0	418.4	7.0	1070.2	13.3	39.1
2	25	0.12	0.1777	0.0044	1.556	0.034	0.0635	0.0011	0.81	2631.2	40.3	397.1	6.9	953.0	13.6	41.7
2	12	0.09	0.3645	0.0073	5.292	0.093	0.1053	0.0018	1.00	3768.6	30.1	645.4	10.7	1867.5	14.9	34.6
2	11	0.05	0.4550	0.0092	6.316	0.109	0.1007	0.0018	1.05	4101.6	29.7	618.5	10.6	2020.7	15.1	30.6

1 rho is the error correlation between the (206Pb/238U) and the (207Pb/235U) ages

[2] the concordance is based on [(238U/206Pb)/(235U/207Pb)] age ratio

Appendix C2

Supplementary monazite isotopic dataset for the samples presented in Chapter 4.

Radiogenic ratios					Ages (Ma)				
$^{208}Pb / ^{232}Th$	1σ	$^{206}Pb / ^{238}U$	1σ	rho	$^{206}Pb / ^{238}U$	1σ	$^{208}Pb / ^{232}Th$	1σ	Conc.
SM15									
0.0155	0.0002	0.0492	0.0006	0.91	309.8	3.5	310.7	3.2	99.7
0.0062	0.0001	0.0204	0.0002	0.82	130.3	1.5	125.4	1.3	103.9
0.0066	0.0001	0.0210	0.0002	0.92	133.7	1.5	133.8	1.4	99.9
0.0118	0.0001	0.0353	0.0004	0.88	223.4	2.6	236.1	2.4	94.6
0.0115	0.0001	0.0363	0.0004	0.90	229.6	2.6	231.2	2.4	99.3
0.0117	0.0001	0.0365	0.0004	0.87	230.9	2.7	234.3	2.4	98.5
0.0065	0.0001	0.0204	0.0002	0.91	130.2	1.5	131.2	1.4	99.2
0.0065	0.0001	0.0201	0.0002	0.94	128.2	1.5	131.3	1.4	97.6
0.0064	0.0001	0.0201	0.0002	0.92	128.0	1.5	128.4	1.3	99.7
0.0062	0.0001	0.0201	0.0002	0.95	128.4	1.5	124.6	1.3	103.0
0.0064	0.0001	0.0208	0.0002	0.94	133.0	1.5	129.8	1.4	102.5
0.0064	0.0001	0.0208	0.0003	0.91	133.0	1.6	129.5	1.4	102.7
0.0124	0.0001	0.0387	0.0005	0.90	244.5	2.8	248.2	2.6	98.5
0.0065	0.0001	0.0210	0.0003	0.91	133.8	1.6	130.6	1.4	102.5
0.0067	0.0001	0.0209	0.0003	0.88	133.3	1.6	134.0	1.4	99.5
0.0066	0.0001	0.0210	0.0003	0.89	133.6	1.6	133.2	1.4	100.3
0.0067	0.0001	0.0209	0.0003	0.87	133.0	1.6	134.9	1.4	98.6
0.0066	0.0001	0.0208	0.0003	0.88	132.7	1.6	133.4	1.4	99.5
0.0056	0.0001	0.0178	0.0002	0.87	113.7	1.4	112.2	1.2	101.3
0.0064	0.0001	0.0207	0.0003	0.90	132.2	1.6	129.6	1.4	102.0
0.0066	0.0001	0.0210	0.0003	0.89	133.9	1.6	132.3	1.4	101.2
0.0059	0.0001	0.0184	0.0002	0.86	117.6	1.4	118.2	1.3	99.5
0.0067	0.0001	0.0208	0.0003	0.87	132.5	1.6	134.4	1.5	98.6
0.0076	0.0001	0.0224	0.0003	0.98	142.5	1.7	153.0	1.8	93.1
0.0053	0.0001	0.0180	0.0002	0.92	115.1	1.4	107.7	1.2	106.9
0.0068	0.0001	0.0207	0.0003	0.98	132.0	1.6	136.6	1.6	96.6
0.0064	0.0001	0.0210	0.0003	0.91	133.6	1.6	129.3	1.4	103.3
0.0056	0.0001	0.0180	0.0002	1.02	115.2	1.4	112.9	1.3	102.0
0.0127	0.0001	0.0407	0.0005	0.92	257.0	3.0	254.7	2.8	100.9
0.0059	0.0001	0.0191	0.0002	0.98	122.2	1.5	119.3	1.3	102.4
0.0096	0.0001	0.0285	0.0004	0.93	181.0	2.2	193.9	2.1	93.3
0.0129	0.0001	0.0404	0.0005	0.89	255.5	3.0	259.2	2.9	98.6
0.0134	0.0002	0.0394	0.0005	0.92	248.9	3.0	269.2	3.0	92.5
0.0066	0.0001	0.0209	0.0003	0.97	133.2	1.6	133.7	1.5	99.6
0.0132	0.0002	0.0405	0.0005	0.94	255.9	3.1	265.4	2.9	96.4
0.0130	0.0002	0.0408	0.0005	0.94	257.9	3.1	260.6	2.9	99.0
0.0129	0.0001	0.0407	0.0005	0.88	257.0	3.1	258.7	2.9	99.3
0.0128	0.0001	0.0403	0.0005	0.88	255.0	3.1	257.8	2.9	98.9
SM24									
0.0144	0.0001	0.0480	0.0005	0.88	302.4	3.3	287.9	2.8	105.0
0.0151	0.0002	0.0483	0.0005	0.89	304.1	3.3	302.9	3.0	100.4
0.0114	0.0001	0.0422	0.0005	0.86	266.4	2.9	229.5	2.3	116.1
0.0135	0.0001	0.0445	0.0005	0.85	280.4	3.1	271.6	2.7	103.2
0.0152	0.0002	0.0480	0.0005	0.89	302.1	3.3	304.9	3.0	99.1

Radiogenic ratios					Ages (Ma)				
$^{208}Pb / ^{232}Th$	1σ	$^{206}Pb / ^{238}U$	1σ	rho	$^{206}Pb / ^{238}U$	1σ	$^{208}Pb / ^{232}Th$	1σ	Conc.
SM24 (continue)									
0.0131	0.0001	0.0392	0.0004	0.89	248.0	2.8	262.2	2.6	94.6
0.0131	0.0001	0.0415	0.0005	0.89	262.4	2.9	263.5	2.6	99.6
0.0143	0.0001	0.0454	0.0005	0.87	286.2	3.1	286.9	2.9	99.8
0.0135	0.0001	0.0429	0.0005	0.92	270.7	3.0	271.8	2.7	99.6
0.0150	0.0002	0.0482	0.0005	0.89	303.4	3.3	301.0	3.0	100.8
0.0151	0.0002	0.0479	0.0005	0.94	301.4	3.3	303.7	3.1	99.2
0.0124	0.0001	0.0401	0.0005	0.92	253.6	2.8	248.4	2.6	102.1
0.0149	0.0002	0.0482	0.0006	0.88	303.2	3.4	299.5	3.1	101.2
0.0151	0.0002	0.0480	0.0006	0.92	302.3	3.4	303.3	3.1	99.7
0.0163	0.0002	0.0523	0.0006	0.91	328.4	3.7	326.6	3.4	100.6
0.0106	0.0001	0.0330	0.0004	0.90	209.5	2.4	213.4	2.2	98.2
0.0120	0.0001	0.0388	0.0005	0.93	245.2	2.8	241.1	2.5	101.7
0.0139	0.0002	0.0444	0.0005	0.92	280.0	3.2	279.4	2.9	100.2
0.0147	0.0002	0.0458	0.0005	0.94	288.5	3.3	295.3	3.1	97.7
0.0140	0.0002	0.0431	0.0005	0.93	272.2	3.1	280.4	2.9	97.1
0.0142	0.0002	0.0443	0.0005	0.90	279.2	3.2	285.0	3.0	98.0
0.0110	0.0001	0.0352	0.0004	0.99	222.8	2.6	221.9	2.6	100.4
0.0057	0.0001	0.0168	0.0002	0.99	107.6	1.3	114.2	1.4	94.2
0.0149	0.0002	0.0478	0.0006	0.90	301.2	3.5	298.6	3.2	100.9
0.0137	0.0002	0.0448	0.0005	0.91	282.2	3.3	275.3	3.0	102.5
0.0124	0.0001	0.0409	0.0005	0.94	258.2	3.0	249.4	2.7	103.5
0.0104	0.0001	0.0330	0.0004	0.87	209.4	2.5	208.6	2.3	100.4
0.0149	0.0002	0.0482	0.0006	0.88	303.6	3.6	299.7	3.3	101.3
0.0135	0.0002	0.0421	0.0005	0.92	265.5	3.2	270.9	3.0	98.0
0.0175	0.0002	0.0548	0.0007	0.90	343.9	4.1	350.4	3.8	98.1
0.0136	0.0001	0.0439	0.0005	0.86	277.2	3.0	272.2	2.6	101.8
0.0150	0.0002	0.0480	0.0005	0.91	302.4	3.3	301.2	2.9	100.4
0.0150	0.0002	0.0476	0.0005	0.90	299.9	3.3	301.8	2.9	99.4
0.0142	0.0001	0.0455	0.0005	0.88	286.6	3.1	284.0	2.8	100.9
0.0151	0.0002	0.0476	0.0005	0.89	299.8	3.3	302.9	2.9	99.0
0.0145	0.0001	0.0476	0.0005	0.85	299.6	3.3	290.2	2.8	103.2
0.0143	0.0001	0.0454	0.0005	0.87	286.4	3.2	287.4	2.8	99.7
0.0149	0.0002	0.0493	0.0006	0.89	310.3	3.4	298.5	2.9	104.0
0.0151	0.0002	0.0483	0.0006	0.87	304.1	3.4	302.7	3.0	100.5
0.0148	0.0002	0.0497	0.0006	0.90	312.5	3.5	297.4	2.9	105.1
0.0152	0.0002	0.0488	0.0006	0.86	307.2	3.5	304.8	3.0	100.8
0.0149	0.0002	0.0482	0.0006	0.86	303.2	3.4	299.7	3.0	101.2
0.0152	0.0002	0.0480	0.0006	0.86	302.0	3.4	305.1	3.1	99.0
0.0157	0.0002	0.0512	0.0006	0.88	321.6	3.6	315.4	3.2	102.0
0.0164	0.0002	0.0521	0.0006	0.90	327.4	3.7	328.0	3.3	99.8
0.0140	0.0001	0.0454	0.0005	0.86	286.3	3.3	280.4	2.8	102.1
0.0093	0.0001	0.0291	0.0003	0.83	184.8	2.1	187.7	1.9	98.5
0.0152	0.0002	0.0478	0.0006	0.90	301.0	3.5	305.5	3.1	98.5
0.0181	0.0002	0.0572	0.0007	0.85	358.3	4.1	362.2	3.7	98.9

Side Work

Gondwana Research 25 (2014) 1230–1241

Contents lists available at ScienceDirect

Gondwana Research

journal homepage: www.elsevier.com/locate/gr

The dispersal of the Gondwana Super-fan System in the eastern Mediterranean: New insights from detrital zircon geochronology

Konstantinos Kydonakis [a,b,*], Dimitrios Kostopoulos [b], Marc Poujol [a], Jean-Pierre Brun [a], Dimitrios Papanikolaou [b], Jean-Louis Paquette [c]

[a] Géosciences Rennes, UMR 6118 CNRS, Université Rennes 1, Campus de Beaulieu, 35042 Rennes, France
[b] Faculty of Geology and Geoenvironment, National and Kapodistrian University of Athens, Panepistimioupoli, Zographou, Athens 15784, Greece
[c] UMR CNRS 6524, Laboratoire Magmas et Volcans, 63038 Clermont-Ferrand Cedex, France

ARTICLE INFO

Article history:
Received 26 January 2013
Received in revised form 18 April 2013
Accepted 1 May 2013
Available online 24 May 2013

Handling Editor: A.S. Collins

Keywords:
Detrital zircon U–Pb ages
Greece
Palaeotethys suture
Cimmerian
Variscan

ABSTRACT

We report here new LA-ICPMS detrital zircon U–Pb ages of a quartzite from the autochthon of Peloponnesus (Feneos locality), southern Greece. The rock classifies as a mature quartz arenite and belongs to an original shale–sandstone succession now metamorphosed into a phyllite–quartzite unit. Zircon age clusters at 0.52–0.75, 0.85, 0.95–1.1, 1.75–2 and 2.4–3 Ga point at the Saharan Metacraton and the Transgondwanan Supermountain as contributing sources; the youngest concordant grain is 522 Ma old. Our data collectively suggest deposition during the Cambro-Ordovician in a collisional setting and are in excellent agreement with those of the virtually intact Cambro-Ordovician sandstone–shale sequences of Libya (Murzuq and Kufrah basins) and the Middle East (Israel and Jordan), interpreted to have been deposited in the Gondwana Super-fan System which draped the northern Gondwanan periphery from ~525 to 460 Ma. By contrast, re-evaluating the available zircon age-distribution pattern and depositional setting of an analogous sequence forming the autochthon of north-central Crete (Galinos beds) we demonstrate that it was originally deposited in a completely different setting, i.e. in an accretionary/fore-arc complex outboard of the south Laurussian active margin (Pelagonia) during the Late Carboniferous. Comparing similar Cambro-Ordovician metasiliciclastic rocks from north-eastern Crete (Sfaka paragneiss), north-central continental Greece (Vertiskos terrane), north-western Turkey (central Sakarya terrane) and the Romanian Carpathians we show that their detrital zircon distribution patterns testify to an original depositional setting similar to that of Peloponnesus (Feneos), Libya and the Middle East. Using key time-frames from previously published palaeogeographic reconstruction models we are able to trace in space and time the Palaeozoic–Early Mesozoic wondering paths of the aforementioned sequences. Thus, time- and facies-equivalent rocks presently cropping out in the eastern Mediterranean share a common provenance from the Gondwana Super-fan System which was diachronously dispersed between Early Silurian and Early Triassic.

1. Introduction

Zircon is an accessory mineral present in most magmatic, metamorphic and sedimentary rocks. Despite its low abundance its resilient nature makes it capable of surviving multiple cycles of physical and chemical weathering, erosion and deposition. Detrital zircon geochronology is extremely useful in resolving provenance- and tectonic-setting-related problems (e.g. Yamashita et al., 2000; Lahtinen et al., 2002; Fernández-Suárez et al., 2003; Linnemann et al., 2004; Nance et al., 2009; Bea et al., 2010; Avigad et al., 2012). Eventually, detrital mineral dating has significantly contributed to the recognition of distinct terranes and their participation in various orogenic phases leading to the refinement of global reconstruction models (e.g. Stampfli and Borel, 2002).

In Greece, such provenance studies are quite scarce. In northern Greece there are the detailed works on the Early–Middle Mesozoic metasedimentary successions of the Circum-Rhodope belt (Meinhold et al., 2009, 2010a; Meinhold and Kostopoulos, 2013), the presumed Early Palaeozoic siliciclastics of the Serbo-Macedonian Massif (Meinhold et al., 2010b) and the anchimetamorphic Late Palaeozoic sequences of Chios Island, eastern Greece (Meinhold et al., 2008). In southern Greece relevant studies include the limited work on the mid-Cretaceous turbidites of the Pindos Unit (Faupl et al., 2006) and the more comprehensive work on the Cycladic archipelago (Keay and Lister, 2002). The Palaeozoic pre-Alpine sedimentary sequences of the External Hellenides (Peloponnesus and Crete) remain quite unexplored as far as their provenance is concerned. The sole exceptions are two sedimentary sequences, one from central (Kock et al., 2007), the other from eastern Crete (Zulauf

* Corresponding author at: Géosciences Rennes, UMR 6118 CNRS, Université Rennes 1, Campus de Beaulieu, 35042 Rennes, France. Tel.: +30 6937502672.
E-mail address: konstantinos.kydonakis@univ-rennes1.fr (K. Kydonakis).

1342-937X/$ – see front matter
http://dx.doi.org/10.1016/j.gr.2013.05.009

et al., 2007); the remaining Peloponnesian territory is totally lacking any detrital zircon data. Thus, the participation of continental southern Greece (Peloponnesus and Crete) in Palaeozoic reconstructions of the eastern Mediterranean could further be assessed as new provenance studies will arise.

Towards that end, we present here the first LA-ICP-MS U/Pb ages on detrital zircons along with whole-rock geochemical data for a quartzite sampled from a key locality in Peloponnesus (Feneos, see Fig. 1), southern Greece, and compare them to available zircon age data from reportedly equivalent sequences from central and eastern Crete. We further compare and re-evaluate similar data for coeval (meta) sedimentary packages from northern Greece, northeastern Romania and northwestern Turkey using as anchoring points non-metamorphosed sandstone–shale successions from Libya and the Middle East. On this basis, we decipher the provenance and tectonic setting of deposition of the aforementioned sequences and proceed to illustrate the dispersal of the northern Gondwana margin in the frame of the palaeogeographic evolution of the eastern Mediterranean during the Palaeozoic.

2. Geological background

2.1. Structure of the Hellenides — recognition of discrete basement terranes

The Hellenides, as a whole, belong to the Alpine–Himalayan mountain chain and have played a key role in the geotectonic evolution of the eastern Mediterranean. They are traditionally subdivided into Internal (lying to the NE) and External (lying to the SW) units with intervening ophiolitic sutures (Vardar and Pindos Oceans) (Fig. 1). The Internal Hellenides lie above the Pindos suture zone and comprise the Pelagonian, Serbo-Macedonian and Rhodopean terranes. These terranes underwent Mesozoic deformation related to the closure of the Vardar Ocean. All Mesozoic deformation fabrics were subsequently strongly reworked during the Tertiary concomitantly with the formation of the Southern Rhodope Core Complex, the intrusion of numerous plutonic bodies and the opening of the Aegean Sea. On the other hand, the External Hellenides were accreted to the southern European margin much later during the Tertiary marking the closure of the Pindos Ocean. They are now exposed beneath the Pindos suture zone.

The Internal Hellenides mainly display crystalline basement and cover lithologies whereas the External ones are dominated by non- to slightly metamorphosed sedimentary sequences (Papanikolaou, 1997; Papanikolaou et al., 2004). The basement terranes of the Internal Hellenides represent discrete fragments of the northern Gondwana margin with major igneous age peaks at ca. 700, 560, and 440 Ma (Anders et al., 2002; Himmerkus et al., 2002; Anders et al., 2003; Himmerkus et al., 2003, 2004; Anders et al., 2006; Himmerkus et al., 2006a, 2007, 2009), diachronously accreted to the southern margin of Laurussia and strongly amalgamated and reworked during the Permo-Carboniferous Variscan magmatism (Yarwood and Aftalion, 1976; De Bono, 1998; Vavassis et al., 2000; Reischmann et al., 2001; Stampfli and Borel, 2002; Most, 2003; Anders et al., 2005; Himmerkus et al., 2006b; Anders et al., 2007; Cornelius et al., 2007; Reischmann and Kostopoulos, 2007; Cornelius, 2008; Turpaud and Reischmann, 2010; Himmerkus et al., 2012). By contrast, outcrops of orthogneissic basement rocks of the External Hellenides (Peloponnesus and Crete) are quite scarce and restricted to Kythira Island (Fig. 1) dated at ca. 320 Ma (Seidel et al., 2006; Xypolias et al., 2006), to a small outcrop in central Crete dated at ca. 300 Ma (Zulauf et al., 2011) and to the Myrsini Syncline in eastern Crete dated at ca. 510 Ma (Romano et al., 2004). In addition, orthogneissic basement rocks often crop out in the Cyclades; they were also dated at ca. 300 Ma (Engel and Reischmann, 1998; Reischmann, 1998; Keay and Lister, 2002; Tomaschek et al., 2008).

2.2. The sedimentary sequences of the External Hellenides: the (para)autochthon — definitions and clarifications

A two-fold classification can be applied to the sedimentary sequences of the External Hellenides: (i) a post-Mid-Triassic carbonate platform cover capped by Tertiary flysch on top and (ii) Palaeozoic to Mid-Triassic siliciclastic horizons (locally involving carbonates and mafic rocks) underneath. The former includes major stratigraphic units such as the Pindos, Gavrovo–Tripolis, Ionian/Mani and pre-Apulian arranged in a SW-verging stack of nappes from NE to SW in the order listed (see Stampfli et al., 2003; van Hinsbergen et al., 2005; Robertson, 2012 and references therein; Papanikolaou, 2013), while the latter encompasses what has been known as the Phyllite–Quartzite Unit s.l. These siliciclastic horizons, which can either be fossiliferous or not, display different degrees of Alpine metamorphism and deformation and a plethora of names depending on locality (e.g. Arna, Kastania, Tyros, Galinos, Ravdoucha, western Crete). They are commonly dated as Late Carboniferous–Early Triassic but fossils as old as Late Ordovician have also been reported (e.g. Kos island; Desio (1931)). In places, the post-Mid-Triassic carbonates are deposited directly on top of the siliciclastics in stratigraphic continuity while elsewhere a major tectonic/sedimentary break is observed.

In Peloponnesus and Crete of the south Aegean domain, two discrete units crop out as tectonic windows through the Pindos and Gavrovo–Tripolis nappes (Fig. 1): the lower Mani Unit made primarily of Triassic to Eocene platform and pelagic limestones and the upper Arna Unit (Papanikolaou and Skarpelis, 1987) built chiefly of shales and sandstones. Both units have undergone subduction-related HP–LT metamorphism (although the Mani Unit to a lower degree) during the Oligo-Miocene (Jolivet et al., 2010) that transformed the rocks into recrystallised limestones/marbles and phyllites–quartzites respectively.

The presence of rocks similar to those of the Arna Unit structurally immediately below or above it has caused considerable confusion and misinterpretations in the literature as exemplified by Papanikolaou and Vassilakis (2010). In addition, numerous names have been given to both the Mani and Arna units depending on locality. In the present paper we retain the terms after the type localities without petrologic connotations. We further consider the terms Mani Unit, Plattenkalk Series, Taygetos Group and Talea Ori Unit interchangeable whereas we use the term Arna Unit to strictly refer to the Phyllite–Quartzite Unit s.s. of other workers (see Deckert et al., 1999; Zulauf et al., 2008; Jolivet et al., 2010; Robertson, 2012; Klein et al., 2013).

In Crete the pre-Mid-Triassic sedimentary sequences are well-dated by fossils to be as old as Late Carboniferous (e.g. Epting et al., 1972; Fytrolakis, 1972; König and Kuss, 1980; Krahl et al., 1983, 1986; see also Dornsiepen and Manutsoglu, 1994). In south Peloponnesus the fossiliferous Late Palaeozoic–Early Triassic sedimentary sequences (e.g. Ktenas, 1924; Fytrolakis, 1971; Lys and Thiebault, 1971) refer exclusively to low-grade series rocks (such as the Tyros beds); the medium-grade Arna Unit has not yet furnished any fossils. The commonly used Late Palaeozoic age for the latter has arisen only from inference by considering it as a time-and-facies equivalent to the former. The perils of lateral correlations of seemingly identical rocks in the field will become apparent below.

2.3. Alpine evolution

The Alpine geodynamic evolution of the Hellenides has been discussed at length by van Hinsbergen et al. (2005), Jolivet and Brun (2010), Ring et al. (2010), Royden and Papanikolaou (2011), Jolivet et al. (2013) and Papanikolaou (2013). The centrepiece of the above studies is the continuous southward retreat of the subducting Hellenic slab since the Eocene that brought about a concomitant, with rollback, southward migration of magmatism in the severely extending Aegean lithosphere (upper plate), a slow-down in the rate of plate convergence as well as a southward shift in the ages of progressively younger subduction-related metamorphism. The

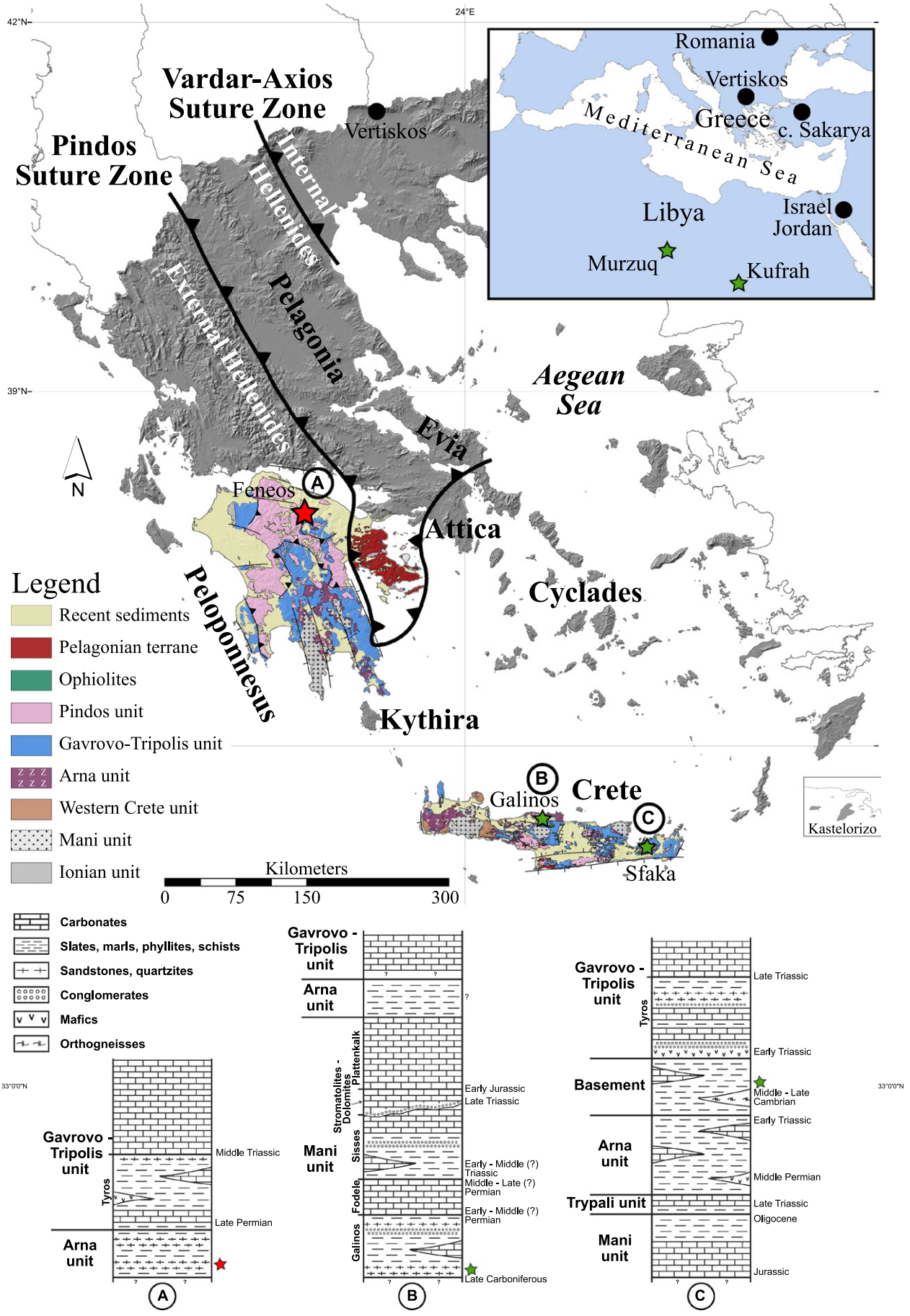

youngest HP–LT metamorphic rocks exhumed in the Hellenic orogen are the Arna and Mani Units that constitute the structurally lowermost nappes.

2.4. Pre-Alpine reconstructions — significance of the phyllite–quartzite sequence s.l

The pre-Alpine palaeogeographic evolution of the eastern Mediterranean has been documented in detail by Stampfli and co-workers (De Bono, 1998; Stampfli and Borel, 2002; Stampfli et al., 2002, 2003; Stampfli, 2005; Stamfli and Kozur, 2006; Kock et al., 2007; Stampfli and Hochard, 2009; Stampfli et al., 2011; see also Dornsiepen et al., 2001). In these reconstructions, the Arna Unit is interpreted as an accretionary/fore-arc complex formed outboard of Pelagonia in the time span 300–230 Ma, at the northern margin of Palaeotethys, while the latter was subducting northwards beneath Laurussia. By contrast, the phyllite–quartzite unit of western Crete is depicted as having been deposited at the slope and outer shelf of the southern margin of Palaeotethys during the same time period. The Late Carboniferous–Early-Middle Permian sandstone–shale Galinos beds, occurring in central-northern Crete and suggested to form the stratigraphic basement of the Talea Ori Unit (Epting et al., 1972), were assigned a northern Neotethyan passive margin origin, deposited at the southern end of the Cimmerian block (Kock et al., 2007).

Evidently, phyllite–quartzite s.l. basal rocks from Crete and Peloponnesus have been deduced to occupy quite distinct palaeogeographic positions in the Late Palaeozoic evolution of the eastern Mediterranean, based mostly on sedimentary facies analysis. This, in conjunction with the ambiguities arising from the difficulties to assign such rocks to the Arna Unit s.s., illustrates the importance of the problem of origin.

2.5. The study area & sample selection

In an effort to clarify the provenance and setting of the Arna Unit we revisited the Feneos window in central-northern Peloponnesus (Fig. 1). A quartzite sample (Fe1) collected from the central part of the Feneos window (37°56′28.62″N/22°19′02.40″E; see details in Kydonakis, 2011) was selected for zircon provenance study. The rock in the field displays only minor foliation. It essentially contains quartz and phengite, with zircon, monazite, rutile and Fe-oxides occurring as accessories.

3. Analytical methods

The sample was crushed first in a steel jaw crusher then ground in an agate mortar. The powder was digested using standard lithium metaborate ($LiBO_2$) fusion and acid dissolution techniques and subsequently chemically analysed for major elements by ICP-AES and trace elements by ICP-MS (SARM laboratory, CRPG-CNRS, Nancy, France). Analytical uncertainties depend on the content and more details can be found in Carignan et al. (2001).

A classic zircon separation procedure was followed at the facilities available at Géosciences Rennes, France. The sample was crushed and the zircon grains were separated using a Wilfley table, heavy liquids and a Frantz isodynamic separator before being handpicked under a binocular microscope and embedded in epoxy resin. Zircons were imaged by cathodoluminescence (CL) before being dated using in-situ laser ablation-inductively coupled plasma-mass spectrometry (LA-ICP-MS) at the Laboratoire Magmas et Volcans in Clermont-Ferrand, France. Ablation spot diameters of 26 μm with repetition rates of 3 Hz were used throughout. The data were corrected for U–Pb and Th–Pb fractionation and for mass bias by standard bracketing with repeated measurements of the GJ-1 zircon (Jackson et al., 2004). Data reduction was carried out using the GLITTER® software package developed by Macquarie Research Ltd. (Jackson et al., 2004). Concordia ages and diagrams were generated using Isoplot/Ex (Ludwig, 2001) updated to ver. 3.75. Further information on the instrumentation and the analytical technique is detailed in Hurai et al. (2010).

4. Results

4.1. Whole-rock geochemistry

The chemical analysis of the bulk rock (see Table A1; supplementary content), coupled with field observations, suggests that our quartzite sample is a metasandstone best classified as a non-calcareous quartzarenite (Fig. A1a; supplementary content). In general, an old, quartzose sedimentary provenance and a possible passive-margin setting are indicated (Fig. A1b, c; supplementary content). The chondrite-normalised REE pattern is strongly reminiscent of that of granitoids shifted, of course, to lower values reflecting lower absolute abundances due to intense quartz dilution as required by the very nature of the rock (Fig. A2a; supplementary content). This indicates derivation from felsic igneous basement sources that were eroded away or from sediments that recycled such sources. When the REE pattern is compared to REE patterns of pre-Alpine (meta-)granitoids from the Greek territory it is striking that it bears no resemblance to the patterns of granitoids from the typical Greek Variscan (i.e. Pelagonia terrane, Anders et al., 2007); the significance of this observation will become clear in Section 5 ("Discussion"). The upper-continental-crust normalised multi-element profile shows a clear positive trend with distinct humps at the K–Rb, Th–Nb–Ta and Zr–Hf parts of the profile suggesting the respective accumulation of white mica, rutile and zircon in accordance with mineralogical observations (Fig. A2b; supplementary content). Interestingly, the quartzite shows a somewhat elevated Cr content suggesting an additional input from mafic/ultramafic detritus.

4.2. Zircon dating

In order to avoid handpicking bias (see discussion in Sláma and Košler, 2012 and references therein) we mounted zircon grains with different colours, shapes and sizes. We measured 120 spots on 102 grains making sure that both core and rim areas were equally analysed. Approximately 92% of the ages obtained fall within the 90–110% concordance limit. The full isotopic dataset is presented in Table A2 (supplementary content). CL images of all the zircon grains and associated spots analysed are shown as Fig. A3 (supplementary content). Although some zircon grains are euhedral to subhedral, the majority are anhedral and rounded with an aspect ratio value of ~1.5, compatible with long transport as already indicated by the geochemical diagrams (Fig. A1b, c; supplementary content). Zircon typology is based on Pupin (1980) with most grains belonging to P2 and P4 types. No relation between zircon characteristics and age is evident.

Fig. 1. Simplified map of the geological entities of Greece with special emphasis on the geology of Peloponnesus and Crete. Shown are the relative positions of the Internal and External Hellenides and intervening Oceanic Suture Zones. Nappe stacking is such that structurally deep units are exposed in the SW whereas structurally shallow units are exposed in the NE (e.g. the External Hellenides lie structurally underneath the Pindos Suture Zone). The geological units for Peloponnesus are mostly after Bornovas and Rondogianni-Tsiambaou (1983) and our own observations whereas those for Crete are after Papanikolaou and Vassilakis (2010). Red star: Feneos quartzite locality of central-northern Peloponnesus used in this study for detrital zircon dating; Green stars: Cretan localities discussed in the text (Galinos sandstone, Kock et al., 2007; Sfaka paragneiss, Zulauf et al., 2007). Composite stratigraphy columns for the localities mentioned are also shown: A after Dornsiepen et al. (1986); B after Kock et al. (2007); C after Zulauf et al. (2008). Inset: Outline of the peri-Mediterranean area with localities discussed in the text. Green stars: Libya (Murzuq basin, sample H6048, Meinhold et al., 2011; Kufrah basin, sample H2553, Morton et al., in press); Black dots: Greece (Vertiskos, sample SM157, Meinhold et al., 2010a), Turkey (central Sakarya, Ustaömer et al., 2012), Israel (Elat, sample K5, Avigad et al., 2003), Jordan (El Quweira, sample US-2, Kolodner et al., 2006) and Romania (Rebra terrane, sample 10-474, Balintoni and Balica, 2013).

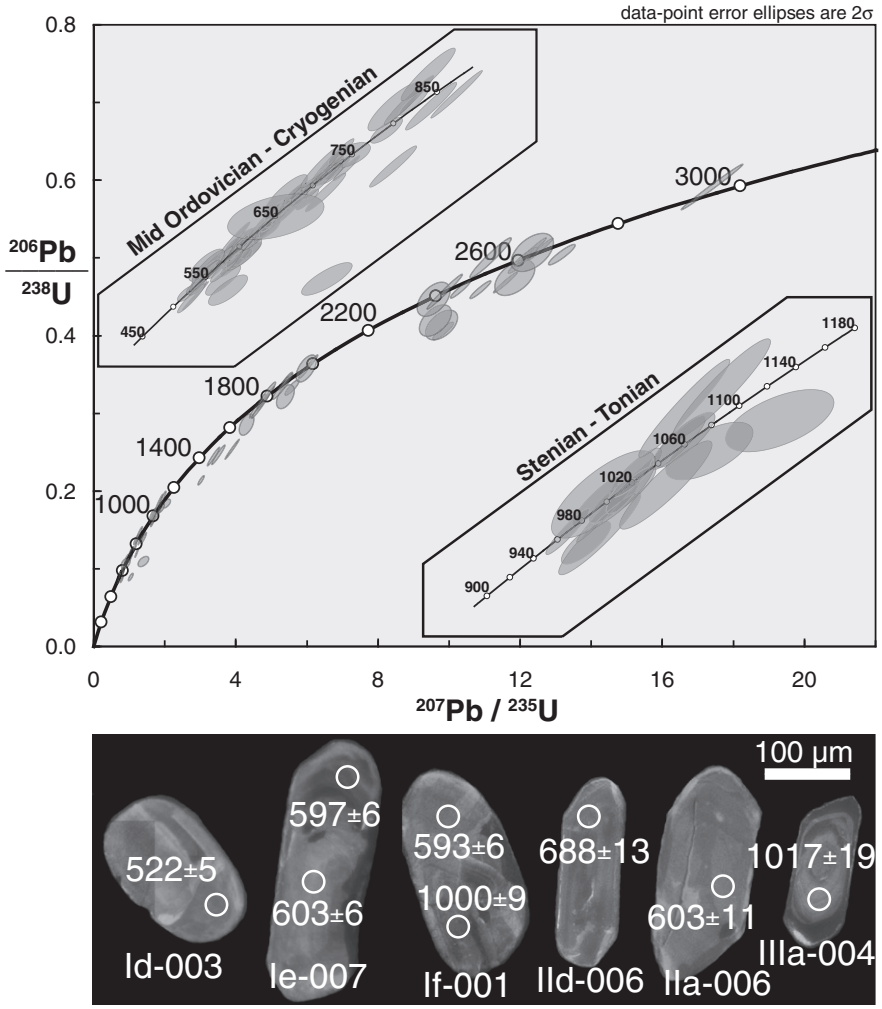

Fig. 2. Wetherill concordia plot for the Feneos quartzite (Fe1) dated in this study (120 spots) and CL images of selected zircon grains with their corresponding $^{238}U/^{206}Pb$ ages (in Ma). Details of the Stenian–Tonian and Mid-Ordovician–Cryogenian intervals are shown as insets. Error ellipses are drawn at the 1-sigma level. Plots were generated using Isoplot/Ex (Ludwig, 2001) updated to version 3.75.

In provenance studies, the most important question still remains the following: "How many grains are needed for a provenance study?" (Vermeesch, 2004). According to Andersen (2005), the measurement of 120 spots eliminates the possibility of not identifying even a small contributing terrane (2% contribution to the total zircon population).

Inspection of Fig. 2 shows that all data plot in a concordant to sub-concordant position but they do not define a simple trend in the Concordia diagram. This demonstrates that several age populations are present in the sample, which confirms the fact that these zircon grains are detrital in origin. For the grains that are 90–110% concordant, the oldest apparent $^{207}Pb/^{206}Pb$ date is 2938.3 ± 19.3 Ma while the

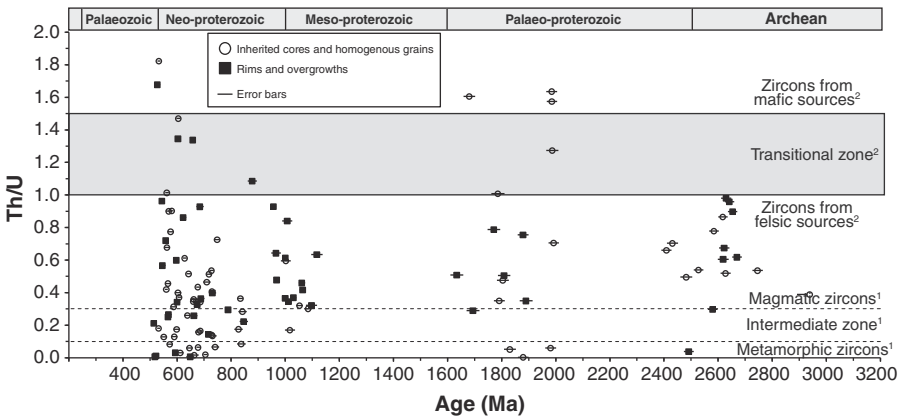

Fig. 3. Zircon Th/U ratio vs. Age plot for the Feneos quartzite (Fe1). The majority of grains come from igneous felsic sources. (1) Magmatic vs. metamorphic zircon fields are from Teipel et al. (2004). (2) Mafic vs. felsic zircon sources fields are from Linnemann et al. (2011).

youngest $^{206}Pb/^{238}U$ date is 521.8 ± 5.5 Ma, this latter constraining the maximum deposition age of our sample. It is noteworthy that not a single Permo-Carboniferous (i.e. Variscan) age was determined.

Furthermore, the measured Th/U ratios strongly suggest that our zircon population was dominated by grains from felsic igneous sources and less so from metamorphic and mafic igneous sources (Teipel et al., 2004; Linnemann et al., 2011) (Fig. 3).

The binned frequency plot (coupled with a probability-density plot) shows that thermal events are recorded at ca. 0.52–0.75 Ga (55%), 0.85 Ga (6%) and 0.95–1.1 Ga (14%) as well as some scattered peaks at ca. 1.75–2 Ga (12%) and 2.4–3 Ga (13%) (Fig. 4a), with varying proportions to the aforementioned distinct thermal events.

5. Discussion

5.1. Provenance and potential sources

The complete absence of Ordovician–Silurian, Permo-Carboniferous and younger ages in detrital zircons from the Feneos quartzite precludes the terranes recognised in the Internal Hellenides from being possible

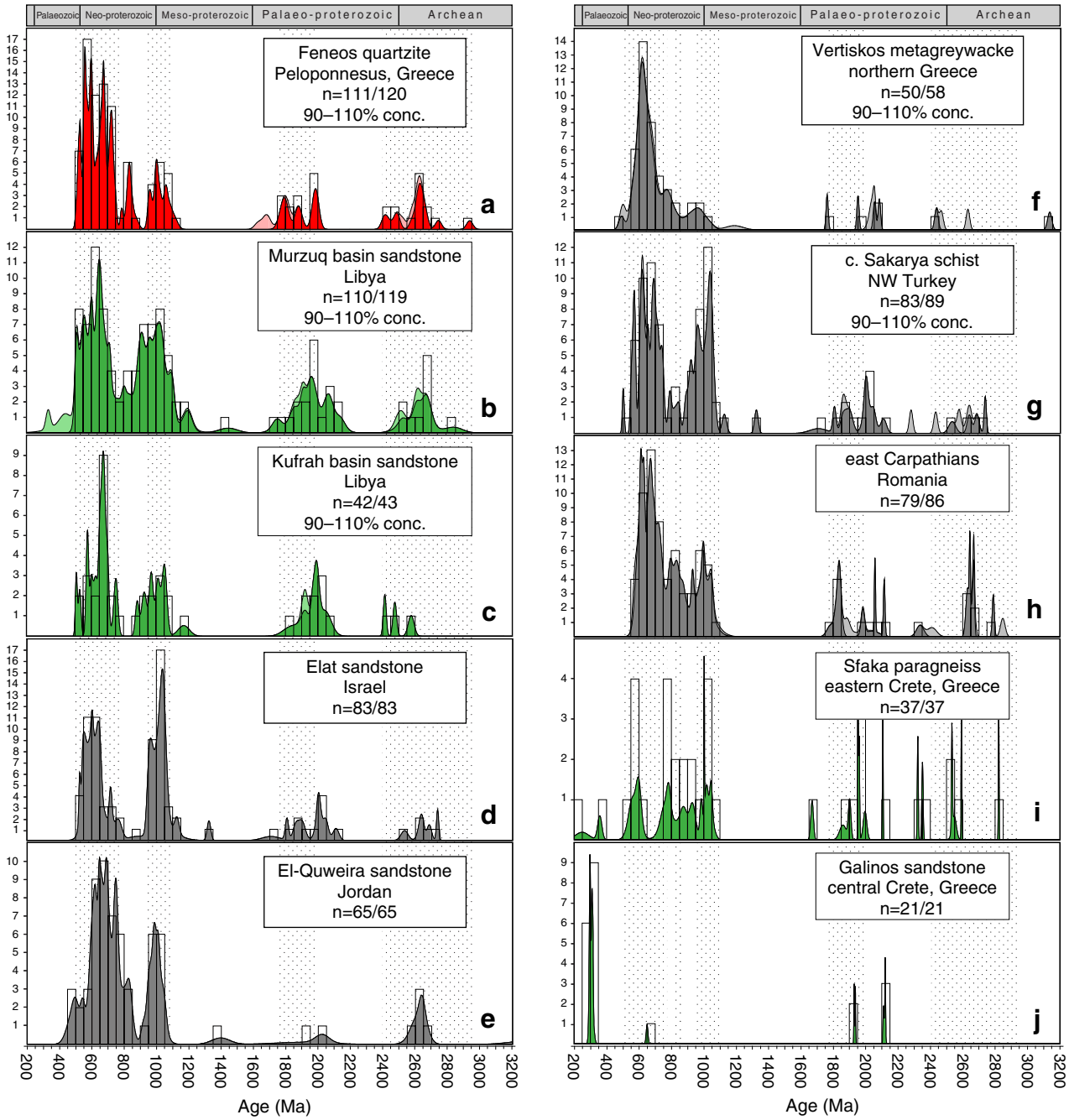

Fig. 4. Age distribution patterns of detrital zircons for the samples discussed in the text (a: Feneos, this study; b–i: remainder eastern Mediterranean localities; see caption of Fig. 1 for references). In a, b, c, f, g & h the $^{238}U/^{206}Pb$ age was used for ages <1.2 Ga (concordance calculated on the basis of $^{238}U/^{206}Pb$ and $^{235}U/^{207}Pb$ apparent ages) while the $^{207}Pb/^{206}Pb$ age was used for ages >1.2 Ga (concordance calculated on the basis of $^{238}U/^{206}Pb$ and $^{207}Pb/^{206}Pb$ apparent ages). In (d), the $^{238}U/^{206}Pb$ age was used for ages <800 Ma and the $^{207}Pb/^{206}Pb$ one for ages >800 Ma. Only concordant ages are plotted. In (e), the weighted mean of $^{238}U/^{206}Pb$ and $^{207}Pb/^{206}Pb$ ages was used according to suggestions in the original publication. In (i, j), the $^{207}Pb/^{206}Pb$ was used without any applied concordance limit due to the limited dataset available. Probability plot: Dark shades: zircon ages within 90–110% concordance; light shades: zircon ages with >10% discordance. Abbreviations: n = number of analyses within the applied concordance limit/number of total analyses. See text for discussion and caption of Fig. 1 for sample localities and references. The binned frequency histograms and the probability-density distributions were created using the AgeDisplay excel workbook (Sircombe, 2004).

sources for this sediment with the exception of the Neoproterozoic Florina and Pirgadikia ones (Anders et al., 2006; Himmerkus et al., 2006a, 2007). Nonetheless, the latter two occur as isolated areas of rather restricted surface outcrop within Variscan basement and for this reason they cannot be considered as likely candidates. By contrast, the prominent Ediacaran–Cryogenian age clusters as well as the peak at the Tonian–Cryogenian boundary seen in Fig. 4a are adequately explicable by invoking sourcing from the Saharan Metacraton (Abdelsalam et al., 2002) and the Arabian-Nubian Shield (Kröner et al., 1987, 1990; Stern, 1994; Blasband et al., 2000). The presence of Palaeoproterozoic and Archean zircon age groups observed in our sample is compatible with sourcing from the Saharan Metacraton (Abdelsalam et al., 2002 — fig. 3B). However, the Arabian Shield while being dominantly Neoproterozoic in age also includes Palaeoproterozoic microplates (Stern and Johnson, 2010 — fig. 7), and thus can be additionally considered as a source for these zircon populations. However, the Stenian–Tonian (0.9–1.1 Ga) peak is nearly totally absent from both the Saharan Metacraton and the Arabian-Nubian Shield basement rocks, the sole exceptions being the volumetrically insignificant Arkenu metasediments of eastern Libya (Meinhold et al., 2011) and the Sa'al metaigneous/metasedimentary complex of Sinai, Egypt (Be'eri-Shlevin et al., 2012), and requires an explanation.

Stenian–Tonian (i.e. 0.9–1.1 Ga-old) grains are invariably present in detrital zircon populations of eastern Mediterranean metasediments (Peloponnesus: this study; Crete: Zulauf et al., 2007; Cyclades: Reischmann, 1998; Keay and Lister, 2002; Vertiskos: Meinhold et al., 2010b; Menderes-Taurus block: Kröner and Şengör, 1990; central Sakarya: Ustaömer et al., 2012; Romanian Carpathians: Balintoni et al., 2009; Balintoni and Balica, 2013) and their existence has long been a puzzle to many researchers. If one invokes a Sunsas–Grenvillian origin (see Gerdes and Zeh, 2006; Nance et al., 2012) then one should also invoke terrane transport from Amazonia, a scenario which is rather not appealing (see also Meinhold et al., 2013). Interestingly, ~1 Ga-old detrital zircons were recently confirmed in Cambro-Ordovician sandstones from the Murzuq and Kufrah basins of Libya (see Figs. 1, 4b & c; Meinhold et al., 2011, 2013) which unconformably overlie the Saharan Metacraton but not in coeval sandstones from the Tassili Ouan Ahaggar basin of eastern Algeria (Linnemann et al., 2011) that lie on the Tuareg Shield, just outside the western confines of the Saharan Metacraton. Similar Cambro-Ordovician sandstones, carrying the enigmatic 1 Ga-age signature, were reported from the northern periphery of Gondwana further east in Israel and Jordan (Avigad et al., 2003; Kolodner et al., 2006). Importantly, the Hf isotopic composition of Neoproterozoic zircons from these sandstones indicates that they were derived from distant terranes, having been transported for several thousands of kilometres before deposition, rather than from the adjacent Arabian-Nubian Shield (Morag et al., 2011). It is now well established that enormous amounts of continentally-derived quartz-rich sandstones were deposited along northern Gondwana, in an area stretching from western northern Africa to eastern Arabia during the time period 525 to 460 Ma (late Early Cambrian–Late Ordovician) (Squire et al., 2006 and references therein). Subarkoses and arkoses dominated the Early and Middle Cambrian switching to mature quartz arenites in the Late Cambrian and Ordovician; palaeocurrent markers indicate that sediment transport was generally from south to north (see Meinhold et al., 2013 and references therein). Detrital zircon U–Pb age patterns suggest that the sequences occurring east of the Tuareg Shield (nearly coincidental with the Algerian–Libyan border) in which 1 Ga-old grains become ubiquitous were sourced from both the Saharan Metacraton and the East African–Antarctic Orogen. The latter is also known as the Transgondwanan Supermountain (including the Arabian-Nubian Shield), and resulted from collision between East and West Gondwana following closure of the Mozambique Ocean between about 650 and 515 Ma (Squire et al., 2006; Meinhold et al., 2013). Approximately 15 M km^3 of Cambro-Ordovician quartz-rich sands was transported by rivers draining the western side of the orogen and deposited in Arabia and northern Africa in a series of giant sedimentary fans that were collectively termed the Gondwana Super-fan System (Squire et al., 2006).

5.2. Equivalent sedimentary sequences of the eastern Mediterranean and their common depositional setting

Reference to Fig. 4 demonstrates the striking resemblance in the detrital zircon age groups between the Feneos (Fig. 4a), Libyan (Fig. 4b, c) and the Middle East (Fig. 4d, e) Cambro-Ordovician sandstones, strongly suggesting a common provenance for all. The same holds true for the metasediments from Vertiskos (Fig. 4f), central Sakarya (Fig. 4g) and the Romanian Carpathians (Fig. 4h) mentioned above for which a similar age of deposition has been proposed based on the youngest concordant detrital zircon ages of 493, 551 and 582 Ma respectively (Balintoni et al., 2009; Meinhold et al., 2010b; Ustaömer et al., 2012; Balintoni and Balica, 2013). Zulauf et al. (2007) published ^{207}Pb–^{206}Pb zircon evaporation ages for a metasediment from eastern Crete (Sfaka paragneiss) summarised in Fig. 4i. The discordance of all grains notwithstanding, the age distribution pattern reminds that of the Feneos and Libya quartzites with a major 1 Ga peak. The two Phanerozoic ages obtained were interpreted to have resulted from radiogenic Pb loss during Alpine fluid migration (Zulauf et al., 2007). The latter authors bracketed the protolith age of the Sfaka paragneiss between Latest Neoproterozoic and Late Cambrian which, in conjunction with the zircon age groups, leaves little doubt that Sfaka was part of the Cambro-Ordovician Gondwana Super-fan System. In stark contrast, the Galinos sandstone from central Crete (see Fig. 1), that was interpreted to constitute the basement of the Mani Unit carbonates (Kock et al., 2007), shows a prominent Late Carboniferous peak, minor scattered Neoproterozoic and Middle Palaeoproterozoic peaks and no sign of Stenian–Tonian zircons (Fig. 4j) testifying to a Variscan provenance.

Based on the evidence presented above we contend that the Feneos quartzite represents the oldest known to date sediment in Greece; it was deposited, in all probability, in a shallow shelf environment north of Libya during the Cambro-Ordovician between 522 Ma, dictated by the youngest concordant zircon age, and 460 Ma, the time of sudden drop in sedimentation rates and eventual shutdown of the Gondwana Super-fan System in this region (see Squire et al., 2006).

Cawood et al. (2012) established that detrital zircon spectra have distinctive age distribution patterns that reflect the tectonic setting of the basin in which they are deposited. They proposed a model that enables prediction of the tectonic setting of sedimentary packages of unknown origin based on the distribution of the differences between the crystallisation and depositional ages (CA–DA) of the zircons. According to these authors, convergent settings include basins lying within a supra-subduction zone setting, extending from the trench to the back-arc basin. Collisional settings incorporate basins formed during and after continental collision, such as foreland basins. Sediment derived from such settings can extend significant distance from the actual site of ocean closure. Extensional settings incorporate rift and post-rift passive margin basins as well intra-cratonic basins. The work of Cawood et al. (2012) showed that: i) convergent margin basins have a high proportion of detrital zircons (generally greater than 50%) with ages close to the age of the sediment, ii) basins formed during continental collision generally contain only minor amounts of zircons with ages approximating the depositional age of the sediment, but contain a significant proportion of grains (50% to 10%) with ages within 150 Ma of the host sediment, and iii) extensional basins are dominated by detrital zircon ages that are much older than the time of sediment accumulation with less than 5% of grains having ages within 150 Ma of the depositional age. Fig. 5 depicts detrital zircon age data plotted with respect to sediment depositional age for the Feneos, Galinos, Sfaka and Libyan sequences as well as the Vertiskos, central Sakarya, Romanian Carpathians and Middle East siliciclastics following Cawood et al.

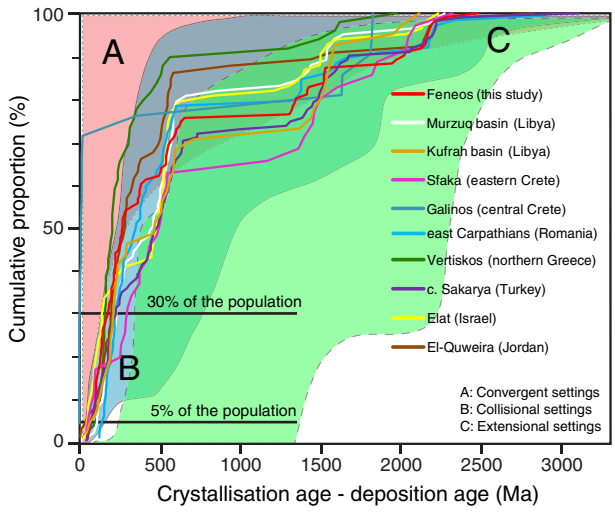

Fig. 5. Crystallisation age minus deposition age vs. cumulative zircon age proportion diagram (after Cawood et al., 2012). The Feneos, Libyan, Sfaka, Vertiskos, central Sakarya and Middle Eastern siliciclastics form a tight cluster strongly suggesting deposition in basins formed during continental collision. The Galinos metasandstone clearly points towards deposition in a convergent setting. The deposition age was provisionally set at 300 Ma (Carboniferous–Permian boundary) for the Galinos sandstone, at 500 Ma (Upper Cambrian) for the Sfaka paragneiss and the Elat sandstone and at 460 Ma (~Mid-Ordovician) for the remainder of the samples. See caption of Fig. 1 for sample localities and references.

(2012). It is clearly evident that the Galinos sandstone was deposited in a convergent margin setting whereas the remainder of the rocks forms a tight cluster at the critical values of the youngest 5 and 30% of the zircons strongly suggesting that they were deposited in basins formed during continental collision. This finding is in excellent agreement with the proposed deposition in the Gondwana Super-fan System for all of the above formations following collision between East and West Gondwana and closure of the Mozambique Ocean. It is also in excellent agreement with the results of Morag et al. (2011) that require long transport of the zircons before deposition and further corroborates the contention of Cawood et al. (2012) that sediment derived from collisional settings can extend significant distance from the actual site of ocean closure.

For the Feneos quartzite, whole-rock geochemistry suggests derivation from felsic igneous basement sources that were eroded away and additional input from mafic/ultramafic detritus. This, in conjunction with long transport as indicated by the rounding effect on the zircon grains, are all compatible with the aforementioned mode of formation of the Transgondwanan Supermountain and its subsequent erosion and deposition of the erosional products in the Gondwana Super-fan System.

5.3. Palaeozoic–Early Mesozoic palaeogeographic evolution — the dispersal of the Gondwana Super-fan System

Our findings have a profound effect on the palaeogeographic evolution of the External Hellenides and require important modifications of previous interpretations. We proceed to show our results in 3 major time steps (Fig. 6).

By Early Silurian (440 Ma; Fig. 6a) the already deposited Cambro-Ordovician Feneos sandstone–shale sequence can be seen to reside at the northern Gondwanan margin, lying north of the Murzuq and Kufrah basins of Libya but south of the future Palaeotethys rift. The depositional site of the Sfaka, Vertiskos, Romanian Carpathians and central Sakarya metasediments is shown to have been north of that of Feneos but also north of the future Palaeotethys rift. The rationale behind the latter interpretation is presented in the following paragraphs. To assist the reader, the relative positions of the Israeli–Jordanian outcrops mentioned earlier in the text are also shown for reference. We

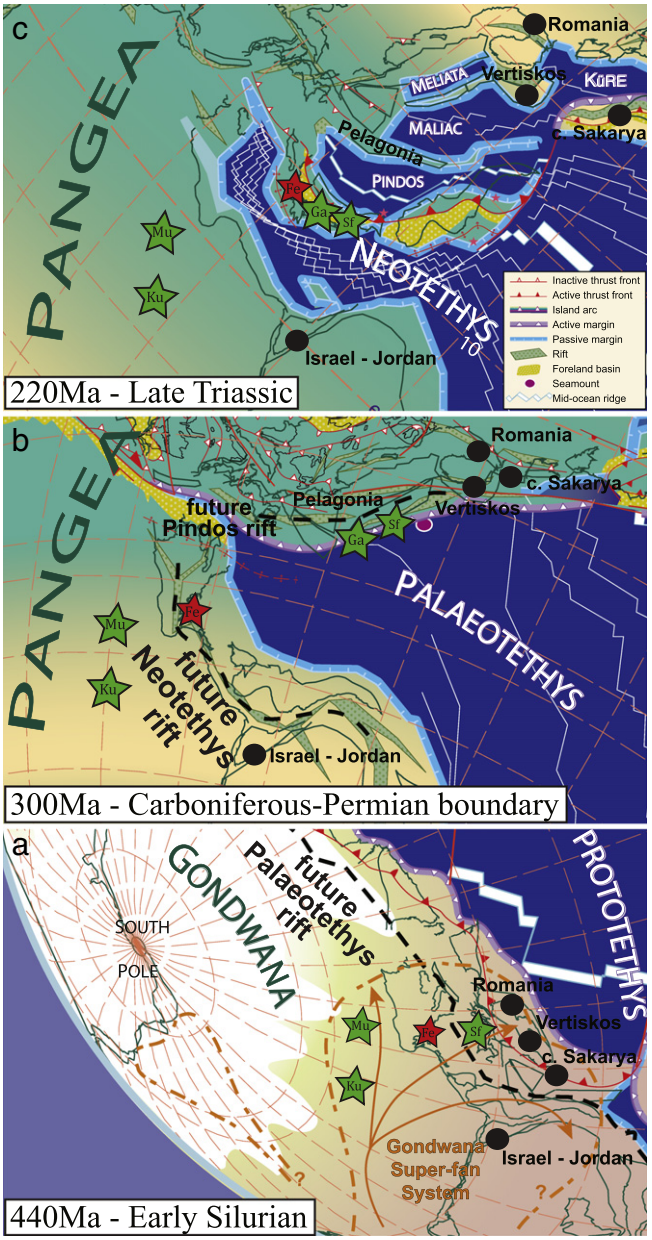

Fig. 6. Palaeozoic (a, b) and Early Mesozoic (c) palaeogeographic reconstructions for the eastern Mediterranean (modified after Stampfli and Borel, 2004). The proposed deposition areas for the samples compared in this study are marked with stars (Peloponnesus, Crete, Libya) and black dots (N. Greece, C. Turkey, Middle East, Romania). Abbreviations: "Fe": Feneos quartzite; "Mu": Murzuq basin sandstone; "Ku": Kufrah basin sandstone; "Ga" Galinos bed metasandstone; "Sf": Sfaka paragneiss. The inferred areal extent of the Gondwana Super-fan System and the Hercynian Pelagonian active margin are also shown. The Gondwana Super-fan System is drawn after Squire et al. (2006) as modified by Meinhold et al. (2013) and our own results and interpretations. See text for discussion and caption of Fig. 1 for sample references and present-day positions.

reiterate that all sequences were deposited within the confines of the Gondwana Super-fan System at the northern Gondwanan margin during the Cambro-Ordovician.

By Late Carboniferous–Early Permian (300 Ma; Fig. 6b) the Feneos sequence is depicted to be still part of northern Gondwana, situated near the southern passive margin of Palaeotethys but north of the future Neotethys rift. As such, it is part of the Cimmerian terranes that were rifted off at around 260 Ma (Stampfli and Borel, 2002). On the other hand, the Galinos succession is illustrated to occupy a fore-arc position at the northern active margin of Palaeotethys while the latter was subducting northwards beneath Laurussia, outboard of Pelagonia,

which is part of the Variscan orogen. This new position of Galinos overcomes the difficulty of very long transport of zircons from the European Variscan Belt through northern Gondwana as proposed by Kock et al. (2007), which is incompatible both with the euhedral to slightly round shape of the zircons and the dearth of zircons with North African age distributions in the sediments. In contrast, it is fully consistent with the provenance and tectonic setting indicated by the isotopic signature of the zircons themselves (Figs. 4j, 5) as well as with the recently identified Variscan basement present only ~5 km away (Rogdia beds; Zulauf et al., 2011). In effect, we propose that the Rogdia beds constitute the real basement of the Galinos sequence. With regard to the evolution of the Sfaka paragneiss it is critical that it belongs to a crystalline basement unit (Myrsini) that was thrust over Late Carboniferous–Early Triassic phyllites–marbles and shows a Middle Carboniferous (~330 Ma) Barrow-type metamorphic overprint (Zulauf et al., 2007 and references therein). As such, Sfaka must have been transported northwards following the opening of Palaeotethys to be eventually accreted to the southern margin of Laurussia and experience the consequences of the Variscan magmatism (Fig. 6b). An amphibolite-facies Barrovian metamorphism is also displayed by the Vertiskos, Romanian Carpathians and central Sakarya paragneisses/schists. Since all three basement terranes have been intruded/reworked by Late Carboniferous granitoids (Vertiskos: Borsi et al., 1965; Sakellariou and Dürr, 1993; Kilias et al., 1999; and our own unpublished data; Romanian Carpathians: Balintoni et al., 2009; Balintoni and Balica, 2013, and references therein; Sakarya: Ustaömer et al., 2012 and references therein), they are shown to occupy a position similar to that of Sfaka, i.e. at the southern active margin of Laurussia. However, in detail, the relative positions between Sfaka, on the one hand, and Vertiskos, the Romanian Carpathians and central Sakarya on the other, within the Variscan belt itself must have differed substantially. Specifically, Sfaka is portrayed south of the future Pindos rift while Vertiskos, the Romanian Carpathians and central Sakarya must have occupied distinctly more northerly positions.

Towards the end of the Triassic (220 Ma; Fig. 6c), Pindos and other small ocean basins were opened in the north whereas Palaeotethys eventually was closed by docking of the northward drifting Cimmerian block at the southern margin of Pelagonia. The opening of these small basins resulted in further dispersal of the once contiguous fragments of the northern margin of Gondwana. In this case, Vertiskos, the Romanian Carpathians and central Sakarya remained north of the Pindos rift yet themselves separated by intervening oceanic tracts, whereas Sfaka and Galinos, together with its underlying Rogdia basement, became isolated to the south within the External Hellenides' domain. The closure of Palaeotethys brought together sedimentary successions from the conjugate margins of this vanished ocean that were sutured and amalgamated. The ensuing carbonate sedimentation of the External Hellenides sealed the suture and concealed areas of different palaeogeographic affinities (see Papanikolaou, 1997). The thus unified terranes together with their sedimentary cover underwent a common Alpine tectonometamorphic evolution, hence the multitude of terms, confusion of units and misinterpretations mentioned earlier in Section 2.2. Opening of Neotethys in the south will keep the Libyan and Middle Eastern Cambro-Ordovician sedimentary formations apart from their consanguineous counterparts discussed herein throughout the Mesozoic and Cenozoic. Present-day convergence between Africa and Europe will consume the extant remains of Neotethys south of Crete thus suturing the long-wandering fragments in a new orogen, the future Mediterranean Mts (http://www.scotese.com).

5.4. Tracing the suture of Palaeotethys in the Hellenic territory

In the light of our new detrital zircon age data for Peloponnesus presented here and the re-evaluation of similar data for Crete on the pre-Mid-Triassic siliciclastic sedimentary sequences of the External Hellenides, it is clear that the Feneos quartzite (north Peloponnesus) represents a fragment of Gondwana that drifted northwards along with the Cimmerian block around the Early Permian, a period during which the Galinos (meta)sandstone (central Crete) was depositing as a fore-arc sequence outboard of the south European Variscan active margin (Fig. 6). The Sfaka paragneiss (eastern Crete) was rifted off northern Gondwana (as part of the "Galatian terrane s.s."; see von Raumer and Stampfli, 2008) during the Late Silurian and accreted to Laurussia by Late Carboniferous where it was affected by Barrow-type Variscan metamorphism (Fig. 6).

We concur with Stampfli et al. (2003) and Stamfli and Kozur (2006) that the suture of Palaeotethys lies, in the Greek area, within the pre-Alpine siliciclastic sequences of Peloponnesus and Crete. Its exact tracing though could be laborious given the lack of detrital zircon age data from these successions. However, we tentatively propose that: (i) in eastern Crete, this suture is most probably the thrust contact itself between the Myrsini crystalline basement unit (including the Sfaka paragneiss) and the underlying phyllite-marble unit and (ii) in Peloponnesus, it lies between the Feneos window and the Variscan orthogneisses of Kythira (Seidel et al., 2006).

Following closure of Palaeotethys and terrane suturing the Variscan active margin underwent rifting along strike that eventually gave birth to the Pindos Ocean by ~220 Ma (Fig. 6c). This resulted in the isolation of a thin stripe of Variscan basement within the External Hellenides, dispersed in small pieces (by later tectonic movements) now recognised in Attica (Liati et al., 2013; our own unpublished data), southern Evia (Chatzaras et al., 2013), the Cyclades (Engel and Reischmann, 1998; Keay and Lister, 2002; Tomaschek et al., 2008), Kythira (Seidel et al., 2006), eastern Crete (Seidel et al., 1982; Zulauf et al., 2011) and central Crete (Zulauf et al., 2011). Collectively, these pieces correspond to the Sitia block as elegantly depicted in the reconstructions of Stampfli and Borel (2002).

Multiple, diachronous rifting of the northern Gondwanan margin and subsequent travelling and dispersal of the resulted Gondwana Super-fan System fragments as presented in Fig. 6 obviate the need to invoke Palaeotethyan sutures north of Pelagonia (e.g. Romanian Carpathians, Balintoni and Balica, 2013).

6. Conclusions

We determined new detrital zircon ages for a quartzite from the Feneos locality of Peloponnesus, southern Greece (Fig. 1) and compared the age distribution pattern to that of similar rocks from central and eastern Crete, northern Greece, NE Romania, NW Turkey, Libya, Israel and Jordan. We further evaluated their tectonic setting of deposition and on this basis we traced their wandering paths in the eastern Mediterranean realm as they were dictated by the opening and closure of oceanic basins throughout the Palaeozoic. Our work can be summarised as follows:

(i) The Feneos quartzite provides evidence of Gondwanan provenance for at least part of the External Hellenides and based on its great similarities with Cambro-Ordovician sequences of the eastern Mediterranean seems to represent the oldest sedimentary rock of Greece known to date.

(ii) There is a clear dichotomy in provenance and tectonic setting between the Feneos (central-northern Peloponnesus) and Galinos (central Crete) rocks but a similarity between those of Feneos and Sfaka (eastern Crete) (Figs. 4 & 5). As a consequence of that Peloponnesus and Crete should be treated independently in palaeogeographic reconstructions although they now constitute an integral part of the External Hellenides. In addition, we highlight the fact that the presence of phyllite–quartzite associations with similar Alpine tectonothermal histories along strike the Hellenic orogen does not necessarily mean that their respective shale–sandstone protoliths were parts of a single sequence that was deposited at a specific site only at a given time. Put another way, the Palaeozoic–Lower Mesozoic sequences of the

External Hellenides known under the names of Tyros, Ravdoucha, Galinos, Kastania, Arna, etc. could reflect deposition at quite distinct palaeogeographic environments, a hypothesis which can efficiently be clarified only by extensive detrital zircon dating.

(iii) Sandstone–shale sequences deposited in collision-related basins of northern Gondwana during the Cambro-Ordovician (Feneos, Sfaka) and similar sequences deposited as accretionary/fore-arc complexes outboard of the active Variscan continental margin of southern Laurussia (Galinos) were sutured and amalgamated upon final closure of the Palaeotethys Ocean during the Late Palaeozoic–Early Triassic (Fig. 6). This amalgamation is strongly supported by their subsequent common burial beneath the extensive carbonate cover of the External Hellenides already by Carnian times. The Palaeotethys suture essentially lies today in southern Greece within the pre-Alpine siliciclastic sequences of Peloponnesus and Crete. Having become a single unit the above sedimentary successions shared a common Alpine tectonometamorphic history and were eventually transformed into phyllite–quartzite s.l. associations in the Oligo-Miocene obscuring their sedimentary characteristics.

(iv) The fate of the northern Gondwanan margin was multiple rifting and travelling of the fragments thereof throughout the Palaeozoic before their final incorporation into younger orogenic belts. Using the key time-frames depicted in Fig. 6, we exemplified that distinct (meta)sedimentary sequences of the eastern Mediterranean (Greece, Romania, Turkey, Libya, Israel and Jordan) showing the same deposition age and setting but substantially different later thermal/metamorphic overprint, were all part of the same Early Palaeozoic megasequence that belonged to the Gondwana Super-fan System. Using as anchoring points the non-metamorphosed Early Palaeozoic outcrops of Libya, Israel and Jordan that remained intact at their original deposition sites we have traced, in space and time, the path of the remainder time- and facies-equivalent rocks presently cropping out in the Balkan and Turkish mountain belts.

Supplementary data to this article can be found online at http://dx.doi.org/10.1016/j.gr.2013.05.009.

Acknowledgements

Dr. G. Meinhold happily made available the isotopic zircon data for the Murzuq and Kufrah basin sandstones of Libya in Excel format and freely shared views and opinions. Prof. G. Stampfli kindly provided high resolution base maps for the palaeogeographic reconstructions of Fig. 6. The comments received by two anonymous reviewers materially helped to improve the original manuscript and are greatly appreciated. D. Kostopoulos acknowledges a University of Athens Kapodistrias travel fund (70/4/7622). K. Kydonakis acknowledges support by an “Empeirikeion Foundation” post-graduate scholarship. A.S. Collins is greatly acknowledged for editorial handling.

References

Abdelsalam, M.G., Liégeois, J.P., Stern, R.J., 2002. The Saharan Metacraton. Journal of African Earth Sciences 34, 119–136.

Anders, B., Reischmann, T., Poller, U., 2002. Geochemistry and geochronology of basement rocks from the Pelagonian Zone, Greece. Geochimica et Cosmochimica Acta 66 (Supplement 1), A19.

Anders, B., Reischmann, T., Poller, U., Kostopoulos, D., 2003. The oldest rocks in Greece: geochronological evidence for remnants of a Precambrian basement within the central Hellenides. Geochimica et Cosmochimica Acta 67 (18 Supplement), A18.

Anders, B., Reischmann, T., Poller, U., Kostopoulos, D., 2005. Age and origin of granitic rocks of the eastern Vardar Zone, Greece: new constraints on the evolution of the Internal Hellenides. Journal of the Geological Society 162, 857–870.

Anders, B., Reischmann, T., Kostopoulos, D., Poller, U., 2006. The oldest rocks of Greece: first evidence for a Precambrian terrane within the Pelagonian Zone. Geological Magazine 143, 41–58.

Anders, B., Reischmann, T., Kostopoulos, D., 2007. Zircon geochronology of basement rocks from the Pelagonian Zone, Greece: constraints on the pre-Alpine evolution of the westernmost Internal Hellenides. International Journal of Earth Sciences 96, 639–661.

Andersen, T., 2005. Detrital zircons as tracers of sedimentary provenance: limiting conditions from statistics and numerical simulation. Chemical Geology 216, 249–270.

Avigad, D., Kolodner, K., McWilliams, M., Persing, H., Weissbrod, T., 2003. Origin of northern Gondwana Cambrian sandstone revealed by detrital zircon SHRIMP dating. Geology 31, 227–230.

Avigad, D., Gerdes, A., Morag, N., Bechstädt, T., 2012. Coupled U–Pb–Hf of detrital zircons of Cambrian sandstones from Morocco and Sardinia: implications for provenance and Precambrian crustal evolution of North Africa. Gondwana Research 21, 690–703.

Balintoni, I., Balica, C., 2013. Carpathian peri-Gondwanan terranes in the East Carpathians (Romania): a testimony of an Ordovician, North-African orogeny. Gondwana Research 23, 1053–1070.

Balintoni, I., Balica, C., Ducea, M.N., Chen, F., Hann, H.P., Şabliovschi, V., 2009. Late Cambrian–Early Ordovician Gondwanan terranes in the Romanian Carpathians: a zircon U–Pb provenance study. Gondwana Research 16, 119–133.

Bea, F., Montero, P., Talavera, C., Abu Anbar, M., Scarrow, J.H., Molina, J.F., Moreno, J.A., 2010. The palaeogeographic position of Central Iberia in Gondwana during the Ordovician: evidence from zircon chronology and Nd isotopes. Terra Nova 22, 341–346.

Be'eri-Shlevin, Y., Eyal, M., Eyal, Y., Whitehouse, M.J., Litvinovsky, B., 2012. The Sa'al volcano-sedimentary complex (Sinai, Egypt): a latest Mesoproterozoic volcanic arc in the northern Arabian Nubian Shield. Geology 40, 403–406.

Blasband, B., White, S., Brooijmans, P., De Boorder, H., Visser, W., 2000. Late Proterozoic extensional collapse in the Arabian-Nubian shield. Journal of the Geological Society 157, 615–628.

Bornovas, J., Rondogianni-Tsiambaou, T., 1983. Geological map of Greece, scale 1:500000, 2nd ed., Inst. of Geol. and Miner. Explor., Athens, 1983.

Borsi, S., Ferrara, G., Mercier, J., 1965. Détermination de l'âge des séries métamorphiques du Massif Serbo-Macédonien au Nord-Est de Thessalonique (Grèce) par les méthodes Rb/Sr et K/Ar. Annales. Société Géologique du Nord 84, 223–225.

Carignan, J., Hild, P., Mevelle, G., More, J., Yeghicheyan, D., 2001. Routine analyses of trace elements in geological samples using flow injection and low pressure on-line liquid chromatography couples to ICP-MS: a study of geochemical reference materials BR, DR-N, UB-N, AN-G and GH. Geostandards Newsletter 25, 187–198.

Cawood, P.A., Hawkesworth, C.J., Dhuime, B., 2012. Detrital zircon record and tectonic setting. Geology 40, 875–878.

Chatzaras, V., Dörr, W., Finger, F., Xypolias, P., Zulauf, G., 2013. U–Pb single zircon ages and geochemistry of metagranitoid rocks in the Cycladic Blueschists (Evia Island): implications for the Triassic tectonic setting of Greece. Tectonophysics 595-596, 125–139.

Cornelius, N.K., 2008. UHP Metamorphic Rocks of the Eastern Rhodope Massif, NE Greece: New Constraints From Petrology, Geochemistry and Zircon Ages. Unpub. PhD Thesis Johannes-Gutenberg Universität, Mainz.

Cornelius, N.K., Reischmann, T., Frei, D., Kostopoulos, D., 2007. Geochronology, geochemistry and isotopes of orthogneisses from the Greek Rhodope. Geochimica et Cosmochimica Acta 71 (15 Supplement), A190.

De Bono, A., 1998. Pelagonian Margins in Central Evia Island (Greece): Stratigraphy and Geodynamic Evolution. Unpub. PhD Thesis Université de Lausanne, Switzerland.

Deckert, C., Plank, M., Seidel, M., Zacher, W., 1999. Die metamorphen Decken des Taygetos-Gebirges (Peloponnes) und ihre Korrelation mit den metamorphen Einheiten auf Kreta–Neugliederung, Vergleiche und Denkmodelle. Zeitschrift der Deutschen Geologischen Gesellschaft 150, 133–158.

Desio, A., 1931. Le isole italiane dell'Egeo. Mem. Carta geol., ftal. 24, 534 S., 87 Abb., 4 Fototat., 9 Ktn., Rom 1931.

Dornsiepen, U.F., Manutsoglu, E., 1994. Zur gliederung der phyllit-Decke Kretas und des Peloponnes. Zeitschrift der Deutschen Geologischen Gesellschaft 145, 286–304.

Dornsiepen, U.F., Gerolymatos, E., Jacobshagen, V., 1986. Die phyllit-quarzit-serie im fenster von Feneos (Nord Peloponnes). Institute of Geological and Mining Research, Geological Geophysical Research, Special Issue, 3, pp. 99–105.

Dornsiepen, U.F., Manutsoglu, E., Mertmann, D., 2001. Permian–Triassic palaeogeography of the external Hellenides. Palaeogeography, Palaeoclimatology, Palaeoecology 172, 327–338.

Engel, M., Reischmann, T., 1998. Single zircon geochronology of orthogneisses from Paros, Greece. Bulletin of the Geological Society of Greece 32, 91–99.

Epting, M., Kudrass, H.R., Leppig, U., Schafer, A., 1972. Geologie der Talea Ori/Kreta. Neues Jahrbuch für Geologie und Paläontologie Abhandlungen 141, 259–285.

Faupl, P., Pavlopoulos, A., Klötzli, U., Petrakakis, K., 2006. On the provenance of mid-Cretaceous turbidites of the Pindos zone (Greece): implications from heavy mineral distribution, detrital zircon ages and chrome spinel chemistry. Geological Magazine 143, 329–342.

Fernández-Suárez, J., Garcia, F.D., Jeffries, T.E., Arenas, R., Abati, J., 2003. Constraints on the provenance of the uppermost allochthonous terrane of the NW Iberian Massif: inferences from detrital zircon U–Pb ages. Terra Nova 15, 138–144.

Floyd, P.A., Leveridge, B.E., 1987. Tectonic environment of the Devonian Gramscatho basin, south Cornwall: framework mode and geochemical evidence from turbiditic sandstones. Journal of the Geological Society 144, 531–542.

Fytrolakis, N., 1971. Die bis heute unbekannten palaeozoischen schichten sudostlhich von Kalamai. Bulletin of the Geological Society of Greece 8, 60–69.

Fytrolakis, N., 1972. Die einwirkung gewisser orogenen Bewegungen und die Gipsbildung in Osekreta (Prov. Sitia). Bulletin of the Geological Society of Greece 9, 28–80.

Gerdes, A., Zeh, A., 2006. Combined U–Pb and Hf isotope LA-(MC-) ICP-MS analyses of detrital zircons: comparison with SHRIMP and new constraints for the provenance and age of an Armorican metasediment in Central Germany. Earth and Planetary Science Letters 249, 47–61.

Herron, M.M., 1988. Geochemical classification of terrigenous sands and shales from core or log data. Journal of Sedimentary Research 58, 820–829.

Himmerkus, F., Reischmann, T., Kostopoulos, D., 2002. First evidence for Silurian magmatism in the Serbo-Macedonian Massif, northern Greece. Geochimica et Cosmochimica Acta 66 (Supplement 1), A330.
Himmerkus, F., Reischmann, T., Kostopoulos, D., 2003. The Serbo-Macedonian Massif, the oldest crustal segment of the Internal Hellenides, identified by zircon ages. Geophysical Research Abstracts 5, 05671.
Himmerkus, F., Reischmann, T., Kostopoulos, D., 2004. The Pirkadikia Unit, the oldest crustal segment in the Serbo-Macedonian terrane assemblage. 5th International Symposium on Eastern Mediterranean Geology, Thessaloniki, Greece, 14–20 April, Ref: T1-63.
Himmerkus, F., Reischmann, T., Kostopoulos, D., 2006a. Late Proterozoic and Silurian basement units within the Serbo-Macedonian Massif, northern Greece: the significance of terrane accretion in the Hellenides. Geological Society, London, Special Publications 260, 35–50.
Himmerkus, F., Reischmann, T., Kostopoulos, D., 2006b. Permo-Carboniferous and upper Jurassic basement ages in the Kerdillion Unit, eastern Serbo-Macedonian Massif, northern Greece. Geophysical Research Abstracts 8, 05758.
Himmerkus, F., Anders, B., Reischmann, T., Kostopoulos, D., 2007. Gondwana-derived terranes in the northern Hellenides. Geological Society of America Memoirs 200, 379–390.
Himmerkus, F., Reischmann, T., Kostopoulos, D., 2009. Serbo-Macedonian revisited: a Silurian basement terrane from northern Gondwana in the Internal Hellenides, Greece. Tectonophysics 473, 20–35.
Himmerkus, F., Zachariadis, P., Reischmann, T., Kostopoulos, D., 2012. The basement of the Mount Athos peninsula, northern Greece: insights from geochemistry and zircon ages. International Journal of Earth Sciences 101, 1467–1485.
Hurai, V., Paquette, J.L., Huraiová, M., Konečný, P., 2010. U–Th–Pb geochronology of zircon and monazite from syenite and pincinite xenoliths in Pliocene alkali basalts of the intra-Carpathian back-arc basin. Journal of Volcanology and Geothermal Research 198, 275–287.
Jackson, S.E., Pearson, N.J., Griffin, W.L., Belousova, E.A., 2004. The application of laser ablation–inductively coupled plasma-mass spectrometry to in situ U–Pb zircon geochronology. Chemical Geology 211, 47–69.
Jolivet, L., Brun, J.-P., 2010. Cenozoic geodynamic evolution of the Aegean. International Journal of Earth Sciences 99, 109–138.
Jolivet, L., Trotet, F., Monié, P., Vidal, O., Goffé, B., Labrousse, L., Agard, P., Ghorbal, B., 2010. Along-strike variations of PT conditions in accretionary wedges and syn-orogenic extension, the HP–LT Phyllite–Quartzite Nappe in Crete and the Peloponnese. Tectonophysics 480, 133–148.
Jolivet, L., Faccenna, C., Huet, B., Labrousse, L., Le Pourhiet, L., Lacombe, O., Lecomte, E., Burov, E., Denèle, Y., Brun, J.-P., Philippon, M., Paul, A., Salaün, G., Karabulut, H., Piromallo, C., Monié, P., Gueydan, F., Okay, A., Oberhänsli, R., Pourteau, A., Augier, R., Gadenne, L., Driussi, O., 2013. Aegean tectonics: strain localisation, slab tearing and trench retreat. Tectonophysics 597-598, 1–33.
Keay, S., Lister, G., 2002. African provenance for the metasediments and metaigneous rocks of the Cyclades, Aegean Sea, Greece. Geology 30, 235–238.
Kilias, A., Falalakis, G., Mountrakis, D., 1999. Cretaceous-Tertiary structures and kinematics of the Serbomacedonian metamorphic rocks and their relation to the exhumation of the Hellenic hinterland (Macedonia, Greece). International Journal of Earth Sciences 88, 513–531.
Klein, T., Craddock, J.P., Zulauf, G., 2013. Constraints on the geodynamical evolution of Crete: insights from illite crystallinity, Raman spectroscopy and calcite twinning above and below the 'Cretan detachment'. International Journal of Earth Sciences 102, 139–182.
Kock, S., Martini, R., Reischmann, T., Stampfli, G.M., 2007. Detrital zircon and micropalaeontological ages as new constraints for the lowermost tectonic unit (Talea Ori unit) of Crete, Greece. Palaeogeography, Palaeoclimatology, Palaeoecology 243, 307–321.
Kolodner, K., Avigad, D., McWilliams, M., Wooden, J.L., Weissbrod, T., Feinstein, S., 2006. Provenance of north Gondwana Cambrian–Ordovician sandstone: U–Pb SHRIMP dating of detrital zircons from Israel and Jordan. Geological Magazine 143, 367–391.
König, H., Kuss, S.E., 1980. Neue daten zur biostratigraphie des permotriadischen autochthons der Insel Kreta (Griechenland). Neues Jahrbuch für Geologie und Paläontologie Monatshefte 9, 525–540.
Krahl, J., Kauffmann, G., Kozur, H., Richter, D., Förster, O., Heinritzi, F., 1983. Neue daten zur biostratigraphie und zur tektonischen lagerung der Phyllit-Gruppe und der Trypali-Gruppe auf der Insel Kreta (Griechenland). Geologische Rundschau 72, 1147–1166.
Krahl, J., Kauffmann, G., Richter, D., Kozur, H., Möller, I., Förster, O., Heinritzi, F., Dornsiepen, U., 1986. Neue fossilfunde in der Phyllit-Gruppe Ostkretas (Griechenland). Zeitschrift der Deutschen Geologischen Gesellschaft 137, 523–536.
Kröner, A., Şengör, A.M.C., 1990. Archean and Proterozoic ancestry in late Precambrian to early Paleozoic crustal elements of southern Turkey as revealed by single-zircon dating. Geology 18, 1186–1190.
Kröner, A., Stern, R.J., Dawoud, A.S., Compston, W., Reischmann, T., 1987. The Pan-African continental margin in northeastern Africa: evidence from a geochronological study of granulites at Sabaloka, Sudan. Earth and Planetary Science Letters 85, 91–104.
Kröner, A., Eyal, M., Eyal, Y., 1990. Early Pan-African evolution of the basement around Elat, Israel, and the Sinai Peninsula revealed by single-zircon evaporation dating, and implications for crustal accretion rates. Geology 18, 545–548.
Ktenas, K., 1924. Formations primaires semimetamorphiques du Peloponnese central. Comptes Rendus Geosciences Société Géologique de France 24, 61–63.
Kydonakis, K., 2011. Kinematic and Structural Analysis in the Feneos Area, N. Peloponnese. Unpub. MSc Thesis University of Athens, Greece.
Lahtinen, R., Huhma, H., Kousa, J., 2002. Contrasting source components of the Paleoproterozoic Svecofennian metasediments: detrital zircon U–Pb, Sm–Nd and geochemical data. Precambrian Research 116, 81–109.
Liati, A., Skarpelis, N., Fanning, C.M., 2013. Late Permian–Early Triassic igneous activity in the Attic Cycladic Belt (Attica): new geochronological data and geodynamic implications. Tectonophysics 595–596, 140–147.
Linnemann, U., McNaughton, N.J., Romer, R.L., Gehmlich, M., Drost, K., Tonk, C., 2004. West African provenance for Saxo-Thuringia (Bohemian Massif): did Armorica ever leave pre-Pangean Gondwana? — U/Pb-SHRIMP zircon evidence and the Nd-isotopic record. International Journal of Earth Sciences 93, 683–705.
Linnemann, U., Ouzegane, K., Drareni, A., Hofmann, M., Becker, S., Gärtner, A., Sagawe, A., 2011. Sands of West Gondwana: an archive of secular magmatism and plate interactions — a case study from the Cambro-Ordovician section of the Tassili Ouan Ahaggar (Algerian Sahara) using U–Pb-LA-ICP-MS detrital zircon ages. Lithos 123, 188–203.
Ludwig, K.R., 2001. Isoplot/Ex rev. 2.49: Berkeley. California, Berkeley Geochronology Center, Special Publication A, 1, p. 56.
Lys, M., Thiebault, F., 1971. Données nouvelles sur l'âge des schistes en Péloponnèse meridional. Comptes Rendus de l'Académie des Sciences Serie D 272, 1–2.
Meinhold, G., Kostopoulos, D.K., 2013. The Circum-Rhodope Belt, northern Greece: age, provenance, and tectonic setting. Tectonophysics 595–596, 55–68.
Meinhold, G., Reischmann, T., Kostopoulos, D., Lehnert, O., Matukov, D., Sergeev, S., 2008. Provenance of sediments during subduction of Palaeotethys: detrital zircon ages and olistolith analysis in Palaeozoic sediments from Chios Island, Greece. Palaeogeography, Palaeoclimatology, Palaeoecology 263, 71–91.
Meinhold, G., Kostopoulos, D., Reischmann, T., Frei, D., BouDagher-Fadel, M.K., 2009. Geochemistry, provenance and stratigraphic age of metasedimentary rocks from the eastern Vardar suture zone, northern Greece. Palaeogeography, Palaeoclimatology, Palaeoecology 277, 199–225.
Meinhold, G., Kostopoulos, D., Frei, D., Himmerkus, F., Reischmann, T., 2010a. U–Pb LA-SF-ICP-MS zircon geochronology of the Serbo-Macedonian Massif, Greece: palaeotectonic constraints for Gondwana-derived terranes in the Eastern Mediterranean. International Journal of Earth Sciences 99, 813–832.
Meinhold, G., Reischmann, T., Kostopoulos, D., Frei, D., Larionov, A.N., 2010b. Mineral chemical and geochronological constraints on the age and provenance of the eastern Circum-Rhodope Belt low-grade metasedimentary rocks, NE Greece. Sedimentary Geology 229, 207–223.
Meinhold, G., Morton, A.C., Fanning, C.M., Frei, D., Howard, J.P., Phillips, R.J., Strogen, D., Whitham, A.G., 2011. Evidence from detrital zircons for recycling of Mesoproterozoic and Neoproterozoic crust recorded in Paleozoic and Mesozoic sandstones of southern Libya. Earth and Planetary Science Letters 312, 164–175.
Meinhold, G., Morton, A.C., Avigad, D., 2013. New insights into peri-Gondwana paleogeography and the Gondwana super-fan system from detrital zircon U–Pb ages. Gondwana Research 23, 661–665.
Morag, N., Avigad, D., Gerdes, A., Belousova, E., Harlavan, Y., 2011. Detrital zircon Hf isotopic composition indicates long-distance transport of North Gondwana Cambrian–Ordovician sandstones. Geology 39, 955–958.
Morton, A.C., Whitham, A., Howard, J., Fanning, M., Abutarruma, Y., El Dieb, M., Elkatarry, F.M., Hamhoom, A.M., Lüning, S., Phillips, R.J., Thusu, B., 2013. In: Salem, M.J. (Ed.), Geology of Southern Libya (in press).
Most, T., 2003. Geodynamic evolution of the Eastern Pelagonian Zone in north-western Greece and the Republic of Macedonia. Implications from U/Pb, Rb/Sr, K/Ar, 40Ar/39Ar Geochronology and Fission Track Thermochronology. Eberhard-Karls-Universität, Tübingen (Unpub. PhD Thesis).
Nance, R.D., Keppie, J.D., Miller, B.V., Murphy, J.B., Dostal, J., 2009. Palaeozoic palaeogeography of Mexico: constraints from detrital zircon age data. Geological Society, London, Special Publications 327, 239–269.
Nance, R.D., Gutiérrez-Alonso, G., Keppie, J.D., Linnemann, U., Murphy, J.B., Quesada, C., Strachan, R.A., Woodcock, N.H., 2012. A brief history of the Rheic Ocean. Geoscience Frontiers 3, 125–135.
Papanikolaou, D., 1997. The tectonostratigraphic terranes of the Hellenides. IGCP Project, pp. 495–514.
Papanikolaou, D., 2013. Tectonostratigraphic models of the Alpine terranes and subduction history of the Hellenides. Tectonophysics 595–596, 1–24.
Papanikolaou, D.J., Skarpelis, N.S., 1987. The blueschists in the external metamorphic belt of the Hellenides: composition, structure and geotectonic significance of the Arna Unit. Annales Géologiques des Pays Helléniques 47–68.
Papanikolaou, D., Vassilakis, E., 2010. Thrust faults and extensional detachment faults in Cretan tectono-stratigraphy: implications for Middle Miocene extension. Tectonophysics 488, 233–247.
Papanikolaou, D., Bargathi, H., Dabovski, C., Dimitriu, R., El-Hawat, A., Ioane, D., Kranis, H., Obeidi, A., Oaie, G., Seghedi, A., 2004. Transect VII: East European Craton–Scythian Platform–Dobrogea–Balkanides–Rhodope Massif–Hellenides–East Mediterranean–Cyrenaica. The TRANSMED Atlas. The Mediterranean Region from Crust to Mantle, Geological and Geophysical Framework. Springer (CDROM content).
Pupin, J.P., 1980. Zircon and granite petrology. Contributions to Mineralogy and Petrology 73, 207–220.
Reischmann, T., 1998. Pre-Alpine origin of tectonic units from the metamorphic complex of Naxos, Greece, identified by single zircon Pb/Pb dating. Bulletin of the Geological Society of Greece 32, 101–111.
Reischmann, T., Kostopoulos, D., 2007. Terrane accretion in the internal Hellenides. Geophysical Research Abstracts 9, 05337.
Reischmann, T., Kostopoulos, D., Loos, S., Anders, B., Avgerinas, A., Sklavounos, A., 2001. Late palaeozoik magnetism in the basement rocks Southwest of MT. Olympos, Central Pelagonian zone, Greece: remnants of a permo-carboniferous magnatic arc. Bulletin of the Geological Society of Greece 34, 985–993.
Ring, U., Glodny, J., Will, T., Thomson, S., 2010. The hellenic subduction system: high-pressure metamorphism, exhumation, normal faulting, and large-scale extension. Annual Review of Earth and Planetary Sciences 38, 45–76.
Robertson, A.H.F., 2012. Late Palaeozoic–Cenozoic tectonic development of Greece and Albania in the context of alternative reconstructions of Tethys in the Eastern Mediterranean region. International Geology Review 54, 373–454.

Romano, S., Dörr, W., Zulauf, G., 2004. Cambrian granitoids in pre-Alpine basement of Crete (Greece): evidence from U–Pb dating of zircon. International Journal of Earth Sciences 93, 844–859.
Roser, B.P., Korsch, R.J., 1988. Provenance signatures of sandstone-mudstone suites determined using discriminant function analysis of major-element data. Chemical Geology 67, 119–139.
Royden, L.H., Papanikolaou, D., 2011. Slab segmentation and late Cenozoic disruption of the Hellenic arc. Geochemistry, Geophysics, Geosystems 12 Q03010.
Rudnick, R.L., Gao, S., 2003. Composition of the continental crust. Treatise on geochemistry 3, 1–64.
Sakellariou, D., Dürr, S., 1993. Geological structure of the Serbo-Macedonian massif in NE Chalkidiki Peninsula. Bulletin of the Geological Society of Greece XXVIII/1, 179–193 (in greek with english abstract).
Seidel, E., Kreuzer, H., Harre, W., 1982. A late Oligocene/early Miocene high pressure belt in the External Hellenides. Geologisches Jahrbuch E23, 165–206.
Seidel, M., Zacher, W., Schwarz, W.H., Jaeckel, P., Reischmann, T., 2006. A Late Carboniferous age of the gneiss of Potamos (Kythira Island, Greece) and new considerations on geodynamic interpretations of the Western Hellenides. Neues Jahrbuch für Geologie und Paläontologie Abhandlungen 241, 325–344.
Sircombe, K.N., 2004. AgeDisplay: an EXCEL workbook to evaluate and display univariate geochronological data using binned frequency histograms and probability density distributions. Computers & Geosciences 30, 21–31.
Sláma, J., Košler, J., 2012. Effects of sampling and mineral separation on accuracy of detrital zircon studies. Geochemistry, Geophysics, Geosystems 13, Q05007. http://dx.doi.org/10.1029/2012GC004106 (17 pp.).
Squire, R.J., Campbell, I.H., Allen, C.M., Wilson, C.J.L., 2006. Did the Transgondwanan Supermountain trigger the explosive radiation of animals on Earth? Earth and Planetary Science Letters 250, 116–133.
Stamfli, G.M., Kozur, H.W., 2006. Europe from the Variscan to the Alpine cycles. Memoirs: Geological Society of London 32, 57–82.
Stampfli, G., 2005. Plate tectonics of the Apulia-Adria microcontinents. CROP Project — Deep Seismic Explorations of the Central Mediterranean and Italy, Section 11, pp. 747–766.
Stampfli, G.M., Borel, G.D., 2002. A plate tectonic model for the Paleozoic and Mesozoic constrained by dynamic plate boundaries and restored synthetic oceanic isochrons. Earth and Planetary Science Letters 196, 17–33.
Stampfli, G., Borel, G., 2004. The TRANSMED transects in space and time: constraints on the paleotectonic evolution of the Mediterranean domain. The TRANSMED Atlas: The Mediterranean Region from Crust to Mantle, pp. 53–80.
Stampfli, G.M., Hochard, C., 2009. Plate tectonics of the Alpine realm. Geological Society, London, Special Publications 327, 89–111.
Stampfli, G.M., Borel, G.D., Marchant, R., Mosar, J., 2002. Western Alps geological constraints on western Tethyan reconstructions. Journal of the Virtual Explorer 8, 77–106.
Stampfli, G., Vavassis, I., De Bono, A., Rosselet, F., Matti, B., Bellini, M., 2003. Remnants of the Paleotethys oceanic suture-zone in the western Tethyan area. Stratigraphic and structural evolution on the Late Carboniferous to Triassic Continental and Marine Successions in Tuscany (Italy): regional reports and general correlation. Bollettino della Societa Geologica Italiana Volume speciale 2, 1–24.
Stampfli, G.M., von Raumer, J., Wilhem, C., 2011. The distribution of Gondwana-derived terranes in the Early Paleozoic. Ordovician of the World 14, 567–574.
Stern, R.J., 1994. Arc-assembly and continental collision in the Neoproterozoic African Orogen: implications for the consolidation of Gondwanaland. Annual Review of Earth and Planetary Sciences 22, 319–351.
Stern, R.J., Johnson, P., 2010. Continental lithosphere of the Arabian Plate: a geologic, petrologic, and geophysical synthesis. Earth-Science Reviews 101, 29–67.
Taylor, S.R., McLennan, S.M., 1985. The continental crust: its composition and evolution. Blackwell, Oxford (312 pp.).
Teipel, U., Eichhorn, R., Loth, G., Rohrmüller, J., Höll, R., Kennedy, A., 2004. U–Pb SHRIMP and Nd isotopic data from the western Bohemian Massif (Bayerischer Wald, Germany): implications for Upper Vendian and Lower Ordovician magmatism. International Journal of Earth Sciences 93, 782–801.
Tomaschek, F., Keiter, M., Kennedy, A.K., Ballhaus, C., 2008. Pre-Alpine basement within the Northern Cycladic Blueschist Unit on Syros Island, Greece. Zeitschrift der Deutschen Gesellschaft für Geowissenschaften 159, 521–531.
Turpaud, P., Reischmann, T., 2010. Characterisation of igneous terranes by zircon dating: implications for UHP occurrences and suture identification in the Central Rhodope, northern Greece. International Journal of Earth Sciences 99, 567–591.
Ustaömer, P.A., Ustaömer, T., Gerdes, A., Robertson, A.H.F., Collins, A.S., 2012. Evidence of Precambrian sedimentation/magmatism and Cambrian metamorphism in the Bitlis Massif, SE Turkey utilising whole-rock geochemistry and U–Pb LA-ICP-MS zircon dating. Gondwana Research 21, 1001–1018.
van Hinsbergen, D.J.J., Hafkenscheid, E., Spakman, W., Meulenkamp, J.E., Wortel, R., 2005. Nappe stacking resulting from subduction of oceanic and continental lithosphere below Greece. Geology 33, 325–328.
Vavassis, I., De Bono, A., Stampfli, G., Giorgis, D., Valloton, A., Amelin, Y., 2000. U–Pb and Ar–Ar geochronological data from the Pelagonian Basement in Evia (Greece): geodynamic implications for the evolution of Paleotethys. Schweizerische Mineralogische und Petrographische Mitteilungen 80, 21–43.
Vermeesch, P., 2004. How many grains are needed for a provenance study? Earth and Planetary Science Letters 224, 441–451.
von Raumer, J.F., Stampfli, G.M., 2008. The birth of the Rheic Ocean — Early Palaeozoic subsidence patterns and subsequent tectonic plate scenarios. Tectonophysics 461, 9–20.
Xypolias, P., Dörr, W., Zulauf, G., 2006. Late Carboniferous plutonism within the pre-Alpine basement of the External Hellenides (Kithira, Greece): evidence from U–Pb zircon dating. Journal of the Geological Society 163, 539–547.
Yamashita, K., Creaser, R.A., Villeneuve, M.E., 2000. Integrated Nd isotopic and U–Pb detrital zircon systematics of clastic sedimentary rocks from the Slave Province, Canada: evidence for extensive crustal reworking in the early-to mid-Archean. Earth and Planetary Science Letters 174, 283–299.
Yarwood, G., Aftalion, M., 1976. Field relations and U–Pb geochronology of a granite from the Pelagonian zone of the Hellenides (High Pieria, Greece). Bulletin de la Société Géologique de France 18, 259–264.
Zulauf, G., Romano, S.S., Dorr, W., Fiala, J., 2007. Crete and the Minoan terranes: age constraints from U–Pb dating of detrital zircons. Geological Society of America Special Papers 423, 401–411.
Zulauf, G., Klein, T., Kowalczyk, G., Krahl, J., Romano, S.S., 2008. The Mirsini Syncline of eastern Crete, Greece: a key area for understanding pre-Alpine and Alpine orogeny in the eastern Mediterranean. Zeitschrift der Deutschen Gesellschaft für Geowissenschaften 159, 399–414.
Zulauf, G., Dörr, W., Krahl, J., 2011. Carboniferous to Triassic felsic magmatism in the external Hellenides of Crete and its implications on the pre-alpine orogeny and paleogeography in the eastern Mediterranean. Geological Processes From Global to Local Scales and Associated Hazards (4–7 September 2011).